Politecnico di Milano

SCUOLA DI INGEGNERIA CIVILE, AMBIENTALE E TERRITORIALE
Laurea Magistrale – Ingegneria Civile

Simplified Design Method of Hysteretic Tuned Mass Dampers for Seismic Protection

Relatore
Prof. Luca MARTINELLI

Candidato
Jorge Andres MILLAN LEYVA – 963870

Academic Year 2021 – 2022

Acknowledgements

I want to start thanking professor Luca Martinelli. I cannot thank you enough for all the help you've given me during this last year. Thank you for your guidance, advice and mentorship.

Quiero agradecer a todas las personas que, de una u otra forma estuvieron presentes durante este proceso. Especialmente a mi mamá, mi papá, mis hermanas y abuelas. A mi familia muchas gracias por apoyarme en cada en cada paso que doy.

Daniela, gracias por tu apoyo durante todo este tiempo. Estoy seguro de que sin ti, todo esto hubiese sido mas difícil.

To my Friends, thanks for always having my back.

To my friends and colleagues from the MSc, thank you very much. Paula, Lamija, Joo, Toro thank you for making the time I spent here better than I could've imagined.

Thanks to all who, in one way or another made this possible.

Augusto, Javier muchas gracias por todo, esto es no hubiese sido posible sin ustedes.

Abstract

Gli Smorzatori a Massa Accordata sono stati ampiamente utilizzati nel controllo delle vibrazioni delle strutture civili. Questi apparecchi sono comunemente utilizzati per mitigare l'effetto del vento e carichi ritmici quando la struttura rimane in regime elastico.

Tuttavia, una volta che la struttura inizia a comportarsi in modo non lineare, l'efficacia degli TMD lineari inizia a diminuire. Questo tipo di comportamento è comune durante l'eccitazione sismica della struttura. Una delle principali conseguenze del danno alla struttura è la perdita di rigidità che genera un cambiamento nella frequenza strutturale.

I TMD isteretici diventano un'alternativa alla riduzione di questo effetto di accordatura, che porta alla perdita di efficienza. Questo tipo di elemento presenta un comportamento softening che gli permette di seguire il deterioramento della struttura a causa dei danni generati dai carichi sismici. Questo tipo di comportamento consente agli smorzatori di ridurre i danni alla struttura.

Questo lavoro presenta una strategia di progettazione semplificata per tale tipo di elemento che, finora, è stata elaborata da ottimizzazione numerica. Uno dei principali vantaggi del metodo presentato è che consente un approccio completamente strutturale al problema. La semplicità del metodo gli consente di far parte delle procedure di progettazione che i progettisti possono utilizzare nelle loro attività quotidiane, a differenza del metodo di ottimizzazione numerica.

A seguito dei risultati sperimentali di una struttura a pareti accoppiate in cemento armato, è stato utilizzato un modello numerico di tale struttura, compreso lo smorzatore, per valutare l'efficacia del TMD. Per modellare la forza isteretica che lo smorzatore fornisce alla struttura, è stato adottato un modello di isteresi di Bouc-Wen.

Le simulazioni numeriche con accelerogrammi scalati mostrano che uno smorzatore con un rapporto di massa del 5% può ridurre lo spostamento quadratico medio (RMS) della struttura del 30%. Quando si considerano i terremoti $1,5$ volte il terremoto di progetto, l'ammortizzatore potrebbe prevenire il collasso riducendo i valori picco degli spostamenti nella struttura del 15%. Lo smorzatore è stato progettato per il terremoto di progetto, dunque questo comportamento conferma ulteriormente l'approccio progettuale dello smorzatore.

La robustezza del metodo è verificata con un'analisi di sensibilità in cui diverse ipotesi di progetto sono state modificate. Tale analisi ha dimostrato che per l'edificio gli smorzatori non lineari sono meno sensibili alla differenza in frequenza rispetto a un sistema lineare.

Keywords:Smorzatori a Massa Accordata, Dinamica non-lineare, Smorzatori Isteretico, Progettazione antisismica

Abstract

Tuned Mass Dampers (TMD) have been widely used in the vibration control of civil engineering structures. These structures are commonly used to mitigate the effects of wind and rhythmic loads. This auxiliary structure is used mainly when the structure remains in the elastic regime.

However, once the structure starts behaving nonlinearly, the effectiveness of such linear TMDs starts to decrease. This type of behaviour is common during seismic excitation of the structure. One of the main consequences of damage to the structure is the loss of stiffness which generates a change in the structural frequency.

Hysteretic TMDs have appeared as an alternative to reduce this detuning effect, leading to the loss of efficiency. This type of element presents a softening behaviour that allows it to follow the deterioration of the structure due to the damage generated by the seismic loads. This type of behavior allows the dampers to reduce the damage in the structure.

This work presents a simplified design strategy for such type of element that, so far, has been done through numerical optimization. One of the main benefits of the presented method is that it allows for a complete structural approach to the problem. The simplicity of the method allows it to be part of design procedures that designers can use in their day-to-day activities, unlike the numerical optimization method.

Following the experimental results of a dual reinforced concrete structure, a numerical model of such structure, including the damper, was used to assess the effectiveness of the TMD. To model the hysteretic force that the damper transfer to the structure, a Bouc-Wen model of hysteresis was adopted.

Numerical simulations with scaled accelerograms show that a damper with a 5% mass ratio can reduce the structure's root mean square (RMS) displacement by 30%. When earthquakes 1.5 times the design earthquake are considered, the damper could prevent collapse by reducing the drifts in the structure by 15%. Note that the damper was designed for the design earthquake, so this behaviour further corroborates the damper design approach.

The robustness of the method is addressed by a sensibility analysis in which several hypotheses of the design and methodology were modified. Such analysis showed that nonlinear dampers are less sensitive to mistuning than a linear system for the building.

Keywords: Tuned Mass Dampers, Nonlinear Dynamics, Seismic Protection, Hysteretic Damper, Design Method

Contents

List of Figures

List of Tables

Chapter 1

Introduction

The consequences of an earthquake may be very different depending on the location where they strike, as the technology of the buildings may lead to an increase in economic losses rather than fatalities. Nowadays, building codes are written to reduce the possibility of a collapse as they focus on ensuring structural damage under great demand rather than a brittle collapse of the building. Thus, allowing the inhabitants to safely exit the structure under this type of event.

Additional elements that enhance the structural performance of buildings can be added. These elements belong to the category of structural control. They can be designed as a retrofitting measure or as an integral part of the structure.

Some of these methods provide significant benefits in the response of the structure. For instance, Tuned Mass Dampers are systems that reduce the vibrations in the structure under loads with a repeating pattern, such as rhythmic crowds or wind flows. Nevertheless, these dampers are less effective in controlling the seismic response of structures.

Recently, the investigation of the design of these elements has required the use of numerical optimization methods. However, these methods are not suitable for design purposes. Therefore, a novel simplified design method for this type of element under seismic will be presented.

1.1 Earthquake and Risk

Earthquakes are one of the most devastating natural disasters, not only for the destruction of the physical environment but also for the social consequences they generate. Earthquakes have become costlier over the years regarding both of those aspects. As seen from Figure 1.1, fatalities and overall costs of earthquakes are usually disassociated, and ideally, a change from fatalities to material costs should be attained.

Population growth has drastically increased the consequences of an earthquake. For instance, according to [2], an earthquake in Teheran, Iran, could kill over a million people. Moreover, the number of vastly populated cities with high seismic hazards is considerably high, for example, Jakarta, New Delhi, Taipei, Mexico City, and Tokyo. Therefore, reducing seismic risk is imperative not only in these locations but in the whole world.

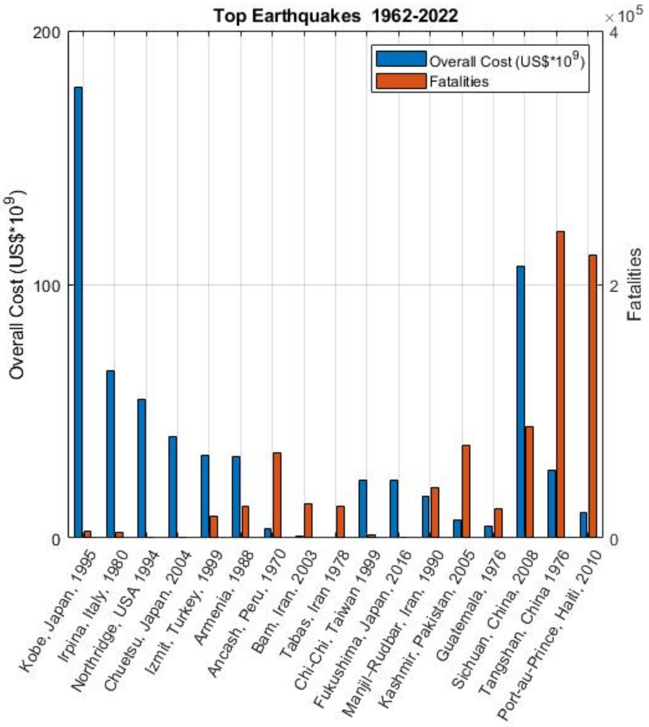

Figure 1.1. Worst Earthquakes in terms of overall costs and fatalities during 1962-2022.
*Values are referred to as the adjusted 2021 value
Retrieved from [1]

It is intended that buildings, when subjected to seismic loads, can ensure that their inhabitants exit the building safely. To do so, they must withstand significant damage during the motion. Resisting damage through deformations allows structures to dissipate part of the energy input by the ground motion. However, most structures dissipate low energy and undergo significant vibrations, even for low-intensity earthquakes.

1.2 Structural Control

New approaches to reducing structural damage have been developed. These aim to limit the damaging deformations and forces in structural components by several methods. Such techniques are denoted as structural control, and they reduce the structure's probability of failure.

By modifying the structure's characteristics, such as stiffness and damping, the auxiliary systems control the response of the main structure and reduce the inelastic energy dissipation demand. Therefore, structural control has been essential in the past decades as it allows us to achieve a satisfactory dynamic response. These methods have also been used as retrofitting techniques as they help to achieve an adequate seismic response in vulnerable buildings such as those reaching the end of their service life.

Protective systems reduce the dynamic demand the main structure would be subjected to and reduce or even mitigate their effects. Structural control can be used for serviceability reasons, such as for the Millennium Bridge in London. Initially, when pedestrians walked across the bridge, they created a vibration that made it move laterally. Due to the discomfort generated by the movement, people began to move in a way resembling the structure. This movement generated a resonant behaviour which led to even greater displacements. Therefore, a retrofitting measure was necessary to avoid discomfort for the bridge users. In this particular situation, a series of Tuned Mass Dampers (TMD), shown in Figure 1.2, were included to reduce the action generated by the moving crowd.

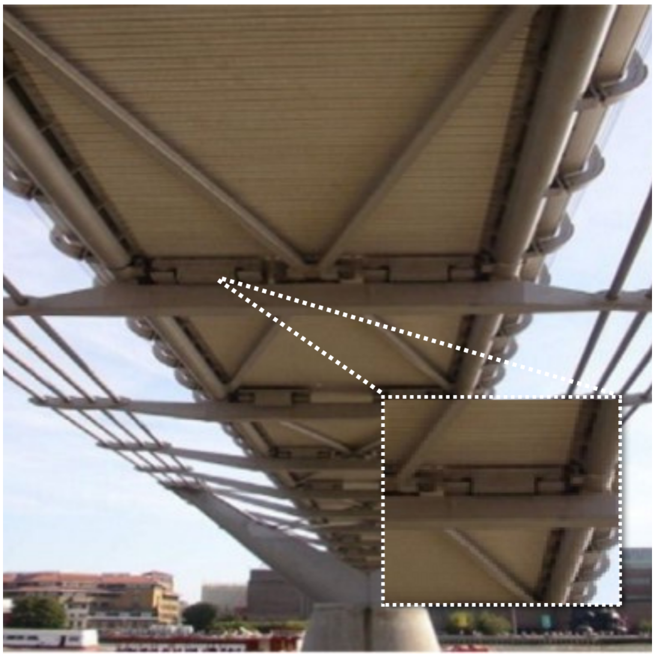

Figure 1.2. Millennium Bridge, London
Retrieved from [3].

Structural control is divided into three classes, active, hybrid and passive. Active and hybrid methods require external energy, while passive methods do not. Due to the great masses that comprise a building, active methods are generally expensive. Instead of stabilizing the whole mass, hybrid methods change the auxiliary structure's parameters to obtain the best response from the building. Passive methods apply to the structural forces that develop due to the structural motion. Some examples of these types of systems are available in Figure 1.3

Passive structural control methods have been widely used in civil engineering as they do not require external energy sources. Their relatively low installation and maintenance cost and the fact that an energy shortage will not impact them are other benefits of this type of mechanism. However, one of the disadvantages of these methods is the impossibility of modifying their working conditions, so their performance depends only on the design conditions. The most used passive devices are base isolation systems, friction dampers, viscoelastic dampers, and tuned mass dampers.

Structural strengthening a building could be a more expensive, and not necessarily adequate, solution for controlling a structure, [3]. Passive structural control techniques

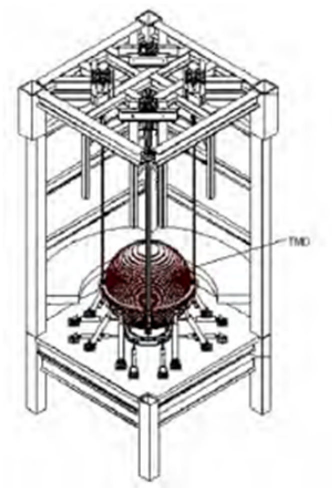

(a) Schematic design of the TMD from Taipei 101

(b) Toushin 24 Ohmori Building basement with its base isolating system

(c) Variable damping mechanism

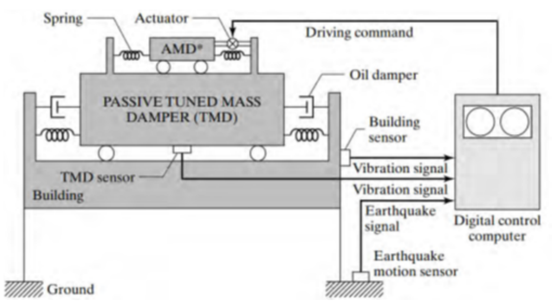

(d) Nishikicho building DUOX Active-Passive TMD

Figure 1.3. Structural Control Systems
Retrieved from [4]

could be used as seismic rehabilitation and retrofit methodologies of existing structures. They could ensure that the dynamic behaviour of the main system is bounded to a certain damage threshold.

Seismic risk assessment is becoming more important every day as many buildings are reaching the end of their service life. It is important to note that a substantial part of the building stock in the world was built before seismic codes. These buildings are more vulnerable to seismic actions, and most do not fulfil today's requirements for new buildings. Therefore, seismic retrofitting is of paramount importance as reconstruction is even more expensive. As a reduction of the input seismic force is generally inconvenient, as it is usually related to seismic isolation systems whose installation is complex in an existing building, another alternative to reduce the seismic risk is tuned mass dampers (TMD).

1.3 TMD

A Tuned Mass Damper (TMD) consists of a mass attached to the structure that contributes to the reduction of its dynamic response [4]. This reduction is possible as such mass moves with a delay with respect to the structure, as shown in Figure 1.4, so its inertial forces dissipate energy. These elements are generally located on the highest floors of the structure as this allows them to be more sensitive to a movement in the structure, for which they will move more and thus dissipate more energy.

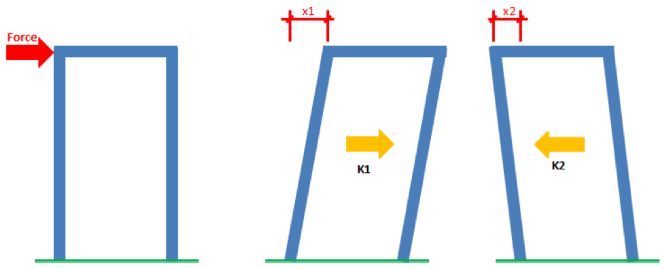

(a) Building without a TMD

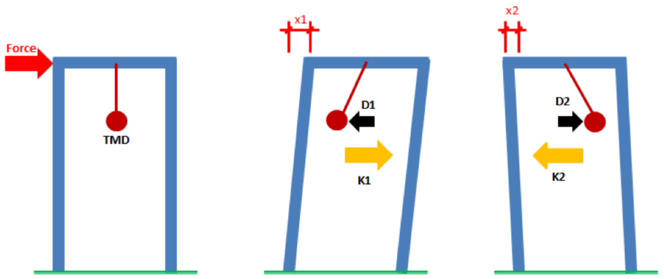

(b) Building with a TMD

Figure 1.4. Schematic Tuned Mass Dampers
Retrieved from [5]

TMDs reduce the response under resonance, meaning that the loading frequency is equal to its natural frequency, hence the "tuned" term. Therefore, if the dynamic load characteristics are known beforehand and present minimum variability, TMDs are an excellent solution. However, TMDs do not necessarily present such a great advantage under seismic loading. For instance, there are several reasons why a TMD could have adverse effects on the structure, [6]. However, if these elements are designed in such a way that they can resemble the behaviour of the structure during seismic excitation, they can keep their effectiveness.

As stated previously, this type of element can be designed as a retrofitting measure or as an integral part of the structure, as in Taipei 101, shown in Figure 1.3a. One of the main benefits of this type of structure as a retrofitting measure is its feasibility.

The TMD can be located at the top of the structure, for instance, on the roof. Thus, allowing to maintain the use and spaces of the building unaltered.

As most of the building stock in the earthquake-prone regions is low-moderate height, they have a higher seismic demand regarding the accelerations they must withstand. However, many do not exhibit high ductility resources that allow them to dissipate large amounts of energy through their deformations. In this scenario, using a TMD would be an excellent solution that allows them to reduce the displacements considerably.

1.4 Simplified Design Approach

The design of the hysteretic TMD, exhibiting a behaviour resembling the structure, allows for a considerable reduction of vibrations. This reduction is because the damper remains tuned to the structure through time. For instance, in [6], using an optimized hysteretic TMD reduced the Root Mean Square (RMS) of the displacements in the structure by more than 50%.

As stated previously, as of now, the way of designing a TMD for seismic applications has been through genetic algorithms (GA). However, a novel approach, now introduced as a simplified design method, would allow a completely structural approach to the problem. Therefore, a ground motion input would no longer be necessary to determine the design of the auxiliary structure.

However, in many third-world countries which are commonly hit by earthquakes, many buildings are still built without regard for the codes; Haiti, for instance, does not have a building code. This lack of good design and construction practices contributes to the high fatalities due to earthquakes in underdeveloped countries. Ergo, having both a retrofitting alternative for existing buildings and a component for new structures could significantly reduce the fatalities and losses derived from earthquakes.

This work presents a simplified design method for TMD for seismic purposes. Using the TMD in numerical simulations of a building considerably reduced the displacements in the structure. In Chapter 2 the theoretical background of the topics that will be discussed will be set. In Chapter 3, the state of the art of Tuned Mass Dampers and their use in seismic settings is shown. In Chapter 4, the benchmark of the analysis and the models used for the design and implementation of the TMD are presented. Chapter 5, discusses the simplified design approach for this type of structure. The numerical results of the structure and the effectiveness of the TMD are discussed in Chapter 6. A sentivity analysis, by changing certain hypothesis of the model are shown in Chapter 7.

Chapter 2

Theoretical Background

2.1 Risk and Vulnerability

Risk denotes the social and economic expected loss that a system is subject to during a specific time due to a hazard. It is the combination, mathematically speaking, the convolution, as expressed in Equation 2.1, of three factors, hazard, exposure, and vulnerability.

$$R = H * E * V \tag{2.1}$$

A hazard is an event that has the potential to produce harm or other undesirable consequences to a person or thing. They depend on the considered location, which is why they exist with or without the presence of people. In this case, it is the expected ground motion or a similar phenomenon. As it cannot be controlled, the most critical aspect is to characterize it in the most exhaustive way possible to work on other risk components and reduce them. In seismic engineering, the hazard is defined by an acceleration response spectrum that is site dependent.

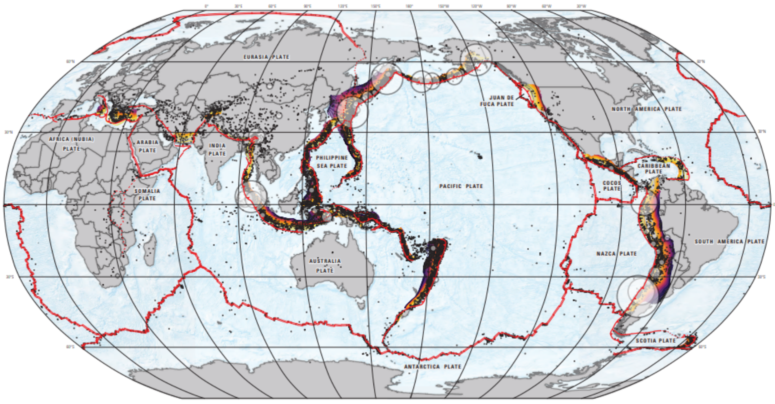

Figure 2.1. Seismicity of the Earth 1900-2018
Retrieved from [7]

Exposure is the people, property, or systems in a location exposed to a hazard. It provides the economic or social value of the system at risk. Generally, exposure includes what lies in the area that the hazard could affect. Reducing risk by reallocating assets and limiting them from hazardous locations is possible, but it becomes unmanageable on larger scales.

Vulnerability is the susceptibility to physical injury, harm, damage, or economic loss and depends on an asset's construction, contents, and economic value of its functions. It is the expected level of damage of a system depending on the hazard's intensity measure. Several authors, for instance [8–10], performed several vulnerability studies regarding buildings in central Italy to characterize their vulnerability.

A particular example is the San Andreas Fault in California. Most of the fault is located in a desertic zone, meaning that the exposure is low, so the risk associated with an earthquake in most of it is low. Nevertheless, this is only the case in some parts of the world. To reduce risk, we must minimize vulnerability as it depends on the building itself. Focusing on it allows engineers to minimize the risk by ensuring that a building can resist a certain amount of damage related to the expected hazard.

2.2 Tuned Mass Dampers (TMD)

Tuned Mass Dampers are designed considering their own frequency and damping and those of the structure, as their behaviour depends on such parameters. TMDs reduce the response under resonance, meaning that the loading frequency is equal to its natural frequency, hence the "tuned" term. Therefore, if the frequency of the load is known beforehand and presents minimum variability, TMDs are an excellent solution.

TMDs are very effective for controlling wind excitations as they can reduce the displacements in the building derived from these loads. Hence, their use has been limited to such applications as controlling displacements and accelerations in tall, flexible buildings. For instance, one of the most iconic buildings with a TMD is the Taipei 101, whose TMD was initially designed to reduce the dynamic effects arising from wind loading.

The system consisted of a mass, m, connected to the ground by a spring, representing its stiffness, k, and a viscous damper, c. The damper with mass m_d, was connected to the structure through a spring, k_d, and a damper, c_d. The TMD was connected to the initial mass, making it a multiple degrees of freedom (MDOF) system, as seen in Figure 2.2.

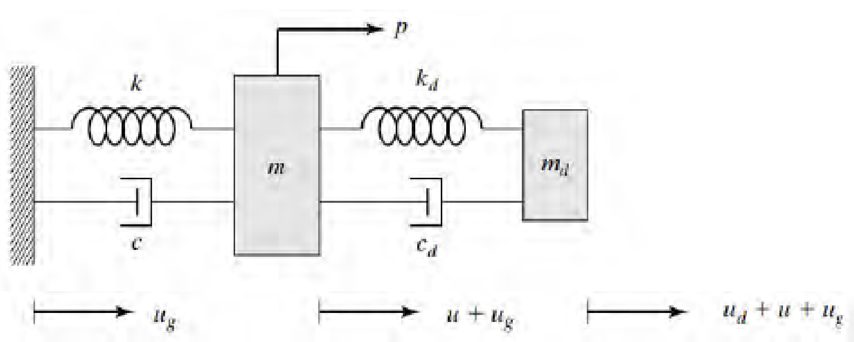

Figure 2.2. Representation of TMD
Retrieved from [4]

Where p is a force function of time to which the main structure is subjected, u_g is the ground excitation, u, is the displacement of the main mass, and u_d is the displacement of the TMD. The equations of motion of the system are those presented in Equation 2.2

$$\begin{aligned} m\ddot{u} + c\dot{u} + ku - c_d\dot{u} - k_d u = & \quad p - m\ddot{u}_g \\ m_d\ddot{u}_d + c_d\dot{u}_d + k_d u_d + m_d\ddot{u} = & \quad m_d\ddot{u}_g \end{aligned} \tag{2.2}$$

Where the overdot denotes differentiation with respect to time. By considering the dynamic properties of each mass, ω, the natural frequency, ξ the damping factor, and μ the mass ratio of the TMD defined as:

$$\begin{aligned} \omega =& \sqrt{\frac{k}{m}} \\ \xi =& \frac{c}{2m\omega} \\ \mu =& \frac{m_d}{m} \end{aligned} \tag{2.3}$$

The equation of motion of the system stated in Equation 2.2 can be represented by diving the equations by their corresponding mass and using their dynamic properties:

$$\begin{aligned} (1+\mu)\ddot{u} + 2\xi_s\omega_s\dot{u} + \omega_s^2 u =& \frac{p}{m} - \mu\ddot{u}_g \\ \ddot{u}_d + 2\xi_d\omega_d\dot{u}_d + \omega_d^2 u_d =& - \ddot{u} \end{aligned} \tag{2.4}$$

Therefore, a new simplified approach concerning this structure is based on reducing such a detuning effect. It uses a hysteretic element to keep a frequency that resembles the one on the structure during damage; in other words, using a TMD with a hysteretic spring which follows the decay of the structural frequency to stay tuned.

The design procedure, explained thoroughly in Chapter 5, would have a TMD whose behaviour can be represented using a Bouc-Wen hysteretic model. This type of element would have a secant stiffness that would allow it to remain tuned to a specific frequency and avoid damage in the building by conserving its effectiveness. Therefore, the design would embrace a global approach as it includes the nonlinearity of the building itself.

2.3 Bouc-Wen Model

The Bouc-Wen (BW) hysteretic model is a well-known physical model that can accurately represent the behaviour of structures. For instance, it was used in [11] to represent the behaviour of a complete structure. This model type can be seen as made up of two parallel springs, a linear and a nonlinear one, as shown in Figure 2.3.

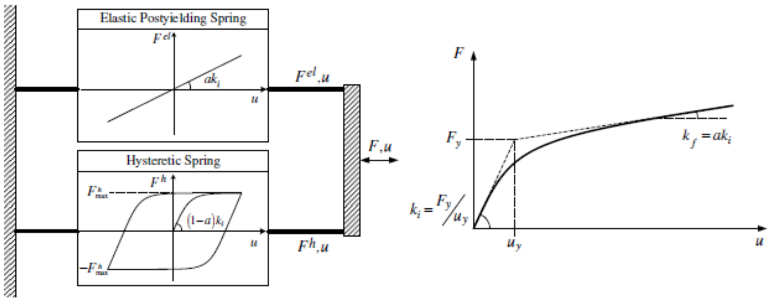

Figure 2.3. Bouc Wen model
Retrieved from [12]

The BW model can be characterized mathematically using Equation 2.5.

$$\begin{aligned} F =& \alpha k x + z \\ \dot{z} =& \left\{(1-\alpha)k - (\beta + \gamma * sgn(z\dot{x}))|z|^n\right\}\dot{x} \end{aligned} \tag{2.5}$$

Where sgn is the signum function. $sgn(x) = 1$ if $x > 0$, $sgn(x) = -1$ if $x < 0$ and $sgn(x) = 0$ if $x = 0$

This model, as expressed in [12], is governed by five parameters β, γ, n, α, and k. k represents the elastic stiffness of the system, α is the relationship between the initial and plastic stiffness (k_i and k_f in Figure 2.3), and parameters β, γ, and n, determine the shape of the hysteretic curve. n determines the velocity or abruptness in the stiffness change from elastic to plastic.

For parameters β and γ, not only is their value interesting but also their difference. As seen from Figure 2.4 the model can reproduce different behaviours depending on the relationship between these coefficients.

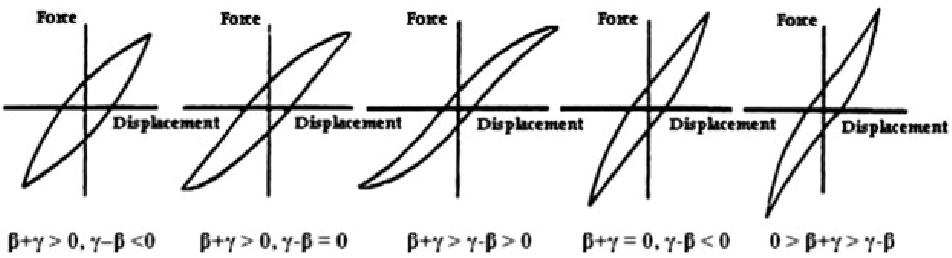

Figure 2.4. Different Hysteretic Cycles $n = 1$
Retrieved from [13]

Chapter 3

State of the Art

The first formulation of a TMD was applied and pattented by Frahm [14] in a field outside of civil engineering. It was later included in the field, through a linear theory, for harmonic excitations to a single degree of freedom (SDOF) system.

The design of a TMD intends to reduce the structural response by exciting the auxiliary mass. The auxiliary structure's damping, stiffness, and mass must be determined. Den Hartog initially proposed an optimal design of a TMD by considering a maximum in the "Den Hartog" points, [4]. In this consideration, the maximum response should be attained at such points. Since then, several studies regarding their optimal design have been made [15, 16]. For instance, Warburton, [17], determined optimal design parameters for white noise excitation.

For seismic applications, several studies such as [18, 19] have provided formulas to obtain the tuning frequencies, f, of the TMD as a function of the mass ratio and damping of the structure. However, these studies are focused on linear TMDs.

However, they necessarily present such a great advantage under seismic loading. For instance, there are several reasons why a linear TMD could have adverse effects on the structure, [20].The frequency bandwidth of the seismic loading and the intrinsic change of the structure's natural period due to damage that characterize nonlinear structures are some of those reasons. The former impedes an effective design as the loading is not known beforehand. The latter is due to a detuning in the TMD, which arises as the structure's initial frequency could decrease as it enters its nonlinear range.

In [21], the effectiveness of the TMD under different ground motion excitations to reduce damage in the structure was reviewed. During the study, it was shown that the effectiveness of the TMD was reduced for systems developing nonlinear behaviour. Ruiz et al. [22], stated that the greater the nonlinearity of the structure, the less effective the TMD would be.

Many authors have used genetic algorithms to find a suitable solution for specific problems, as per [23–25], but a consensus has yet to be reached.

Recently, in [26] the concept of a hysteretic TMD is proposed, allowing a more general approach to the problem. Analysis of this type of structure, [6], has led to a considerable reduction in the dynamic response of the building.

Additionally, in [27] designed a hysteretic TMD through an analytical approach and by GA. In such study a resonance condition was imposed, yet it differed from the results obtained in through GA.

Chapter 4

Experimentation and Modelling

A numerical simulation was performed to assess the effectiveness and feasibility of the hysteretic TMD. The benchmark for such simulation came from the experimentation campaign at the ELSA Laboratory of the JPRC in Ispra, [28] . In the campaign, a low-rise reinforced concrete building was subjected to a Pseudo-Dynamic (PSD) test to compare two different design approaches, [29]. After the campaign, the building was modelled numerically within a MS thesis work, obtaining satisfactory results compared to the real one, [30, 31].

4.1 Experimental Campaign

The experiment aimed to compare the behaviour of two different design methods, the Force-Based Design (FBD) and the Displacement-Based Design (DBD). The FBD is the method on which structural codes rely, the Eurocode 8 (EC8), for instance, for which it will be referred to in such a way in further comparisons. It is based on the strength and stiffness that a building should have to resist the loading derived from an earthquake. Meanwhile, the DBD considers the displacement to which the structure would be subjected to obtain those parameters.

For the experimentation, a real-scale 4-story dual reinforced concrete building, made up of two parallel frames, each designed through a different approach, shown in Figure 4.1, was built. Each frame was composed of two columns and two shear walls connected with a coupling beam. The building is consider dual as the walls and columns resist the the seismic shear forces. However, most of this load is sustained by the walls, in this structure they resisted 70% of the lateral loads considered.

The 4-storey building was $12.5m$ tall, with a first floor of $3.5m$ and the remaining floors with a constant height of $3m$. The wall on the exterior of the structure was shaped like an "L" with dimensions 100x50x25cm and the interior one was rectangular with dimensions 100x25 cm. The columns of the structure had the same section as the beams, 40x25 cm. The beams, including the coupling beam had the same cross section, yet, they spanned through different lengths. Both frames were $4m$ apart and were connected by means of transversal beams a 15cm slab. The frames were designed considering a tributary width of $5m$,for such, in the experiment the remaining mass was added in the form of water tanks to simulate the design loads. The characteristic material strengths were $25MPa$ for concrete and 500 for steel.

The structure was designed considering a behavior factor $q = 5$ for a high ductility class. To attain such value, the procedure of EC8 requires detailing of the the columns in bending at joints and elements in shear as to prevent brittle collapse. This is done to ensure the capacity design procedure,allowing for ductile failure in the structure.

For this structure, a difference in the steel quantities per frame is significant. The DBD side is reported to have in average 30% less steel than the EC8 side. This is done as a considerable reduction in the longitudinal and transversal reinforcement was obtained by the designers.

One of the biggest differences between both design procedures is the reinforcement within the critical zone. In this case, the EC8 required twice the height of the cross section while the DBD design requieres 1.5. The reinforcement within this zone is also considerably reduced. For instance, the stirrups, all of 8mm in diameter, in the EC8 side had a separation of $6cm$,while in the DBD side, a separation of $21cm$ in the first two floors and $22.5cm$ were used in the upper ones. Yet, unlike in the EC8 side, the BDB required diagonal reinforcement in the coupling beams of the first floor.

The complete reinforcement layout of the tested structure is presented in Appendix A. For further information regarding the characteristics of the structure and the experimental campaign, please refer to [29] and [28].

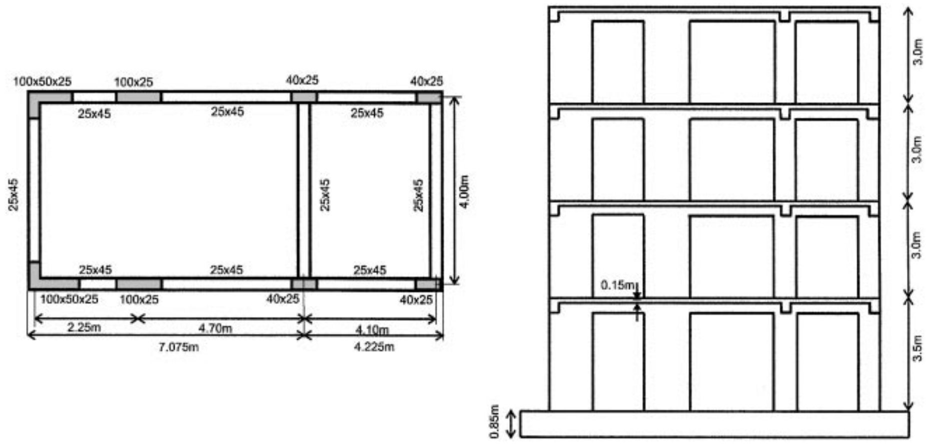

Figure 4.1. Experimental Structure
Member cross sections are in cm. Retrieved from [29] .

Pseudo-dynamic tests are an easy and beneficial way to approach the dynamic behaviour of structures. It is a hybrid-numerical experimental test that combines the simulation of the dynamic aspects of the problem with an experiment that can be carried out at low velocities.

The inertial dynamic forces are computed by solving the equations of motion at each time interval using numerical integration. For instance, this can be done through Newmark's equation. In this way, the displacements at each step can be computed and imposed on the structure using actuators. Then the reaction forces are read from the load cells and used to compute the displacement in the next step. By obtaining the forces, as a result, the instantaneous stiffness can be computed at every time instant. A flow chart of this type of test is presented in Annex A, Figure A.1.

One of the main benefits of this type of experiment is that as inertial forces are computed numerically, there is no need to perform the test on a real-time scale.

This procedure considerably reduces the power required from the hydraulic hammers compared to those in shaking tables. It also allows visual inspections as there is easy tracking of damage progression. The test can also be interrupted to perform such inspections.

As the term of the equation regarding the reaction forces is read directly from the load cells, it is not necessary to know the beforehand properties or assume models about the behaviour of the material or the components related to damage as they are intrinsically considered. In the same way, the hysteretic damping coming from the inelastic deformation and propagation of damage, which is one of the most effective mechanisms of energy dissipation, is also considered.

The PSD test was conducted by considering a response spectrum in line with that of EC8. For such a spectrum, a soil type B and a PGA of $0.4g$ were considered with structural damping of 5%. The structure was subjected to three accelerograms, corresponding to a service earthquake, a design earthquake, and 1.5 times the design earthquake referred to as D04, D05 and D06, respectively. The accelerogram of the test was modulated after the 1995 Kobe earthquake, as presented in Figure 4.2.

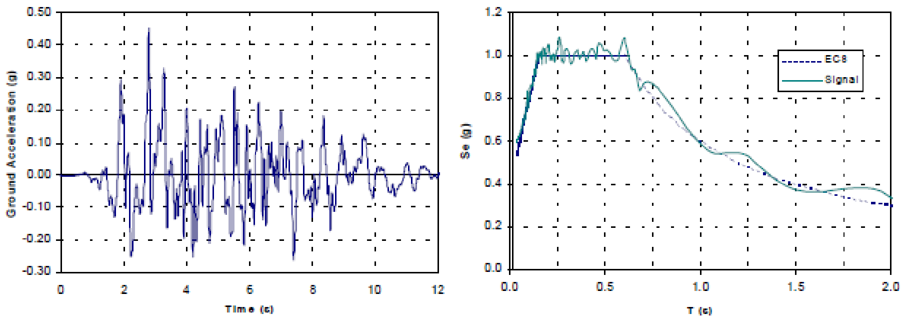

Figure 4.2. Ground motion and Response Spectrum D05
Retrieved from [28]

The test was performed in the direction parallel to the frames, the longest direction of the structure. In the short direction, the displacements were constrained to zero, which impedes torsional behaviour. Therefore, 4 traslational degrees of freedom, one on each floor in the direction of the frames, are considered.

Under the design earthquake, the structure had good behaviour, with both sides presenting similar hysteretic cycles. As stated by [28] the EC8 side had higher restoring forces, yet both frames dissipated the same amount of energy.

A significant variation in the fundamental frequency of the structure occurred during the test. Initially, a structural frequency of $2.7Hz$, representing the uncracked structure, decreased to around $1.2Hz$, which was the estimated frequency with member secant stiffness to yielding, [28] , shown in Figure 4.3. This remarkable difference shows why a linear viscous elastic tuned mass damper is not able to protect the building during the whole earthquake, but losses its tuning frequency relatively fast.

During the last accelerogram, D06, the structure was severely damaged, for which it was decided to stop the test to repair the structure and continue the test. However, the retrofitted structure will not be considered. It will be assumed that the test was finished at the moment in which the structure was repaired.

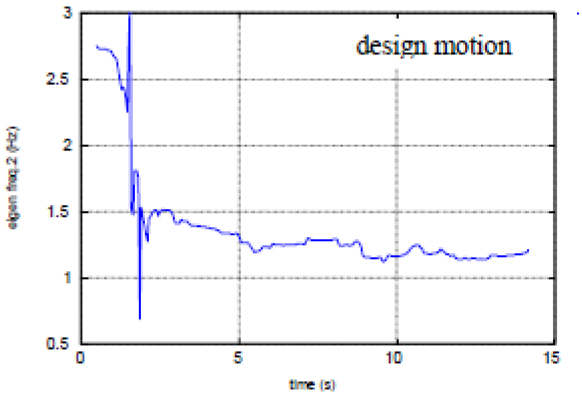

Figure 4.3. Evolution of fundamental frequency
Retrieved from [28]

At the end of the D06 test, both frames had sustained great amount of damage. Cracking, due to either flexure or shear were present in the coupling beams and the walls. The width of such cracks were increased during the last motion. The result of the test was that the reduction on the steel quantity did not impaired the overall behavior of the structure, [28]. The final crack configuration is shown in Figure 4.4

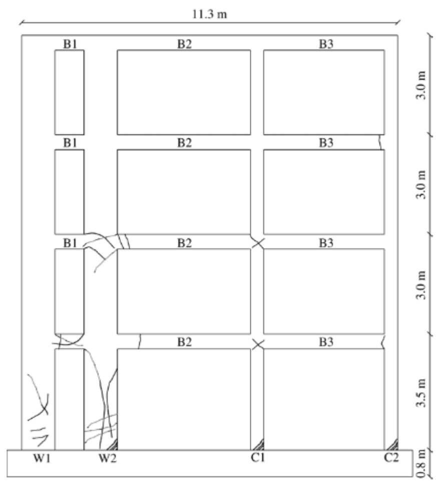

Figure 4.4. Damaged structure

4.2 Numerical Modelling

Two different types of models were carried out for the structure. The first model was carried out using a commercial software, which would allow us to evaluate the suitability of the method for the design of this type of structure. The second model, a more refined one, was carried out by [30, 31] and is a numerical model which resembles the behaviour of the structure. This second model will be used to assess the effectiveness of the designed TMD by comparing the controlled structure (the one containing the TMD) and the uncontrolled one.

In both cases, the same modelling procedure of the elements was used. Meaning that the weights, definition of the materials, cross sections, and reinforcements have been reproduced similarly.

4.2.1 SAP2000 Model

The structure was modelled in the commercial software SAP2000, presented in Figure 4.5. In it, vertical elements were modelled in the sections centroid, while horizontal elements were modelled at the height of the upper face of the slab. In this horizontal elements, a part of the slab is considered as a collaborating width in the beams. This value is determined by the minimum suggested in [32]. Additionally, rigid zones in the nodes between horizontal and vertical elements were considered. The masses in each frame were assumed to be concentrated as shown in Figure 4.6 where the dead and live loads are considered.

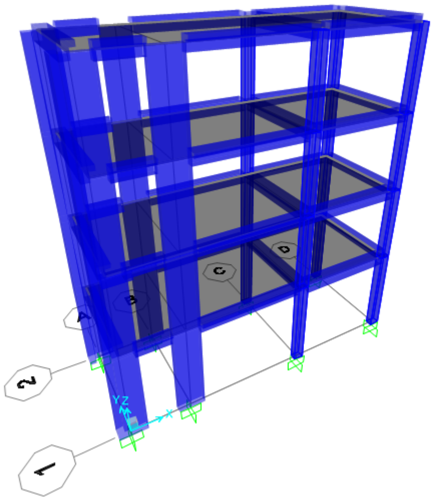

Figure 4.5. SAP2000 model

The section designer of the software was used to model the L-shaped columns and the reinforcement details from [28] which are necessary for determining the hinge characteristics. In the model, plastic hinges were assumed to happen only close to the nodes, following a lumped plasticity hypothesis. The skeleton curve stated in [34] was adopted for the hinges. For the beams only the bending moment in principal axis is considered for the hinge, while in the columns the coupling between axial force and bending moment is used. The length of the plastic zones is assumed to be equal to the height of the cross section.

In this model, a nonlinear static analysis was carried out. As the structure is not symmetrical, the analysis results in each direction differ. The first mode controls the structure's dynamic behaviour, and the soft story collapse mechanism was not possible as, in the pushover analysis, the curve resulting from such a load pattern was greater than the modal one. This type of behavior was anticipated due to the presence of the coupled walls. It is important to state that such walls resist most of the shear forces in the building as expected from a dual system.

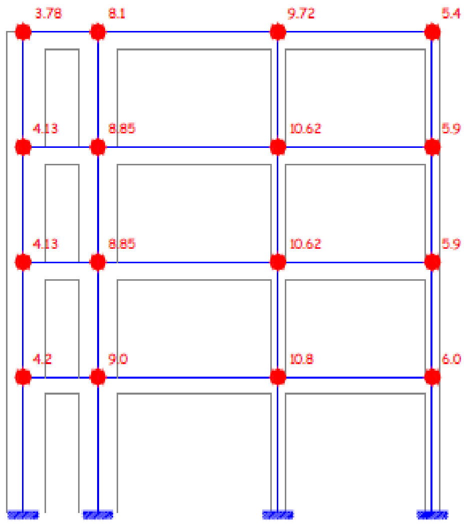

Figure 4.6. Lumped mass distribution
Retrieved from [33].

Therefore the capacity curve of the structure, to a load pattern in agreement with its first mode of vibration in the considered direction, is shown in Figure 4.8a. The control point for the capacity curve is the center of gravity of the 4^{th} floor. The pushover curve is obtained by means of the SAP2000 model and is computed in both directions of the structure due to its asymmetry.

This type of analysis is now considered standard to evaluate the performance of a structure, and is very beneficial as it allows to understand the damage propagation in the structure. From the model it was possible to see that initially the coupling beams yielded, thus generating a reduction of stiffness in the structure. This is exactly what happened in the real structure. Ergo, this type of analysis allow to comprehend the behavior of the structure and design corrective measures if necessary. The final hinge configuration of the pushover analysis in the positive direction is shown in Figure 4.7. In the figure the color scale refer to the skeleton curve of the plastic hinges.

A comparison between the observed behaviour of the system and the pushover curve is present in Figure 4.8b. In such figure, the broken line coming from the experimental frame under the design earthquake is compared to the pushover curve from the SAP2000. A good agreement between both sets of data is attained as the pushover curve envelopes the experimental values.

Even if this method can be considered relatively easy nowadays, there are several factors that lead can to different pushover curves. Due to this variability the expertise of the designer to model structures is crucial to obtain a response of the structure that would actually resemble the behaviour of the structure. This is a very important remark as a comparison between the real structure and the model is generally not possible.

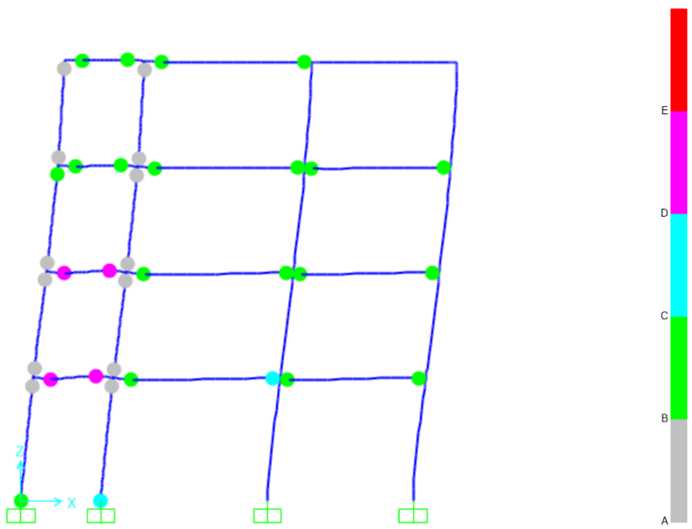

Figure 4.7. Hinge activation

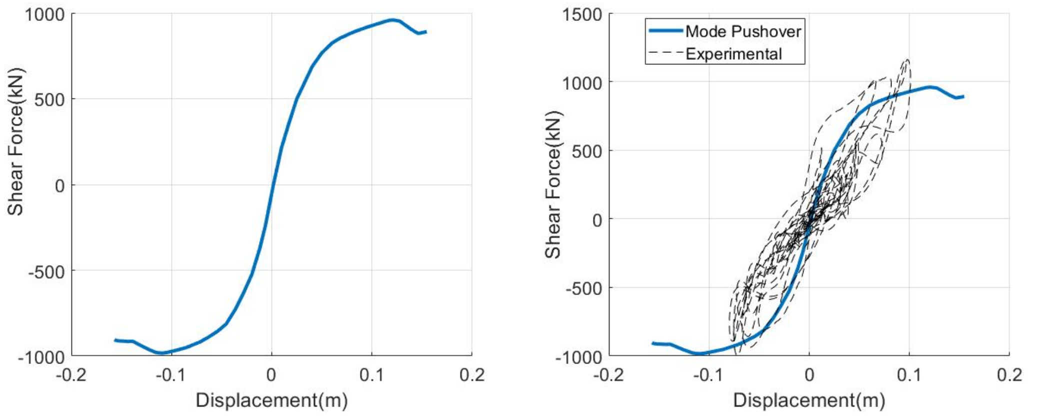

(a) Pushover Curve (b) Pushover curve vs Experimental results

Figure 4.8. SAP2000 Model Verification

4.2.2 Refined Model

The second model is a numerical model made up of R.C.I.Z elements for the reinforced concrete elements, originally developed in [35]. Through these elements, [30] modeled the structure using the NONDA computer code shown in [36]. This type of element is capable of capturing the interaction between between the shear resistance and the inelastic flexural behaviour. As it is a fiber model element, the structural member is discretized in fibers of the corresponding material for which the stress-strain history is evaluated through their uniaxial constitutive laws, [33].

This fiber model was set up similarly to the SAP2000 model, yet only the direction parallel to the frames was considered for the analysis. Hence, displacements and rotations perpendicular to the analyzed direction were restrained.

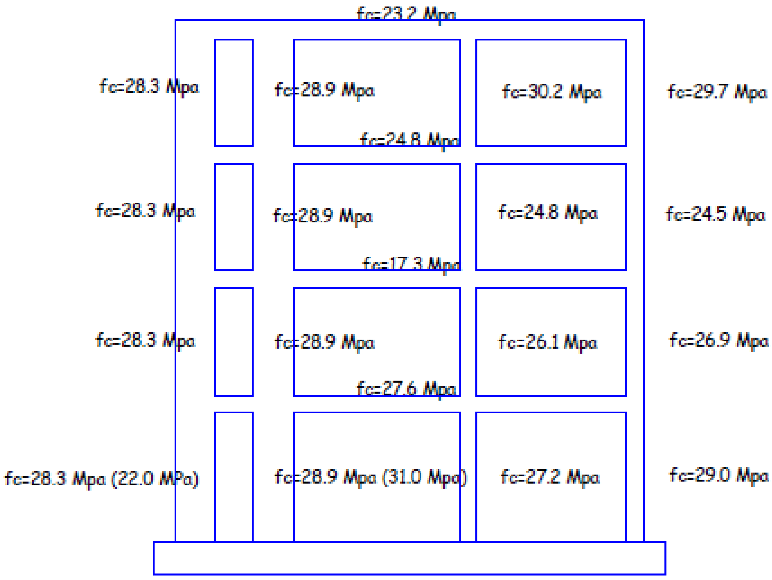

Figure 4.9. Concrete strength (MPa)
Values in parenthesis relate to the DBD side
Retrieved from [30]

In the model, the same collaborating width of the slab was considered in the modelling of the beams. The slab itself was not modelled as a rigid diaphragm as it would impose an axial constraint in the element thus affecting the flexural response of the horizontal elements.Thus, the displacements in the traslational DOF of the inner walls were set equal to each other in order to model the rigid diaphragm hypothesis.

According to the R.C.I.Z. formulation the element had to be discretized in 5 cross sections throughout its length. In the model, all of the sections were equal to each other, meaning that a total of 56 fiber sections were modelled, one per each element. Each element had the real concrete strength, shown in Figure 4.9.

Depending on the type of element, a different amount of fibers, both of concrete and steel were required to model it. For instance, walls required a total of 22 concrete fibers. Both walls were modelled the same way, yet due to the L shape of a wall some fibers had an increase in their area. For the same element, another criteria that had to be taken into consideration is that the centroid of the fiber is not longer coincident with the axis of the element

Elements had the same characteristics through the height, only the concrete strength was varied. Beams had the same amount of concrete fibers, yet coupling beams had two additional steel fibers. It is important to note that the numerical code NONDA had to be modified in order to account for the diagonal reinforcement of such beam, [33].

A comparison between the slabs displacements and the base shear force obtained from the experimental analysis of the frame and the model was performed to validate it. The model represents the global behaviour of the structure, especially the roof displacement and the shear force where the agreement between the experimental data and the numerical model is almost perfect. The comparison for the design test can be seen in Figures 4.10 and 4.11.

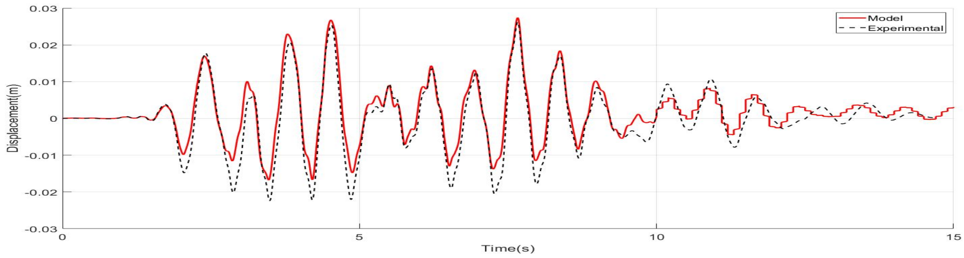

(a) 1^{st}

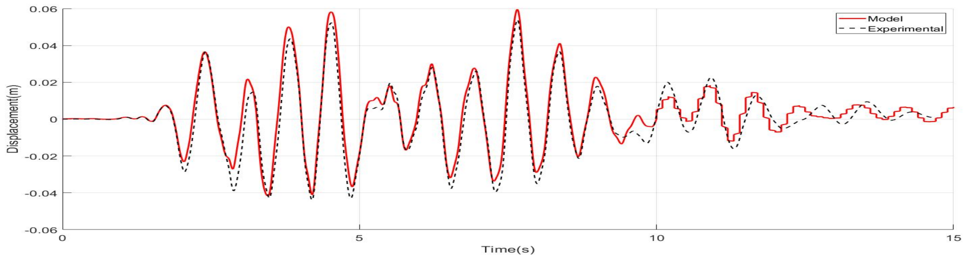

(b) 2^{nd}

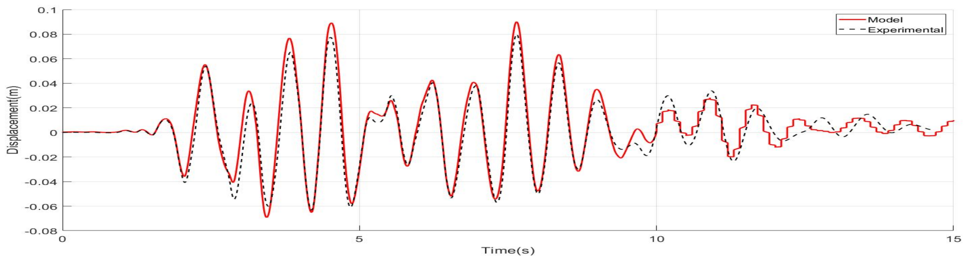

(c) 3^{rd}

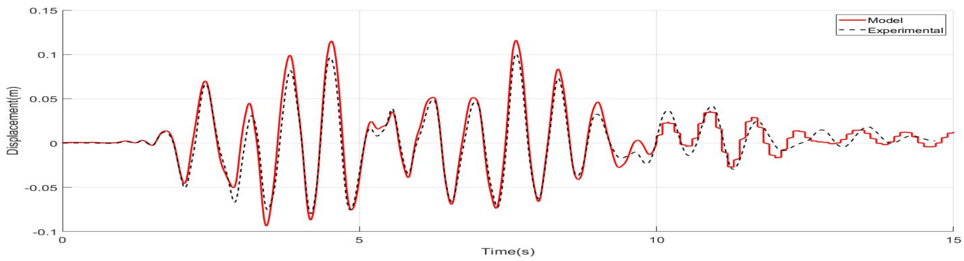

(d) 4^{th}

Figure 4.10. Floor Displacements

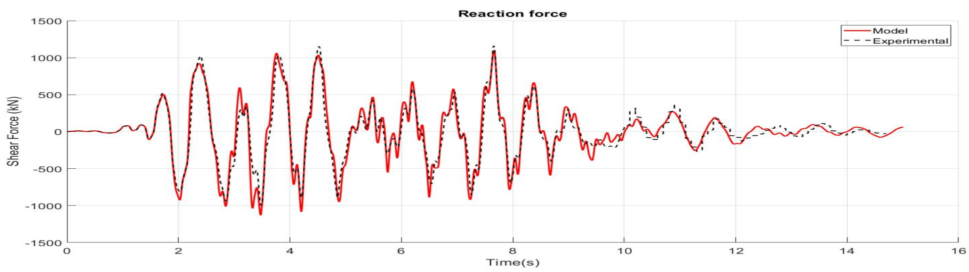

Figure 4.11. Shear Force at the Base

Due to the resemblance of this model to the real structure a series of nonlinear time history analyses can be carried out ensuring that it would reproduce the behavior of the actual structure with significant accuracy. Therefore, an element intended to represent the TMD will be included in the numerical code to determine its efficiency.

4.2.3 Bouc Wen Element

The TMD was modelled as a Bouc Wen element so that it would be possible to include it in the more refined structural model. To do so, an additional element with the BW hysteretic behavior was modelled in such a way to be compatible with the existing NONDA code in which the structure was analyzed.

Therefore, a reading and writing procedure for the input and output file respectively for the parameters of the element just as for the other types of elements was necessary. The element had to be coded in a path independent way that permitted to save the last equilibrated state and advance from it to the next step. In this way, both the tangential stiffness and forces of the element at each step had to be computed independently by solving the related differential equation of the system shown in Equation 2.5. In this way, the integration of the BW equations is decoupled from the integration scheme of the systems response.

The design of the element will be explained in Section 5. Examples of different hysteretic behaviour of the BW element by varying certain characteristics are presented in Figure 4.12. It is important to note that in the figure, a sinusoidal load with a maximum displacement of $30cm$ is applied and the relationship of $\gamma = \beta$ is imposed.

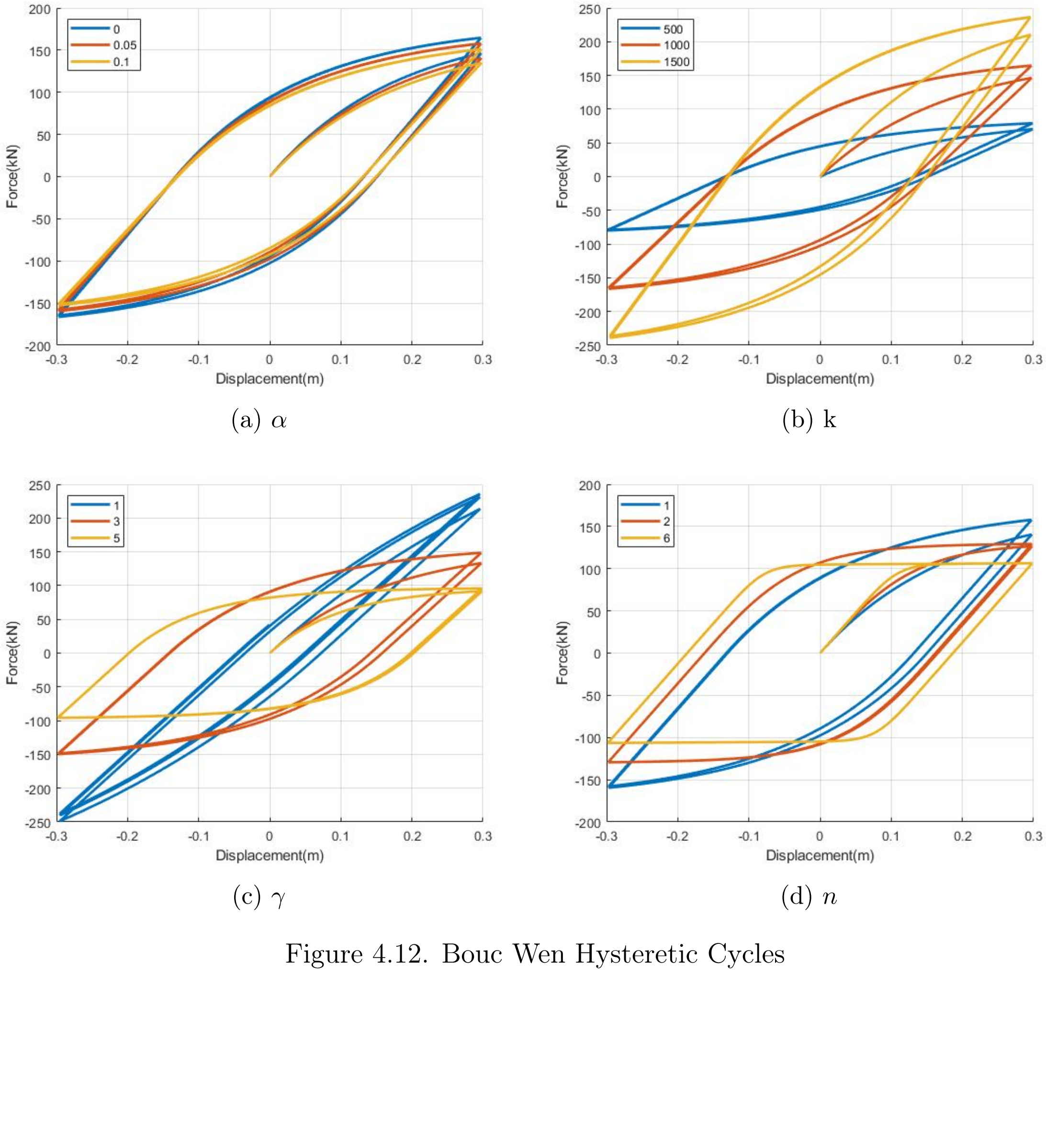

(a) α (b) k (c) γ (d) n

Figure 4.12. Bouc Wen Hysteretic Cycles

Chapter 5

Design

5.1 Design Procedure

The main benefit of using for the TMD a spring following a BW element law is that as the structure deteriorates and enters the nonlinear range, as shown in Figure 4.3, the hysteretic TMD can continue to perform as intended, unlike a linear TMD. Therefore, the main task is to have an element that reduces the damage in the structure by behaving similarly to it in both the elastic and plastic range.

The new methodology for designing the hysteretic TMD avoids using genetic algorithms (GA) and numerical optimization, which are time-consuming and unsuitable for design. Instead, an approach using the capacity curve of the structure can lead to results comparable to those obtained by employing GA.

The design procedure of the TMD is based on a nonlinear static "pushover" analysis. This type of analysis results in a curve that relates the displacement of a certain control point of the structure, typically one on the last floor of the structure and the shear force at the base. This curve is also called the capacity curve. In the case of the considered structure, the pushover curve is available in Figure 4.8a.

It is noteworthy that the TMD's behaviour depends on the structure's displacement at its location. For such, the control point chosen for the pushover analysis should be the one where ideally, it would be installed.

A bilinearization procedure can be done in the capacity curve. This procedure allows seeing the pushover curve in a more simplified way, as it would only consist of two linear branches intersecting at the yielding point. Such linear segments are attained using an energetic equivalence between the areas enclosed by curves, the bilinear one and the actual pushover. Structures with trilinear curves are also common; however, in those cases, the first two branches will be considered.

The procedure presented in FEMA 440, [37], for defining the biliearization of the pushover curve is recommended as it allows for an elastic branch more representative of the elastic behaviour of the system. This procedure is iterative, although it converges in a few iterations, as it depends on the ductility of the system, which at the same time depends on the yielding point. This method also provides an estimation of the damping of the structure. The Italian Building Code (NTC2018) provides a similar method for bilinearizing pushover curves. Nevertheless, both methods differ due to the assumption over the initial elastic branch. It is important to state that commercial softwares usually includes a bilinearization of such curves.

The Bilinearized Pushover curve is presented in Figure 5.1.

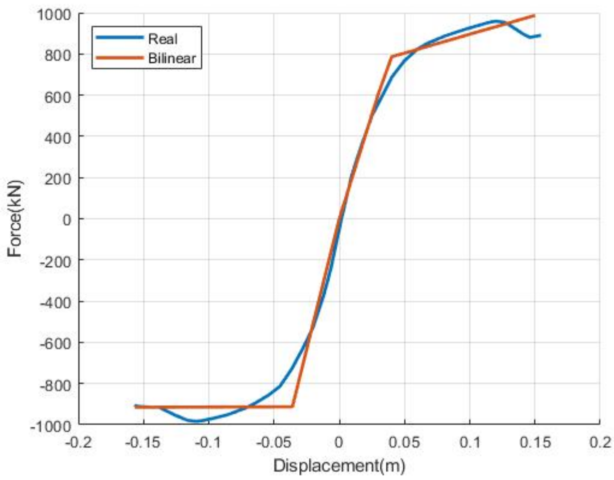

Figure 5.1. Pushover Curve

The capacity curve can be modified into the capacity spectrum using Equation 5.1.

$$d^* = \frac{d}{\Gamma}; \qquad F^* = \frac{F}{m^* * \Gamma * g} \tag{5.1}$$

Where m^*,Γ, F^* and d^* correspond to the modal mass, mass participation factor, and equivalent shear force and displacement, respectively. This modification allows analyzing the structure, which is a Multi Degree of Freedom (MDOF) as an equivalent Single Degree of Freedom (SDOF) system.

$$\Gamma = \frac{\boldsymbol{\varphi^T M r}}{\boldsymbol{\varphi^T M \varphi}}; \qquad m^* = \boldsymbol{\varphi M r} \tag{5.2}$$

With $\boldsymbol{M}$ as the mass matrix, $\boldsymbol{\varphi}$ the mode shape related to the loading pattern of the pushover curve and $\boldsymbol{r}$ as the vector relating the masses to the considered direction of analysis.

The purpose of the TMD is to reduce the structure's displacements through an inertial mass moving out of phase with the structure. Therefore, the designer must select a level of displacement that can be considered suitable for the structure. In this way, the designer could increase the damping of the structure to find that new performance point. This modification can be done in the ADRS spectrum, as in the bilinearization procedure, by accounting for additional damping. The additional damping required, as shown in Equation 5.3, to attain such displacements is the one the TMD should provide to the structure.

$$\xi_r = \xi_t - \xi_0 \tag{5.3}$$

Where ξ_r is the required equivalent damping, ξ_0 is the initial damping of the structure obtained through the bilinearization procedure and ξ_t is the structural damping for which the desired performance point is attained.

It is important to note that the equivalent damping provided by the damper heavily depends on the mass ratio, $\mu = \frac{m_d}{m}$, shown in Figure 5.2, which refers to Optimal linear TMD. Therefore, it can be assumed that the damper's mass ratio is equal, or approximately equal, to the equivalent damping required by the structure to attain the desired performance point, $\xi_r \approx \mu$. Hence, the mass ratio is a function of the desired performance point selected by the designer. This value usually varies between 1% and 5% of the mass of the structure.

This consideration can be used in be used in both directions. Thus, allowing the designer to choose a mass ratio needed to attain the displacement of the performance point or to check the displacement assuming a mass ratio. It is then important to note that these two steps are interchangeable in order, as they depend on the limiting characteristics of the structure or the needs of the designer.

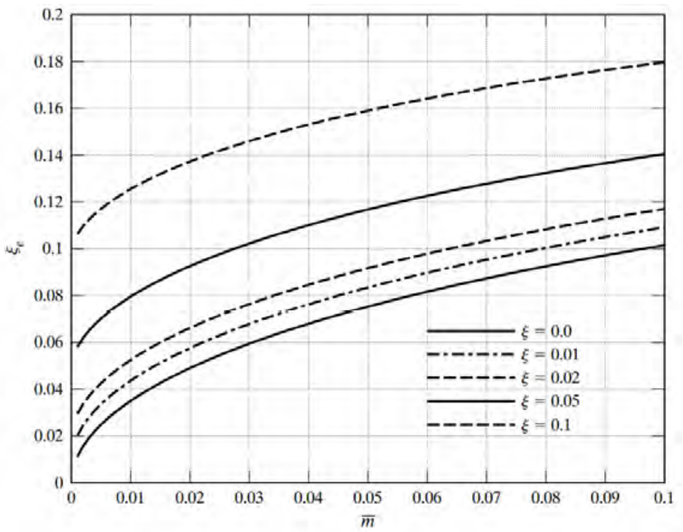

Figure 5.2. Equivalent Damping from an Optimal TMD
Retrieved from [4]

For the design, several parameters should be retrieved from the pushover curve; these are the initial stiffness of the structure (k_0) from the bilinear pushover, the damping (ξ), and the secant stiffness at the desired performance point (k_{sec}). The secant stiffness must be determined using the real pushover of the structure, yet the difference with the one computed by the bilinear curve is commonly negligible. In the following, the damper characteristics will be denoted with a subscript d to distinguish them from the structure's characteristics.

By considering these parameters, the period of the equivalent bilinear structure can be computed as

$$T^* = 2\pi\sqrt{\frac{m^*}{k_0}} \tag{5.4}$$

The TMD should be then tuned to the frequency f stated by [19], which depends on the mass ratio μ and the structural damping ξ. The key aspect of the design is that this tuning frequency should be attained in two moments, at the beginning of the motion and both when the structure reaches the performance point. It is assumed that the structure will reach its performance point while the TMD reaches its maximum displacement.

$$
\begin{aligned}
f =& \frac{T_0}{T_{d,0}} = \frac{\omega_{d,0}}{\omega_0} \\
f =& \frac{T_{sec}}{T_{d,sec}} = \frac{\omega_{d,sec}}{\omega_{sec}}
\end{aligned}
\tag{5.5}
$$

Where T_{sec} and $T_{d,sec}$ are the secant period of the structure and the BW element at their corresponding maximum displacement. Thus intending that the damper is again tuned to the structure at that moment. With f computed according to 5.6 following the recommendations of [19].

$$
\begin{aligned}
f =& (\frac{\sqrt{1-0.5\mu}}{1+\mu} + \sqrt{1-2\xi^2} - 1) \\
& - (2.375 - 1.034\sqrt{\mu} - 0.426\mu)\xi\sqrt{\mu} \\
& - (0.3730 - 16.903\sqrt{\mu} + 20.496\mu)\xi^2\sqrt{\mu}
\end{aligned}
\tag{5.6}
$$

From the tunning frequency, the initial period of the structure, $T^* = T_0$ and the mass of the damper, known through the mass ratio, the initial stiffness of the TMD can be computed. In the same way, the secant stiffness of the damper can be obtained by considering Equation 5.4 and 5.5, using the secant period of the structure at the selected performance point rather than the initial one.

The following must be considered regarding the parameters that control the Bouc Wen model. First, the parameter n will be fixed as $n = 1$ as it allows for smooth behaviour with great dissipation and analytical solution of the equation, [38]. The relationship $\gamma = \beta$ is assumed as this allows for a softening behaviour in the structure and mostly linear unloading, [13]. The hardening coefficient α_d depends on the material used for the damper and its arrangement.

The secant stiffness of the damper $k_{d,sec}$ can be computed by considering the tuning at the performance point through Equation 5.7. Imposing that the damper achieves such secant stiffness at its maximum displacement, $u_{d,max}$ the value of the parameter γ and β can be obtained. This can be done by means of an iterative procedure or by assuming a value of the stroke. In the following section, 5.1.1, the iterative procedure to determine $u_{d,max}$ is presented. An example of the application of such procedure is shown in Section 5.2

The secant stiffness of the damper can be computed according to Equation 5.7 retrieved from [39].

$$
k_{d,sec}(u) = k_{d,0}\left\{\alpha_d + \frac{1-\alpha_d}{u(\beta+\gamma)}(1-e^{-u(\beta+\gamma)})\right\}
\tag{5.7}
$$

5.1.1 Iterative Procedure

As stated previously, the damper is displacement-dependent, meaning that its maximum displacement depends on the displacement of the structure at the point at which it is installed. Therefore, considering a SDOF system excited by a sinusoidal load with the secant frequency of the structure and an amplitude equal to the desired performance point of the structure, the displacement of the TMD at such point can be estimated through Eq 5.8.

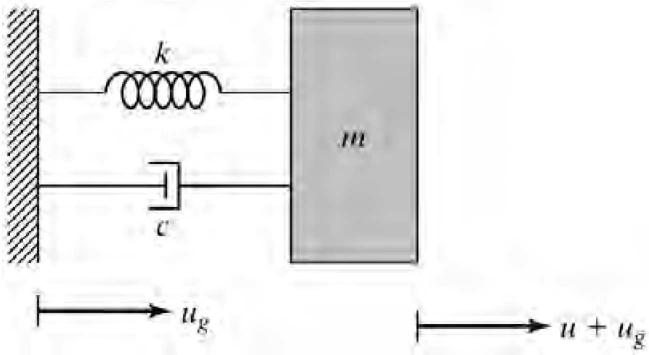

Figure 5.3. Base excitation of SDOF
Taken from [4]

$$u_{d,max} = x_{pp}\sqrt{\frac{\rho^4}{(1-\rho^2)^2 + (2\xi_d\rho)^2}} \tag{5.8}$$

Where $\rho = \frac{1}{f}$ and x_{pp} is the displacement of the structure at the new performance point.

This is an iterative procedure which requires the tuning frequency, the secant period (or stiffness) of the structure, and the displacement of the control node. It is iterative, as the maximum displacement of the SDOF depends on its frequency response function, which depends on the damping of the BW, which is again a function of its displacement. To initialize the BW model, the maximum working displacement $u_{max} = u_{max}(f, u_g, \xi_d)$ is required to compute the secant stiffness at u_{max}.

Through Equation 5.7, by considering that $\gamma = \beta$, the values of such parameters can be computed. Therefore, all of the parameters defining the BW hysteretic model are defined, for which the hysteretic curve of the model can be drawn.

With such curve,the damping of the element can be obtained by considering the hysteretic energy dissipated A_h and the elastic energy A_e. The former refers to the energy dissipated during a full hysteretic loop loading cycle, while the latter refers to the elastic energy of a system with secant stiffness. For example, Figure 5.4 shows both energies within a hysteretic cycle.

The equivalent damping of the element can be computed as:

$$\begin{aligned} A_h &= \int F dx \\ A_e &= \frac{1}{2}k_{sec}u_{max}^2 \\ \xi_e &= \frac{A_h}{4\pi A_e} \end{aligned} \tag{5.9}$$

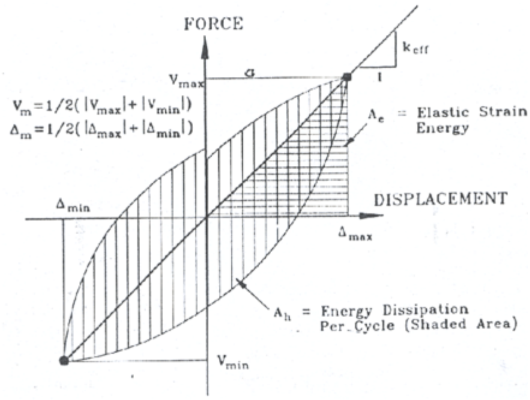

Figure 5.4. Equivalent Viscous Damping
Retrieved from [40]

In case the damping of the structure is different from the one assumed at the beginning of the step, the damping should be set to the new one and repeated until convergence under the desired tolerance. A flow chart with the iterative procedure is available in Figure 5.5.

Once the characteristics of the element are determined, the real equivalent damping that it would provide to the system can be computed. As the damper dissipates energy that otherwise would have to be dissipated by the structure, the equivalent damping can be computed as:

$$\xi_{eq} = \frac{Ah_d}{4\pi A_e} \tag{5.10}$$

Considering that A_e is the elastic energy of the structure. Equation 5.10 can be modified to:

$$\begin{aligned} \xi_{eq} &= \xi_h \mu^* \left(\frac{fU_{max}}{x_{max}} \right)^2 \\ \mu^* &= \frac{m_d}{m^*} \end{aligned} \tag{5.11}$$

In this way, it is possible to check the initial assumption of the equivalent damping added by the TMD.

It is important to note that as stated by [41], the BW element does not possess an elastic domain unless $\gamma = 0$. As this will not be the case, the element will always have a residual deformation. Therefore the actual maximum displacement of the moving damper could be greater than the considered stroke $u_{d,max}$. It is then recommended, for a real damper, to have a space greater than that for which it is designed.

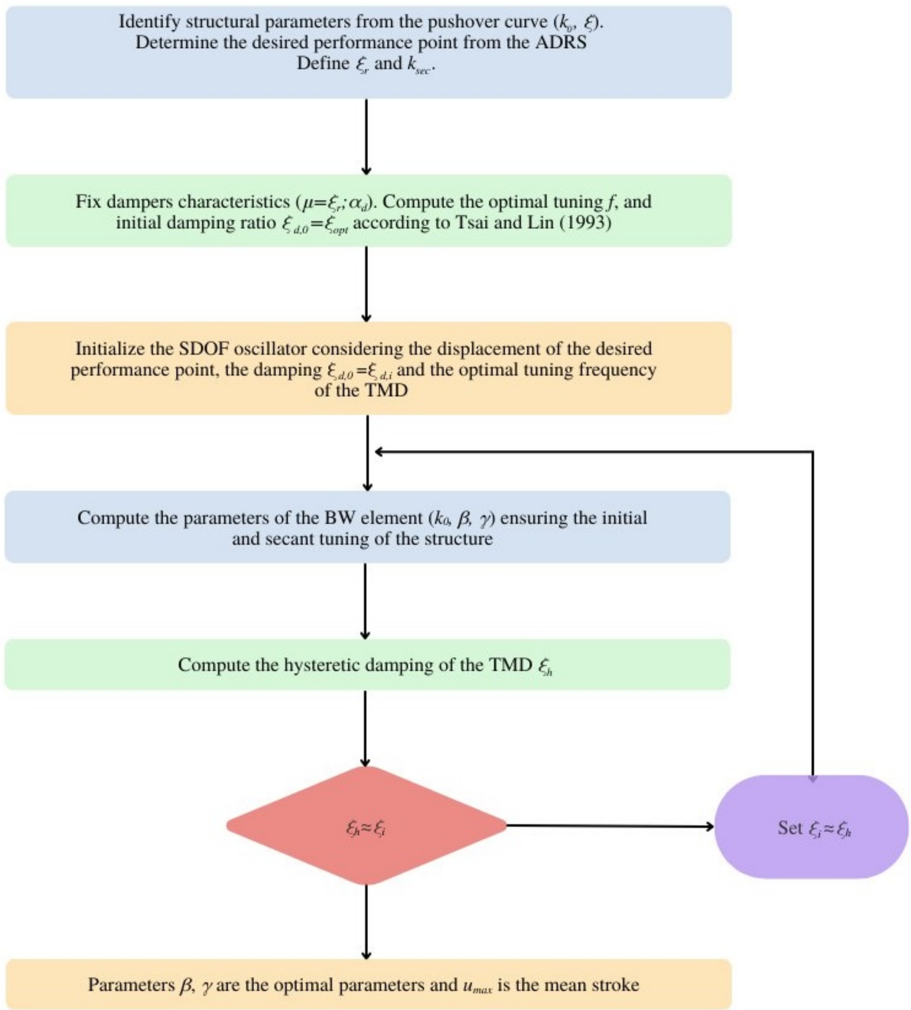

Figure 5.5. Iterative Design Procedure

5.1.2 Direct Procedure

By removing the iterative procedure shown in the previous design strategy it cannot be ensured that the damper will be tuned at the desired secant stiffness. This is because the displacement of the TMD is not optimized at the performance point and so it could be lower or greater than anticipated.

For assuming a stroke of the TMD, u_{max}, an amplification value of the floor displacement is needed. In the iterative procedure this was done by means of the SDOF system under ground motion. However in this alternative, as the BW element will not be iterated, the actual hysteretic damping will be unknown, and so the actual amplification value. Therefore, a recommended value for the assumed stroke lies between 2 to 3.5 times the floor displacement. These values correspond to the magnification factor of an element with 14% equivalent damping under tunings close to resonance. Under this study all elements that were designed in such manner provided an equivalent viscous damping greater than such value.

As u_{max} is set beforehand, Equation 5.7, can be used to impose $f\omega_{sec} = \omega_{d,sec}$ considering $k_{d,sec} = k_{d,sec}(u_{max})$ and so compute the values of $\gamma = \beta$. f is computed by means of Equation 5.6.

A greater maximum displacement than the designed one is also possible and so the same consideration regarding the feasibility of the structures should be stated.

5.2 Results

In the case presented in Chapter 4, the design was performed considering the displacement in the positive direction, as shown in Figure 5.6. The results derived from the bilinearized pushover curve are summarized in Table 5.1.

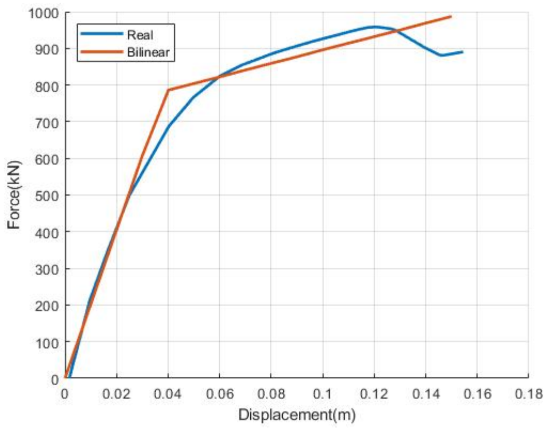

Figure 5.6. Pushover Curve Positive Direction

Table 5.1. Results Bilinearized Pushover

$k_0(kN/m)$	$d_y(m)$	$\xi(\%)$	PP SDOF (m)*	PP MDOF (m)*	$k_{sec}(kN/m)$
20240.6	0.039	16	0.091	0.12	8208.9

*PP:Performance Point

Where ξ is computed, for instance, through the formulas presented in [37]. Other formulas to approximate structural damping are available for instance in the Italian NTC2018, [42], Method B for bilinearizing the pushover curve. Both methods provide similar results for the structural damping. The modal mass of the SDOF system is $m^* = 155ton$ and the mass participation factor is $\Gamma = 1.31$.

Following the recommendations of [37], three different conditions for the effective cases for the effective damping depending on the ductility of the structure are considered. According to the NTC2018, [42], the structural damping can be computed, in % ,as:

$$\xi_{eq} = k\frac{63.7 * (F_Y^* d_{max}^* - F_{max}^* d_y^*)}{F_{max}^* d_{max}^*} + 5 \tag{5.12}$$

It is important to note that the equation is given within an iterative procedure, for which it was required to update the damping in every step until convergence. The coefficient k depends on the characteristics of the expected hysteretic cycle of the structure and can adopt three different values. F_y, d_y, F_{max} and d_{max} corresponds to the force and displacement, yielding and maximum, that the bilinear structure presents.

For this case, the procedure assuming initially the mass ratio will be followed. By using a mass ratio $\mu = 0.05$, an equivalent damping of 21% could be assumed for the structure, by considering $\xi_r = \mu$.

$$\begin{aligned} \xi_r =& \xi_t - \xi_0 \\ 0.05 =& \xi_t - 0.16 \\ \xi_t =& 0.21 \end{aligned} \tag{5.13}$$

When considering such damping in the ADRS spectrum, the expected performance point of the SDOF system would be $0.077m$ meaning $0.10m$ in the real structure. The uncontrolled and controlled situations are represented in Figure 5.7.

Next, as the the mass ratio is already defined, the tuning frequency can be computed according to [19], through Equation 5.6, the optimal value considering $\mu = 0.05$ and $\xi = 16\%$ is $f = 0.83$.

$$\begin{aligned} f =& (\frac{\sqrt{1-0.5\mu}}{1+\mu} + \sqrt{1-2\xi^2} - 1) \\ & - (2.375 - 1.034\sqrt{\mu} - 0.426\mu)\xi\sqrt{\mu} \\ & - (0.3730 - 16.903\sqrt{\mu} + 20.496\mu)\xi^2\sqrt{\mu} \\ f =& (\frac{\sqrt{1-0.5*0.05}}{1+0.05} + \sqrt{1-2*0.16^2} - 1) \\ & - (2.375 - 1.034\sqrt{0.05} - 0.426*0.05)*0.16*\sqrt{0.05} \\ & - (0.3730 - 16.903\sqrt{0.05} + 20.496*0.05)*0.16^2*\sqrt{0.05} \\ f =& 0.83 \end{aligned} \tag{5.14}$$

Considering the initial stiffness of the structure, k_0, the initial stiffness of the damper $k_{d,0}$ can be computed, and the hardening coefficient α_d can be defined. For this case the hardening coefficient will be set as $\alpha_d = 0.05$ as a design choice. Taking into account the mass ratio of $\mu = 0.05$, the mass of the TMD is $m_d = 11.6ton$. It is important to note that even if for the mass of the damper the mass of the whole structure is considered, for the computation of the element's stiffness, the modal mass is used instead of the total mass of the structure. In Chapter 7 a comparison of the results when using the total mass of the structure in this calculation is available.

$$\begin{aligned} \mu =& \frac{m_d}{m} \\ 0.05 =& \frac{m_d}{232} \\ m_d =& 11.6ton \end{aligned} \tag{5.15}$$

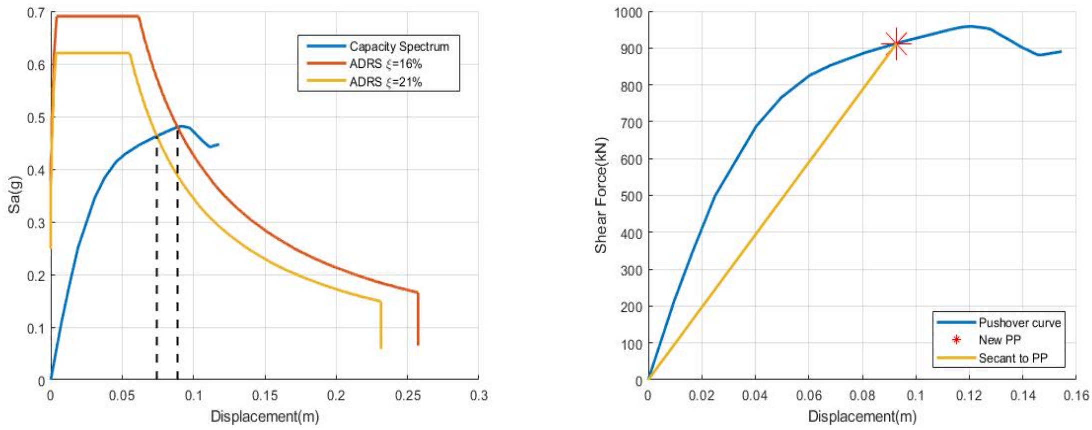

(a) Reduction of the Demand spectrum (b) Secant stiffness to the new Performance Point

Figure 5.7. Performance Point with Added Damping

With the mass of the TMD and imposing that it is tuned as per f one gets the initial stiffness of the damper, $k_{d,0}$, as:

$$
\begin{aligned}
f^2\frac{k_0}{m^*} &= \frac{k_{d,0}}{m_d} \\
0.83^2 * \frac{20240.6}{155} &= \frac{k_{d,0}}{11.6} \\
k_{d,0} &= 1050.5kN/m
\end{aligned}
\tag{5.16}
$$

5.2.1 Iterative Procedure

Based on the new performance point of the structure an initial estimate of the stroke can be computed by assuming an initial $\xi_{d,0}$ and considering the TMD as a SDOF under base excitation with a ground displacement equal to the displacement of the performance point as per Equation 5.8.

By assuming an initial value of $\xi = 16\%$, which is the result of the optimal parameter of the TMD according to [19], the SDOF system would be subjected to an initial motion of $0.24m$ and shown in Figure 5.8.

$$
\begin{aligned}
u_{d,max} &= x_{pp}\sqrt{\frac{\rho^4}{(1-\rho^2)^2+(2\xi_d\rho)^2}} \\
u_{d,max} &= 0.1 * \sqrt{\frac{1.2^4}{(1-1.2^2)^2+(2*0.16*1.2)^2}} \\
u_{d,max} &= 0.24m
\end{aligned}
\tag{5.17}
$$

Considering this displacement as u_{max} the values of the remaining parameters of the BW model can be computed by considering the tuning under secant frequency.

With the stroke, the values of γ and β can be computed using Equation 5.7 so a first attempt of the BW can be drawn.

$$\begin{aligned} f^2 \frac{k_{sec}}{m^*} * m_d =& k_{d,0} \left\{ \alpha_d + \frac{1-\alpha_d}{u(\beta+\gamma)} (1 - e^{-u(\beta+\gamma)}) \right\} \\ 0.83^2 * \frac{9844}{155} * 11.6 =& 1045 * \left\{ 0.05 + \frac{0.95}{0.24*(\beta+\gamma)} (1 - e^{-0.24*(\beta+\gamma)}) \right\} \end{aligned} \tag{5.18}$$

Imposing $\gamma = \beta$ the equation can be solved for one of the two variables resulting in $\gamma = \beta = 4.22$.

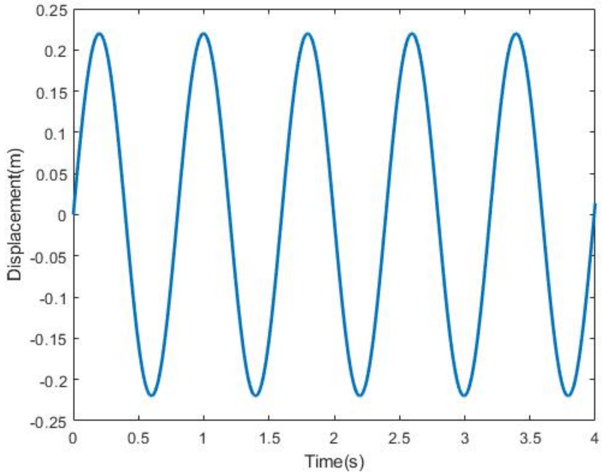

Figure 5.8. First Sinusoidal Motion

The resulting BW hysteretic cycle is shown in Figure 5.9a. However, the result of computing the damping of the BW element is $\xi = 14.1\%$. As this value differs from the original one, the process is repeated by considering this new damping value to compute the stroke of the system. In this study, the process converged at the second iteration resulting in a maximum displacement of $u_{max} = 0.237m$. Figure 5.9b presents the resulting BW cycle, and its characteristics are resumed in Table 5.2.

Table 5.2. Results BW Element

Mass (ton)	$k_{d,0}(kN/m)$	$k_{d,sec}(kN/m)$	$\xi(\%)$	Displacement at PP (m)*
11.6	1050.5	509.61	14.6	0.237

*Performance Point

By considering the BW equivalent viscous damping, and using 5.11 the actual equivalent damping that the TMD would provide to the structure is:

$$\begin{aligned}
\xi_{eq} =& \xi_h \mu^* \left(\frac{fU_{max}}{x_{max}}\right)^2 \\
\xi_{eq} =& 0.146 * 0.075^* \left(\frac{0.83 * 0.237}{0.077}\right)^2 \\
\xi_{eq} =& 0.07
\end{aligned} \tag{5.19}$$

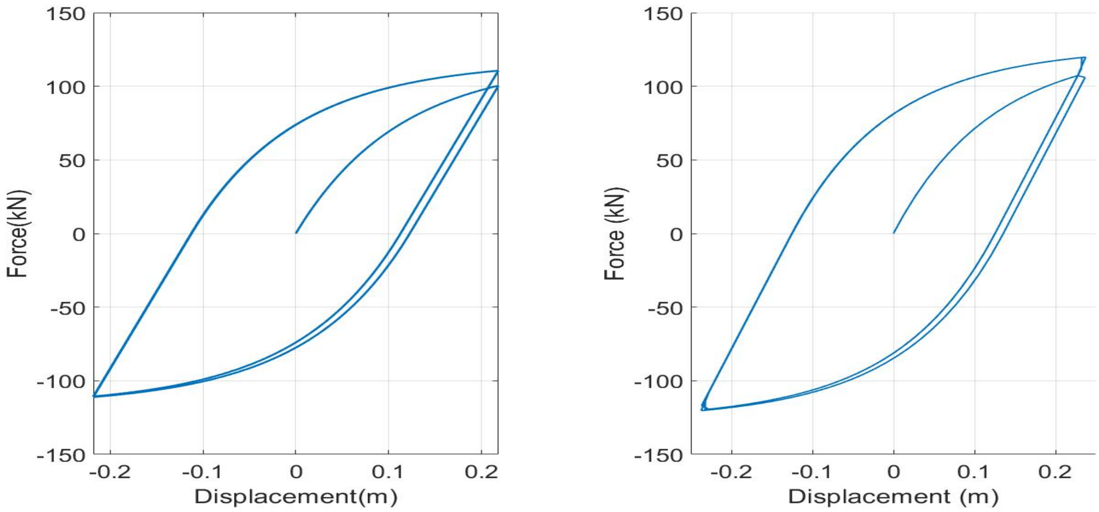

(a) Initial

(b) Final

Figure 5.9. BW Hysteretic Cycle

5.2.2 Direct Procedure

Considering beforehand a stroke of the TMD as $30cm$ would allow to avoid the iterative procedure at the expense of not ensuring the tuning at the performance point.

$$\begin{aligned} f^2\frac{k_{sec}}{m^*} * m_d =& k_{d,0}\left\{\alpha_d + \frac{1-\alpha_d}{u(\beta+\gamma)}(1-e^{-u(\beta+\gamma)})\right\} \\ 0.83^2 * \frac{9844}{155} * 11.6 =& 1045 * \left\{0.05 + \frac{0.95}{0.30*(\beta+\gamma)}(1-e^{-0.30*(\beta+\gamma)})\right\} \end{aligned} \tag{5.20}$$

Imposing $\gamma = \beta$ the equation can be solved for one of the two variables resulting in $\gamma = \beta = 3.1$. Therefore, the characteristics of this system are assumed to be optimal, yet the average displacement at the performance point remains unknown.

By having an element with a secant stiffness tuned at a greater displacement it is expected to have a greater hysteretic cycle. The comparison between the hysteretic cycles of the resulting elements, alongside the desired secant stiffness of the element are presented in Figure 5.10.

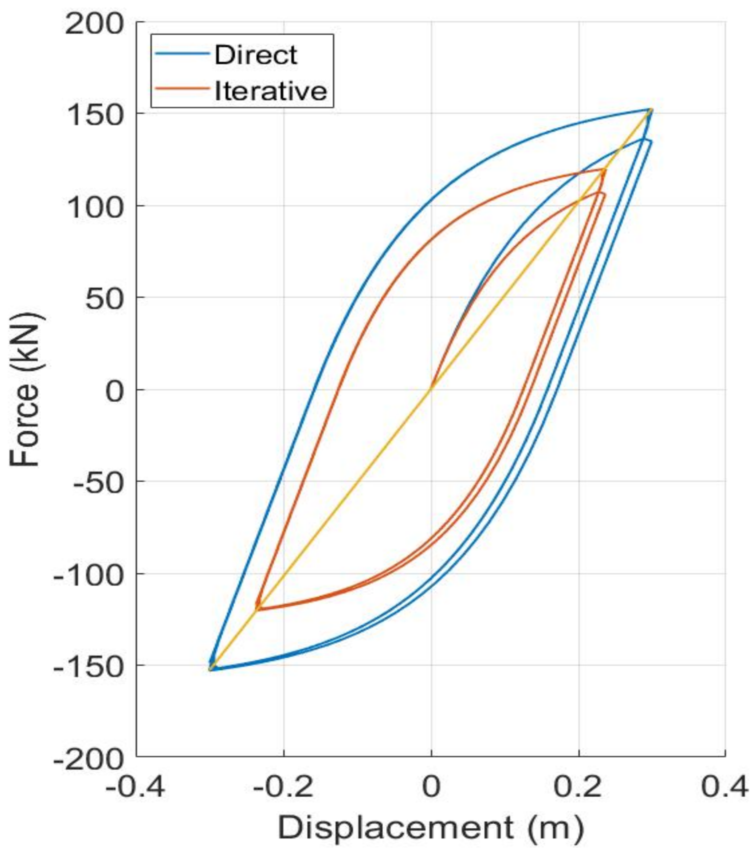

Figure 5.10. Comparison of the BW Hysteretic Cycles

Chapter 6

Numerical Results

As stated previously, to assess the TMD's effectiveness, the numerical model shown in Chapter 4 and validated in [30] was used. The performance indices shown in Table 6.1 were used to understand the behaviour of the structure after introducing the TMD. In addition to the performance indices, the results of the uncontrolled structure for the considered indices in each of the ground motions considered are presented.

Table 6.1. Definition of Performance Indices

System	Response	Peak	RMS
Structure	Displacement	$J_1 = \frac{max(x)_{W,TMD}}{max(x)_{W/O,TMD}}$	$J_4 = \frac{RMS(x)_{W,TMD}}{RMS(x)_{W/O,TMD}}$
	Shear force at the base	$J_2 = \frac{max(F)_{W,TMD}}{max(F)_{W/O,TMD}}$	$J_5 = \frac{RMS(F)_{W,TMD}}{RMS(F)_{W/O,TMD}}$
	Acceleration	$J_3 = \frac{max(\ddot{x})_{W,TMD}}{max(\ddot{x})_{W/O,TMD}}$	$J_6 = \frac{RMS(\ddot{x})_{W,TMD}}{RMS(\ddot{x})_{W/O,TMD}}$
TMD	Stroke	$J_7 = max(u_d)$	

x refers to the displacement of the center of gravity in the 4^{th} floor.

The behavior of the remaining floors of the structures will be analyzed by means of the inter-storey drifts, defined as relative displacements between two successive floors divided by the floor height. The accelerations considered for the Performance indices are the relative accelerations.

6.1 Benchmark

Initially, the behaviour of the controlled and uncontrolled structures will be compared under the excitations of the experimental structure in [28]. Meaning that the structure will be studied using different accelerograms, D04 (service), D05 (design), and D06 (1.5 design). A case in which two and all of them occur in sequence will also be analyzed. This case helps to understand the behaviour of the structure when it has been affected by a previous earthquake. The accelerograms are presented in Figure 6.1

The behavior of the uncontrolled structure for the earthquakes considered is summarized in Table 6.2. In the table the components for each performance index are indicated, meaning that the peak and RMS displacements, forces and accelerations of the structure are shown.

Table 6.2. Uncontrolled Structure Benchmark

Earthquake	Response Index Component					
	$J_1(m)$	$J_2(kN)$	$J_3(m/s^2)$	$J_4(m)$	$J_5(kN)$	$J_6(m/s^2)$
D04	0.009	347.858	2.833	0.003	109.981	0.770
D05	0.116	1118.582	10.722	0.036	380.606	2.967
D45	0.116	1112.258	10.643	0.032	343.162	2.692
D456	0.234	1629.567	15.462	0.050	392.796	3.148

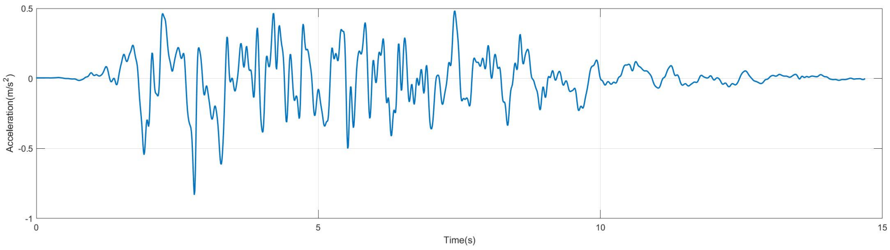

(a) D04

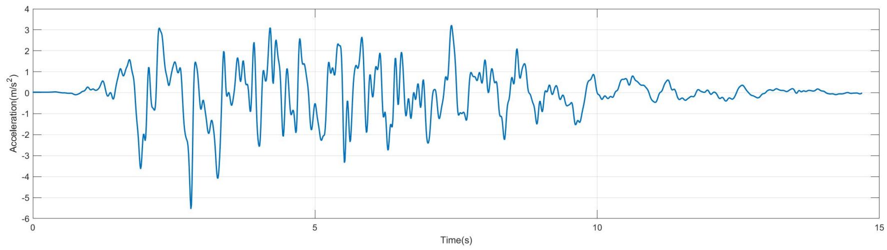

(b) D05

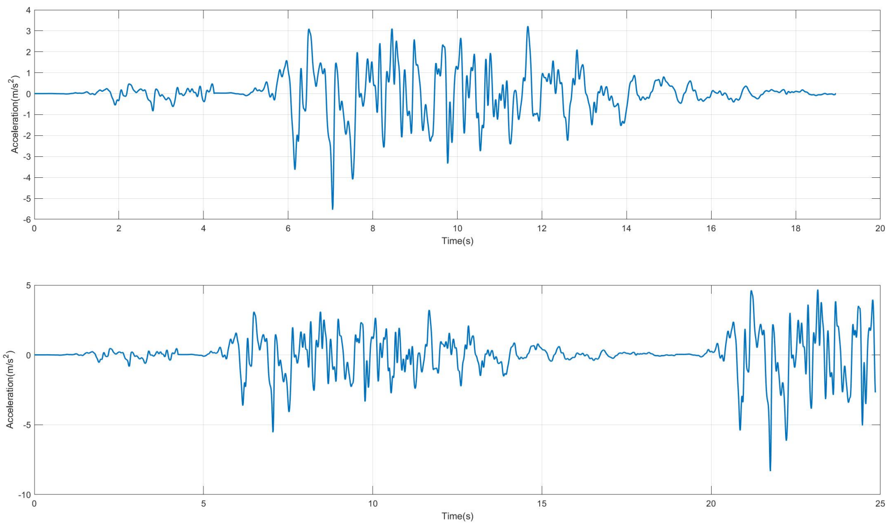

(c) D456

Figure 6.1. Accelerograms

6.1.1 D04

Test D04 refers to a frequent accelerogram, meaning it is 15% of the design earthquake. It is important to note that the location at which the TMD is located moves less than $1cm$. Even under such circumstances, the TMD can dissipate energy as it reduces the response of the building. Both, the structure and the TMD work in a linear way during this excitation as seen from their hysteretic curves. The performance indices are summarized in Table 6.3, and the behavior is presented in Figure 6.2.

Table 6.3. Performance Indices D04

Earthquake	Response Index						
	J_1	J_2	J_3	J_4	J_5	J_6	J_7(m)
D04	0.902	1.063	1.028	0.809	0.828	0.856	0.028

6.1.2 D05

The TMD can reduce the structure's response in terms of displacement in the studied direction. However, its effectiveness under this type of ground motion will be studied in Section 6.2 to avoid particularising the results to this ground motion.The performance indices are summarized in Table 6.4, and the behavior is presented in Figure 6.3.

Table 6.4. Performance Indices D05

Earthquake	Response Index						
	J_1	J_2	J_3	J_4	J_5	J_6	J_7(m)
D05	0.782	0.942	1.187	0.7246	0.950	1.069	0.195

Under the design earthquake the effects of introducing the TMD in the structure are more evident. Its displacement time history is significantly modified reducing both peak and RMS of the response of the roof. From the hysteretic curve, the shear force time history and the performance indices J_2 and J_5 a reduction in the shear forces is not present. Yet from the reduction in the displacements, a more compact hysteretic curve is attained. It is also noteworthy that the TMD did not achieve the design displacement at the moment in which the structure did.

6.1.3 D45

This accelerogram consists of D05 preceded by the initial 4.3 seconds of the D04.The performance indices are summarized in Table 6.5, and the behavior is presented in Figure 6.4.

Table 6.5. Performance Indices D45

Earthquake	Response Index						
	J_1	J_2	J_3	J_4	J_5	J_6	J_7(m)
D45	0.791	0.955	1.074	0.752	0.952	0.98	0.186

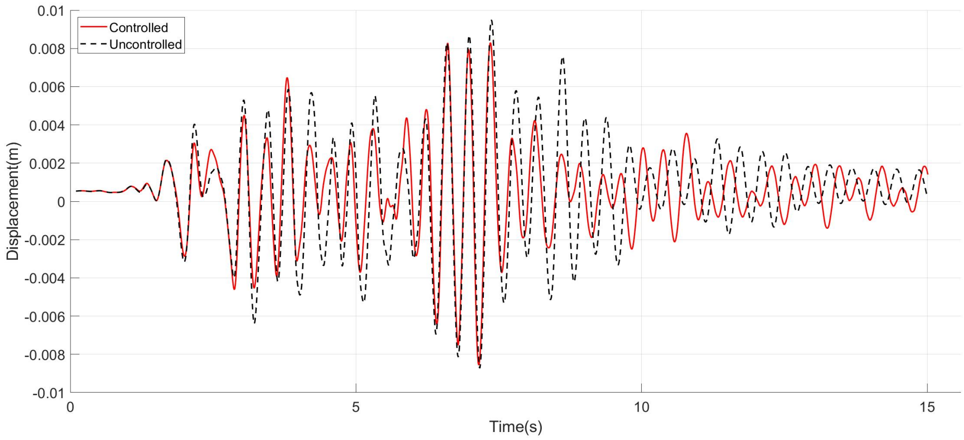

(a) Roof Displacements

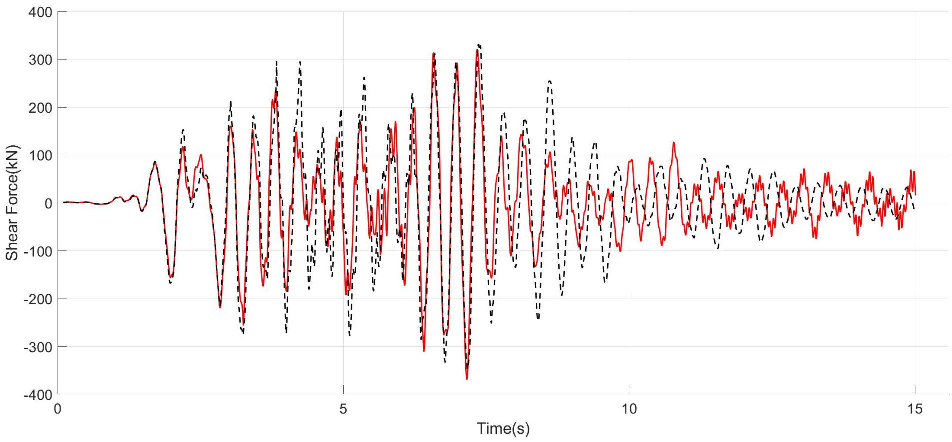

(b) Shear Forces at the base

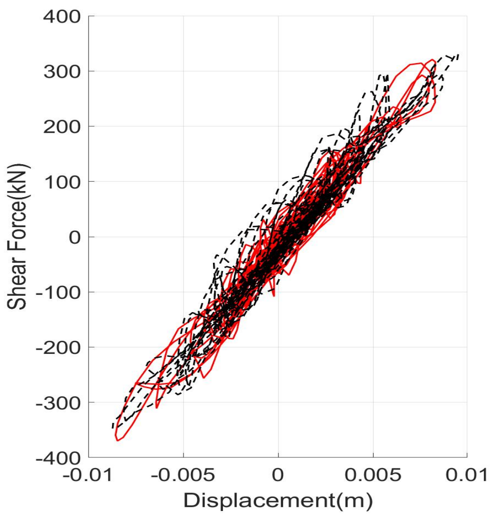

(c) Structural Hysteretic Curve

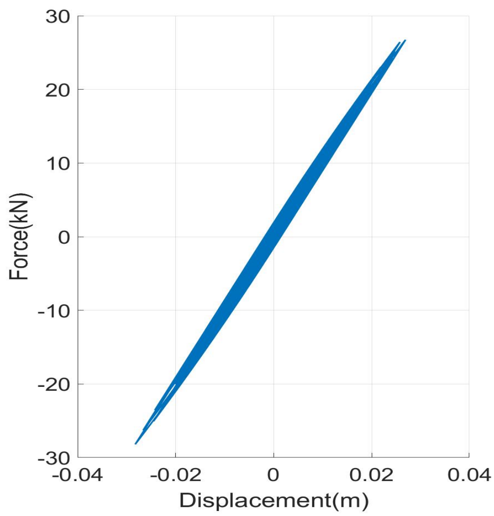

(d) TMD Hysteretic Curve

Figure 6.2. D04

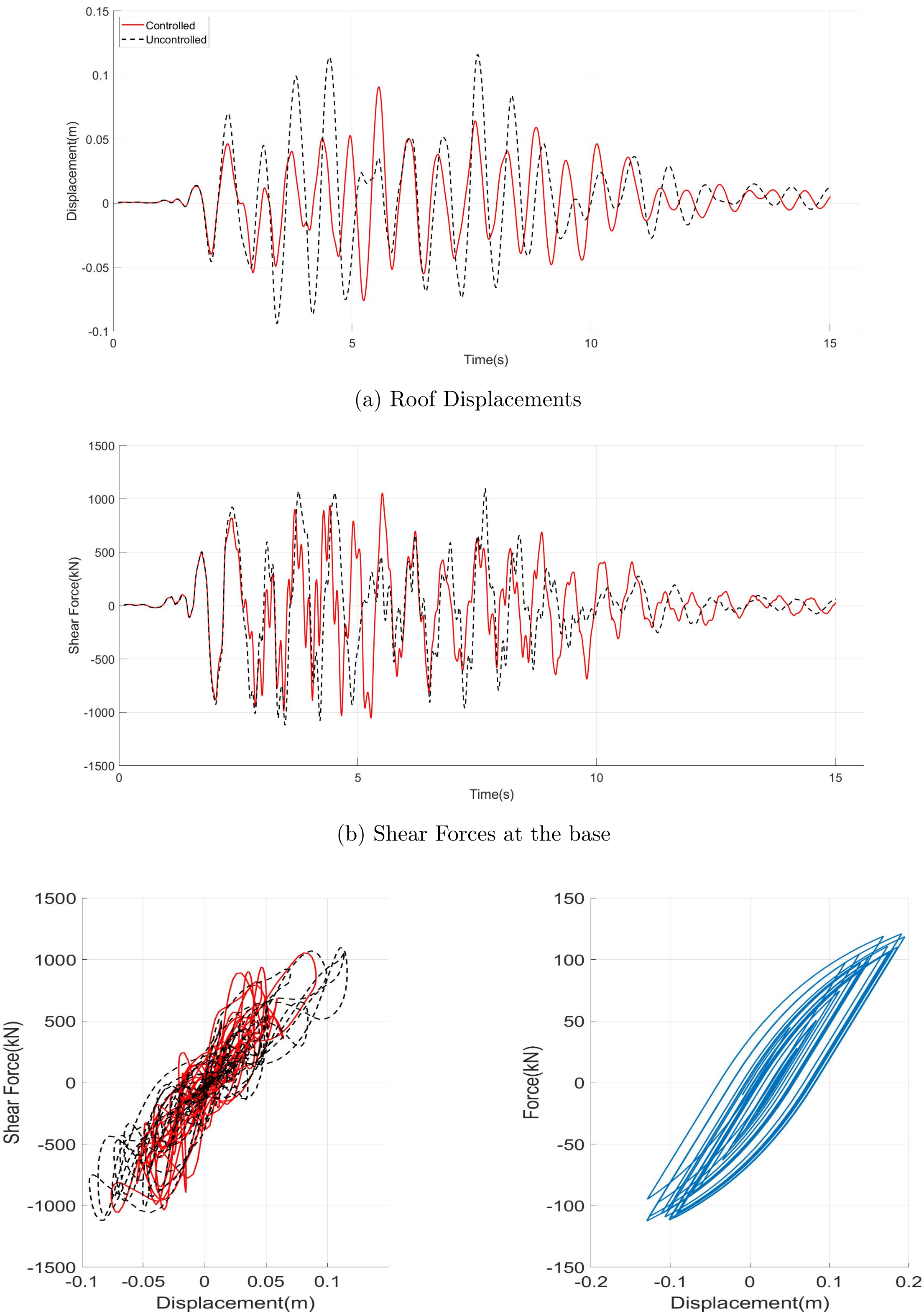

(a) Roof Displacements

(b) Shear Forces at the base

(c) Structural Hysteretic Curve

(d) TMD Hysteretic Curve

Figure 6.3. D05

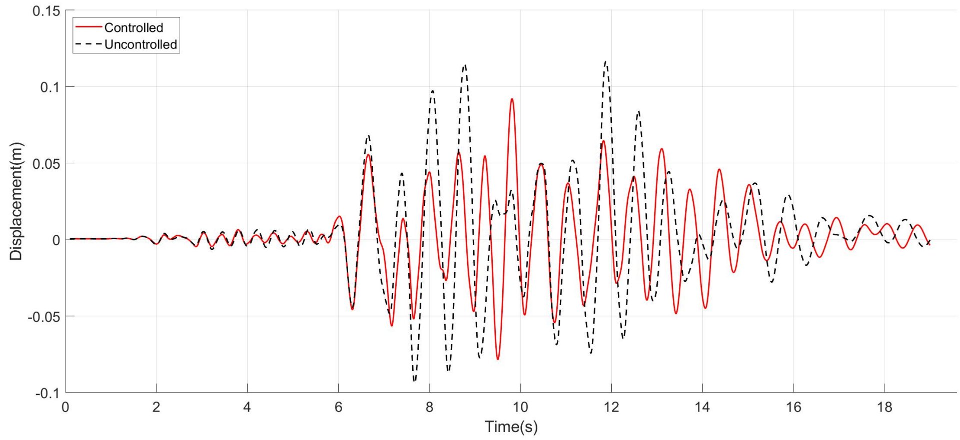

(a) Roof Displacements

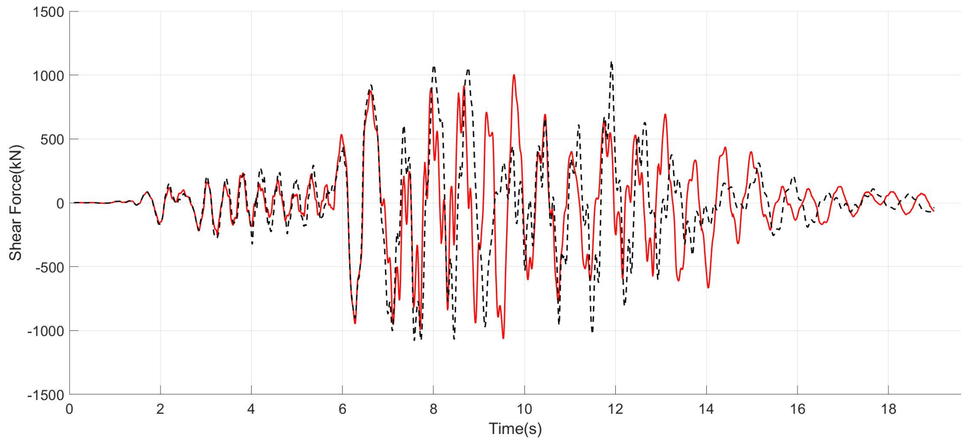

(b) Shear Forces at the base

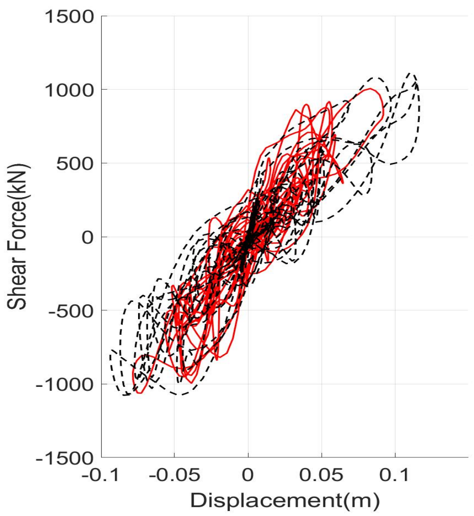

(c) Structural Hysteretic Curve

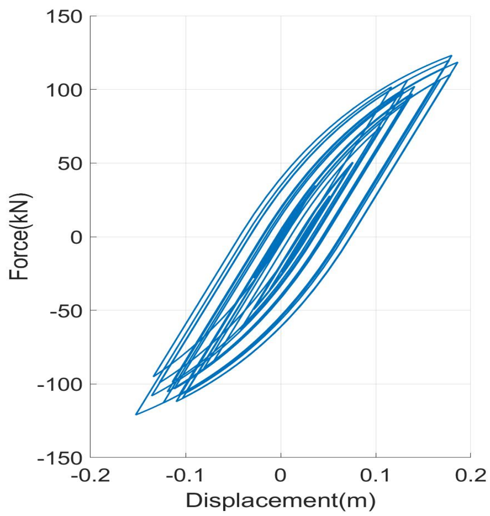

(d) TMD Hysteretic Curve

Figure 6.4. D45

The behavior of the uncontrolled structure subjected to the consecutive accelerograms is different from that when it is subjected only to test D05. There are several reason for which this may have happened. For instance, damage in the real structure or the fact that that by the beginning of the design earthquake the structure was already moving. Under any of those scenarios, the damper was still able to attenuate the response of the building, again reducing its displacement but not the shear forces. In this case the TMD did not reach the design displacement.

6.1.4 D456

Test D456 is the accelerogram that the experimental structure suffered, leading to the results shown in [28] . As D45, it has the initial 4.5s of the service accelerogram proceeded by the design accelerogram. Once the design accelerogram is done, test D06, representing 1.5 times the design accelerogram, is performed. The accelerogram is stopped at the moment in which the test was concluded. The performance indices are summarized in Table 6.6, and the behavior is presented in Figure 6.5.

Table 6.6. Performance Indices D456

Earthquake	Response Index						
	J_1	J_2	J_3	J_4	J_5	J_6	J_7(m)
D456	0.743	0.886	0.862	0.783	0.961	0.969	0.330

The code implemented for this analysis is not able to reproduce steel failure so it would not be able to demonstrate the structural collapse. Therefore, if the accelerogram D456 were to be continued to the end, an equilibrated solution would be found for every step, yet such states would not represent the actual behaviour of the structure. It is interesting to note that the damper reduces the peak displacement in the same order of magnitude for this type of earthquake than to the design one. This is considering that for this ground motion the structure had already suffered damage from the previous ones. It is important to note that the controlled structure, at the point in which the test was stopped, reached maximum displacement values 1.5 times greater than the uncontrolled structure under the design test while the uncontrolled case had a displacement twice as big than that of the design earthquake.

It is also important to note that even when the structure deepens into its nonlinear state the damper is still able to work accordingly. When the structure is subjected to this ground motion, the damper is still able to reduce the response, in terms of displacements, in a good manner. However to do so, it requires a displacement greater than the designed one, as the structural displacement is greater than anticipated. In this hysteretic curve the plastic deformation of the BW element is clearly displayed. After two important strokes, the element starts vibrating in a location different from the initial one. This aspect would need to be considered for a real damper as more space should be provided for it to dissipate energy.

Regarding the displacements of the remaining floors, the uncontrolled structure is above the Life Safety criteria under the design ground motion of the recommendations in FEMA 356, [34], for the maximum drift in walls, reported as 1%. The criteria for walled structures is considered, as there is no recommendation for dual systems, and

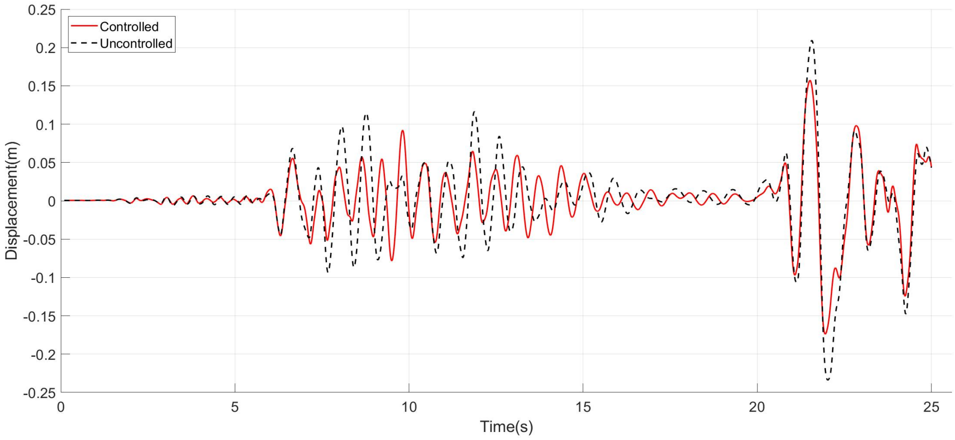

(a) Roof Displacements

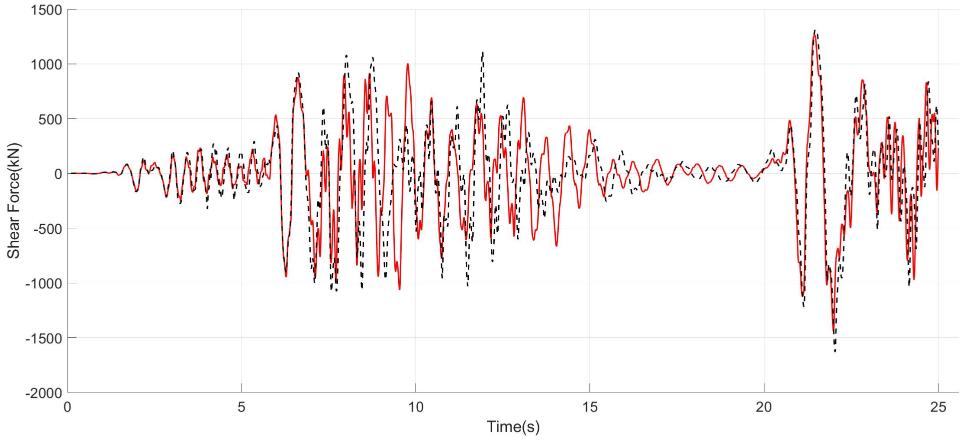

(b) Shear Forces at the base

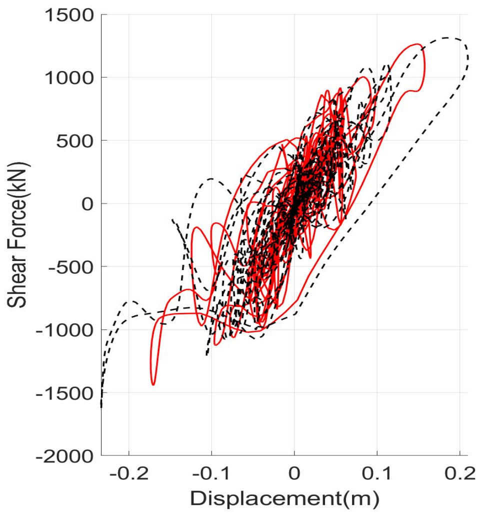

(c) Structural Hysteretic Curve

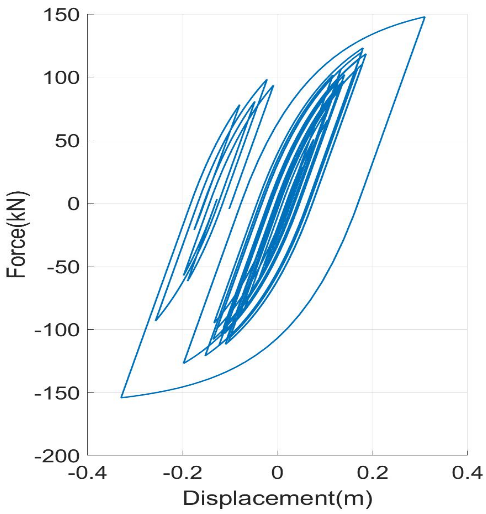

(d) TMD Hysteretic Curve

Figure 6.5. D456

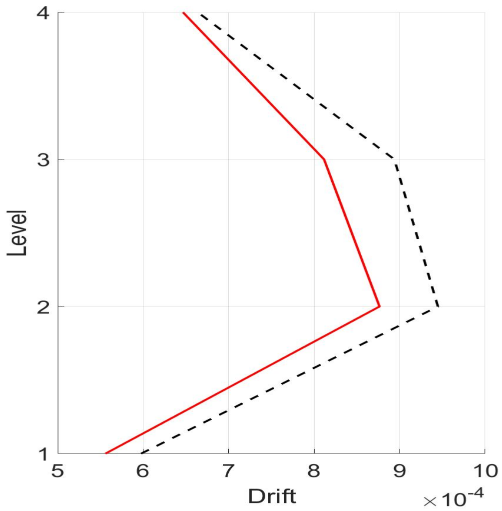

(a) D04

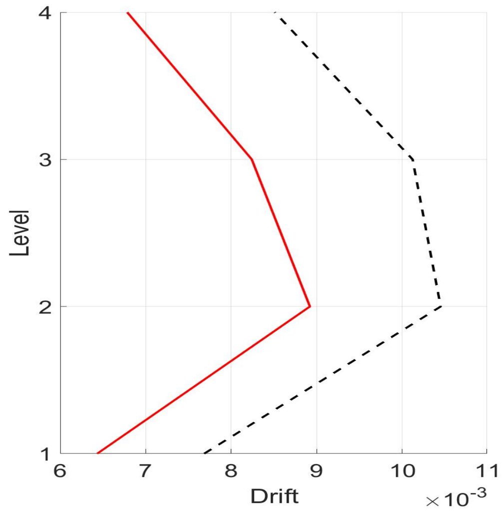

(b) D05

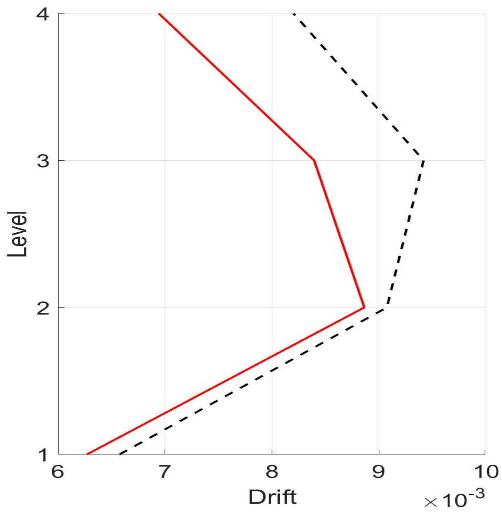

(c) D45

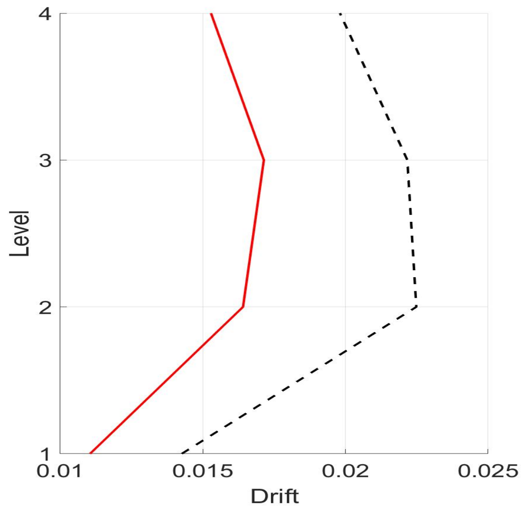

(d) D456

the coupled walls take most of the horizontal load of the structure. However, that is different from the uncontrolled situation, as the controlled structure can remain below that threshold.

Interestingly, the TMD kept the drifts at the same level in both tests D05 and D45. Nevertheless, the uncontrolled structure performed differently. In it, the drifts were reduced. Thus, showing that the behaviour of the structure was indeed affected by the previous earthquake. The roof displacements, however, were kept almost constant in both cases.

It is very important to understand the behaviour of the drifts for test D456. In the uncontrolled structure, the drifts are above the limits recommended in [34] of 2% as collapse prevention limit of walls. Yet, the use of the TMD could avoid collapse or delay it as at the time in which the test was stopped the structure could still resist an increment in loads. This is in accordance to the behavior shown in 6.5 by means of the structural hysteretic cycle.

6.2 Natural accelerograms

A series of eight-scaled accelerograms were used to determine the effectiveness of the TMD. They were matched with a EC8 spectrum with a PGA of $0.4g$, soil calss B and structural damping of 5%. This is the same spectrum used for matching the Kobe ground motion used in the PSD test of the building [28] and shown in Figure 4.2.

This demonstrates that the method is not optimized for a particular accelerogram but for the site response spectrum. The response spectrum used for scaling the accelerograms corresponded to the design response spectrum of the building and for which test D05 was scaled. The matched response spectrum of the accelerograms and their mean are presented in Figure 6.7. The accelerograms to which the model was subjected are shown in Figure 6.8.

The behavior of the uncontrolled structure is summarized in Table 6.7.

Table 6.7. Uncontrolled Structure Natural Accelerograms

Earthquake	Response Index Component					
	$J_1(m)$	$J_2(kN)$	$J_3(m/s^2)$	$J_4(m)$	$J_5(kN)$	$J_6(m/s^2)$
Chalfant	0.197	1180.286	9.289	0.053	369.412	2.655
Chi-Chi	0.097	1063.792	9.470	0.012	156.903	1.142
Erzincan	0.159	1090.676	8.898	0.036	336.526	2.347
Friulli	0.132	1225.124	9.409	0.029	274.004	1.963
Imperial Valley	0.156	1258.762	10.824	0.031	302.861	2.332
Kobe	0.177	1252.272	9.855	0.035	280.009	2.186
Loma Prieta	0.138	1276.549	12.542	0.028	258.233	2.070
Northridge	0.138	1255.761	10.318	0.047	371.781	2.662
Average	0.149	1200.403	10.076	0.034	293.716	2.170

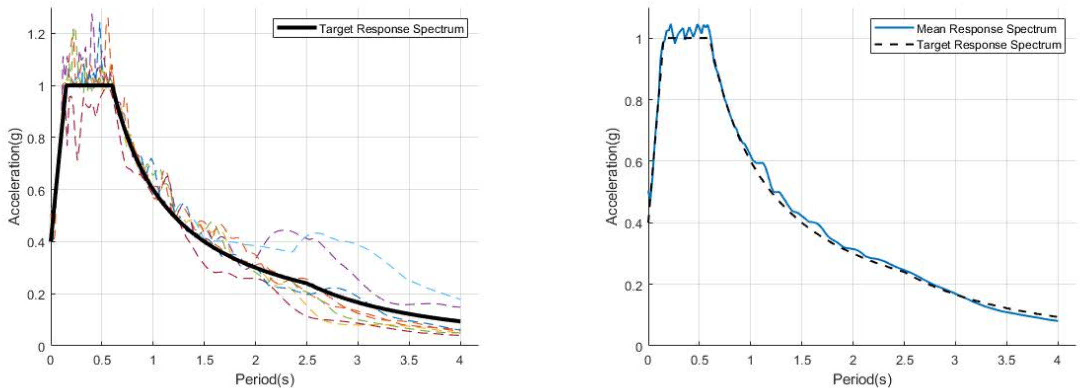

(a) Matched (b) Mean

Figure 6.7. Matched Response Spectrum

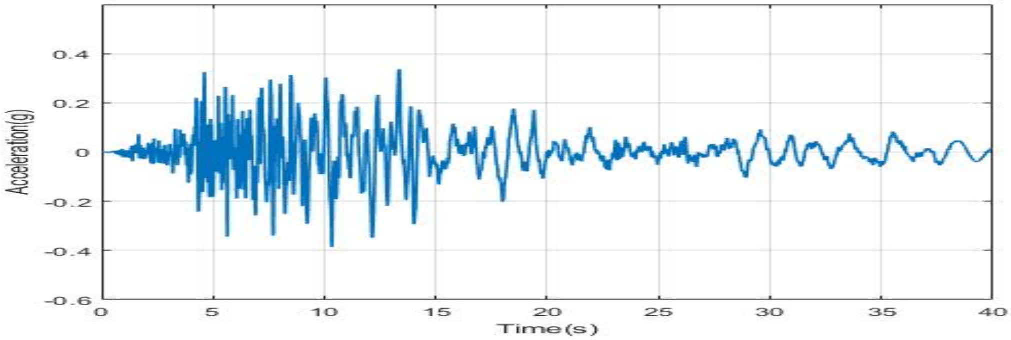

(a) Chalfant

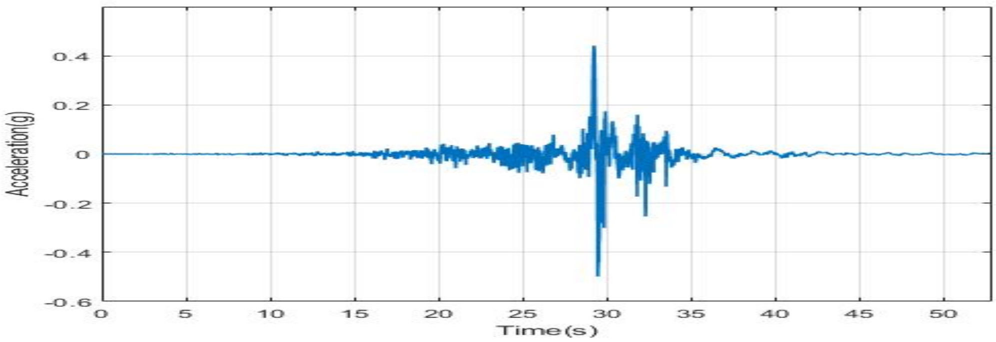

(b) Chi Chi

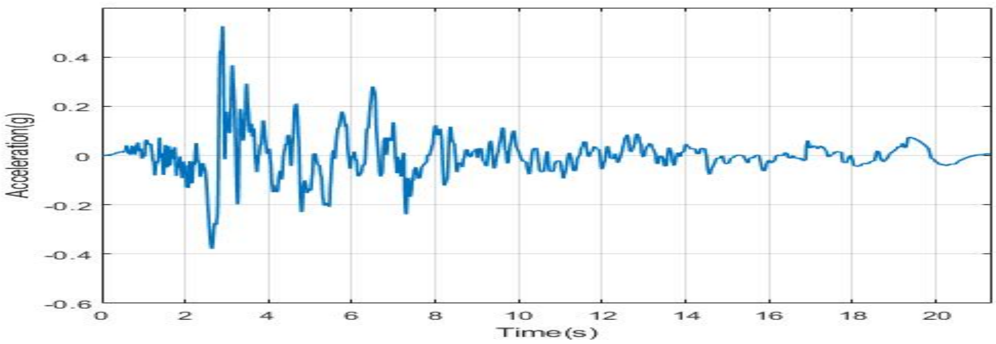

(c) Erzincan

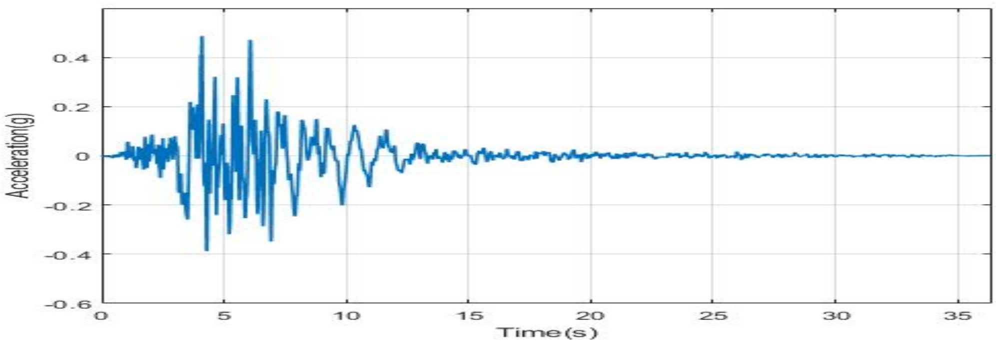

(d) Friulli

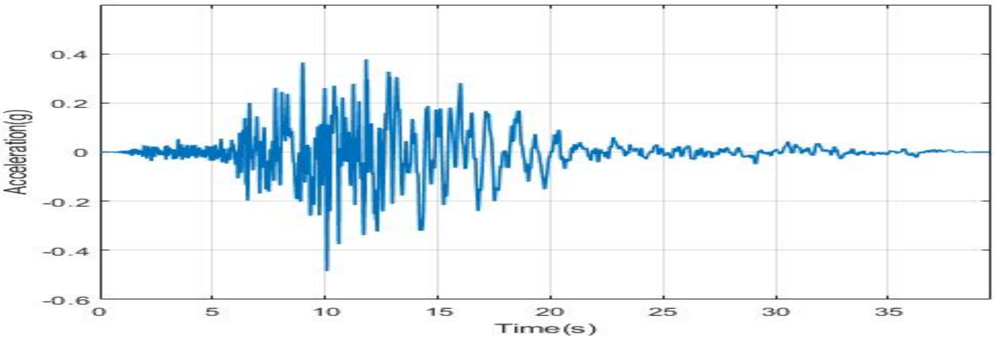

(e) Imperial Valley

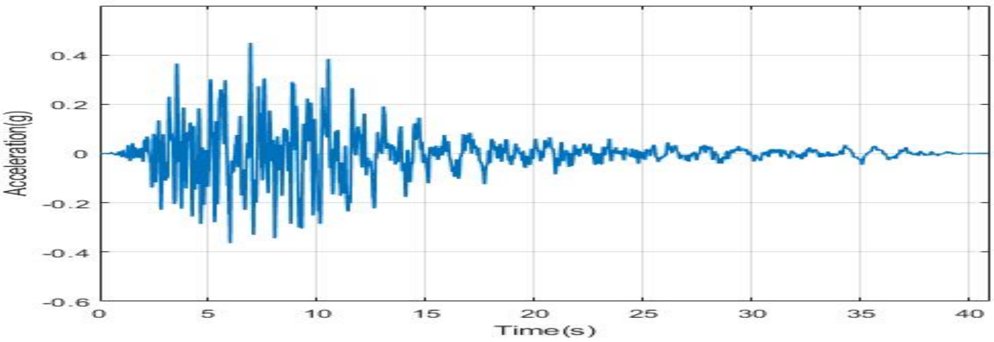

(f) Kobe

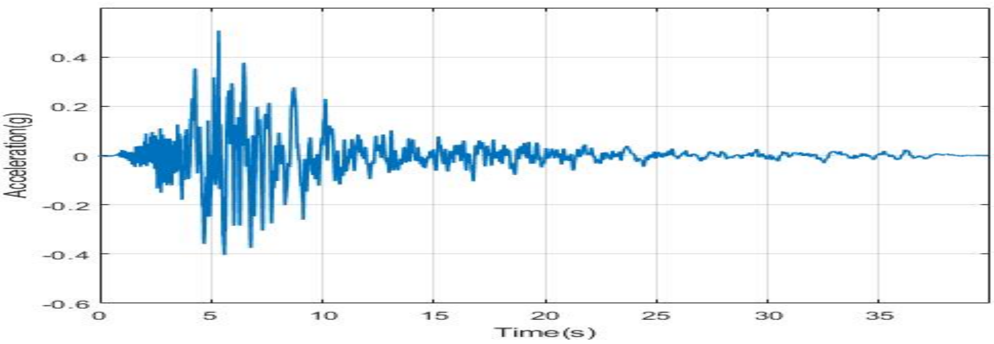

(g) Loma Prieta

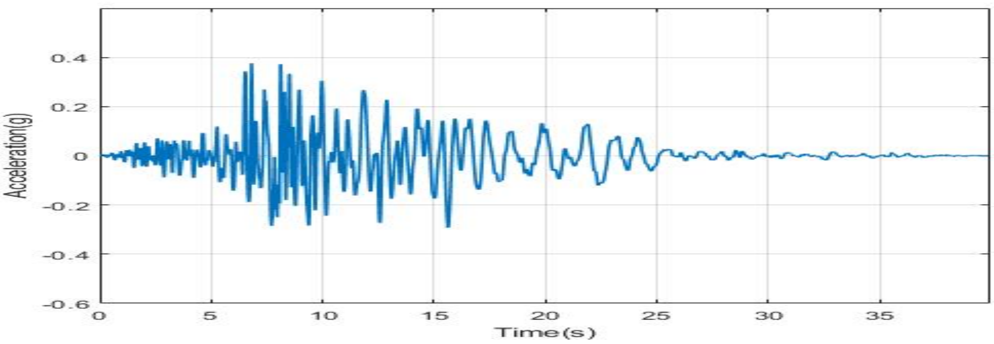

(h) Northridge

Figure 6.8. Accelerograms

6.2.1 Chalfant

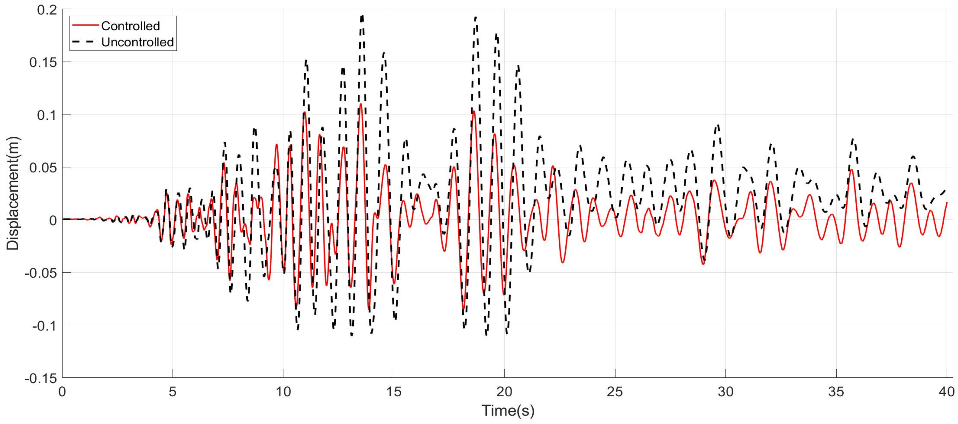

(a) Roof Displacements

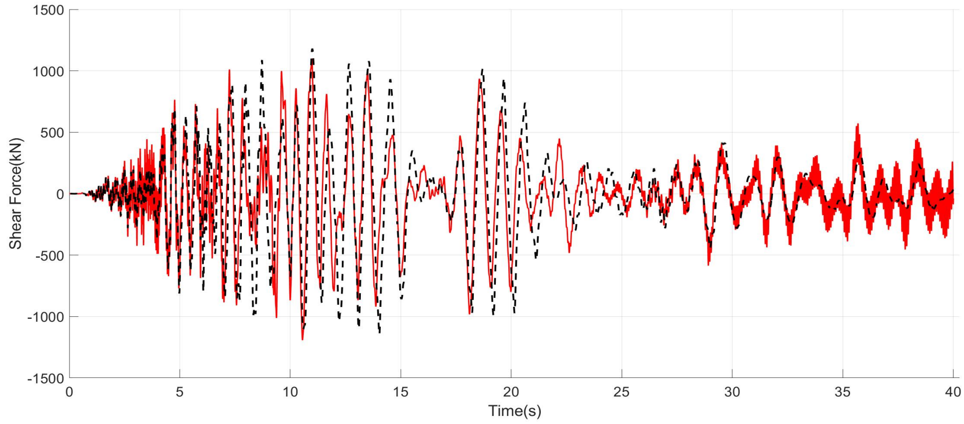

(b) Shear Forces at the base

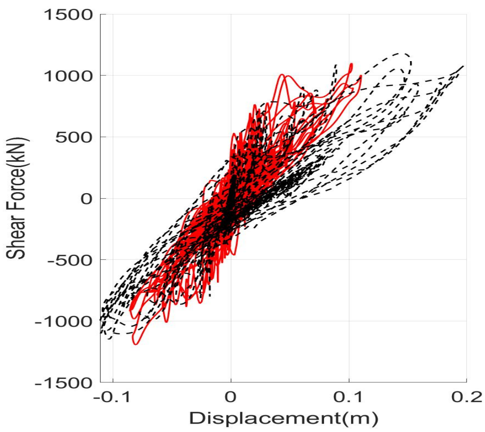

(c) Structural Hysteretic Curve

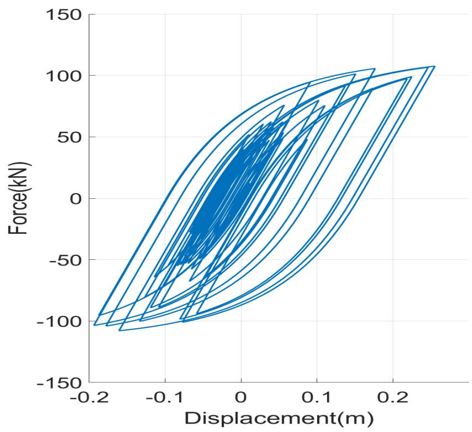

(d) TMD Hysteretic Curve

Figure 6.9. Chalfant

6.2.2 Chi-Chi

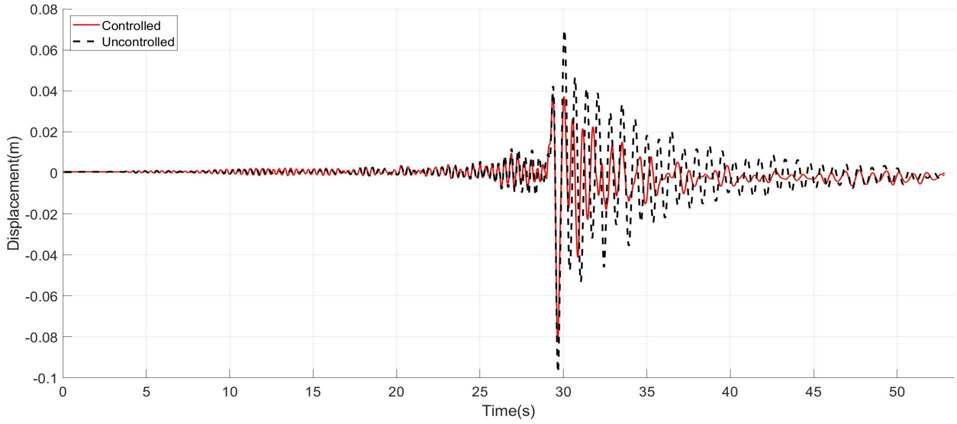

(a) Roof Displacements

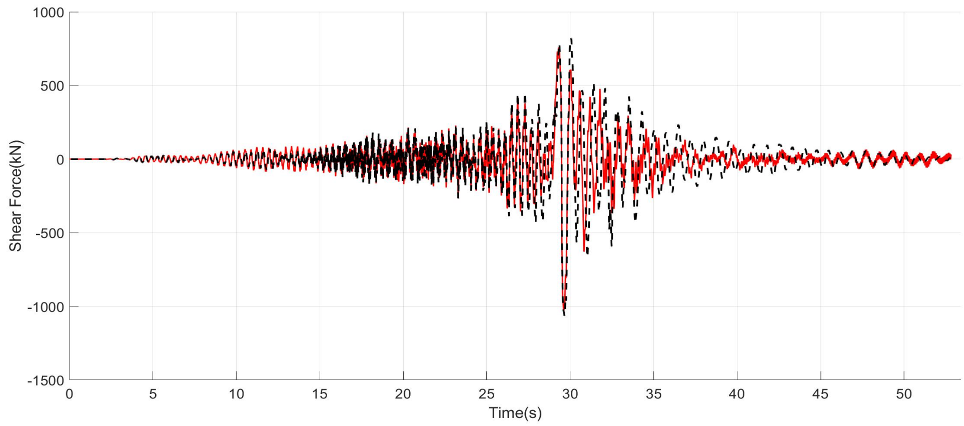

(b) Shear Forces at the base

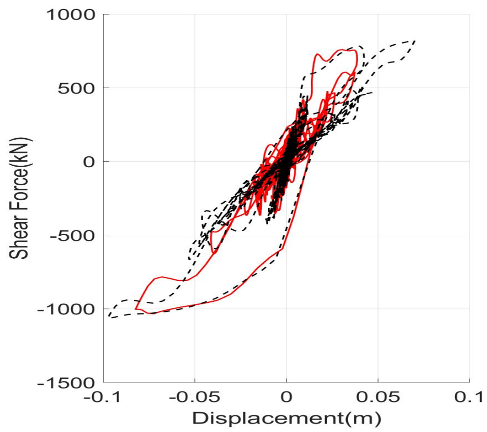

(c) Structural Hysteretic Curve

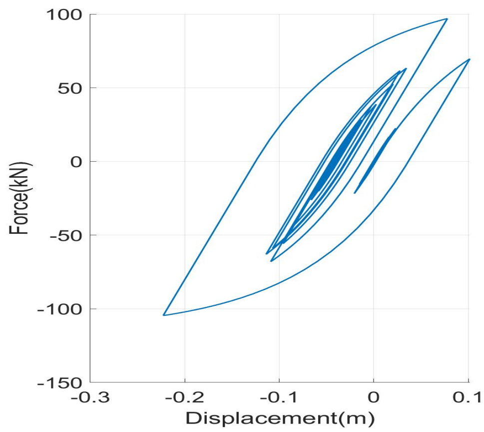

(d) TMD Hysteretic Curve

Figure 6.10. Chi Chi

6.2.3 Erzincan

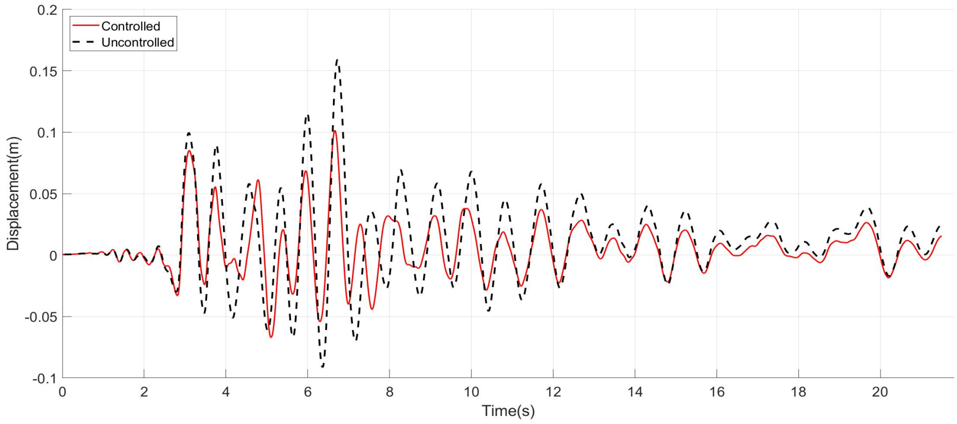

(a) Roof Displacements

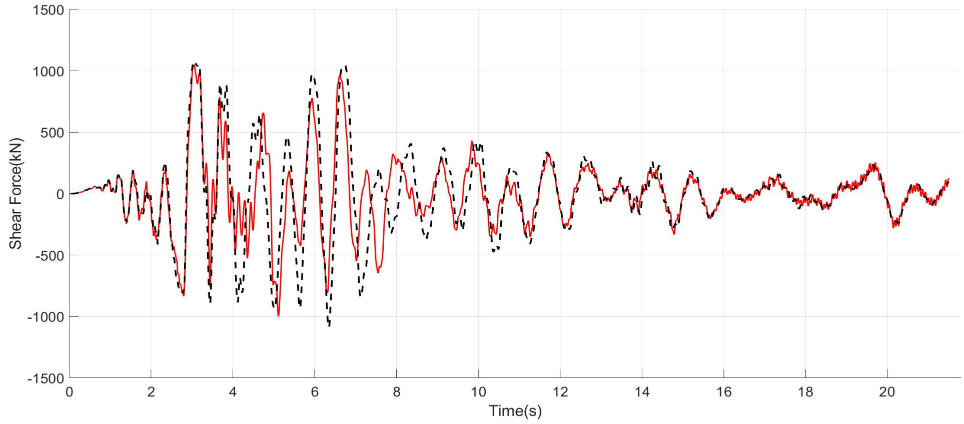

(b) Shear Forces at the base

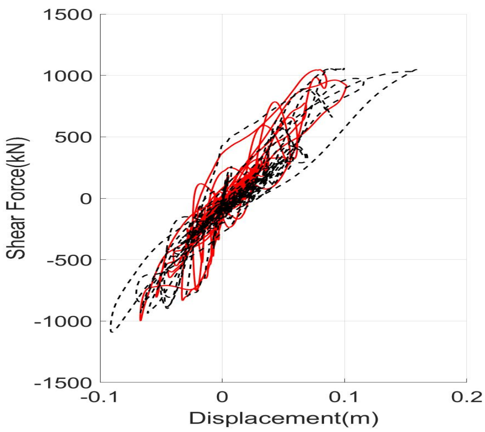

(c) Structural Hysteretic Curve

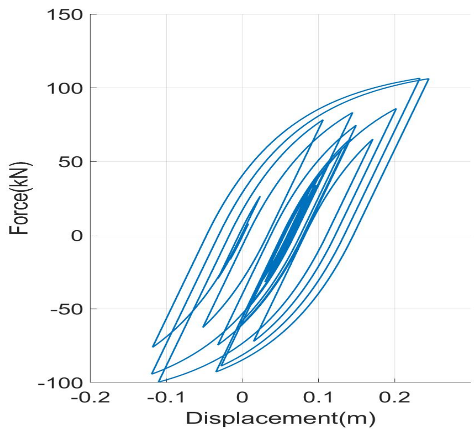

(d) TMD Hysteretic Curve

Figure 6.11. Erzincan

6.2.4 Friulli

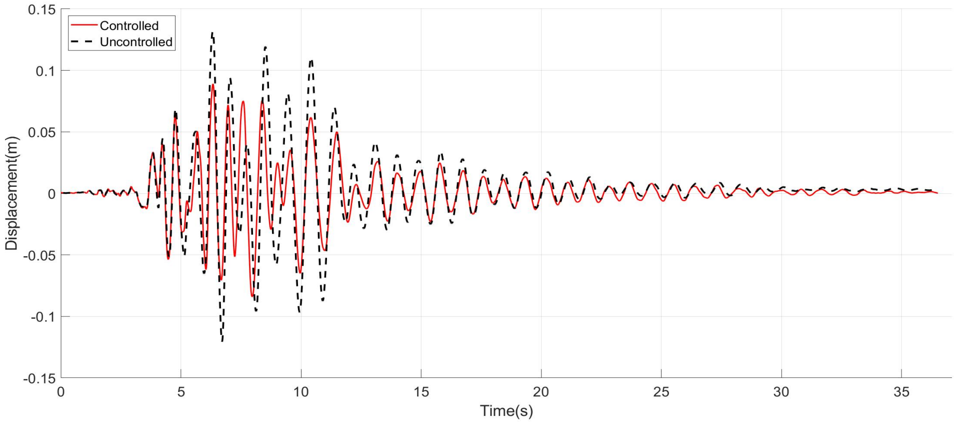

(a) Roof Displacements

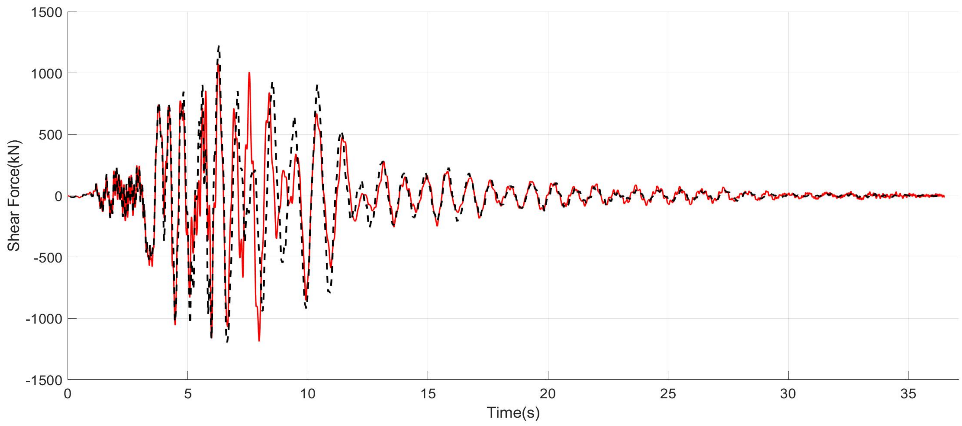

(b) Shear Forces at the base

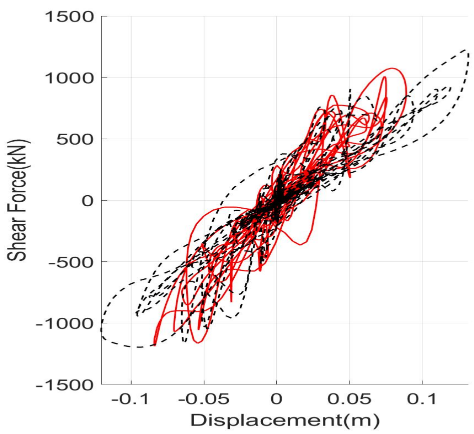

(c) Structural Hysteretic Curve

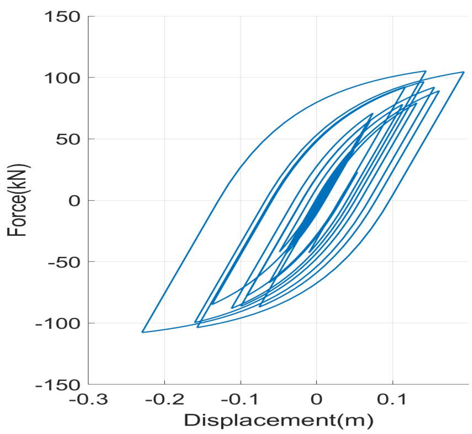

(d) TMD Hysteretic Curve

Figure 6.12. Friulli

6.2.5 Imperial Valley

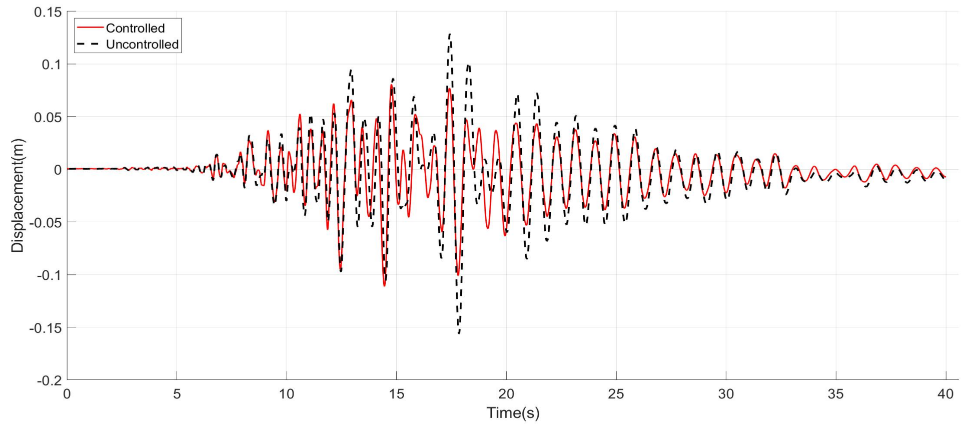

(a) Roof Displacements

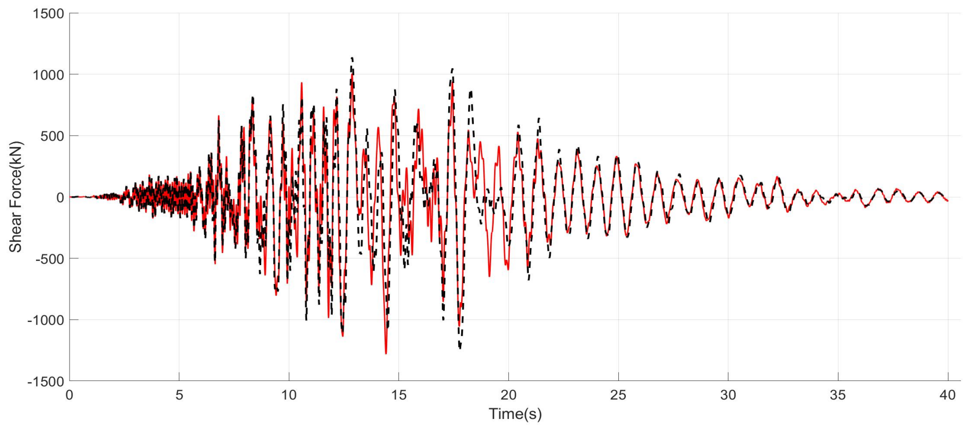

(b) Shear Forces at the base

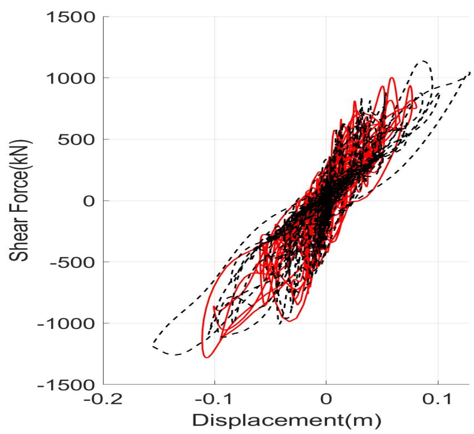

(c) Structural Hysteretic Curve

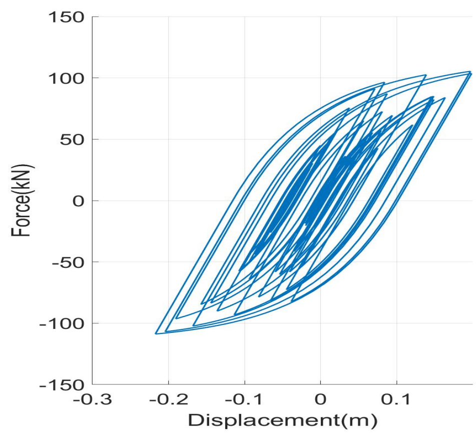

(d) TMD Hysteretic Curve

Figure 6.13. Imperial Valley

6.2.6 Kobe

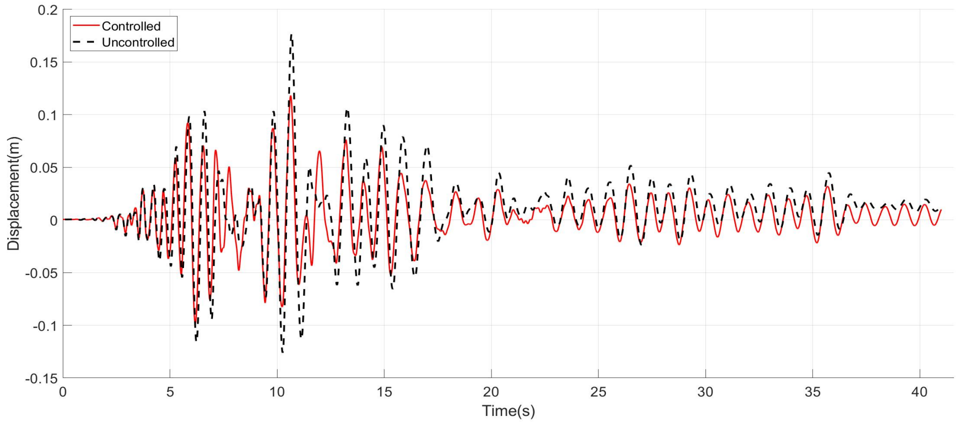

(a) Roof Displacements

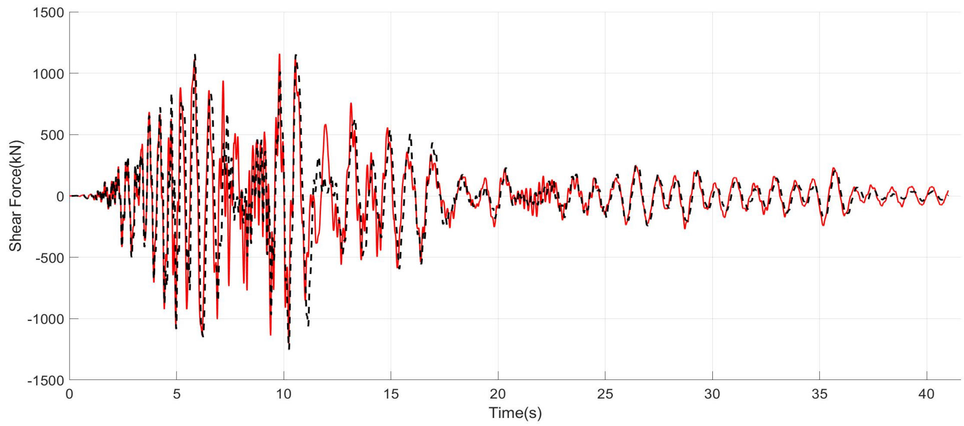

(b) Shear Forces at the base

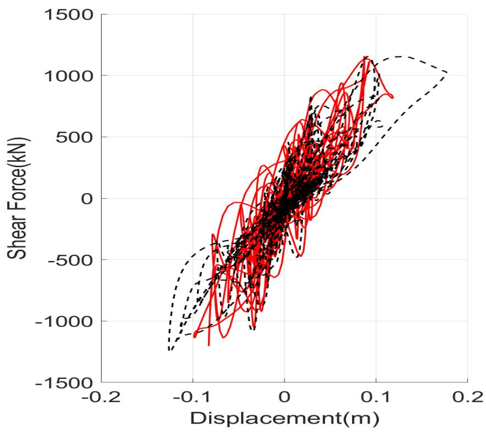

(c) Structural Hysteretic Curve

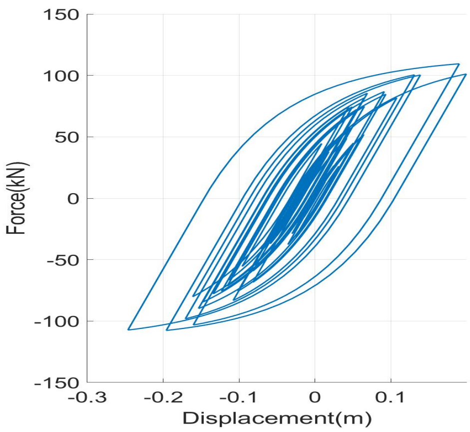

(d) TMD Hysteretic Curve

Figure 6.14. Kobe

6.2.7 Loma Prieta

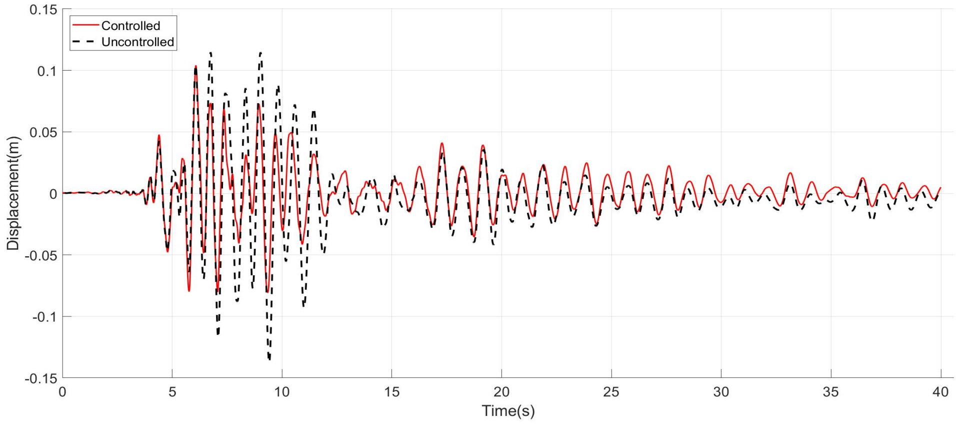

(a) Roof Displacements

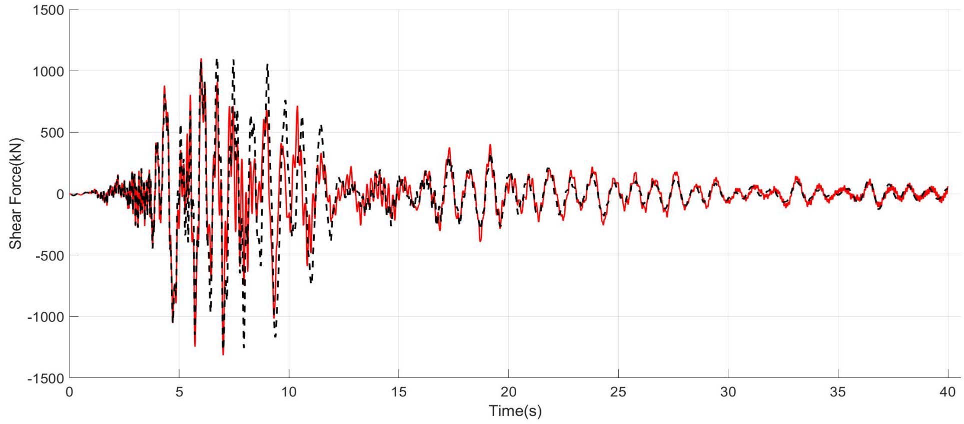

(b) Shear Forces at the base

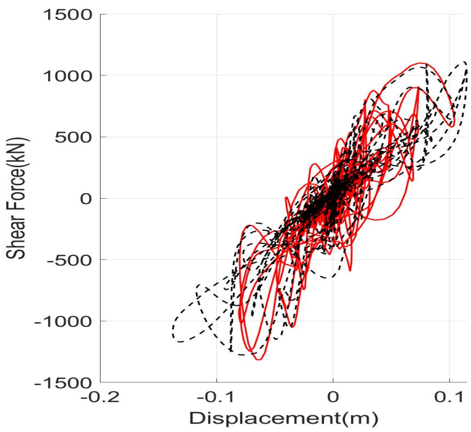

(c) Structural Hysteretic Curve

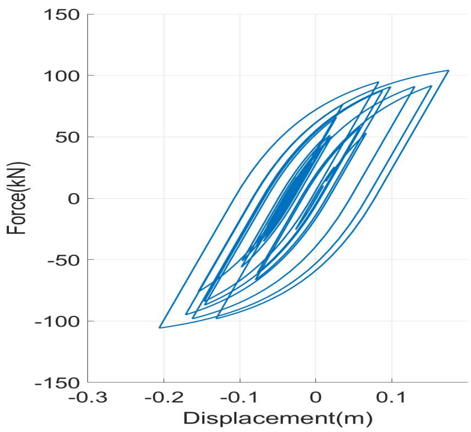

(d) TMD Hysteretic Curve

Figure 6.15. Loma Prieta

6.2.8 Northridge

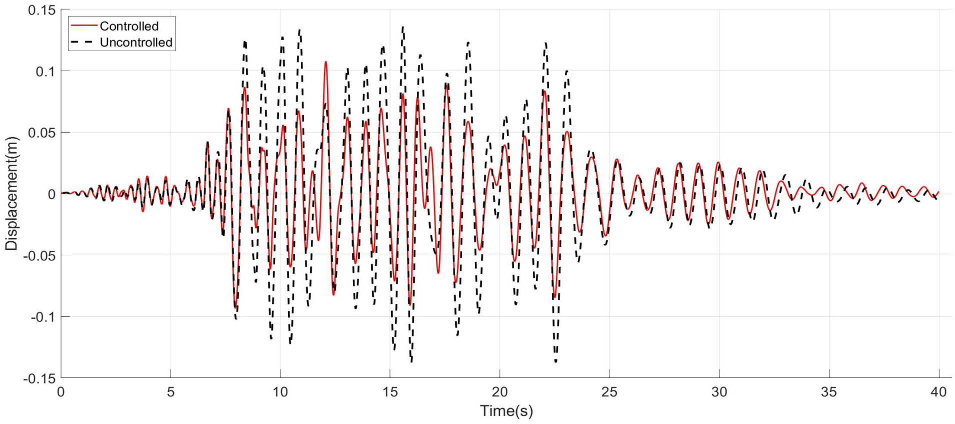

(a) Roof Displacements

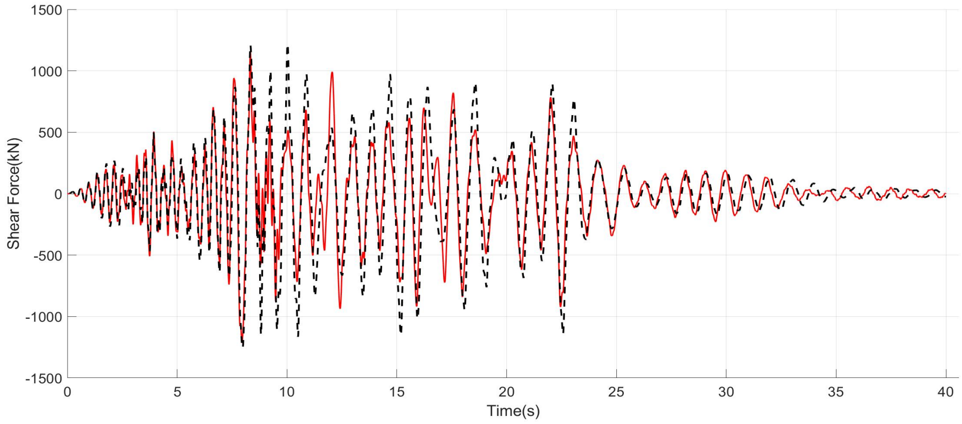

(b) Shear Forces at the base

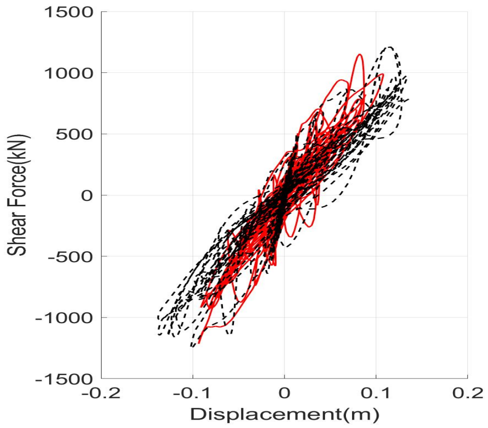

(c) Structural Hysteretic Curve

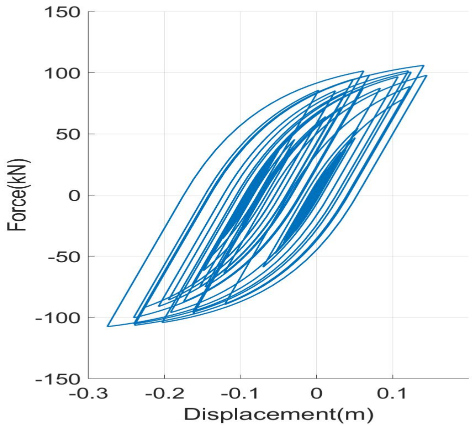

(d) TMD Hysteretic Curve

Figure 6.16. Northridge

6.2.9 Comparison

As seen from Figures 6.9- 6.16 that there is a considerable reduction in the roof displacement and the drifts in the structure. However, it is also evident that the shear forces of the structure remain constant. The drifts in the structure were considerably reduced, in many cases remaining below the FEMA 356 threshold of Life Safety, which never happened in the uncontrolled case. In Table 6.8 the peak displacements of the controlled and uncontrolled cases are compared alongside the Performance index J_1. The definition of the performance indices is available in Table 6.1

Table 6.8. Peak Displacements

Earthquake	Peak displacement		
	Uncontrolled (m)	Controlled (m)	J_1
Chalfant	0.197	0.110	0.560
Chi-Chi	0.097	0.083	0.847
Erzincan	0.159	0.102	0.638
Friulli	0.132	0.089	0.676
Imperial Valley	0.156	0.111	0.712
Kobe	0.177	0.118	0.668
Loma Prieta	0.138	0.104	0.757
Northridge	0.138	0.108	0.782
Average	0.149	0.103	0.705

From Table 6.8 it can be seen that the average response of the uncontrolled structure was greater than the one anticipated through the performance point of the pushover curve shown in Section 5 . Nevertheless, the displacement of the real structure was limited to the one expected and shown in the same section by using a mass ratio of $\mu = 0.05$. Thus, showing that the TMD worked more efficiently than anticipated. This was expected as the additional equivalent damping to the main structure was computed considering a linear TMD model. Ergo, analysis on the equivalent damping depending on the mass ratio for non linear TMD are requiered in the near future.

Under the suite of selected accelerograms, the TMD reduced the average roof displacement by $4.6cm$. Regarding the displacements, the greatest reduction was when subjected to Chalfant ground motion, where a reduction of almost 50% was obtained. On the other hand, the TMD was less effective under Chi Chi ground motion, where a reduction of 15% was reached. In this last case, the peculiarity of the ground motion could be the reason for the reduction in the effectiveness. In it he response of the TMD resembled more the response under a blast than to an earthquake. Therefore, the parameters are not optimal for this type of loading and so they would have to be redesigned accordingly. Thus demonstrating that the optimal design parameters for these two types of loading are different and that the hysteretic TMD here design could provide low effectiveness on reducing the peak displacements under this type of excitation.

Concerning the behavior of the other floors in the building, from Figure 6.17 show the adimensional interstorey drifts of the structure at the different levels over the

Table 6.9. Performance Indices Natural Accelerograms

Earthquake	Performance Index						
	J_1	J_2	J_3	J_4	J_5	J_6	J_7(m)
Chalfant	0.560	1.010	0.962	0.543	0.865	0.922	0.255
Chi-Chi	0.847	0.971	0.854	0.625	0.809	0.856	0.223
Erzincan	0.638	0.961	0.923	0.645	0.811	0.822	0.245
Friulli	0.676	0.970	1.042	0.696	0.902	0.926	0.230
Imperial Valley	0.712	1.018	1.007	0.771	0.926	0.954	0.217
Kobe	0.668	0.961	1.197	0.748	0.990	1.030	0.247
Loma Prieta	0.757	1.030	0.987	0.693	0.851	0.895	0.206
Northridge	0.782	0.967	0.914	0.632	0.815	0.795	0.275
Average	0.705	0.986	0.986	0.669	0.871	0.900	0.237

ground motions considered. It is evident that a considerable reduction in such values is obtained by adopting the TMD in the structure. Drifts, as displacements, were reduced in average 30% at each floor. They followed very similar behavior than the roof displacements, being the most effective under the Chalfant ground motion and least effective in Chi Chi.

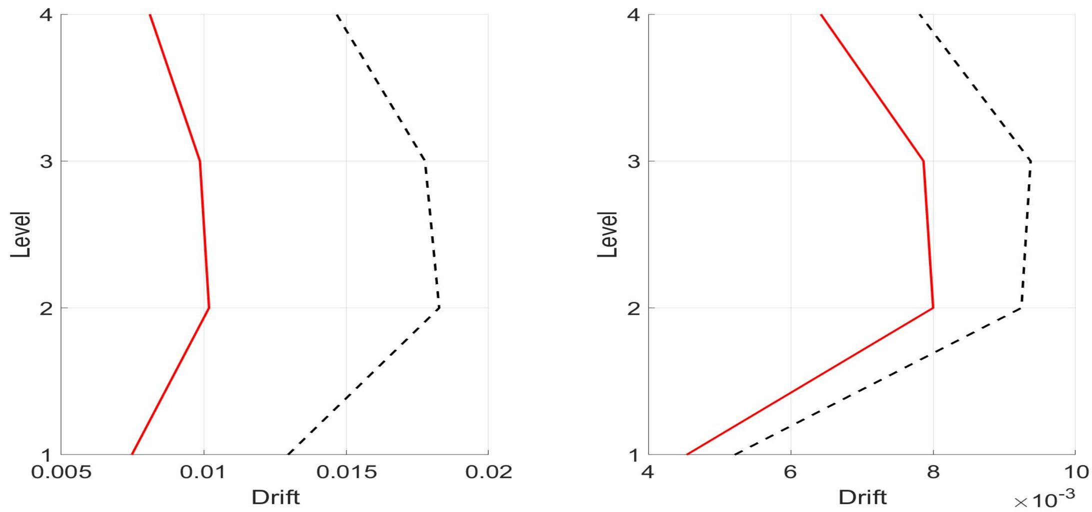

(a) Chalfant (b) Chi Chi

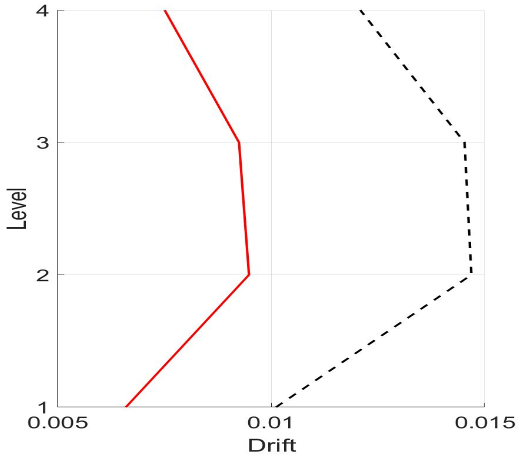

(c) Erzincan

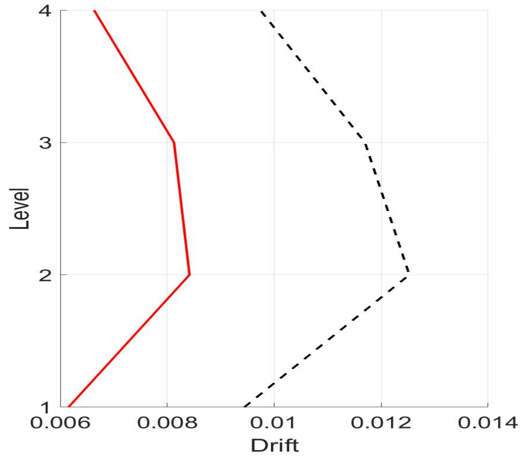

(d) Friulli

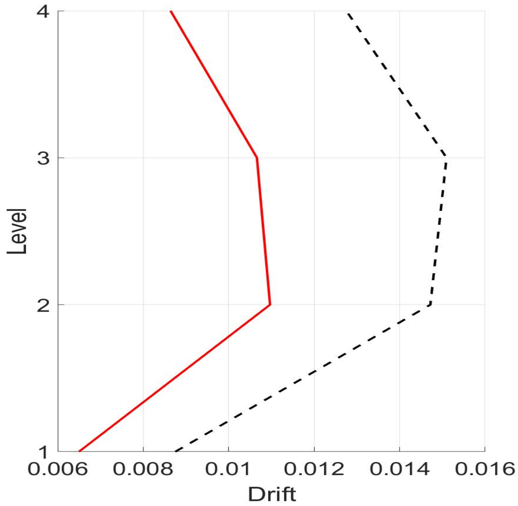

(e) Imperial Valley

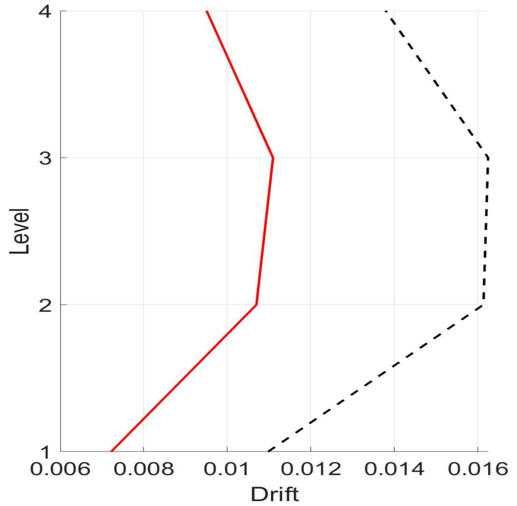

(f) Kobe

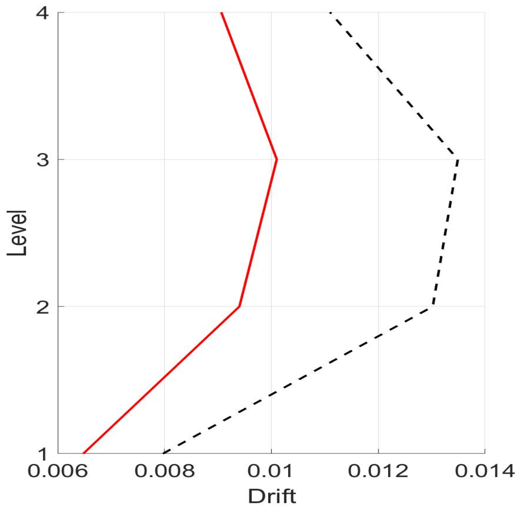

(g) Loma Prieta

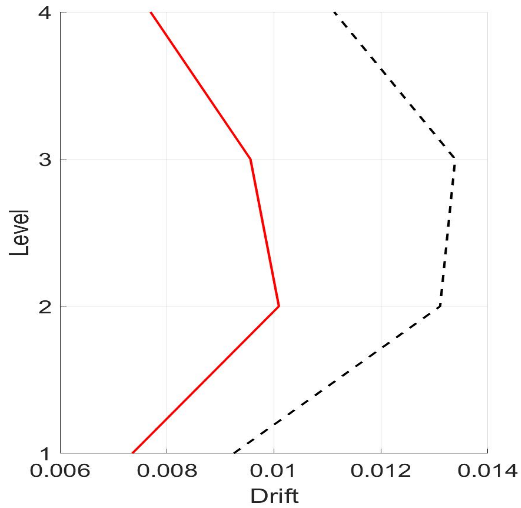

(h) Northridge

Figure 6.17. Drifts

The hysteretic behavior of the building is considerably improved when the TMD is introduced. For instance, in Figure 6.9, the reduction in the nonlinear deformations is evident. This is repeated under all of the ground motions but one, Chi Chi. Due to the peculiarity of this ground motion, the damper does not attenuate the response of the structure until the big displacement at around $30sec$. From that point the damper is able to reduce the roof displacement by working in the way it is intended to. As a matter of fact, it manages to mitigate the dynamic response of the building rather fast.

The TMD improved the global behavior of the building in all ground accelerations considered. In all of them, the RMS of the displacements and accelerations were reduced. The damper is far more efficient reducing the displacements in the structure than the relative accelerations it is being subjected to due to the motion. However, under some ground motions, the peak acceleration in the roof was increased when introducing the TMD.

It is important to note that the average stroke value, Performance index J_7, is equal to that estimated in Chapter 5. However, as stated previously, greater values were be obtained due to the different displacements of the roof. Yet, under none of the ground motions considered a stroke of $30cm$ was obtained.

In terms of shear forces at the base, the structure would have to withstand approximately the same peak forces even if a TMD is added. Nevertheless, a reduction in the RMS of the forces was also obtained. This means, that if the structure were to yield, the introduction of the TMD would not impede such yielding. Yet the plastic displacements that it would undergo after such yielding would be reduced.

This last point is of vital importance in the design of retrofitting measures. Many buildings approaching the end of their service life that are not compliant with actual codes in terms of ductility can still withstand the required forces. The problem of such buildings lies more in their ability to resist deformations rather than their strength. Suppose this were to be the case, where the building does not exhibit the required global ductility. In that case, this type of retrofitting technique could become a great alternative to reduce the displacements demands.

Another important way of measuring the effectiveness of the TMD is by considering the energy absorbed by the building. It is expected, from the introduction of the TMD that the accelerations in the floors reduce, thus reducing the input energy of the building. This reduction in the input energy translates to a reduction of the energy absorbed by the structure that its components should resist in terms of deformation. For example, Figure 6.18 depicts the evolution of the input, kinetic and absorbed energy in the building under the Northridge ground motion. It is evident that there is a decrease in all of the energies by introducing the TMD.

Using Figure 6.18 and 6.16 simultaneously, it can be understood that from the first spike in the roof displacement, which inputs a considerable displacement in the TMD, the energies and therefore deformations are reduced when compared to the uncontrolled case. In this particular case, a reduction in the absorbed energy of 10% was obtained. These reductions indicate that the structural members suffer less damage from the earthquakes and thus have a lower probability of compromising the safety of the inhabitants.

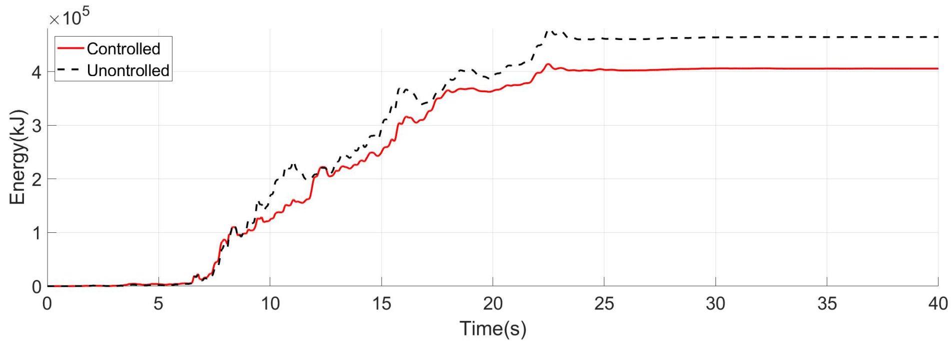

(a) Input

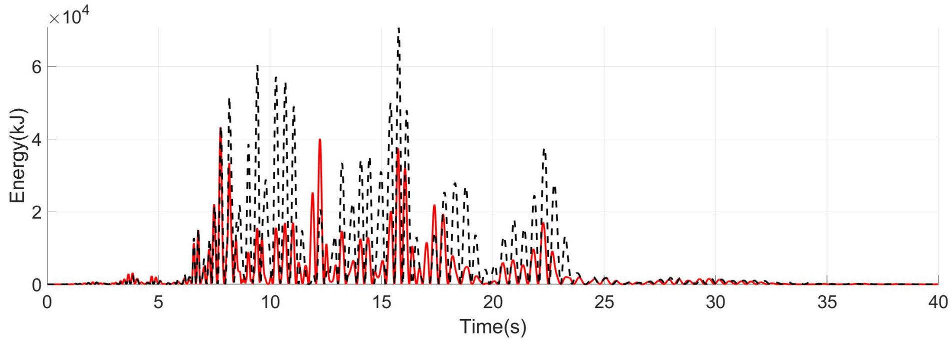

(b) Kinetic

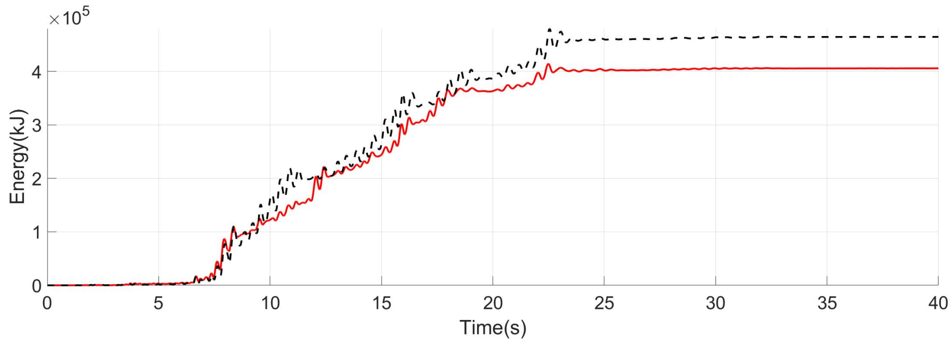

(c) Absorbed

Figure 6.18. Energies

Chapter 7

Sensibility Analysis

As the analyzed structure contains a significant amount of degrees of freedom, a numerical approach to the optimization problem is rather cumbersome. Following the same procedure of Chapter 5, several hypotheses were modified to comprehend further the behavior of this type of auxiliary structure and its interaction with the main structure. Therefore, alongside the modified damper, the damper results shown in Chapter 6 are displayed for reference. The modifications of such hypotheses allow for proving the robustness of the design procedure. It is well known, for instance, that the behavior of an undamped TMD on a SDOF system is highly dependent on the tuning parameter. In such way, it is essential to understand the behavior of the structure when dampers with different properties are used.

Please refer to Annex B for the figures comparing the behavior of the analyzed structure under each earthquake.

7.1 Linear damper

A linear damper, designed following the considerations of [19] of tuning and damping was included in the system instead of the nonlinear one used for this study. This element was modelled in NONDA considering a linear spring, which is a particular case of the BW model with $\alpha_d = 1$.

The design of these elements consisted in adopting a stiffness, that with the same mass of the hysteretic damper, attained the same desired structural frequency. Thus, two different linear dampers will be considered, one with each of the considered frequencies of the hysteretic damper. The damper tuned to the initial frequency of the structure will be referred to as case Linear Initial while the damper tuned to the secant frequency will be Linear Secant.

As in the design of the hysteretic damper, the stiffness of the damper is determined by means of the tuning with respect to the main structure. As the same tuning and mass ratio will be used, the stiffness of the dampers will be those considered in Chapter 5 for the hysteretic damper. Once the stiffness of the structure was defined, the viscous damping, c can be computed by means of Equation 7.1

$$\xi = \frac{c}{2\sqrt{km}} \tag{7.1}$$

Where ξ is the damping ratio, k, c, m are the stiffness, damping and mass of the system respectively. As stated previously, for the mass ratio of $\mu = 0.05$, and a structural damping ratio of 0.16 the recommended optimal damping ratio is recommeded by [19] $\xi = 0.16$.

With the equivalent damping ratio, the viscous damping of the linear TMDs can be computed, in this case, the Linear Initial case had a value of $c_d = 35.3kN/(m/s)$ while $c_d = 24.63kN/(m/s)$ was used for the Linear Secant TMD.

Table 7.1. Performance Indices Linear Damper

Type	Performance Index						
	J_1	J_2	J_3	J_4	J_5	J_6	J_7(m)
Hysteretic	0.705	1.010	0.986	0.669	0.883	0.900	0.237
Linear Initial	0.895	1.033	1.044	0.928	0.973	0.976	0.292
Linear Secant	1.023	1.015	0.996	1.124	1.040	1.032	0.449

It is evident that the benefits of installing a linear damper are very limited within a seismic context. By considering the same mass ratio, the auxiliary structure does not ensure controlling the structure in a great manner. On the contrary, under several ground excitations the protected structure had greater drifts than the uncontrolled structure, meaning that it worsen the seismic behavior of the system.

It is important to recall that TMDs are generally used to control vibrations that have a limited frequency bandwidth. However, that is not the case under seismic loading. Due to the great frequency content and the deterioration in the structure, the linear TMD is not capable of reducing the vibrations in the structure in a significant way.

7.2 Direct procedure

As expressed in Chapter 5, it is possible to modify the procedure to assume the stroke of the TMD and avoid the iterative procedure. By proceeding in such a way, several input strokes will be assumed for instance, $15cm$, $20cm$, and $30cm$. The first value ensures that the TMD will be tuned to the mode of vibration by using a low value of the tuning displacement. The last two correspond to the hypothesis expressed previously of assuming that the TMD will move approximately two or three times the floor displacement.

The damper's characteristics are determined to be tuned with the secant frequency at the stroke displacement. The average performance indices obtained by introducing the different dampers in the structure are shown in Table 7.2 and in Figure 7.1.

As stated previously, by using the direct procedure, the design secant tuning is not ensured. This is because the relationship between the displacement of the damper and the structure is not known. Therefore, it is not possible to know if the damper will reach or surpass the displacement at which it is being tuned to the main structure.

This is exactly what parameter J_7 reflects in Table 7.2. Using values lower than the optimized stroke means that the secant stiffness at the working condition is lower than expected and so the tuning frequency is smaller. On the other hand, when using greater displacements, the secant stiffness will be greater than anticipated and so will

Table 7.2. Summary Performance Indices Direct Procedure

Input Stroke(cm)	Performance Index						
	J_1	J_2	J_3	J_4	J_5	J_6	J_7(m)
23.7	0.705	1.010	0.986	0.669	0.883	0.900	0.237
15	0.733	1.010	1.001	0.695	0.883	0.921	0.246
20	0.709	0.999	1.003	0.674	0.873	0.911	0.240
30	0.675	0.974	0.990	0.662	0.874	0.898	0.234
35	0.668	0.971	0.982	0.665	0.880	0.911	0.233
45	0.672	0.969	1.000	0.684	0.888	0.899	0.233
60	0.705	0.963	1.000	0.726	0.904	0.903	0.236

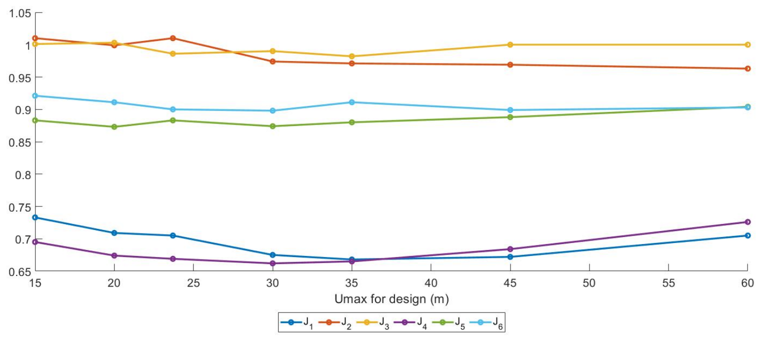

Figure 7.1. Performance Indices Direct Procedure

the tuning frequency. However, when comparing the strokes, it is evident that they gravitate towards the same value, one very similar to the one computed using the iterative approach.

Interestingly, the iterative procedure did not have the best results under the considered accelerograms. By considering input strokes from $30cm$ to $45cm$ the behavior of the performance indices regarding the displacements are reduced. However, the results against the optimized method were similar, with an average of 1.7% between the performance indices 1 through 6. A similar behavior was obtained when using the input stroke of $20cm$, having a mean difference of 3% in such indices. Such a difference confirms that a direct method could be as effective as the iterative procedure.

This demonstrates that the design of the TMD is not very sensitive to a non-accurate determination of the performance point in the neighboring areas of the study. This increases the robustness of the method as high expertise for designing the numerical model of the structure for the retrieval of the pushover curve would not be necessary. In this way, a model that could fairly reproduce the behavior of the building would be enough for the design of the auxiliary structure.

It shows as well that a particular secant tuning frequency is not as important as the initial one. In particular, it shows that it is this nonlinear behavior shown by the TMD that prevents it from damaging the structure. Meaning that, with a TMD tuned to the initial frequency and showing a softening behavior, in case of the BW through $\gamma = \beta$, the response of the structure would not be worsened under ground motion excitation.

Therefore, the element could be designed using the direct method, considering a stroke $2-3$ times, or even more, the expected displacement of the control point. The sensibility of the results considering different performance points will be discussed in Section 7.6.

7.3 Stiffness

As expressed previously, there are several ways to bilinearize the pushover curve. In the method presented in Section 5, a secant stiffness crossing the pushover curve at 60% of the yielding force following the recommendations of FEMA440, [37], was adopted. Nevertheless, it is also possible to adopt a tangent stiffness of the pushover to bilinearize the curve and design the TMD. For instance, the Italian Building Code, NTC2018, follows this approach for deriving the bilinear curve. Following such recommendations, the results of the bilinearized pushover curve are presented in Table 7.3 and in Figure 7.2.

Table 7.3. Results Bilinearized Pushover

$k_0(kN/m)$	$d_y(m)$	$\xi(\%)$	PP SDOF (m)*	PP MDOF (m)*
30717.79	0.015	15	0.093	0.122

*PP:Performance Point

Due to the change in the structure's considered initial stiffness, the damper's initial stiffness will change. The initial tangent stiffness will also be reduced by 50% to emulate the structure's stiffness after cracking. In addition to these results, a reduction and increase of 10% in the considered initial stiffness to determine the sensibility to such parameter will be studied. Therefore in Table 7.4 they will be referred to as the code that was followed for the bilinearization, and the corresponding modification.

Table 7.4. Summary Performance Indices Stiffness

Code	Stiffness	Performance Index						
	(kN/m)	J_1	J_2	J_3	J_4	J_5	J_6	J_7(m)
FEMA440	20240.6	0.705	1.010	0.986	0.669	0.883	0.900	0.237
NTC2018	30717.8	0.746	0.963	0.928	0.750	0.905	0.869	0.177
50%NTC2018	15358.9	0.771	1.009	1.017	0.743	0.912	0.952	0.273
90%FEMA440	18216.5	0.734	1.001	0.998	0.699	0.876	0.902	0.248
110%FEMA440	22264.7	0.671	0.976	0.969	0.660	0.872	0.891	0.222

From Table 7.4, it is evident that the most significant differences when considering the tangent stiffness, and 50% of such value in the performance indices are in terms of displacements. Both displacements indices, peak and RMS, suffered an increase by changing the considered stiffness of the structure to the ones relating the tangent stiffness. However, this behavior was not evident when values closer to the secant stiffness were used. In these cases the structure kept similar behaviors in most of the performance indices.

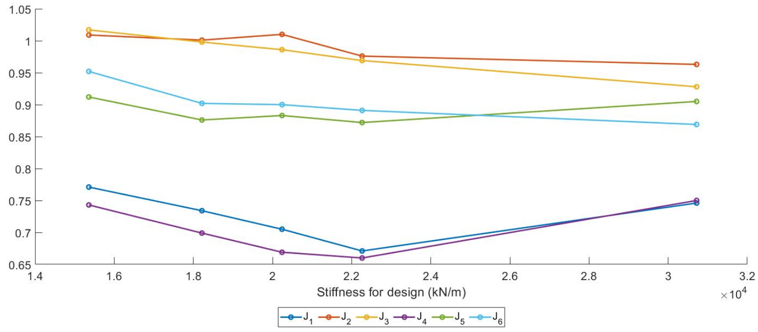

Figure 7.2. Performance Indices Stiffness

It is interesting to note that by considering a stiffness 10% greater than the one initially assumed a better performance of the structure was obtained. This behavior could be due to a modeling mistake in the SAP2000 model. Other reason for this behavior could be that due to the non linearity of the damper the optimal tuning frequency is no longer that recommended by [19]. However, a single study over a particular building is not enough to ensure such behavior.

This indicates that a secant stiffness of the structure, as the one considered in [34] for the bilinearization procedure, which is more characteristic of the elastic branch of the structure, works in a better way for defining the characteristics of the damper. This allows for a damper that is more effective through accounting for structural damage. Yet, even considering the different stiffness alternatives, the damper is still capable to improve the behavior of the structure.

7.4 Mass of the structure

During the design procedure, it was stated that the modal mass of the equivalent SDOF should be used for the computation of the initial frequency. Therefore, Table 7.5 compares the TMD's behavior when tuned to a frequency referring to the whole mass of the structure and the frequency of the equivalent SDOF. The considered stiffness remains constant and thus the frequency is reduced.

Table 7.5. Performance Indices Mass of the structure

Mass (ton)	Performance Index						
	J_1	J_2	J_3	J_4	J_5	J_6	J_7(m)
155 (m^*)	0.705	1.010	0.986	0.669	0.883	0.900	0.237
232 (m)	0.814	1.000	0.991	0.765	0.916	0.955	0.302

If the total mass were to be considered for the design of the TMD without regard for the modal analysis, it is evident that the structural frequency would be lower. This detuning generates a significant difference in terms of displacements of the controlled structure. In this case, the displacements indices were affected more severely, 15%, than by varying the considered initial stiffness of the element. Therefore demonstrating that the TMD effectively reduces the response of the mode for which it was designed.

However, for the structure under consideration, using the total mass of the building and an initial tangent stiffness derives in a structural frequency similar to that considered in the design.

7.5 Tuning

In [25] this type of TMD was designed and analyzed by assuming that the element should vibrate in resonance with the structure, as it attained the best results when compared to other tuning conditions. In such a study, a Takeda model was used to represent the structure, the element design was carried out employing GA, and the simplified method presented here. The numerical optimization intended to keep the damper tuned as much as possible to the structure in a limited search, considering $\gamma = \beta$. Finally, both designs were compared regarding the model's parameters and displacement in the structure, leading to similar designs and resulting displacements. Other authors have also worked on the problem under similar tuning conditions such as [27, 39].

However, as additional tuning frequencies were considered to comprehend the behavior if the inital hypothesis of adopting the tuning by [19] is correct. Therefore, a lower tuning frequency of $f = 0.75$, and two greater ones of $f = 0.86$ and $f = 0.90$ were included in addition to the resonant damper. Their results are presented in Table 7.6 and in Figure 7.3.

Table 7.6. Summary Performance Indices Tuning

$f = \frac{\omega_d}{\omega_s}$	Performance Index						
	J_1	J_2	J_3	J_4	J_5	J_6	J_7(m)
0.83	0.705	1.010	0.986	0.669	0.883	0.900	0.237
0.90	0.686	0.967	0.992	0.673	0.870	0.883	0.211
1	0.803	0.953	0.922	0.832	0.920	0.874	0.169
0.75	0.753	1.000	0.993	0.714	0.891	0.935	0.257
0.86	0.683	1.012	0.993	0.660	0.867	0.894	0.231

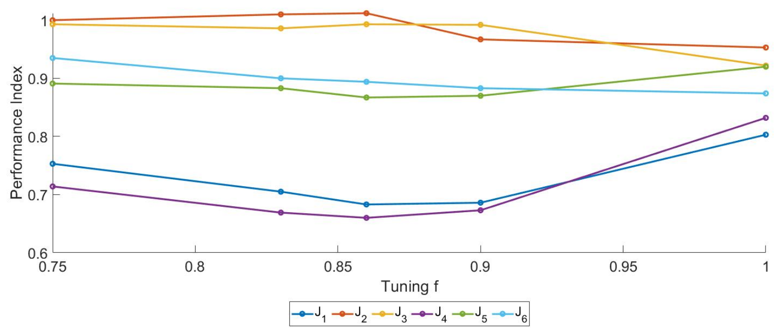

Figure 7.3. Performance Indices Tuning

By having a frequency of the structure equal to that of the damper, the structural response is interesting. Unlike the results expressed by [25], the resonant damper is outperformed in terms of displacements, both RMS and peak, by approximately 14% and 24% respectively when compared to the tuning frequency recommended by [19]. The other values had similar responses varying approximately 5% between them.

This could indicate that the Takeda model was an oversimplification of the behavior of the building. In the [25], however, it was shown that the global behavior of the building, in terms of displacements and shear forces were captured by the model. This type of behaviors that cannot be captured by SDOF systems generates more design uncertainties.

Similar results were obtained by [27], where an analytically designed TMD in resonance was compared to one obtained through GA. In such work, a similar hypothesis regarding the BW model were imposed, for instance, $n = 1$ and $\gamma = \beta$. This allows solving the design problem by assuming a tuning frequency. In such case, a resonance condition was imposed. However, when searching for the optimal design of the TMD such limitations were not imposed. Therefore, the optimal characteristics for the BW model were obtained. Such characteristics varied significantly from those obtained using the analytical method.

In [27], the optimal TMDs analyzed were able to reduce the structural displacement by approximately 50% with lower mass ratios. It is important to note that none of the optimal TMDs in the study presented characteristics of $\gamma = \beta$. This confirms that the optimal TMD might not be obtained by the design method presented here. Yet, the [25] showed that the optimal TMD within the search space considering by $\gamma = \beta$ could be obtained, with enough accuracy, by implementing the simplified method here presented.

Therefore when considering the structure as a MDOF system, a better response is obtained by considering the tuning obtained through Equation 5.6. However such tuning is for an optimally tuned linear TMD, thus further investigating the optimal tuning parameters for the nonlinear TMD is required.

When a lower tuning was imposed, $f = 0.75$ the results were worse than that of the TMD initially designed. However, with greater tuning frequencies, $f = 0.86$ and $f = 0.9$, better or similar behaviours were obtained. This could means that the optimal tuning frequency of this type of dampers is indeed higher than the one adopted initially.

7.6 Different mass ratio

The optimization procedure explained in Section 5was used assuming a $\mu = 1\%$ and so an additional equivalent damping $\xi = 1\%$ is considered in the structure. In this way, the new performance point leads to a $0.118m$ in the real structure. Considering $\mu = 1\%$ the optimal tuning according to [19] is $f = 0.92$.

The results of the analysis using such TMD are resumed in shown in Table 7.7. An important remark is that for such design the stroke of the TMD was greater than that of the $\mu = 0.05$, as it was $u_{max} = 28cm$.

From Table 7.7, we can see that even with a 1% mass can reduce both displacement indices by around 10%. The forces and accelerations, however, were not significantly modified.

It is interesting to note that the peak displacement under considering a TMD with

Table 7.7. Summary Performance Indices Mass Ratio

Mass Ratio (μ)	Performance Index						
	J_1	J_2	J_3	J_4	J_5	J_6	J_7(m)
0.05	0.705	1.010	0.986	0.669	0.883	0.900	0.237
0.01	0.915	0.993	1.011	0.879	0.956	0.964	0.277
0.01*	0.920	0.990	1.012	0.882	0.955	0.964	0.275

a lower mass ratio was greater than anticipated. Initially, the performance point of the structure was considered as $11cm$, yet, after the analysis, an effective displacement at the roof of $13cm$ was computed. This means that the iterative procedure done to compute the displacement of the damper is incorrect as the displacement of the performance point was miscalculated.

The behavior of the control structure by assuming a displacement in the performance point of $0.13m$ was also considered, shown in Table 7.7 as entry 0.01*, yet the results did not vary much with those presented in the mass ratio $\mu = 0.01$. This demonstrates that incorrectly assessing the displacement of the performance point may be not detrimental to the design. This is in line with the behavior presented in Section 7.2 as the controlled structural behavior did not present significant changes by considering different levels of input stroke. Thus confirming the robustness of the design procedure as the numerical model in the nonlinear stage is not as critical as the elastic branch, which is usually easier to capture through the models. It also shows that the most important parameters are the initial tuning and mass ratio to reduce the displacements in the building.

Therefore computing the stroke of the TMD as shown in Section 5.1.1, may be unnecessary for the design of the but crucial for further understanding its behavior. It is important to note that with the different mass ratios the stroke of the damper remained similar under the design earthquake.

Regarding the behavior of the controlled structure, on average the TMD can reduce the RMS displacements in all cases and reduce their average value in approximately 10% with respect to the uncontrolled structure. However, under the Northridge ground motion, the peak displacement in the roof and the drifts in the three upper floors were increased. This increase was of 3%, 5% and 7% in the drifts of the structure and 5% in the peak displacement to the uncontrolled structure. In all other cases, the drifts and peak displacements were either reduced or unaltered, for instance as when subjected to Chi Chi.

This result is in line with what was stated previously. The importance of the secant tuning is secondary to the initial tuning and is the global behavior of the TMD helps to control the response of the building. Nevertheless, it is important to emphasize the fact that the hysteretic curves of the building were not significantly modified by the addition of the TMD with a mass ratio of 1%. This contrasts with the behavior shown when a mass ratio of 5% was used,except for the Chi Chi case. However, under this ground motion, the behavior of the controlled structure was similar to the one seen with a 5% mass ratio.

7.7 1.5 Design Earthquake

As stated previously, the NONDA code does not consider steel fiber failures, therefore it will be capable to obtain an equilibrated solution for every time step. Thus, it cannot reproduce the structural collapse. For such the structural results here presented may have been impossible for the real structure to obtain, however it allows to understand the behavior of the structure under such earthquakes. According to the NTC2018, the return period for such ground motion is approximately 975 years for the considered class of the structure. Meaning that the probability of an earthquake with those characteristics, or greater, is 5% during the service life of a structure.

Table 7.8. Performance Indices 1.5 Design Earthquake

Earthquake	Performance Index						
Multiplier	J_1	J_2	J_3	J_4	J_5	J_6	J_7(m)
1	0.705	1.010	0.986	0.669	0.883	0.900	0.237
1.5	0.848	0.957	0.998	0.876	0.968	0.970	0.327

It is clear from Table 7.8, that the TMD is not as effective when the structure faces such solicitations. Yet it is still capable to reduce the structural response even when the structure deepens into its non linear range. A mean reduction of 15% in both of the displacement indexes was attained. This reduction can be owned to the fact that the damper was not designed to work under such ground motions. Nevertheless, even under such conditions the damper is still capable of reducing, and not worsening, the response of the building.

To assess the collapse condition the criteria recommended by [34] for walls is considered. Such criteria states that the adimensional interstorey drift should not exceed 2%. However, when the structure is subjected to the considered ground motions, the average drift in the second and third level were 2.07% and 2.08% respectively. The drift threshold was exceeded in six of the eight ground motions considered, with "Chi Chi" and "Loma Prieta" being the only ones in which the those values were not attained.

When introducing the damper into the model, the drifts in all levels were reduced in approximately 15%. With such reduction, the structure was only facing higher drifts than those recommended by FEMA in two scenarios, "Northridge" and "Chalfant". The average drift in those two levels were limited to 1.74% and 1.79%. Therefore, the damper would allow to effectively reduce the damage of the structure to a point in which structural collapse could be prevented. Showing that the hysteretic damper is capable of achieving some tuning in the plastic regime of the structure.

Chapter 8

Conclusions

Nowadays, taller buildings are being built to accommodate the urban population, which is overgrowing. It is not sustainable for the environment to continue this process. Therefore, retrofitting existing structures becomes necessary to fulfil housing needs. However, the main problem with retrofitting such structures is that most do not satisfy the safety criteria of current building codes, especially regarding their seismic behaviour.

Design codes prevent structures' failure by ensuring they can withstand great damage. Yet, many structures built in the past century are approaching the end of their service life and cannot sustain significant plastic deformations generated by such damage. This is usually owned to the fact that they do not exhibit high ductility, which is fundamental for current codes regarding seismic design.

Therefore, considering their natural deterioration and the change in national regulations, a significant part of the building stock requires retrofitting to fulfil current requirements. Recently, many approaches to reduce seismic vulnerability have been used. For instance, [43], worked on under-designed beam-to-column joints that could exhibit brittle behaviour under seismic action. This reduces or impedes weak column strong beam mechanism, which is opposite to capacity design. Nevertheless, other ways to reduce seismic vulnerability have been through seismic control devices.

Many seismic-resistant buildings are implementing this strategy to have more slender and economic structures. Therefore, structures with structural control methods will be more common.

Within the passive methods of structural control, those that do not require energy, base isolation, structural bracing, and TMDs are the most common methods nowadays. However, TMDs were considered not advantageous within a seismic context as they are effective within a narrow frequency bandwidth.

A new type of TMD with a spring exhibiting a hysteretic behavior has been adopted during the last decade. This type of element has proven to be beneficial as it avoids the main problem of a linear TMD, the detuning generated by the frequency shift due to the damage in the system. This type of element presents itself as an ideal retrofitting technique, as it could be installed on the roof of many buildings permitting their diffusion in vast territories.

As of now, the element's design relies on numerical optimization methods. However, a novel simplified method for this type of structure was shown and proven in a dual reinforced concrete building whose behaviour was tested numerically following its experimental results.

The design method delivered the characteristics of a TMD that improved the overall behaviour of the building. The design procedure, explained thoroughly in Chapter 5, is a fully structural approach to the problem. Therefore, it requires only the characteristics of the structure and the site response spectrum. Therefore, it would not require modelling additional input variables, for instance, ground motions.

The element reduced the displacements in each floor of the structure by approximately 30% by using a mass ratio of 5%. With such a mass ratio, the RMS of the structure's displacements, accelerations, and shear forces were reduced. Under the same ground motions, a linear TMD was only able to reduce such value by around 10%.

It was also shown that the element could work even when the structure deepens into the nonlinear range. In this case, the damper was able to reduce the structure's drifts to a level that, according to FEMA in [34], is deemed to prevent structural collapse. However, the element could have been more effective under those ground motions.

The behaviour of the controlled structure was shown to be determined, especially by the mass ratio considered. However, an overall improvement in the structure was obtained with a lower mass ratio of 1%. With this mass ratio, the controlled structure exhibited a response worse than the uncontrolled structure for one of the eight considered ground motions. It is important to note that this damper had better results to the implementation of the linear damper with 5%.

The resulting element cannot be considered optimal as several hypotheses on its behaviour were assumed beforehand. Nevertheless, the method showed robustness as the structure's response remained within the expected range even when changing several input values substantially. This is a critical aspect as the method depends on the nonlinear static analysis and therefore depends on the designer. It was shown that a change of up to 10% in the considered stiffness lead to similar results in terms of RMS.

However, several dampers used for the sensibility analysis outperformed the one obtained by means of the iterative approach. All of these dampers presented a longer tuning to the initial stiffness of the structure. This was achieved either means of a higher stiffness, higher tuning tuning. or through a secant tuning at a displacement higher than the actual one. This induces a slowlier decay of the stiffness of the element and therefore longer initial tuning. This could mean that nonlinear dampers require different tuning values for which further analysis are recommended.

Further studies within this field could allow, for instance, to include pinching within the BW element as [44]. Excite the element in both directions to start generalizing the problem and understanding the possibility of extending the theory to MTMDs. This could be important as the TMD vibrates for a longer time than the earthquake generating an oscillatory variation around that of the uncontrolled structure in the base shear. Numerical tests in order to confirm the validity of tuning conditions used in this study are also required. Within such study, a different initial and secant tuning could be introduced as happened in this study for the dampers showing the best behavior.

Nevertheless, the essential part would be to continue the experimental efforts. Experimenting with different materials and set-ups that allow obtaining different hysteretic cycles is the key to understanding the damper's feasibility.

This is not intended to be a final design of the element, as there is space to continue improving the method proposed here. On the other hand, it is intended to be the second step to a design method that can be implemented within national regulations.

Appendix A

Experimentation Set-up

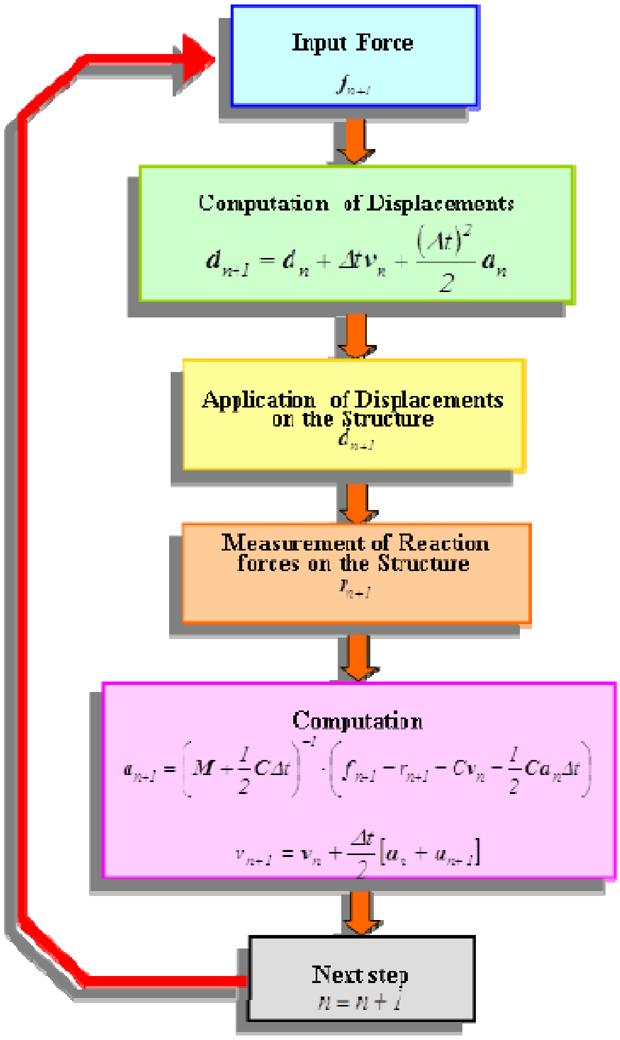

Figure A.1. PSD procedure
Retrieved from [30].

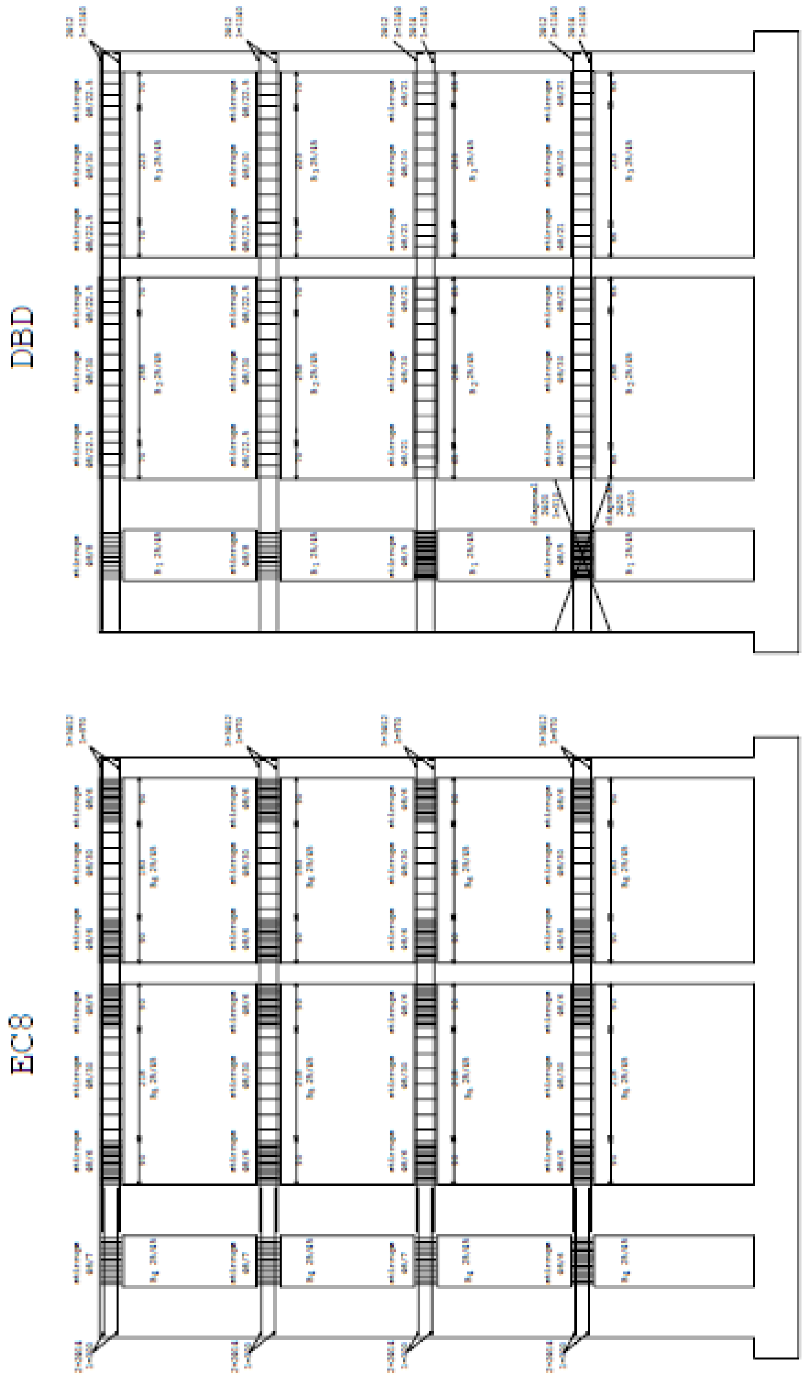

Figure A.2. Reinforcement layout: Horizontal elements
Retrieved from [28]

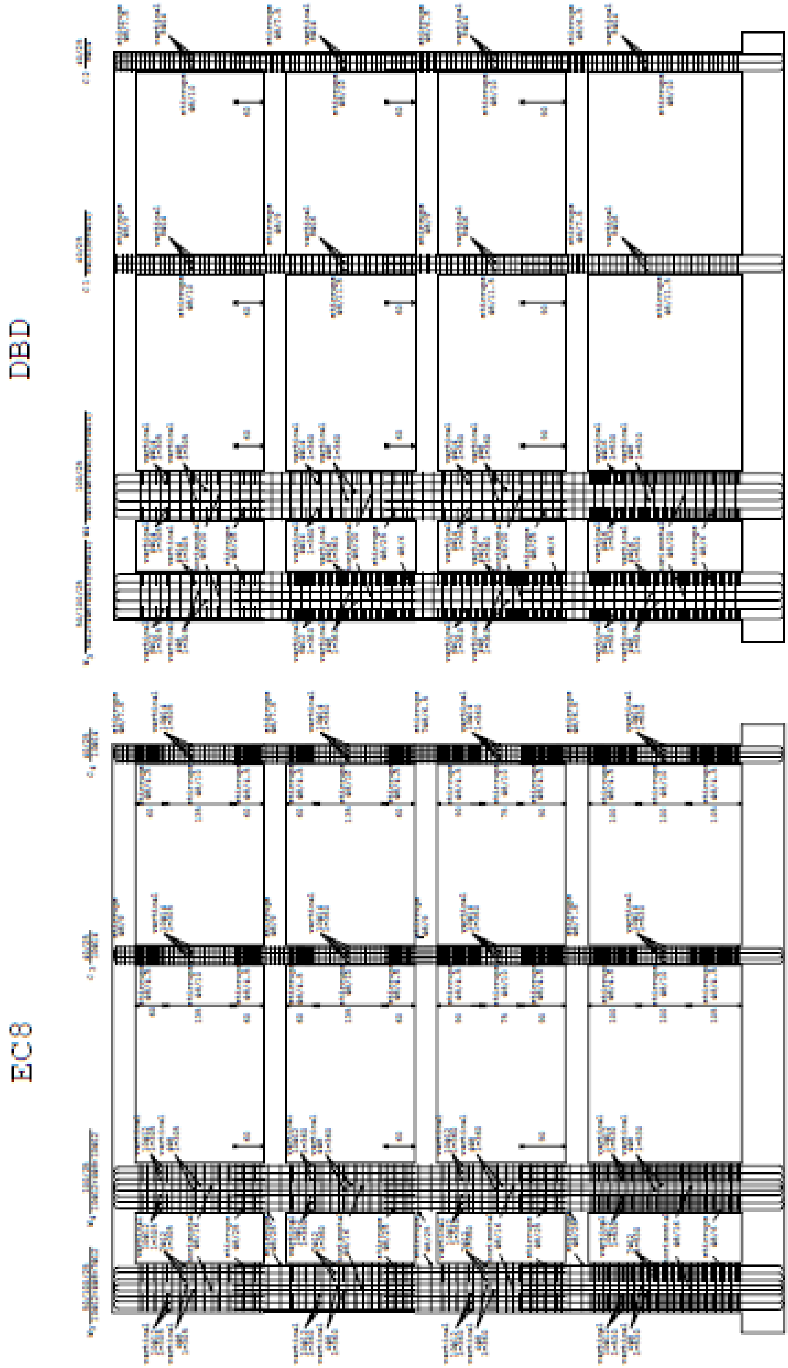

Figure A.3. Reinforcement layout: Vertical elements
Retrieved from [28]

Appendix B

Sensibility Analysis

B.1 Linear Damper

B.1.1 Initial Stiffness

By considering a linear damper tuned to the initial frequency instead of a hysteretic one the following results are obtained.

Table B.1. Performance Indices Linear Initial Damper

Earthquake	Performance Index						
	J_1	J_2	J_3	J_4	J_5	J_6	J_7(m)
Chalfant	0.836	1.087	1.312	0.800	0.948	0.959	0.311
Chi-Chi	0.825	0.968	0.876	0.583	0.758	0.797	0.224
Erzincan	0.751	1.054	0.952	0.882	0.936	0.952	0.271
Friulli	0.853	0.955	1.096	0.941	0.988	0.967	0.272
Imperial Valley	1.025	1.259	0.986	1.259	1.042	0.968	0.291
Kobe	0.695	0.965	1.209	0.837	1.062	1.099	0.354
Loma Prieta	0.920	0.984	0.965	0.945	1.014	1.069	0.302
Northridge	1.258	0.988	0.952	1.173	1.037	0.995	0.314
Average	0.895	1.033	1.044	0.928	0.973	0.976	0.292

Chalfant

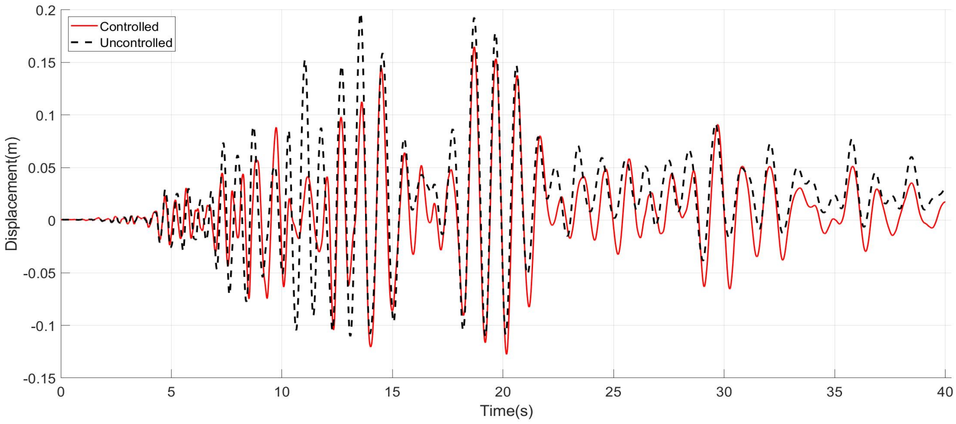

(a) Roof Displacements

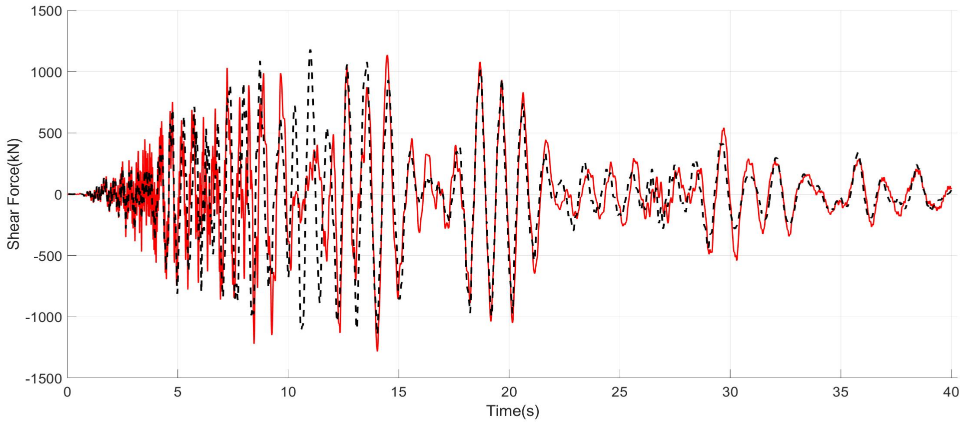

(b) Shear Forces at the base

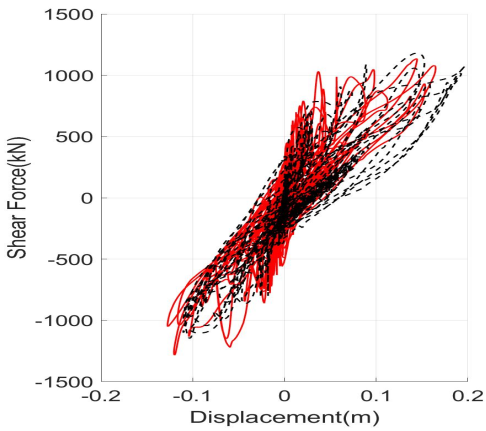

(c) Structural Hysteretic Curve

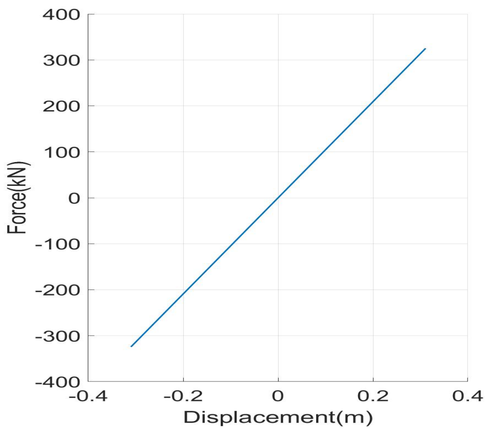

(d) TMD Hysteretic Curve

Figure B.1. Chalfant Linear Initial TMD

Chi-Chi

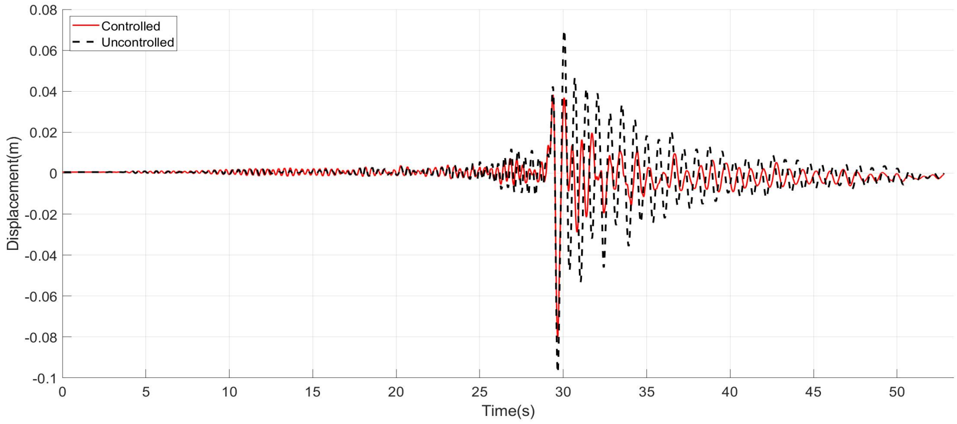

(a) Roof Displacements

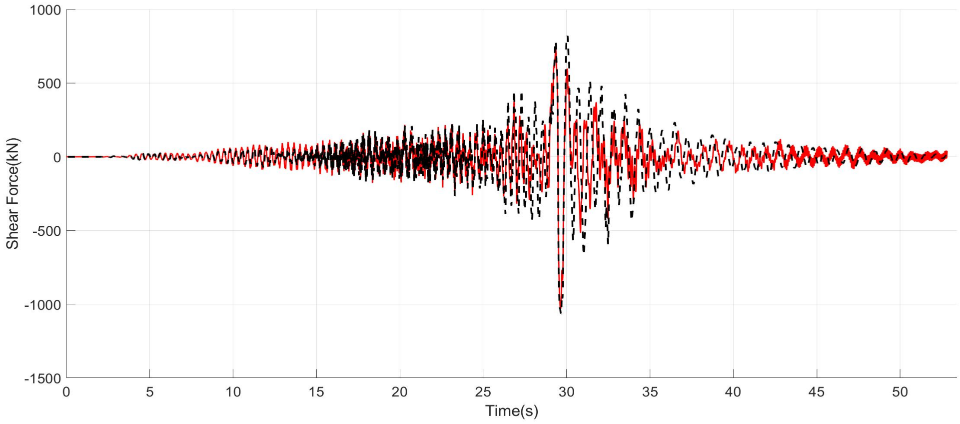

(b) Shear Forces at the base

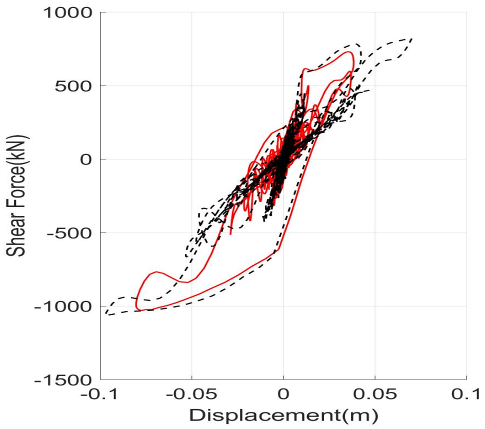

(c) Structural Hysteretic Curve

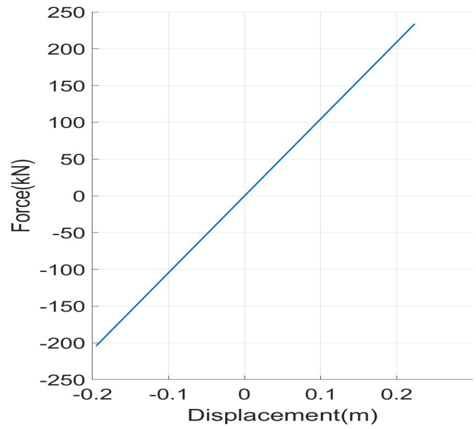

(d) TMD Hysteretic Curve

Figure B.2. Chi Chi Linear Initial TMD

Erzincan

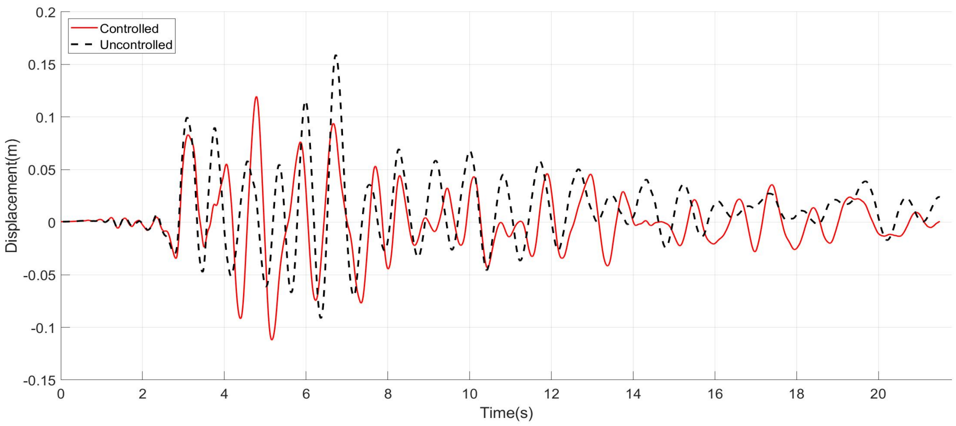

(a) Roof Displacements

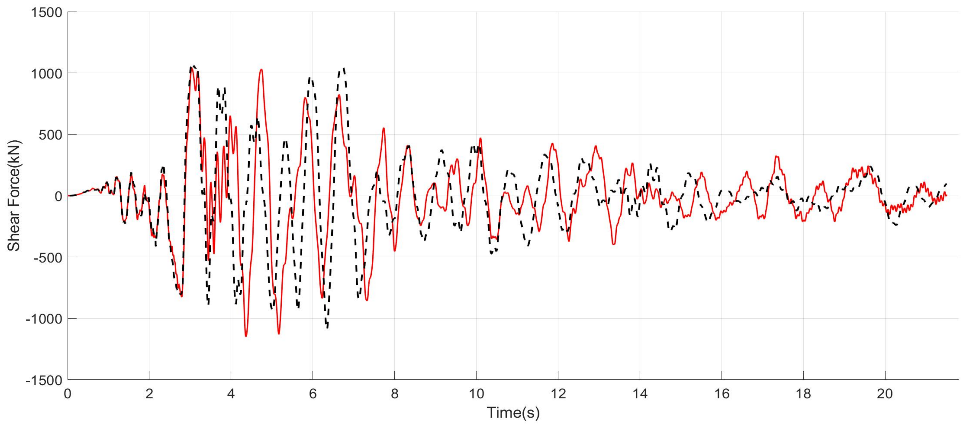

(b) Shear Forces at the base

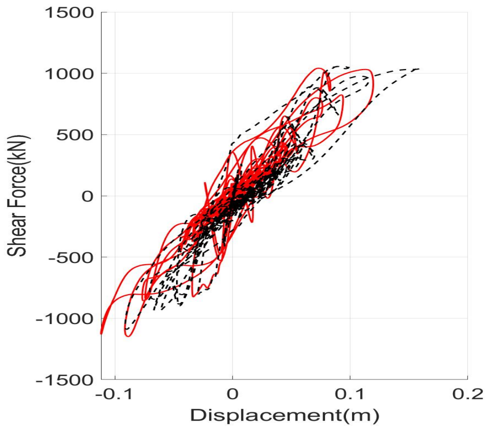

(c) Structural Hysteretic Curve

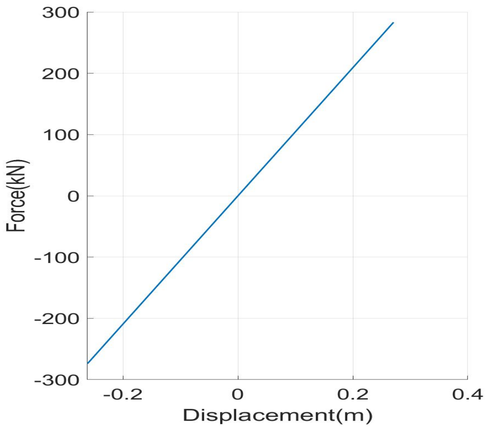

(d) TMD Hysteretic Curve

Figure B.3. Erzincan Linear Initial TMD

Friulli

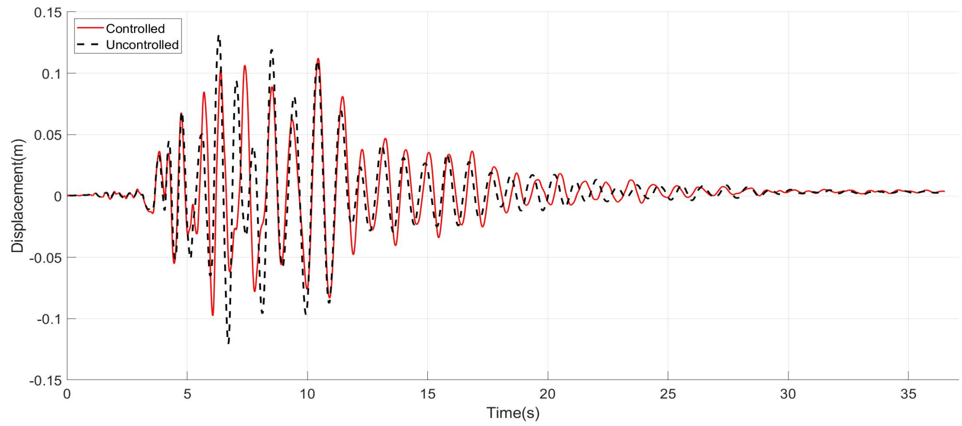

(a) Roof Displacements

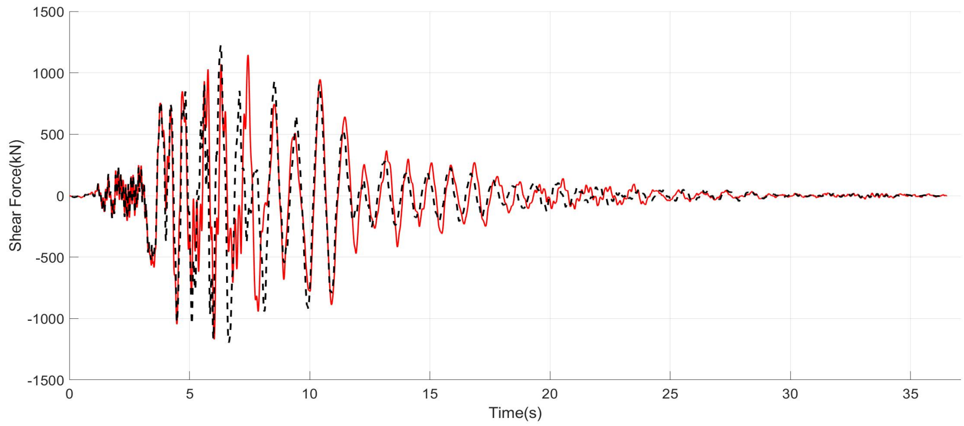

(b) Shear Forces at the base

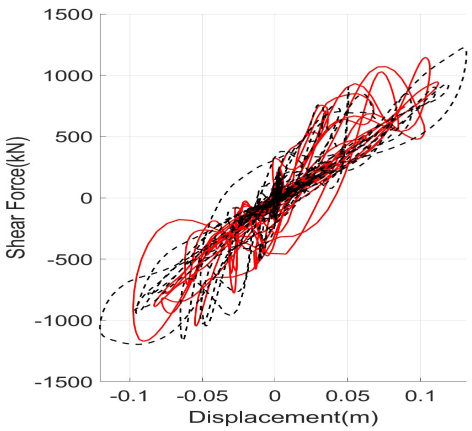

(c) Structural Hysteretic Curve

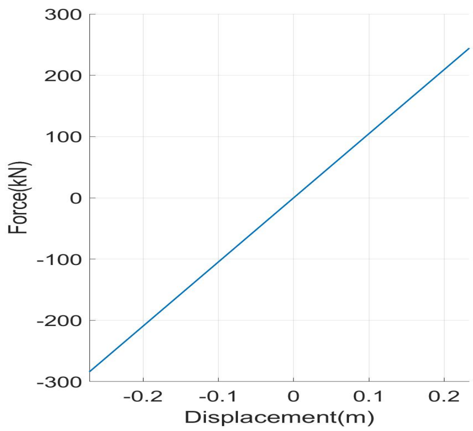

(d) TMD Hysteretic Curve

Figure B.4. Friulli Linear Initial TMD

Imperial Valley

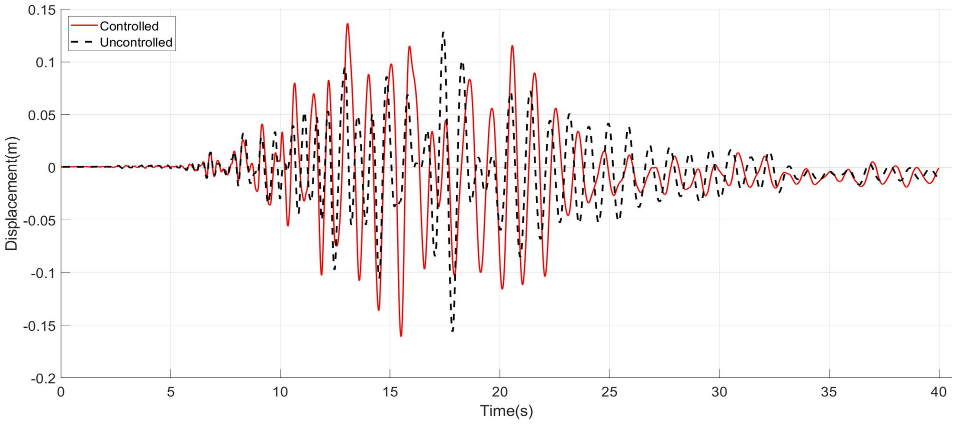

(a) Roof Displacements

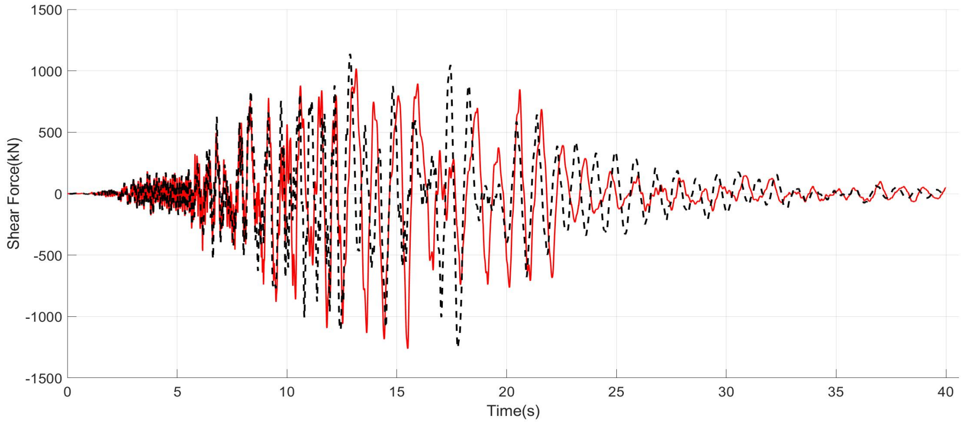

(b) Shear Forces at the base

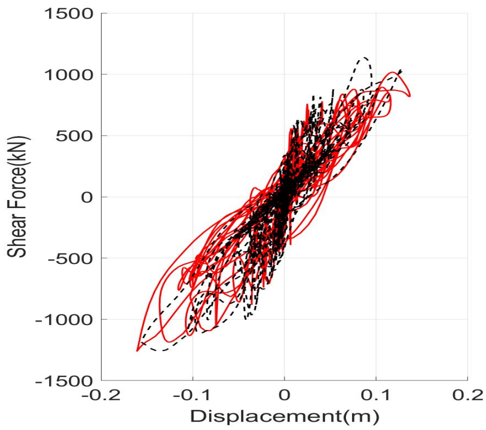

(c) Structural Hysteretic Curve

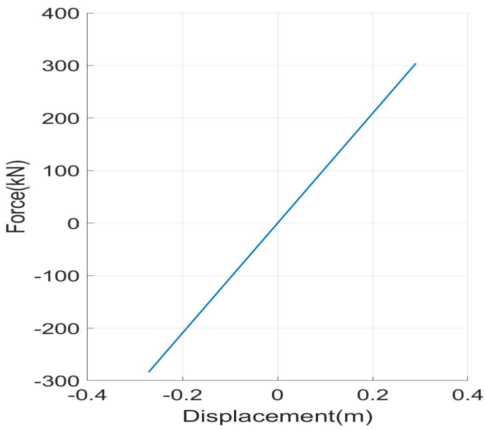

(d) TMD Hysteretic Curve

Figure B.5. Imperial Valley Linear Initial TMD

Kobe

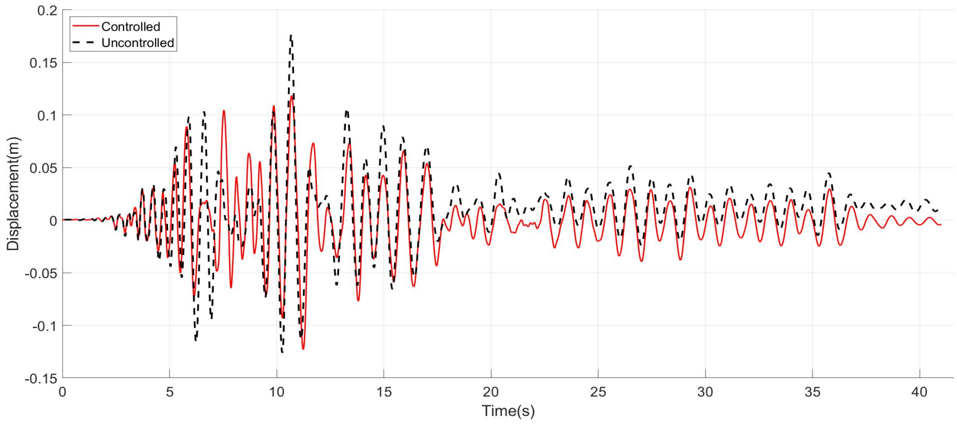

(a) Roof Displacements

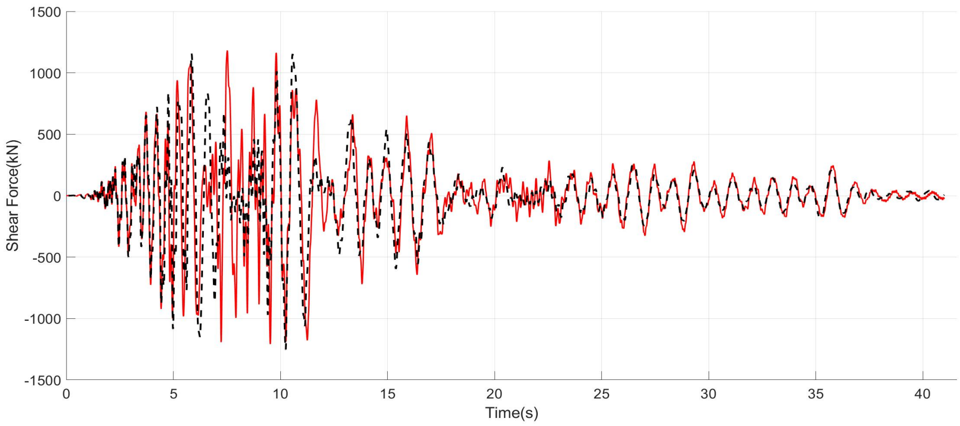

(b) Shear Forces at the base

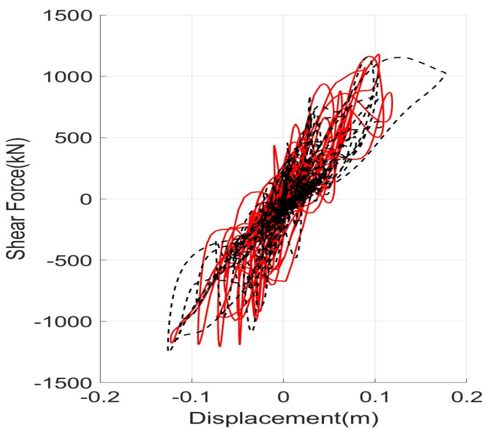

(c) Structural Hysteretic Curve

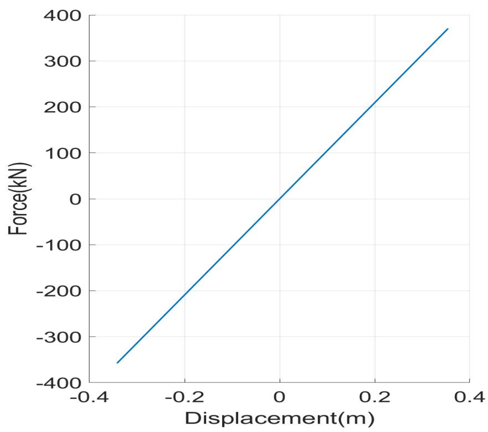

(d) TMD Hysteretic Curve

Figure B.6. Kobe Linear Initial TMD

Loma Prieta

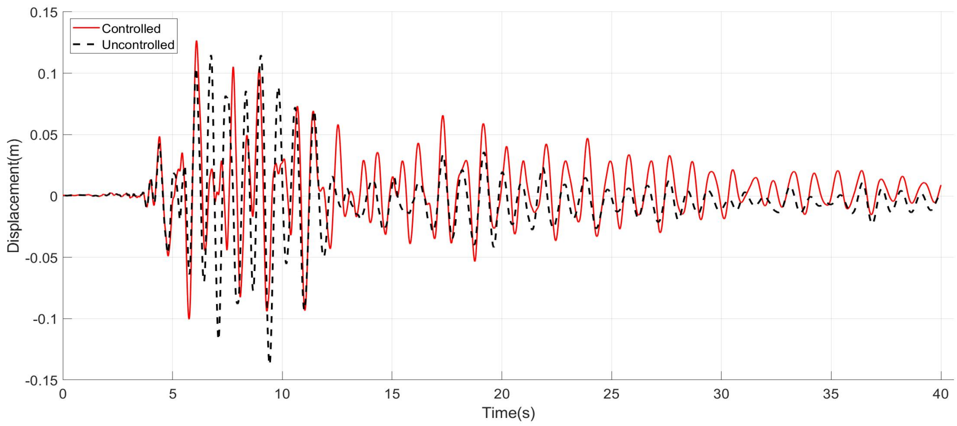

(a) Roof Displacements

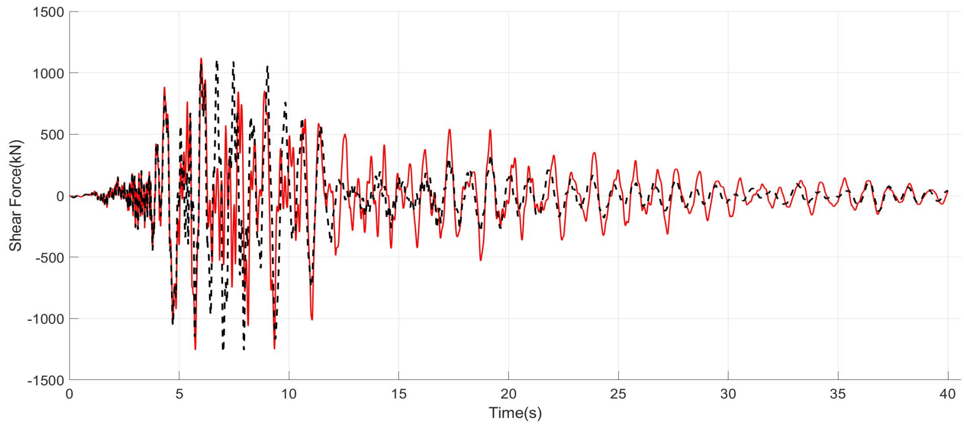

(b) Shear Forces at the base

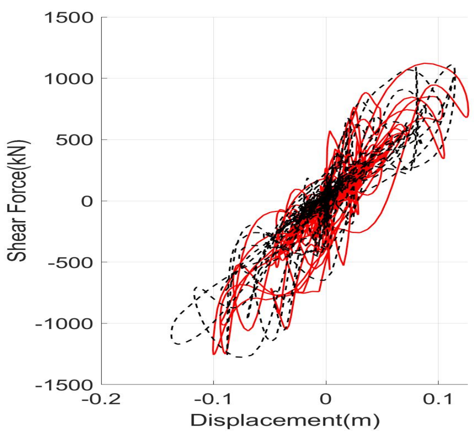

(c) Structural Hysteretic Curve

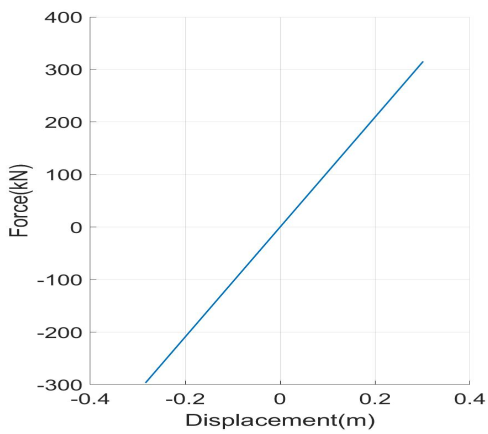

(d) TMD Hysteretic Curve

Figure B.7. Loma Prieta Linear Initial TMD

Northridge

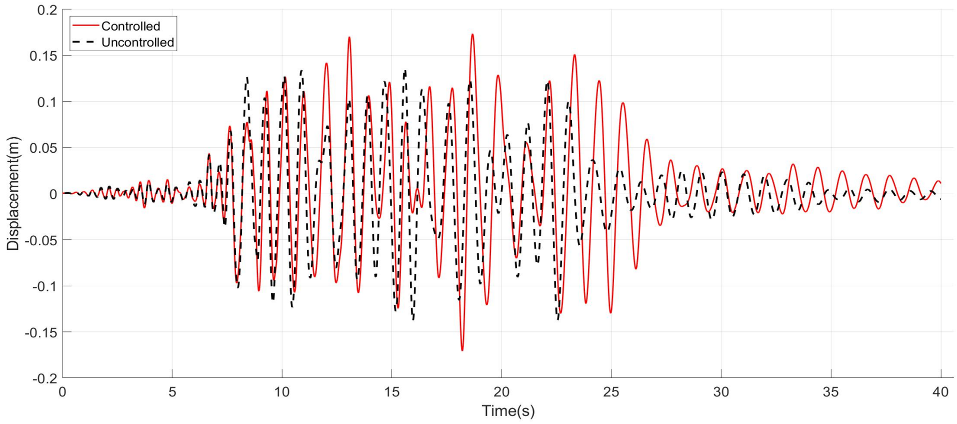

(a) Roof Displacements

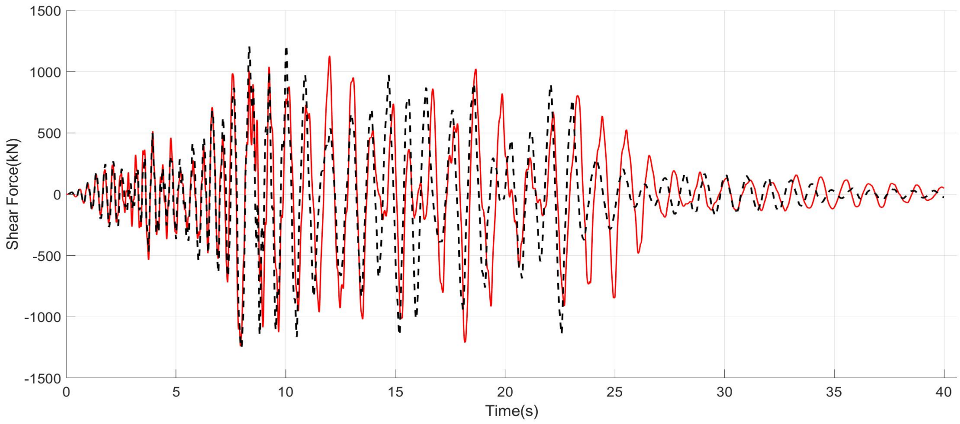

(b) Shear Forces at the base

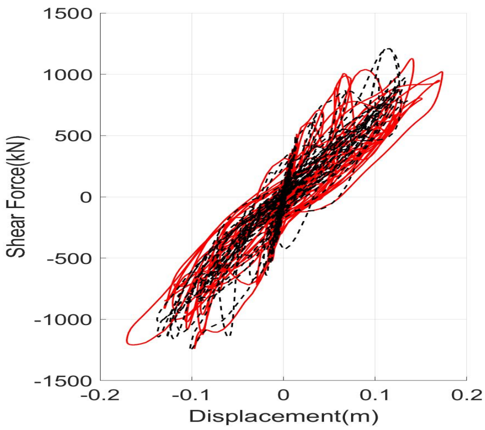

(c) Structural Hysteretic Curve

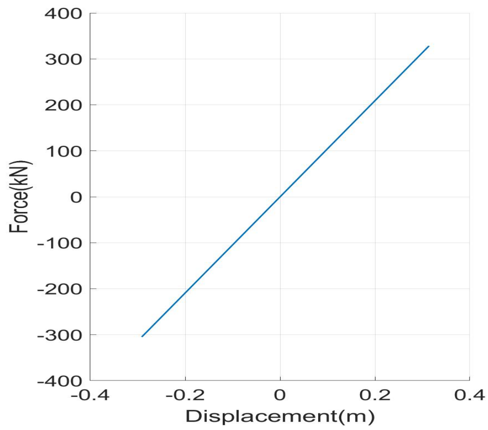

(d) TMD Hysteretic Curve

Figure B.8. Northridge Linear Initial TMD

Drifts

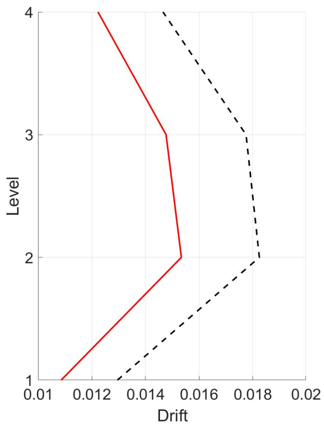

(a) Chalfant

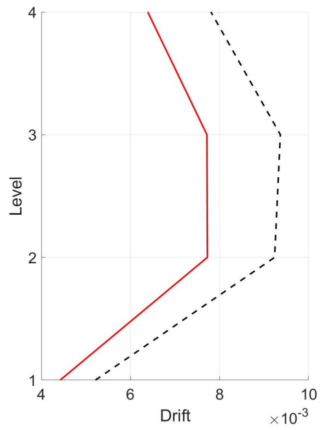

(b) Chi Chi

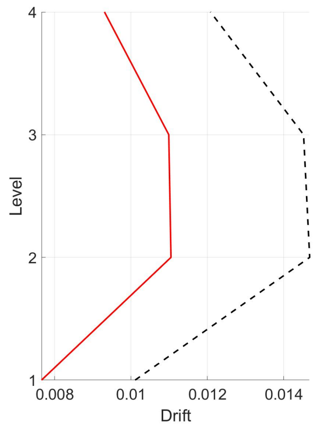

(c) Erzincan

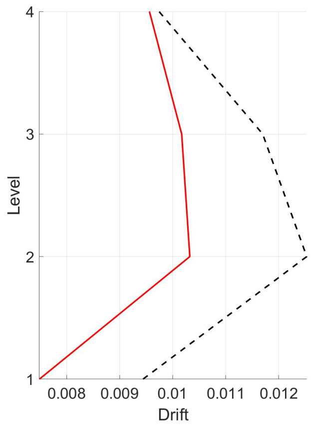

(d) Friulli

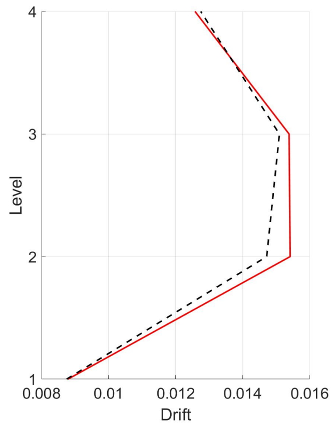

(e) Imperial Valley

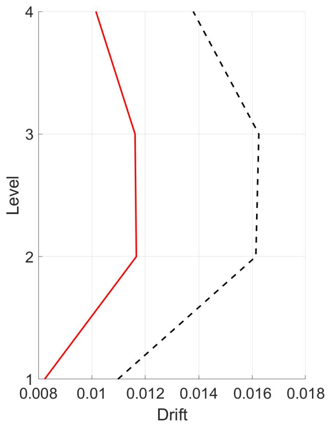

(f) Kobe

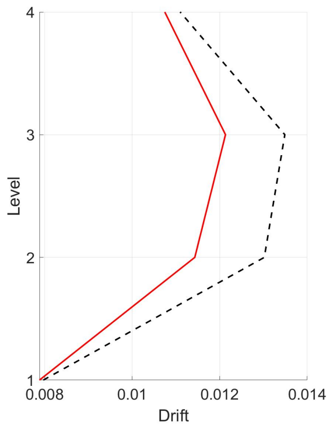

(g) Loma Prieta

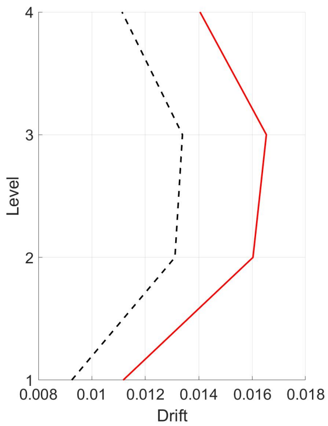

(h) Northridge

Figure B.9. Drifts Linear Initial TMD

B.1.2 Secant Stiffness

By considering a linear damper tuned to the secant stiffness the following results are obtained.

Table B.2. Performance Indices Linear Secant Damper

Earthquake	Performance Index						
	J_1	J_2	J_3	J_4	J_5	J_6	J_7(m)
Chalfant	0.706	1.057	1.077	0.660	0.879	0.925	0.506
Chi-Chi	0.919	1.012	0.928	1.133	1.081	1.065	0.331
Erzincan	0.780	1.102	1.114	0.938	1.042	1.065	0.379
Friulli	1.023	1.040	0.981	1.256	1.142	1.121	0.495
Imperial Valley	0.978	0.940	0.977	1.293	1.108	1.077	0.455
Kobe	1.019	0.894	1.023	1.100	1.054	1.046	0.543
Loma Prieta	1.385	1.076	0.937	1.466	0.992	0.980	0.379
Northridge	1.370	0.999	0.930	1.143	1.022	0.975	0.504
Average	1.023	1.015	0.996	1.124	1.040	1.032	0.449

Chalfant

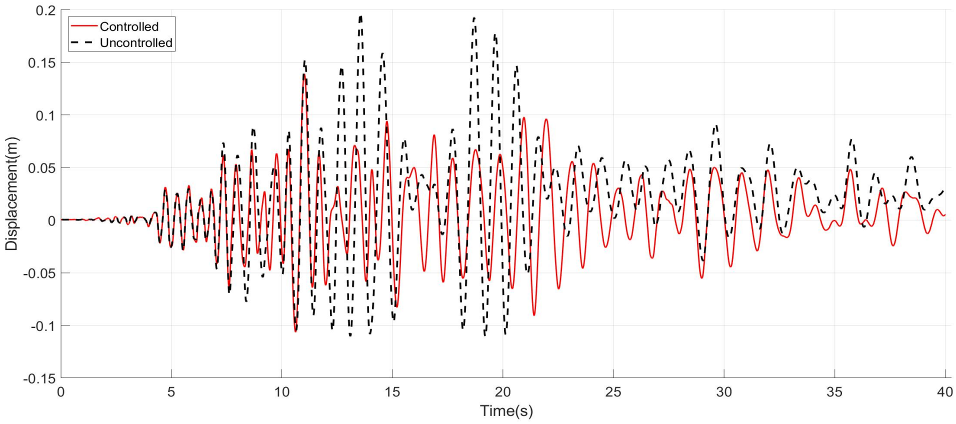

(a) Roof Displacements

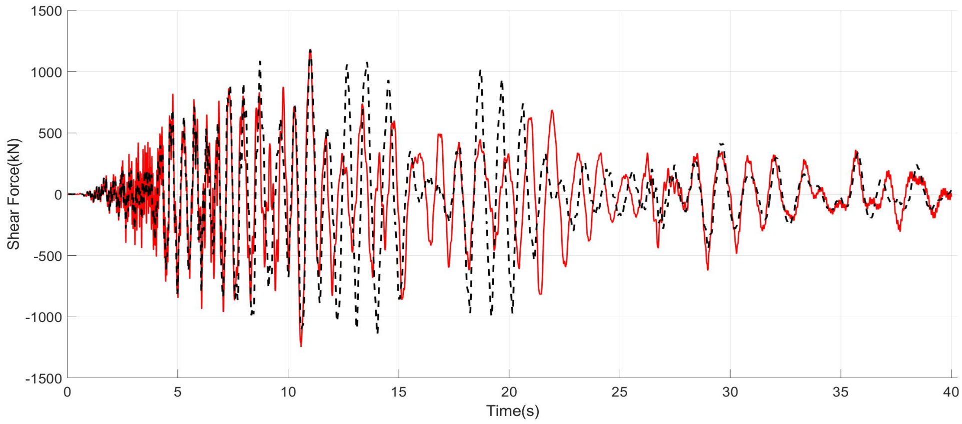

(b) Shear Forces at the base

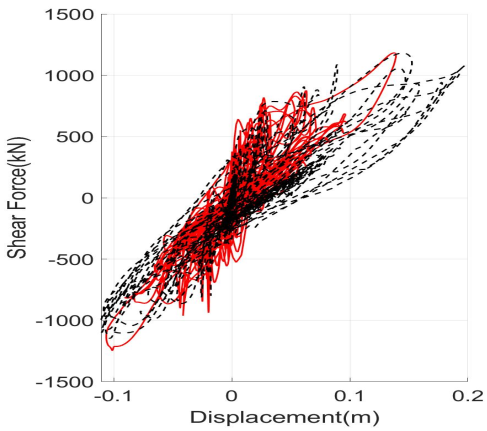

(c) Structural Hysteretic Curve

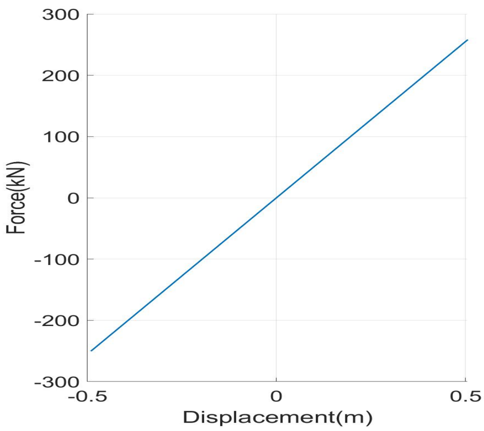

(d) TMD Hysteretic Curve

Figure B.10. Chalfant Linear Secant TMD

Chi-Chi

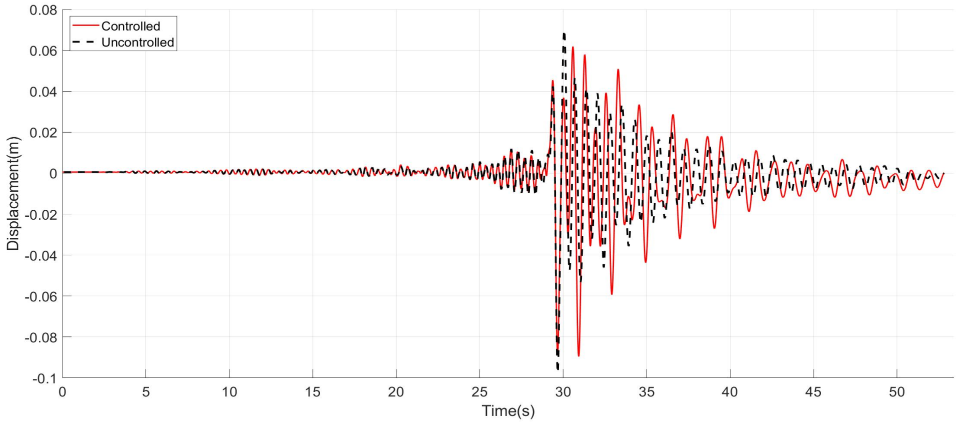

(a) Roof Displacements

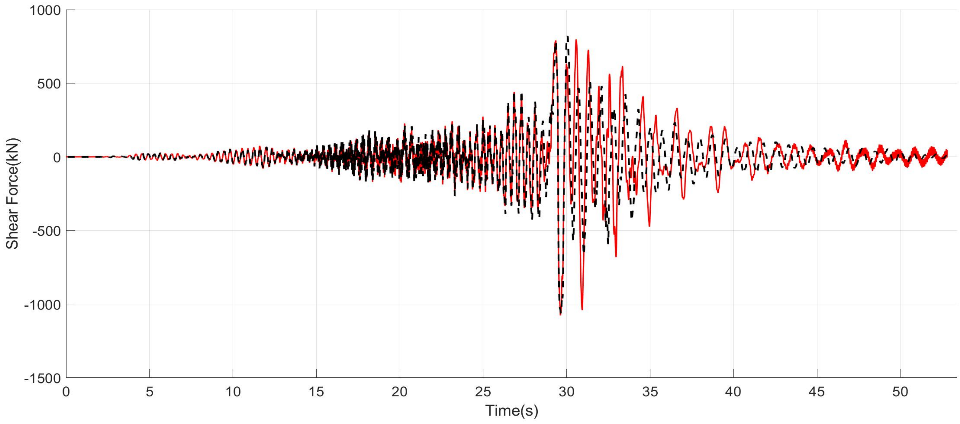

(b) Shear Forces at the base

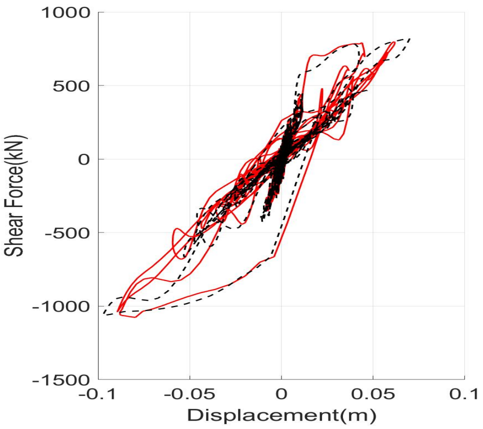

(c) Structural Hysteretic Curve

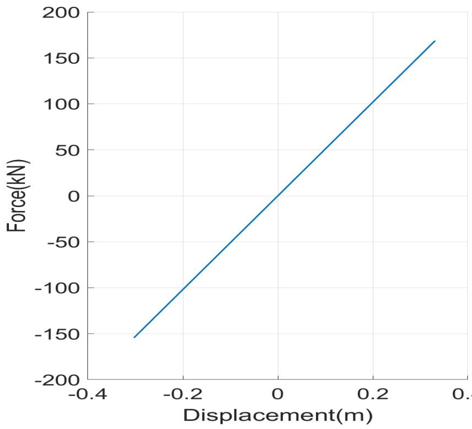

(d) TMD Hysteretic Curve

Figure B.11. Chi Chi Linear Secant TMD

Erzincan

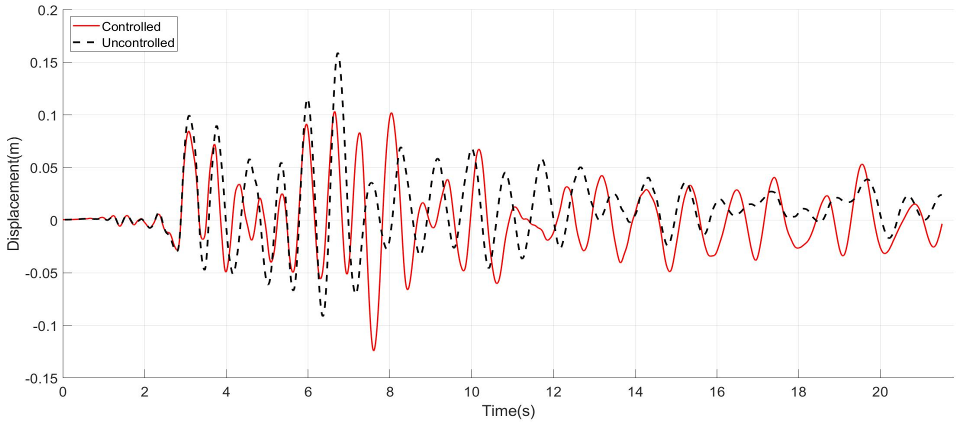

(a) Roof Displacements

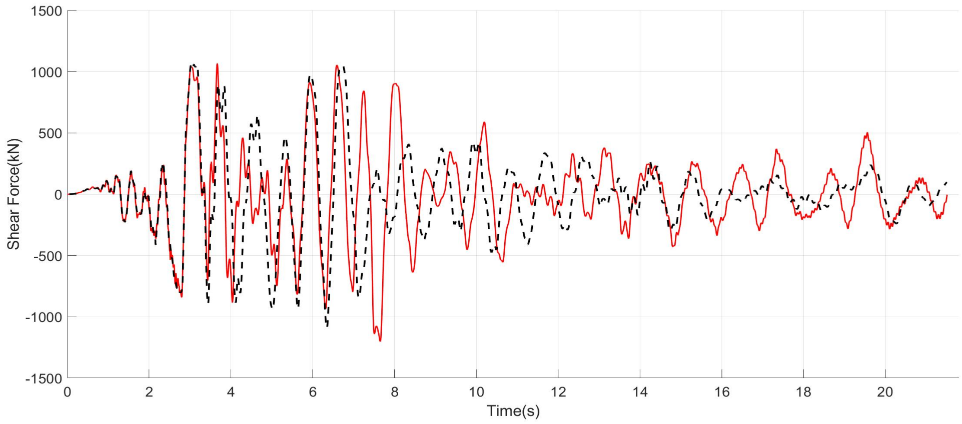

(b) Shear Forces at the base

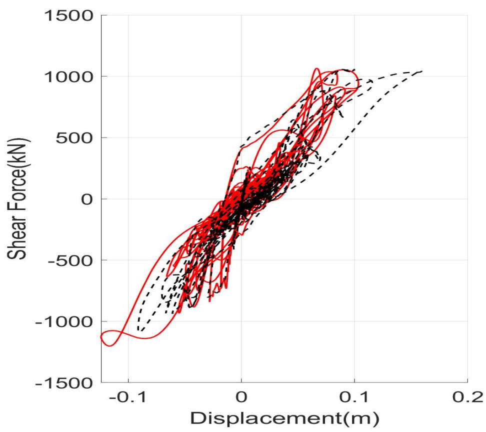

(c) Structural Hysteretic Curve

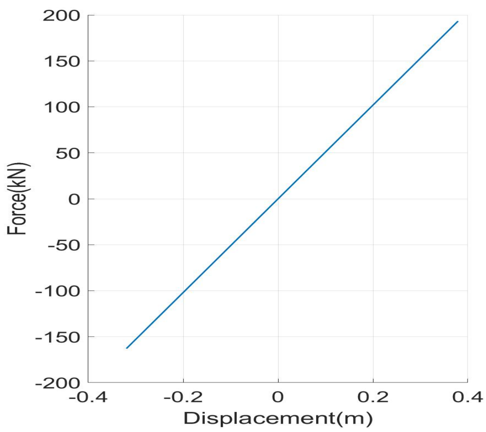

(d) TMD Hysteretic Curve

Figure B.12. Erzincan Linear Secant TMD

Friulli

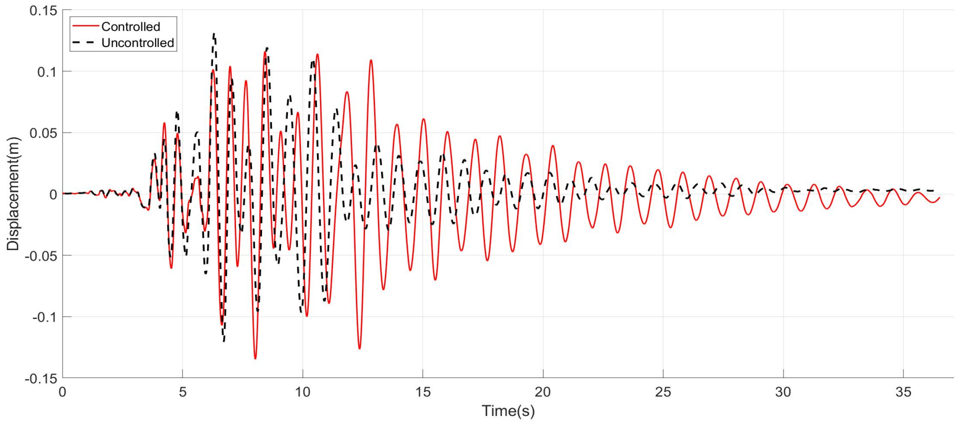

(a) Roof Displacements

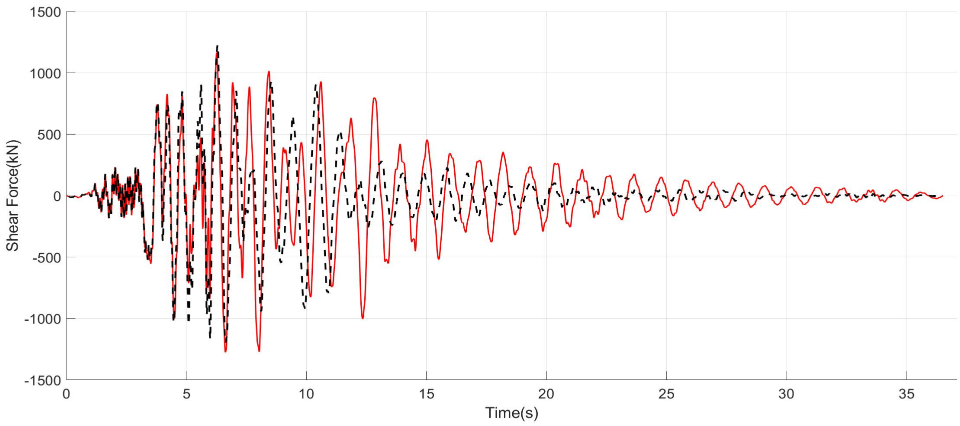

(b) Shear Forces at the base

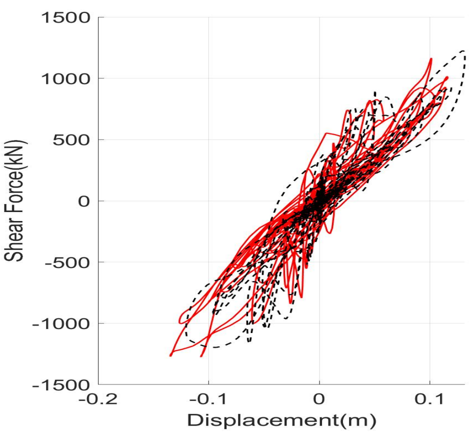

(c) Structural Hysteretic Curve

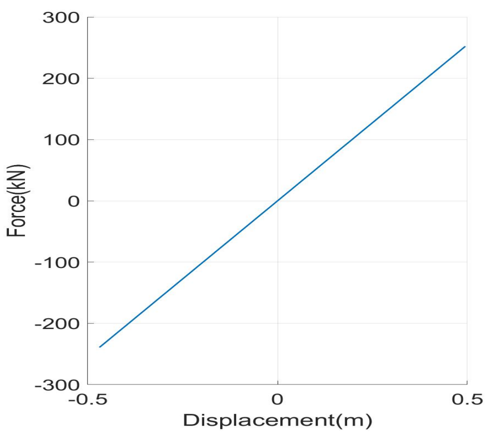

(d) TMD Hysteretic Curve

Figure B.13. Friulli Linear Secant TMD

Imperial Valley

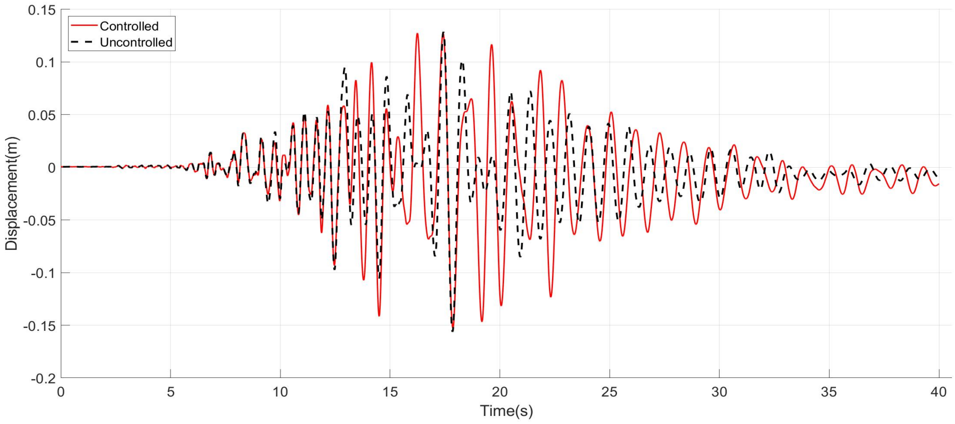

(a) Roof Displacements

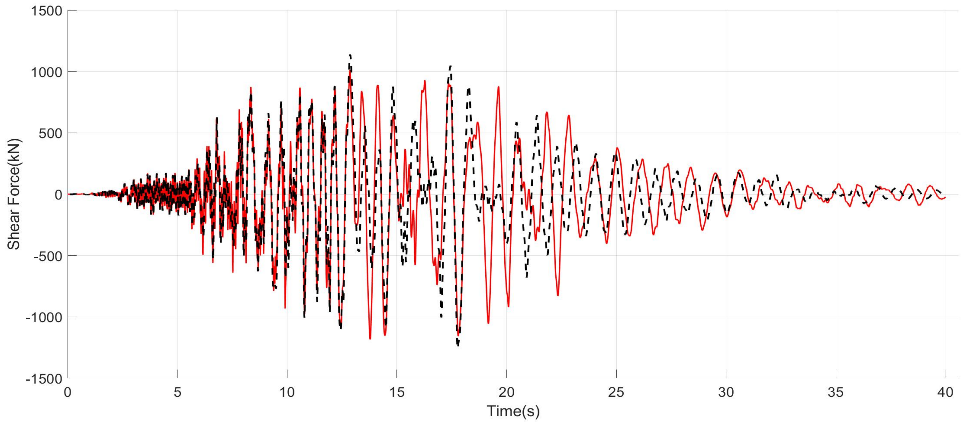

(b) Shear Forces at the base

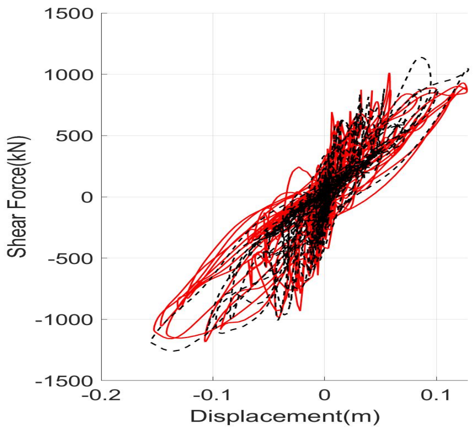

(c) Structural Hysteretic Curve

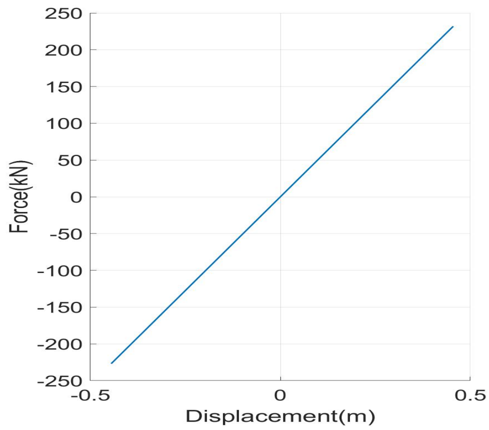

(d) TMD Hysteretic Curve

Figure B.14. Imperial Valley Linear Secant TMD

Kobe

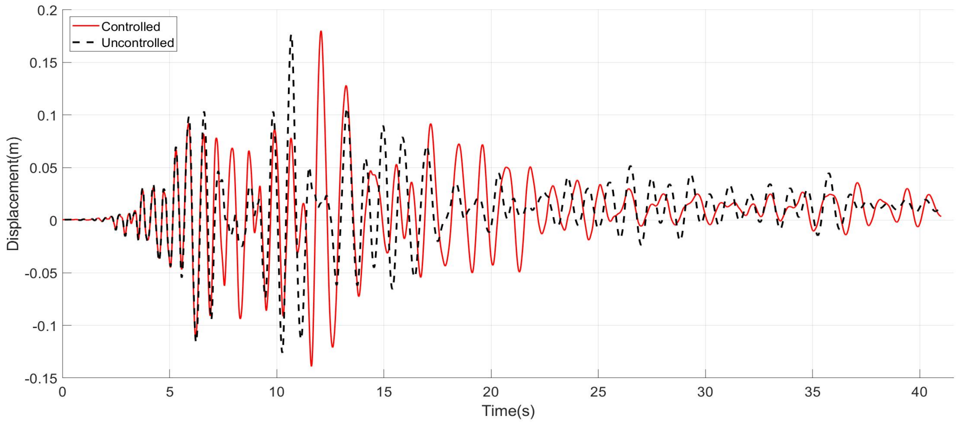

(a) Roof Displacements

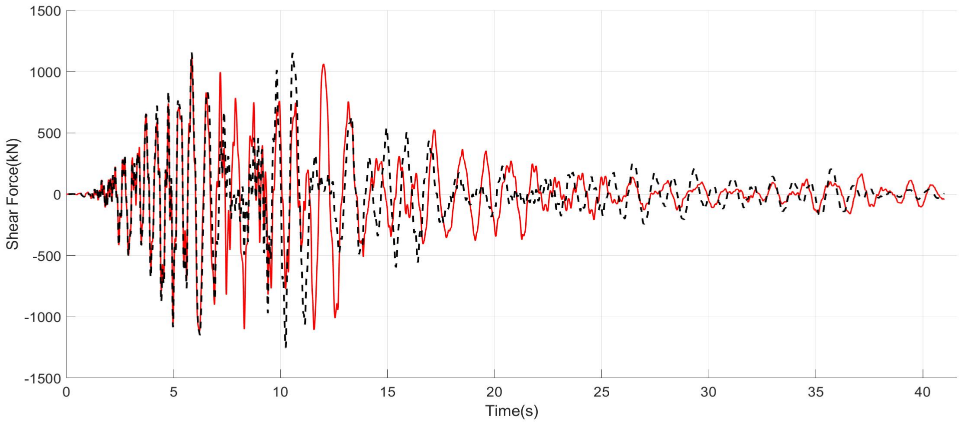

(b) Shear Forces at the base

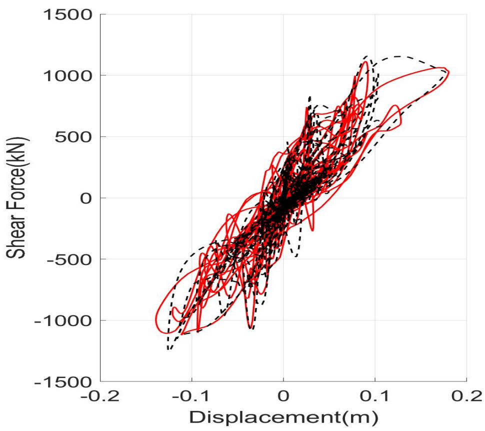

(c) Structural Hysteretic Curve

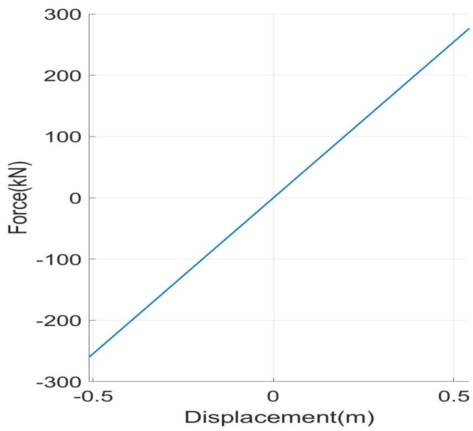

(d) TMD Hysteretic Curve

Figure B.15. Kobe Linear Secant TMD

Loma Prieta

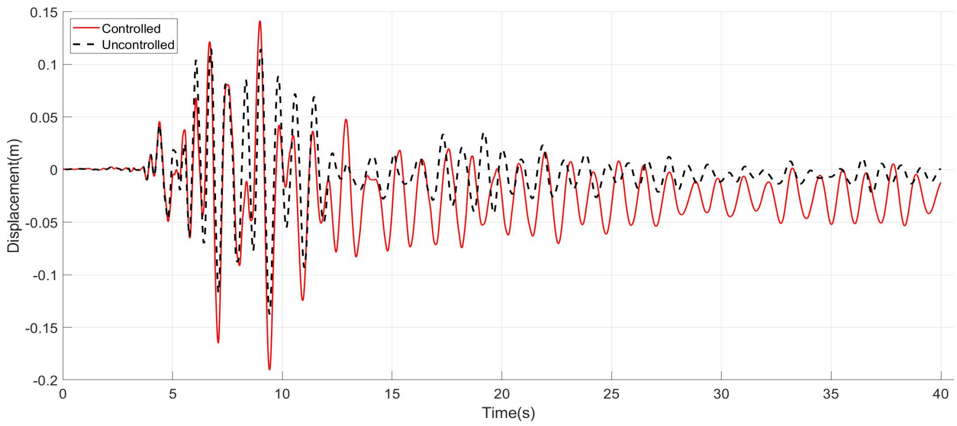

(a) Roof Displacements

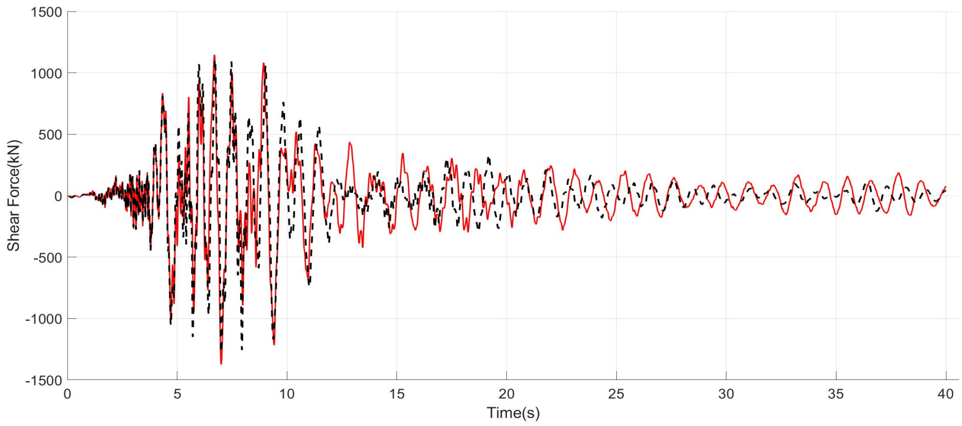

(b) Shear Forces at the base

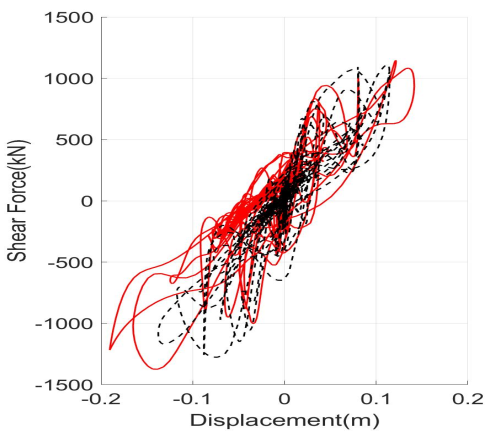

(c) Structural Hysteretic Curve

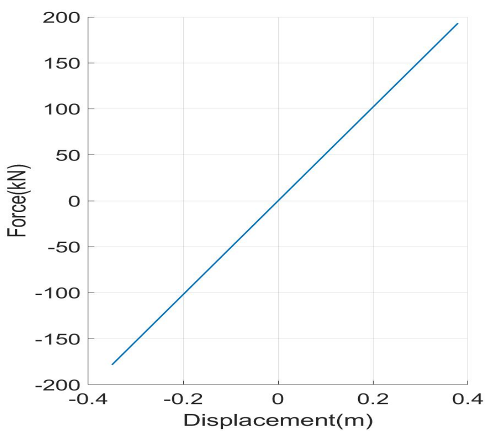

(d) TMD Hysteretic Curve

Figure B.16. Loma Prieta Linear Secant TMD

Northridge

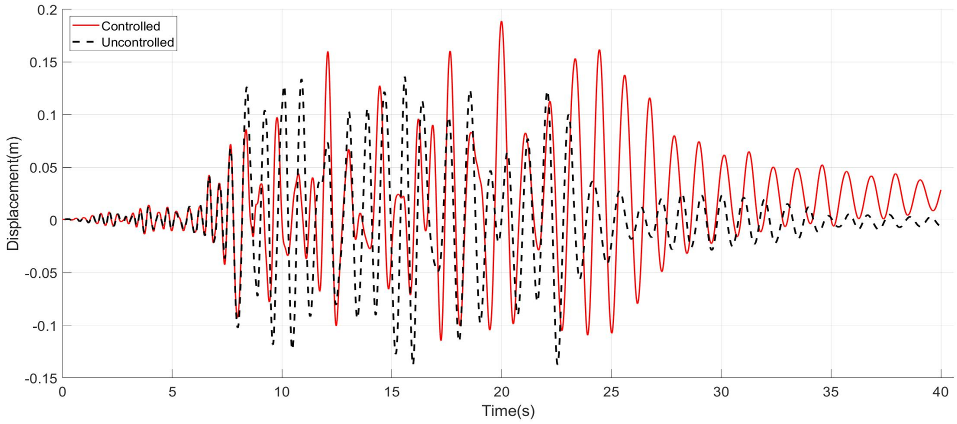

(a) Roof Displacements

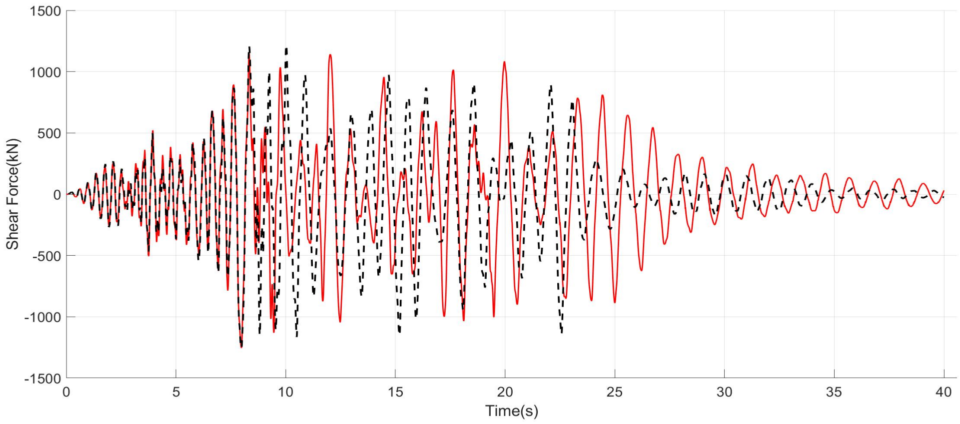

(b) Shear Forces at the base

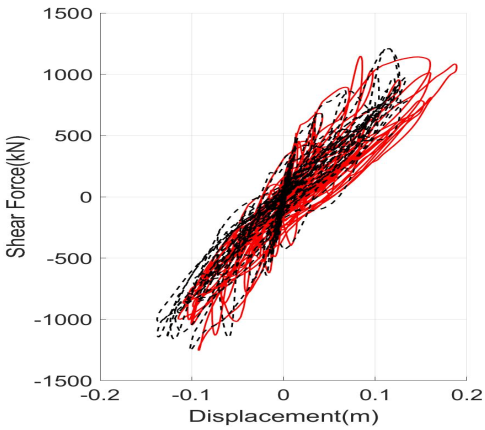

(c) Structural Hysteretic Curve

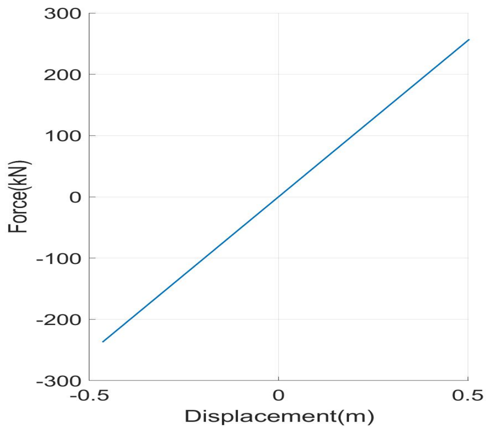

(d) TMD Hysteretic Curve

Figure B.17. Northridge Linear Secant TMD

Drifts

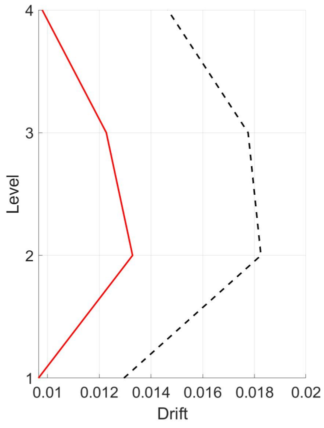

(a) Chalfant

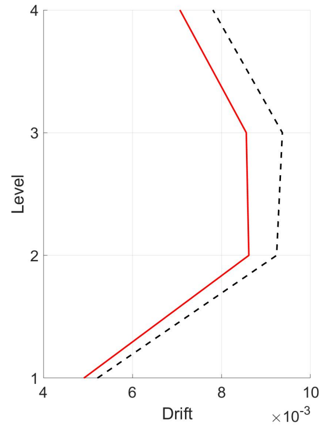

(b) Chi Chi

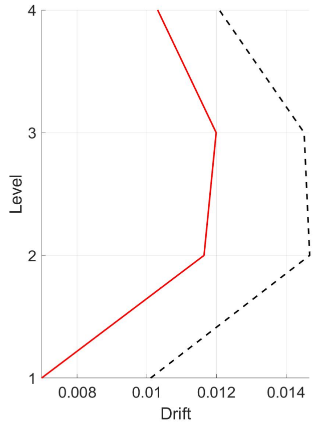

(c) Erzincan

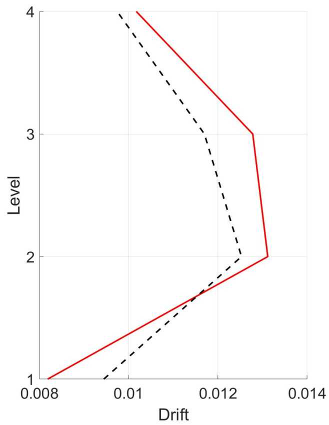

(d) Friulli

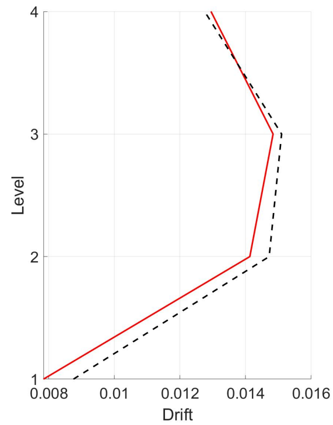

(e) Imperial Valley

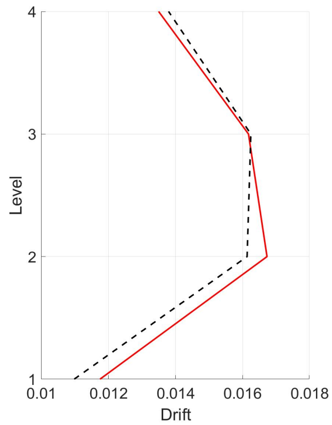

(f) Kobe

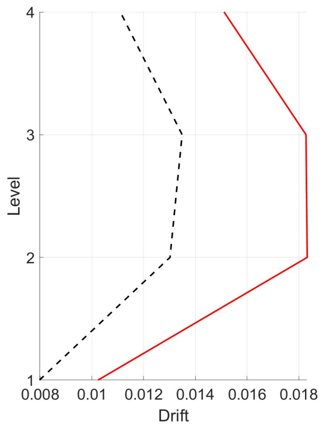

(g) Loma Prieta

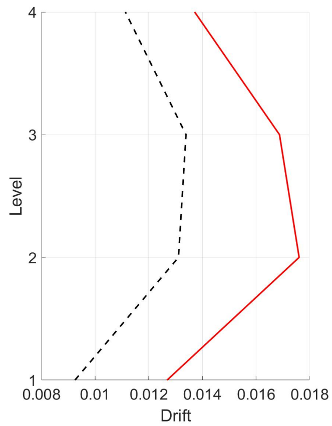

(h) Northridge

Figure B.18. Drifts Linear Secant TMD

B.2 Direct Procedure

B.2.1 $U_{max} = 15cm$

The results of the matched natural accelerograms using a direct desing procedure assuming a maximum displacement of the TMD of $15cm$ are presented.

Table B.3. Performance Indices $U_{max} = 15cm$

Earthquake	Performance Index						
	J_1	J_2	J_3	J_4	J_5	J_6	J_7(m)
Chalfant	0.577	0.996	1.032	0.531	0.847	0.951	0.302
Chi-Chi	0.836	0.976	0.881	0.639	0.808	0.855	0.237
Erzincan	0.705	0.987	1.014	0.676	0.850	0.891	0.264
Friulli	0.733	1.019	1.003	0.716	0.911	0.945	0.225
Imperial Valley	0.756	1.045	1.093	0.792	0.927	0.965	0.226
Kobe	0.737	0.996	1.072	0.792	0.982	1.012	0.229
Loma Prieta	0.724	1.081	1.007	0.771	0.908	0.927	0.237
Northridge	0.797	0.979	0.905	0.641	0.827	0.819	0.246
Average	0.733	1.010	1.001	0.695	0.883	0.921	0.246

Chalfant

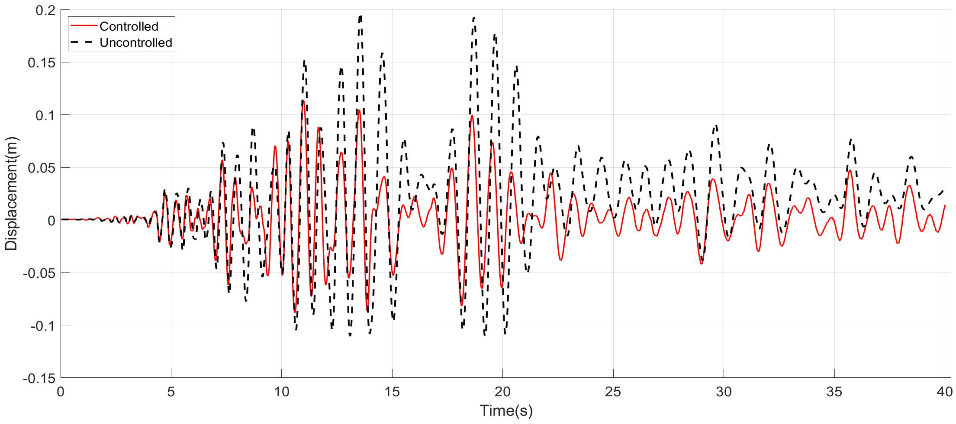

(a) Roof Displacements

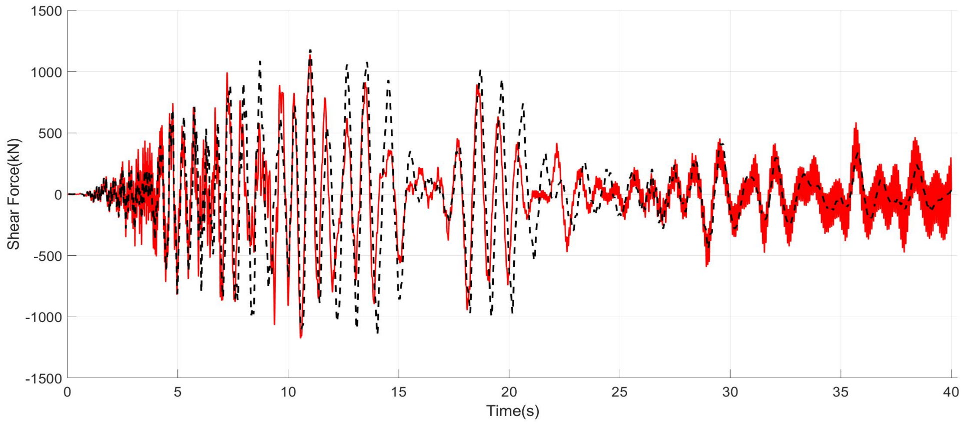

(b) Shear Forces at the base

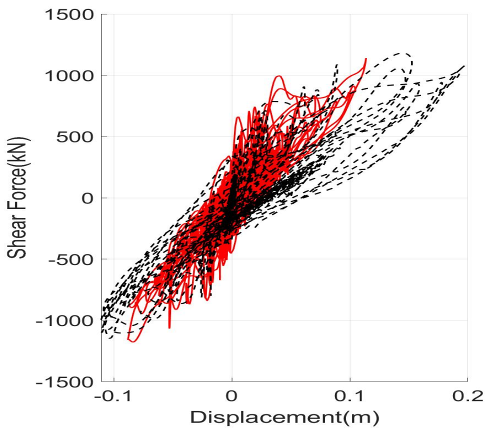

(c) Structural Hysteretic Curve

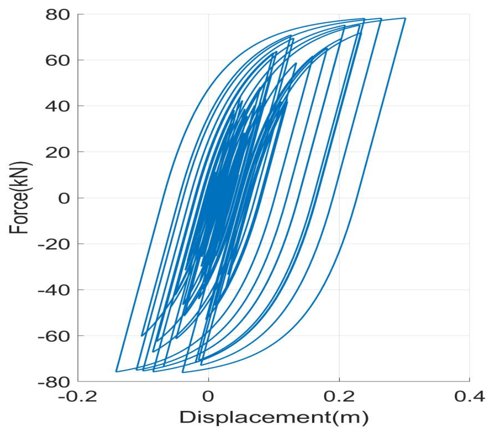

(d) TMD Hysteretic Curve

Figure B.19. Chalfant $U_{max} = 15cm$

Chi-Chi

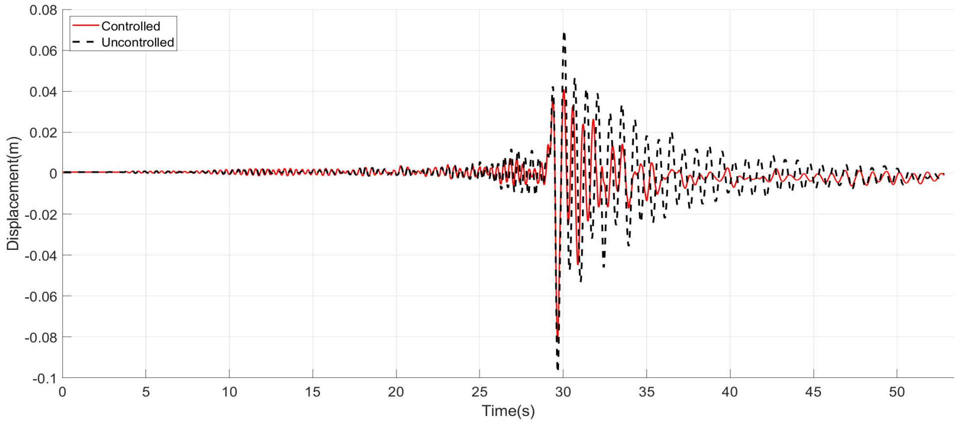

(a) Roof Displacements

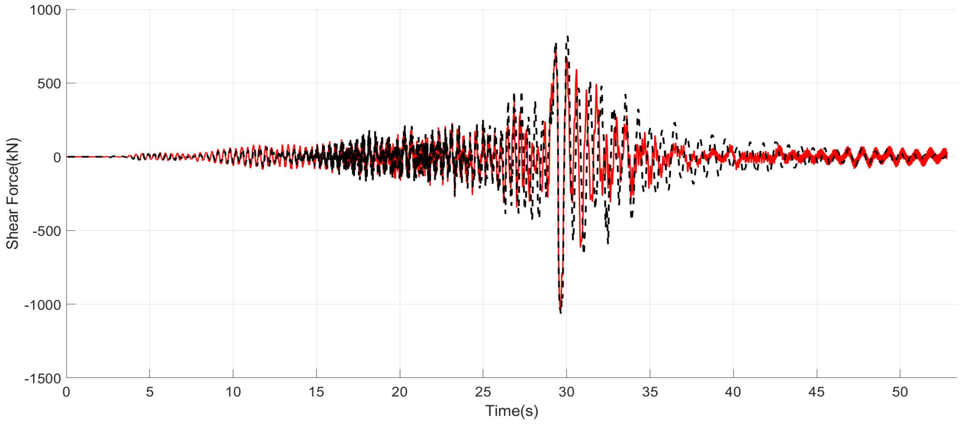

(b) Shear Forces at the base

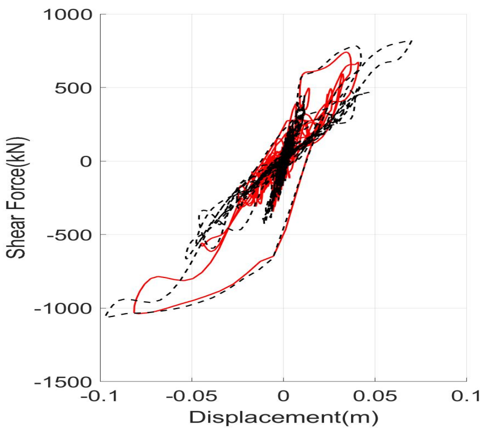

(c) Structural Hysteretic Curve

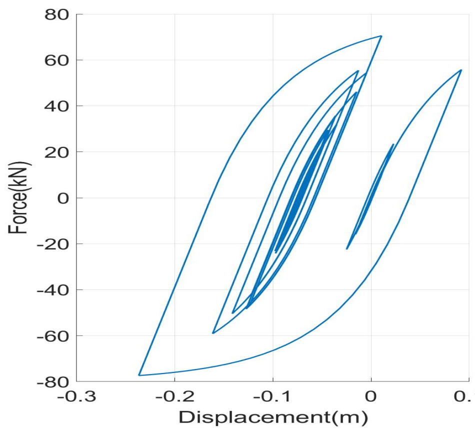

(d) TMD Hysteretic Curve

Figure B.20. Chi Chi $U_{max} = 15cm$

Erzincan

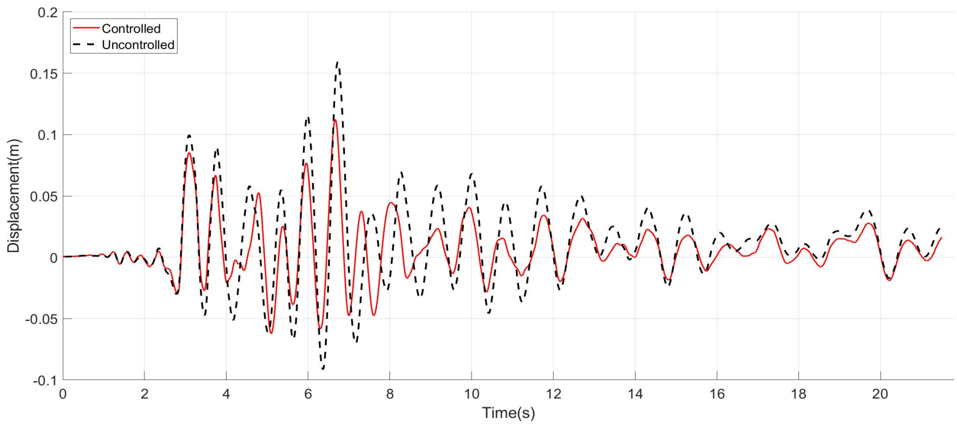

(a) Roof Displacements

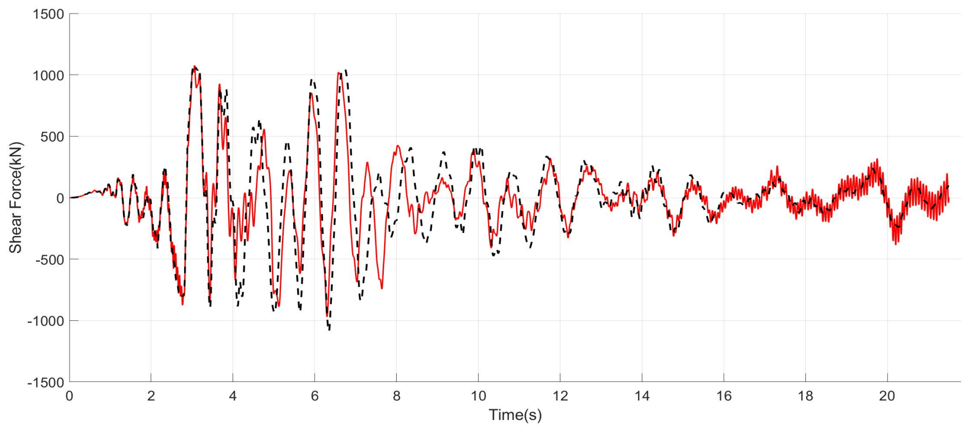

(b) Shear Forces at the base

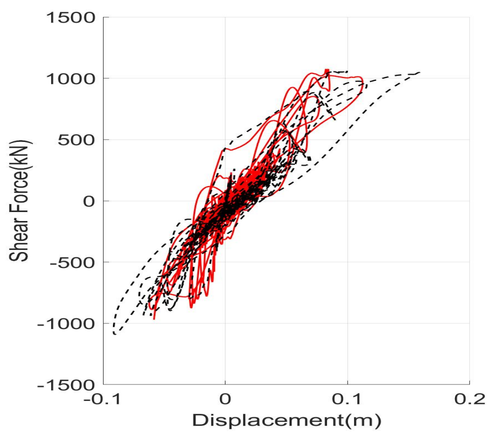

(c) Structural Hysteretic Curve

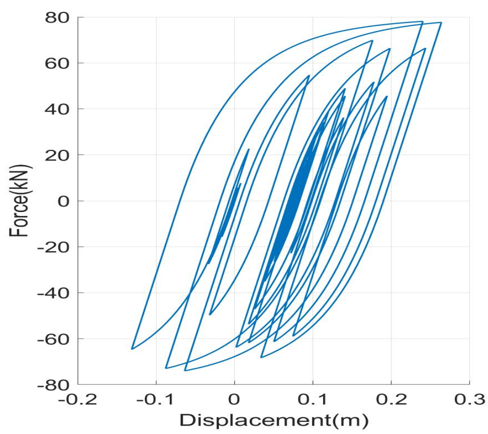

(d) TMD Hysteretic Curve

Figure B.21. Erzincan $U_{max} = 15cm$

Friulli

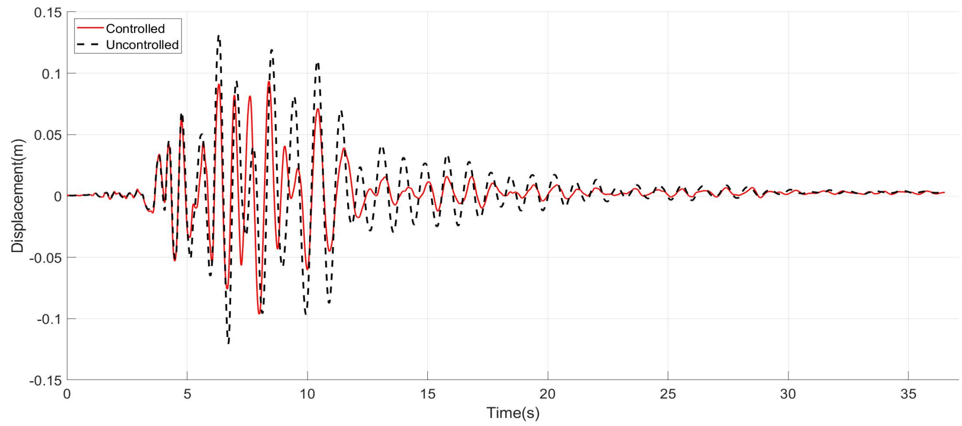

(a) Roof Displacements

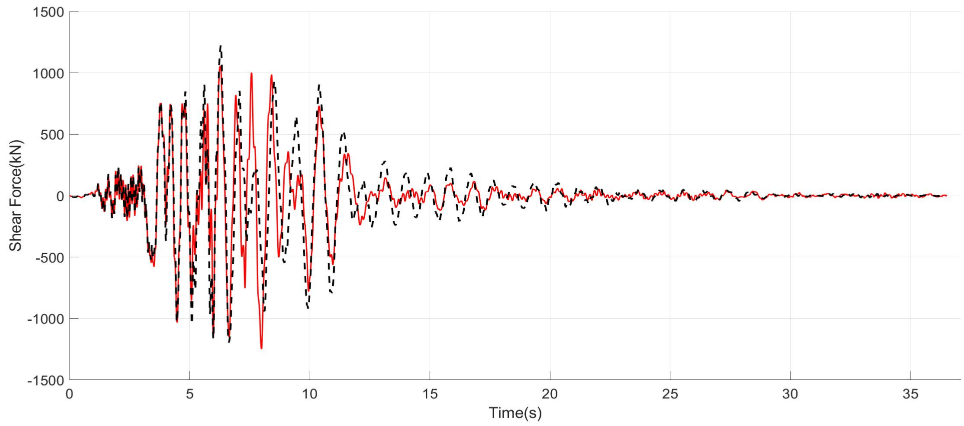

(b) Shear Forces at the base

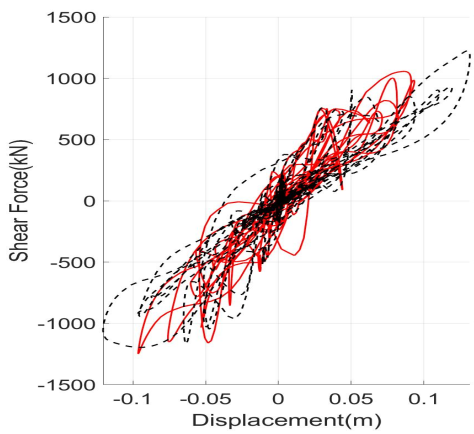

(c) Structural Hysteretic Curve

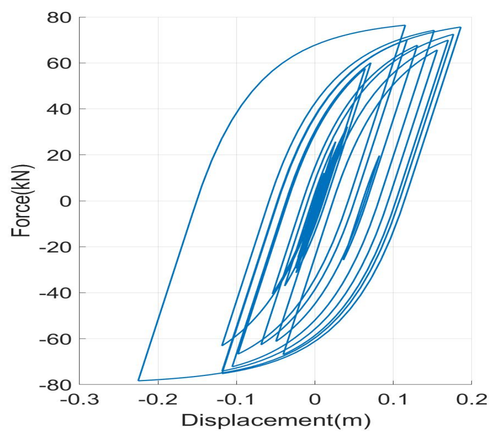

(d) TMD Hysteretic Curve

Figure B.22. Friulli $U_{max} = 15cm$

Imperial Valley

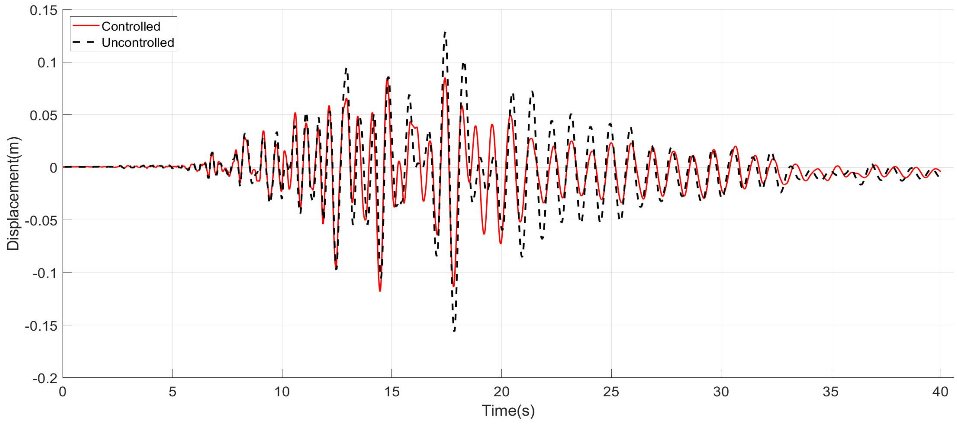

(a) Roof Displacements

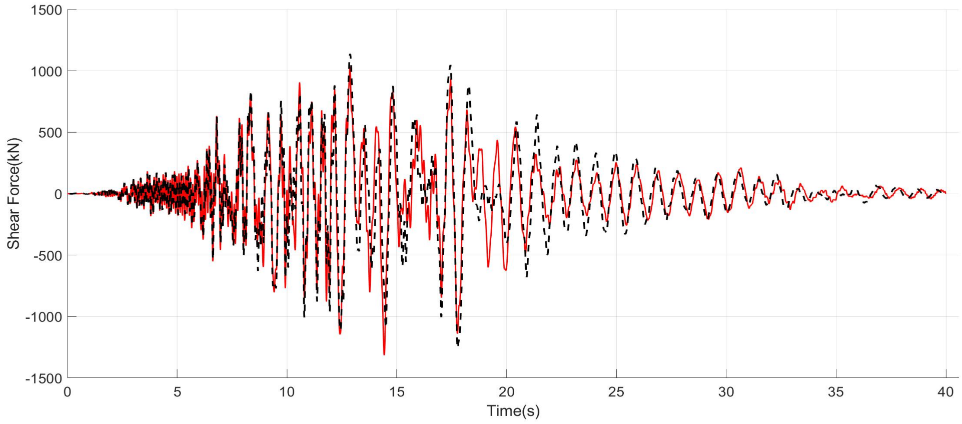

(b) Shear Forces at the base

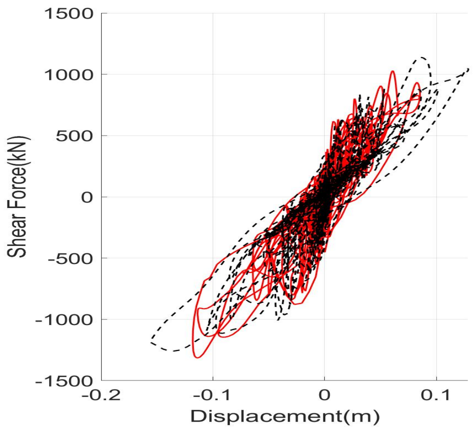

(c) Structural Hysteretic Curve

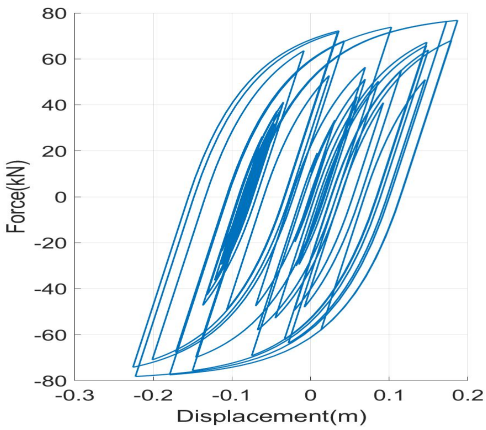

(d) TMD Hysteretic Curve

Figure B.23. Imperial Valley $U_{max} = 15cm$

Kobe

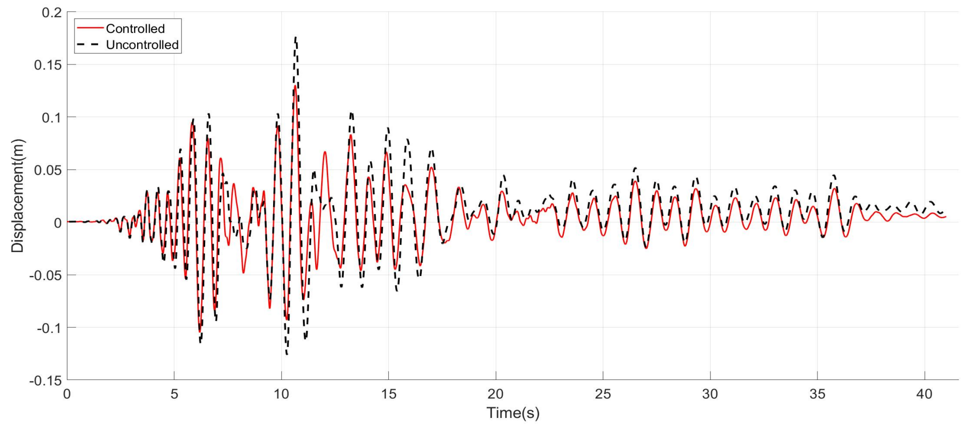

(a) Roof Displacements

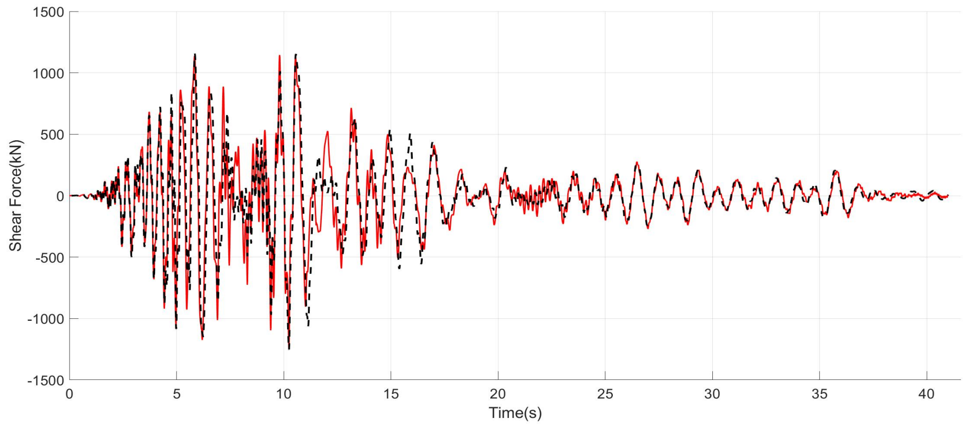

(b) Shear Forces at the base

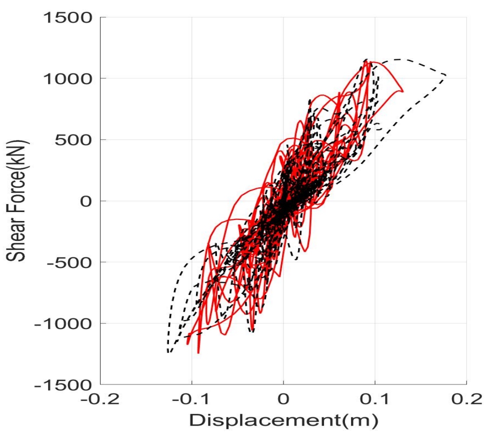

(c) Structural Hysteretic Curve

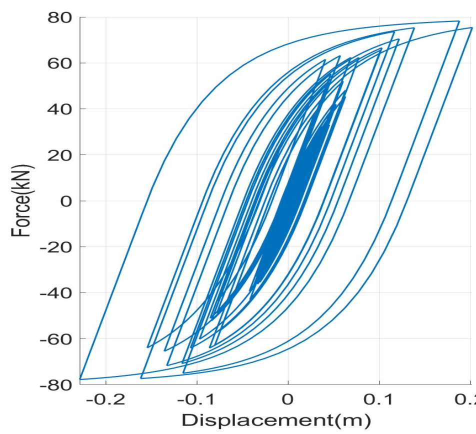

(d) TMD Hysteretic Curve

Figure B.24. Kobe $U_{max} = 15cm$

Loma Prieta

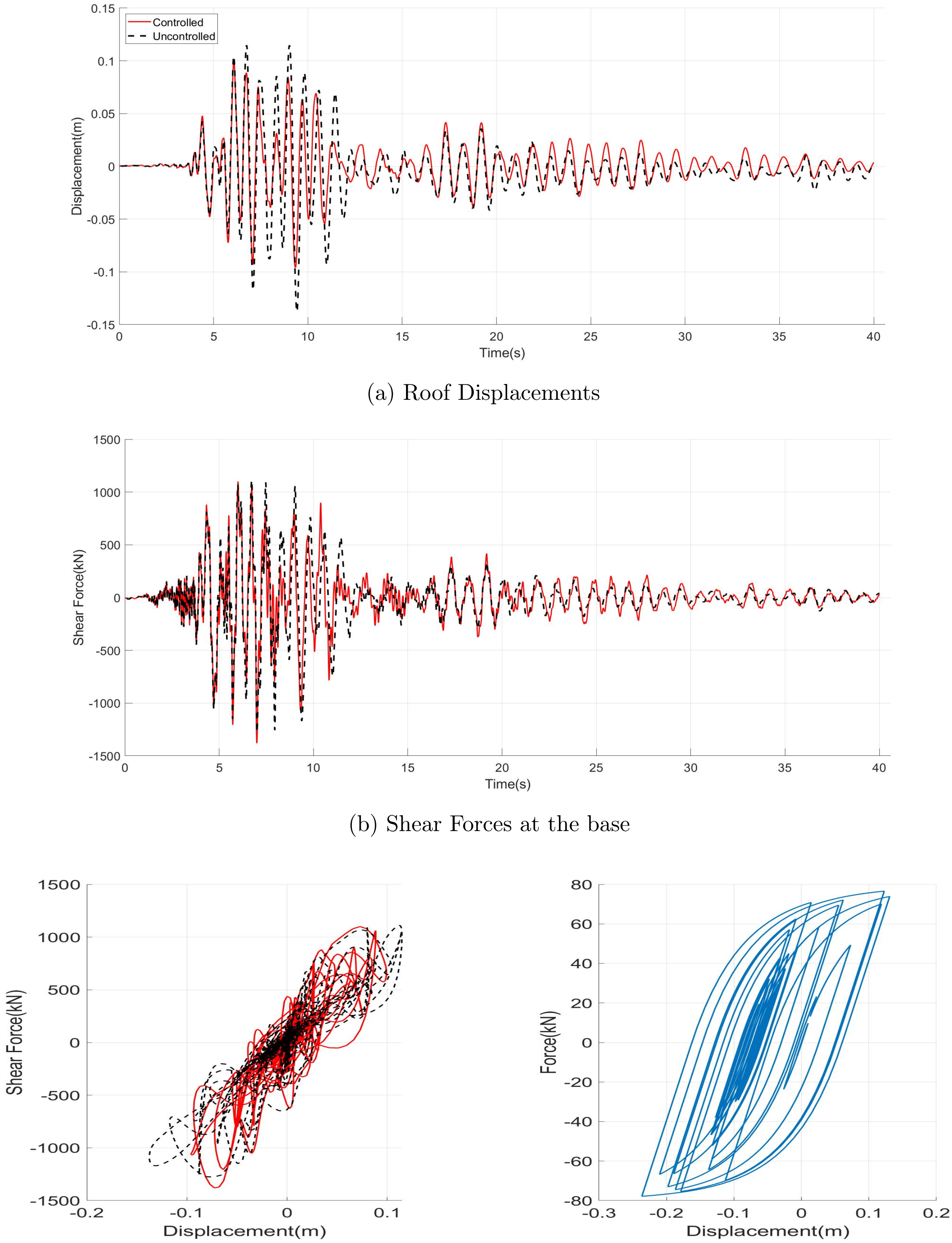

(a) Roof Displacements

(b) Shear Forces at the base

(c) Structural Hysteretic Curve

(d) TMD Hysteretic Curve

Figure B.25. Loma Prieta $U_{max} = 15cm$

Northridge

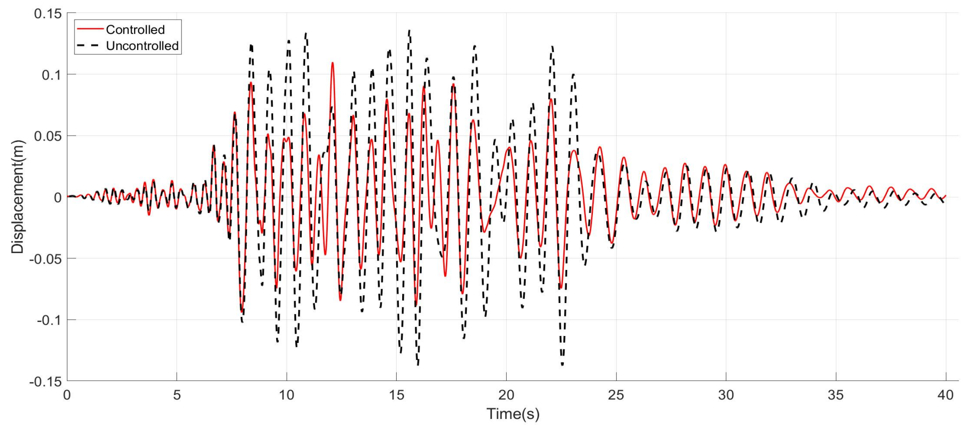

(a) Roof Displacements

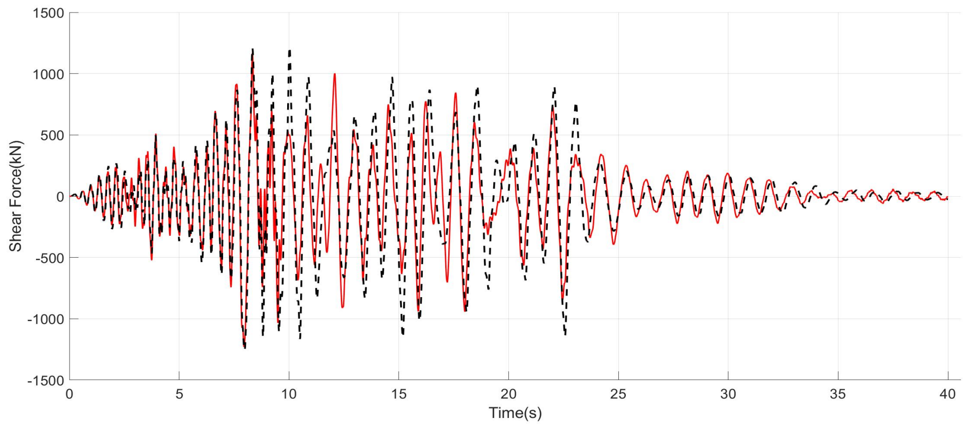

(b) Shear Forces at the base

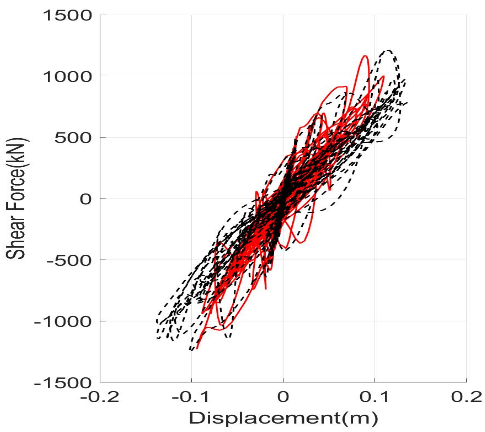

(c) Structural Hysteretic Curve

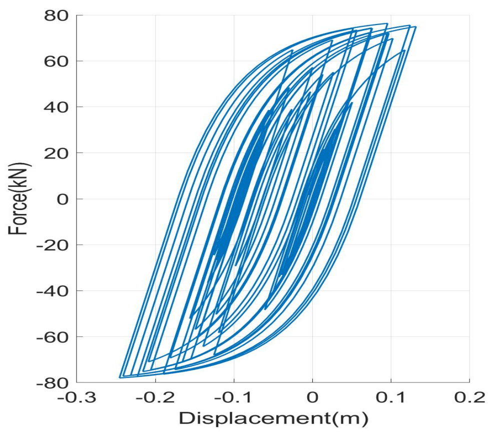

(d) TMD Hysteretic Curve

Figure B.26. Northridge $U_{max} = 15cm$

Drifts

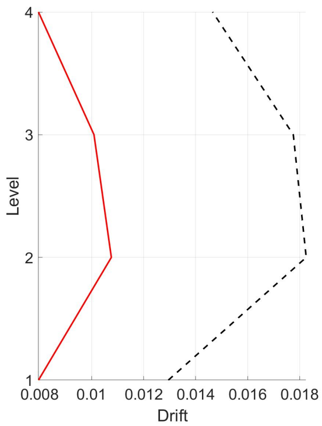

(a) Chalfant

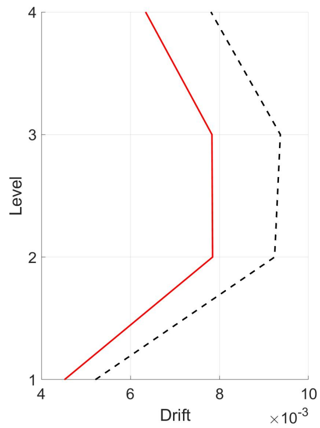

(b) Chi Chi

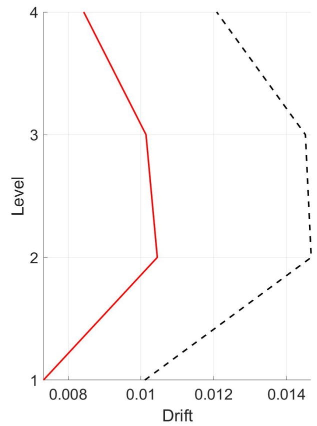

(c) Erzincan

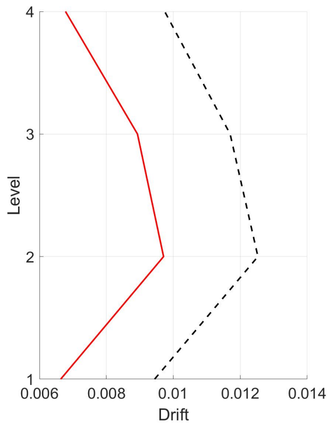

(d) Friulli

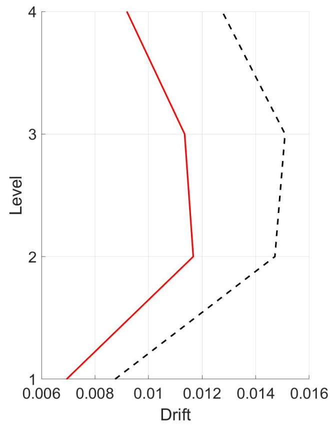

(e) Imperial Valley

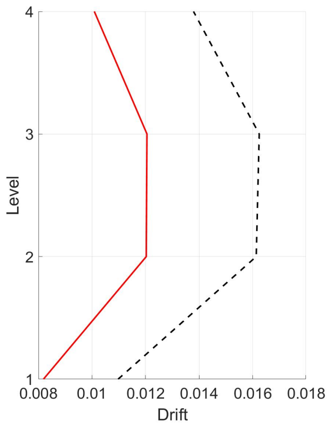

(f) Kobe

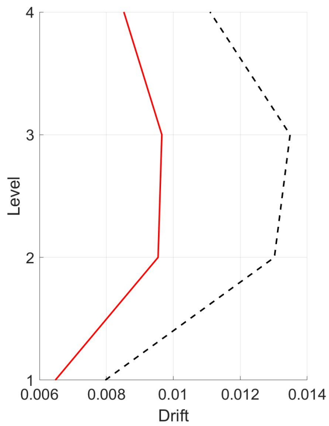

(g) Loma Prieta

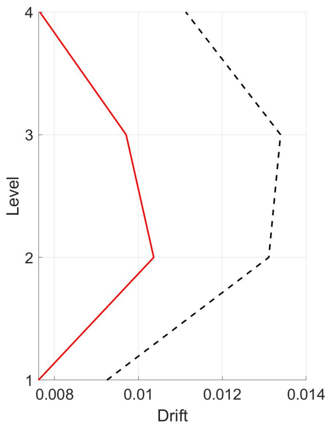

(h) Northridge

Figure B.27. Drifts $U_{max} = 15cm$

B.2.2 $U_{max} = 20cm$

Using a stroke of $20cm$ for the direct design procedure the following results are obtained.

Table B.4. Performance Indices $U_{max} = 20cm$

Earthquake	Performance Index						
	J_1	J_2	J_3	J_4	J_5	J_6	J_7(m)
Chalfant	0.559	1.015	0.997	0.537	0.851	0.907	0.271
Chi-Chi	0.818	0.981	0.913	0.612	0.799	0.876	0.224
Erzincan	0.662	0.980	0.992	0.656	0.827	0.857	0.253
Friulli	0.674	0.979	1.048	0.698	0.907	0.938	0.230
Imperial Valley	0.732	1.032	1.015	0.782	0.930	0.966	0.215
Kobe	0.691	0.968	1.178	0.765	0.991	1.031	0.254
Loma Prieta	0.741	1.065	0.983	0.713	0.870	0.914	0.207
Northridge	0.795	0.971	0.899	0.628	0.814	0.798	0.267
Average	0.709	0.999	1.003	0.674	0.873	0.911	0.240

Chalfant

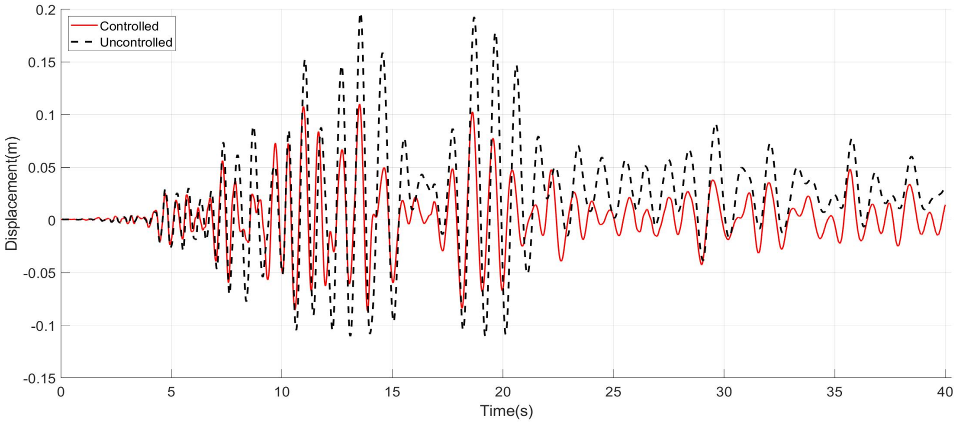

(a) Roof Displacements

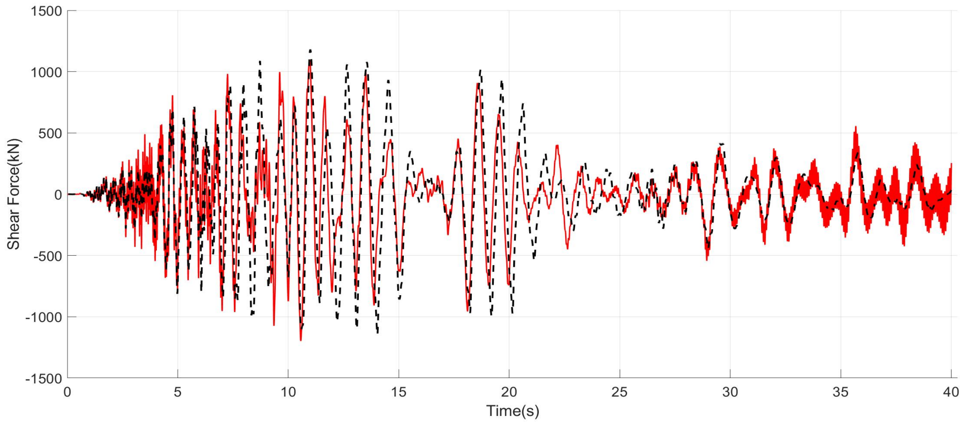

(b) Shear Forces at the base

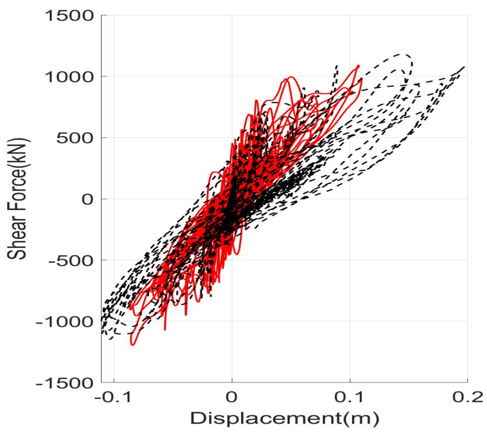

(c) Structural Hysteretic Curve

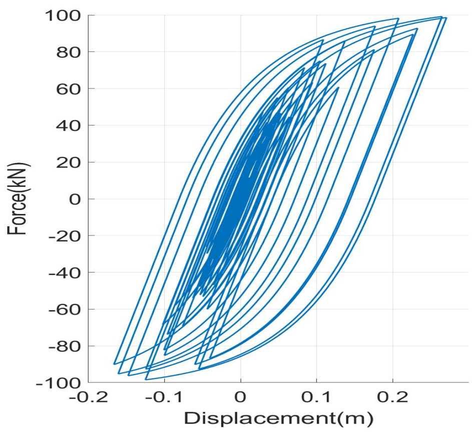

(d) TMD Hysteretic Curve

Figure B.28. Chalfant $U_{max} = 20cm$

Chi-Chi

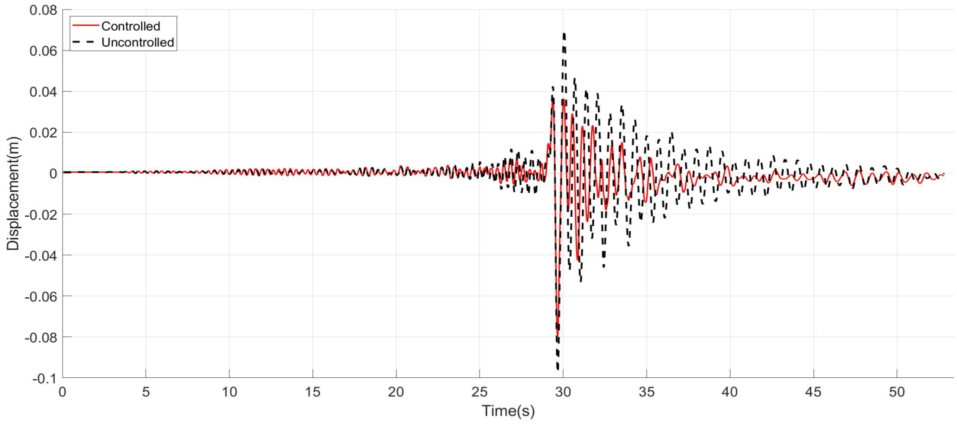

(a) Roof Displacements

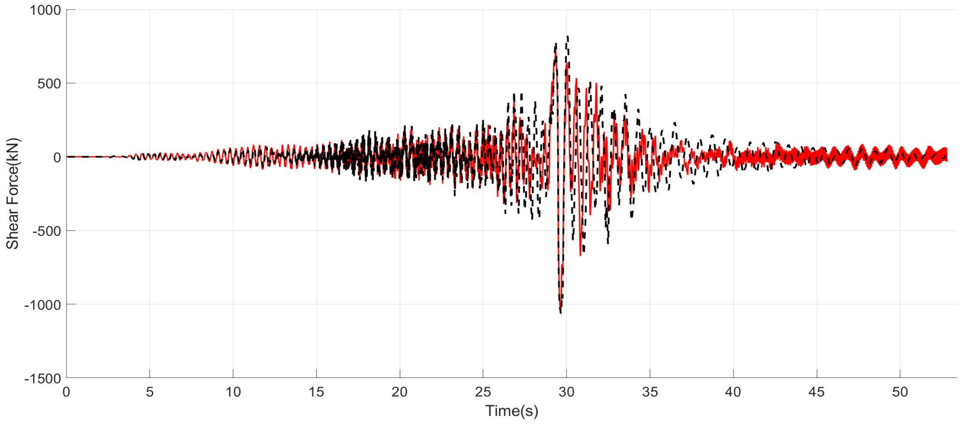

(b) Shear Forces at the base

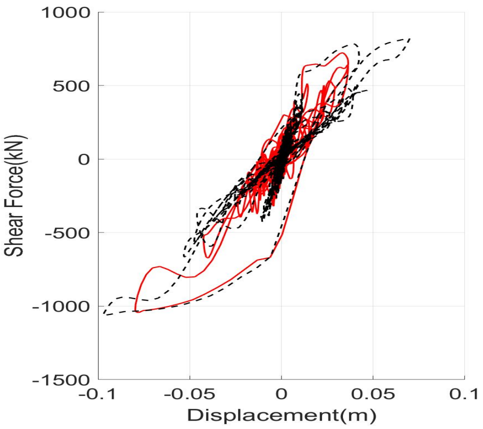

(c) Structural Hysteretic Curve

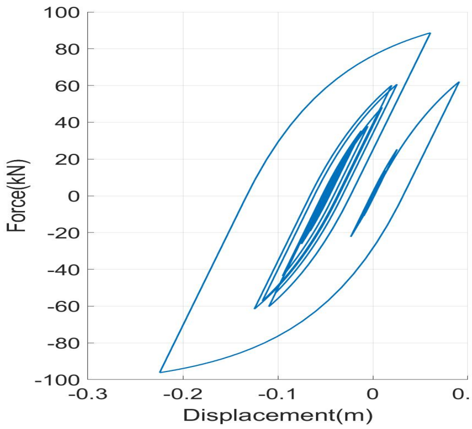

(d) TMD Hysteretic Curve

Figure B.29. Chi Chi $U_{max} = 20cm$

Erzincan

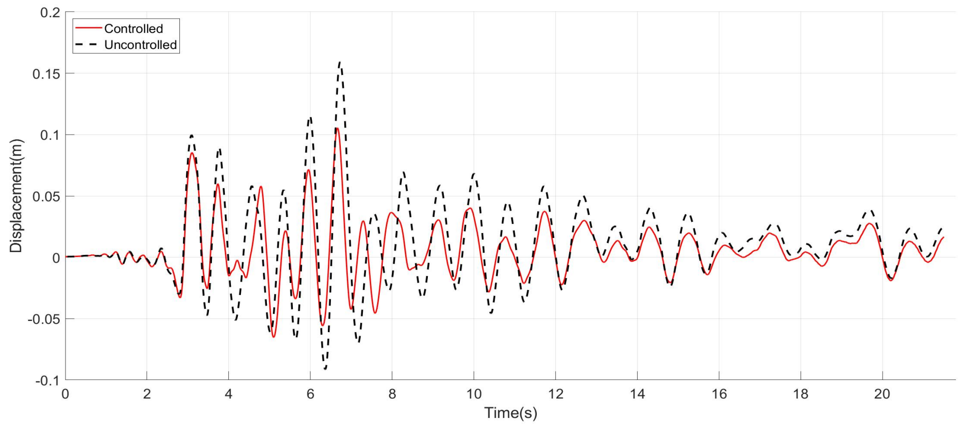

(a) Roof Displacements

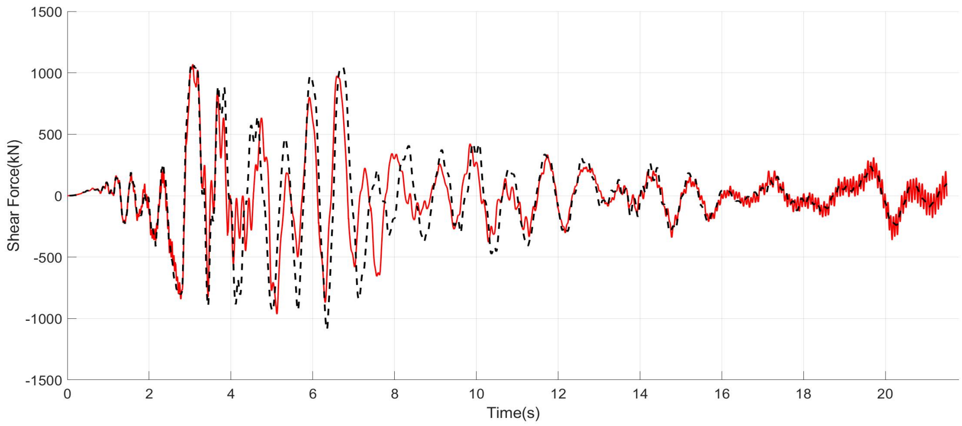

(b) Shear Forces at the base

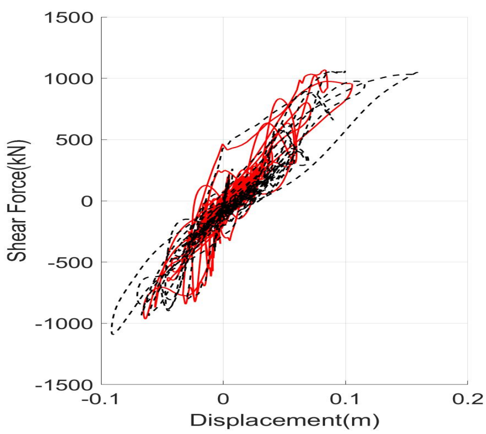

(c) Structural Hysteretic Curve

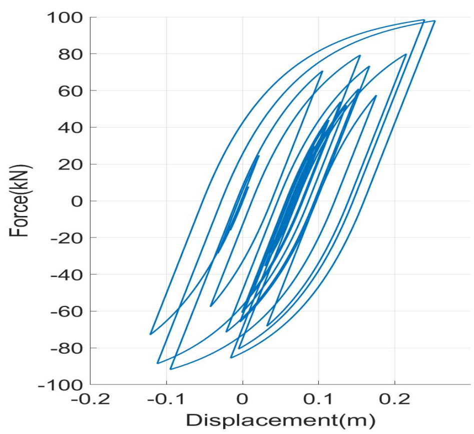

(d) TMD Hysteretic Curve

Figure B.30. Erzincan $U_{max} = 20cm$

Friulli

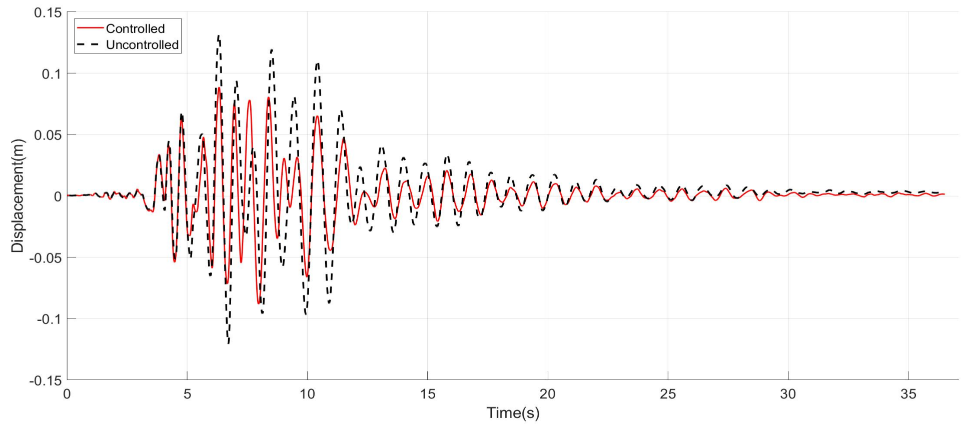

(a) Roof Displacements

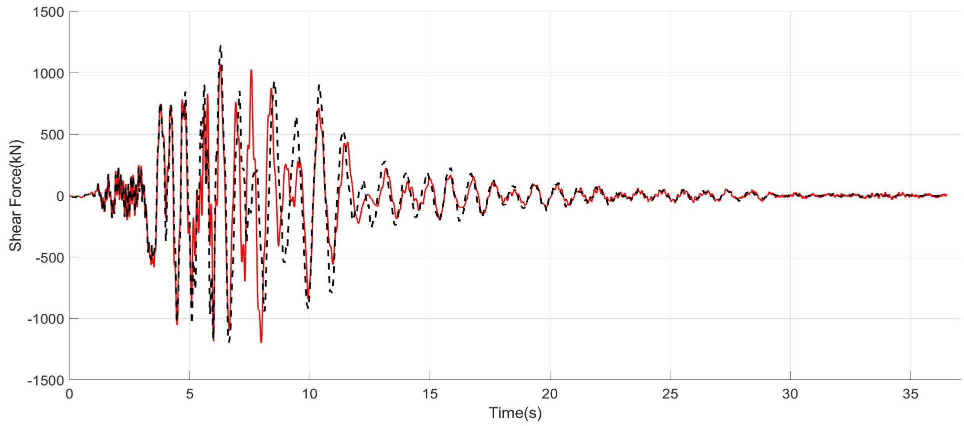

(b) Shear Forces at the base

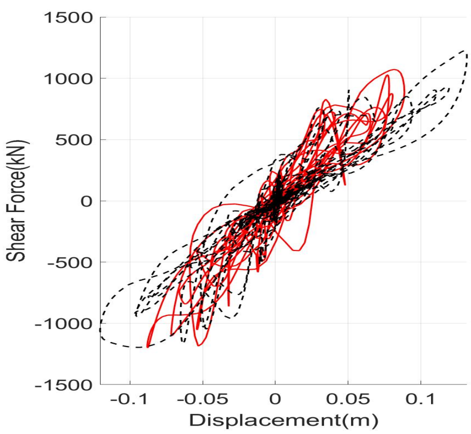

(c) Structural Hysteretic Curve

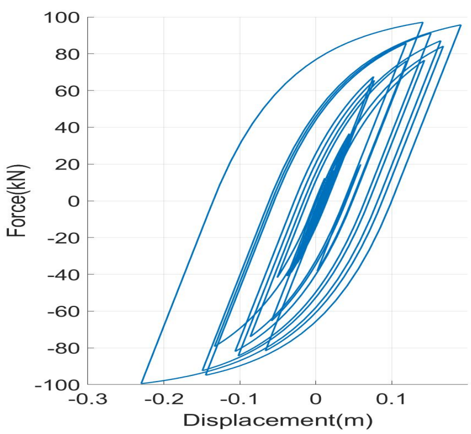

(d) TMD Hysteretic Curve

Figure B.31. Friulli $U_{max} = 20cm$

Imperial Valley

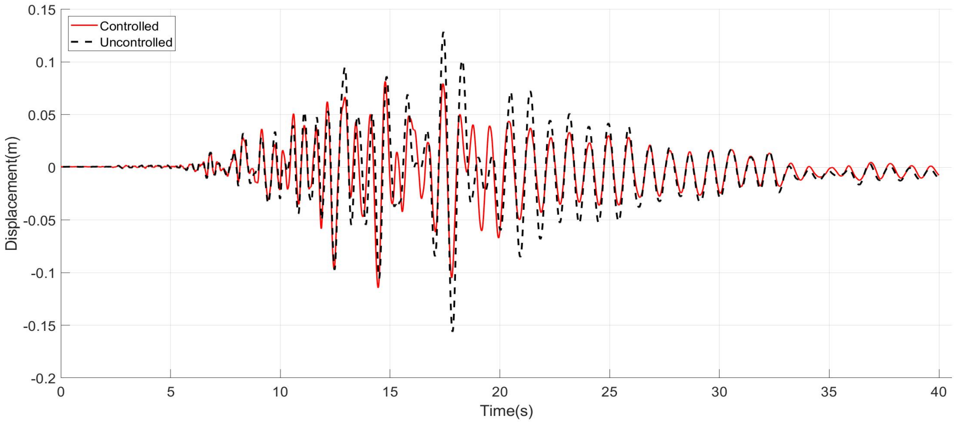

(a) Roof Displacements

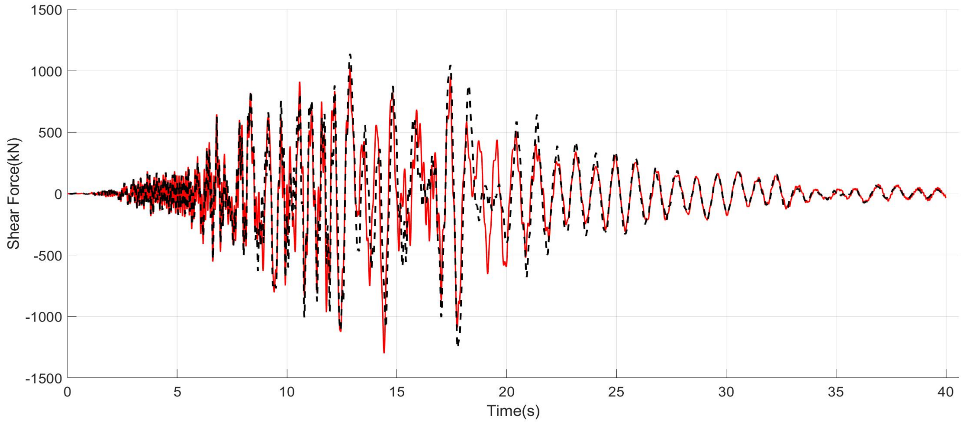

(b) Shear Forces at the base

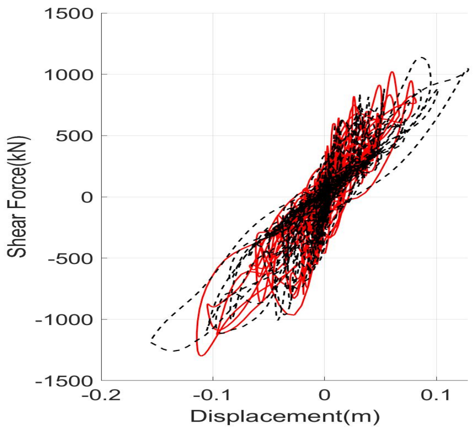

(c) Structural Hysteretic Curve

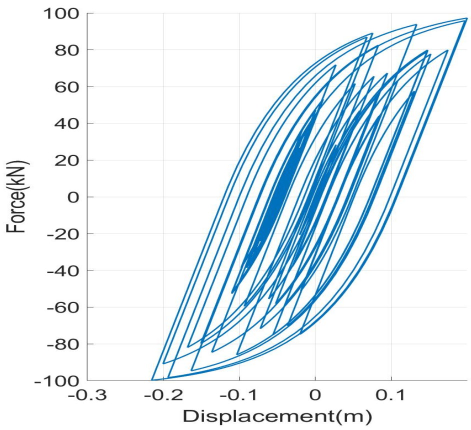

(d) TMD Hysteretic Curve

Figure B.32. Imperial Valley $U_{max} = 20cm$

Kobe

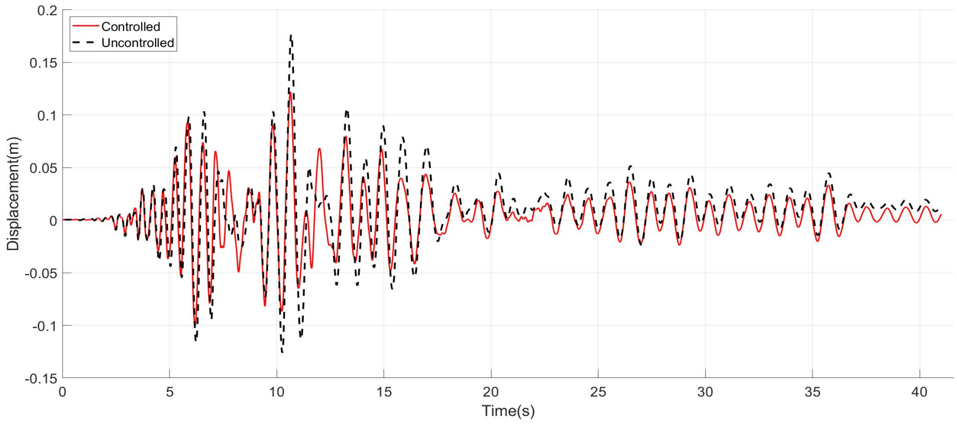

(a) Roof Displacements

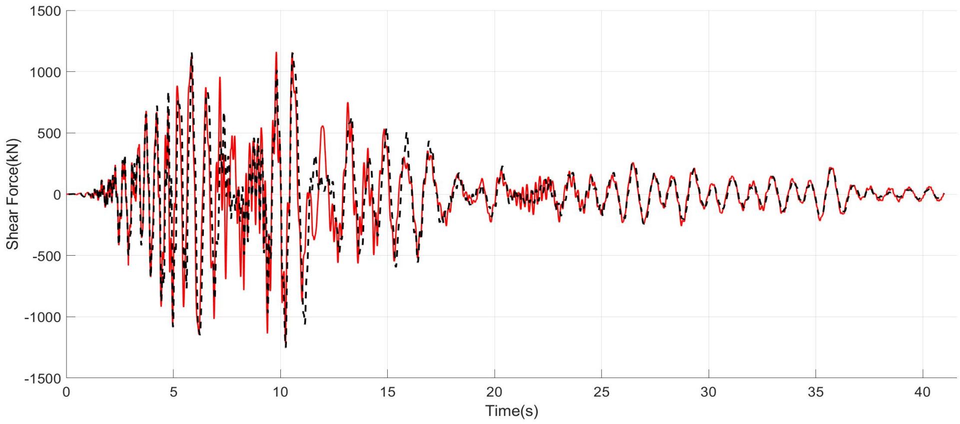

(b) Shear Forces at the base

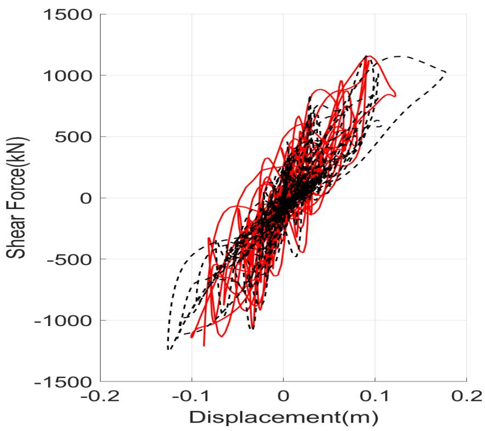

(c) Structural Hysteretic Curve

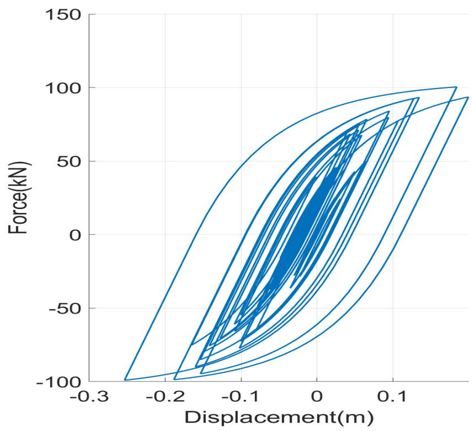

(d) TMD Hysteretic Curve

Figure B.33. Kobe $U_{max} = 20cm$

Loma Prieta

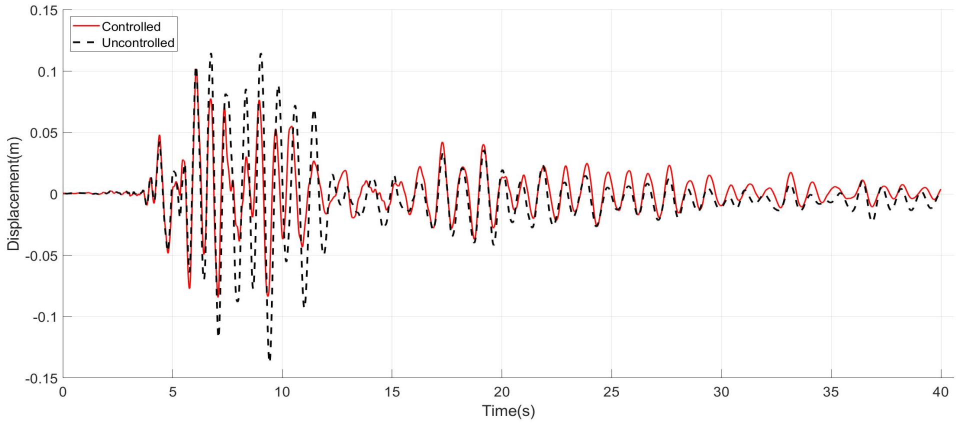

(a) Roof Displacements

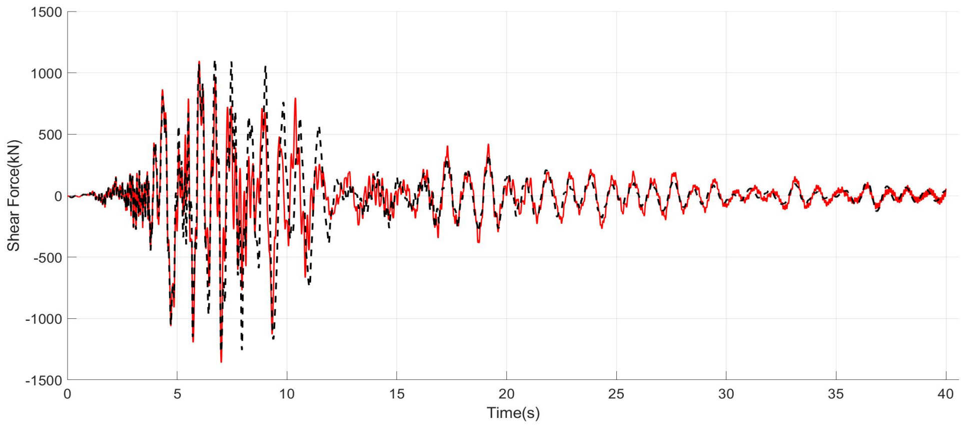

(b) Shear Forces at the base

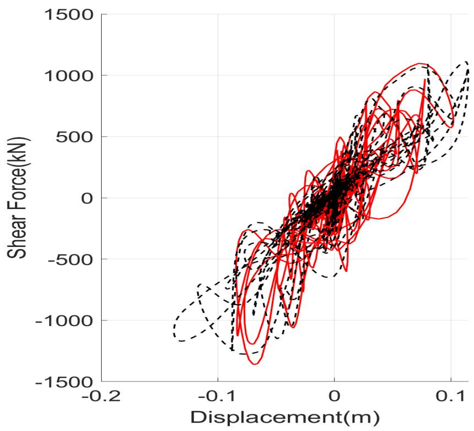

(c) Structural Hysteretic Curve

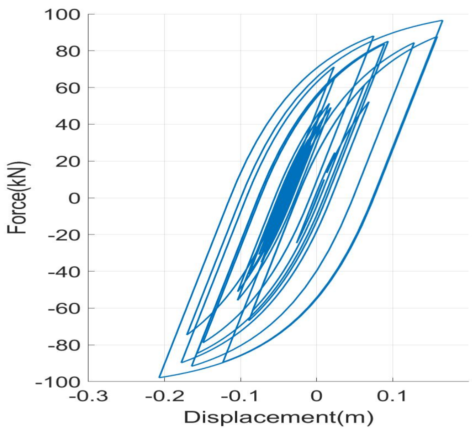

(d) TMD Hysteretic Curve

Figure B.34. Loma Prieta $U_{max} = 20cm$

Northridge

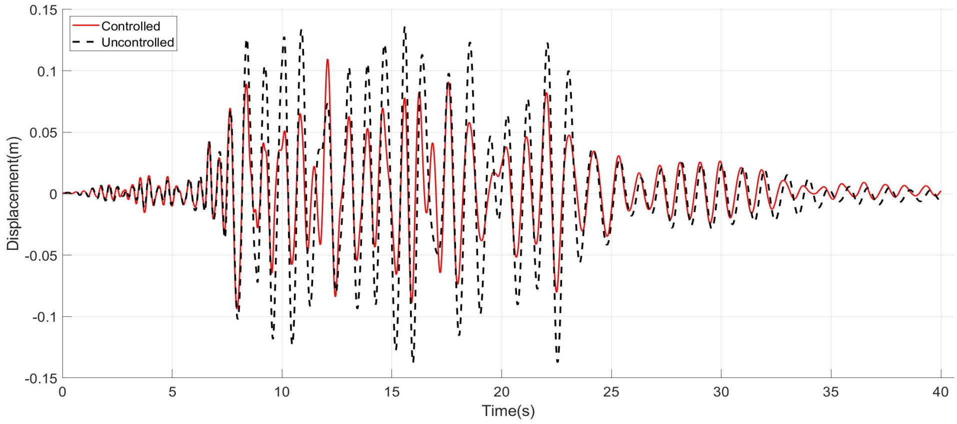

(a) Roof Displacements

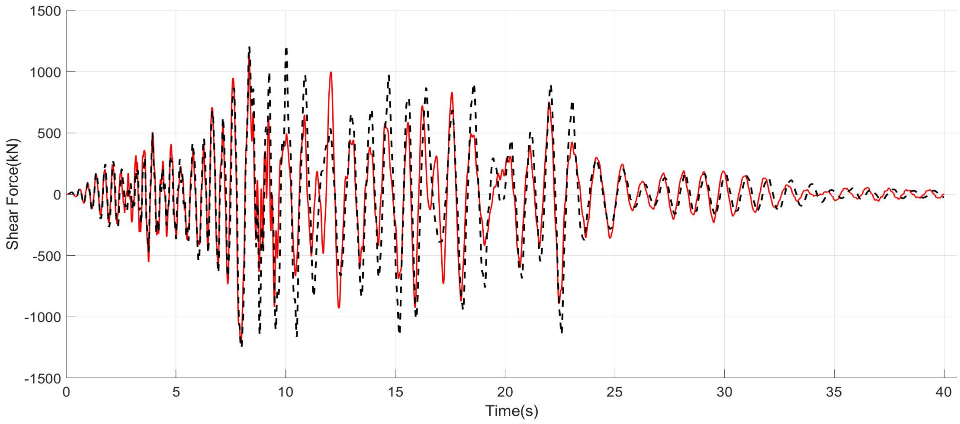

(b) Shear Forces at the base

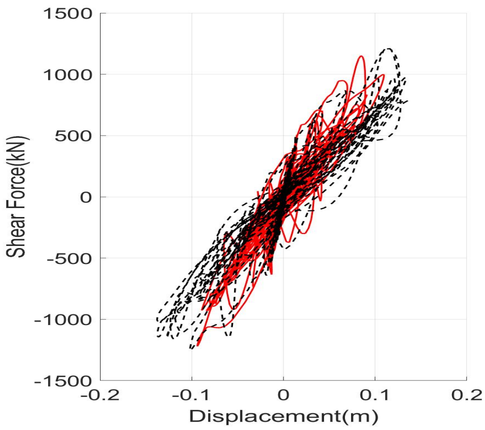

(c) Structural Hysteretic Curve

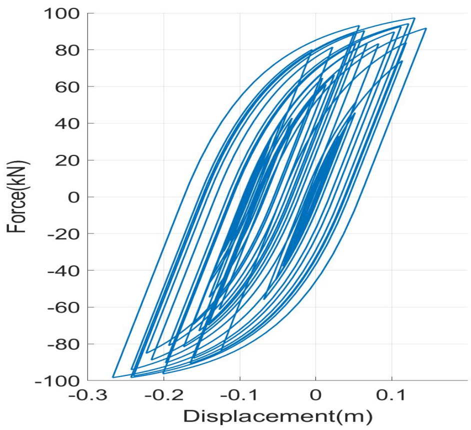

(d) TMD Hysteretic Curve

Figure B.35. Northridge $U_{max} = 20cm$

Drifts

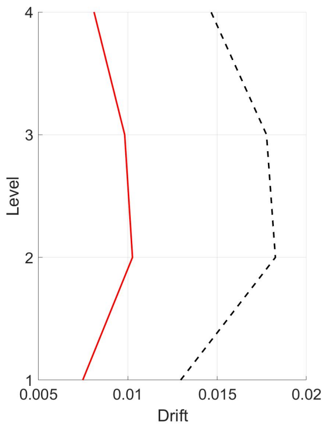

(a) Chalfant

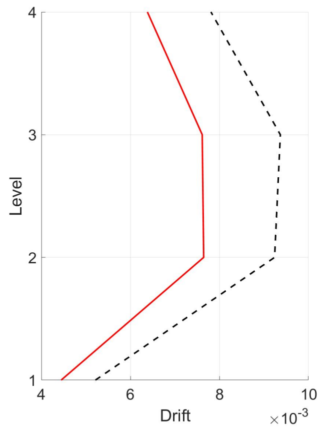

(b) Chi Chi

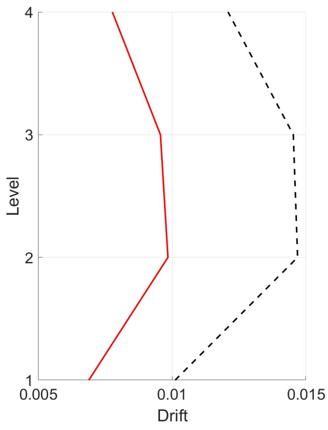

(c) Erzincan

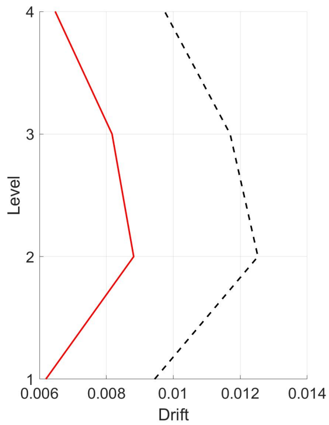

(d) Friulli

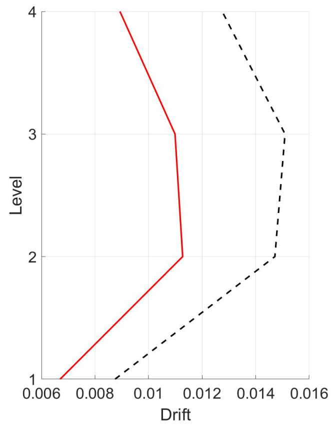

(e) Imperial Valley

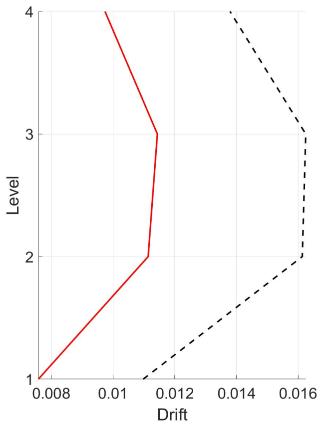

(f) Kobe

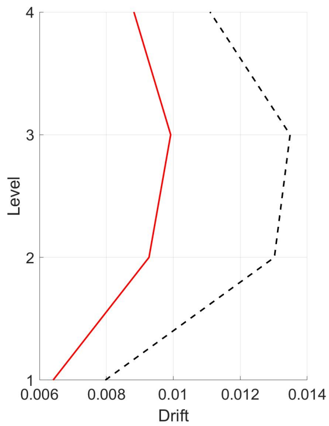

(g) Loma Prieta

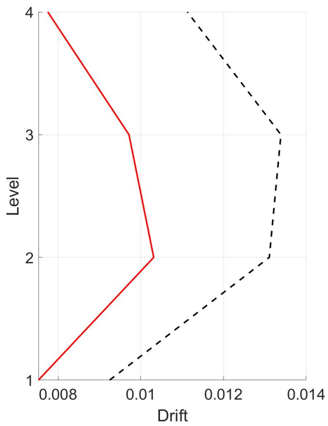

(h) Northridge

Figure B.36. Drifts $U_{max} = 20cm$

B.2.3 $U_{max} = 30cm$

Setting the stroke as a desing parameter and using a value of $30cm$ for the tuning at the performance point, the results following results are obtained.

Table B.5. Performance Indices $U_{max} = 30cm$

Earthquake	Performance Index						
	J_1	J_2	J_3	J_4	J_5	J_6	J_7(m)
Chalfant	0.491	1.008	1.026	0.538	0.901	0.956	0.245
Chi-Chi	0.802	0.964	0.845	0.599	0.789	0.831	0.212
Erzincan	0.589	0.963	0.904	0.623	0.808	0.821	0.237
Friulli	0.663	0.958	1.064	0.688	0.897	0.910	0.226
Imperial Valley	0.695	0.991	1.014	0.769	0.929	0.946	0.227
Kobe	0.607	0.969	1.219	0.714	0.986	1.031	0.237
Loma Prieta	0.780	0.966	0.956	0.702	0.836	0.872	0.214
Northridge	0.772	0.977	0.895	0.660	0.848	0.813	0.278
Average	0.675	0.974	0.990	0.662	0.874	0.898	0.234

Chalfant

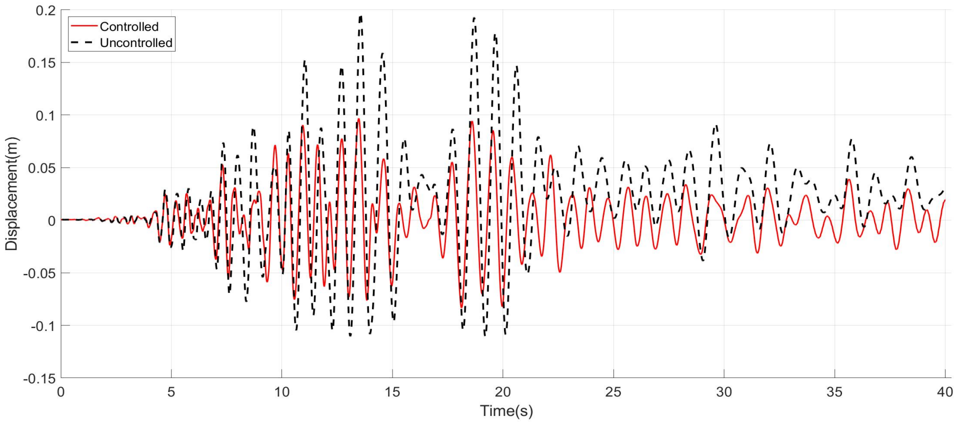

(a) Roof Displacements

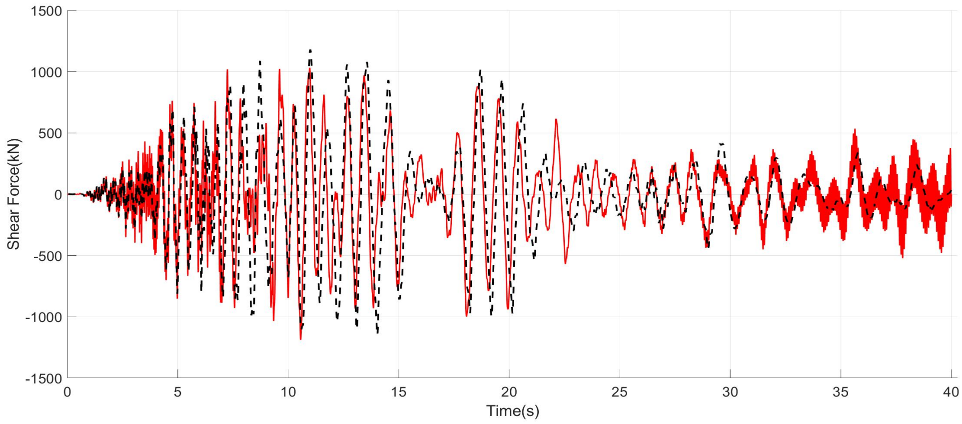

(b) Shear Forces at the base

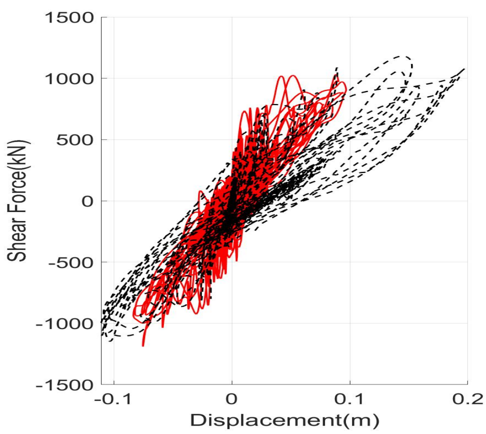

(c) Structural Hysteretic Curve

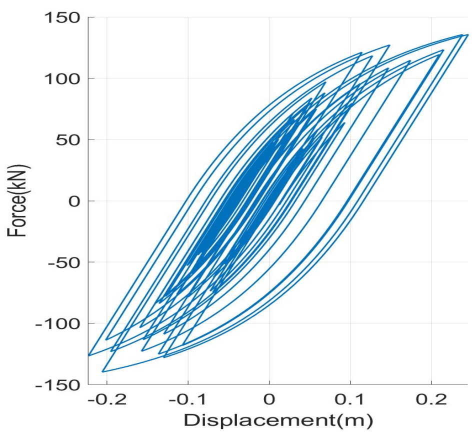

(d) TMD Hysteretic Curve

Figure B.37. Chalfant $U_{max} = 30cm$

Chi-Chi

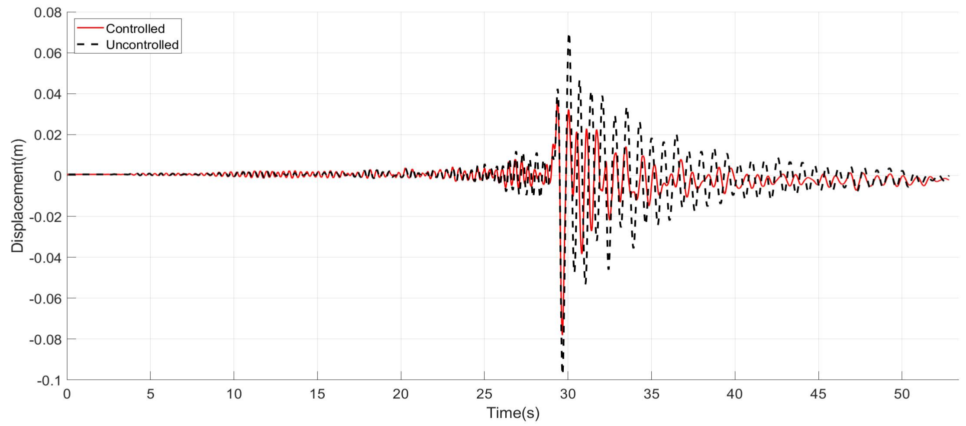

(a) Roof Displacements

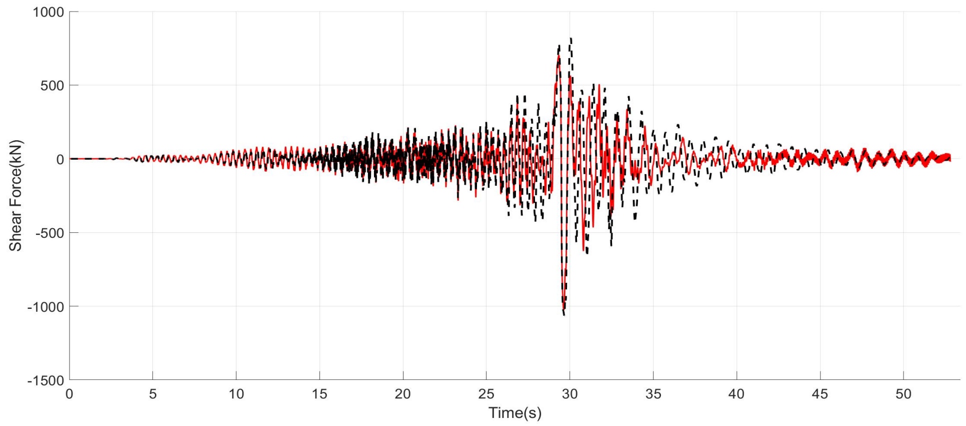

(b) Shear Forces at the base

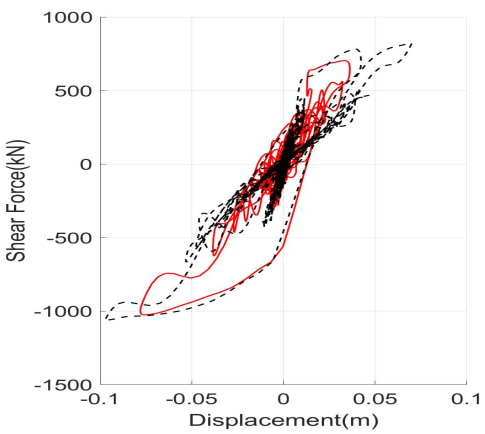

(c) Structural Hysteretic Curve

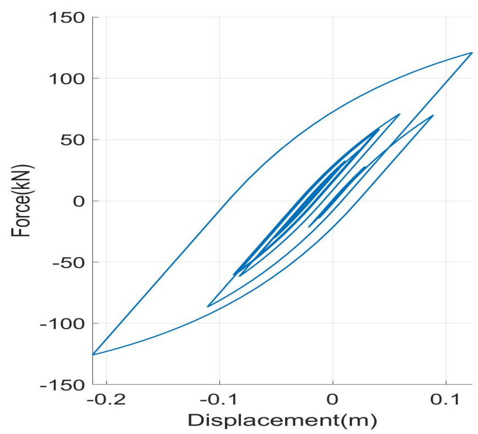

(d) TMD Hysteretic Curve

Figure B.38. Chi Chi $U_{max} = 30cm$

Erzincan

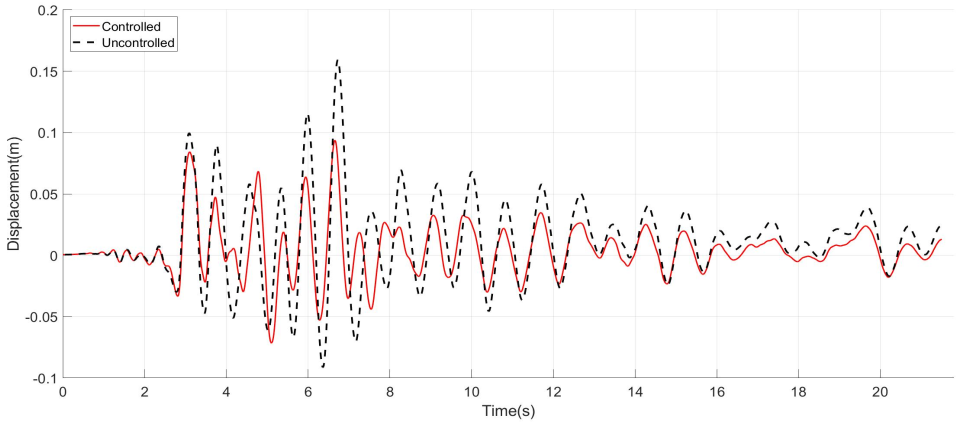

(a) Roof Displacements

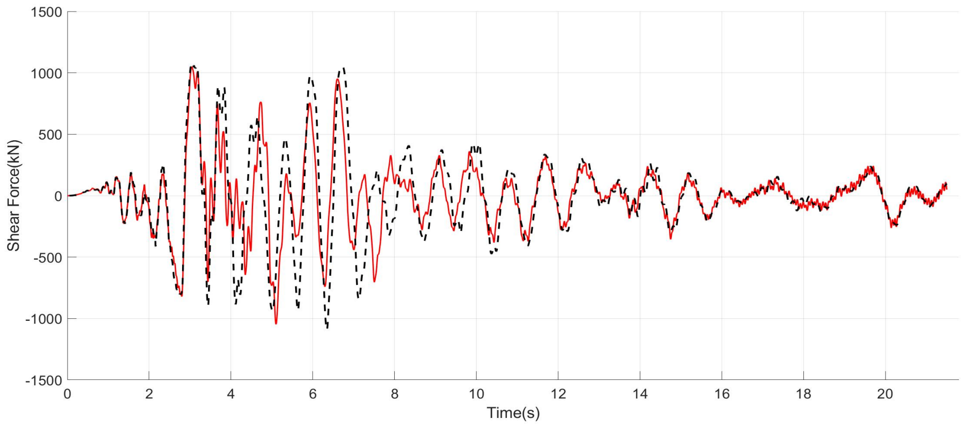

(b) Shear Forces at the base

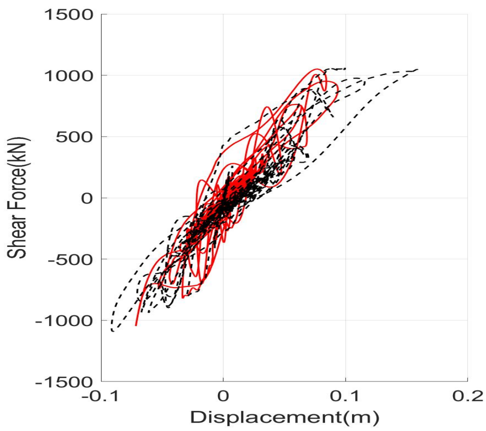

(c) Structural Hysteretic Curve

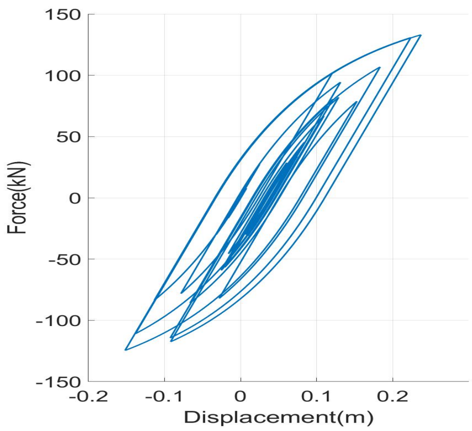

(d) TMD Hysteretic Curve

Figure B.39. Erzincan $U_{max} = 30cm$

Friulli

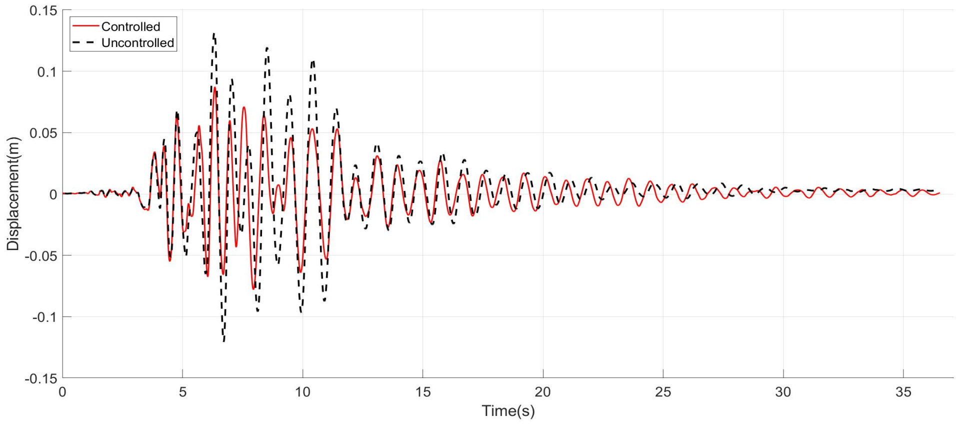

(a) Roof Displacements

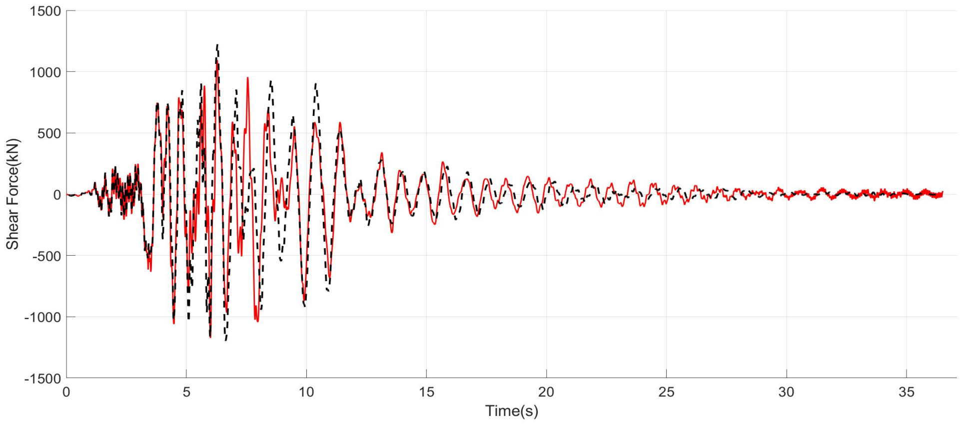

(b) Shear Forces at the base

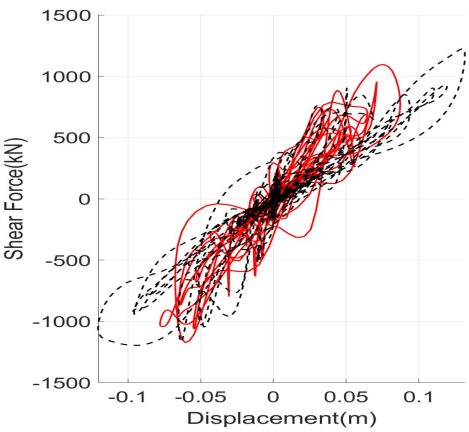

(c) Structural Hysteretic Curve

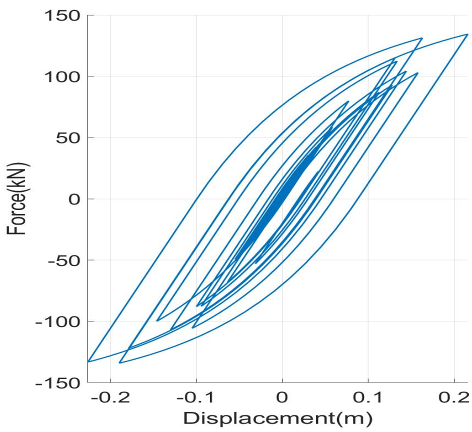

(d) TMD Hysteretic Curve

Figure B.40. Friulli $U_{max} = 30cm$

Imperial Valley

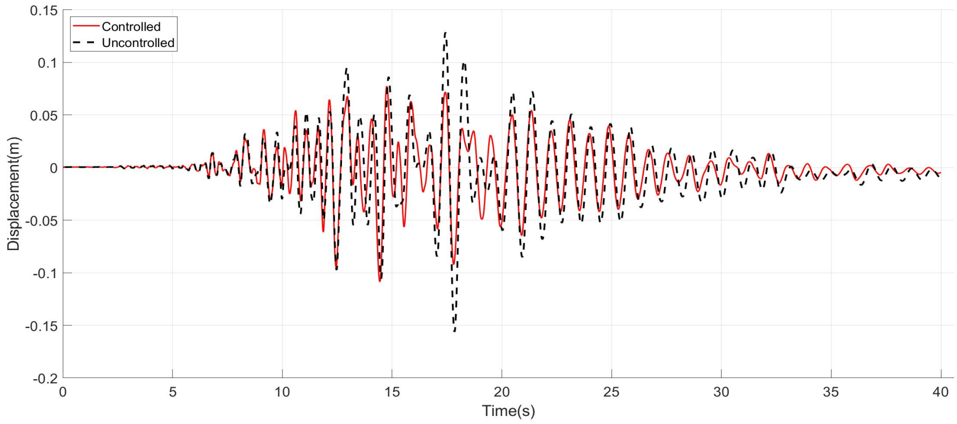

(a) Roof Displacements

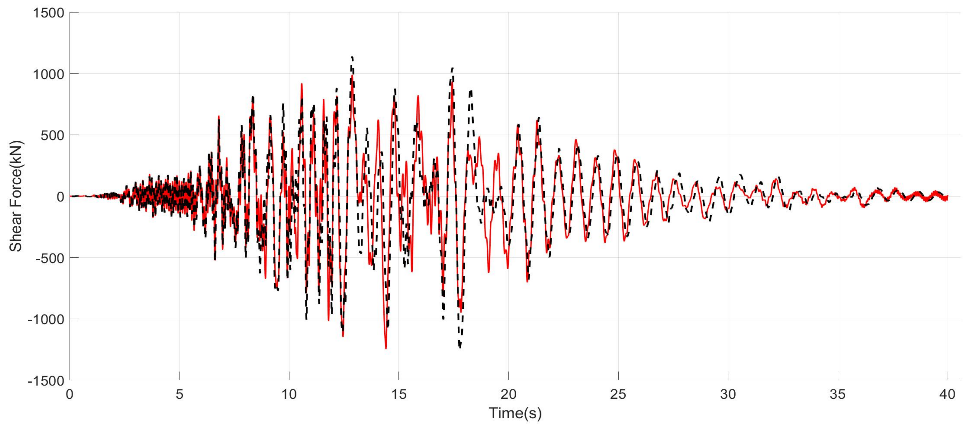

(b) Shear Forces at the base

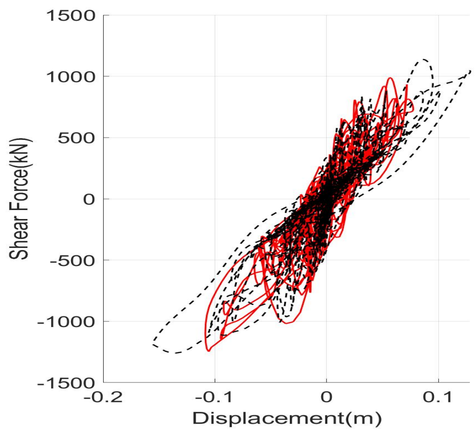

(c) Structural Hysteretic Curve

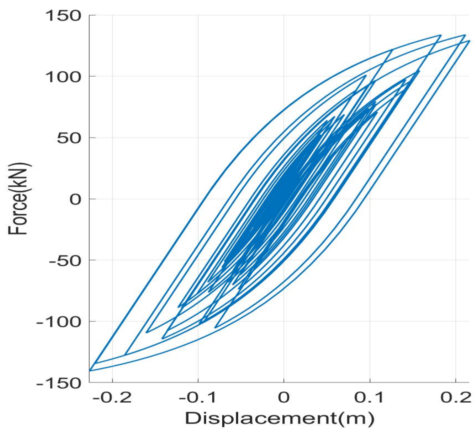

(d) TMD Hysteretic Curve

Figure B.41. Imperial Valley $U_{max} = 30cm$

Kobe

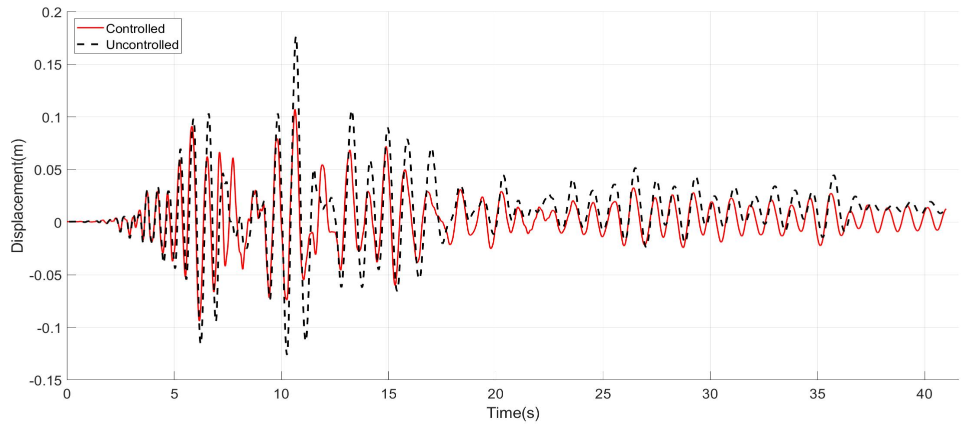

(a) Roof Displacements

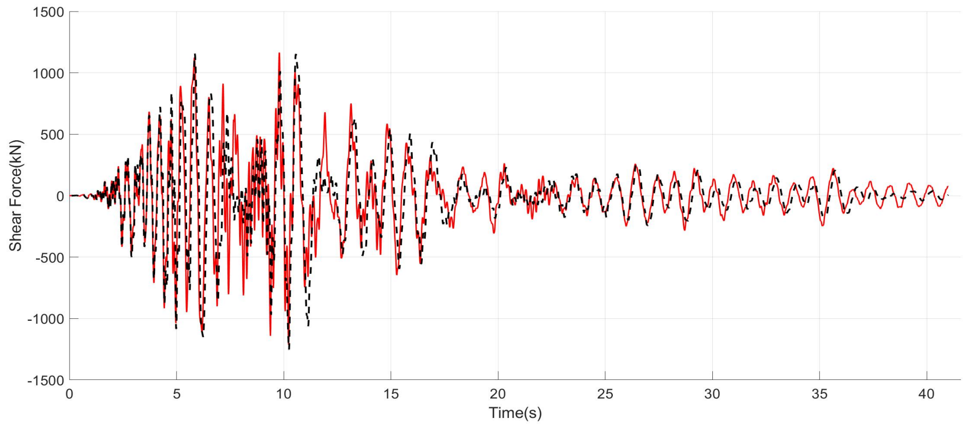

(b) Shear Forces at the base

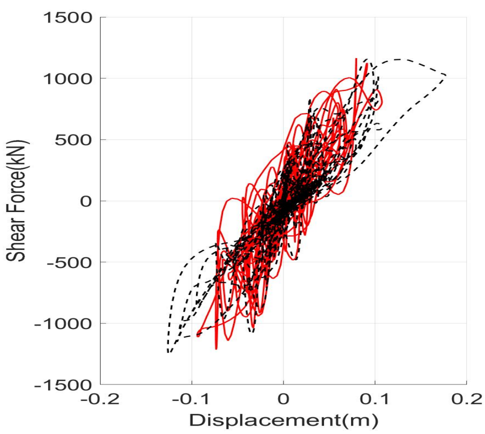

(c) Structural Hysteretic Curve

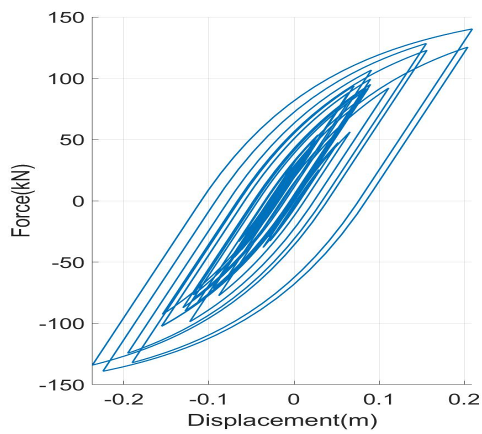

(d) TMD Hysteretic Curve

Figure B.42. Kobe $U_{max} = 30cm$

Loma Prieta

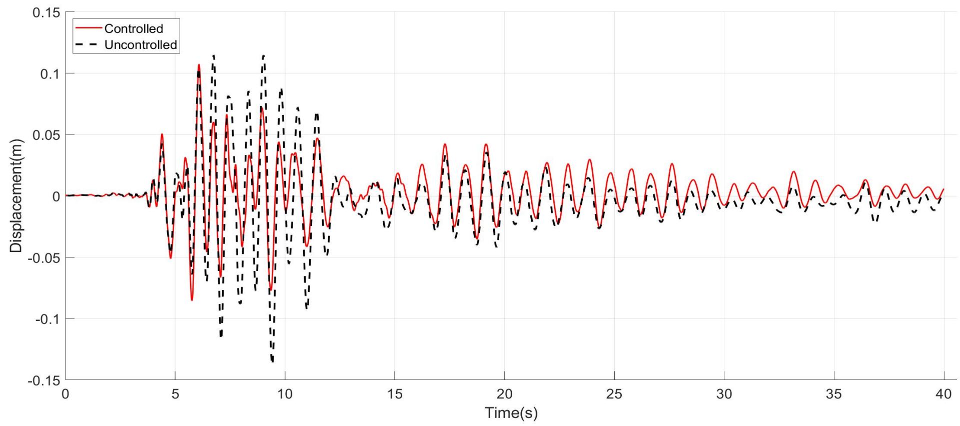

(a) Roof Displacements

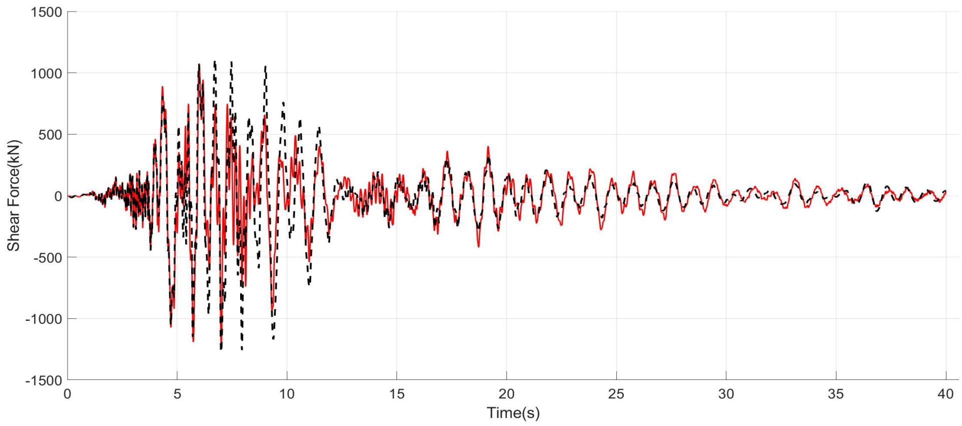

(b) Shear Forces at the base

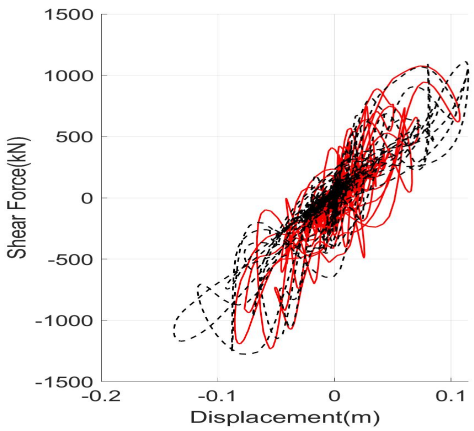

(c) Structural Hysteretic Curve

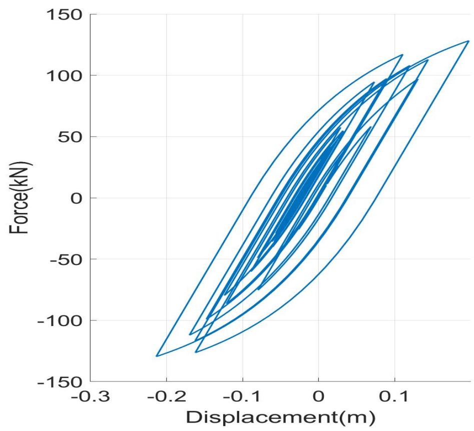

(d) TMD Hysteretic Curve

Figure B.43. Loma Prieta $U_{max} = 30cm$

Northridge

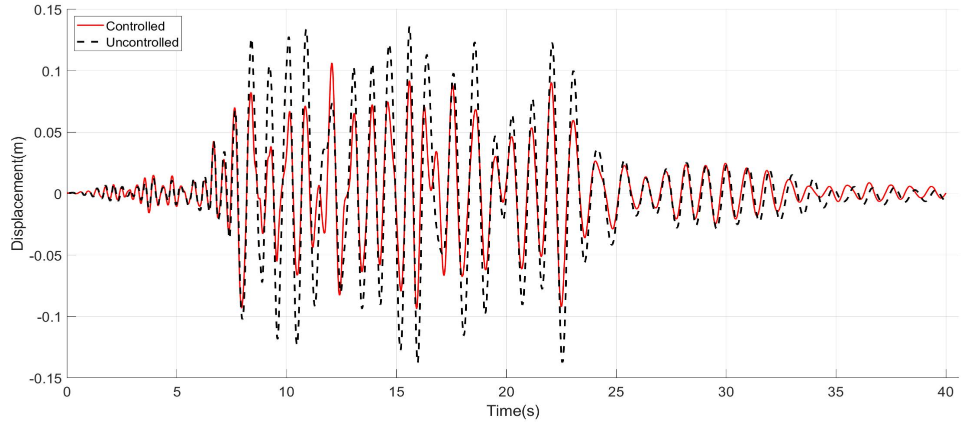

(a) Roof Displacements

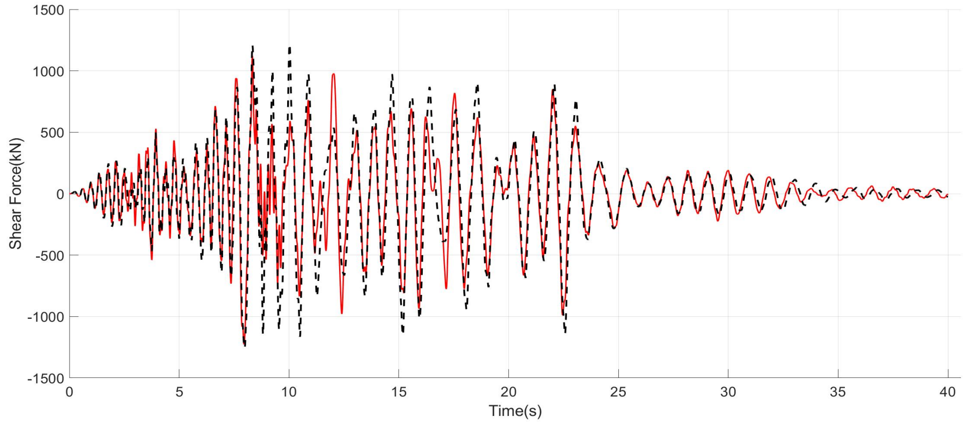

(b) Shear Forces at the base

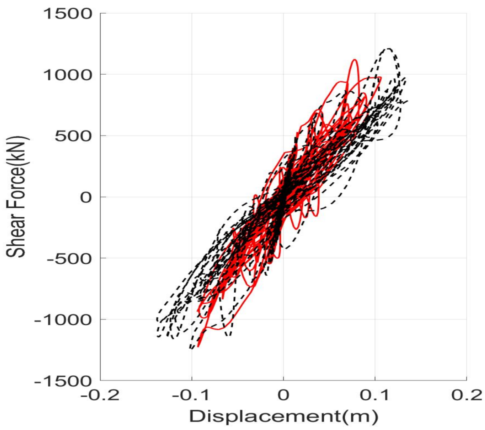

(c) Structural Hysteretic Curve

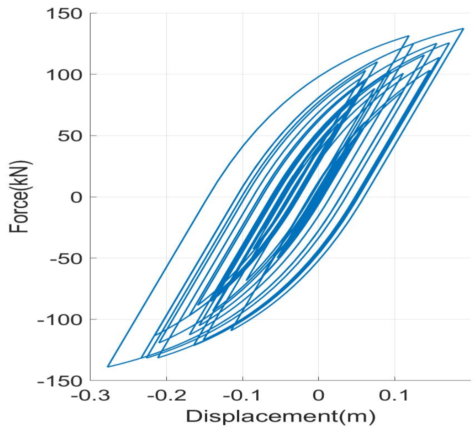

(d) TMD Hysteretic Curve

Figure B.44. Northridge $U_{max} = 30cm$

Drifts

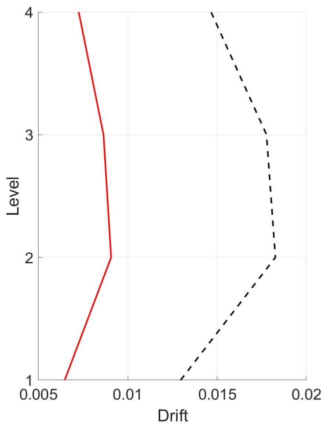

(a) Chalfant

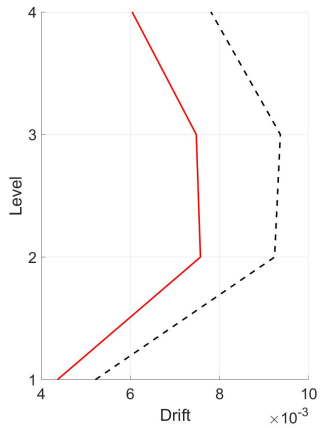

(b) Chi Chi

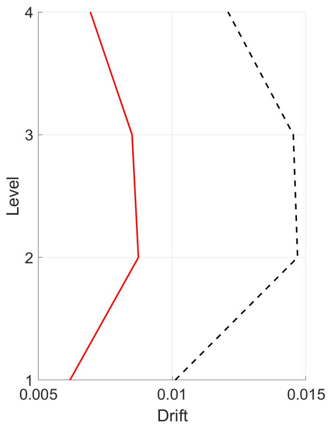

(c) Erzincan

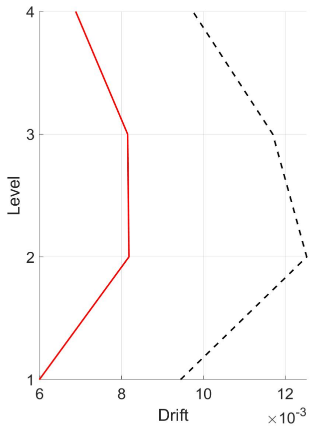

(d) Friulli

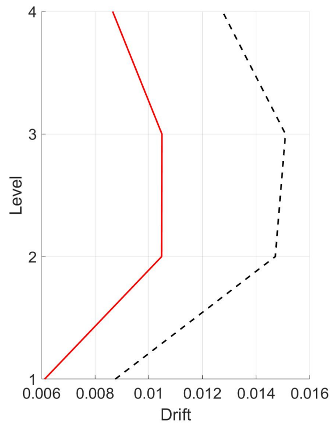

(e) Imperial Valley

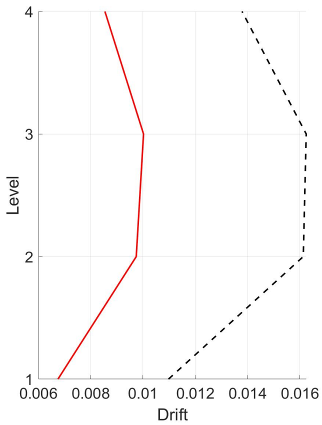

(f) Kobe

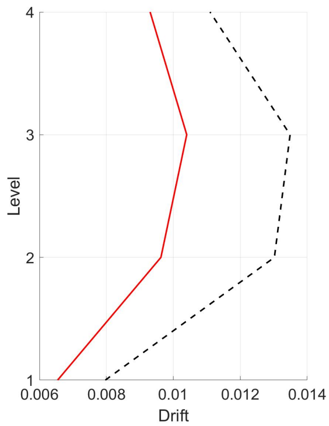

(g) Loma Prieta

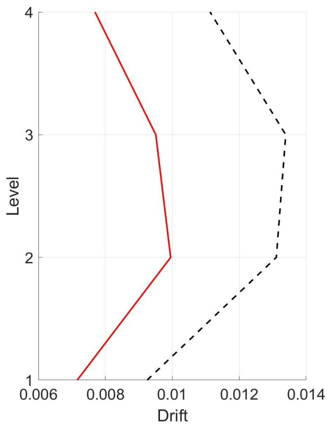

(h) Northridge

Figure B.45. Drifts $U_{max} = 30cm$

B.2.4 $U_{max} = 35cm$

Setting the stroke as a desing parameter and using a value of $35cm$ for the tuning at the performance point, the results following results are obtained.

Table B.6. Performance Indices $U_{max} = 35cm$

Earthquake	Performance Index						
	J_1	J_2	J_3	J_4	J_5	J_6	J_7(m)
Chalfant	0.471	1.015	1.020	0.541	0.920	0.976	0.244
Chi-Chi	0.805	0.969	0.830	0.597	0.784	0.835	0.210
Erzincan	0.568	0.960	0.882	0.621	0.823	0.899	0.233
Friulli	0.668	0.977	1.051	0.696	0.895	0.902	0.223
Imperial Valley	0.683	0.951	1.018	0.771	0.934	0.941	0.232
Kobe	0.591	0.981	1.265	0.704	0.984	1.034	0.236
Loma Prieta	0.797	0.944	0.905	0.707	0.836	0.878	0.212
Northridge	0.763	0.970	0.883	0.682	0.867	0.826	0.273
Average	0.668	0.971	0.982	0.665	0.880	0.911	0.233

Chalfant

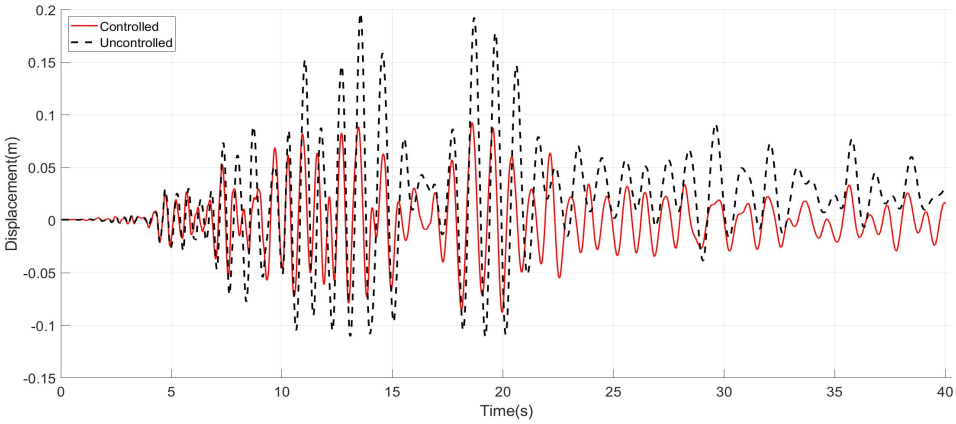

(a) Roof Displacements

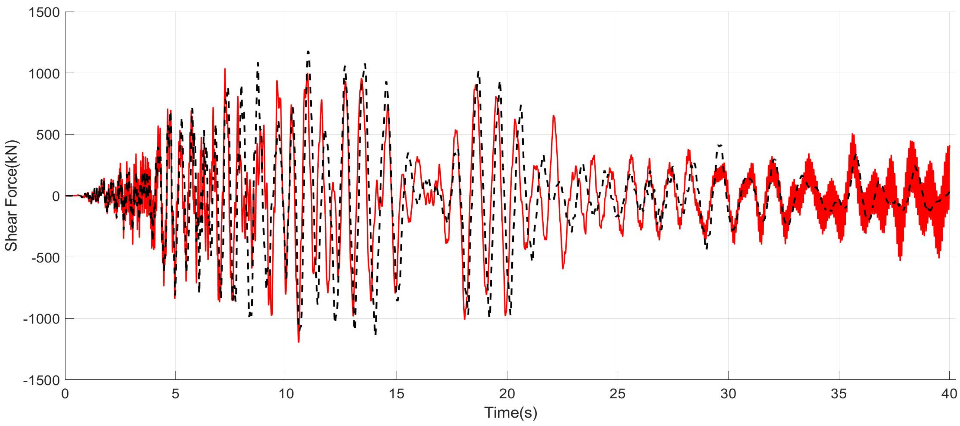

(b) Shear Forces at the base

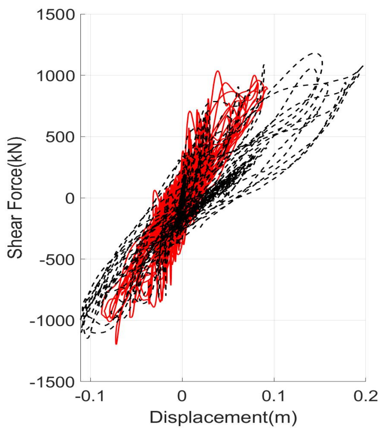

(c) Structural Hysteretic Curve

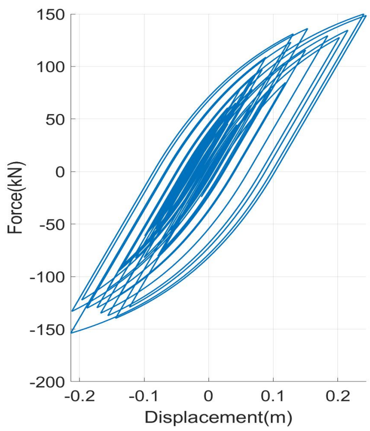

(d) TMD Hysteretic Curve

Figure B.46. Chalfant $U_{max} = 35cm$

Chi-Chi

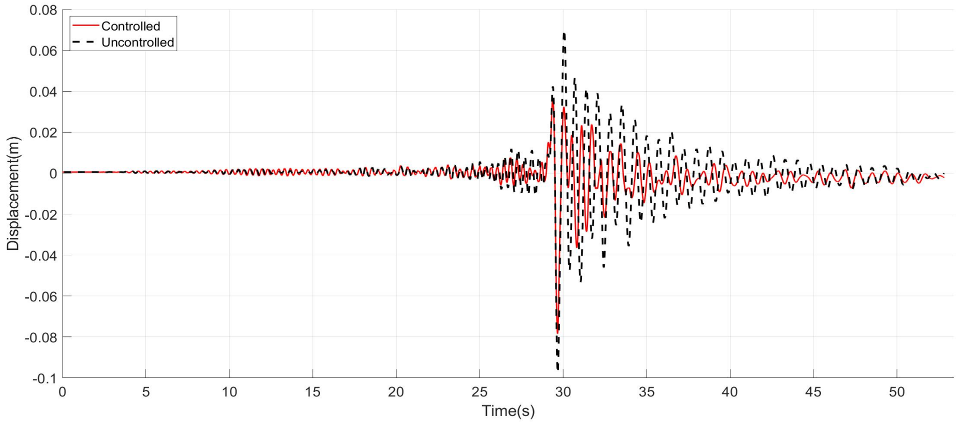

(a) Roof Displacements

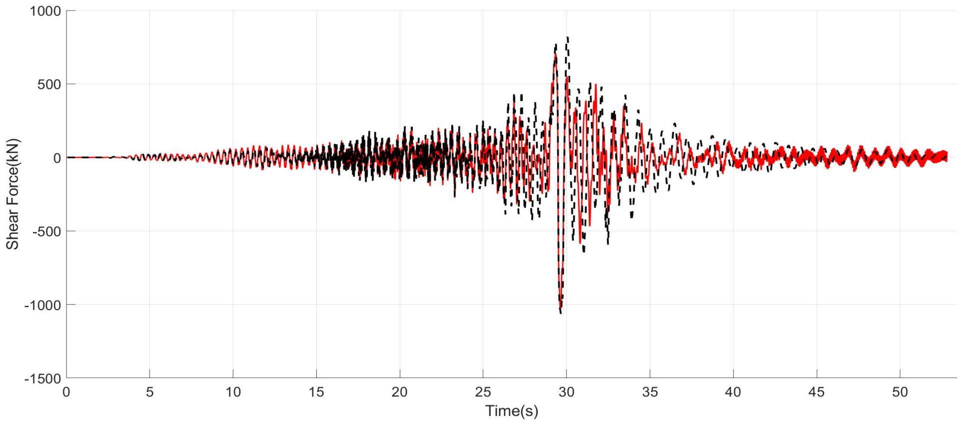

(b) Shear Forces at the base

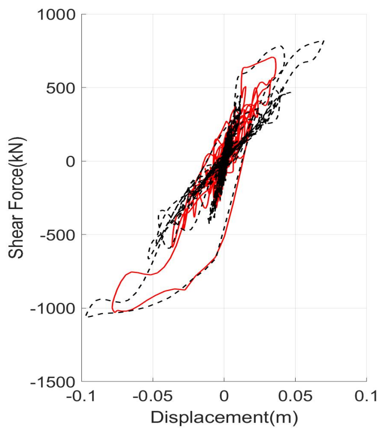

(c) Structural Hysteretic Curve

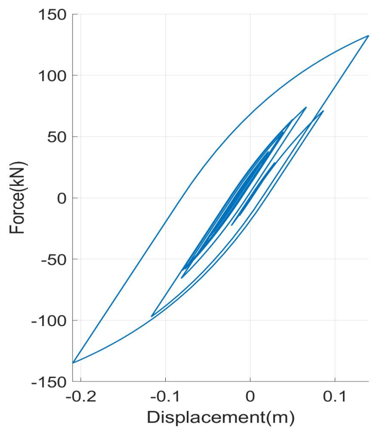

(d) TMD Hysteretic Curve

Figure B.47. Chi Chi $U_{max} = 35cm$

Erzincan

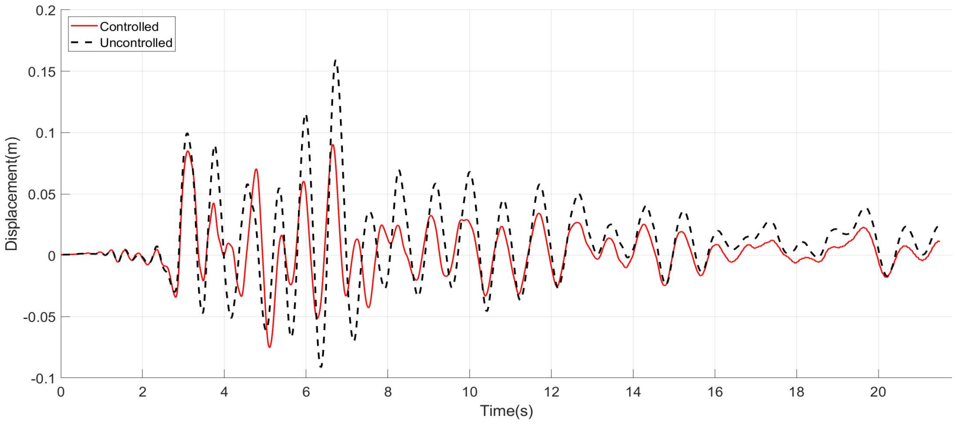

(a) Roof Displacements

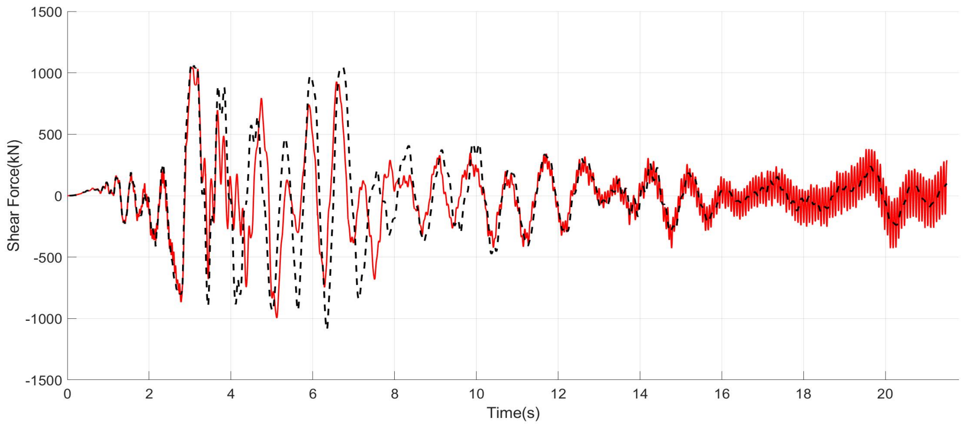

(b) Shear Forces at the base

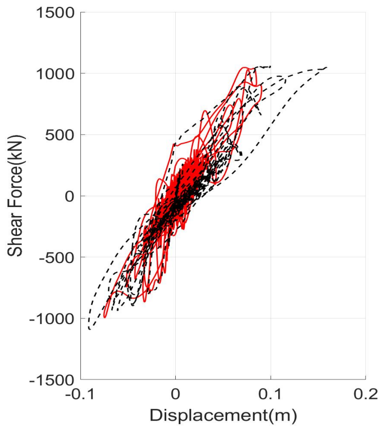

(c) Structural Hysteretic Curve

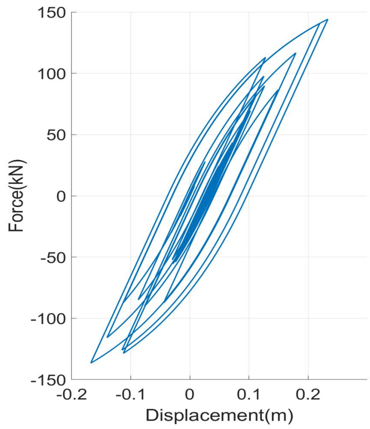

(d) TMD Hysteretic Curve

Figure B.48. Erzincan $U_{max} = 35cm$

Friulli

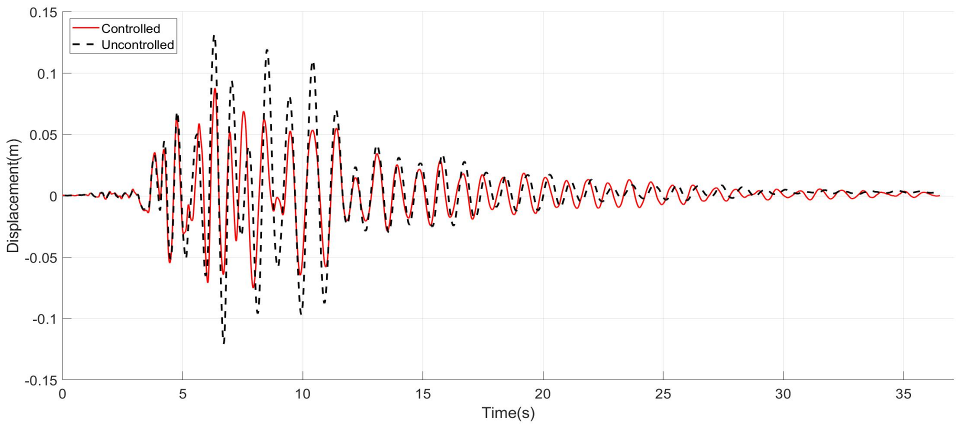

(a) Roof Displacements

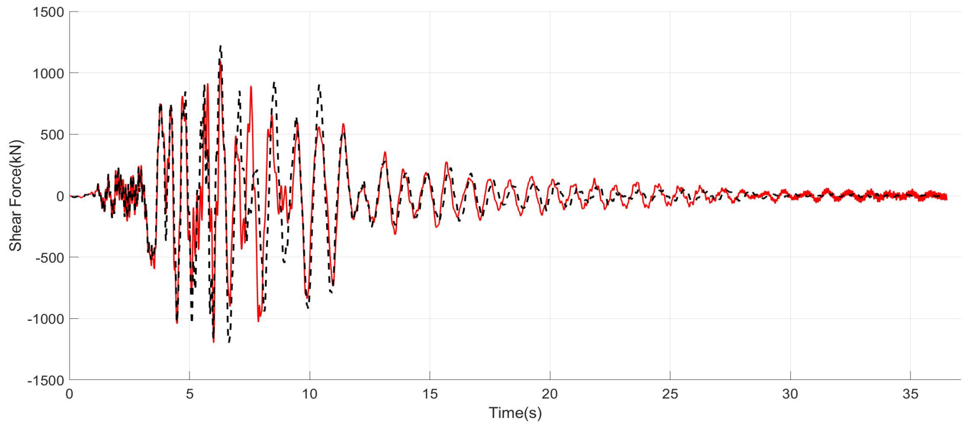

(b) Shear Forces at the base

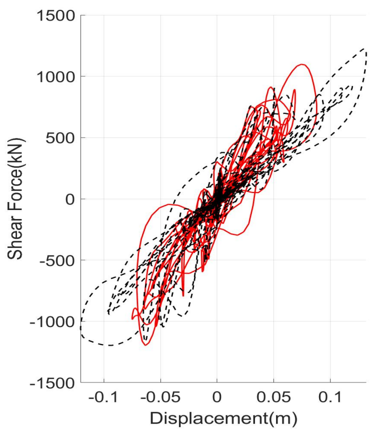

(c) Structural Hysteretic Curve

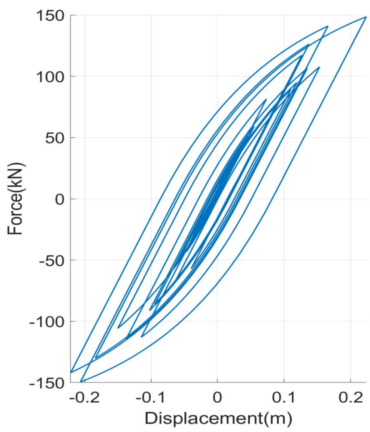

(d) TMD Hysteretic Curve

Figure B.49. Friulli $U_{max} = 35cm$

Imperial Valley

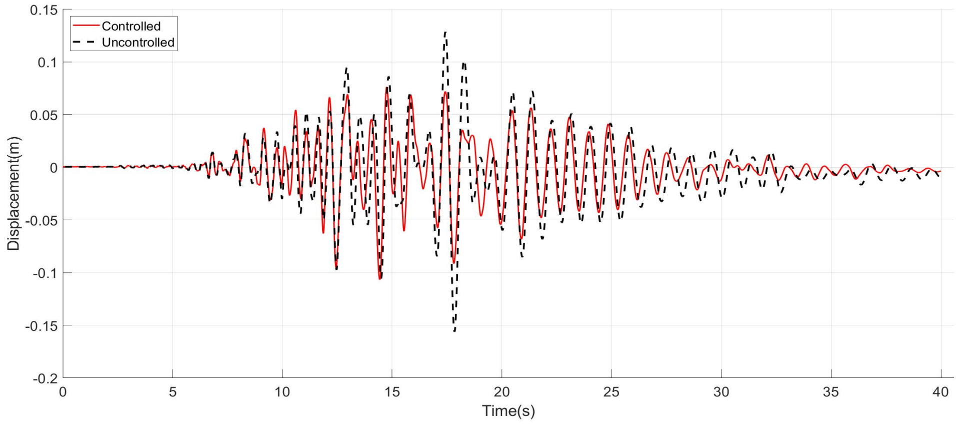

(a) Roof Displacements

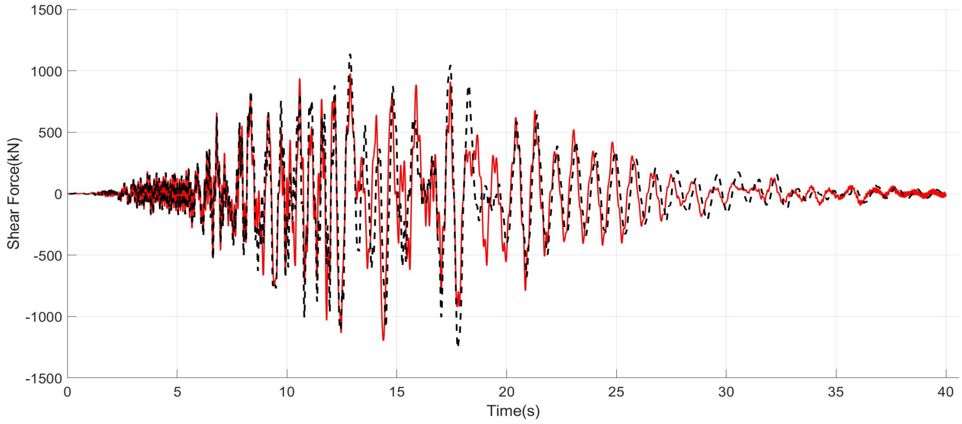

(b) Shear Forces at the base

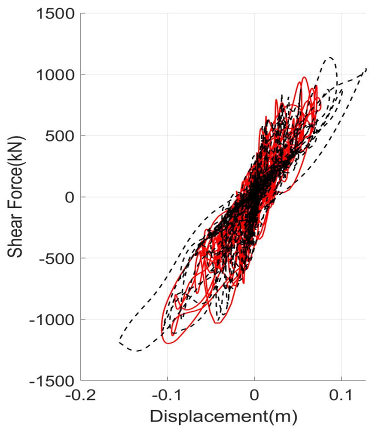

(c) Structural Hysteretic Curve

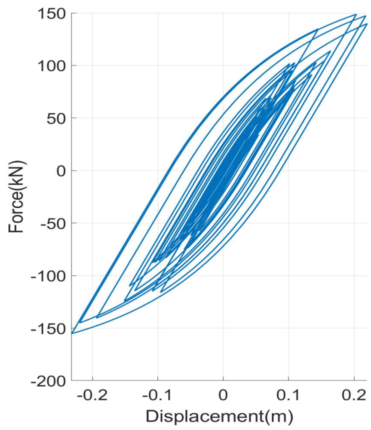

(d) TMD Hysteretic Curve

Figure B.50. Imperial Valley $U_{max} = 35cm$

Kobe

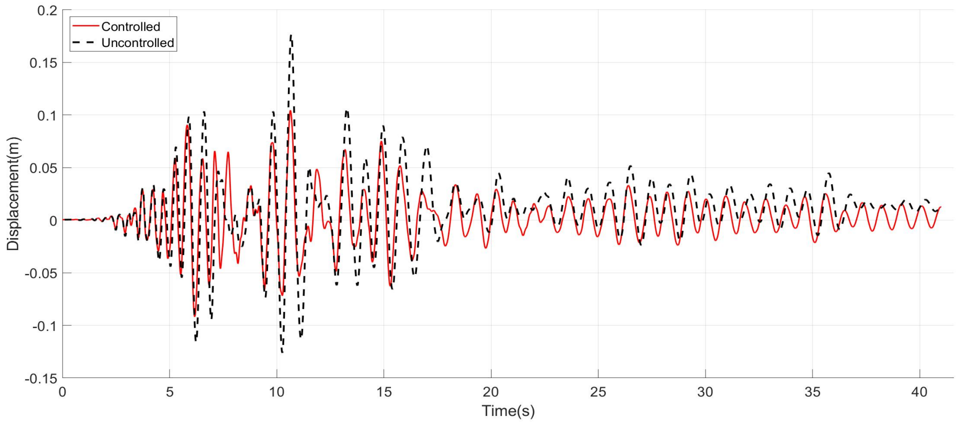

(a) Roof Displacements

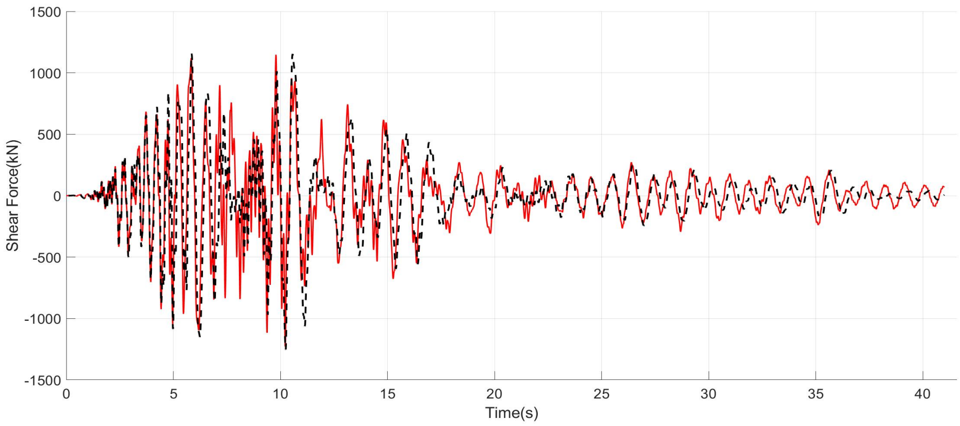

(b) Shear Forces at the base

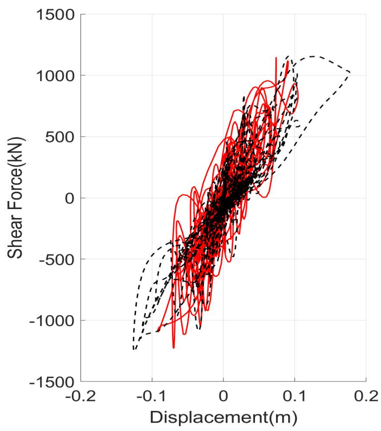

(c) Structural Hysteretic Curve

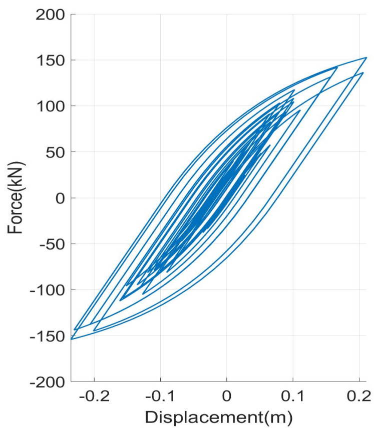

(d) TMD Hysteretic Curve

Figure B.51. Kobe $U_{max} = 35cm$

Loma Prieta

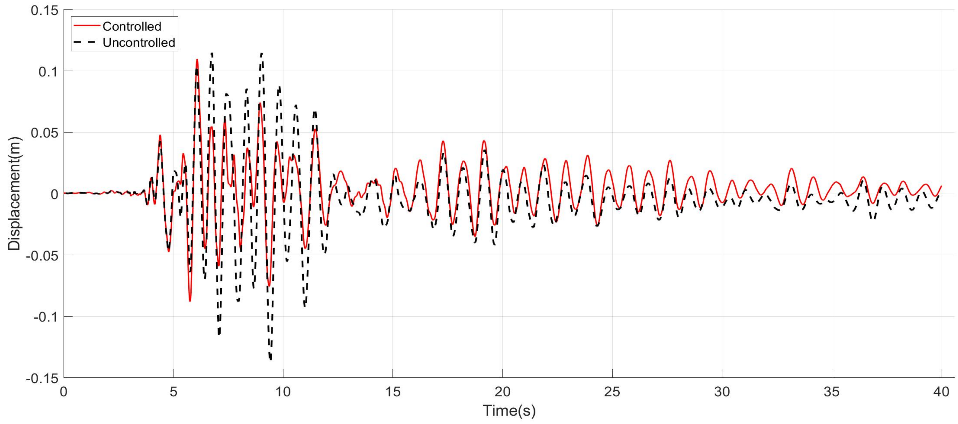

(a) Roof Displacements

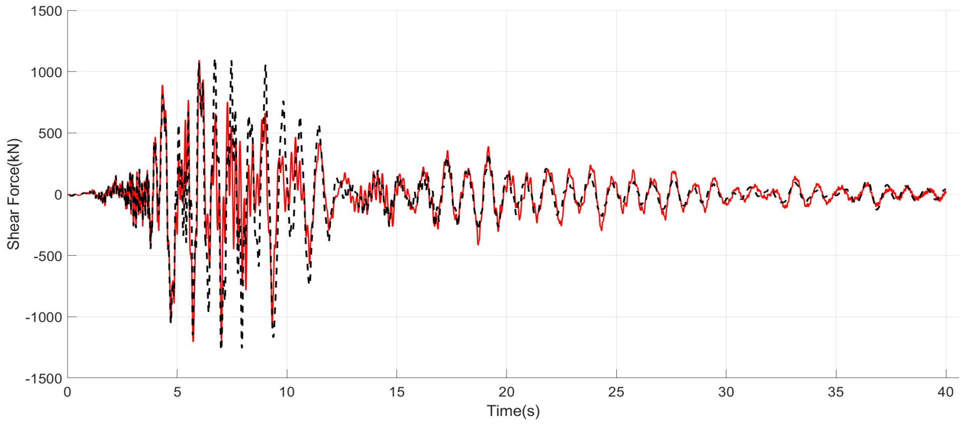

(b) Shear Forces at the base

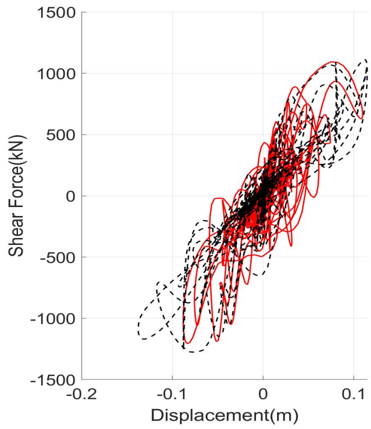

(c) Structural Hysteretic Curve

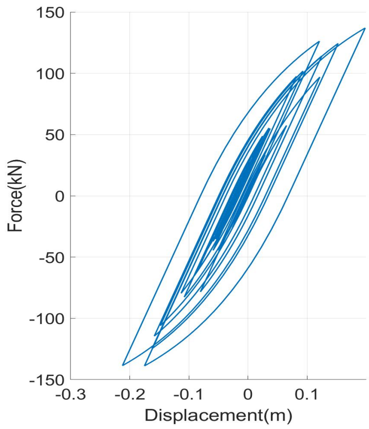

(d) TMD Hysteretic Curve

Figure B.52. Loma Prieta $U_{max} = 35cm$

Northridge

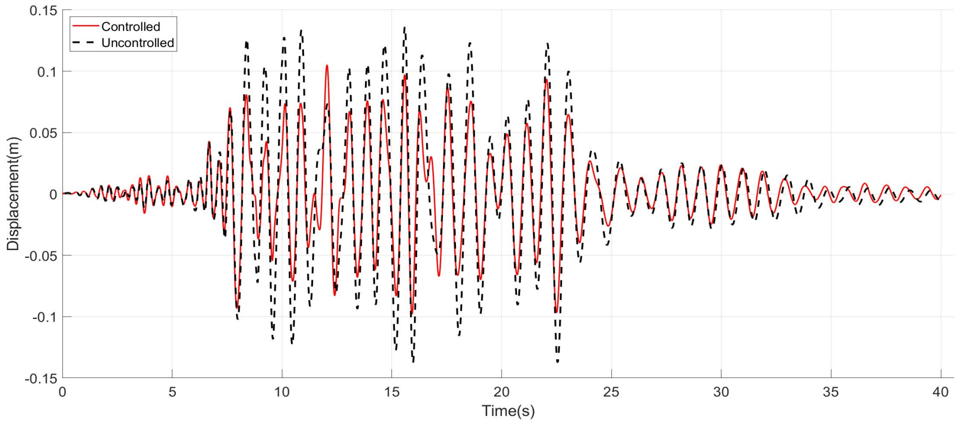

(a) Roof Displacements

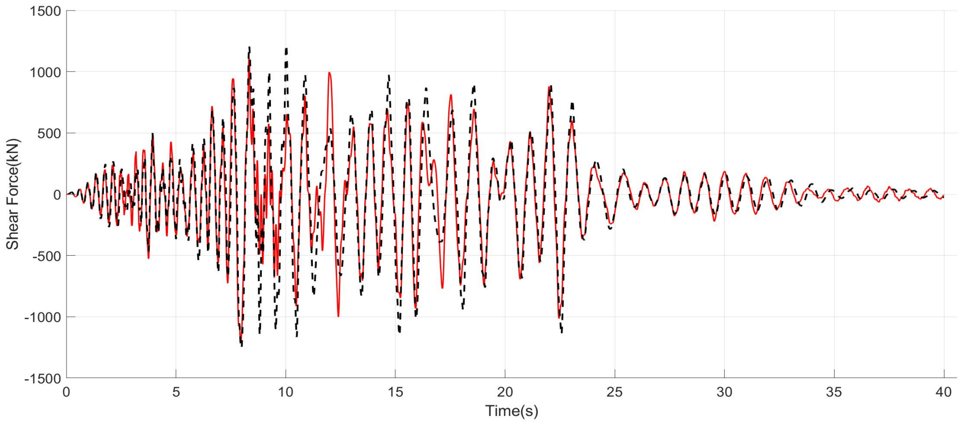

(b) Shear Forces at the base

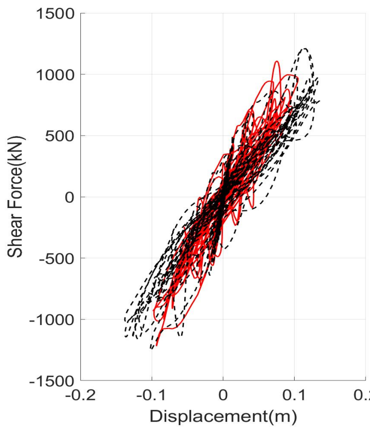

(c) Structural Hysteretic Curve

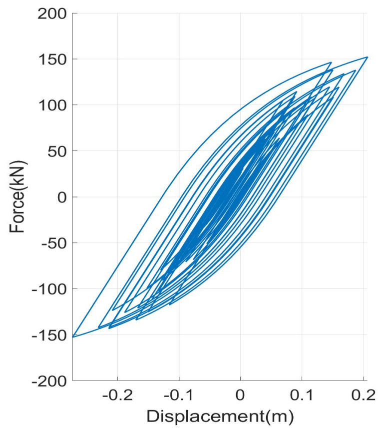

(d) TMD Hysteretic Curve

Figure B.53. Northridge $U_{max} = 35cm$

Drifts

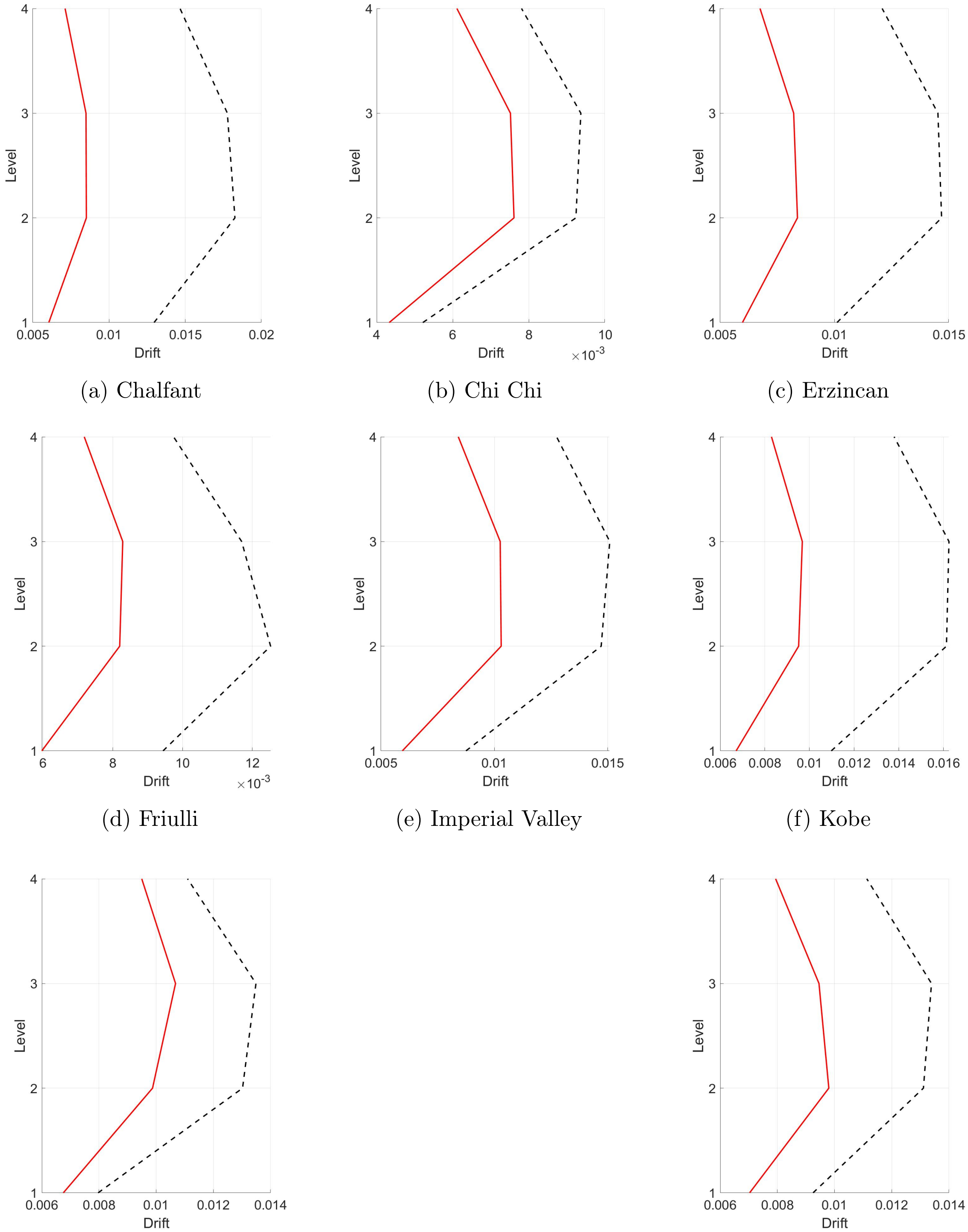

(a) Chalfant

(b) Chi Chi

(c) Erzincan

(d) Friulli

(e) Imperial Valley

(f) Kobe

(g) Loma Prieta

(h) Northridge

Figure B.54. Drifts $U_{max} = 35cm$

B.2.5 $U_{max} = 45cm$

Setting the stroke as a desing parameter and using a value of $45cm$ for the tuning at the performance point, the results following results are obtained.

Table B.7. Performance Indices $U_{max} = 45cm$

Earthquake	Performance Index						
	J_1	J_2	J_3	J_4	J_5	J_6	J_7(m)
Chalfant	0.515	1.002	1.088	0.574	0.947	0.960	0.245
Chi-Chi	0.801	0.971	0.865	0.600	0.782	0.838	0.205
Erzincan	0.535	0.970	0.860	0.627	0.805	0.801	0.228
Friulli	0.677	0.981	1.078	0.717	0.894	0.892	0.233
Imperial Valley	0.666	0.941	1.068	0.795	0.946	0.939	0.237
Kobe	0.590	0.994	1.281	0.709	0.991	1.039	0.253
Loma Prieta	0.817	0.917	0.884	0.723	0.839	0.875	0.207
Northridge	0.776	0.978	0.877	0.729	0.902	0.851	0.259
Average	0.672	0.969	1.000	0.684	0.888	0.899	0.233

Chalfant

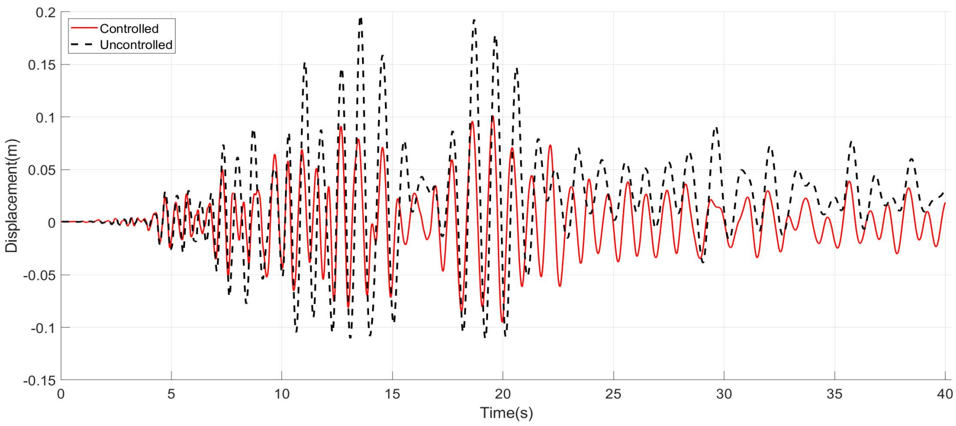

(a) Roof Displacements

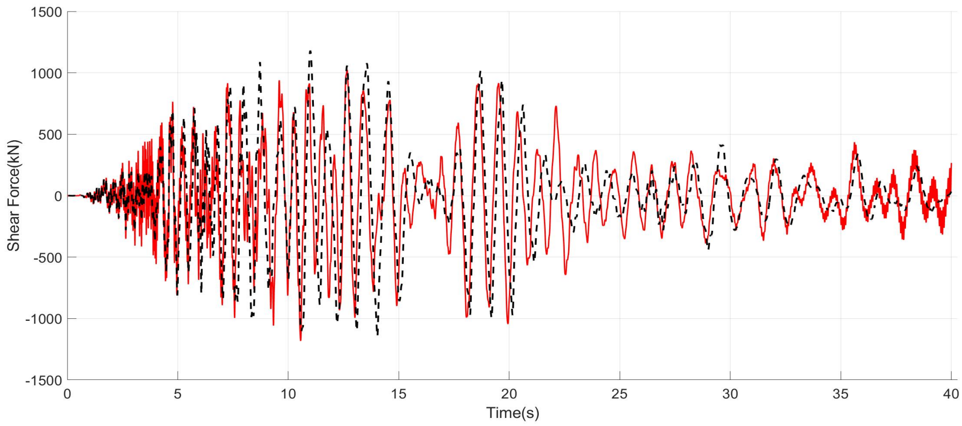

(b) Shear Forces at the base

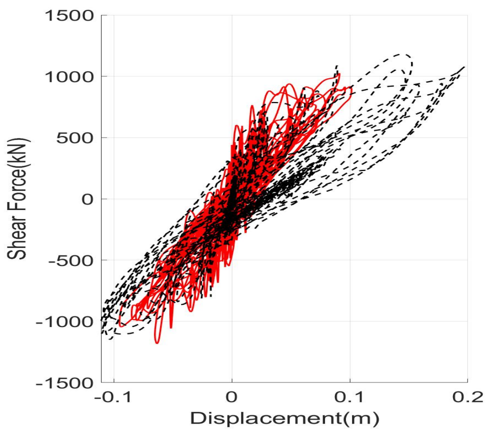

(c) Structural Hysteretic Curve

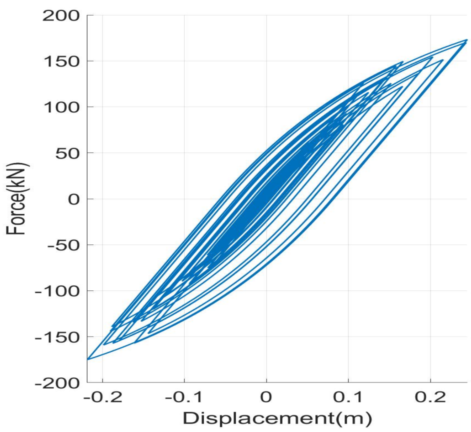

(d) TMD Hysteretic Curve

Figure B.55. Chalfant $U_{max} = 45cm$

Chi-Chi

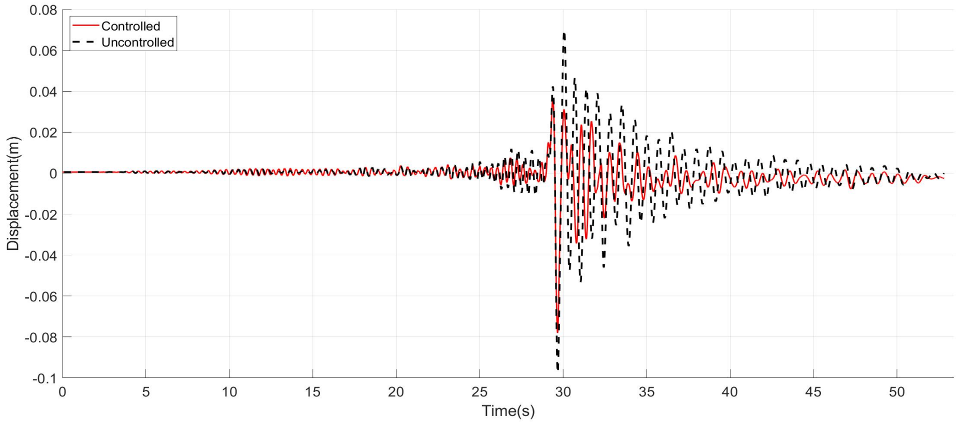

(a) Roof Displacements

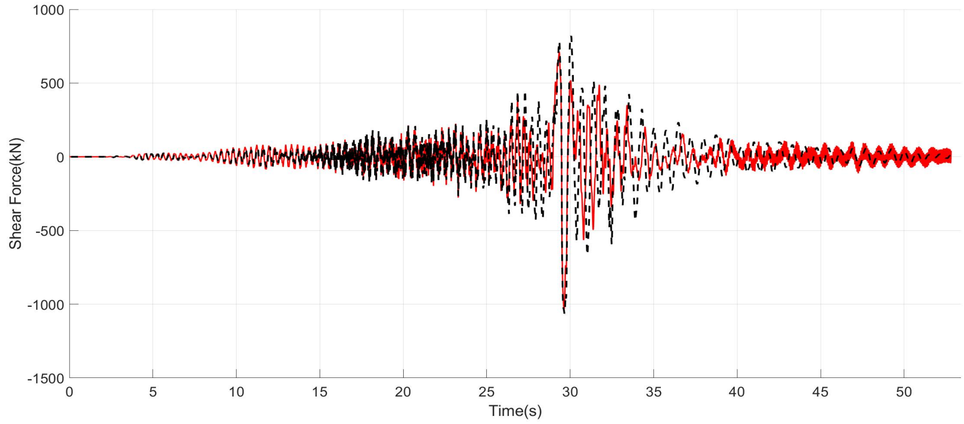

(b) Shear Forces at the base

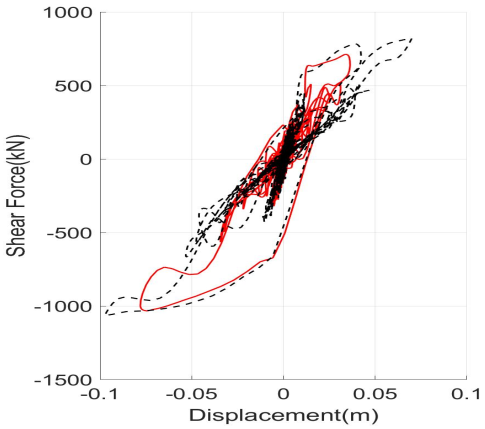

(c) Structural Hysteretic Curve

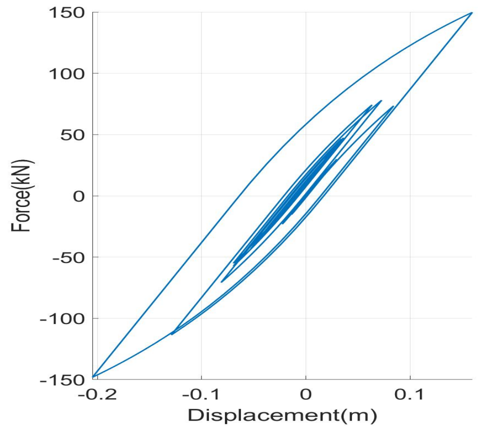

(d) TMD Hysteretic Curve

Figure B.56. Chi Chi $U_{max} = 45cm$

Erzincan

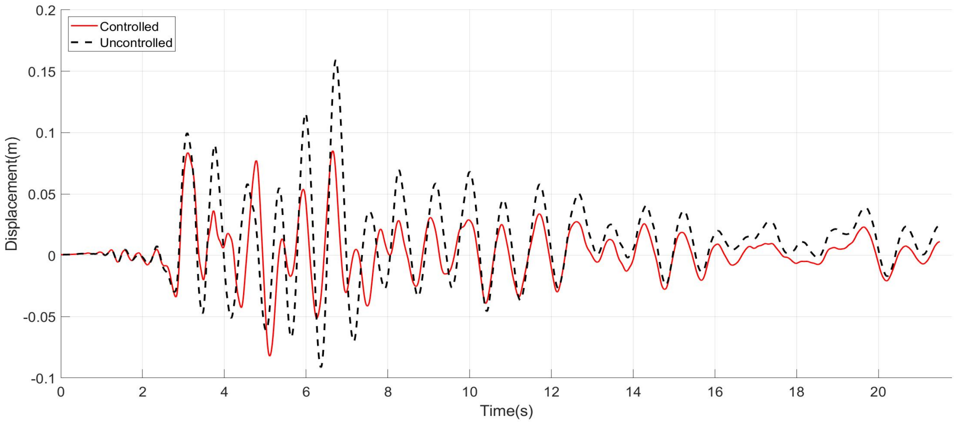

(a) Roof Displacements

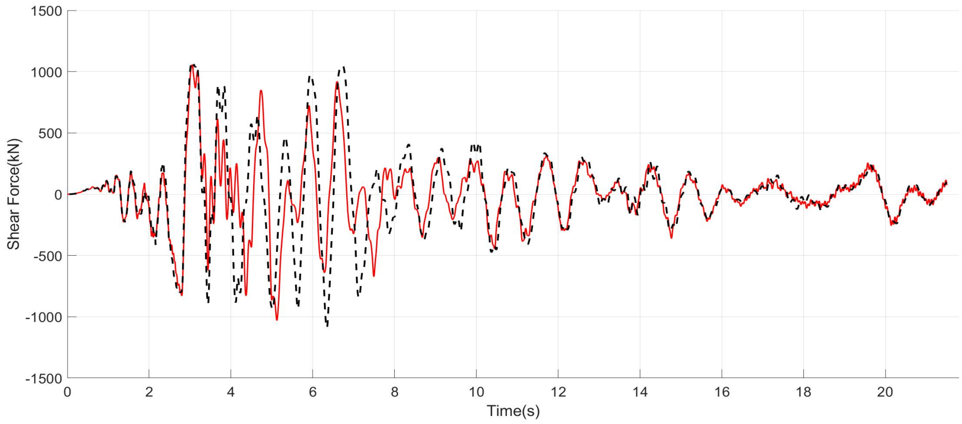

(b) Shear Forces at the base

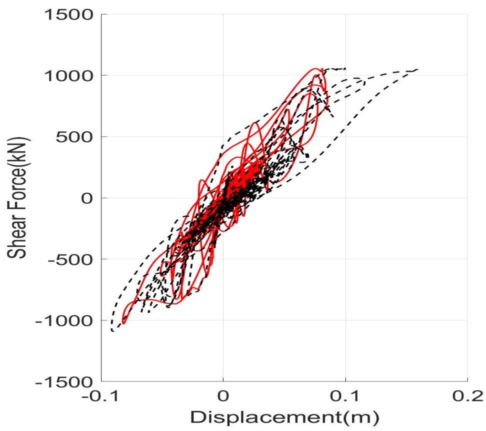

(c) Structural Hysteretic Curve

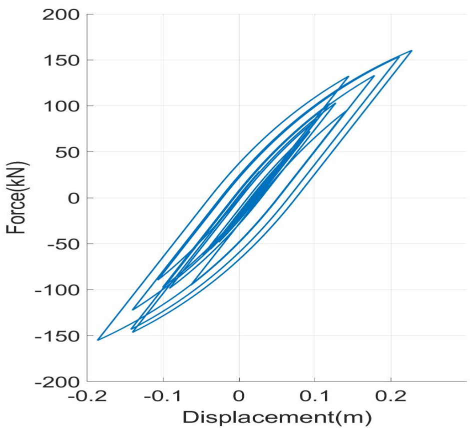

(d) TMD Hysteretic Curve

Figure B.57. Erzincan $U_{max} = 45cm$

Friulli

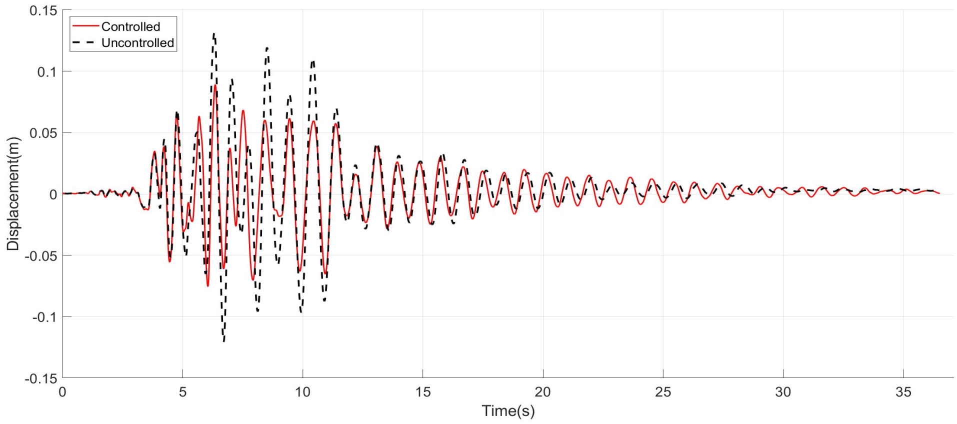

(a) Roof Displacements

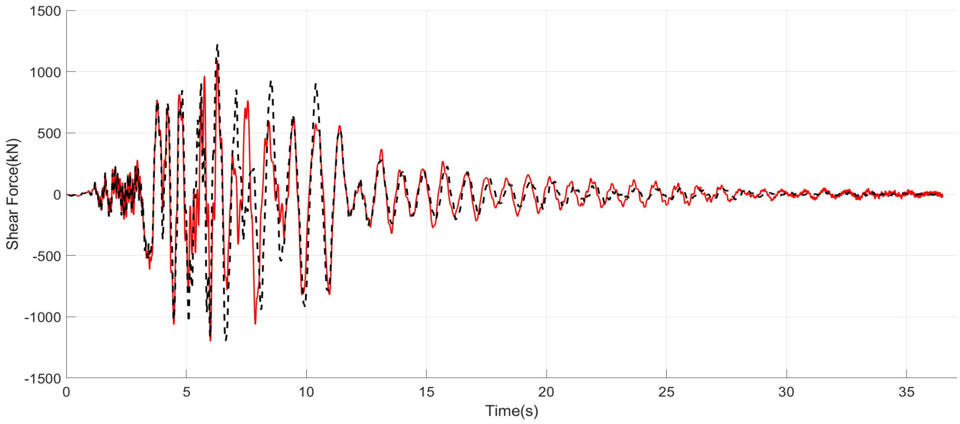

(b) Shear Forces at the base

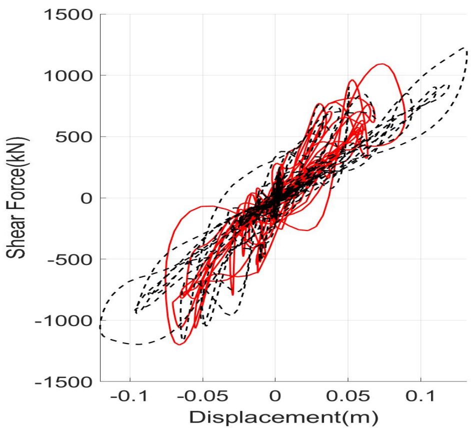

(c) Structural Hysteretic Curve

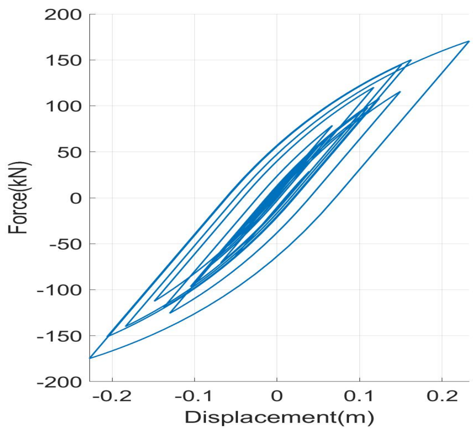

(d) TMD Hysteretic Curve

Figure B.58. Friulli $U_{max} = 45cm$

Imperial Valley

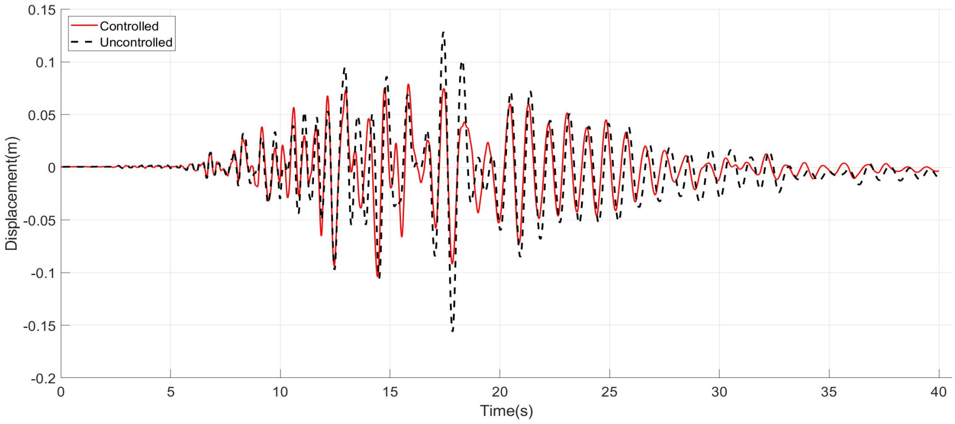

(a) Roof Displacements

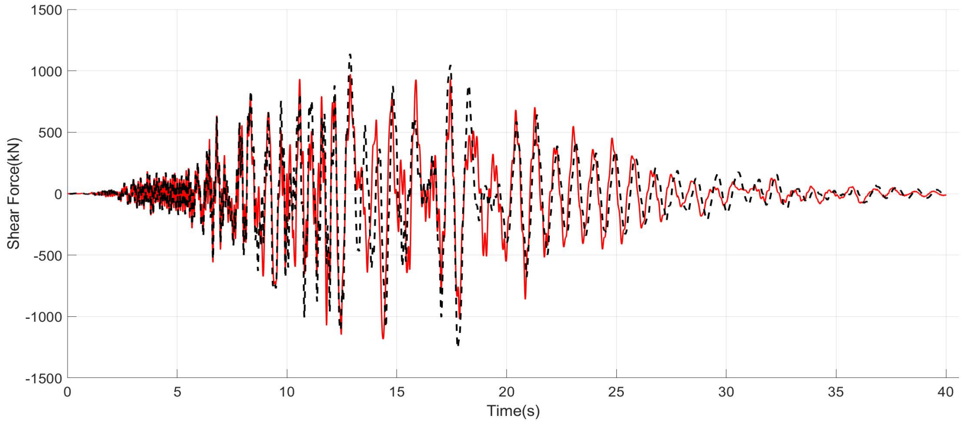

(b) Shear Forces at the base

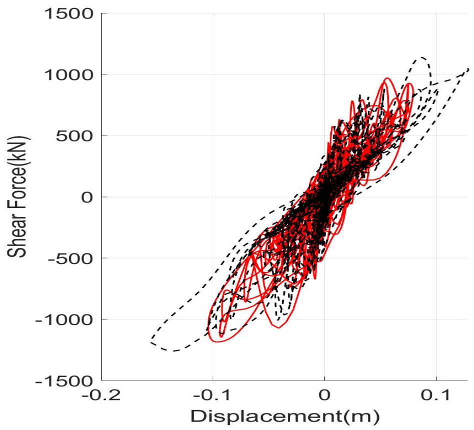

(c) Structural Hysteretic Curve

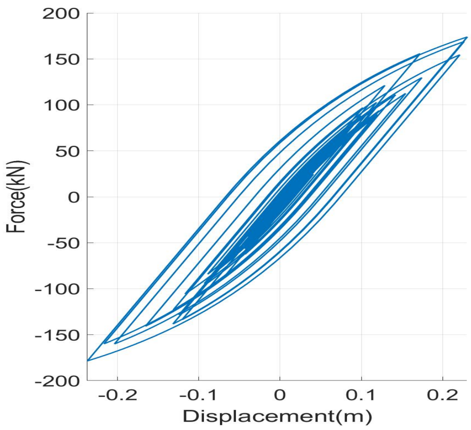

(d) TMD Hysteretic Curve

Figure B.59. Imperial Valley $U_{max} = 45cm$

Kobe

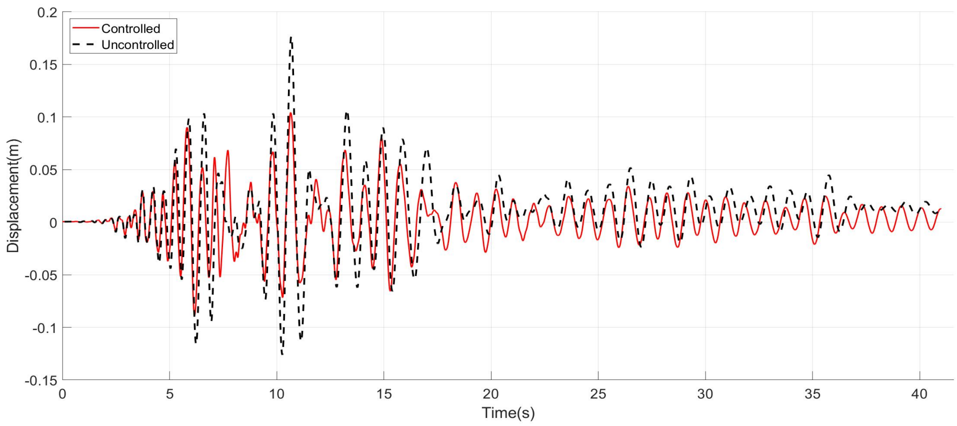

(a) Roof Displacements

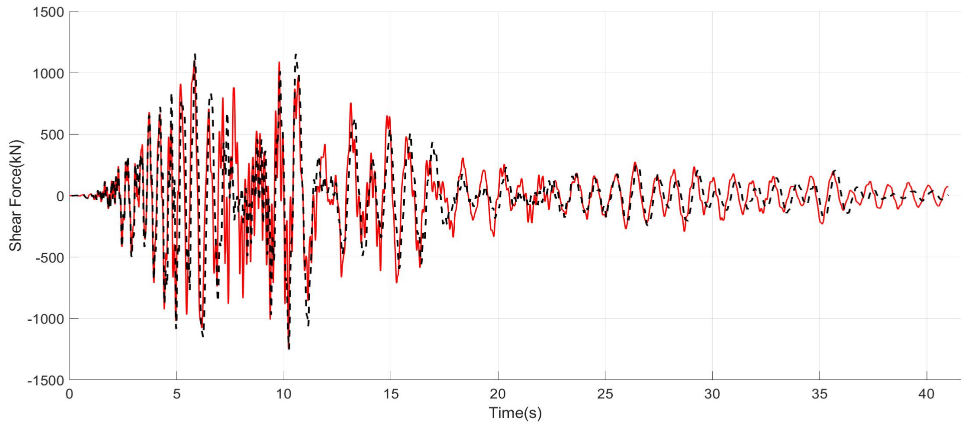

(b) Shear Forces at the base

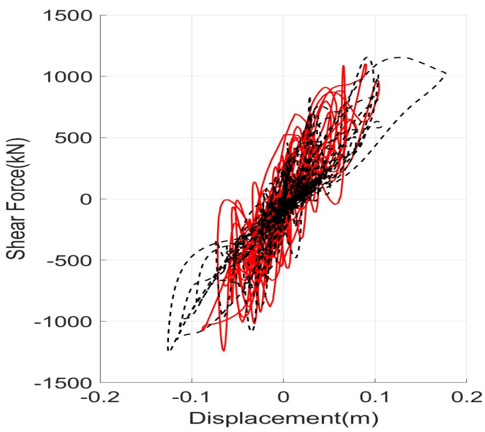

(c) Structural Hysteretic Curve

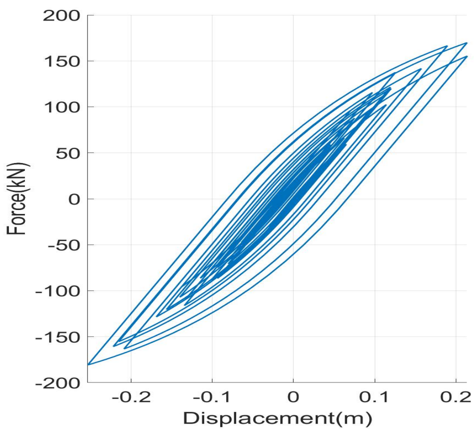

(d) TMD Hysteretic Curve

Figure B.60. Kobe $U_{max} = 45cm$

Loma Prieta

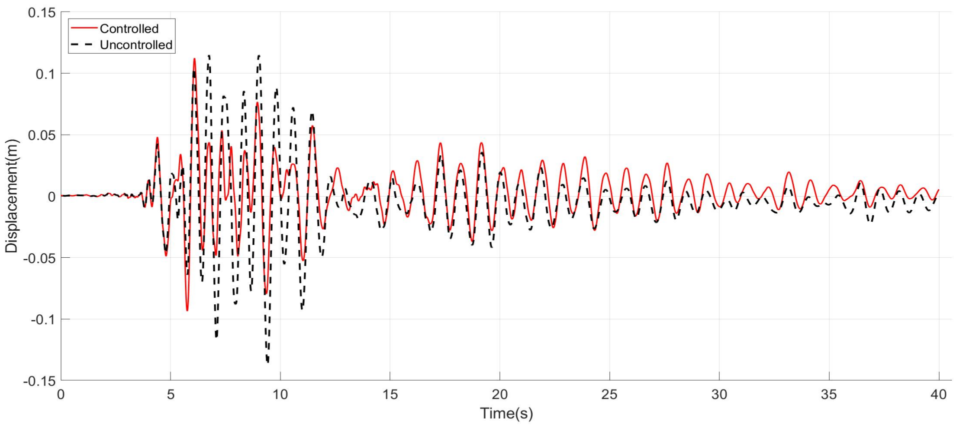

(a) Roof Displacements

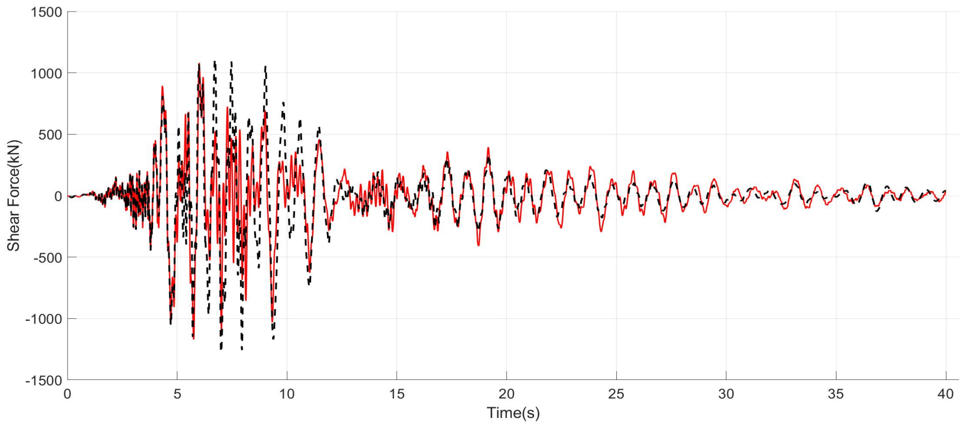

(b) Shear Forces at the base

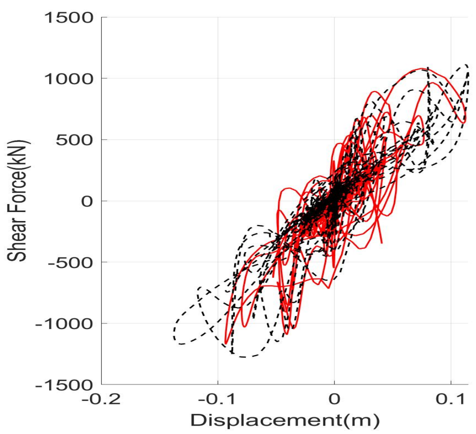

(c) Structural Hysteretic Curve

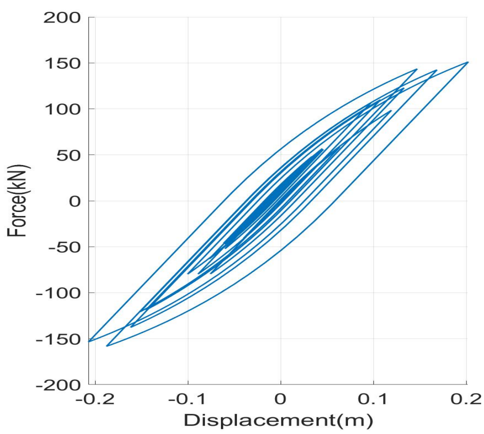

(d) TMD Hysteretic Curve

Figure B.61. Loma Prieta $U_{max} = 45cm$

Northridge

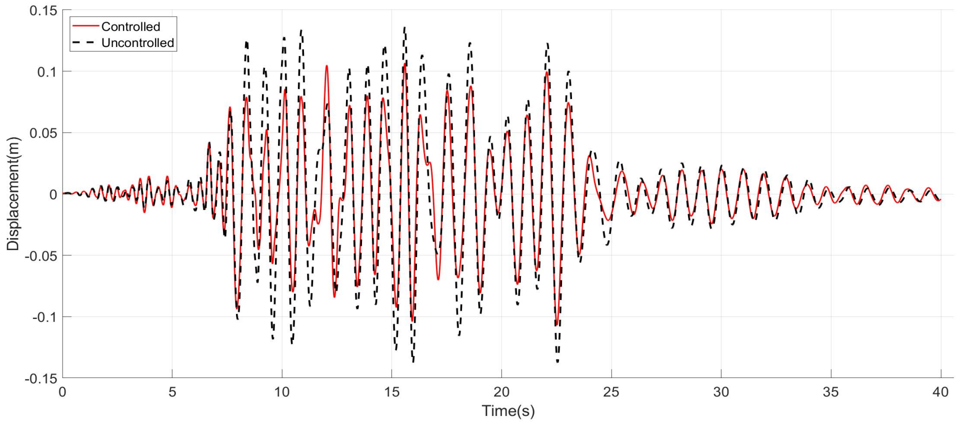

(a) Roof Displacements

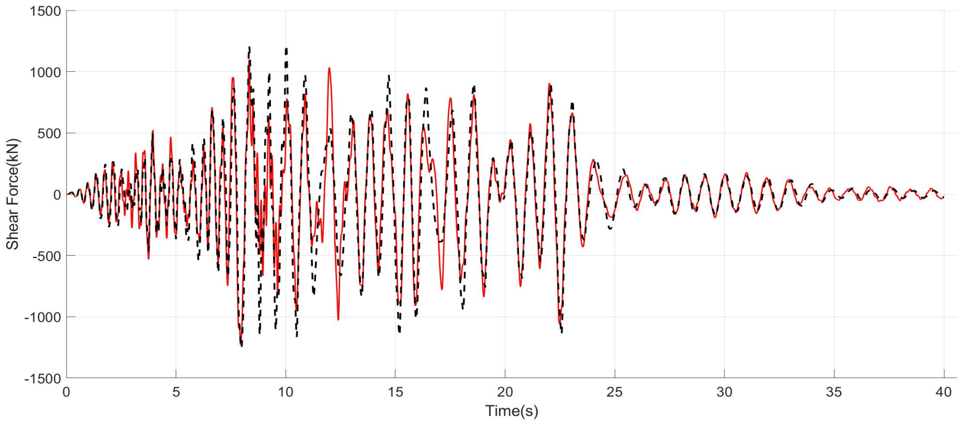

(b) Shear Forces at the base

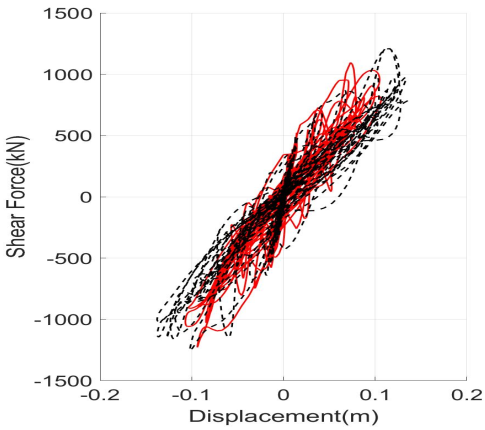

(c) Structural Hysteretic Curve

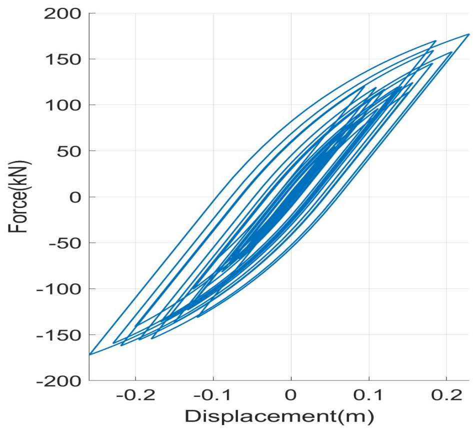

(d) TMD Hysteretic Curve

Figure B.62. Northridge $U_{max} = 45cm$

Drifts

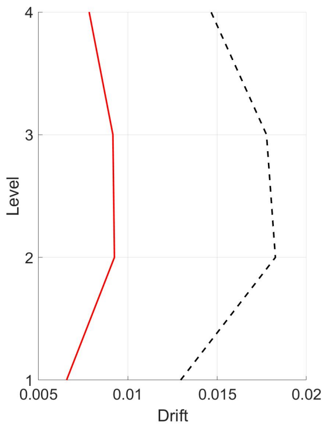

(a) Chalfant

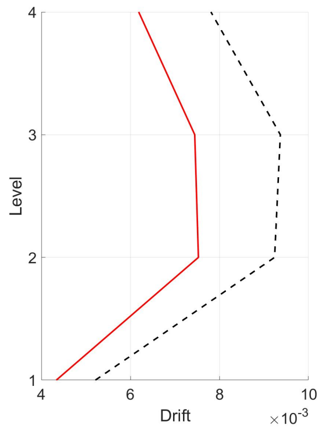

(b) Chi Chi

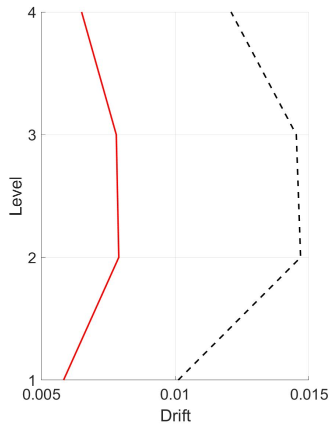

(c) Erzincan

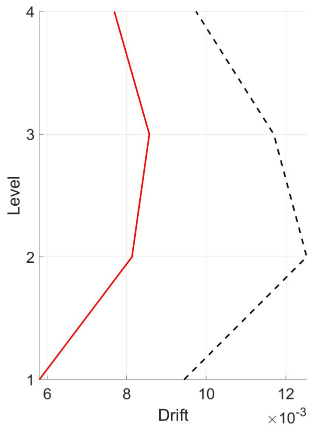

(d) Friulli

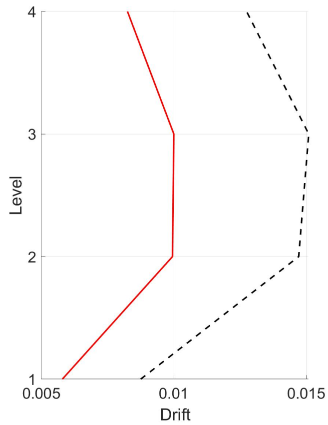

(e) Imperial Valley

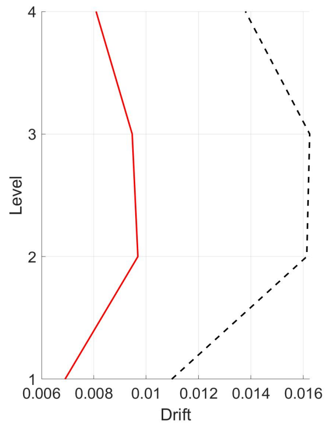

(f) Kobe

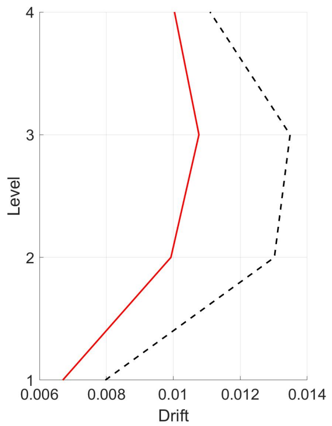

(g) Loma Prieta

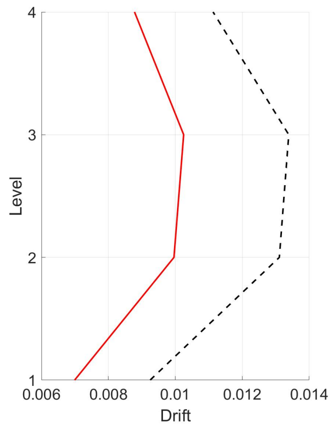

(h) Northridge

Figure B.63. Drifts $U_{max} = 45cm$

B.2.6 $U_{max} = 60cm$

Setting the stroke as a desing parameter and using a value of $60cm$ for the tuning at the performance point, the results following results are obtained.

Table B.8. Performance Indices $U_{max} = 60cm$

Earthquake	Performance Index						
	J_1	J_2	J_3	J_4	J_5	J_6	J_7(m)
Chalfant	0.603	0.941	1.058	0.637	0.949	0.957	0.250
Chi-Chi	0.790	0.970	0.846	0.596	0.780	0.807	0.200
Erzincan	0.561	0.959	0.891	0.664	0.827	0.826	0.225
Friulli	0.692	0.985	1.094	0.736	0.895	0.882	0.244
Imperial Valley	0.664	0.963	1.023	0.860	0.973	0.947	0.2487
Kobe	0.630	0.988	1.332	0.734	0.999	1.042	0.271
Loma Prieta	0.844	0.920	0.803	0.780	0.863	0.877	0.205
Northridge	0.853	0.976	0.958	0.797	0.943	0.882	0.246
Average	0.705	0.963	1.000	0.726	0.904	0.903	0.236

Chalfant

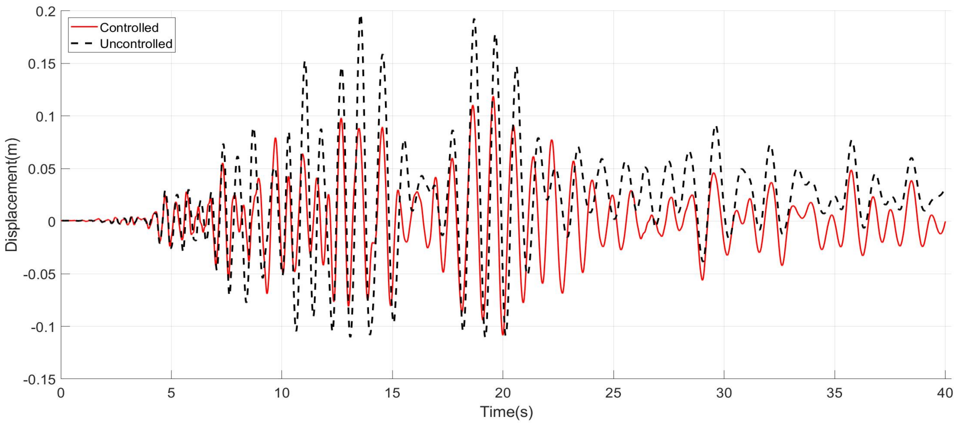

(a) Roof Displacements

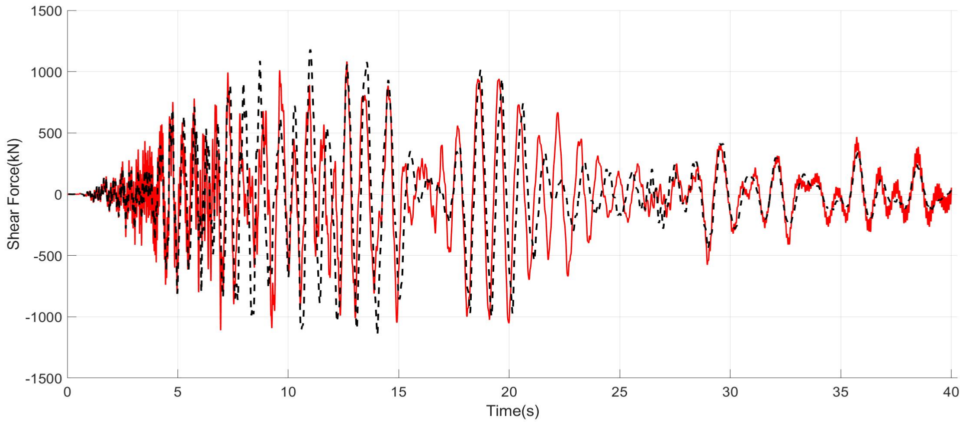

(b) Shear Forces at the base

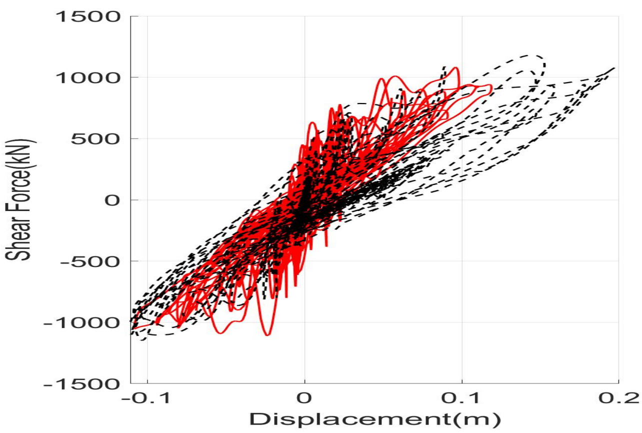

(c) Structural Hysteretic Curve

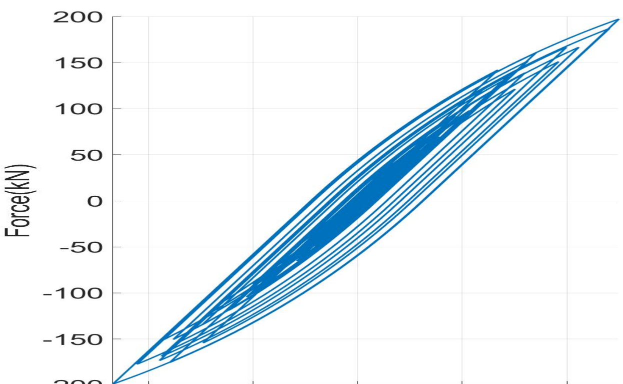

Chi-Chi

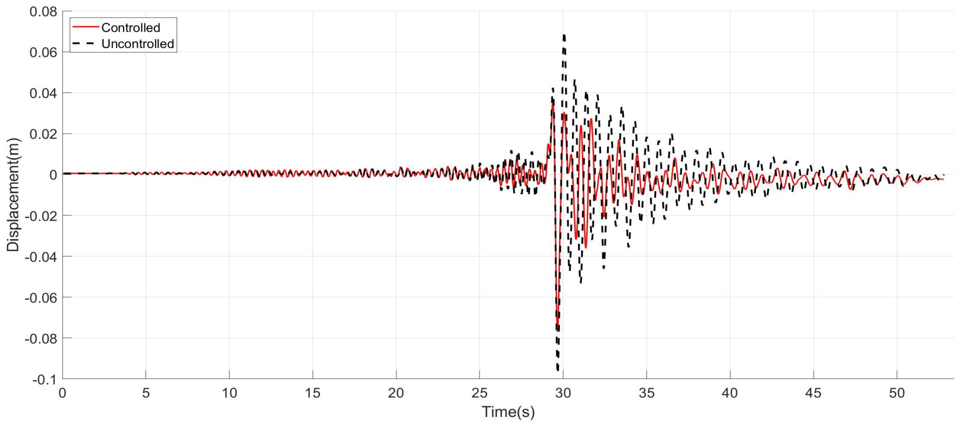

(a) Roof Displacements

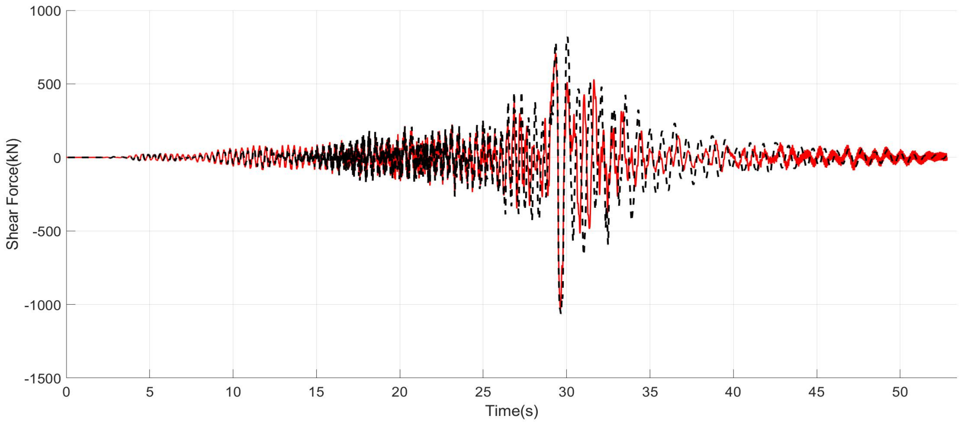

(b) Shear Forces at the base

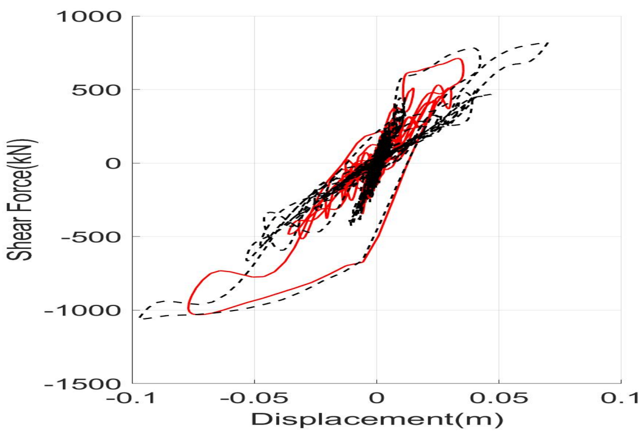

(c) Structural Hysteretic Curve

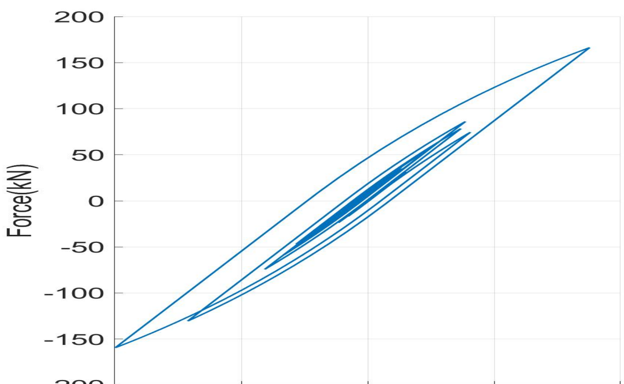

Erzincan

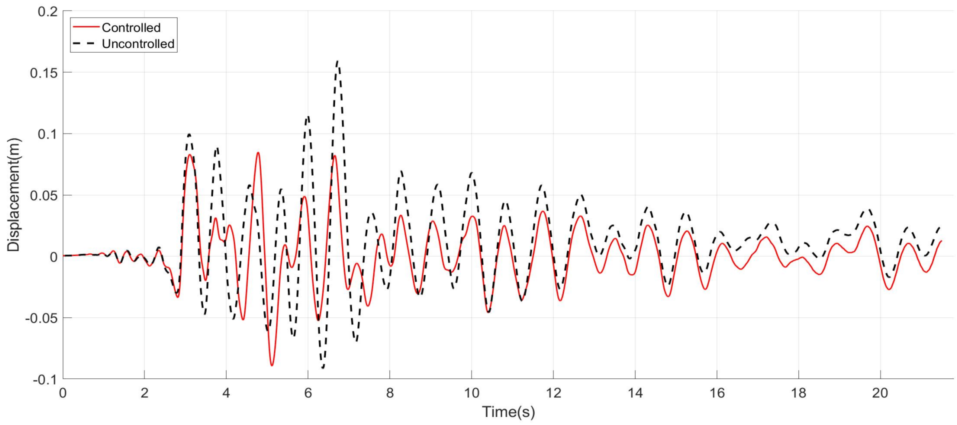

(a) Roof Displacements

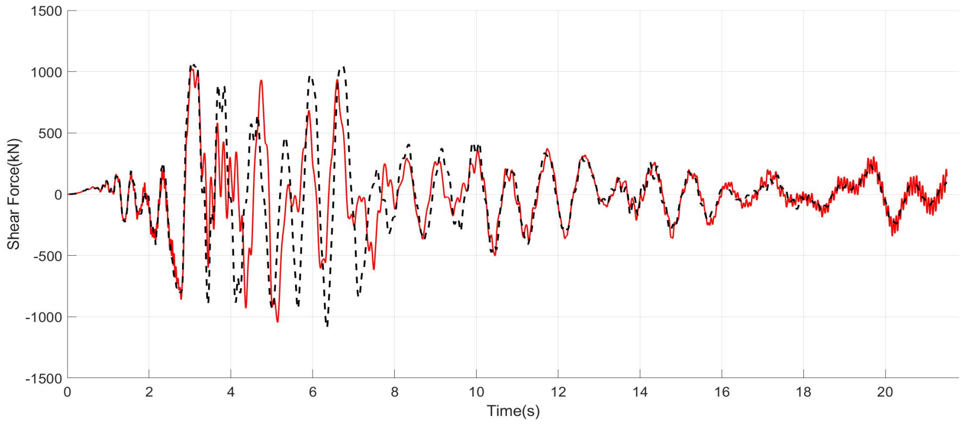

(b) Shear Forces at the base

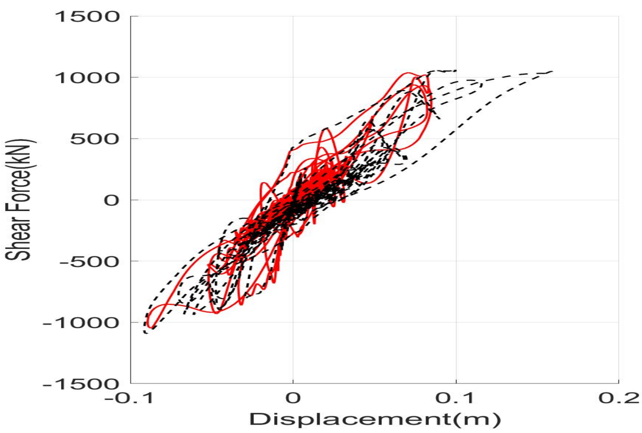

(c) Structural Hysteretic Curve

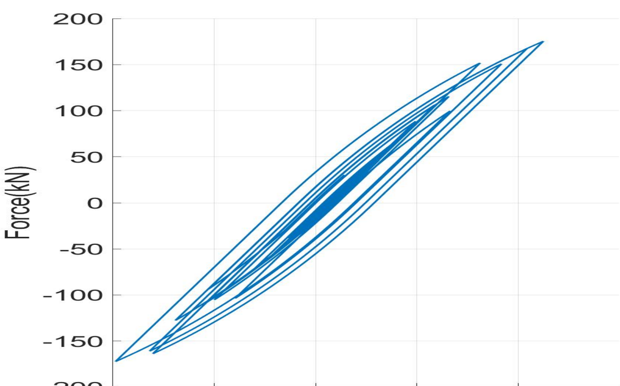

Friulli

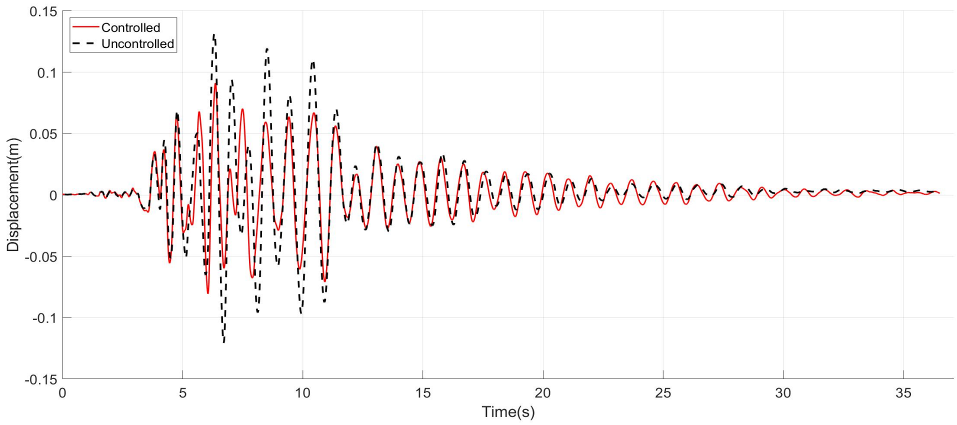

(a) Roof Displacements

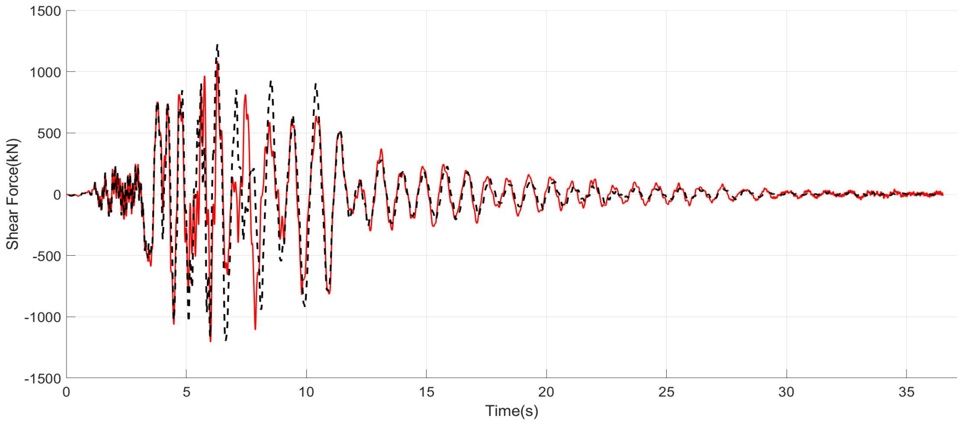

(b) Shear Forces at the base

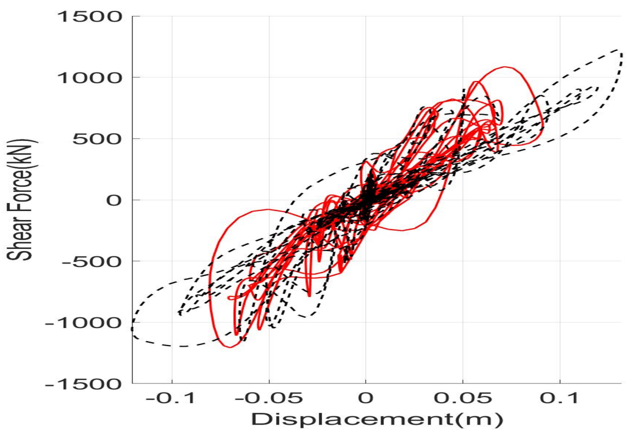

(c) Structural Hysteretic Curve

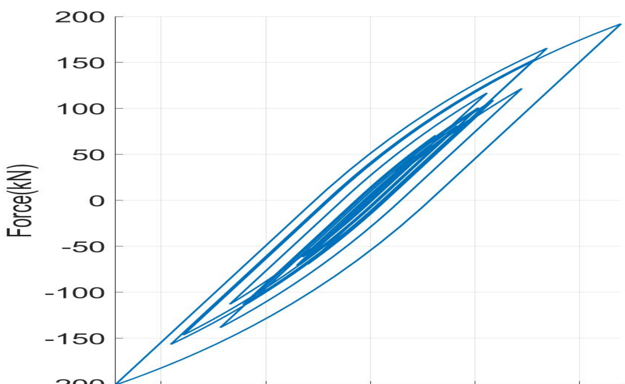

Imperial Valley

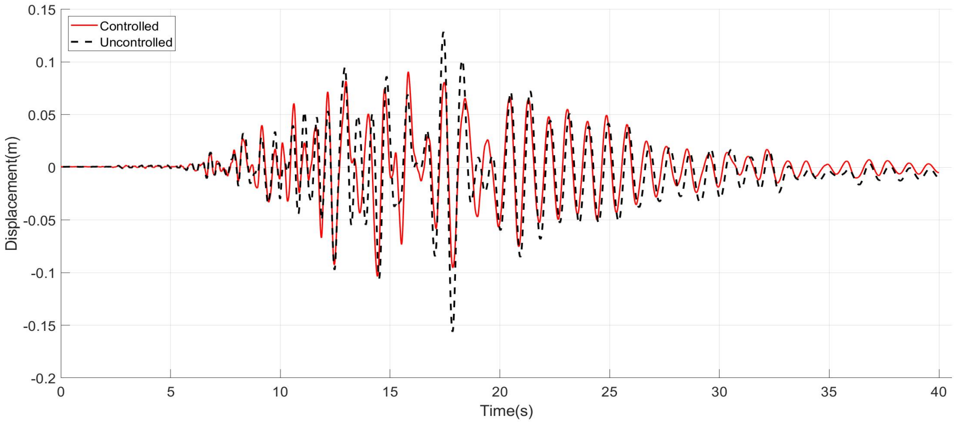

(a) Roof Displacements

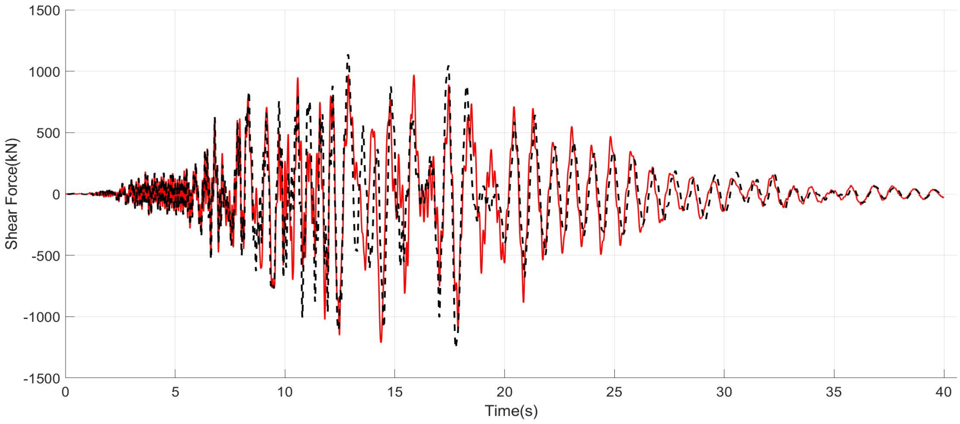

(b) Shear Forces at the base

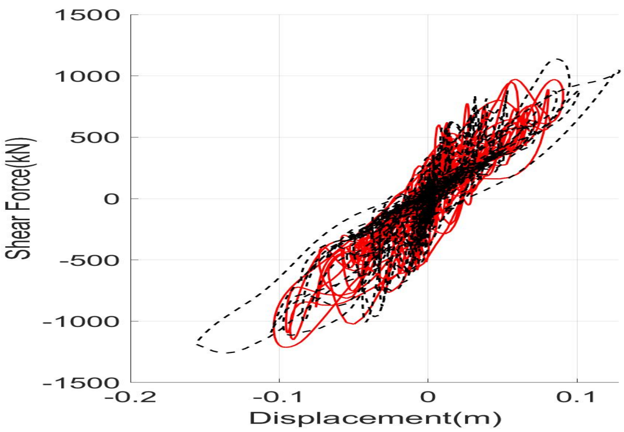

(c) Structural Hysteretic Curve

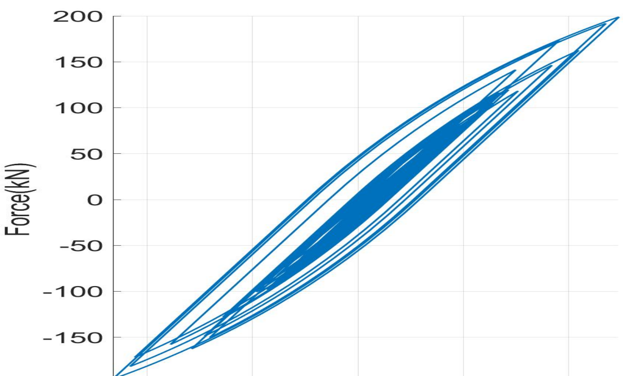

Kobe

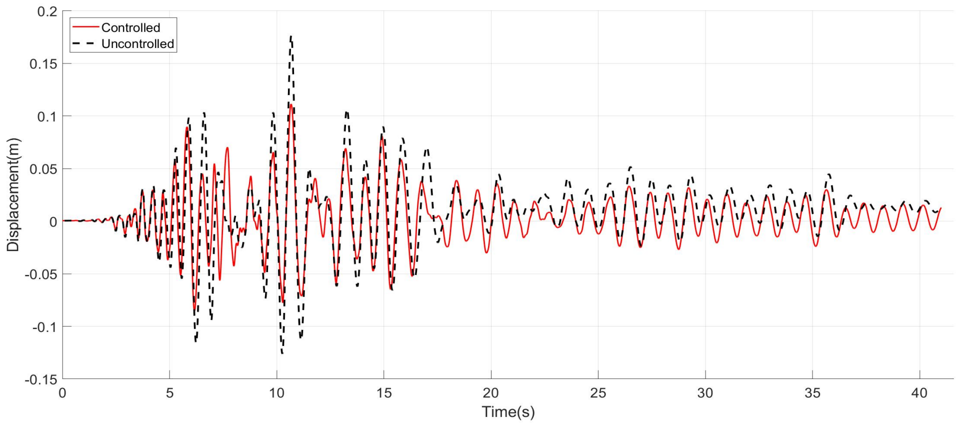

(a) Roof Displacements

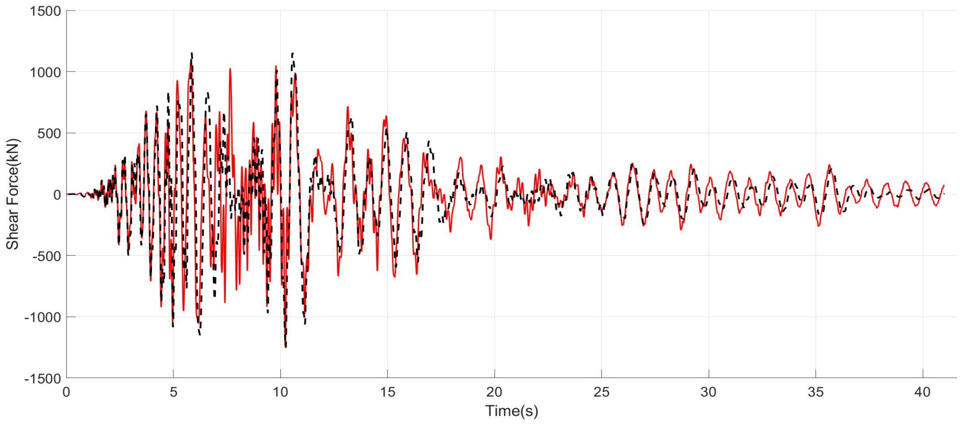

(b) Shear Forces at the base

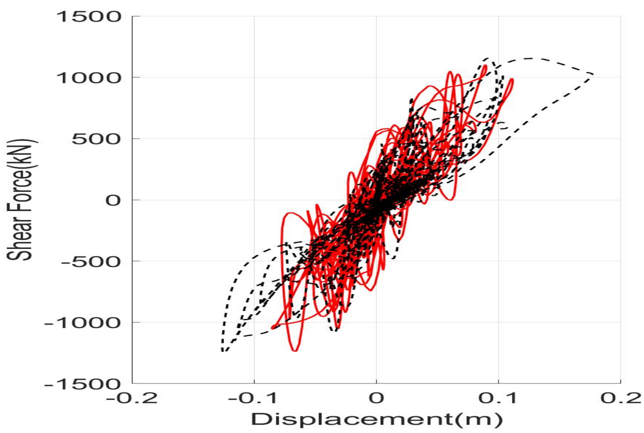

(c) Structural Hysteretic Curve

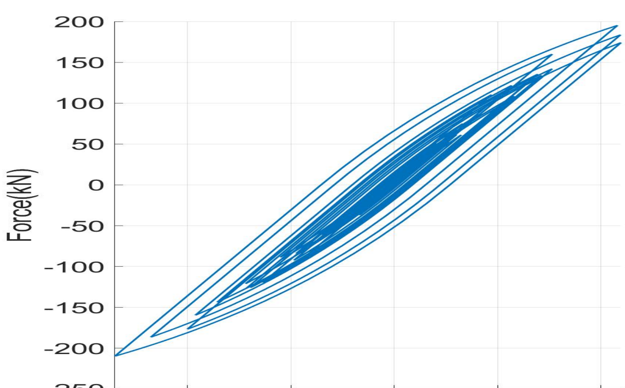

Loma Prieta

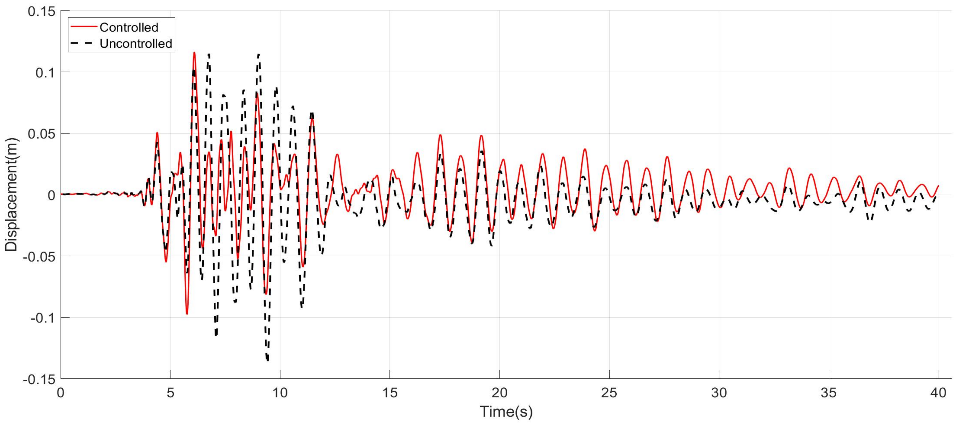

(a) Roof Displacements

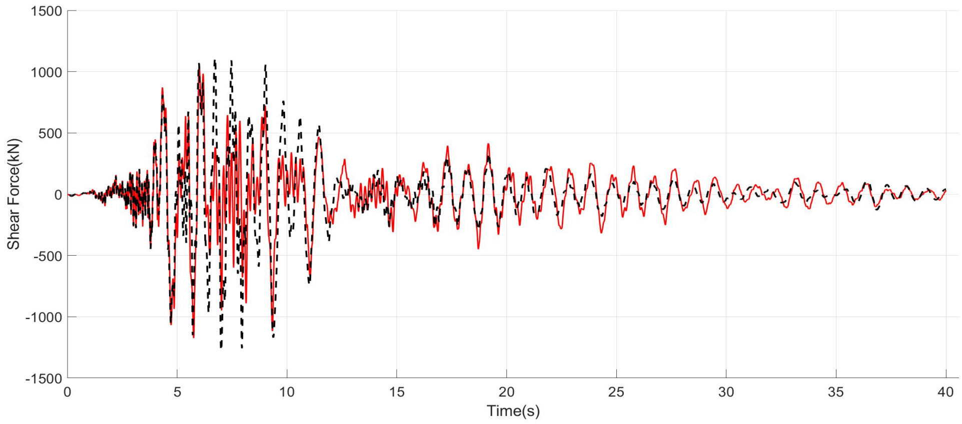

(b) Shear Forces at the base

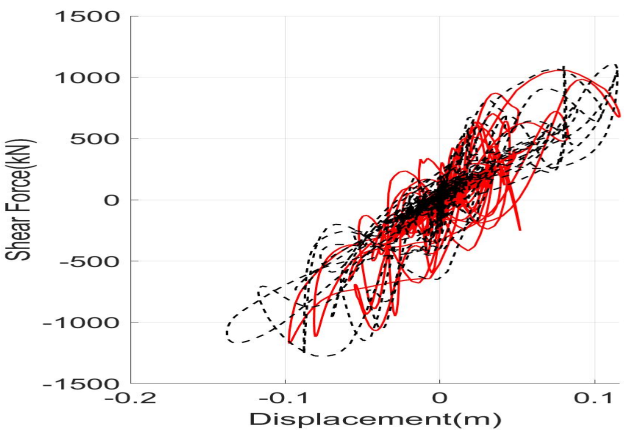

(c) Structural Hysteretic Curve

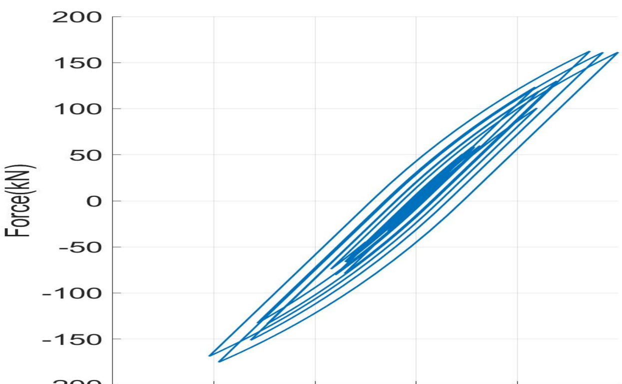

Northridge

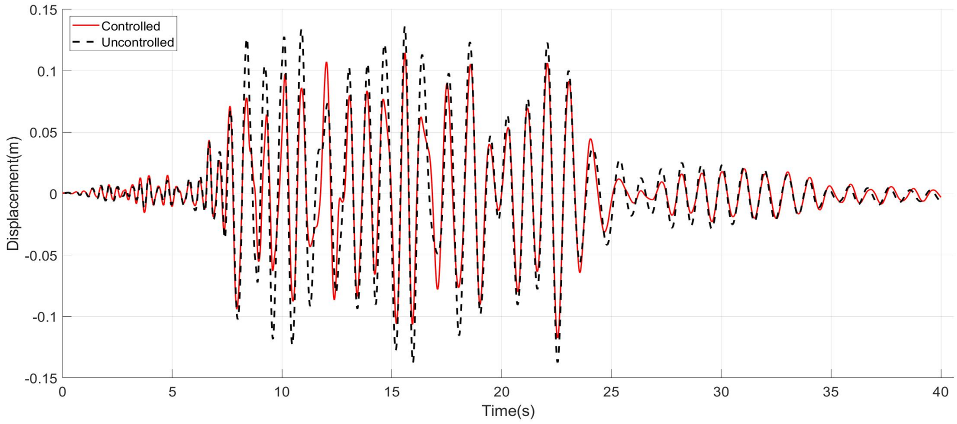

(a) Roof Displacements

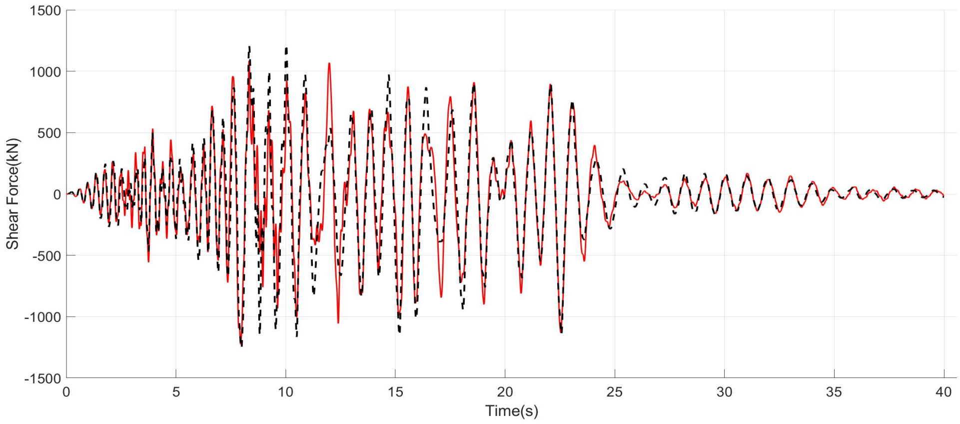

(b) Shear Forces at the base

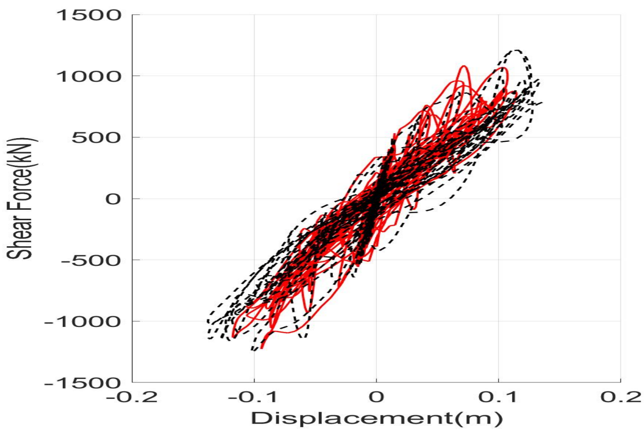

(c) Structural Hysteretic Curve

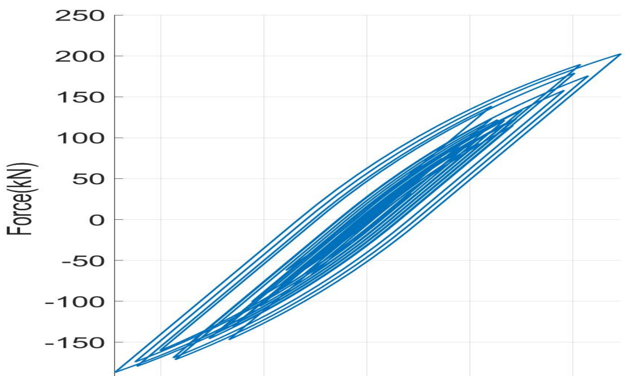

Drifts

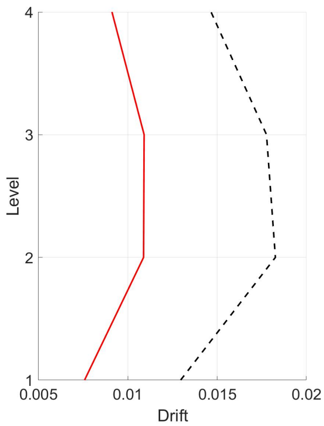

(a) Chalfant

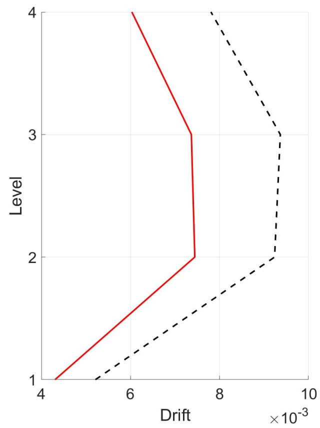

(b) Chi Chi

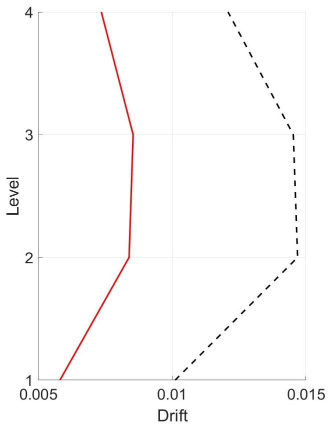

(c) Erzincan

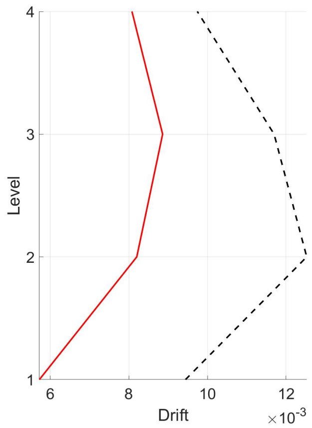

(d) Friulli

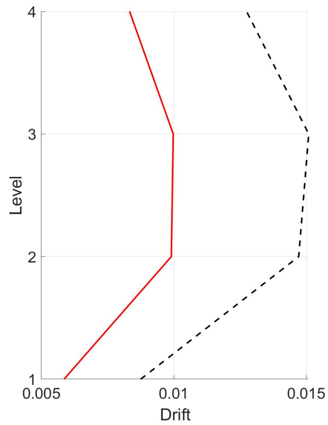

(e) Imperial Valley

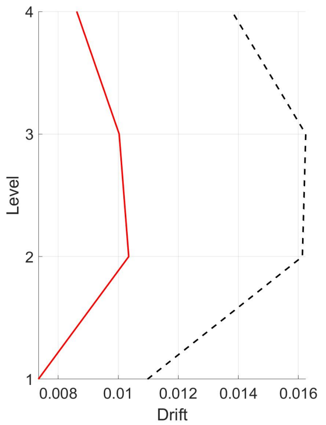

(f) Kobe

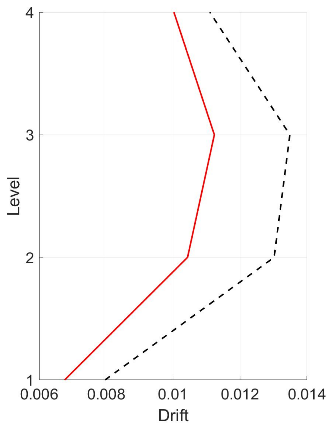

(g) Loma Prieta

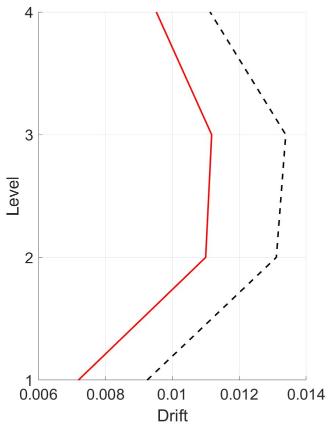

(h) Northridge

Figure B.72. Drifts $U_{max} = 60cm$

B.3 Stiffness

B.3.1 Tangent Stiffness

Assuming a tangent stiffness of the structure for the initial tuning derives in the following results.

Table B.9. Performance Indices Tangent Stiffness

Earthquake	Performance Index						
	J_1	J_2	J_3	J_4	J_5	J_6	J_7(m)
Chalfant	0.654	0.961	1.045	0.671	0.955	0.943	0.171
Chi-Chi	0.959	0.989	0.883	0.694	0.754	0.720	0.167
Erzincan	0.634	1.019	0.866	0.742	0.833	0.788	0.160
Friulli	0.776	0.968	0.999	0.755	0.887	0.855	0.163
Imperial Valley	0.726	0.881	0.904	0.958	0.991	0.908	0.194
Kobe	0.558	0.968	1.079	0.644	0.979	0.965	0.159
Loma Prieta	0.734	0.984	0.831	0.734	0.895	0.901	0.166
Northridge	0.925	0.936	0.815	0.800	0.948	0.870	0.239
Average	0.746	0.963	0.928	0.750	0.905	0.869	0.177

Chalfant

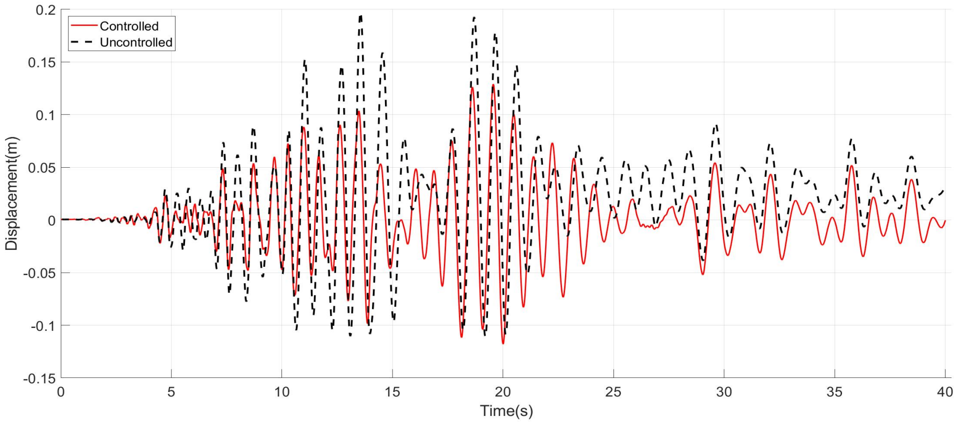

(a) Roof Displacements

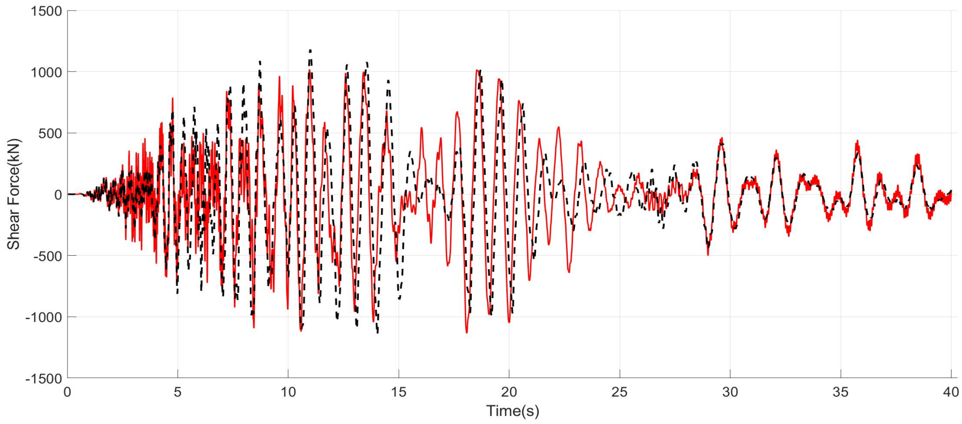

(b) Shear Forces at the base

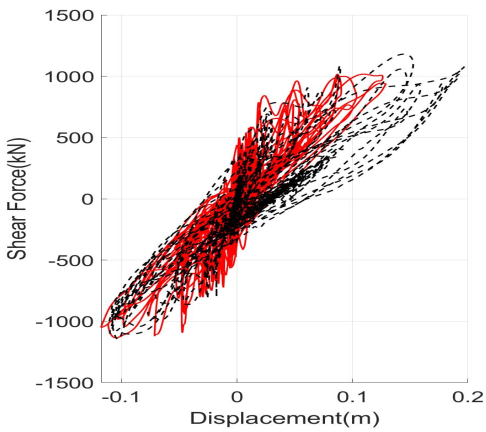

(c) Structural Hysteretic Curve

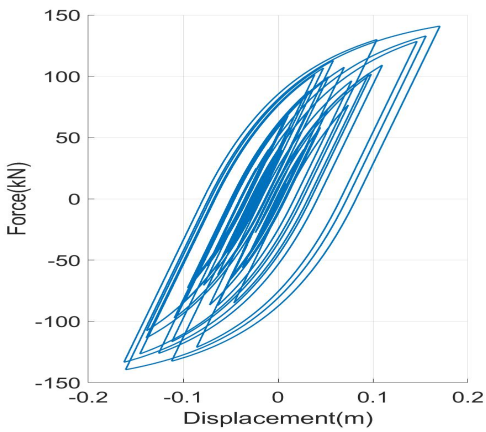

(d) TMD Hysteretic Curve

Figure B.73. Chalfant Tangent Stiffness

Chi-Chi

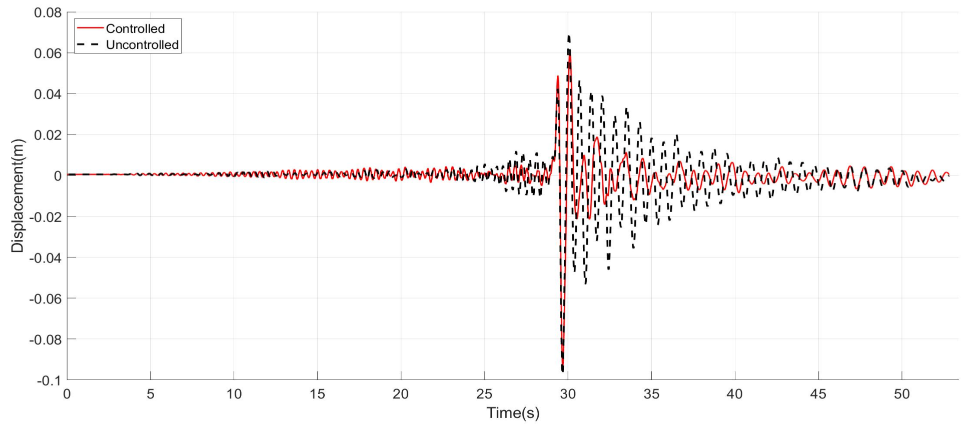

(a) Roof Displacements

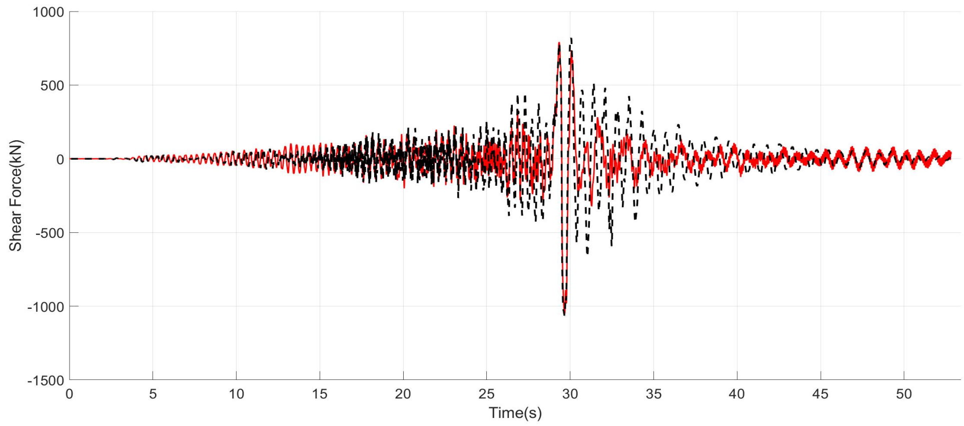

(b) Shear Forces at the base

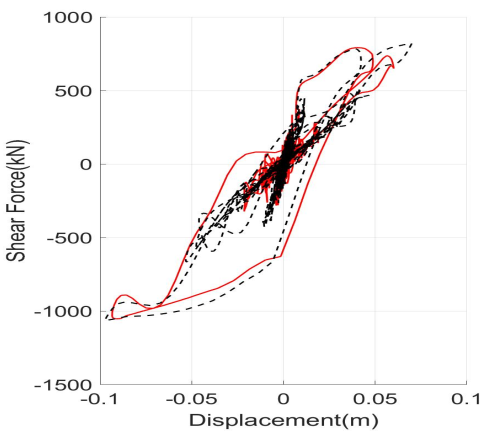

(c) Structural Hysteretic Curve

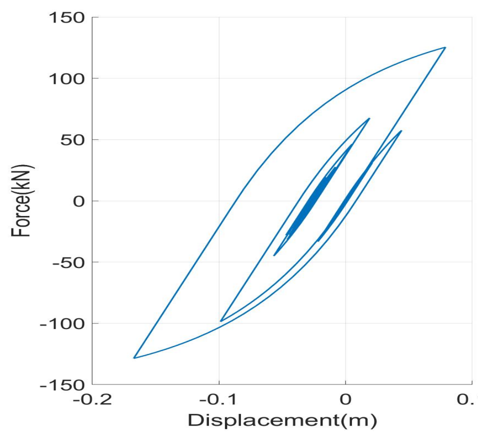

(d) TMD Hysteretic Curve

Figure B.74. Chi Chi Tangent Stiffness

Erzincan

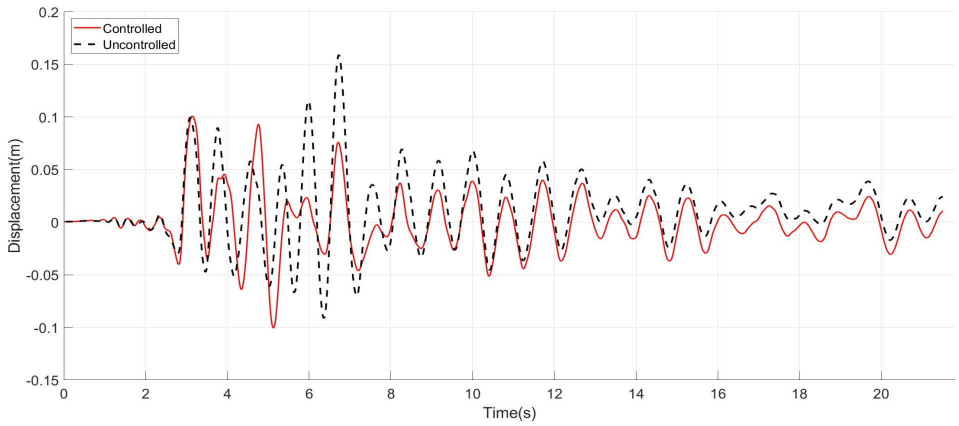

(a) Roof Displacements

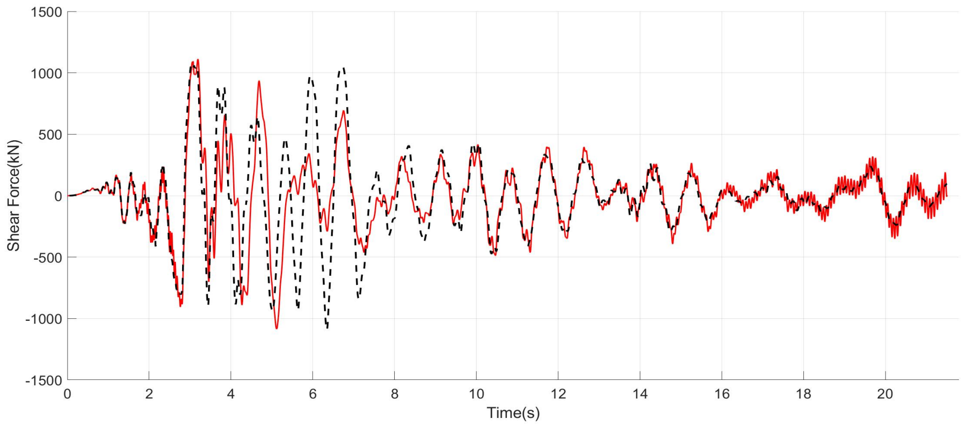

(b) Shear Forces at the base

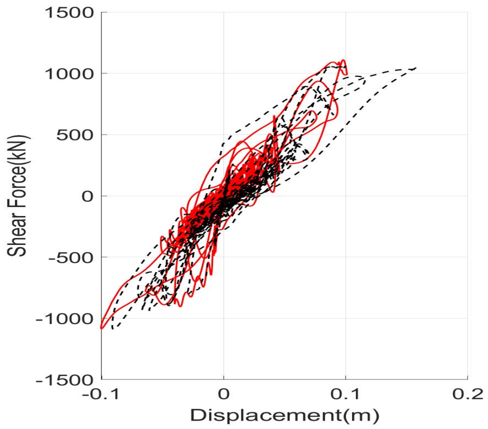

(c) Structural Hysteretic Curve

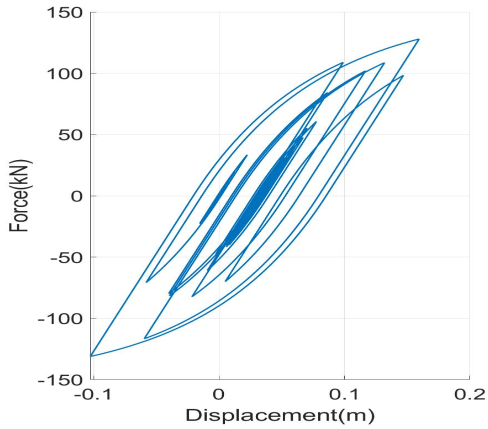

(d) TMD Hysteretic Curve

Figure B.75. Erzincan Tangent Stiffness

Friulli

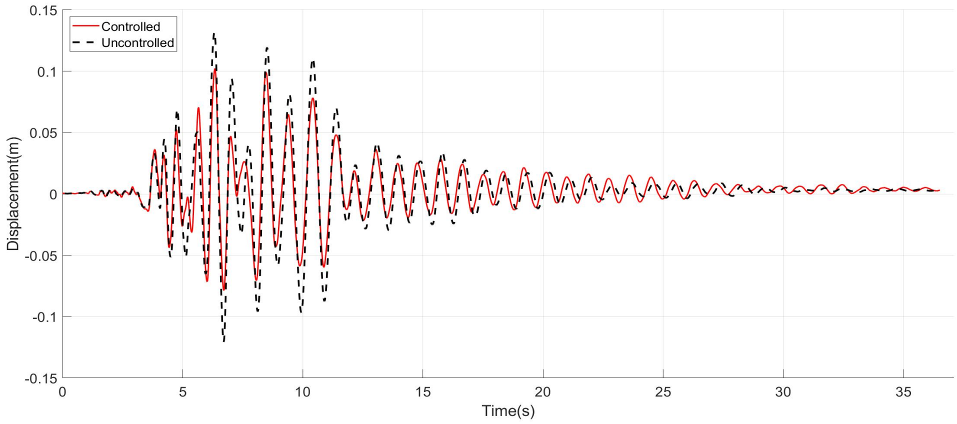

(a) Roof Displacements

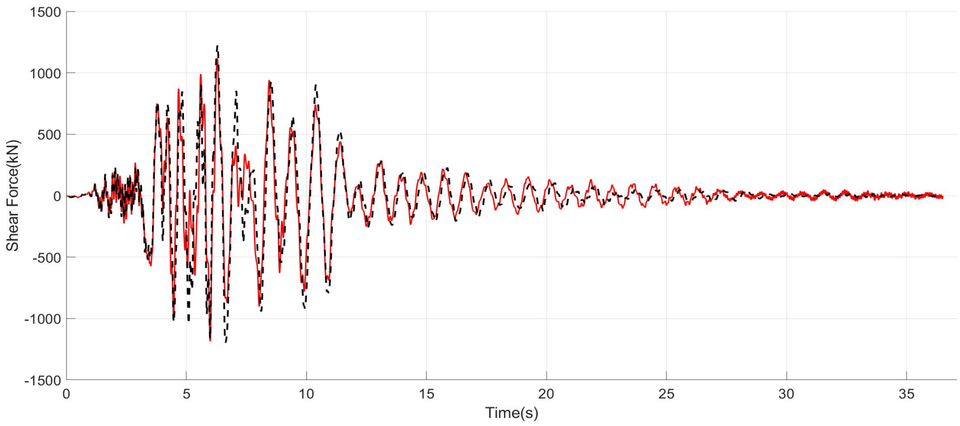

(b) Shear Forces at the base

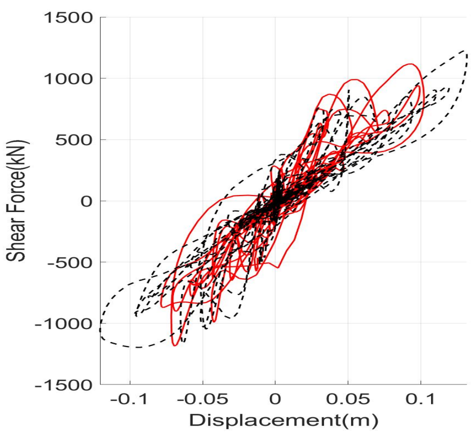

(c) Structural Hysteretic Curve

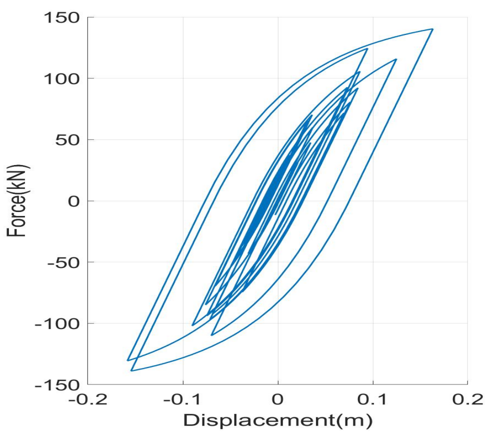

(d) TMD Hysteretic Curve

Figure B.76. Friulli Tangent Stiffness

Imperial Valley

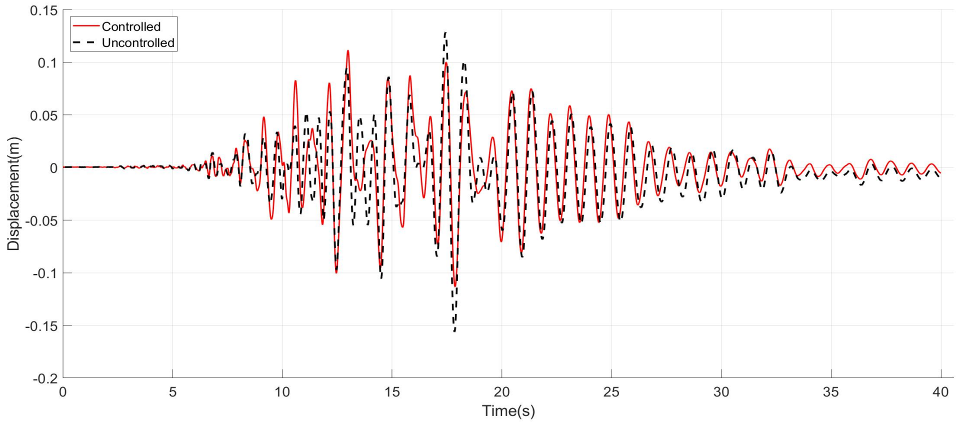

(a) Roof Displacements

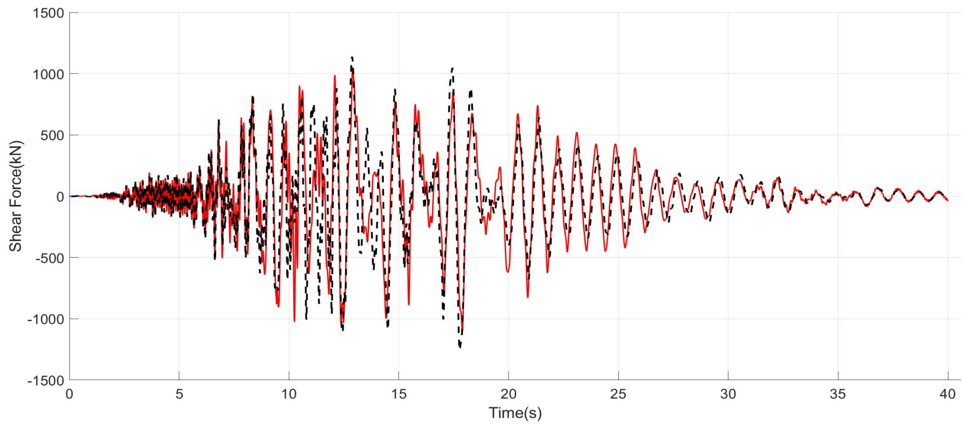

(b) Shear Forces at the base

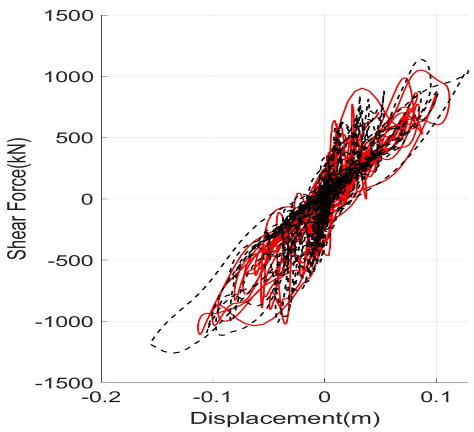

(c) Structural Hysteretic Curve

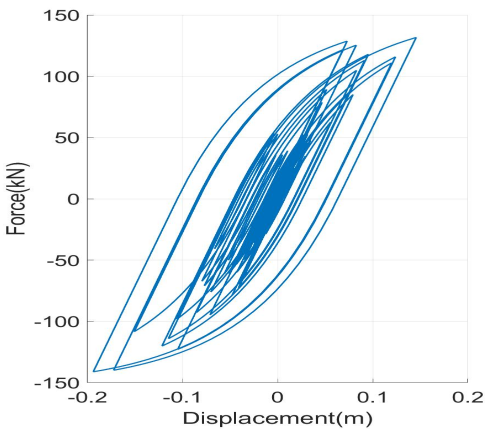

(d) TMD Hysteretic Curve

Figure B.77. Imperial Valley Tangent Stiffness

Kobe

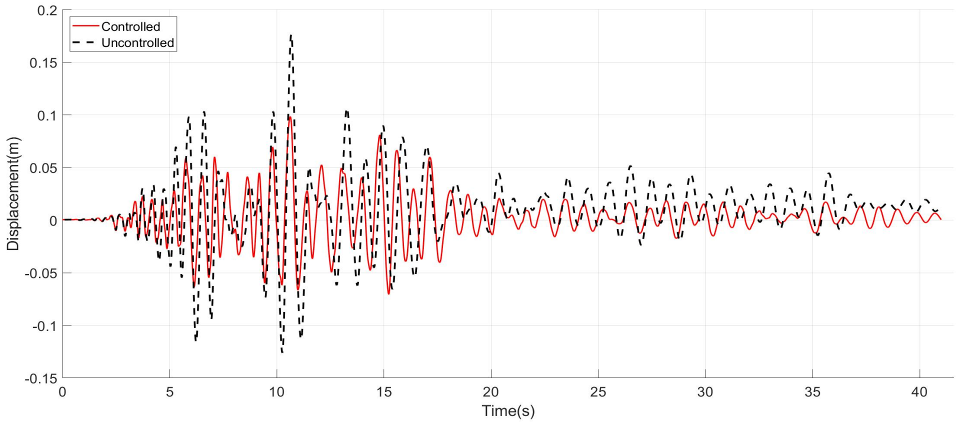

(a) Roof Displacements

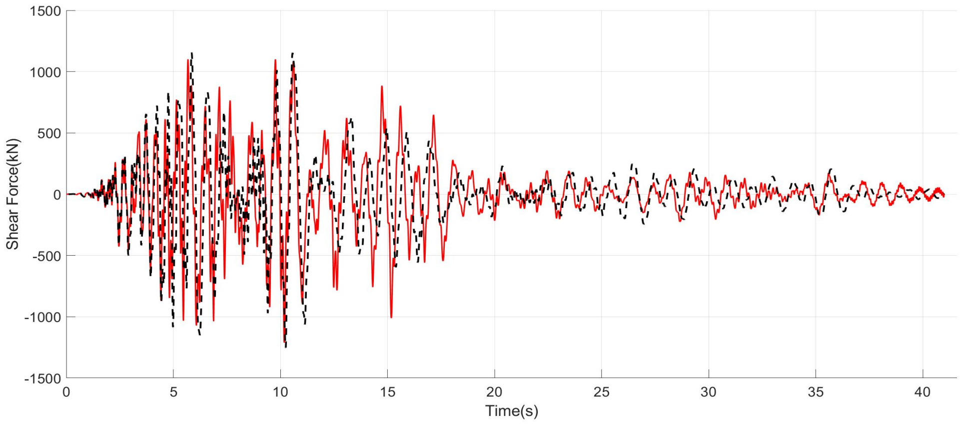

(b) Shear Forces at the base

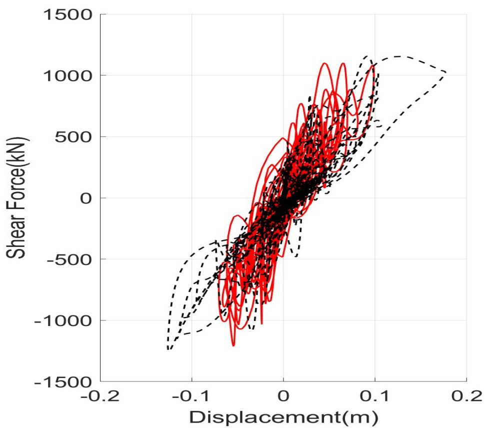

(c) Structural Hysteretic Curve

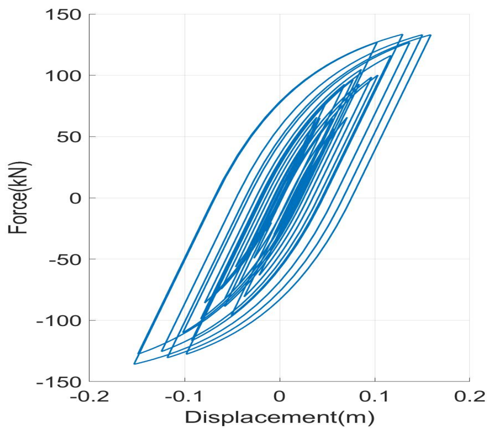

(d) TMD Hysteretic Curve

Figure B.78. Kobe Tangent Stiffness

Loma Prieta

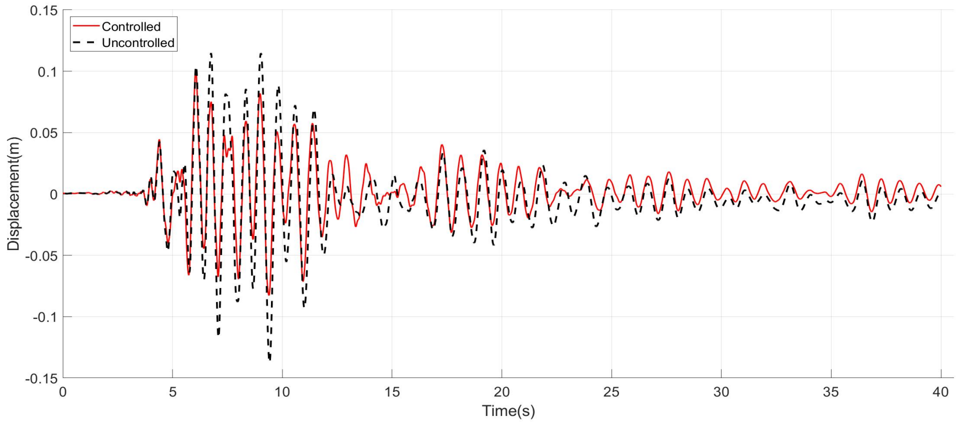

(a) Roof Displacements

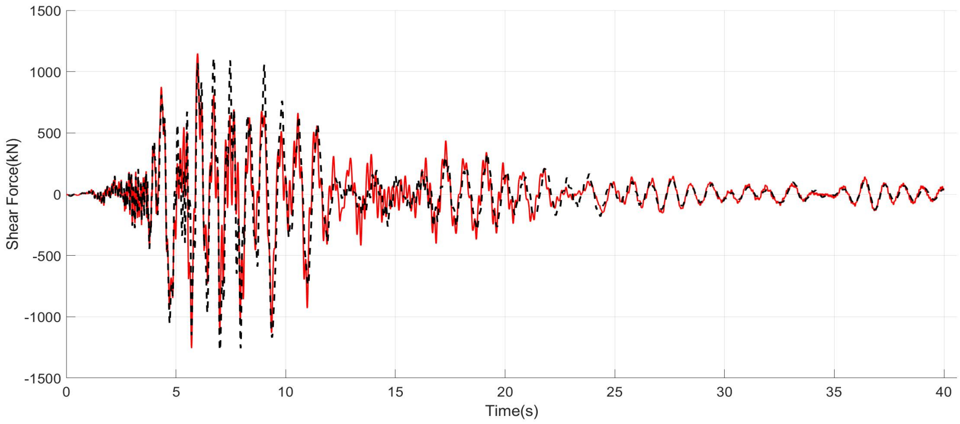

(b) Shear Forces at the base

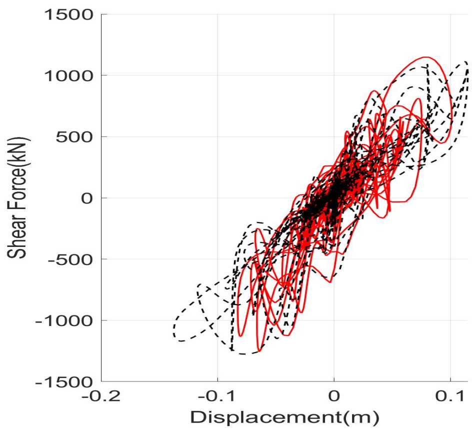

(c) Structural Hysteretic Curve

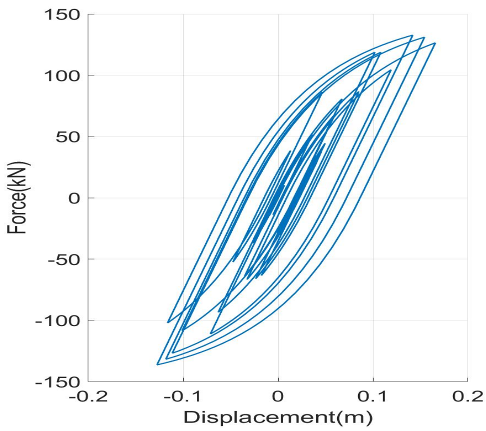

(d) TMD Hysteretic Curve

Figure B.79. Loma Prieta Tangent Stiffness

Northridge

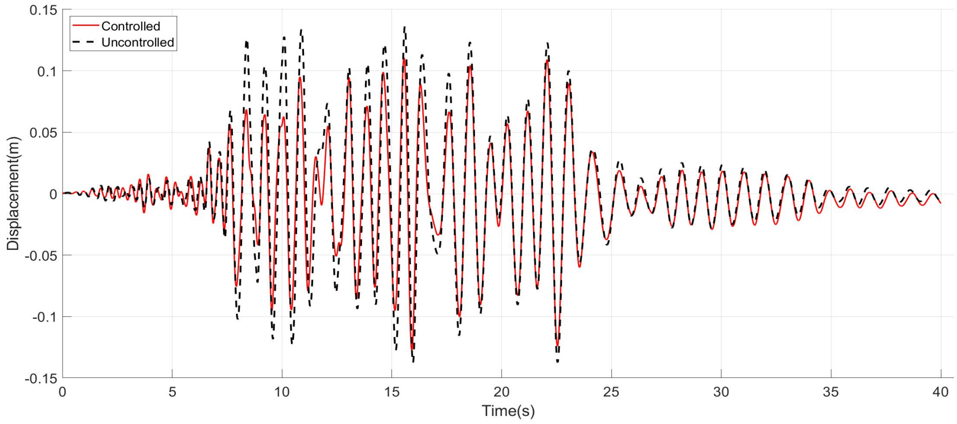

(a) Roof Displacements

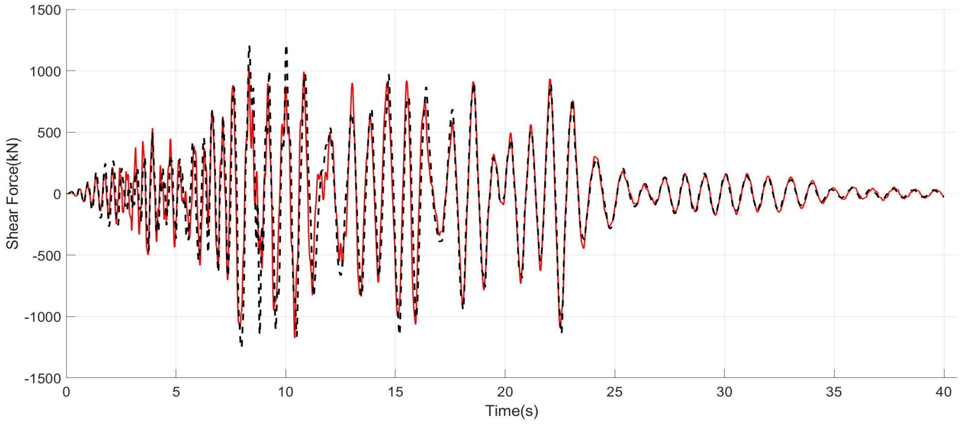

(b) Shear Forces at the base

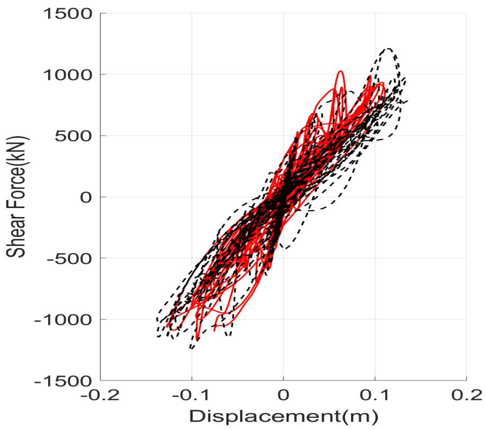

(c) Structural Hysteretic Curve

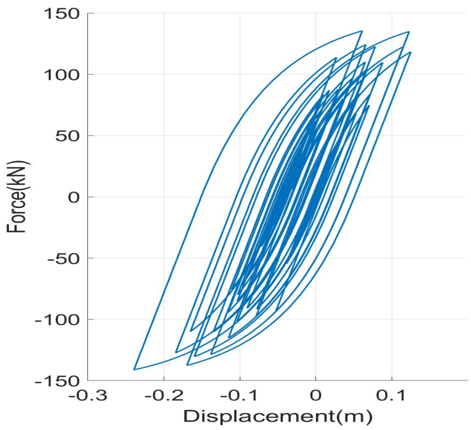

(d) TMD Hysteretic Curve

Figure B.80. Northridge Tangent Stiffness

Drifts

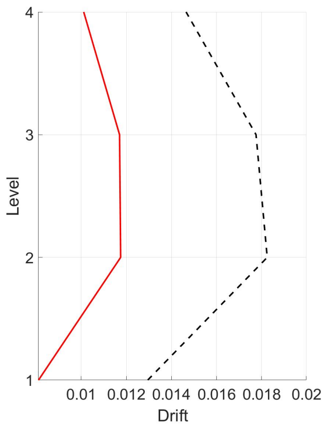

(a) Chalfant

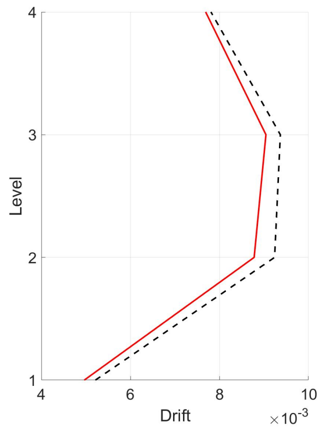

(b) Chi Chi

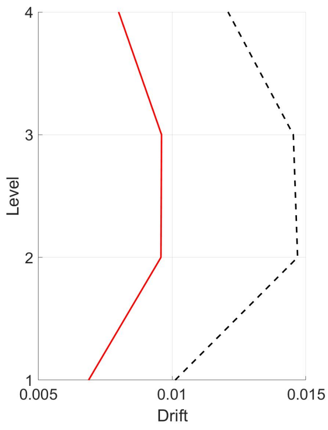

(c) Erzincan

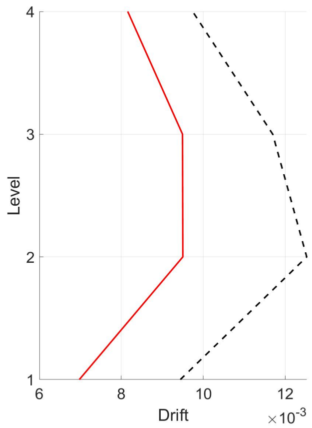

(d) Friulli

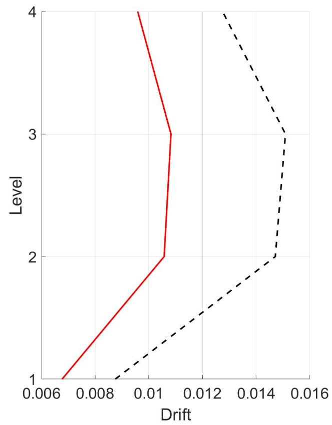

(e) Imperial Valley

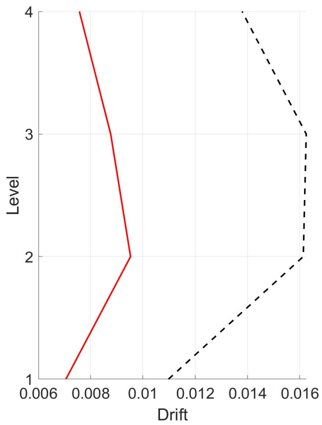

(f) Kobe

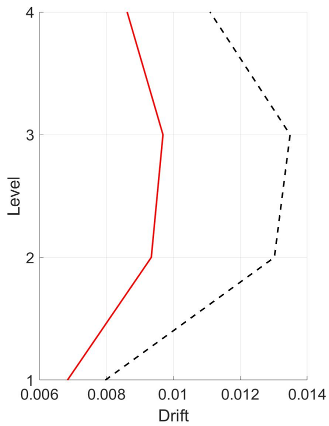

(g) Loma Prieta

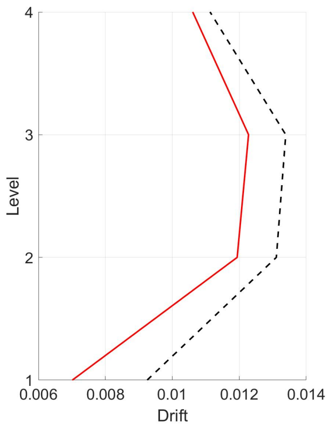

(h) Northridge

Figure B.81. Drifts Tangent Stiffness

B.3.2 50% **Tangent Stiffness**

Assuming a 50% of tangent stiffness of the structure to account for cracking leads to the following results.

Table B.10. Performance Indices 50% Tangent Stiffness

Earthquake	Performance Index						
	J_1	J_2	J_3	J_4	J_5	J_6	J_7(m)
Chalfant	0.582	0.994	1.140	0.534	0.841	0.935	0.270
Chi-Chi	0.848	0.991	0.872	0.772	0.906	0.955	0.244
Erzincan	0.729	0.978	0.945	0.719	0.885	0.943	0.283
Friulli	0.777	0.977	1.098	0.778	0.967	0.991	0.274
Imperial Valley	0.889	1.047	1.001	0.875	0.955	0.984	0.256
Kobe	0.679	0.954	1.206	0.819	1.030	1.077	0.302
Loma Prieta	0.684	1.135	0.991	0.754	0.905	0.943	0.261
Northridge	0.983	0.998	0.881	0.695	0.807	0.786	0.293
Average	0.771	1.009	1.017	0.743	0.912	0.952	0.273

Chalfant

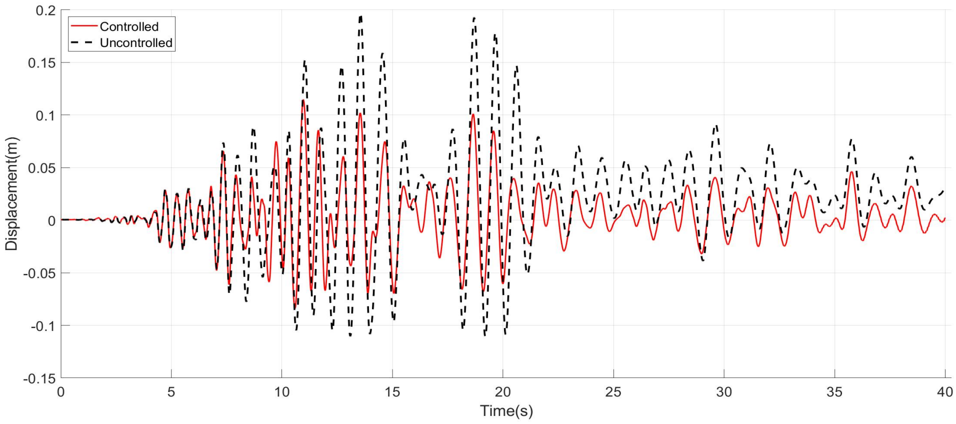

(a) Roof Displacements

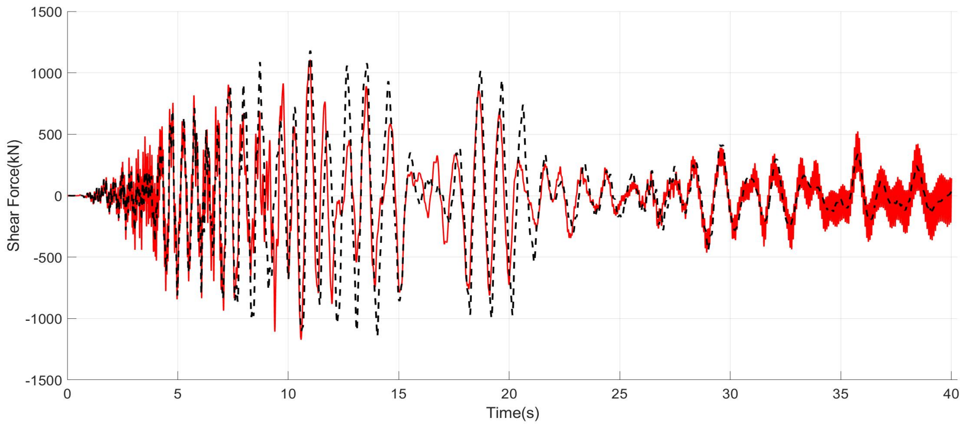

(b) Shear Forces at the base

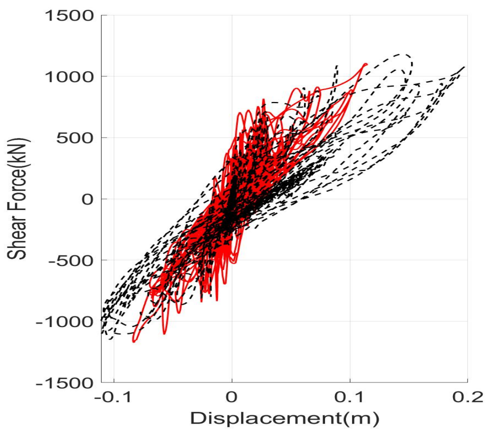

(c) Structural Hysteretic Curve

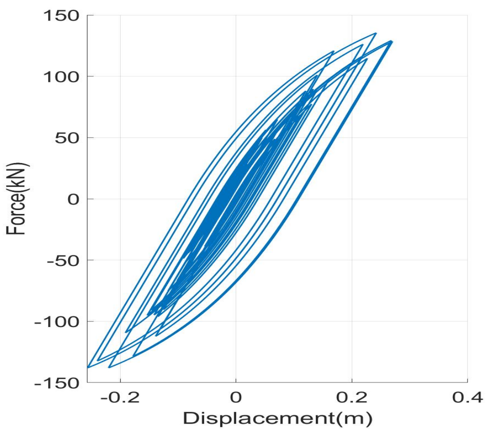

(d) TMD Hysteretic Curve

Figure B.82. Chalfant 50% Tangent Stiffness

Chi-Chi

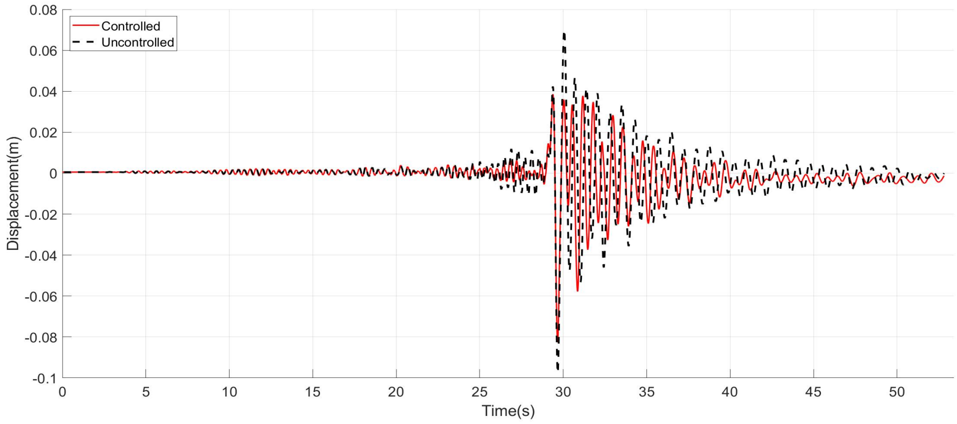

(a) Roof Displacements

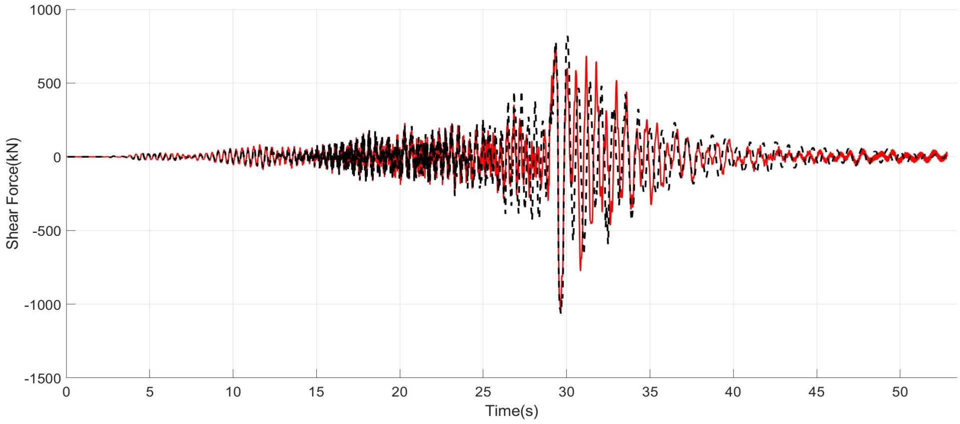

(b) Shear Forces at the base

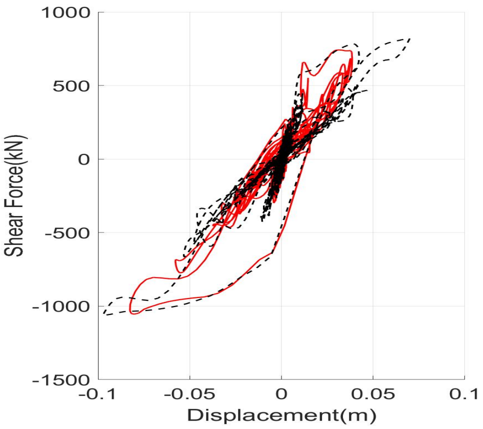

(c) Structural Hysteretic Curve

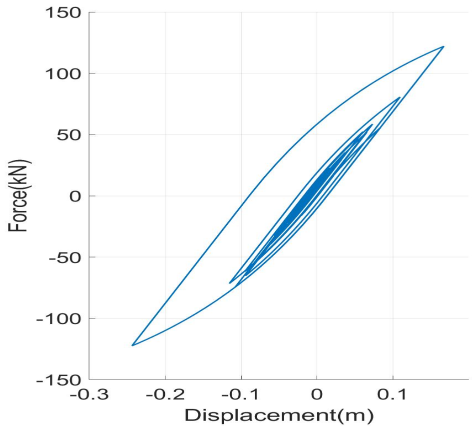

(d) TMD Hysteretic Curve

Figure B.83. Chi Chi 50% Tangent Stiffness

Erzincan

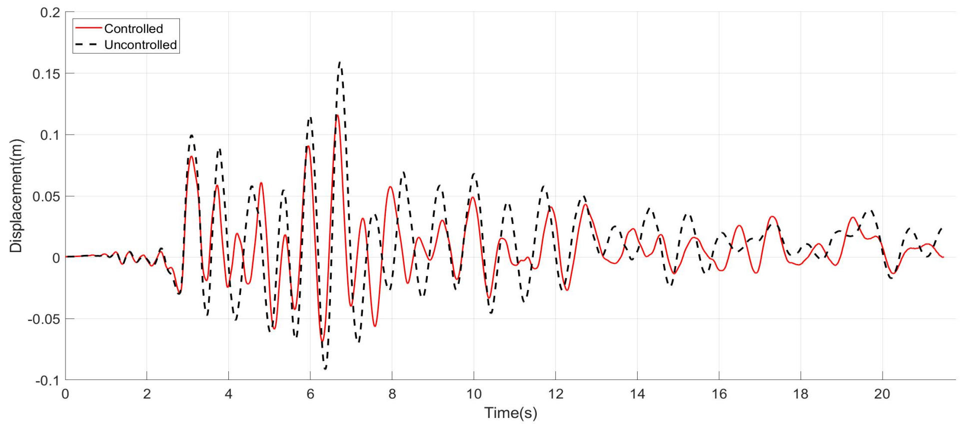

(a) Roof Displacements

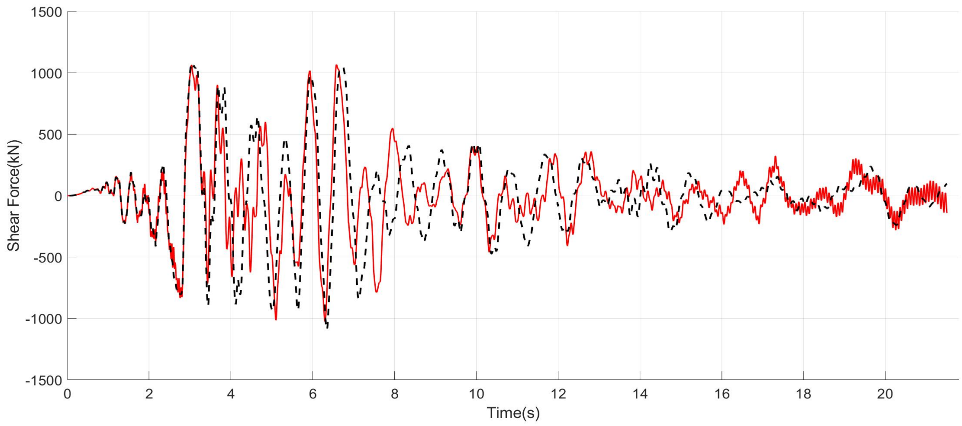

(b) Shear Forces at the base

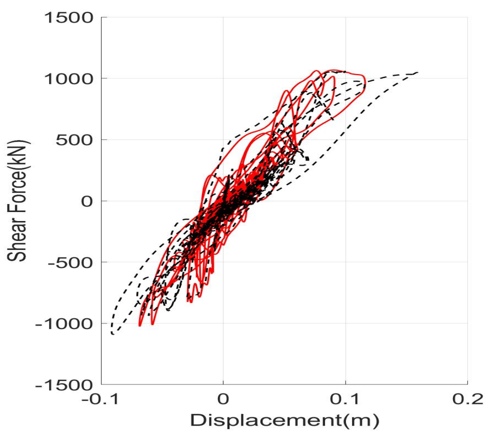

(c) Structural Hysteretic Curve

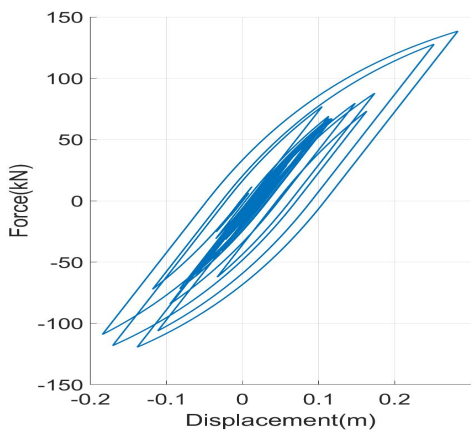

(d) TMD Hysteretic Curve

Figure B.84. Erzincan 50% Tangent Stiffness

Friulli

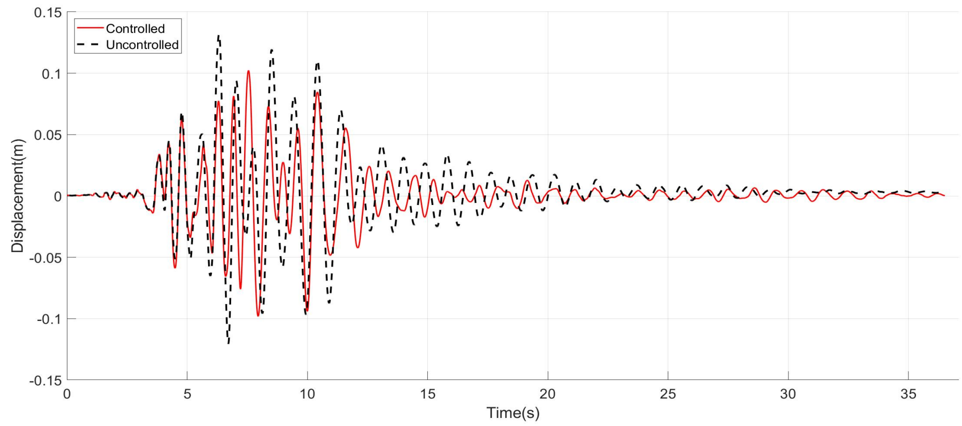

(a) Roof Displacements

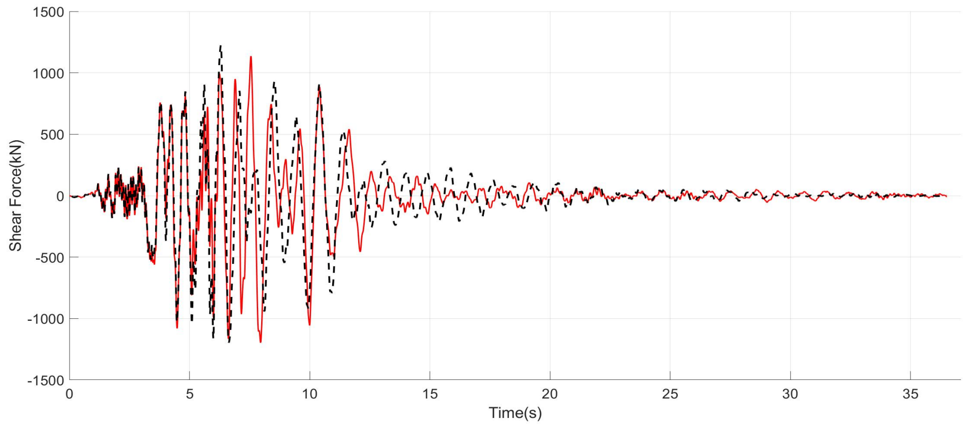

(b) Shear Forces at the base

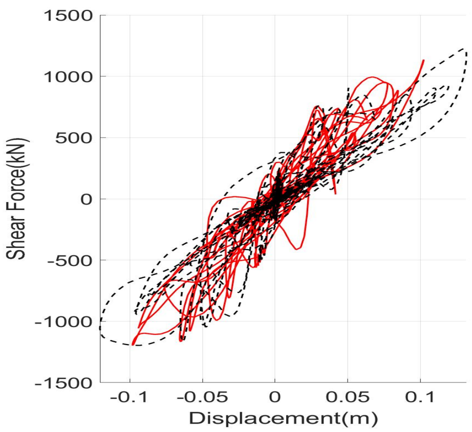

(c) Structural Hysteretic Curve

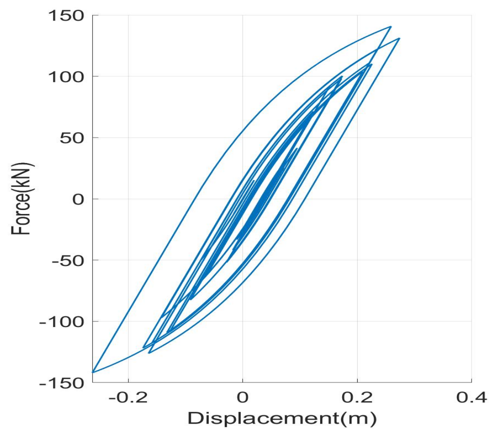

(d) TMD Hysteretic Curve

Figure B.85. Friulli 50% Tangent Stiffness

Imperial Valley

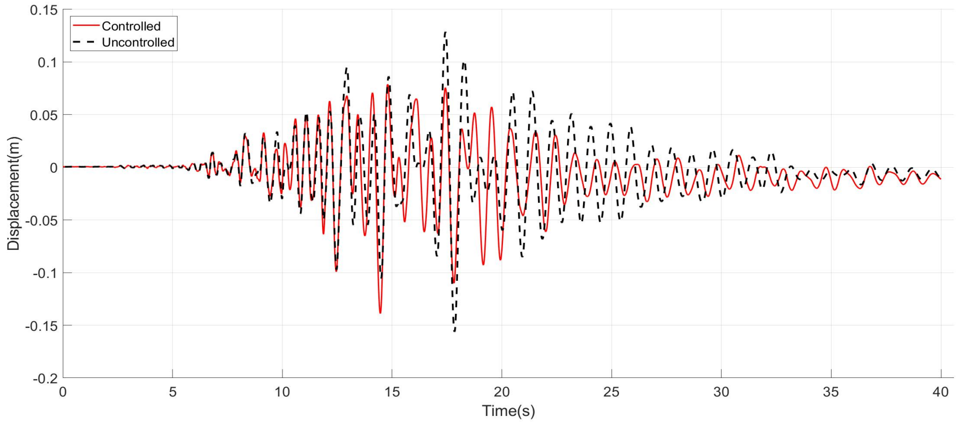

(a) Roof Displacements

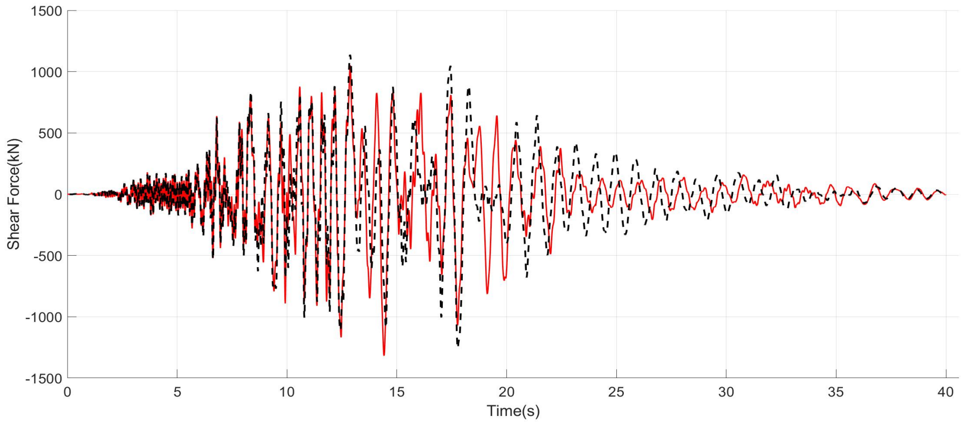

(b) Shear Forces at the base

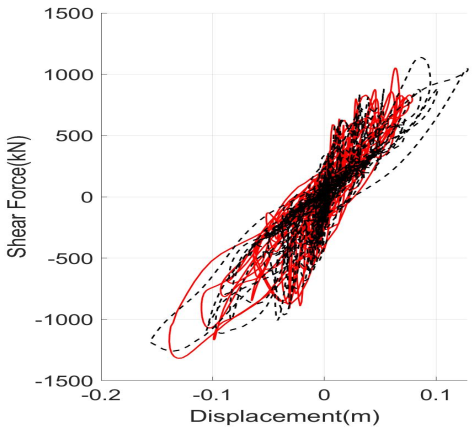

(c) Structural Hysteretic Curve

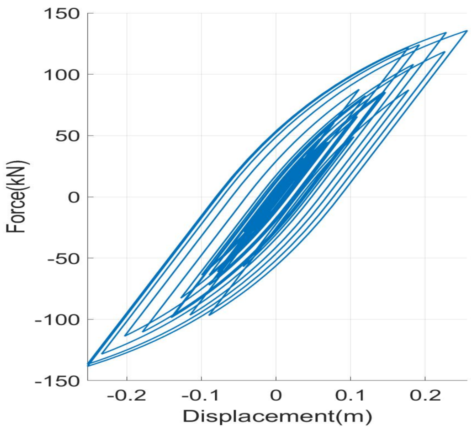

(d) TMD Hysteretic Curve

Figure B.86. Imperial Valley 50% Tangent Stiffness

Kobe

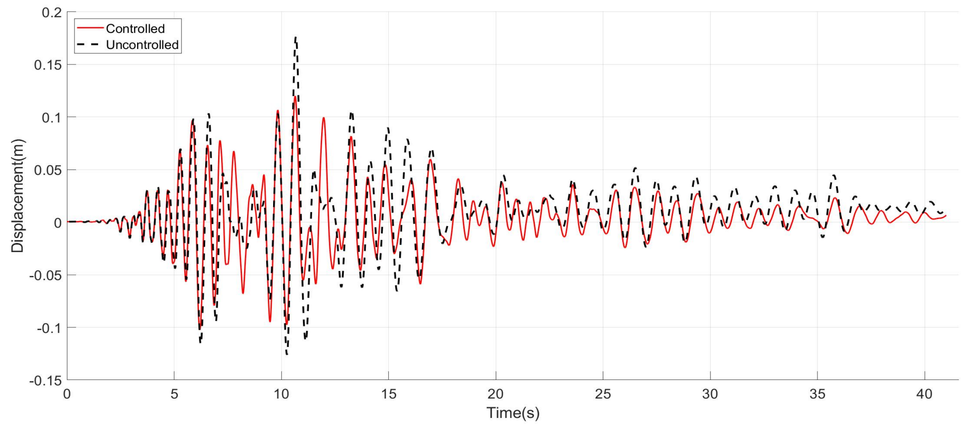

(a) Roof Displacements

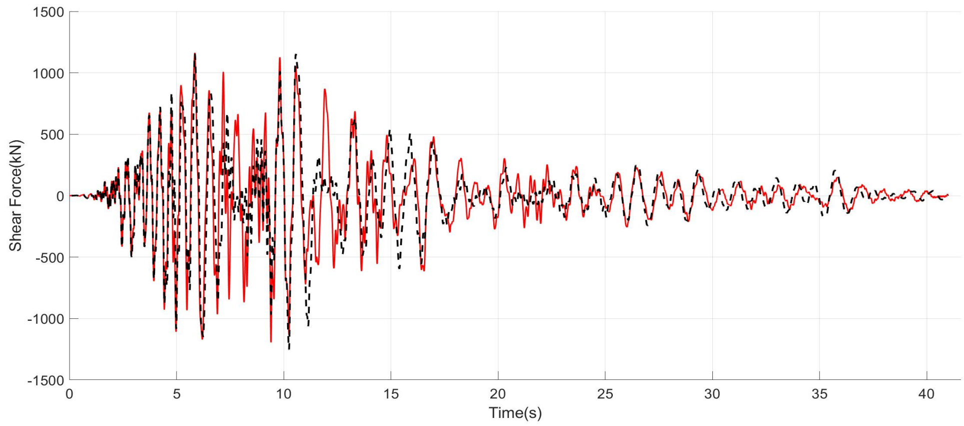

(b) Shear Forces at the base

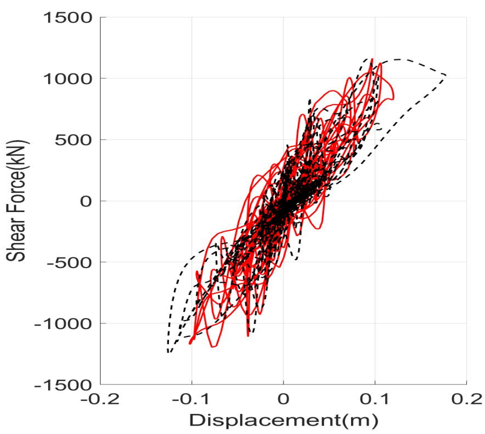

(c) Structural Hysteretic Curve

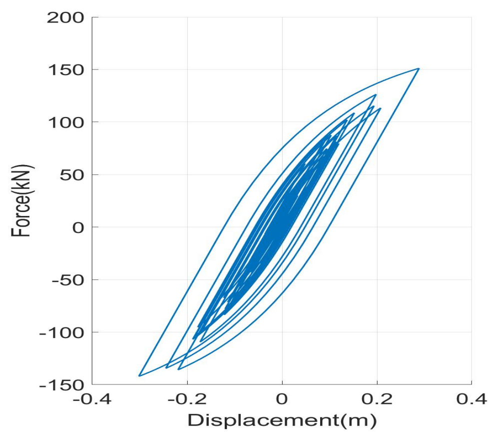

(d) TMD Hysteretic Curve

Figure B.87. Kobe 50% Tangent Stiffness

Loma Prieta

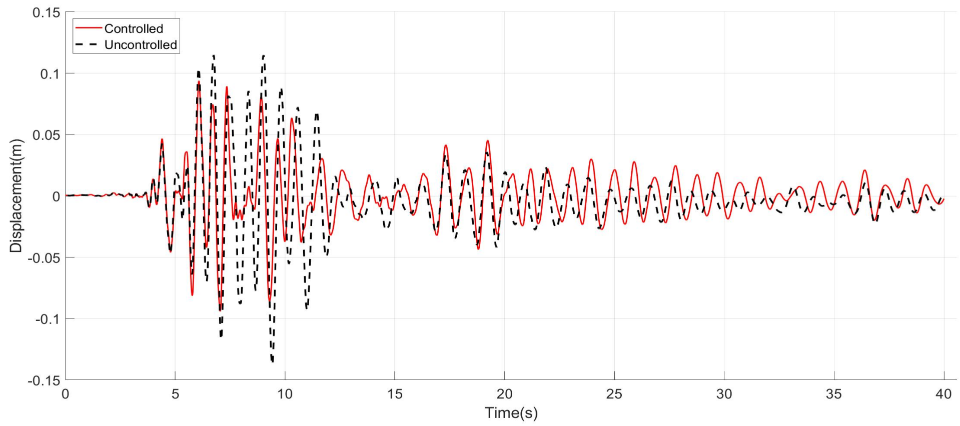

(a) Roof Displacements

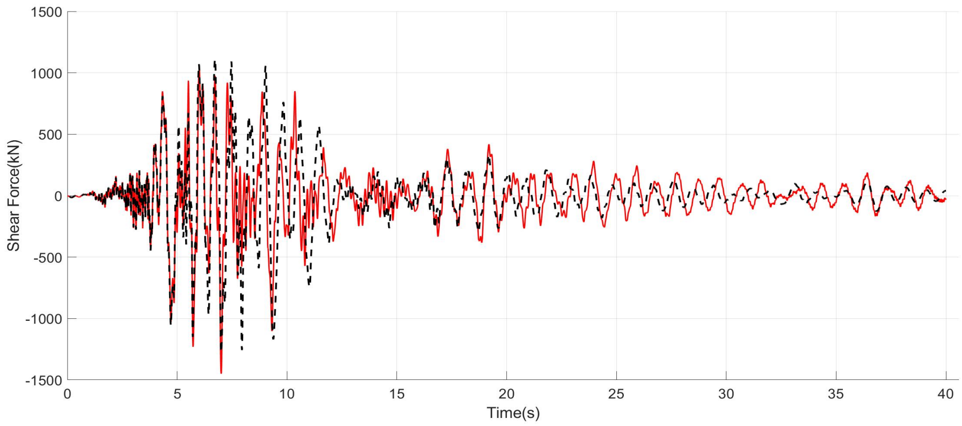

(b) Shear Forces at the base

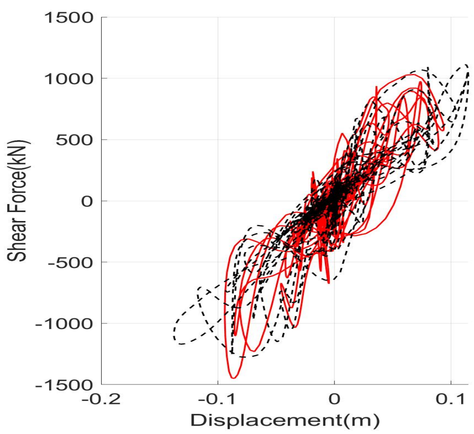

(c) Structural Hysteretic Curve

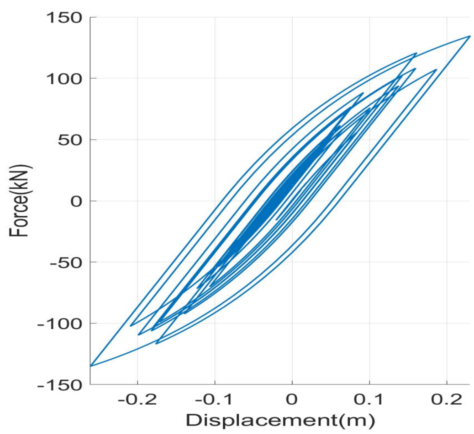

(d) TMD Hysteretic Curve

Figure B.88. Loma Prieta 50% Tangent Stiffness

Northridge

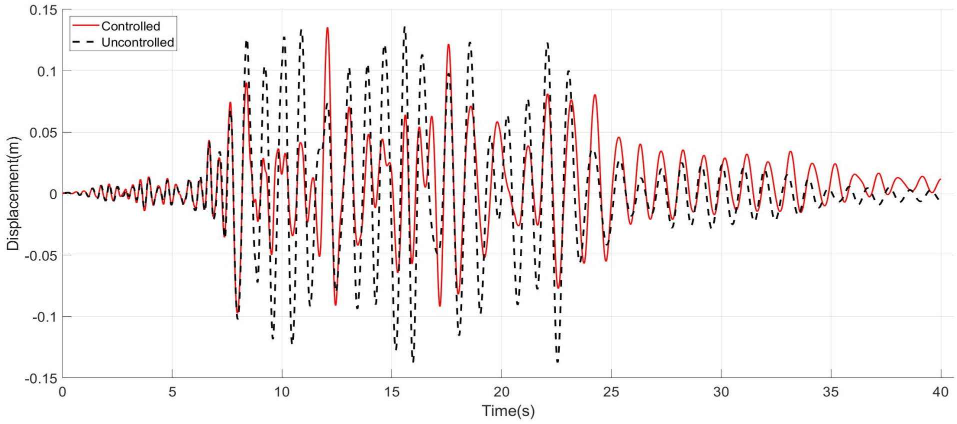

(a) Roof Displacements

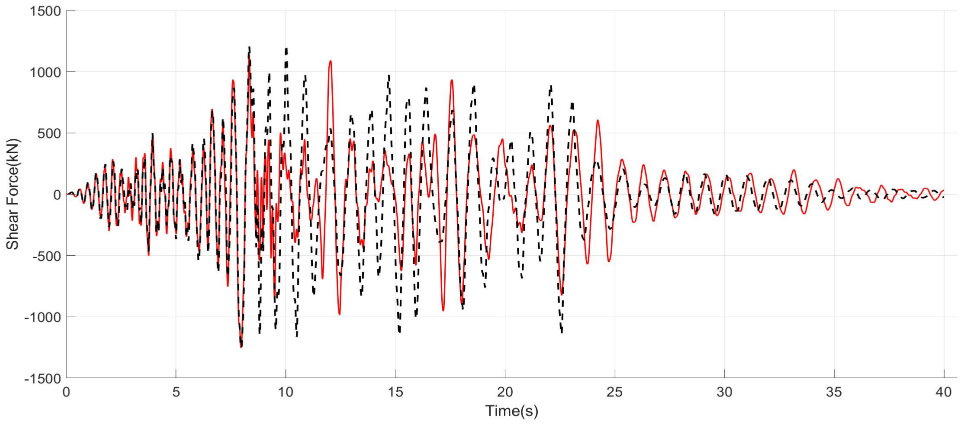

(b) Shear Forces at the base

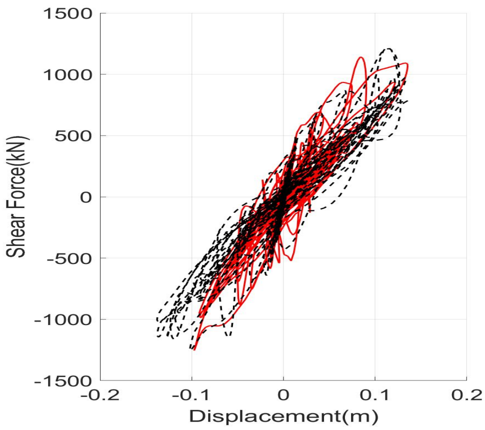

(c) Structural Hysteretic Curve

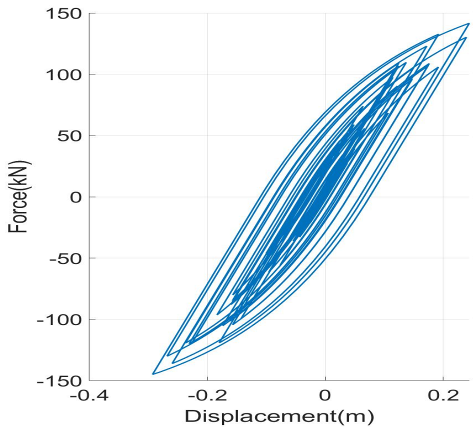

(d) TMD Hysteretic Curve

Figure B.89. Northridge 50% Tangent Stiffness

Drifts

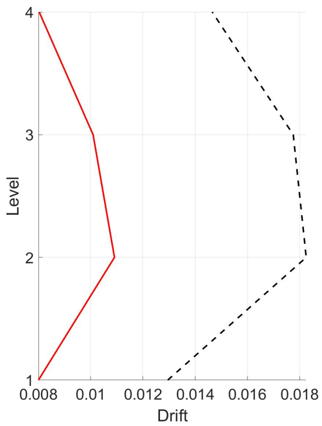

(a) Chalfant

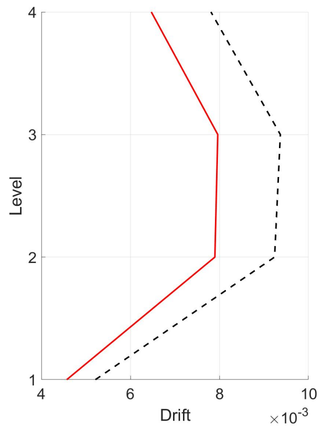

(b) Chi Chi

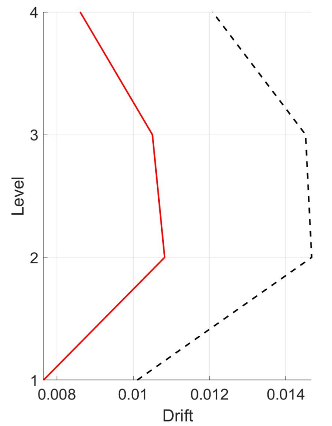

(c) Erzincan

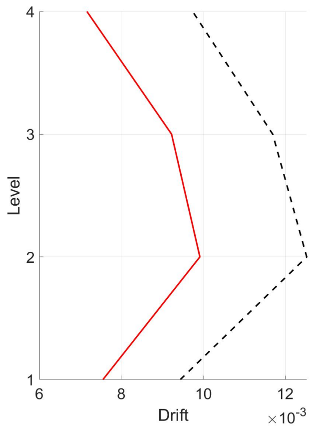

(d) Friulli

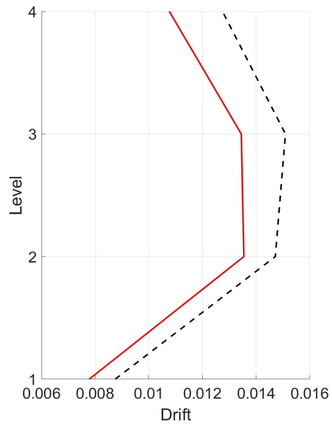

(e) Imperial Valley

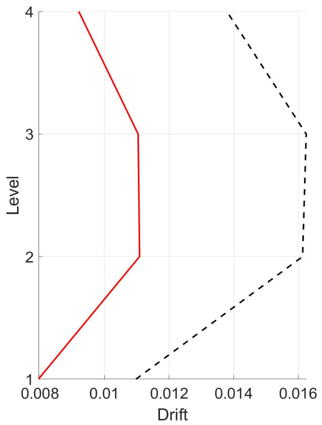

(f) Kobe

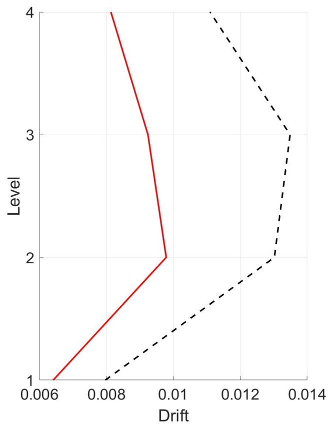

(g) Loma Prieta

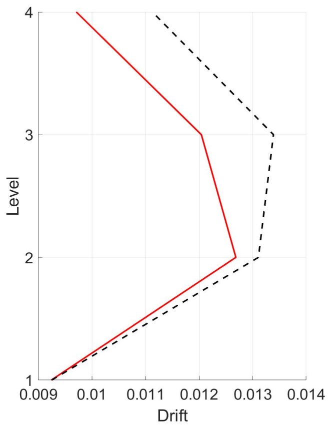

(h) Northridge

Figure B.90. Drifts 50% Tangent Stiffness

B.3.3 90% Stiffness

By reducing the considered stiffness of the structure by 10% the following results are obtained.

Table B.11. Performance Indices 90% Stiffness

Earthquake	Performance Index						
	J_1	J_2	J_3	J_4	J_5	J_6	J_7(m)
Chalfant	0.611	1.017	1.024	0.587	0.841	0.868	0.267
Chi-Chi	0.889	0.990	0.847	0.710	0.795	0.828	0.234
Erzincan	0.675	0.969	0.942	0.669	0.839	0.867	0.258
Friulli	0.658	0.968	1.050	0.700	0.925	0.947	0.232
Imperial Valley	0.776	1.060	1.044	0.817	0.949	0.970	0.234
Kobe	0.666	0.958	1.202	0.763	0.992	1.038	0.275
Loma Prieta	0.736	1.055	0.987	0.699	0.858	0.902	0.225
Northridge	0.860	0.990	0.889	0.648	0.813	0.793	0.257
Average	0.734	1.001	0.998	0.699	0.876	0.902	0.248

Chalfant

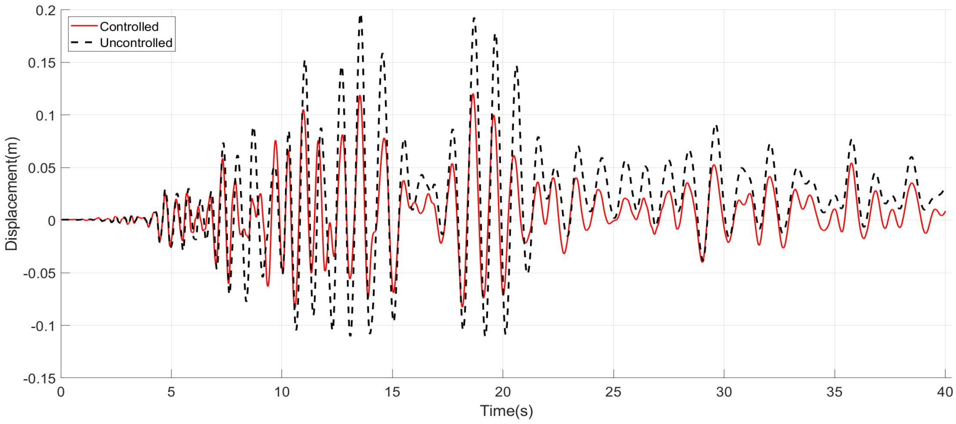

(a) Roof Displacements

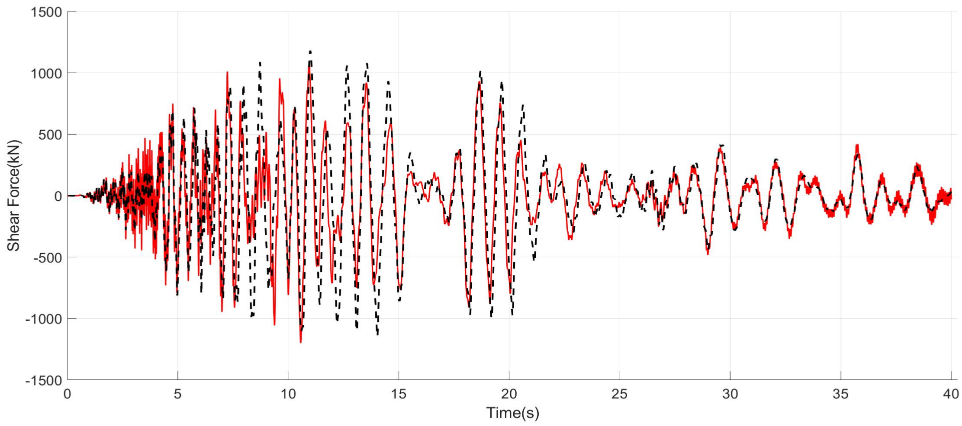

(b) Shear Forces at the base

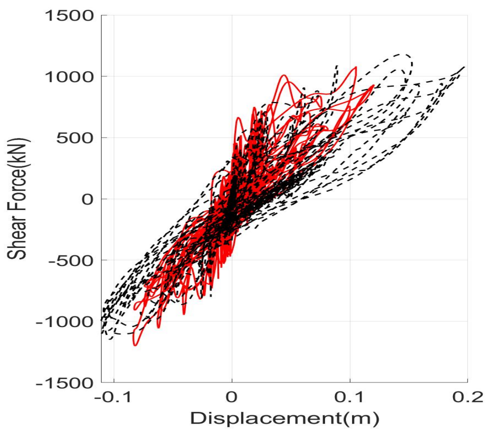

(c) Structural Hysteretic Curve

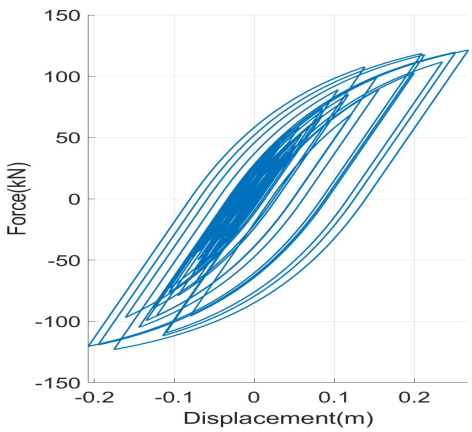

(d) TMD Hysteretic Curve

Figure B.91. Chalfant 90% Stiffness

Chi-Chi

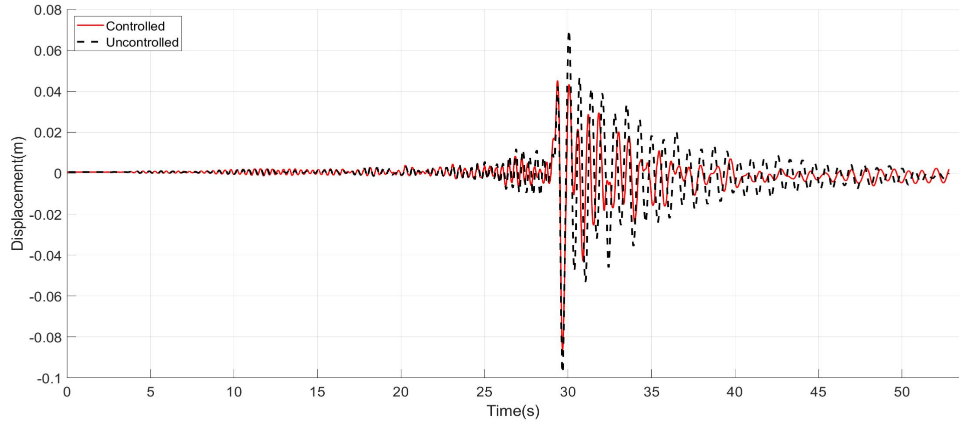

(a) Roof Displacements

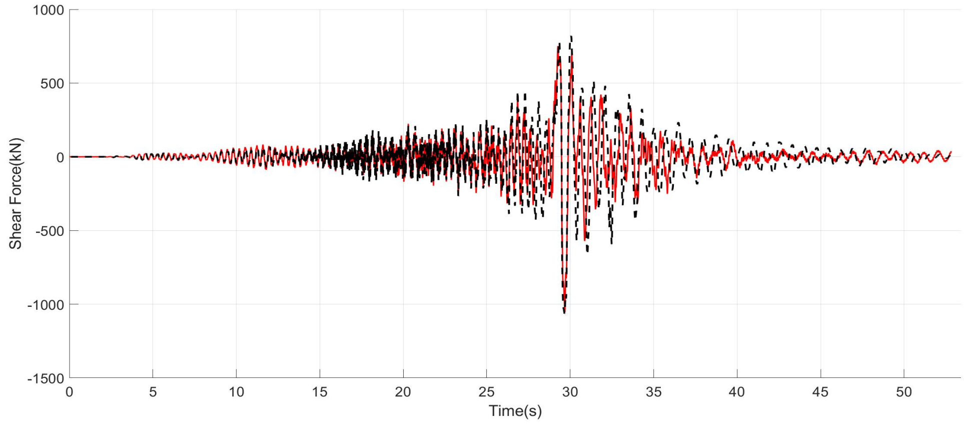

(b) Shear Forces at the base

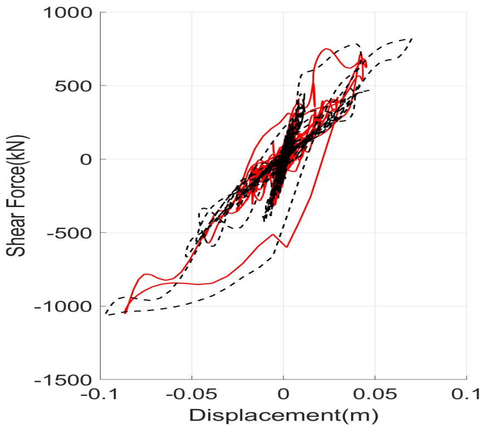

(c) Structural Hysteretic Curve

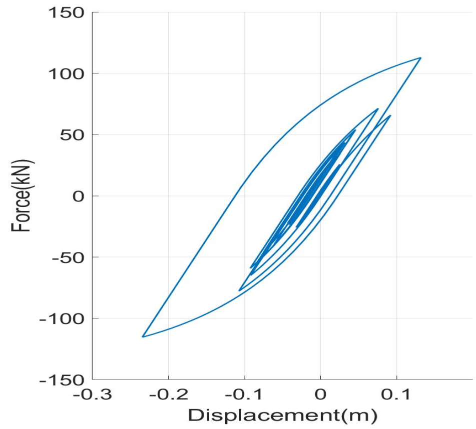

(d) TMD Hysteretic Curve

Figure B.92. Chi Chi 90% Stiffness

Erzincan

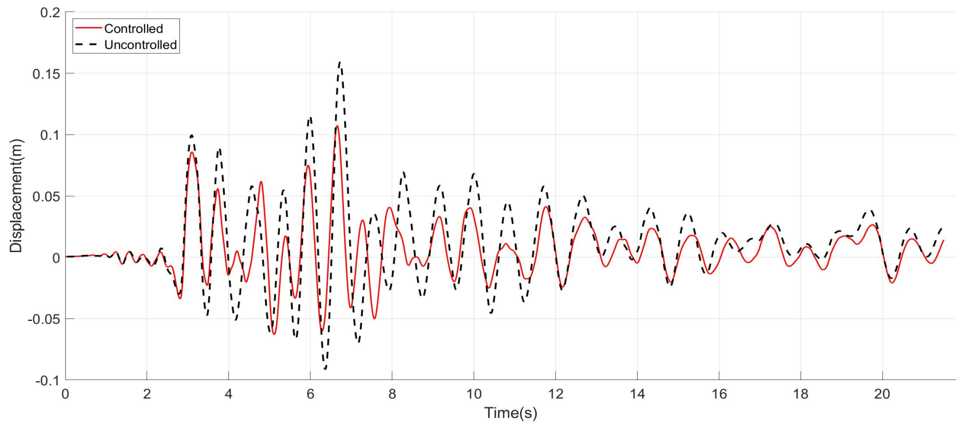

(a) Roof Displacements

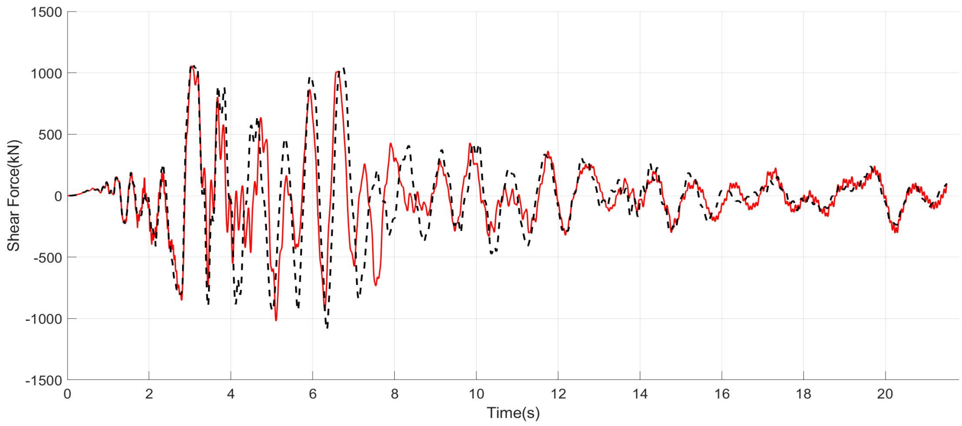

(b) Shear Forces at the base

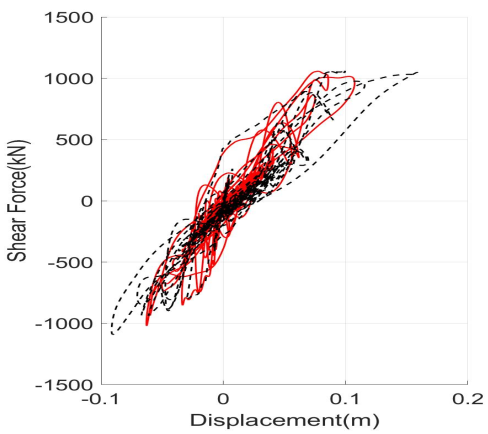

(c) Structural Hysteretic Curve

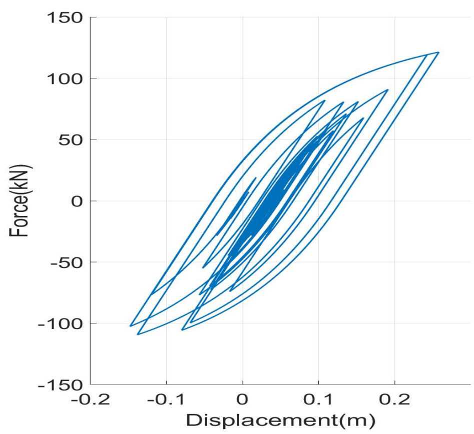

(d) TMD Hysteretic Curve

Figure B.93. Erzincan 90% Stiffness

Friulli

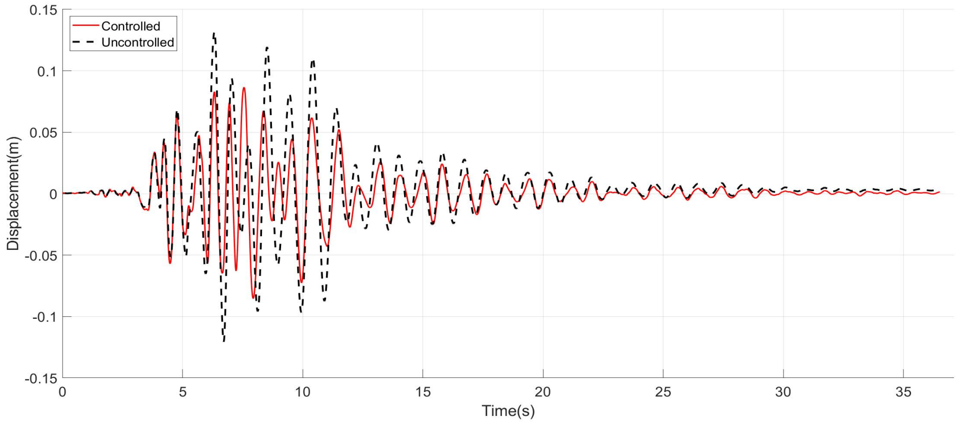

(a) Roof Displacements

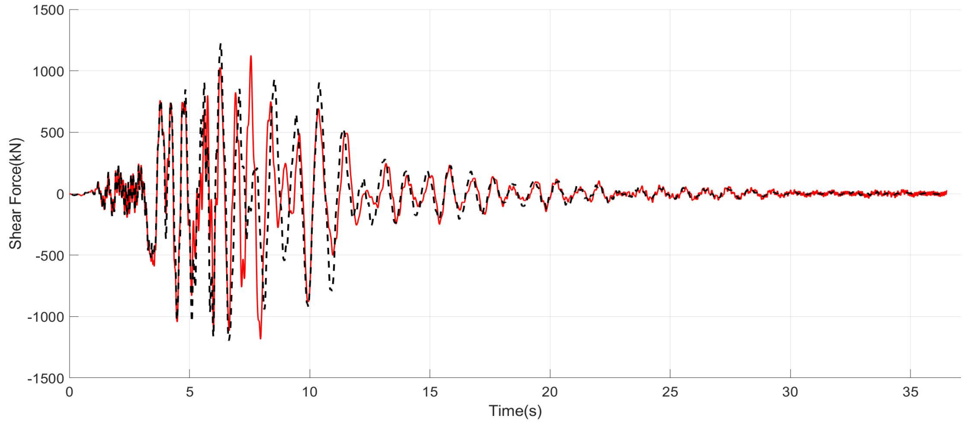

(b) Shear Forces at the base

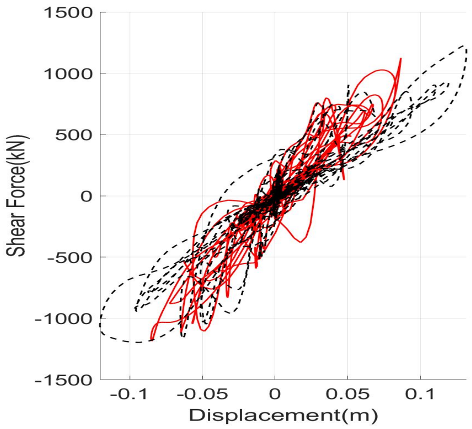

(c) Structural Hysteretic Curve

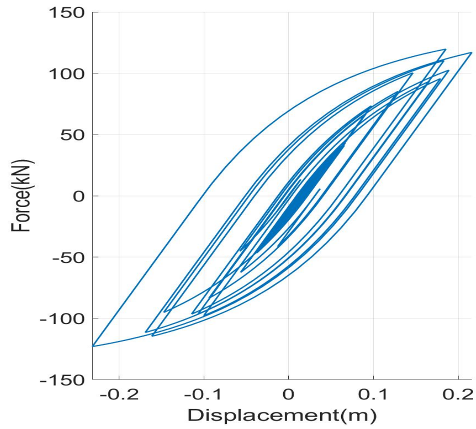

(d) TMD Hysteretic Curve

Figure B.94. Friulli 90% Stiffness

Imperial Valley

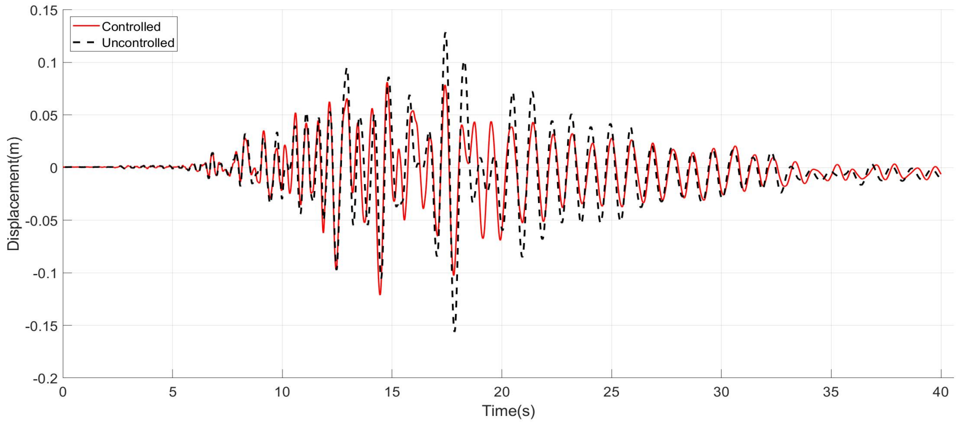

(a) Roof Displacements

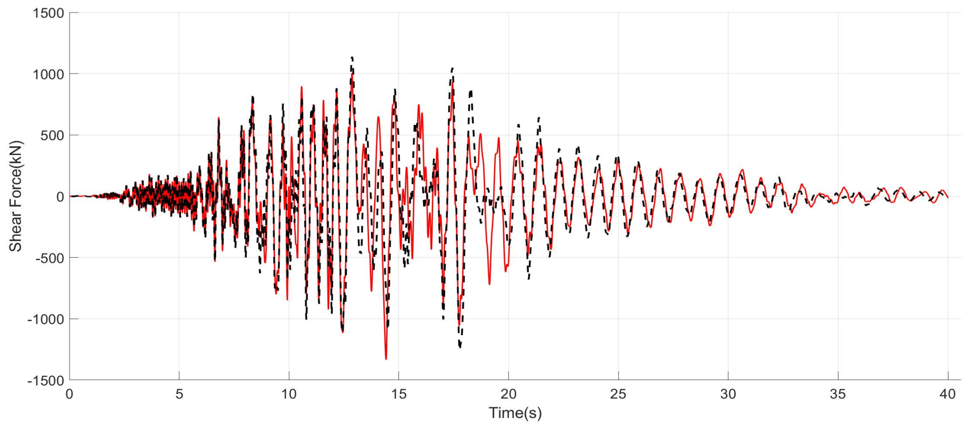

(b) Shear Forces at the base

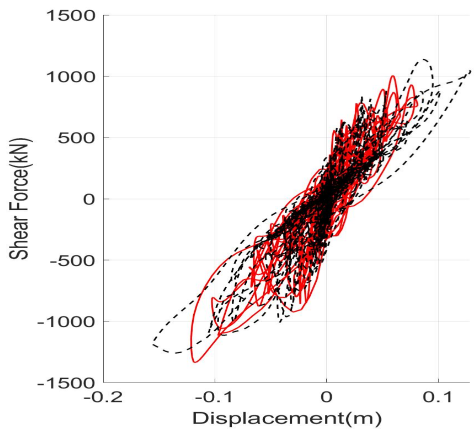

(c) Structural Hysteretic Curve

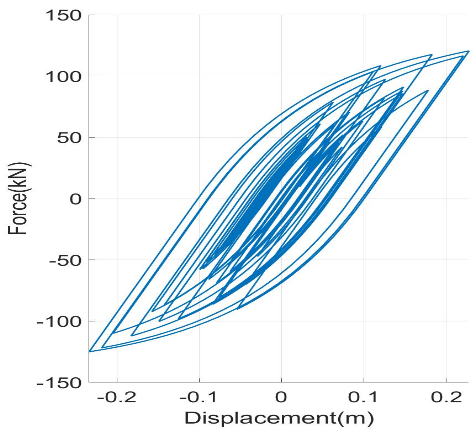

(d) TMD Hysteretic Curve

Figure B.95. Imperial Valley 90% Stiffness

Kobe

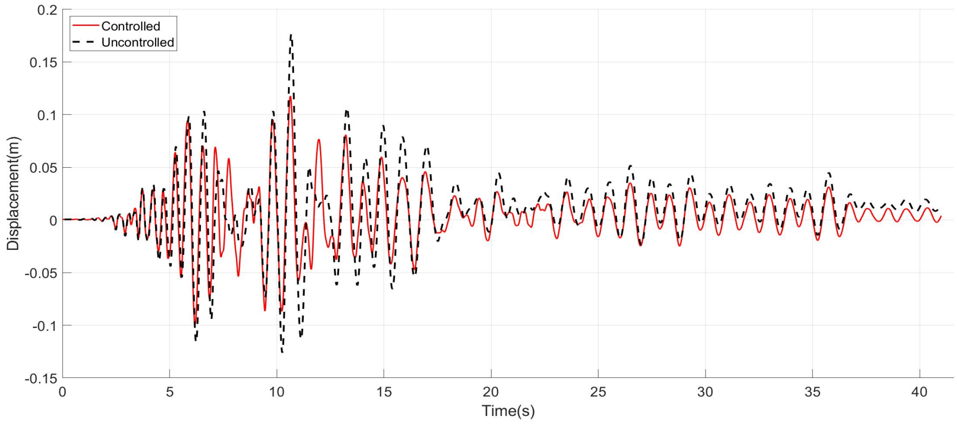

(a) Roof Displacements

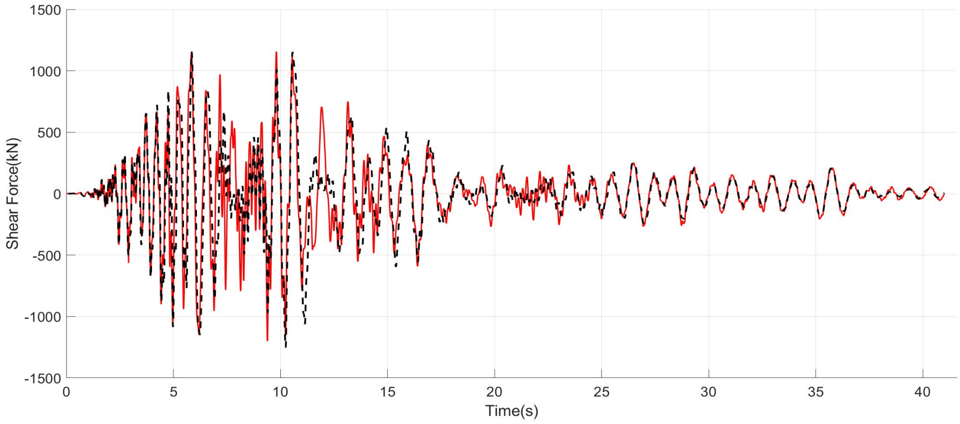

(b) Shear Forces at the base

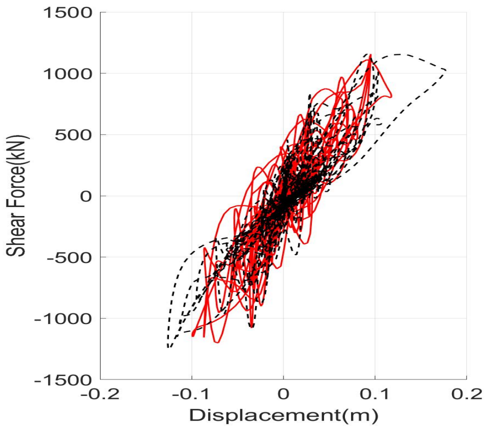

(c) Structural Hysteretic Curve

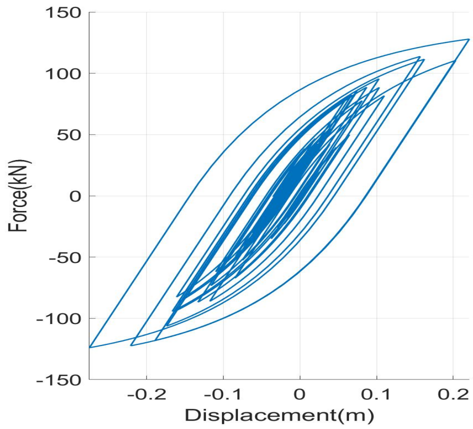

(d) TMD Hysteretic Curve

Figure B.96. Kobe 90% Stiffness

Loma Prieta

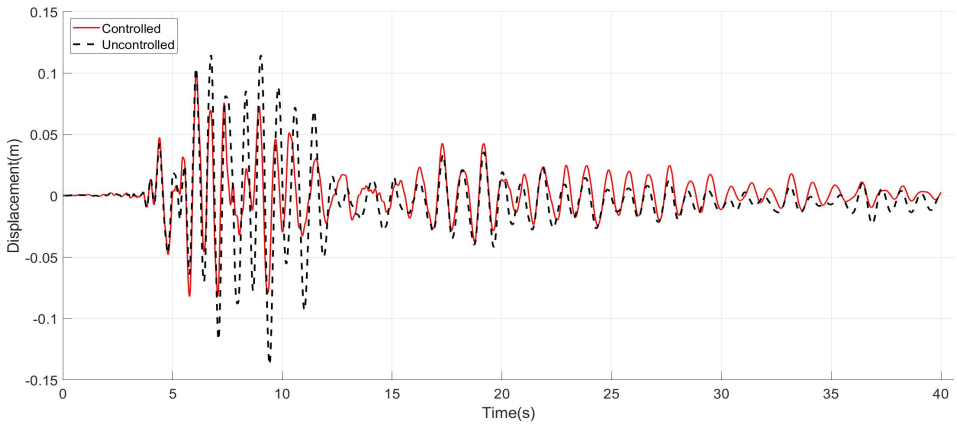

(a) Roof Displacements

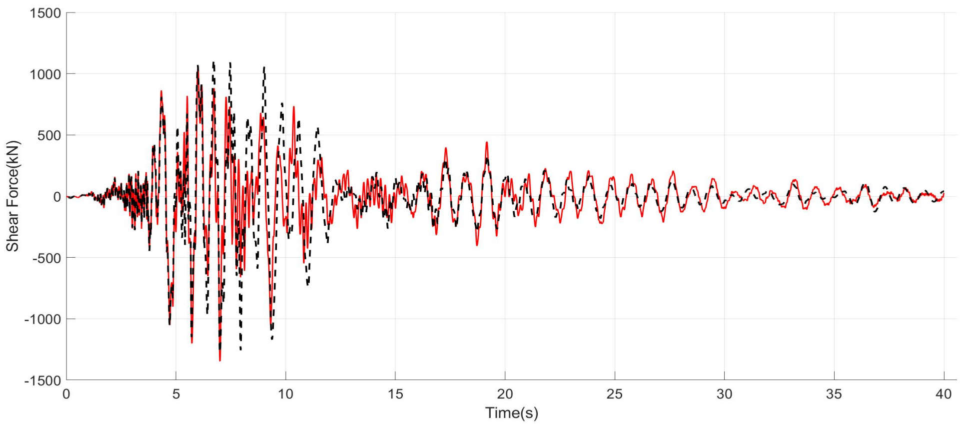

(b) Shear Forces at the base

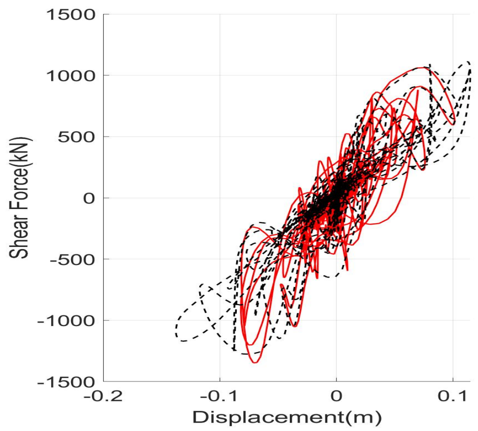

(c) Structural Hysteretic Curve

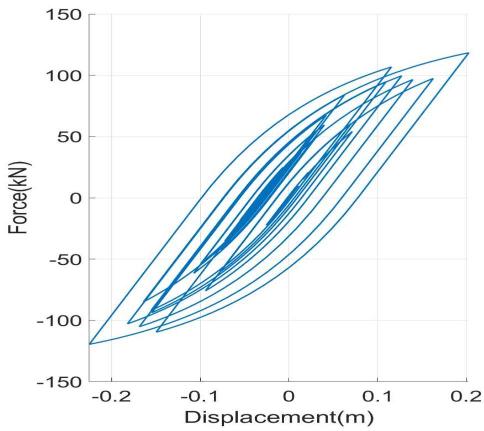

(d) TMD Hysteretic Curve

Figure B.97. Loma Prieta 90% Stiffness

Northridge

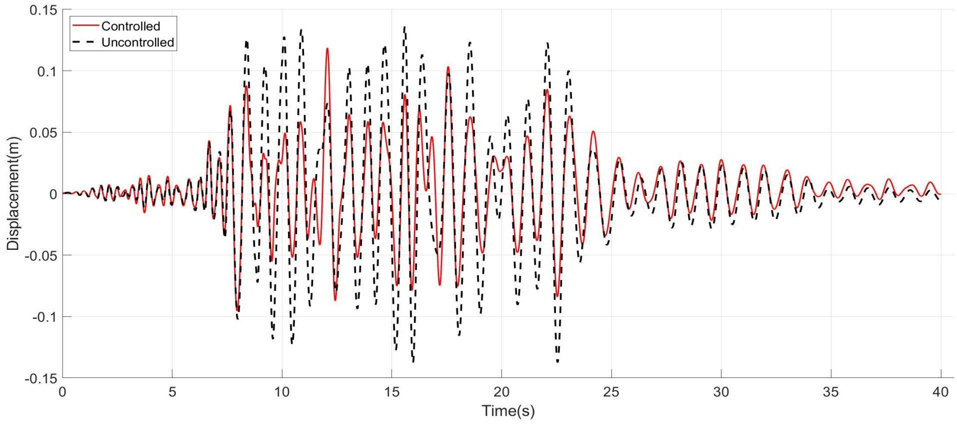

(a) Roof Displacements

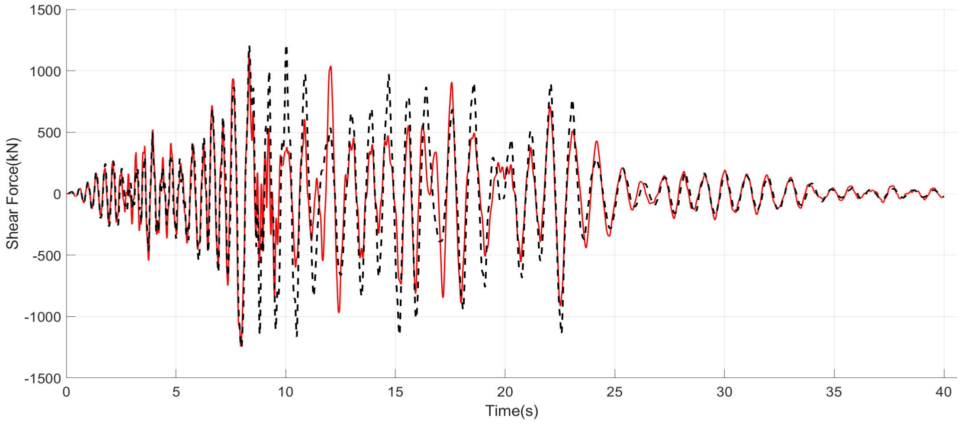

(b) Shear Forces at the base

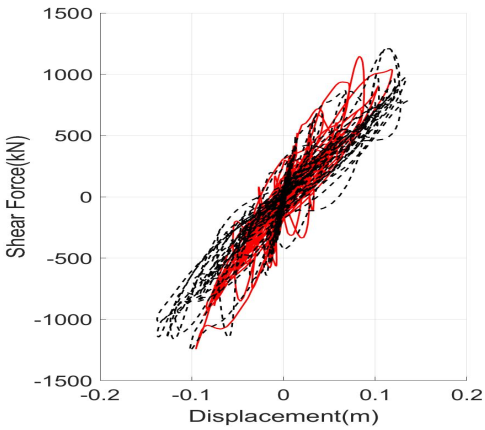

(c) Structural Hysteretic Curve

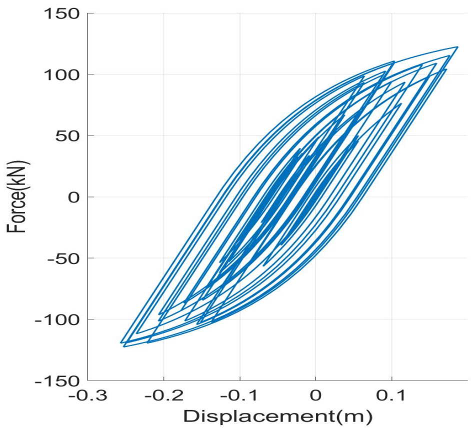

(d) TMD Hysteretic Curve

Figure B.98. Northridge 90% Stiffness

Drifts

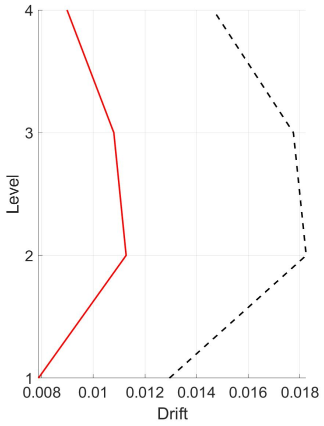

(a) Chalfant

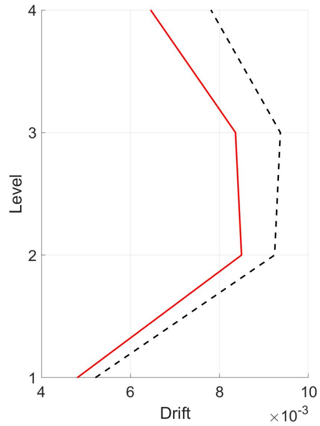

(b) Chi Chi

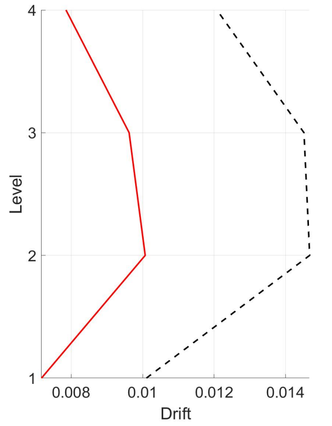

(c) Erzincan

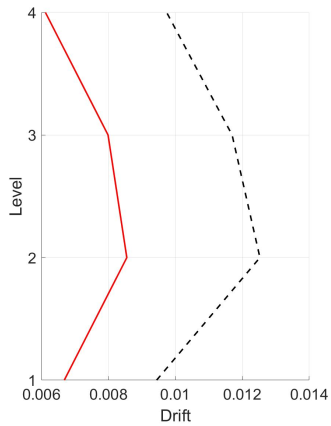

(d) Friulli

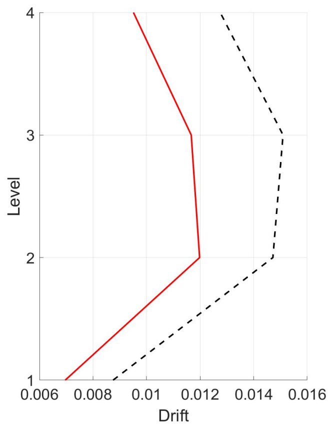

(e) Imperial Valley

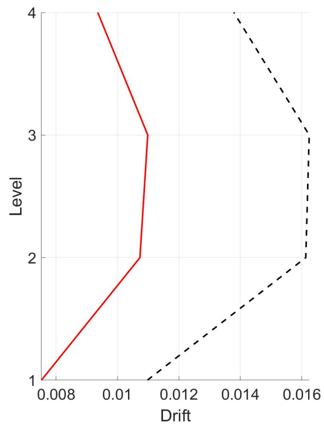

(f) Kobe

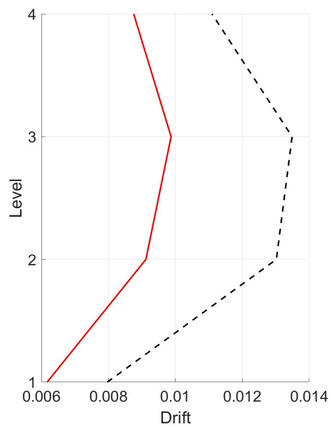

(g) Loma Prieta

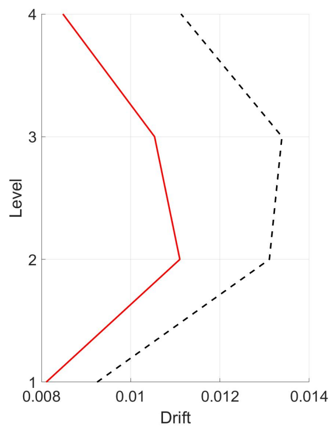

(h) Northridge

Figure B.99. Drifts 90% Stiffness

B.3.4 110% **Stiffness**

By considering a stiffness 10% greater than the initial one, the following results are obtained.

Table B.12. Performance Indices 110% Stiffness

Earthquake	Performance Index						
	J_1	J_2	J_3	J_4	J_5	J_6	J_7(m)
Chalfant	0.449	1.031	0.968	0.526	0.926	0.992	0.2357
Chi-Chi	0.825	0.968	0.876	0.583	0.758	0.797	0.207
Erzincan	0.547	0.972	0.840	0.616	0.795	0.818	0.218
Friulli	0.717	0.986	1.059	0.725	0.891	0.889	0.205
Imperial Valley	0.621	0.898	0.984	0.753	0.920	0.913	0.223
Kobe	0.598	1.016	1.217	0.701	0.979	1.010	0.212
Loma Prieta	0.805	0.969	0.928	0.702	0.834	0.875	0.197
Northridge	0.802	0.965	0.877	0.677	0.874	0.833	0.278
Average	0.671	0.976	0.969	0.660	0.872	0.891	0.222

Chalfant

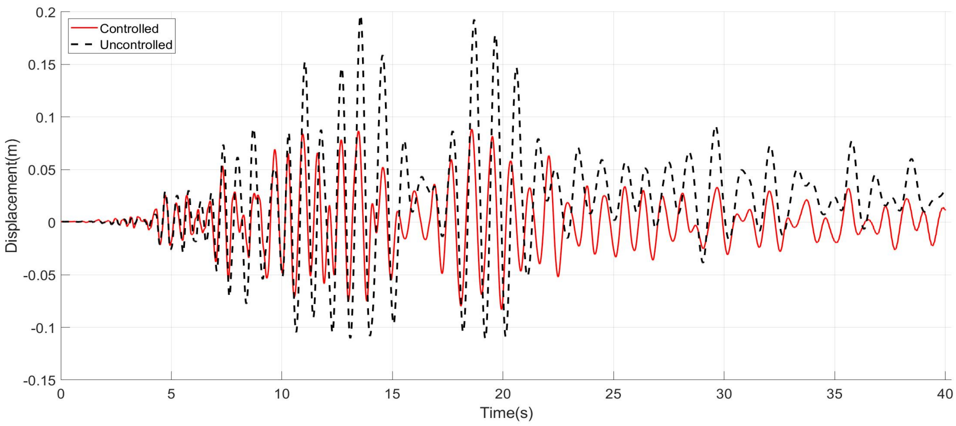

(a) Roof Displacements

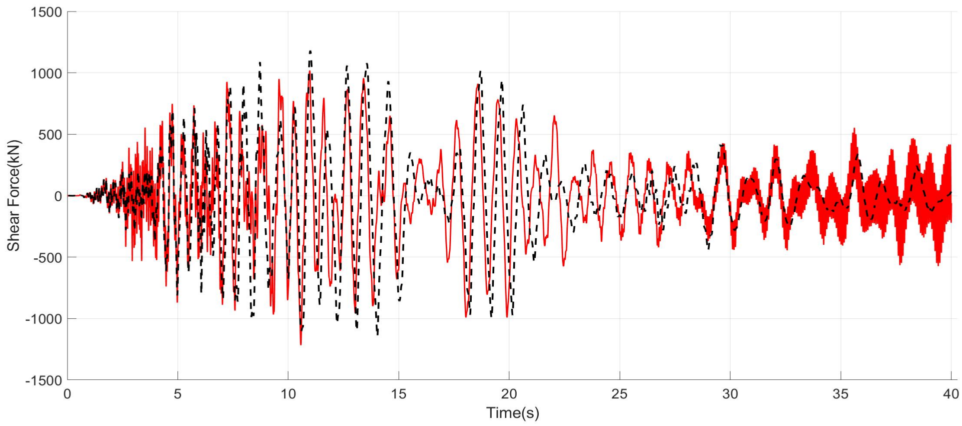

(b) Shear Forces at the base

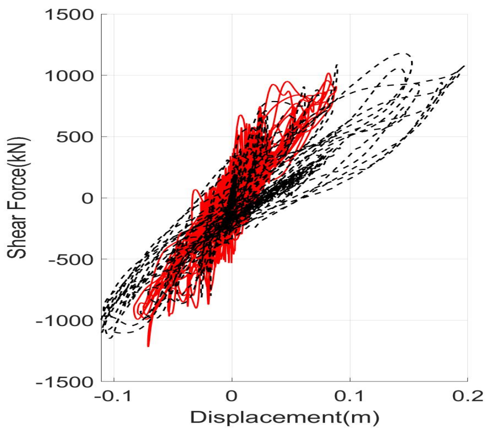

(c) Structural Hysteretic Curve

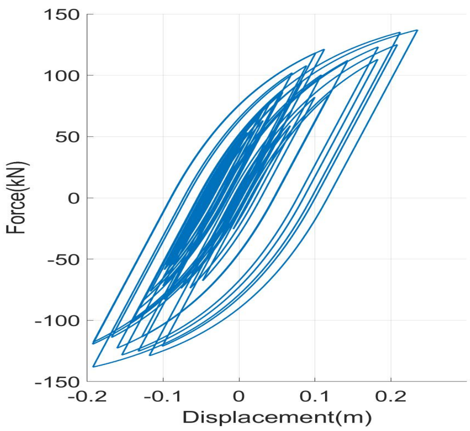

(d) TMD Hysteretic Curve

Figure B.100. Chalfant 110% Stiffness

Chi-Chi

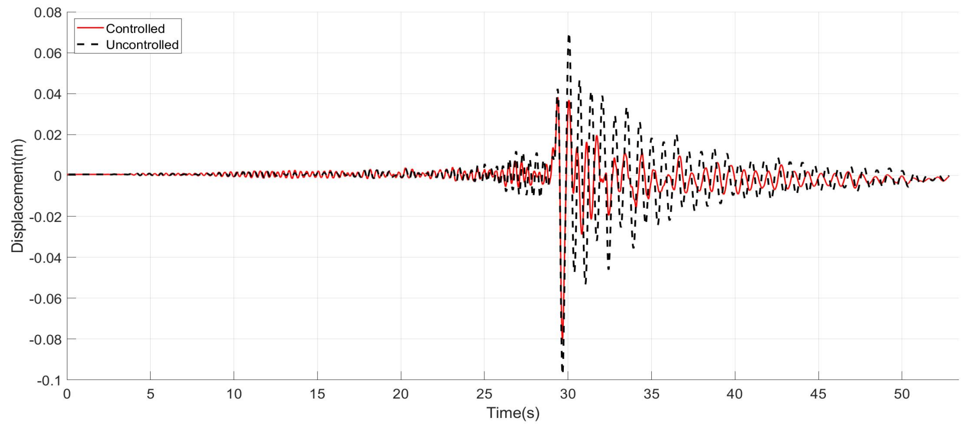

(a) Roof Displacements

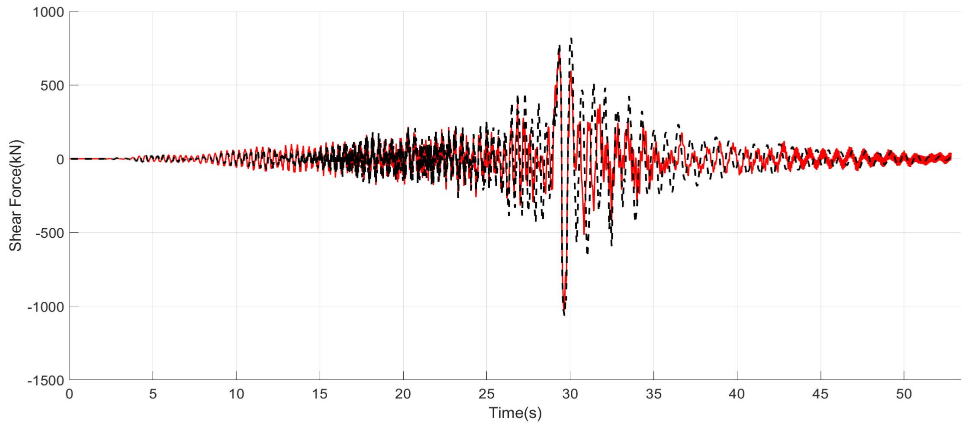

(b) Shear Forces at the base

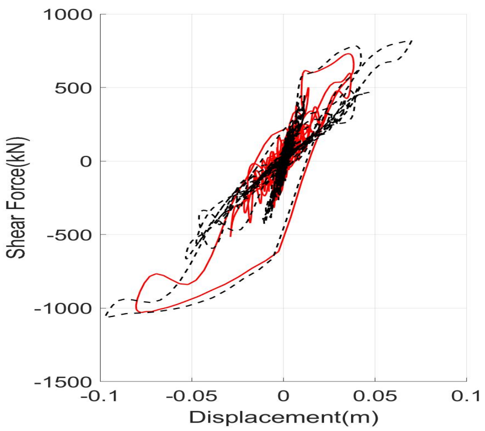

(c) Structural Hysteretic Curve

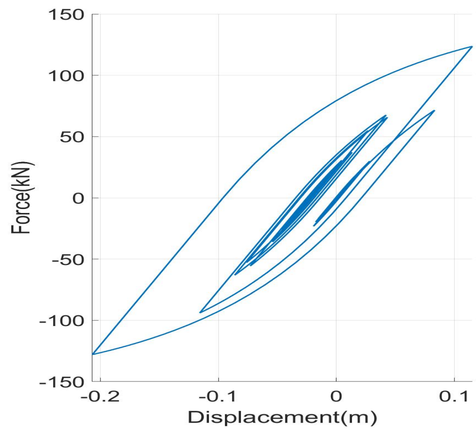

(d) TMD Hysteretic Curve

Figure B.101. Chi Chi 110% Stiffness

Erzincan

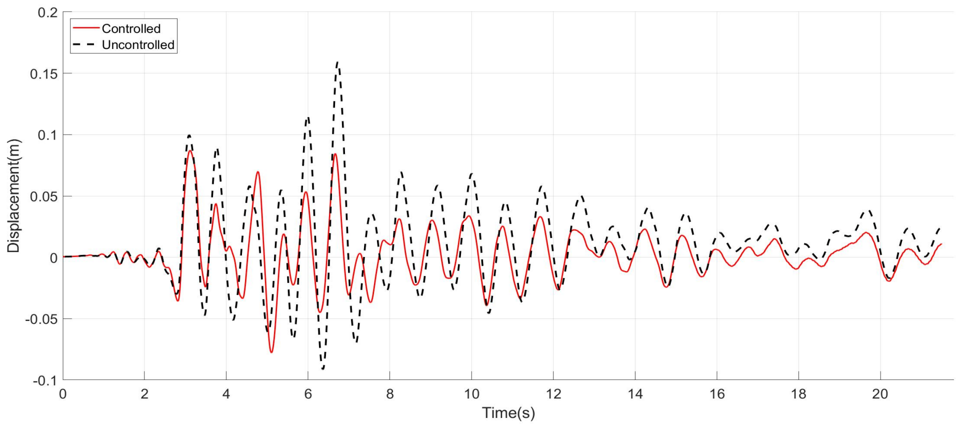

(a) Roof Displacements

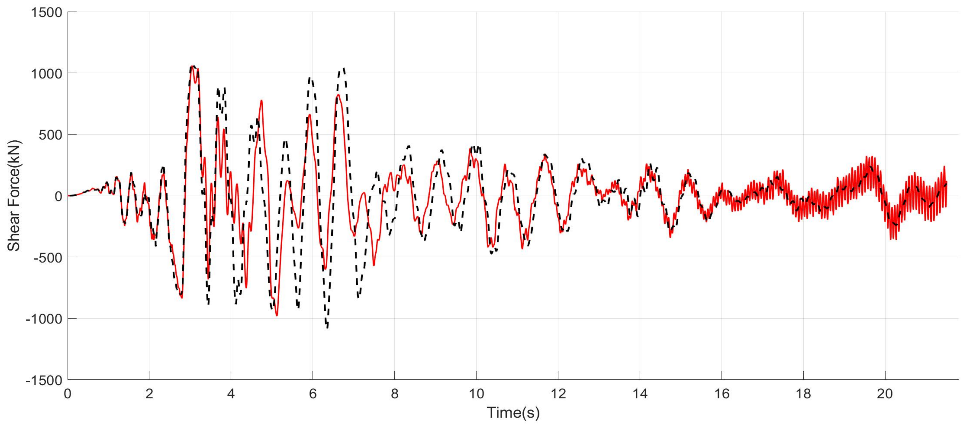

(b) Shear Forces at the base

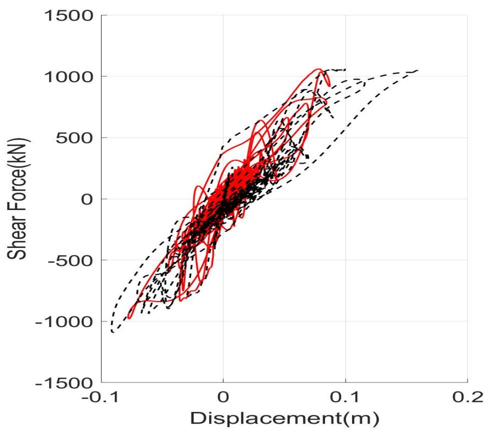

(c) Structural Hysteretic Curve

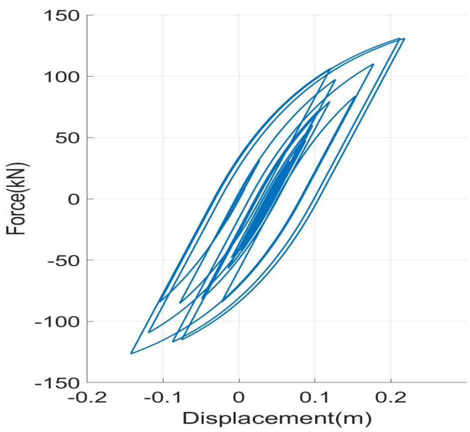

(d) TMD Hysteretic Curve

Figure B.102. Erzincan 110% Stiffness

Friulli

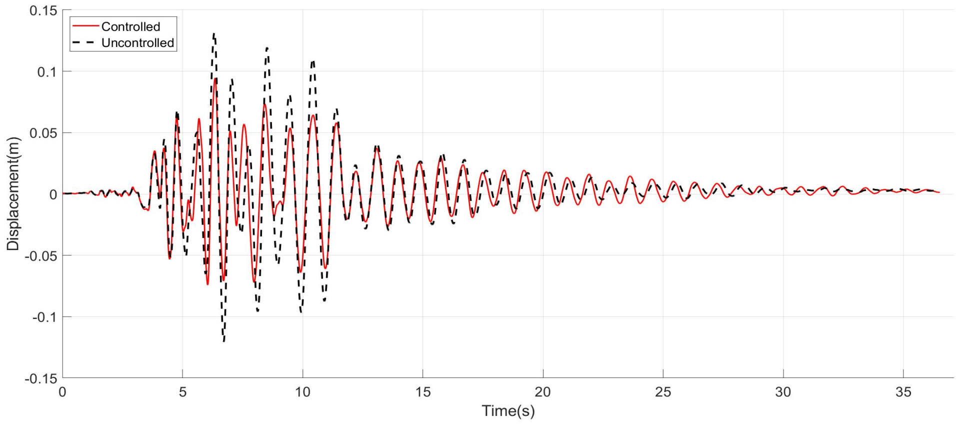

(a) Roof Displacements

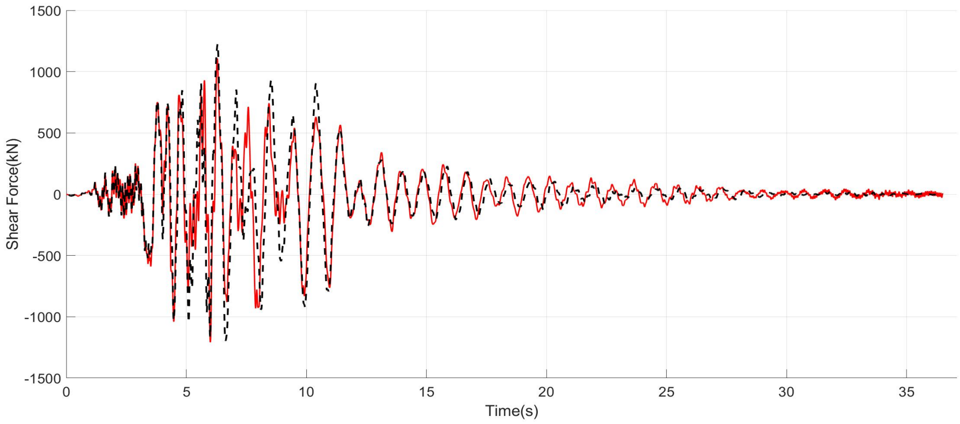

(b) Shear Forces at the base

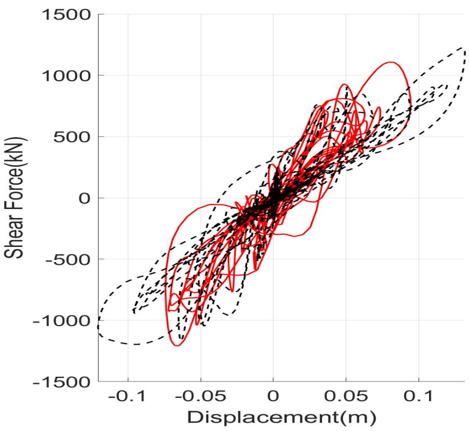

(c) Structural Hysteretic Curve

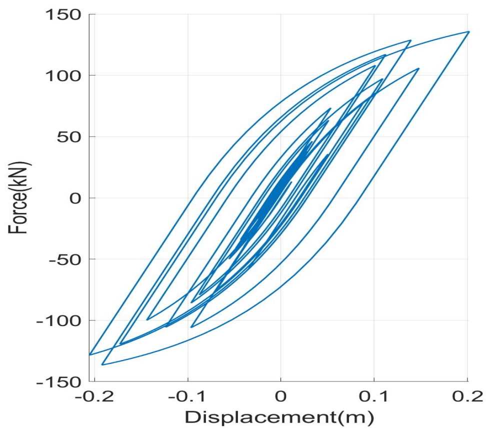

(d) TMD Hysteretic Curve

Figure B.103. Friulli 110% Stiffness

Imperial Valley

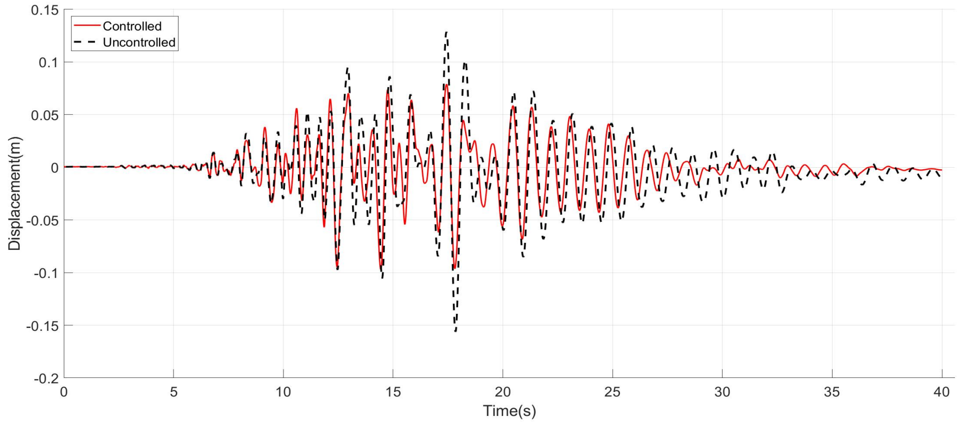

(a) Roof Displacements

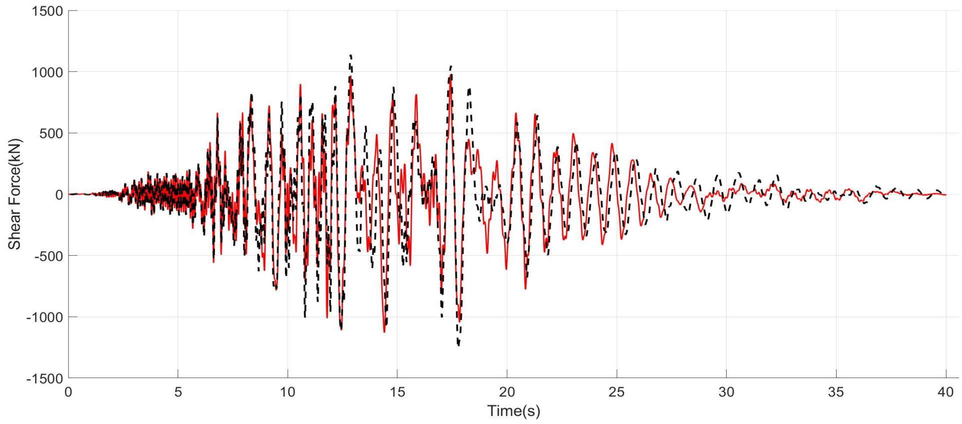

(b) Shear Forces at the base

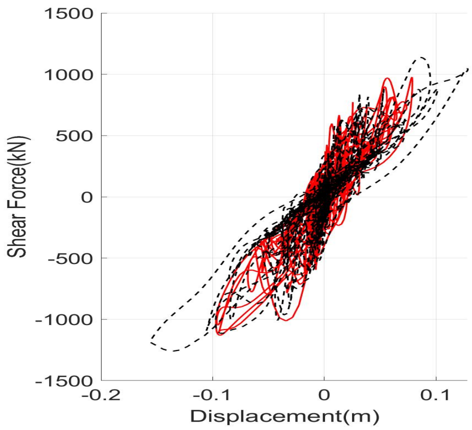

(c) Structural Hysteretic Curve

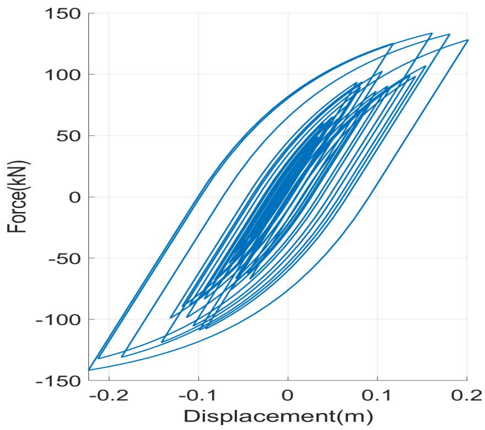

(d) TMD Hysteretic Curve

Figure B.104. Imperial Valley 110% Stiffness

Kobe

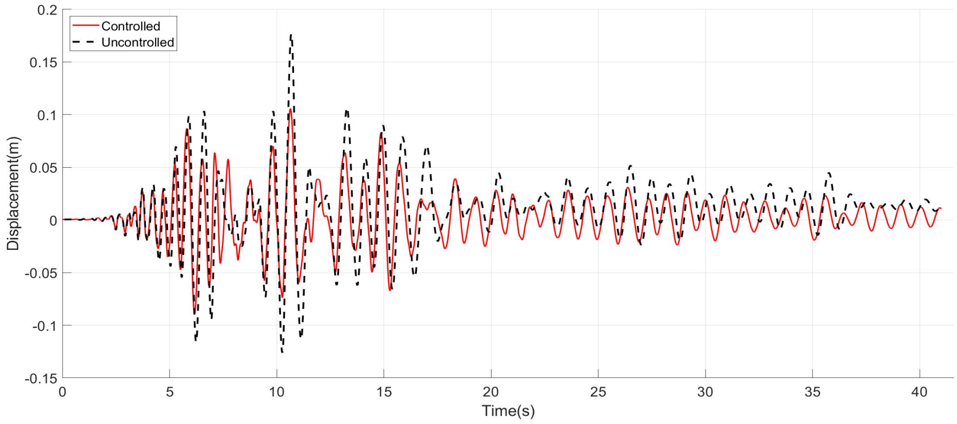

(a) Roof Displacements

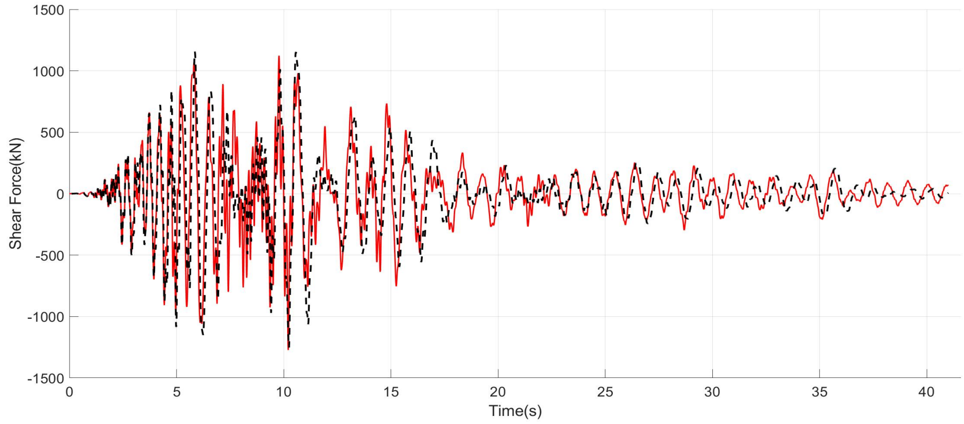

(b) Shear Forces at the base

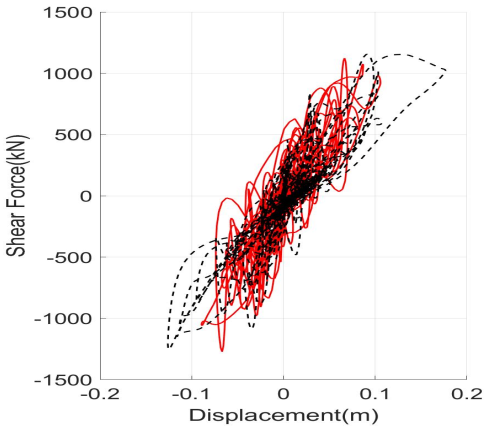

(c) Structural Hysteretic Curve

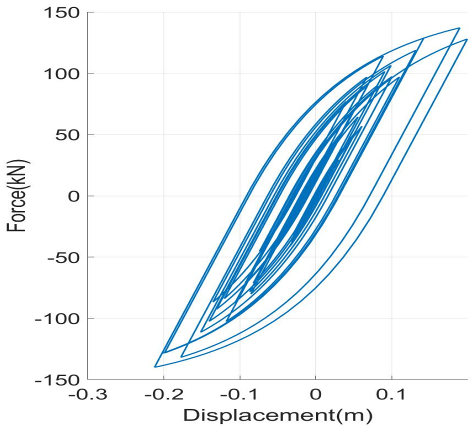

(d) TMD Hysteretic Curve

Figure B.105. Kobe 110% Stiffness

Loma Prieta

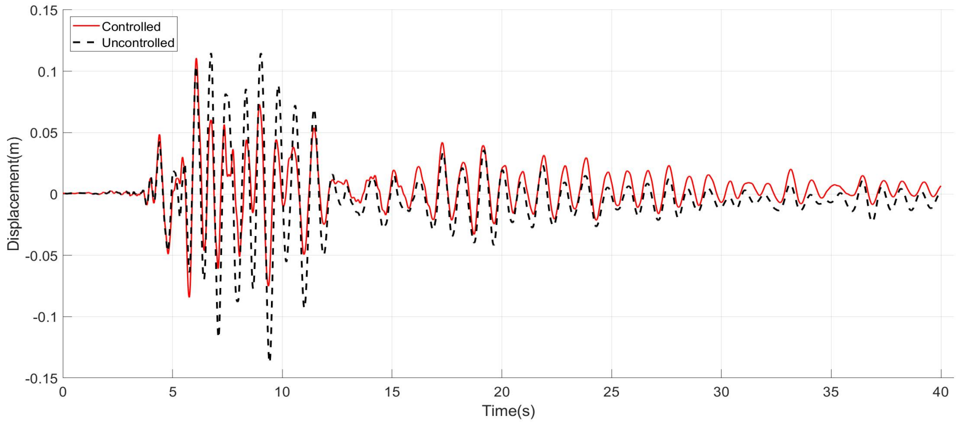

(a) Roof Displacements

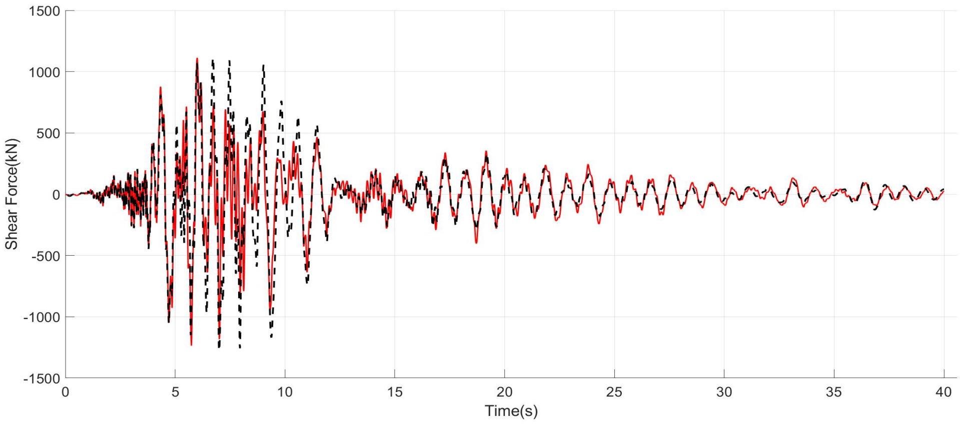

(b) Shear Forces at the base

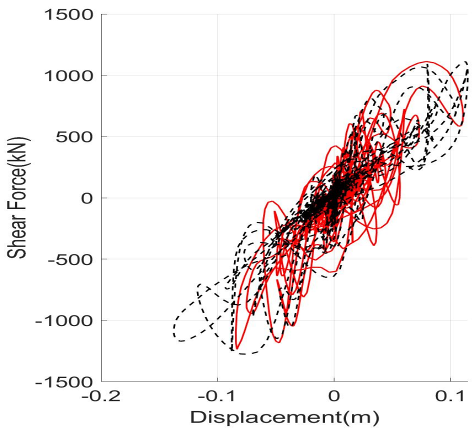

(c) Structural Hysteretic Curve

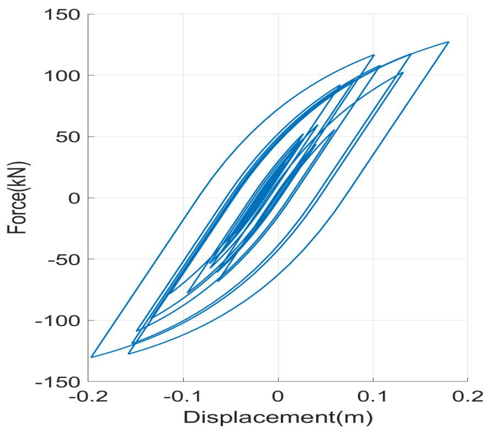

(d) TMD Hysteretic Curve

Figure B.106. Loma Prieta 110% Stiffness

Northridge

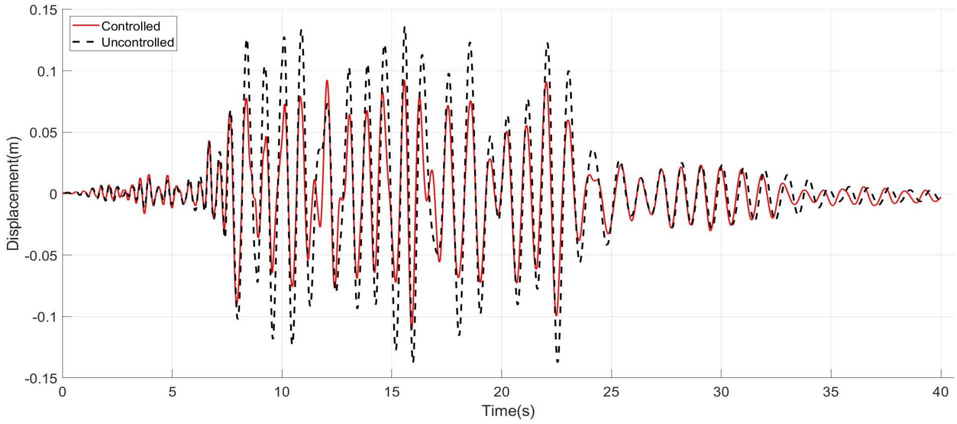

(a) Roof Displacements

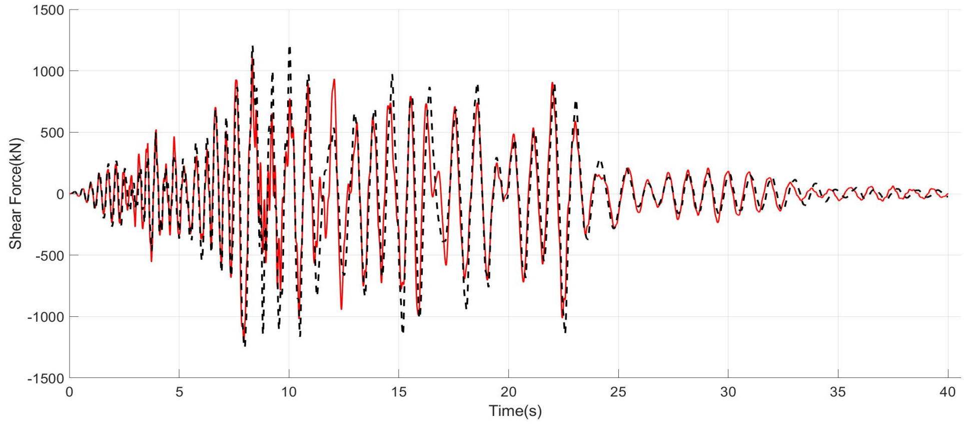

(b) Shear Forces at the base

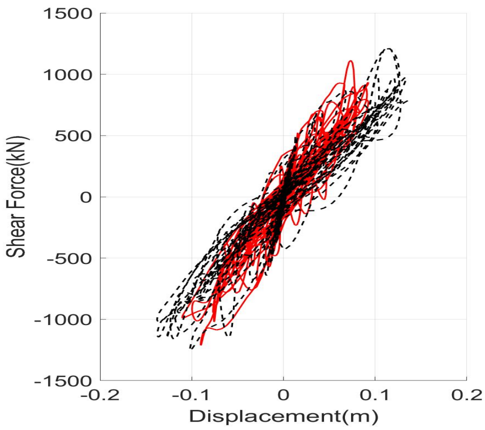

(c) Structural Hysteretic Curve

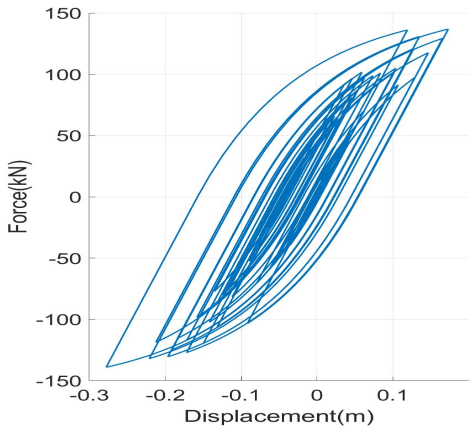

(d) TMD Hysteretic Curve

Figure B.107. Northridge 110% Stiffness

Drifts

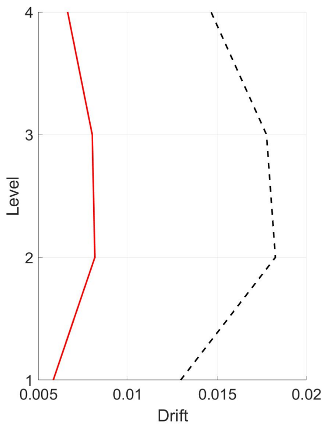

(a) Chalfant

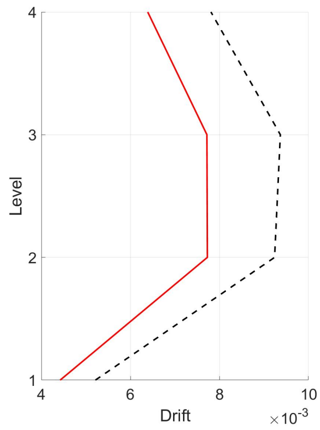

(b) Chi Chi

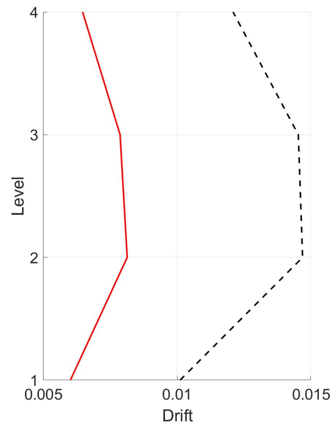

(c) Erzincan

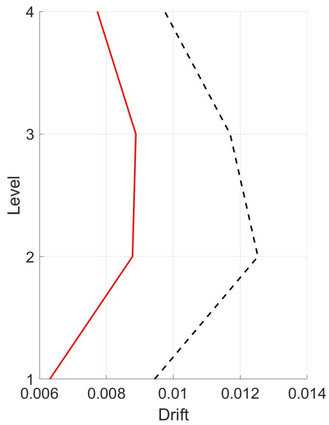

(d) Friulli

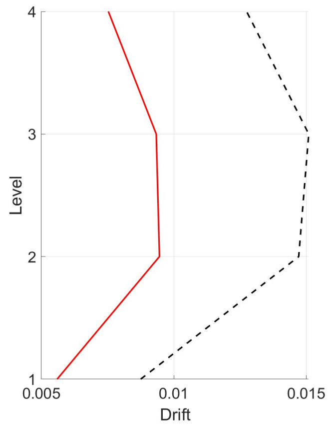

(e) Imperial Valley

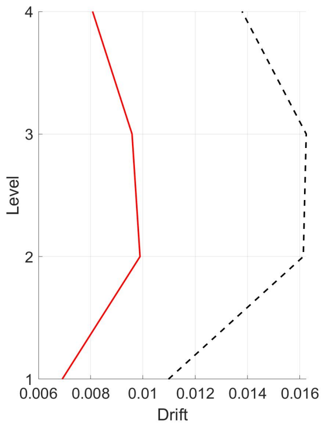

(f) Kobe

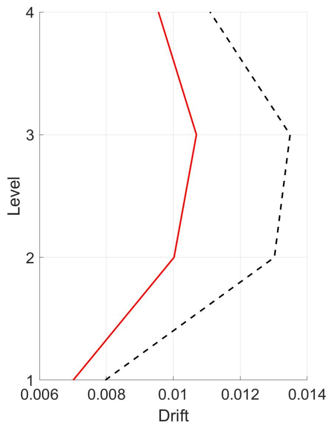

(g) Loma Prieta

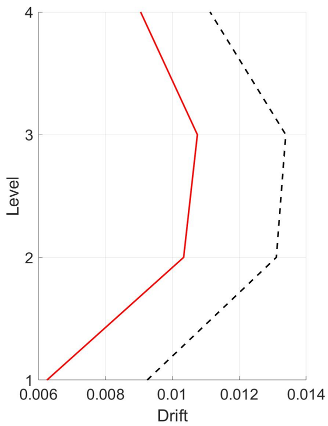

(h) Northridge

Figure B.108. Drifts 110% Stiffness

B.4 Mass of the Structure

Considering a total mass of the structure to obtain the initial frequency of the structure leads to the results here presented.

Table B.13. Performance Indices Mass of the Structure

Earthquake	Performance Index						
	J_1	J_2	J_3	J_4	J_5	J_6	J_7(m)
Chalfant	0.584	0.991	1.102	0.493	0.808	0.905	0.368
Chi-Chi	0.912	1.018	0.913	0.837	0.936	0.975	0.276
Erzincan	0.776	0.994	1.021	0.734	0.896	0.932	0.281
Friulli	0.859	1.052	1.028	0.814	0.958	0.991	0.287
Imperial Valley	0.837	0.968	1.003	0.839	0.941	0.976	0.242
Kobe	0.761	0.952	0.996	0.804	0.966	0.999	0.298
Loma Prieta	0.862	1.071	0.951	0.872	0.960	0.971	0.396
Northridge	0.917	0.956	0.912	0.725	0.861	0.889	0.271
Average	0.814	1.000	0.991	0.765	0.916	0.955	0.302

Chalfant

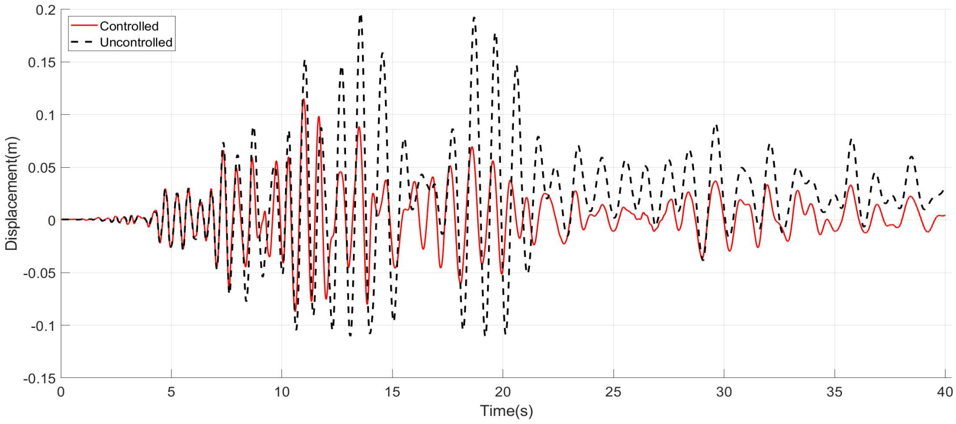

(a) Roof Displacements

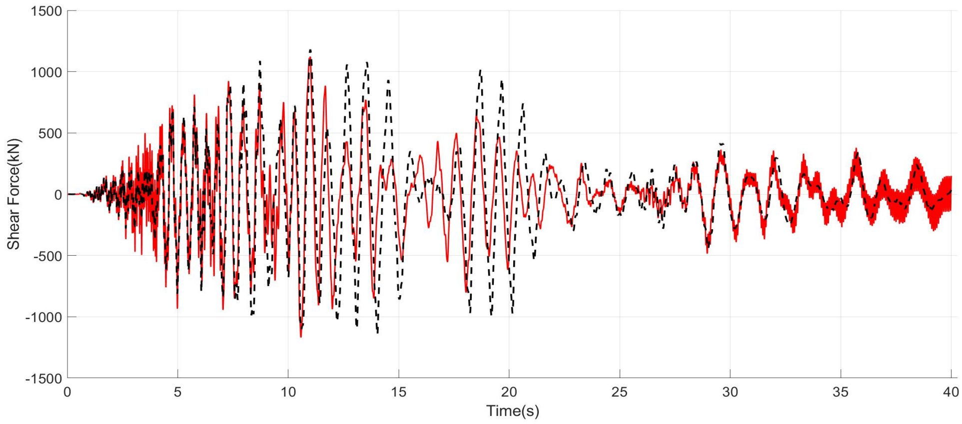

(b) Shear Forces at the base

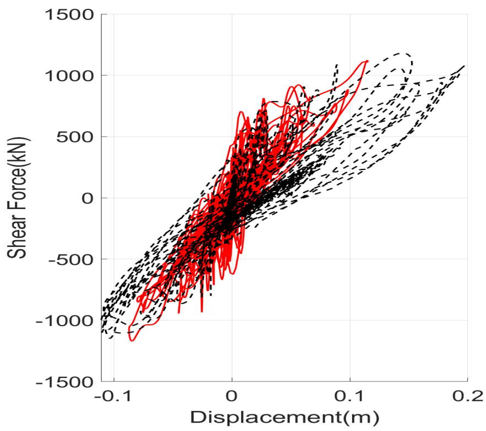

(c) Structural Hysteretic Curve

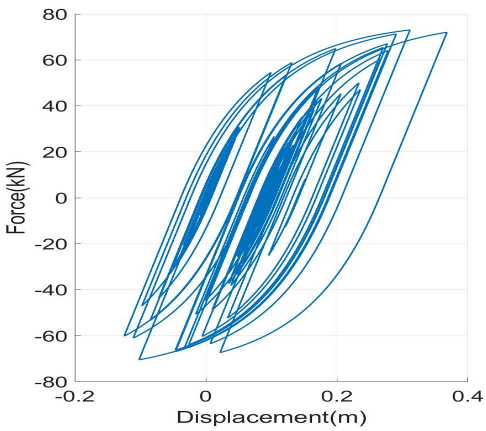

(d) TMD Hysteretic Curve

Figure B.109. Chalfant Mass of the Structure

Chi-Chi

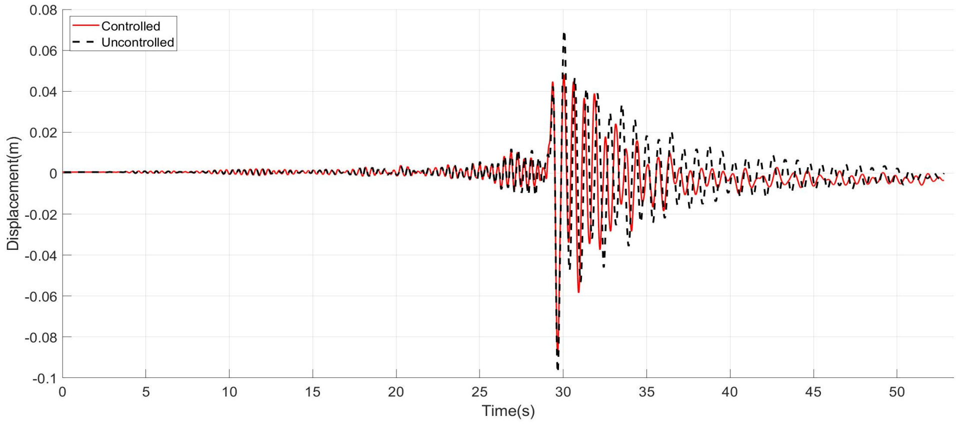

(a) Roof Displacements

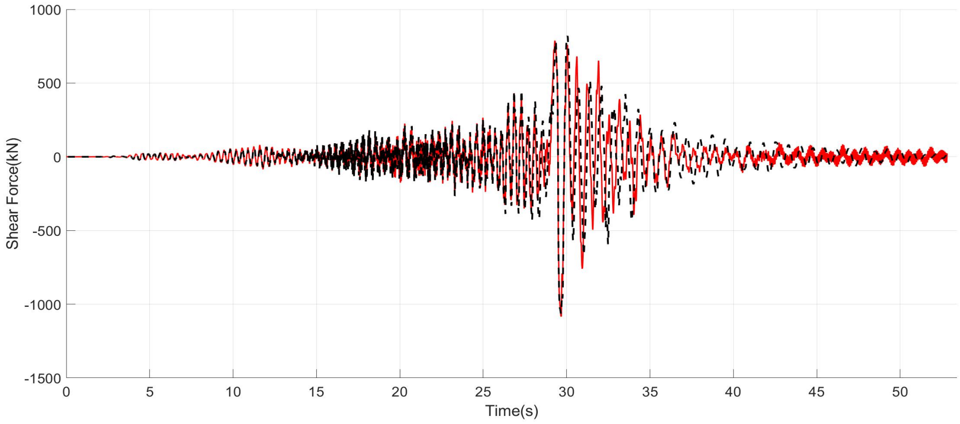

(b) Shear Forces at the base

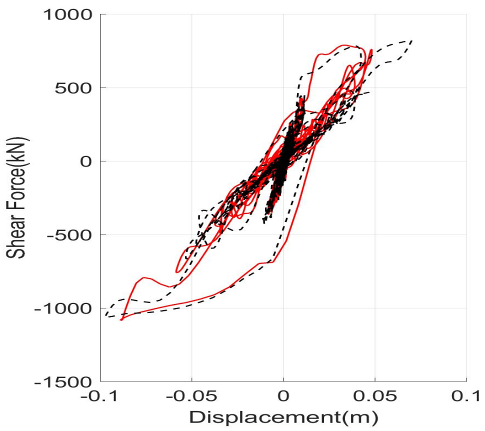

(c) Structural Hysteretic Curve

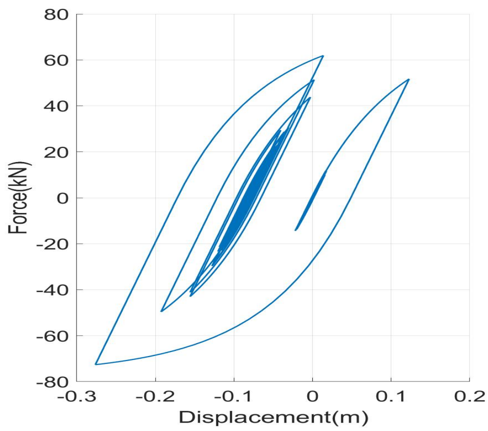

(d) TMD Hysteretic Curve

Figure B.110. Chi Chi Mass of the Structure

Erzincan

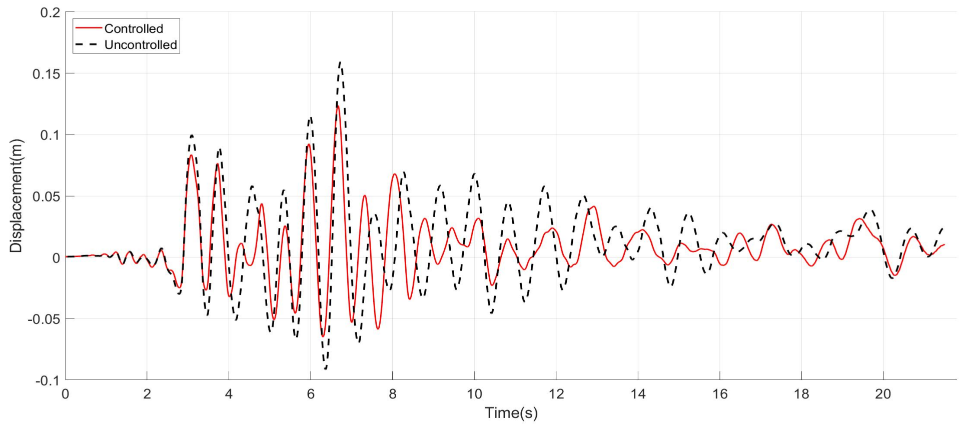

(a) Roof Displacements

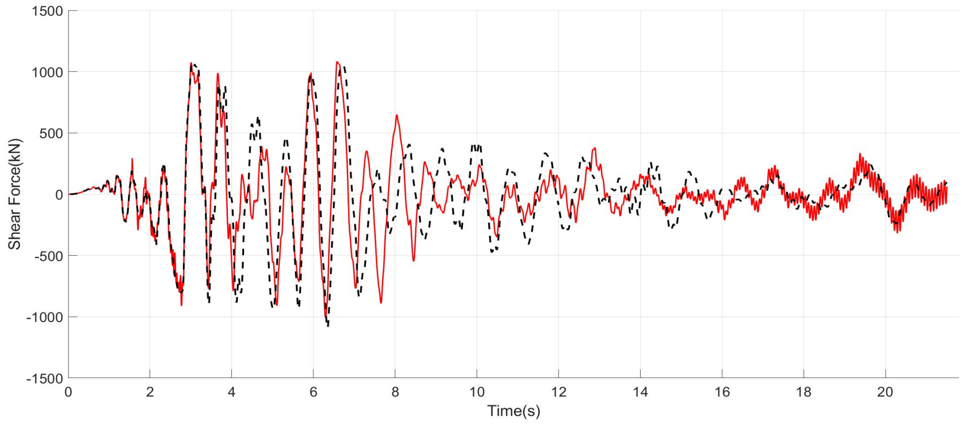

(b) Shear Forces at the base

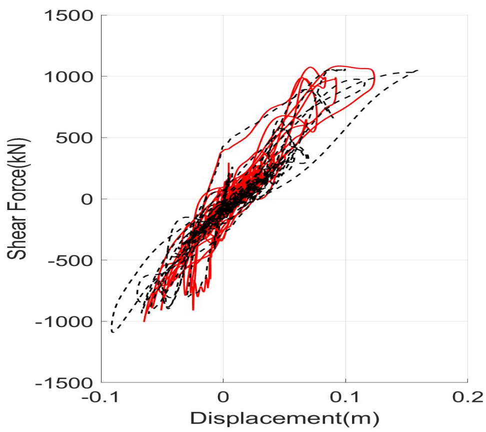

(c) Structural Hysteretic Curve

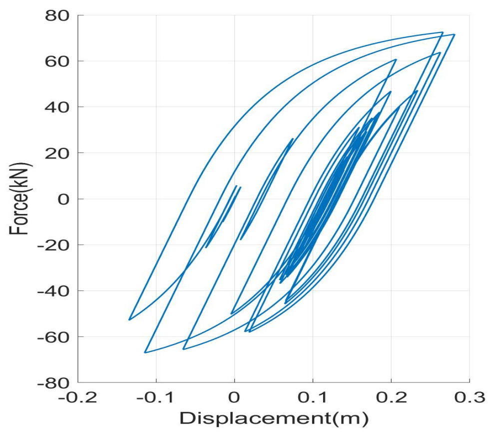

(d) TMD Hysteretic Curve

Figure B.111. Erzincan Mass of the Structure

Friulli

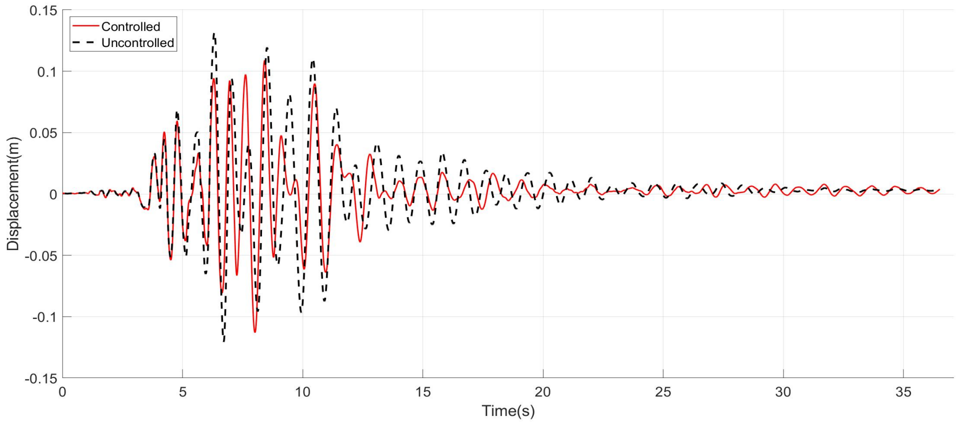

(a) Roof Displacements

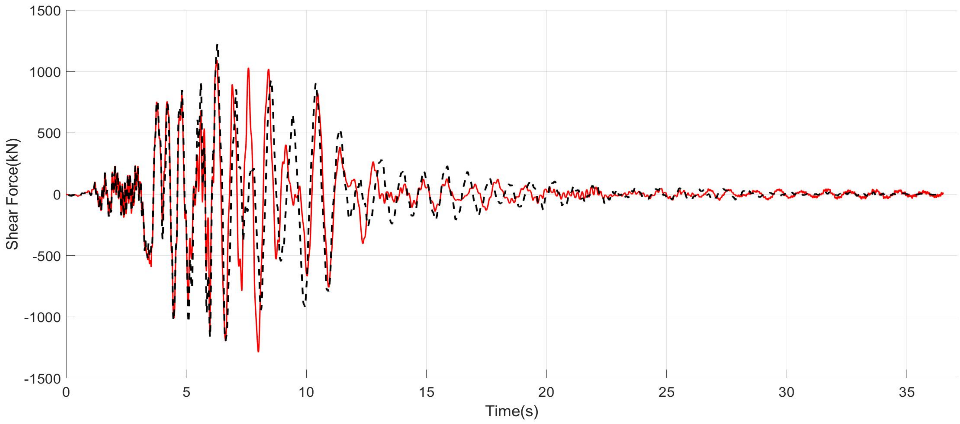

(b) Shear Forces at the base

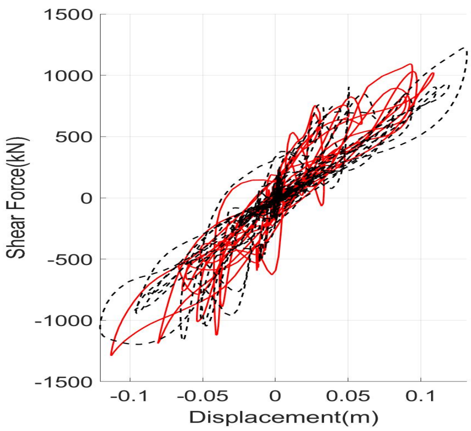

(c) Structural Hysteretic Curve

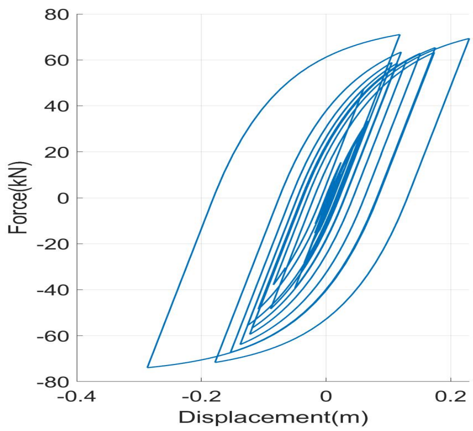

(d) TMD Hysteretic Curve

Figure B.112. Friulli Mass of the Structure

Imperial Valley

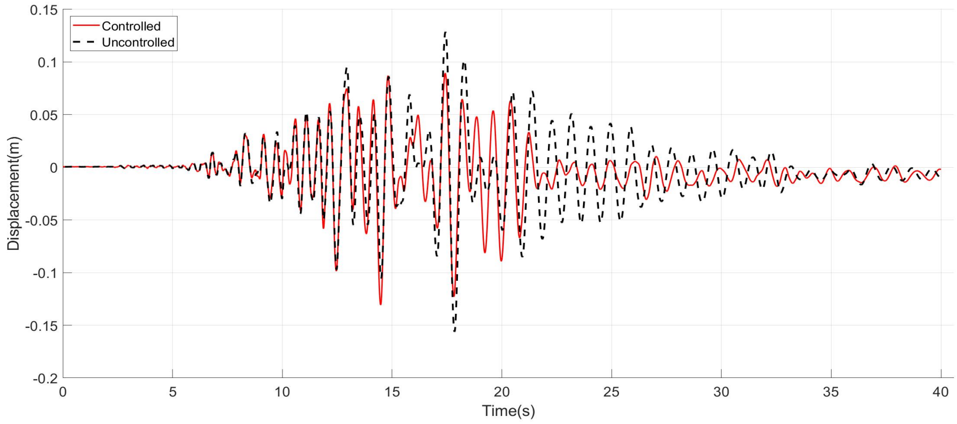

(a) Roof Displacements

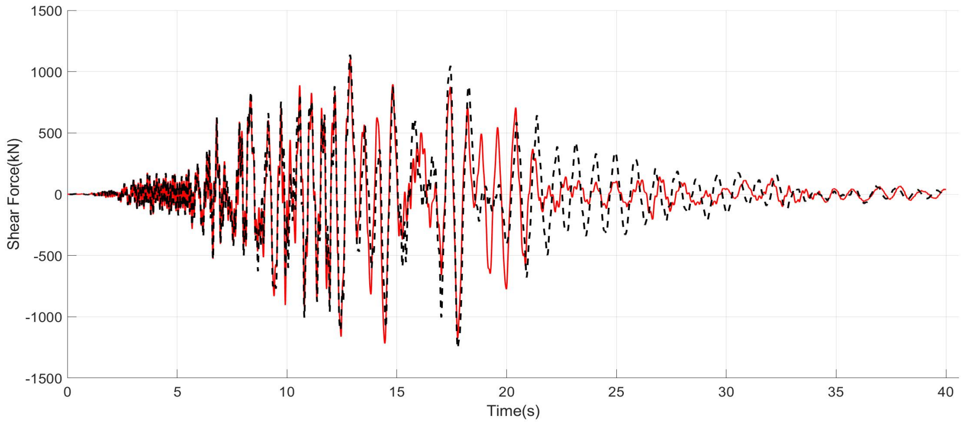

(b) Shear Forces at the base

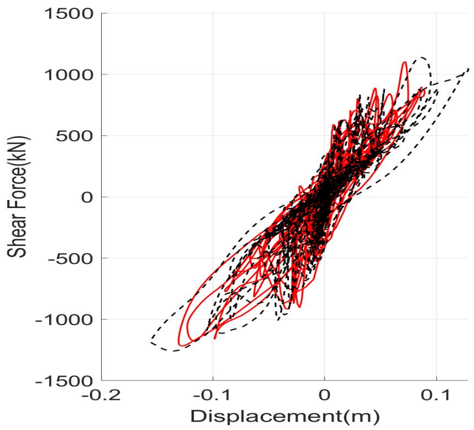

(c) Structural Hysteretic Curve

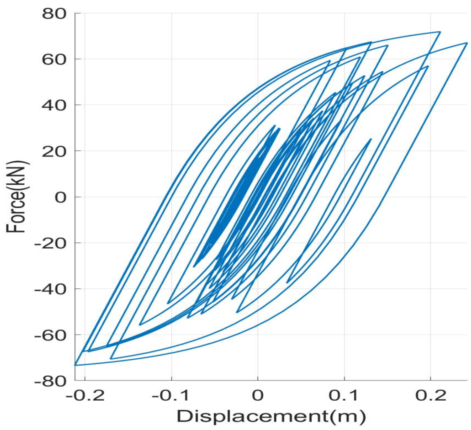

(d) TMD Hysteretic Curve

Figure B.113. Imperial Valley Mass of the Structure

Kobe

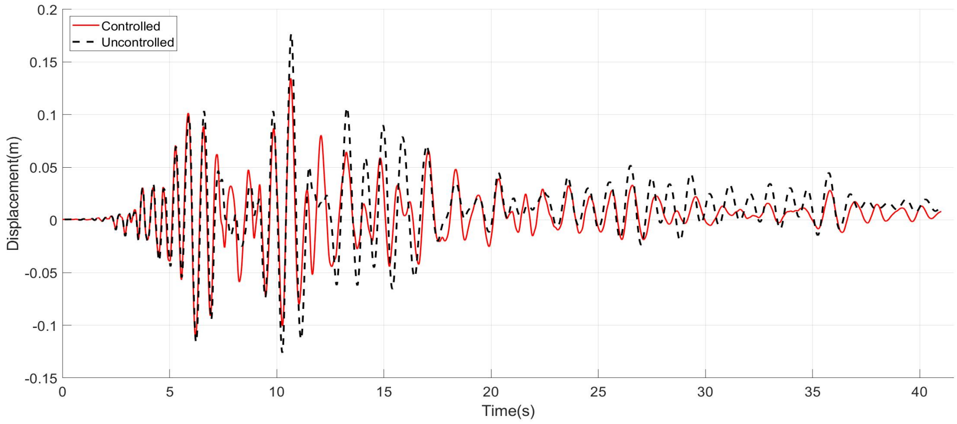

(a) Roof Displacements

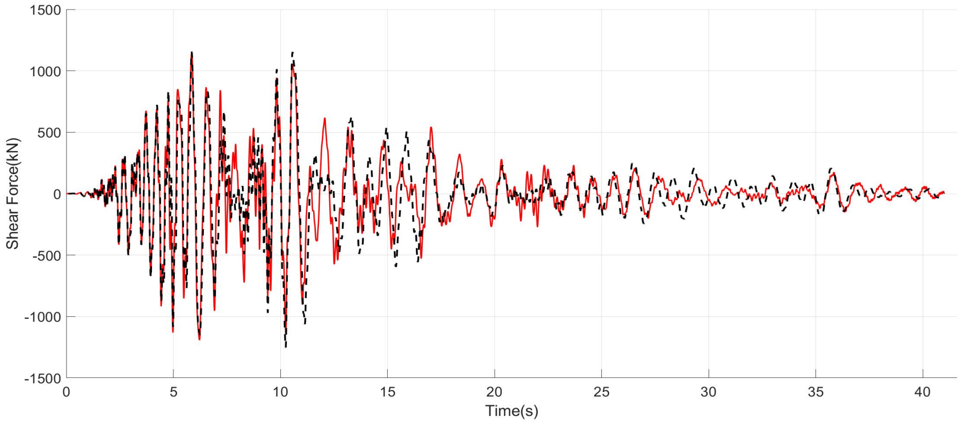

(b) Shear Forces at the base

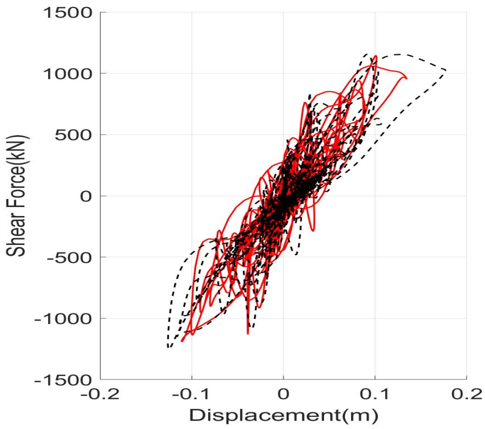

(c) Structural Hysteretic Curve

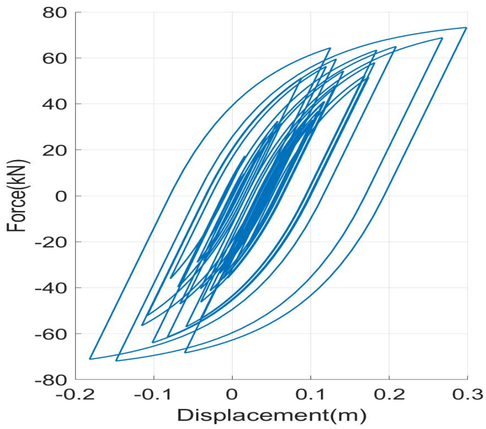

(d) TMD Hysteretic Curve

Figure B.114. Kobe Mass of the Structure

Loma Prieta

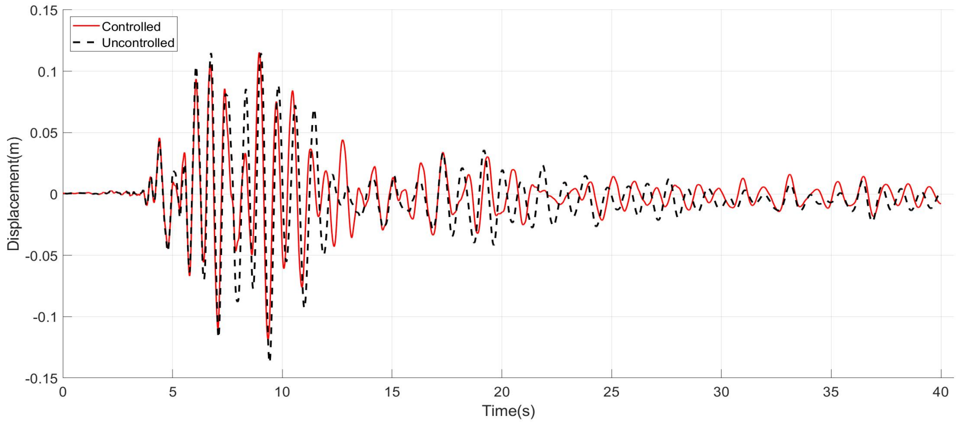

(a) Roof Displacements

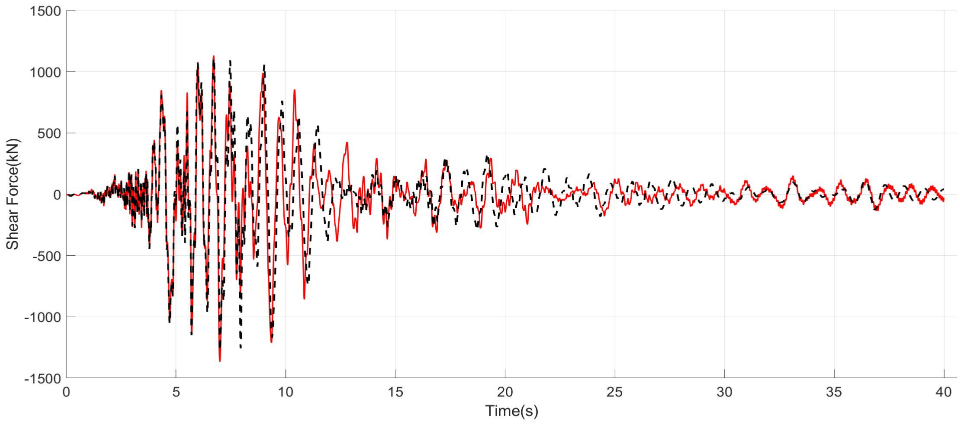

(b) Shear Forces at the base

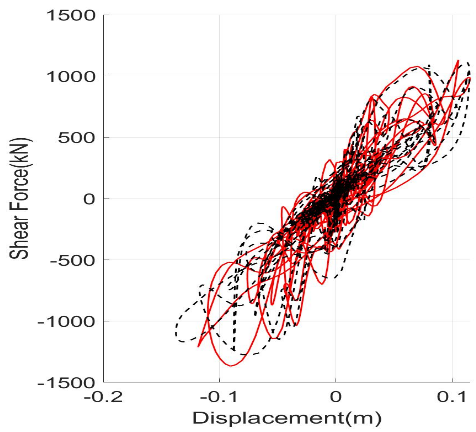

(c) Structural Hysteretic Curve

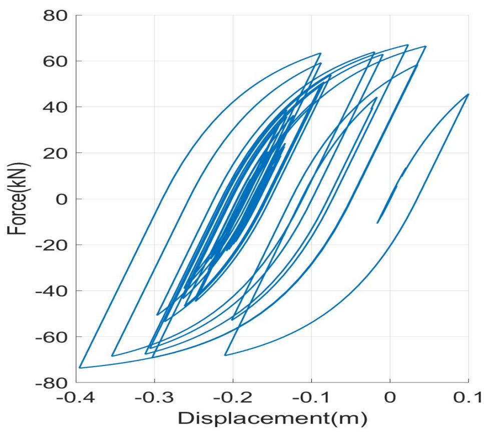

(d) TMD Hysteretic Curve

Figure B.115. Loma Prieta Mass of the Structure

Northridge

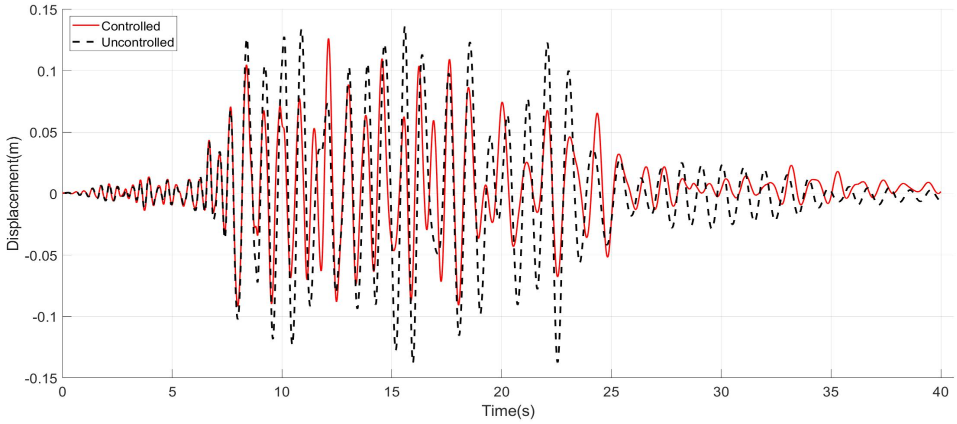

(a) Roof Displacements

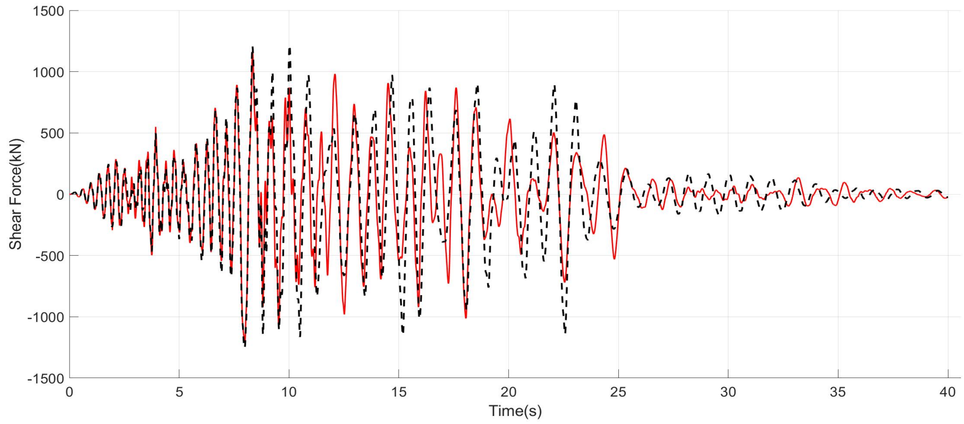

(b) Shear Forces at the base

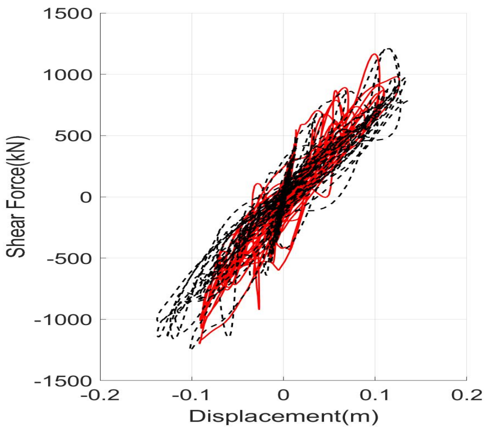

(c) Structural Hysteretic Curve

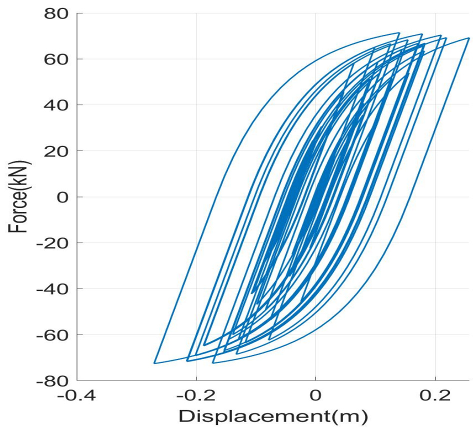

(d) TMD Hysteretic Curve

Figure B.116. Northridge Mass of the Structure

Drifts

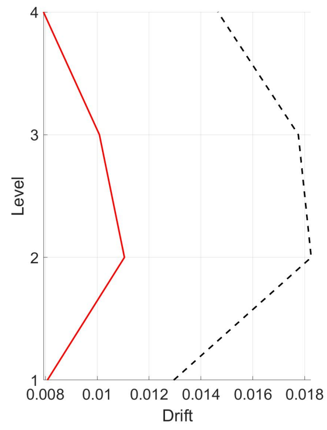

(a) Chalfant

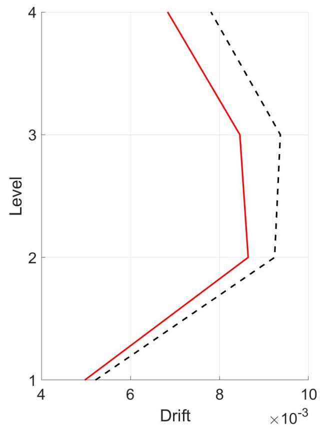

(b) Chi Chi

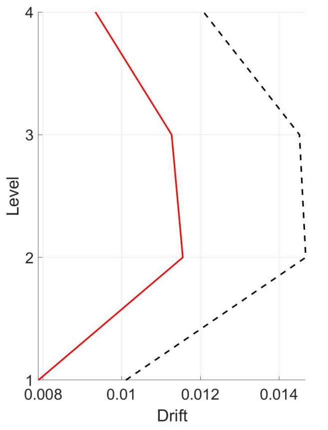

(c) Erzincan

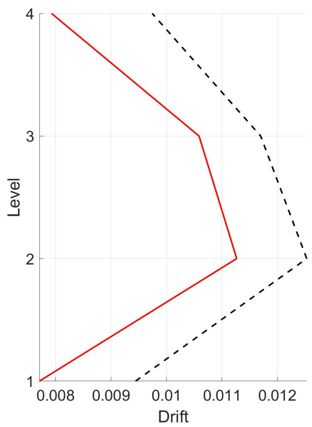

(d) Friulli

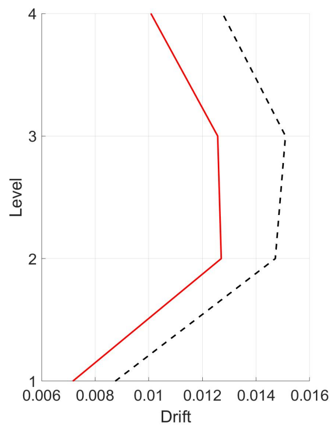

(e) Imperial Valley

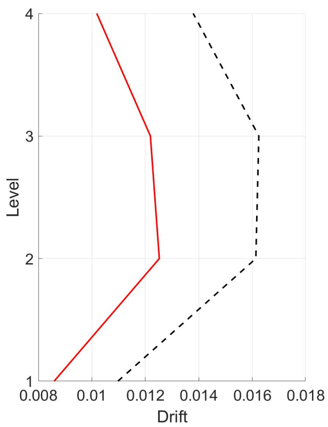

(f) Kobe

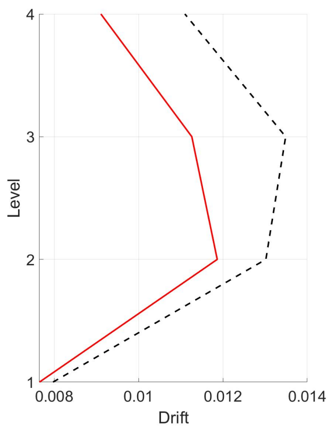

(g) Loma Prieta

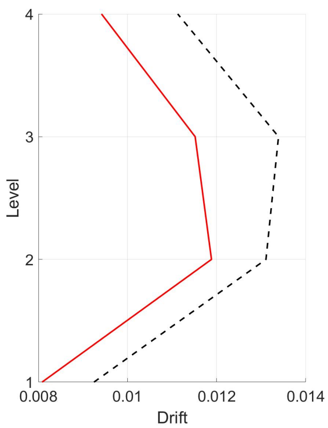

(h) Northridge

Figure B.117. Drifts Mass of the Structure

B.5 Tuning

B.5.1 $f = 1$

Using a tuning frequency of 1, meaning that the TMD and the structure have the same natural period derives in the following results.

Table B.14. Performance Indices $f = 1$

Earthquake	Performance Index						
	J_1	J_2	J_3	J_4	J_5	J_6	J_7(m)
Chalfant	0.747	0.999	1.069	0.751	0.958	0.939	0.181
Chi-Chi	0.963	0.973	0.863	0.746	0.792	0.766	0.157
Erzincan	0.673	1.019	0.882	0.812	0.867	0.805	0.145
Friulli	0.759	0.935	1.006	0.753	0.870	0.843	0.175
Imperial Valley	0.866	0.946	0.970	1.163	1.053	0.958	0.189
Kobe	0.754	0.856	0.932	0.839	0.957	0.911	0.158
Loma Prieta	0.723	0.971	0.819	0.749	0.898	0.888	0.165
Northridge	0.938	0.927	0.836	0.843	0.966	0.881	0.181
Average	0.803	0.953	0.922	0.832	0.920	0.874	0.169

Chalfant

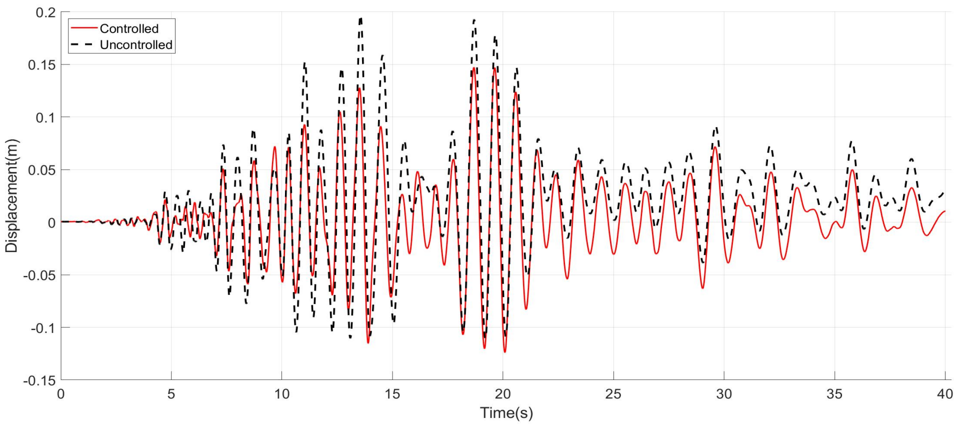

(a) Roof Displacements

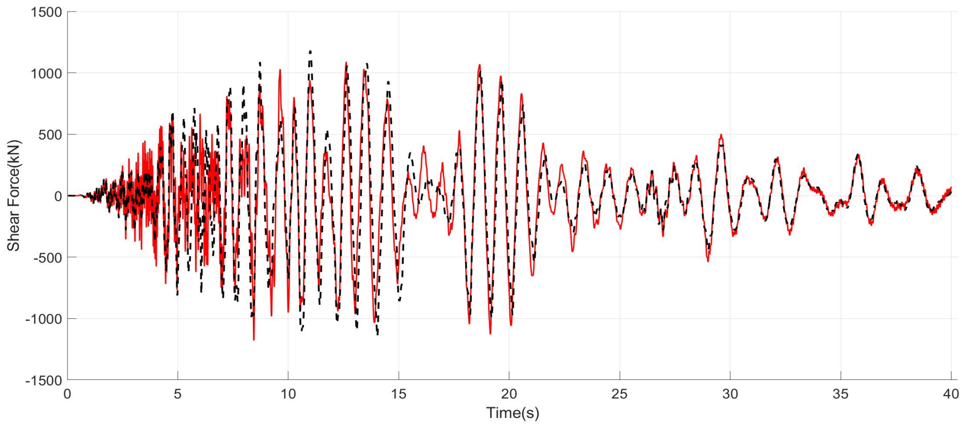

(b) Shear Forces at the base

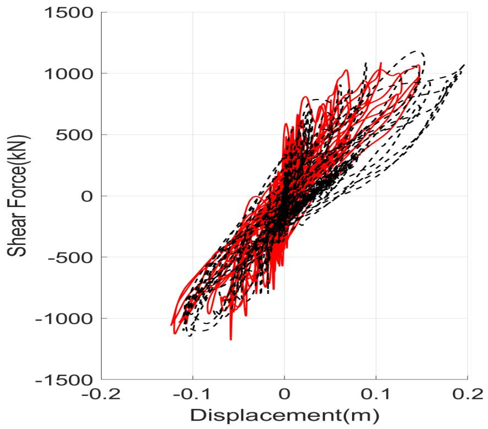

(c) Structural Hysteretic Curve

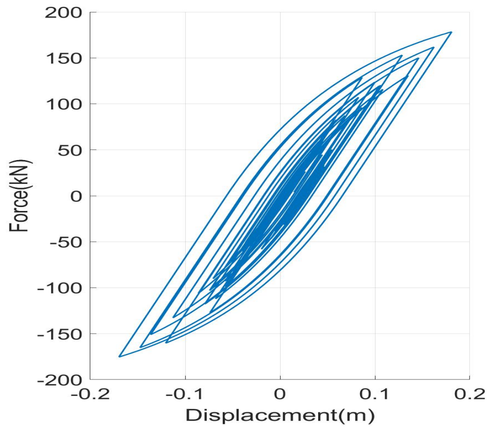

(d) TMD Hysteretic Curve

Figure B.118. Chalfant $f = 1$

Chi-Chi

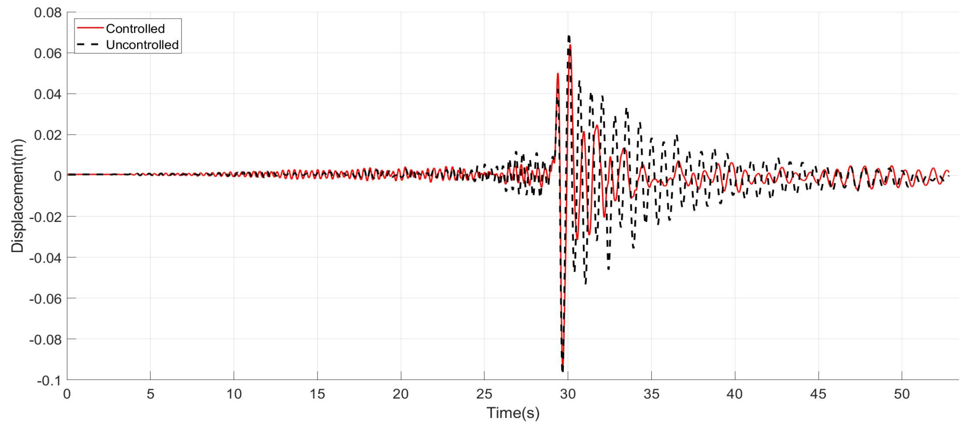

(a) Roof Displacements

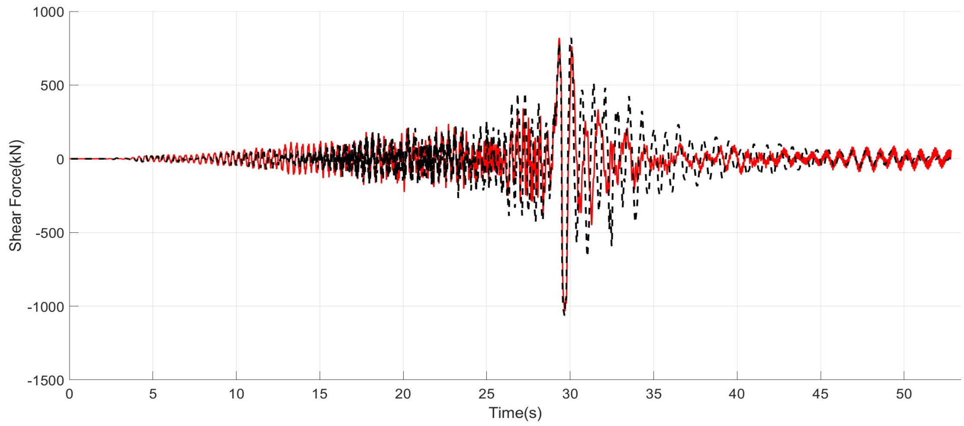

(b) Shear Forces at the base

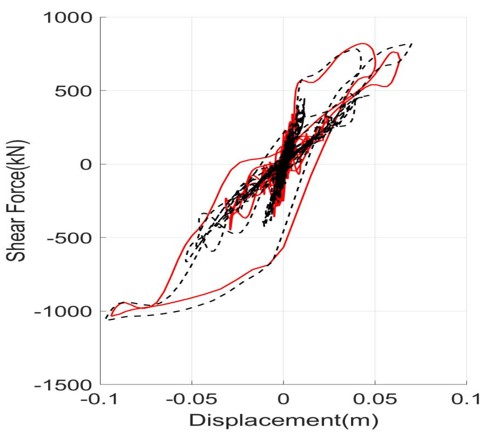

(c) Structural Hysteretic Curve

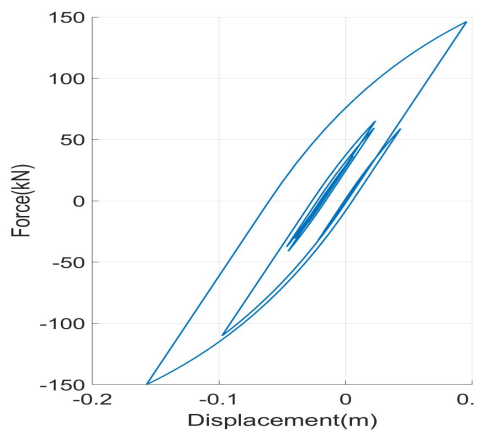

(d) TMD Hysteretic Curve

Figure B.119. Chi Chi $f = 1$

Erzincan

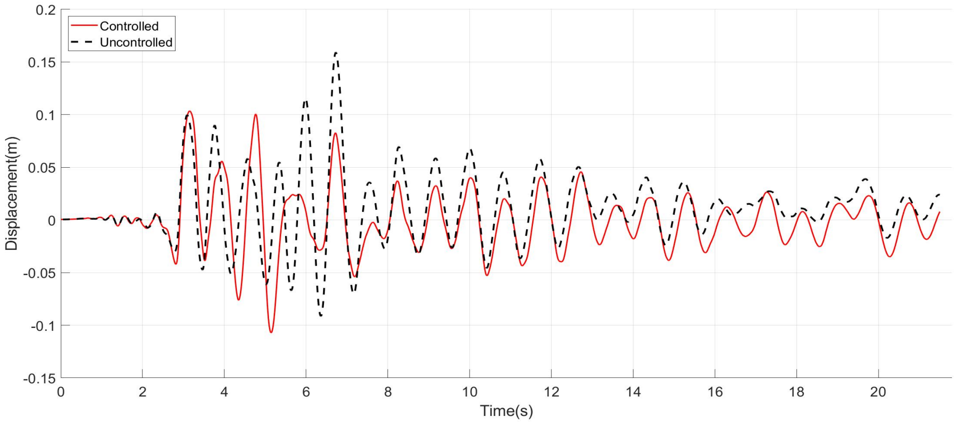

(a) Roof Displacements

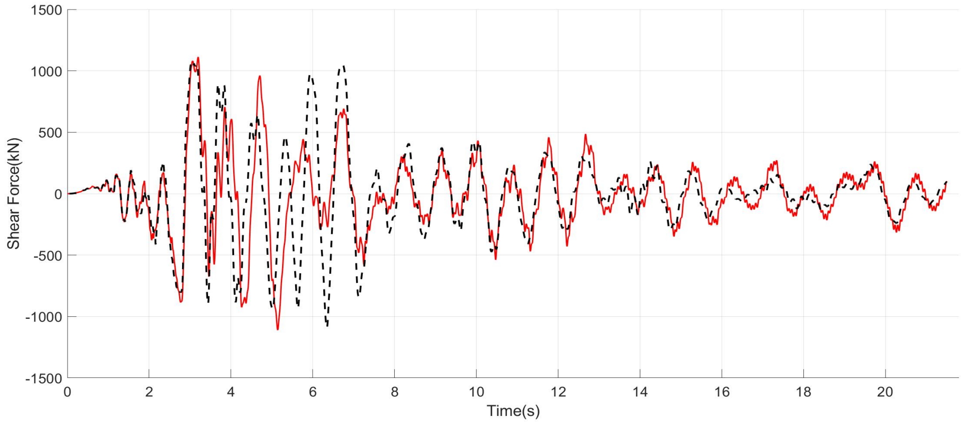

(b) Shear Forces at the base

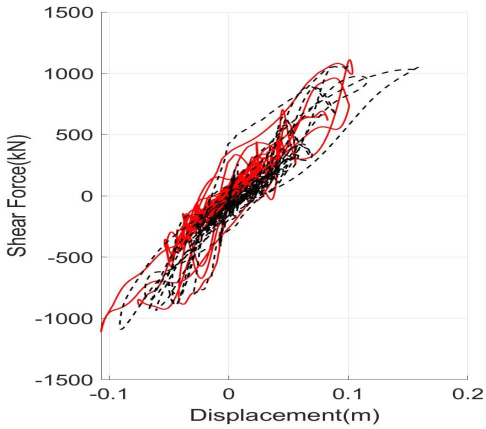

(c) Structural Hysteretic Curve

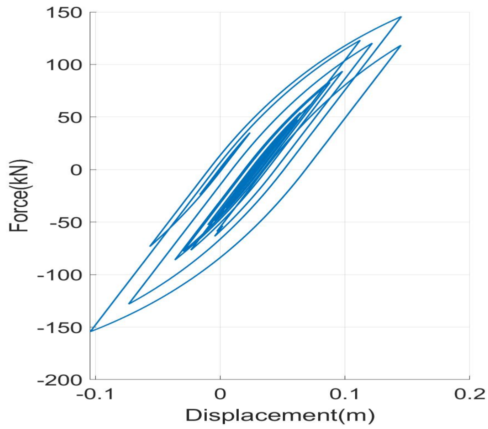

(d) TMD Hysteretic Curve

Figure B.120. Erzincan $f = 1$

Friulli

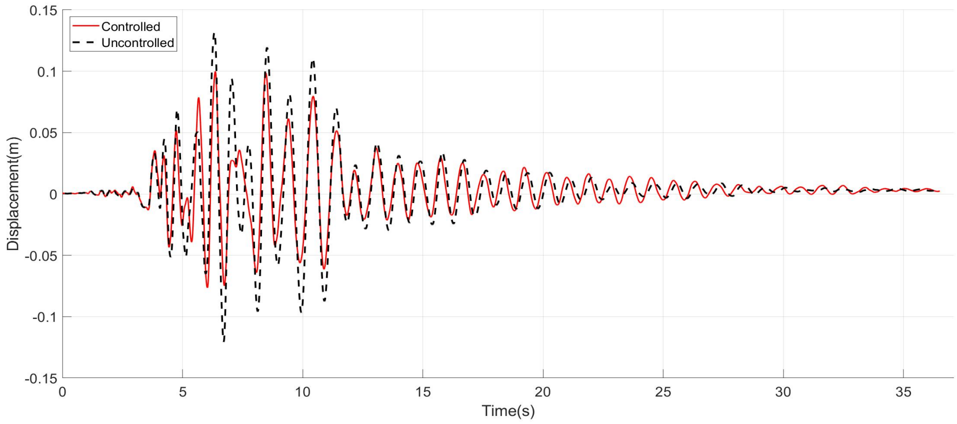

(a) Roof Displacements

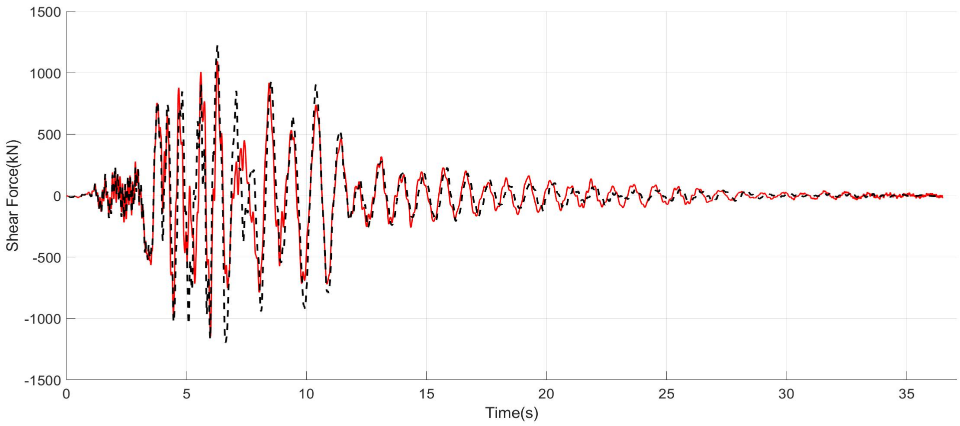

(b) Shear Forces at the base

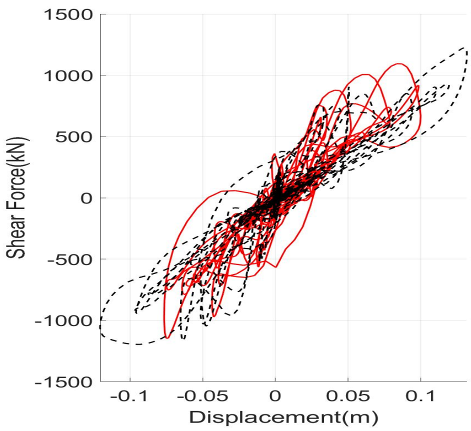

(c) Structural Hysteretic Curve

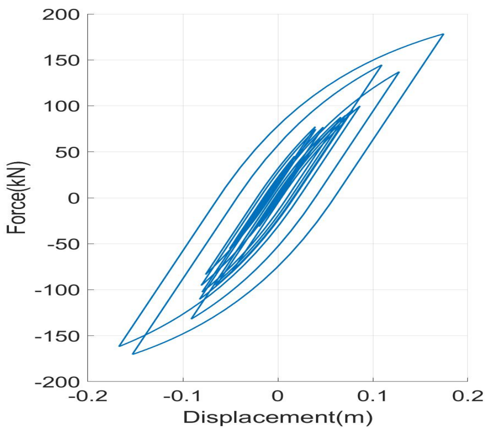

(d) TMD Hysteretic Curve

Figure B.121. Friulli $f = 1$

Imperial Valley

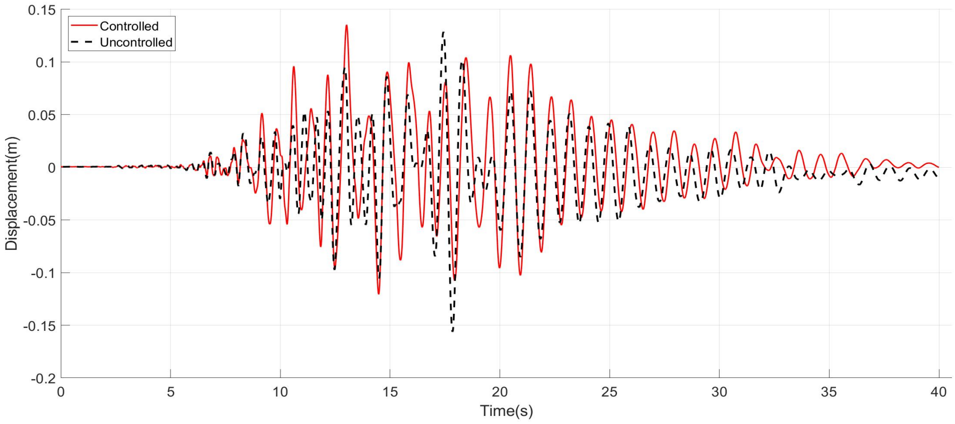

(a) Roof Displacements

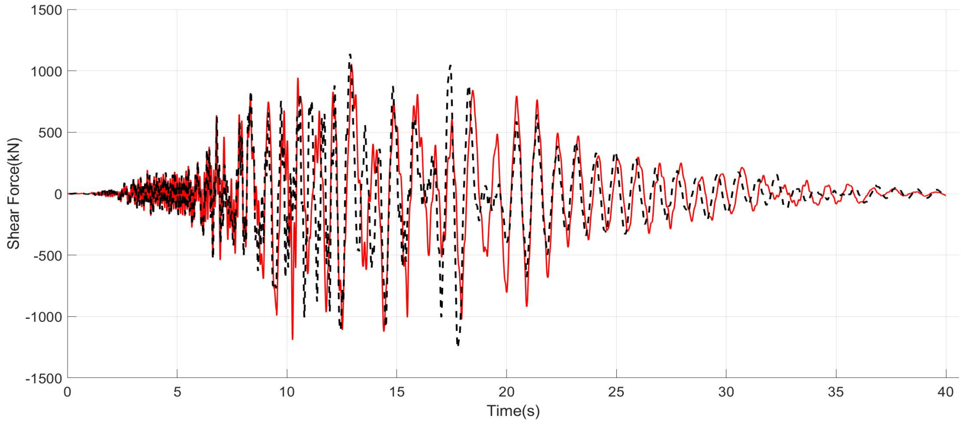

(b) Shear Forces at the base

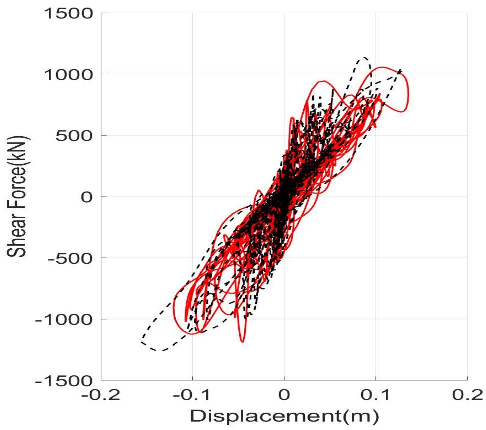

(c) Structural Hysteretic Curve

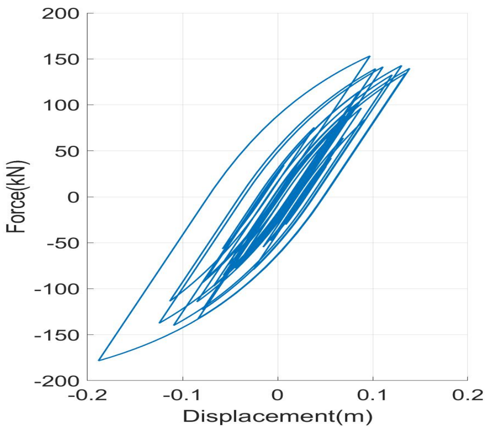

(d) TMD Hysteretic Curve

Figure B.122. Imperial Valley $f = 1$

Kobe

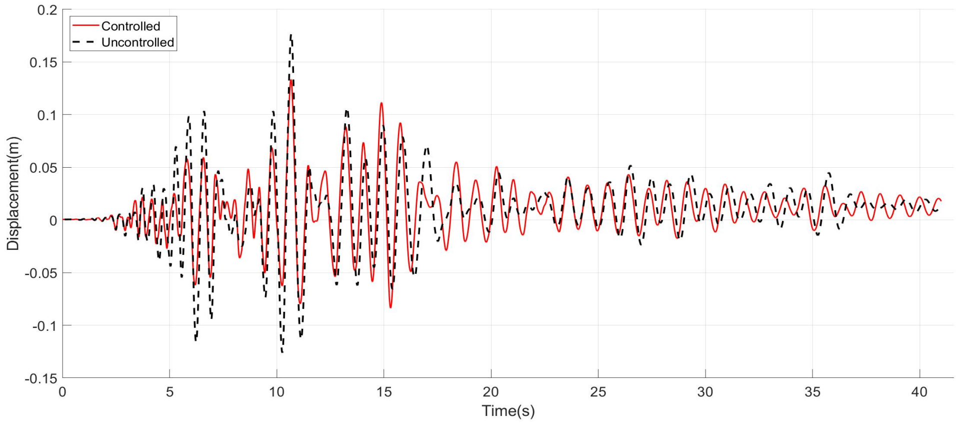

(a) Roof Displacements

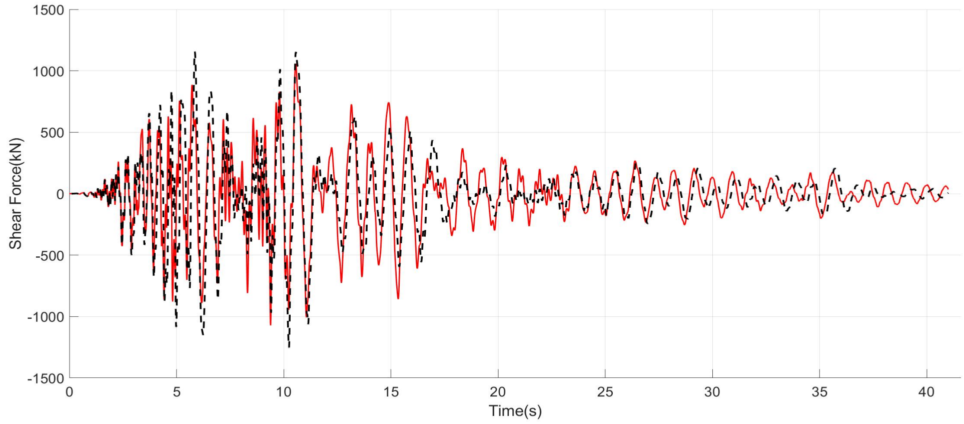

(b) Shear Forces at the base

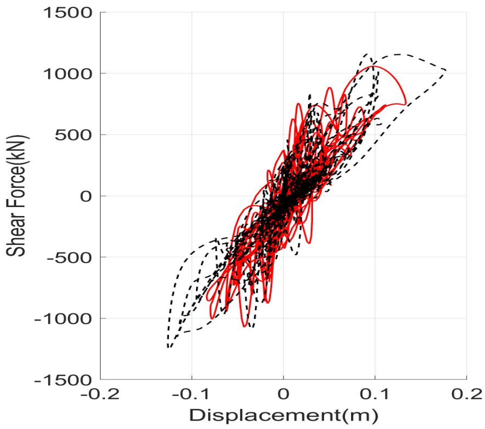

(c) Structural Hysteretic Curve

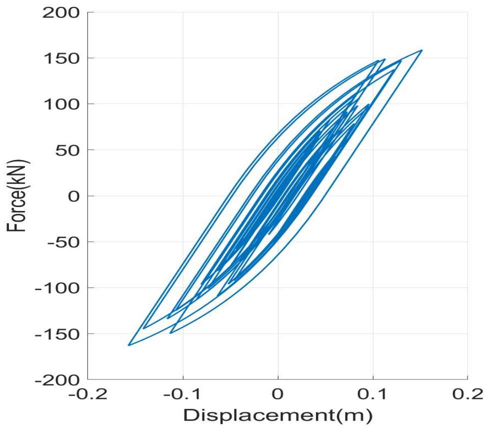

(d) TMD Hysteretic Curve

Figure B.123. Kobe $f = 1$

Loma Prieta

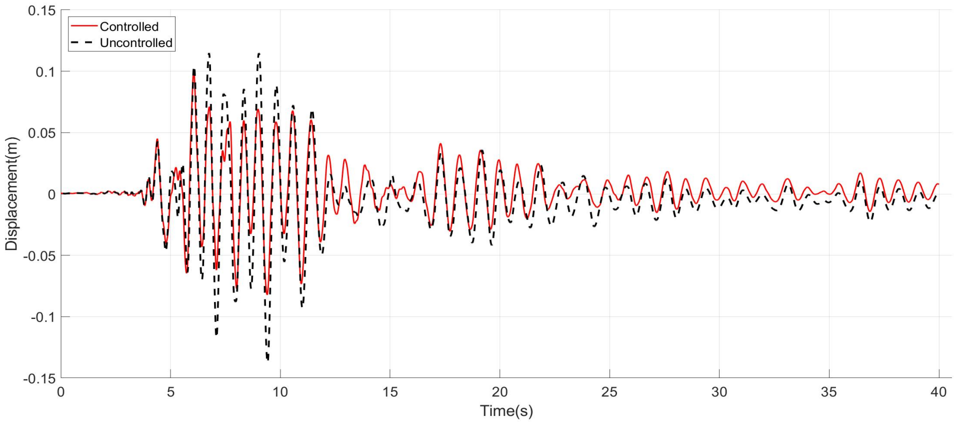

(a) Roof Displacements

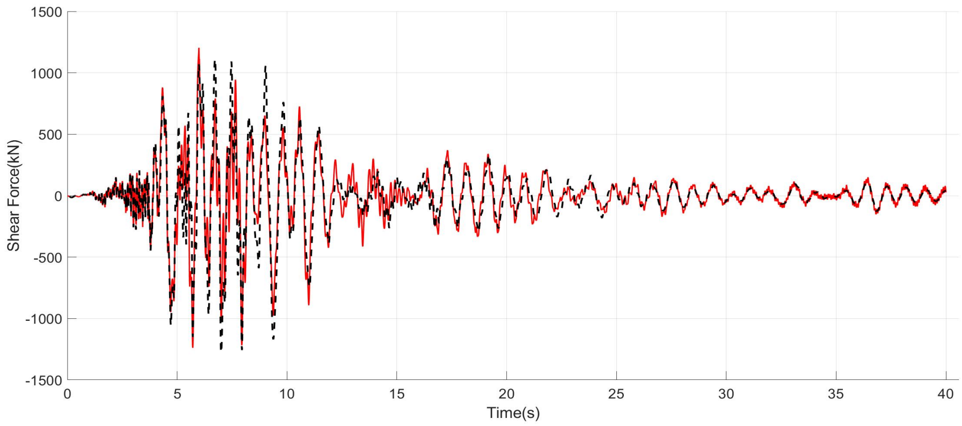

(b) Shear Forces at the base

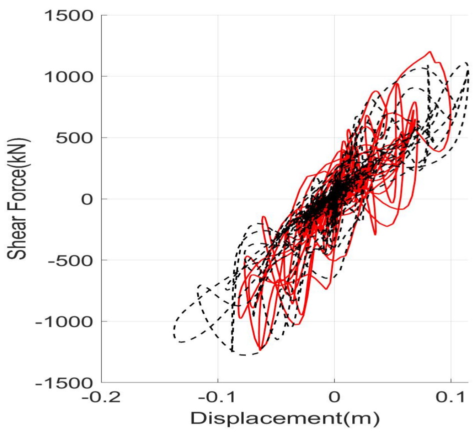

(c) Structural Hysteretic Curve

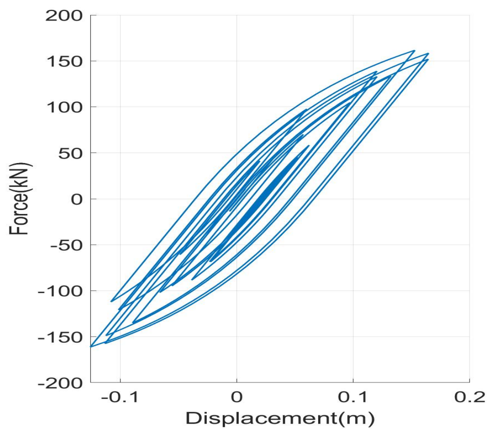

(d) TMD Hysteretic Curve

Figure B.124. Loma Prieta $f = 1$

Northridge

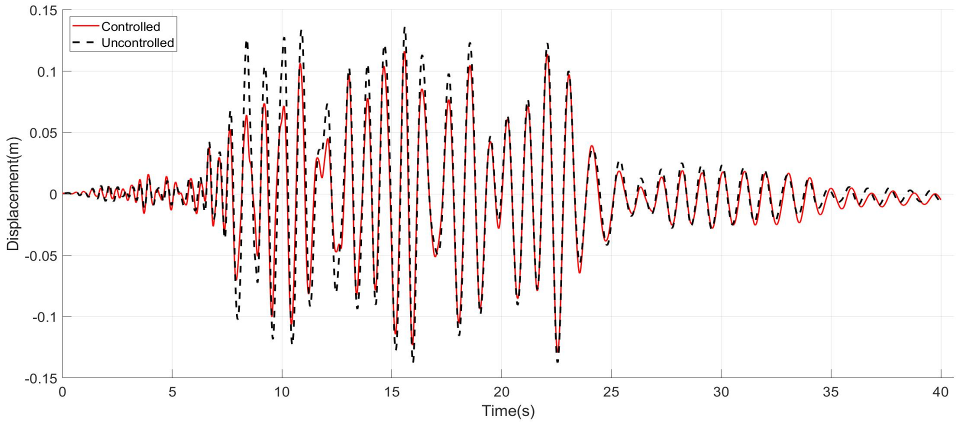

(a) Roof Displacements

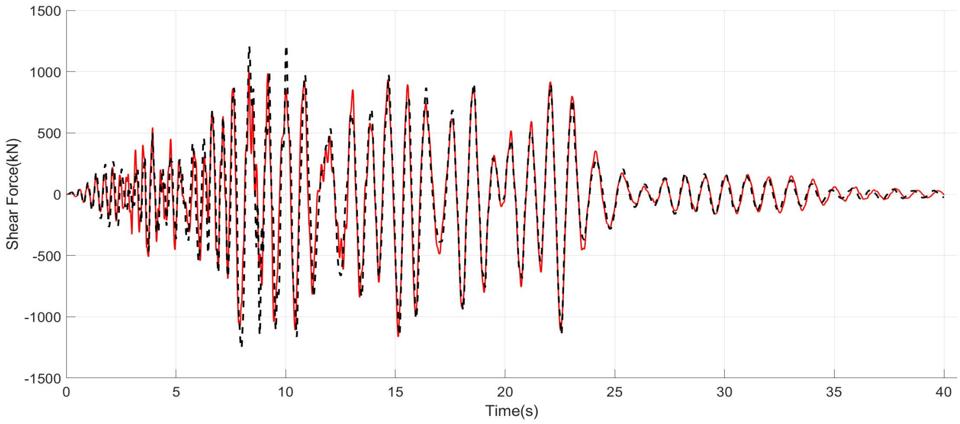

(b) Shear Forces at the base

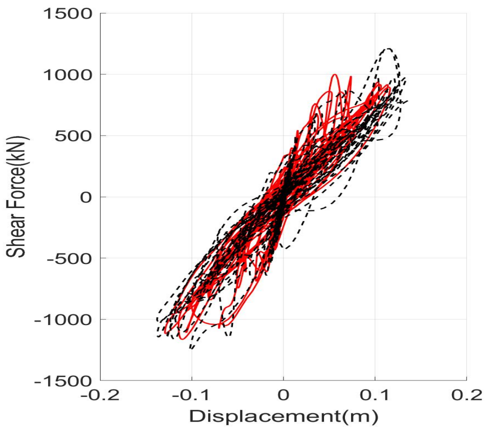

(c) Structural Hysteretic Curve

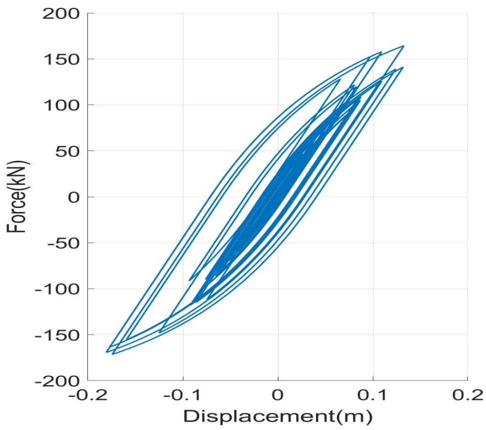

(d) TMD Hysteretic Curve

Figure B.125. Northridge $f = 1$

Drifts

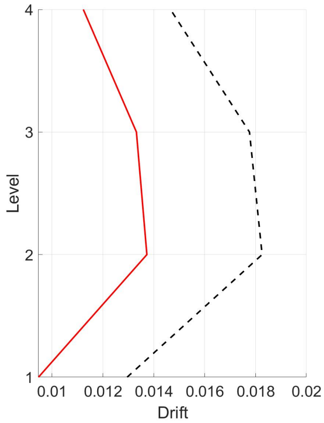

(a) Chalfant

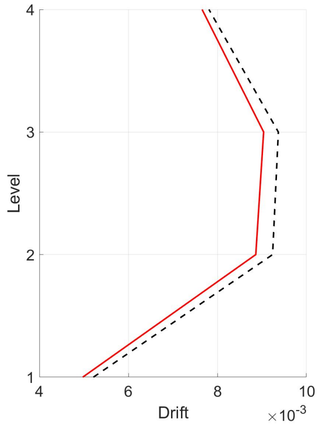

(b) Chi Chi

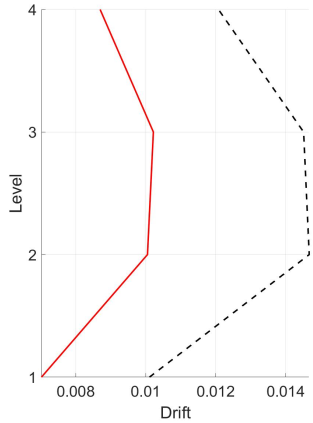

(c) Erzincan

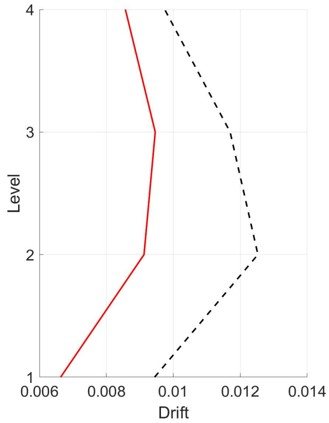

(d) Friulli

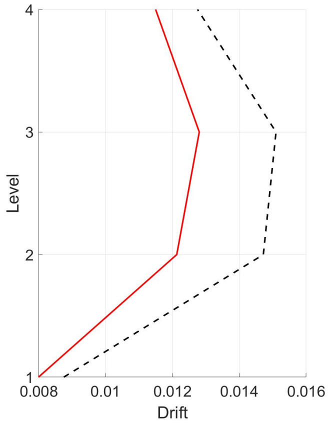

(e) Imperial Valley

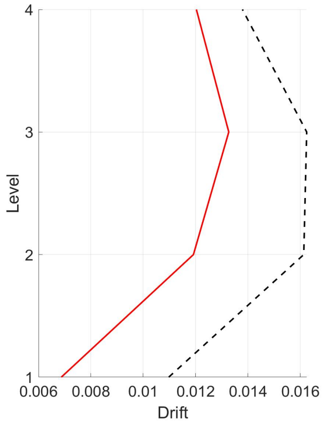

(f) Kobe

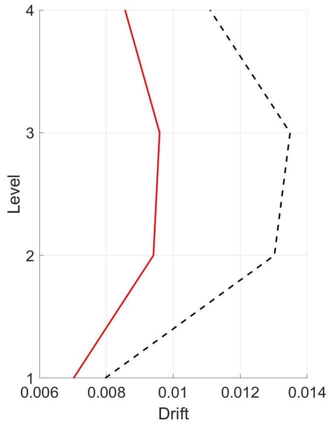

(g) Loma Prieta

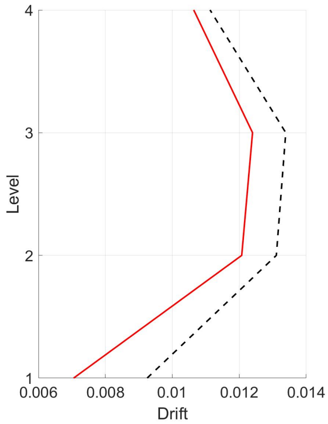

(h) Northridge

Figure B.126. Drifts $f = 1$

B.5.2 $f = 0.90$

Using a tuning frequency of 0.90 the following results are obtained

Table B.15. Performance Indices 0.90

Earthquake	Performance Index						
	J_1	J_2	J_3	J_4	J_5	J_6	J_7(m)
Chalfant	0.443	1.037	1.061	0.517	0.927	1.006	0.208
Chi-Chi	0.886	0.983	0.874	0.628	0.752	0.785	0.206
Erzincan	0.552	0.974	0.859	0.619	0.797	0.828	0.203
Friulli	0.718	0.917	1.266	0.760	0.874	0.867	0.189
Imperial Valley	0.654	0.901	0.905	0.780	0.907	0.875	0.224
Kobe	0.587	1.015	1.163	0.688	0.977	0.991	0.200
Loma Prieta	0.803	0.963	0.909	0.707	0.836	0.875	0.184
Northridge	0.843	0.945	0.898	0.684	0.887	0.838	0.276
Average	0.686	0.967	0.992	0.673	0.870	0.883	0.211

Chalfant

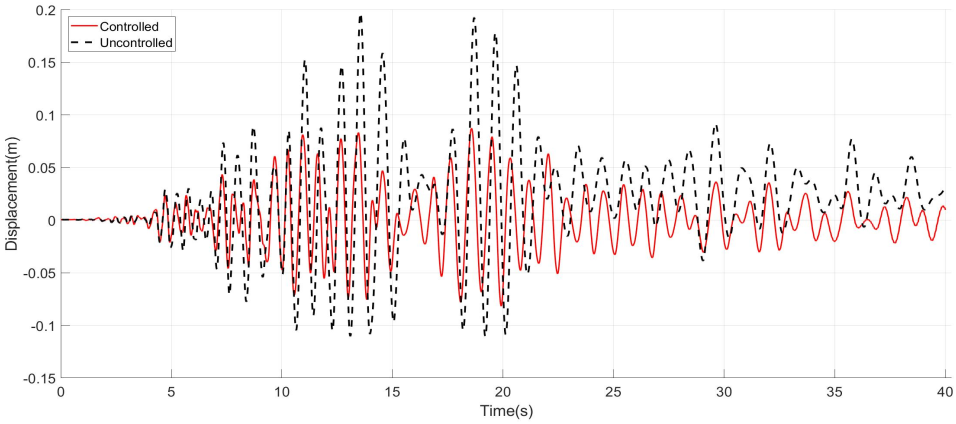

(a) Roof Displacements

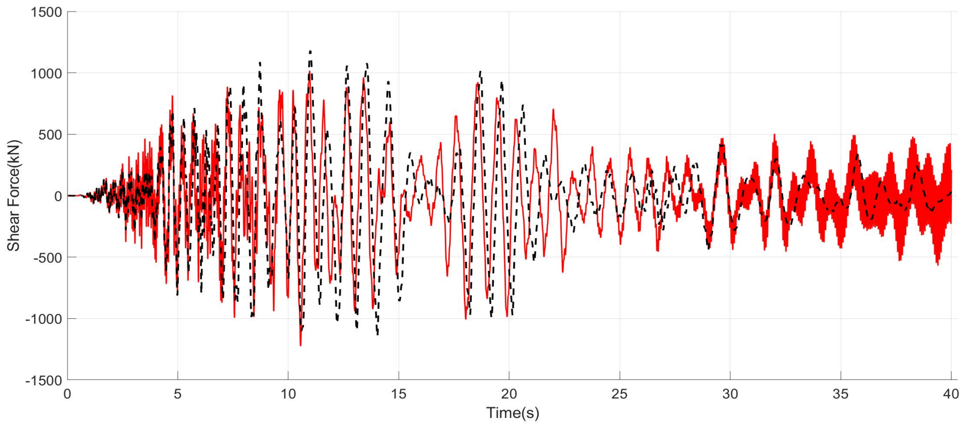

(b) Shear Forces at the base

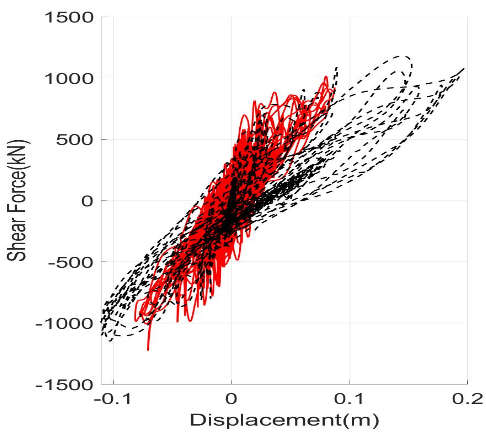

(c) Structural Hysteretic Curve

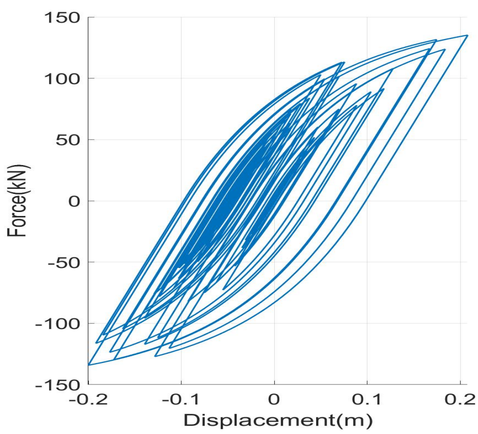

(d) TMD Hysteretic Curve

Figure B.127. Chalfant $f = 0.90$

Chi-Chi

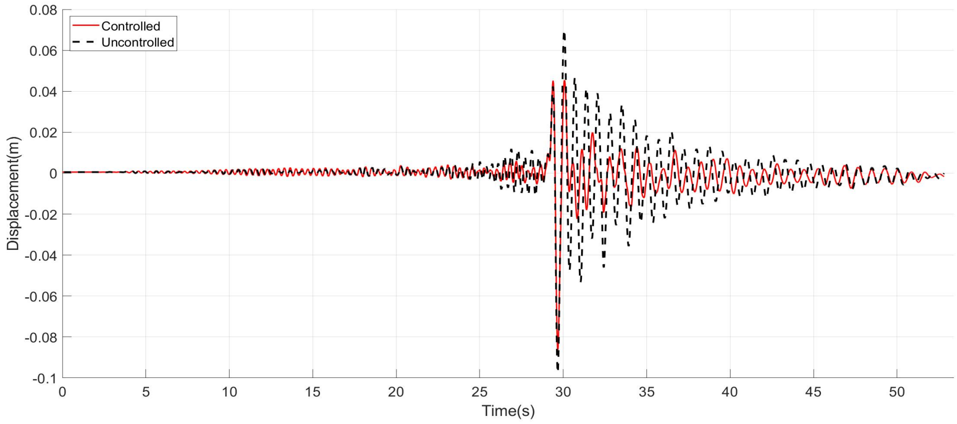

(a) Roof Displacements

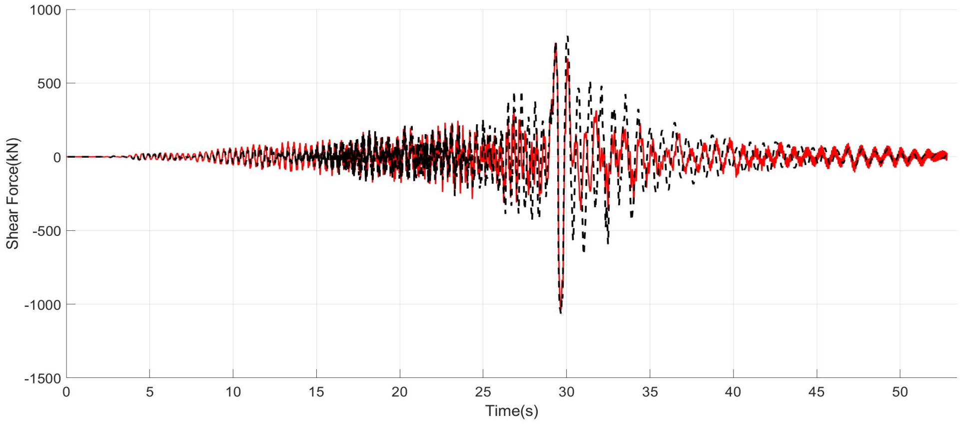

(b) Shear Forces at the base

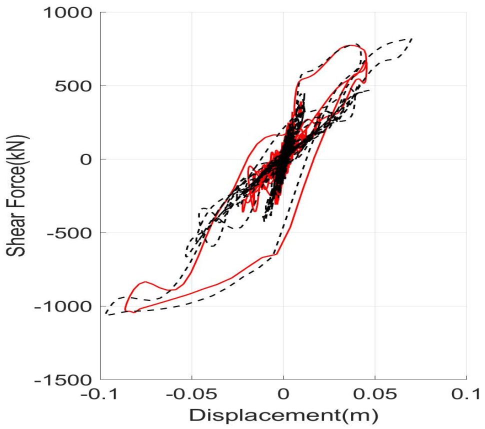

(c) Structural Hysteretic Curve

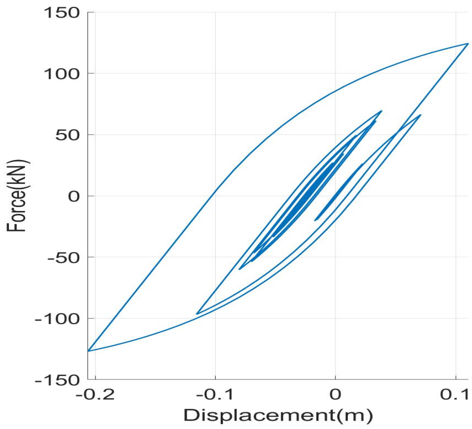

(d) TMD Hysteretic Curve

Figure B.128. Chi Chi $f = 0.90$

Erzincan

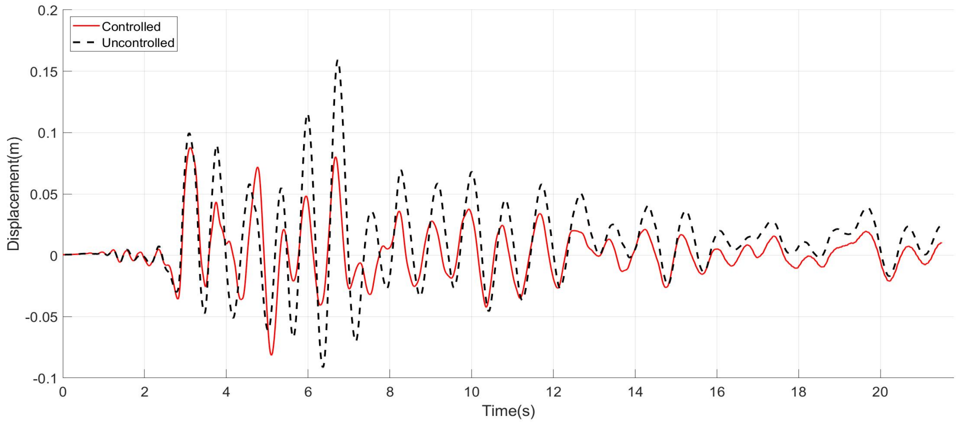

(a) Roof Displacements

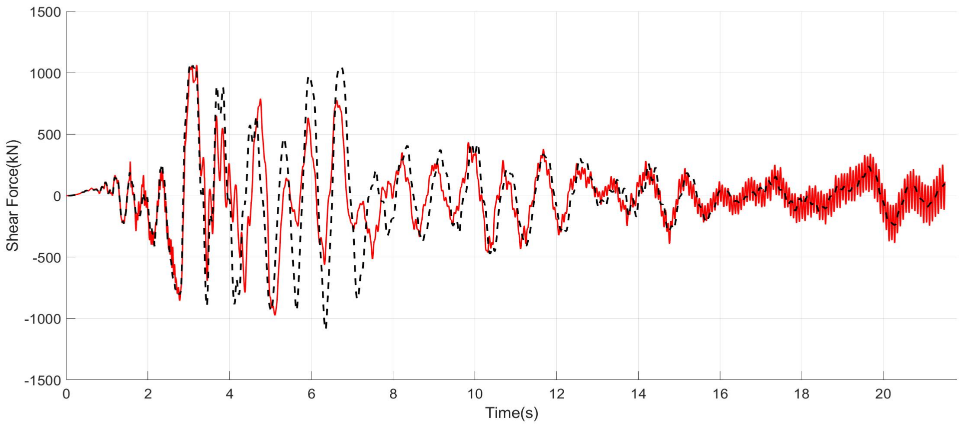

(b) Shear Forces at the base

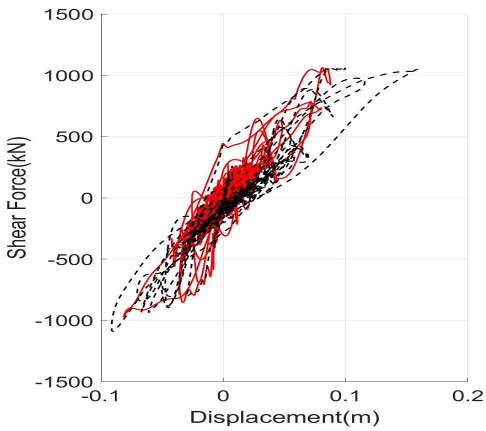

(c) Structural Hysteretic Curve

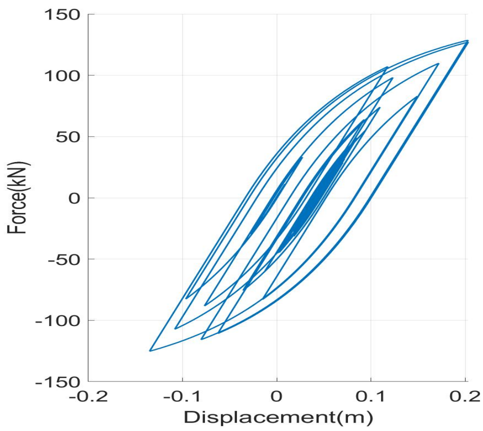

(d) TMD Hysteretic Curve

Figure B.129. Erzincan $f = 0.90$

Friulli

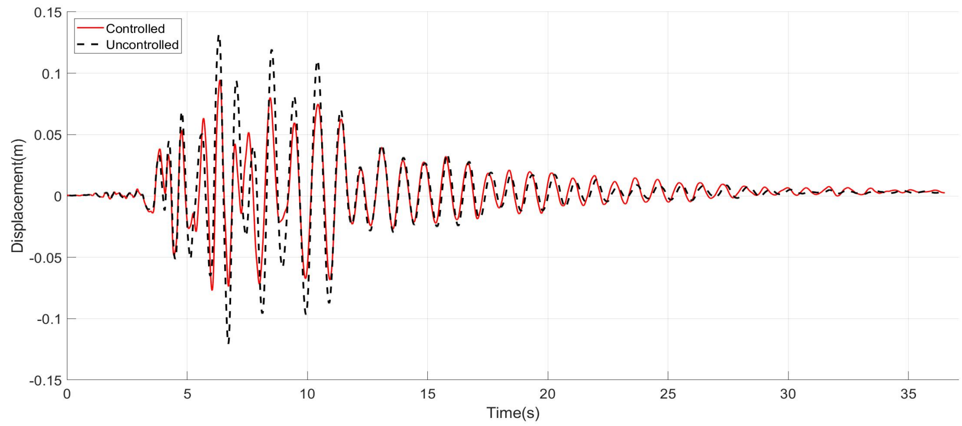

(a) Roof Displacements

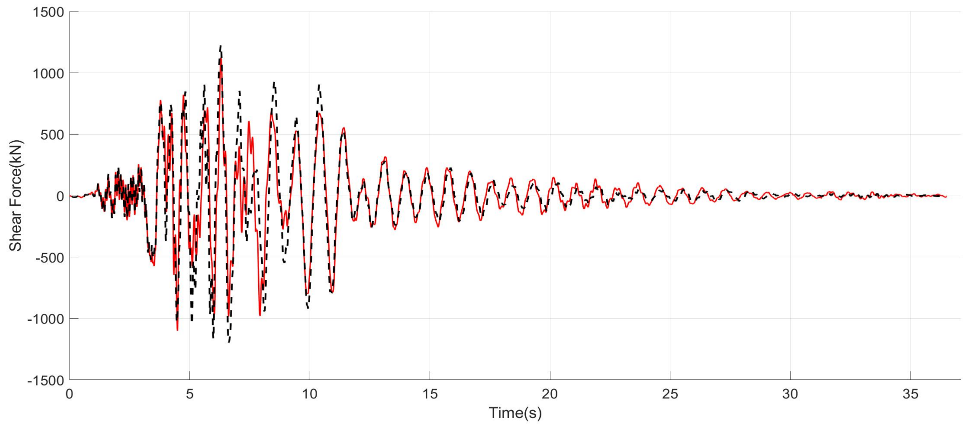

(b) Shear Forces at the base

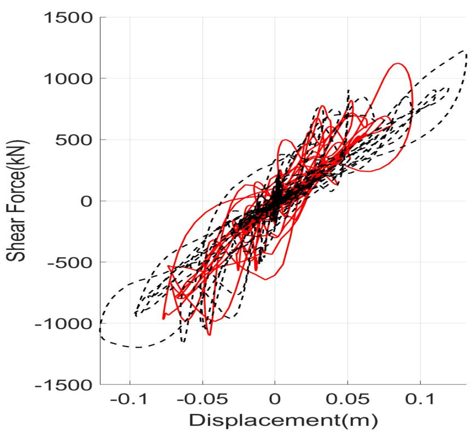

(c) Structural Hysteretic Curve

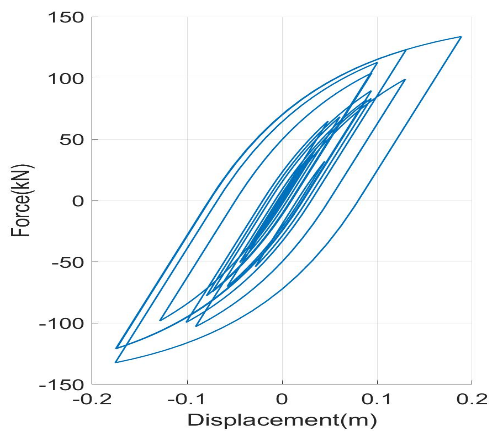

(d) TMD Hysteretic Curve

Figure B.130. Friulli $f = 0.90$

Imperial Valley

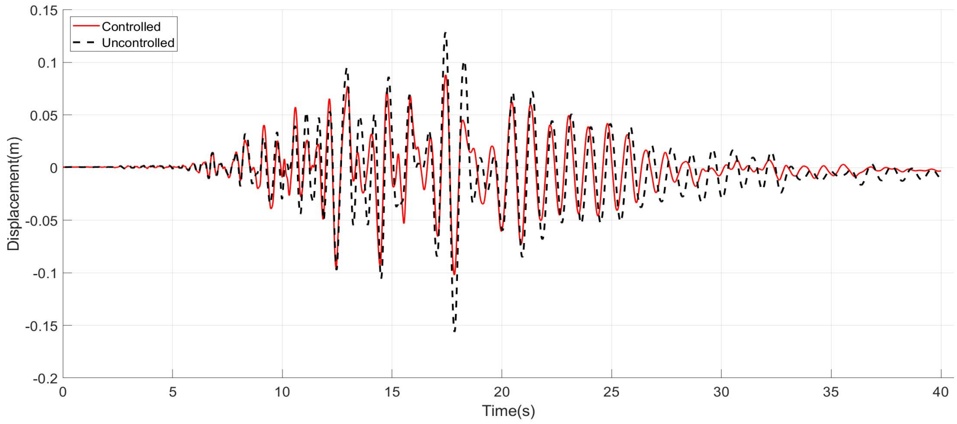

(a) Roof Displacements

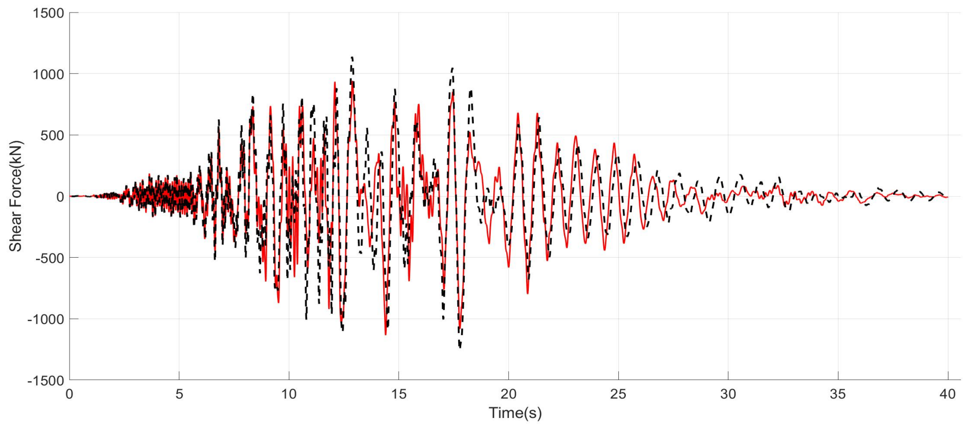

(b) Shear Forces at the base

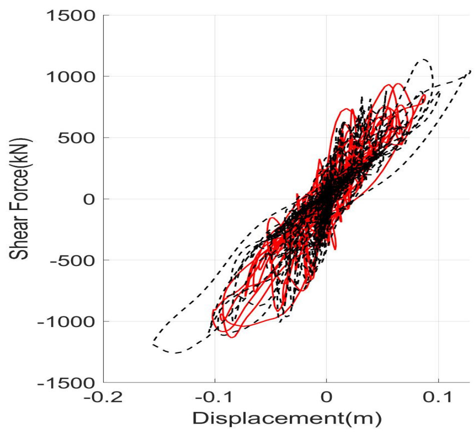

(c) Structural Hysteretic Curve

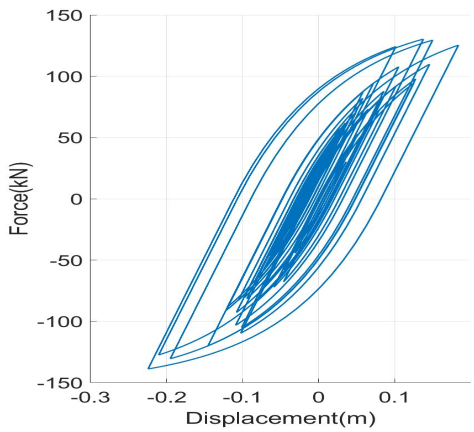

(d) TMD Hysteretic Curve

Figure B.131. Imperial Valley $f = 0.90$

Kobe

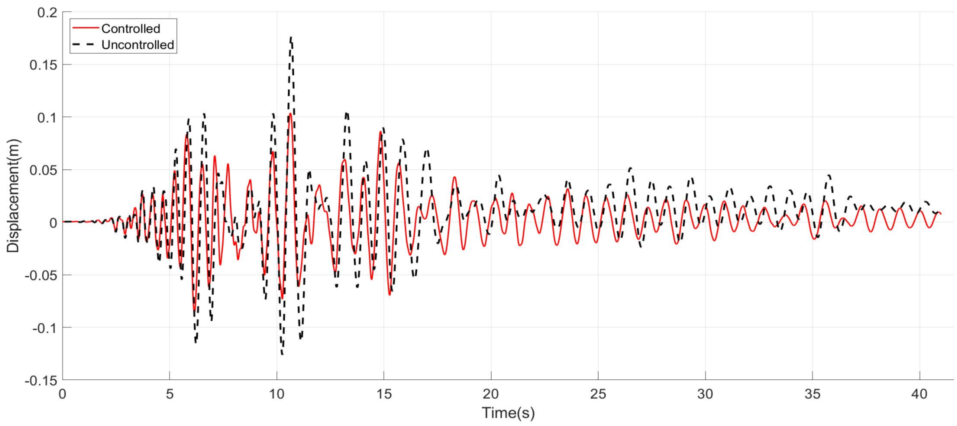

(a) Roof Displacements

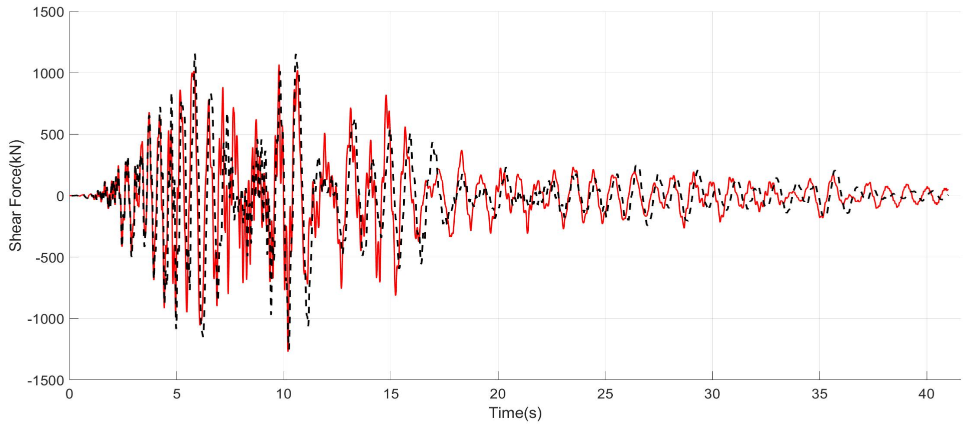

(b) Shear Forces at the base

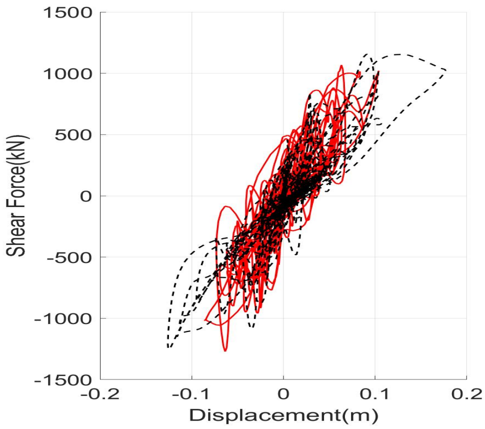

(c) Structural Hysteretic Curve

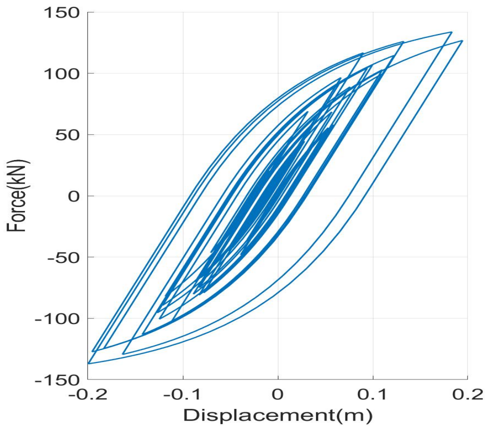

(d) TMD Hysteretic Curve

Figure B.132. Kobe $f = 0.90$

Loma Prieta

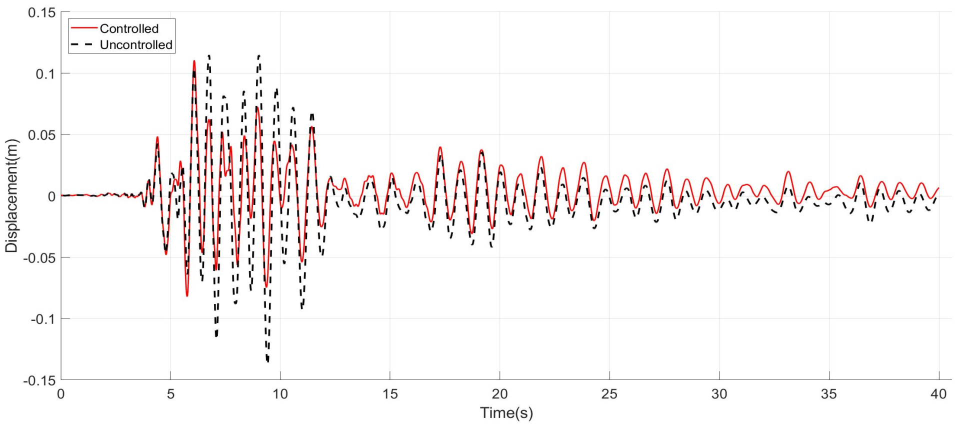

(a) Roof Displacements

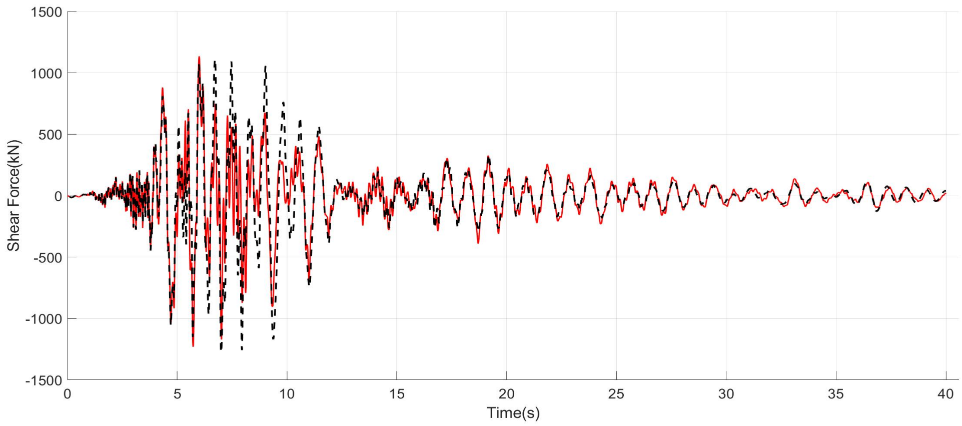

(b) Shear Forces at the base

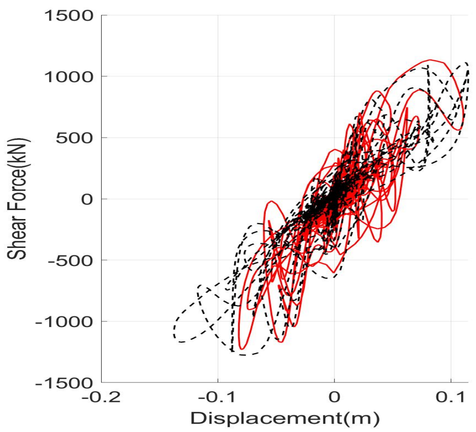

(c) Structural Hysteretic Curve

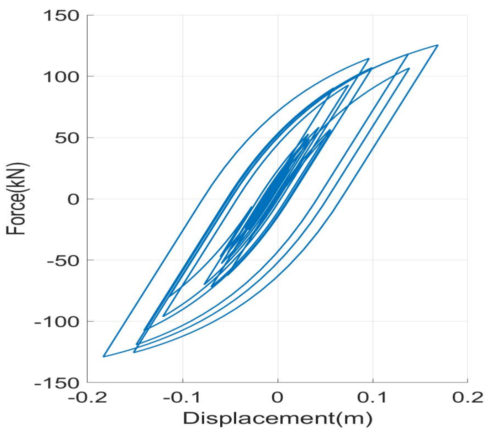

(d) TMD Hysteretic Curve

Figure B.133. Loma Prieta $f = 0.90$

Northridge

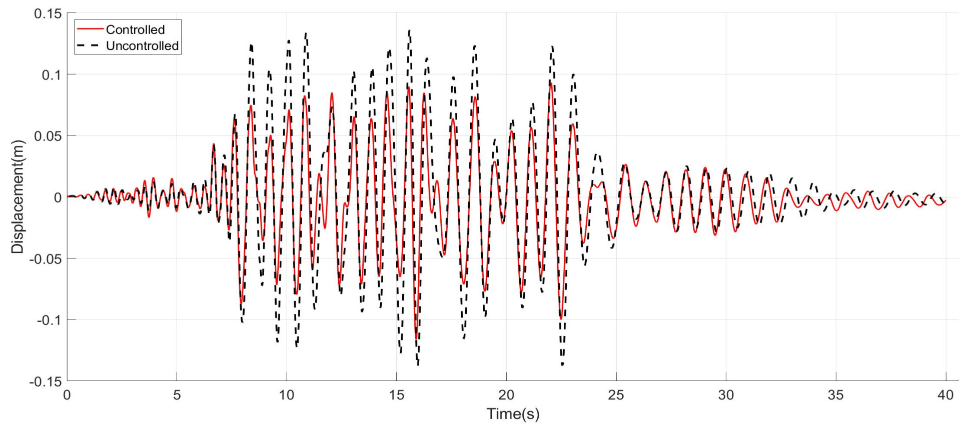

(a) Roof Displacements

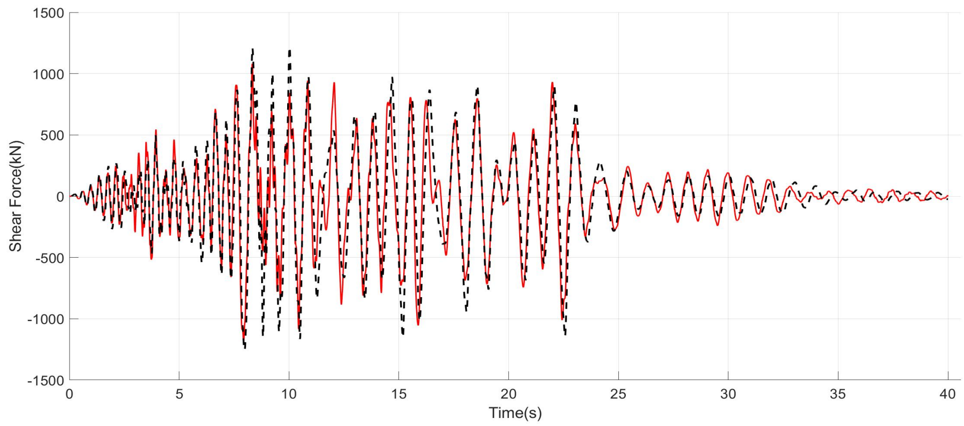

(b) Shear Forces at the base

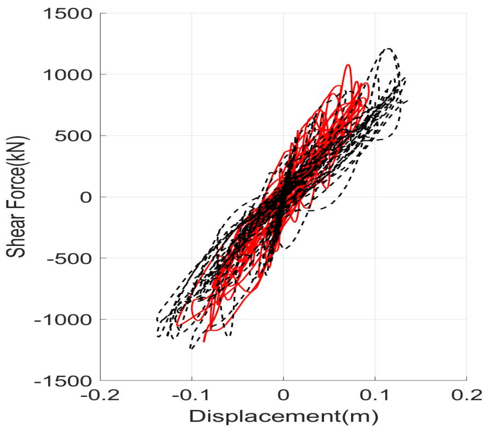

(c) Structural Hysteretic Curve

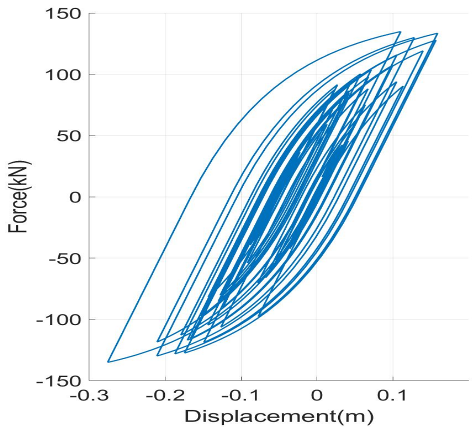

(d) TMD Hysteretic Curve

Figure B.134. Northridge $f = 0.90$

B.5.3 $f = 0.75$

Using a tuning frequency of 0.70 delivers the following results.

Table B.16. Performance Indices $f = 0.75$

Earthquake	Performance Index						
	J_1	J_2	J_3	J_4	J_5	J_6	J_7(m)
Chalfant	0.562	0.999	1.099	0.501	0.832	0.973	0.293
Chi-Chi	0.838	0.999	0.855	0.717	0.873	0.923	0.250
Erzincan	0.730	0.999	0.946	0.719	0.848	0.893	0.275
Friulli	0.749	0.942	0.991	0.722	0.916	0.947	0.232
Imperial Valley	0.818	1.037	1.062	0.819	0.935	0.969	0.229
Kobe	0.721	0.937	1.067	0.803	0.991	1.023	0.251
Loma Prieta	0.701	1.108	1.023	0.775	0.916	0.949	0.258
Northridge	0.905	0.977	0.902	0.656	0.814	0.808	0.265
Average	0.753	1.000	0.993	0.714	0.891	0.935	0.257

Chalfant

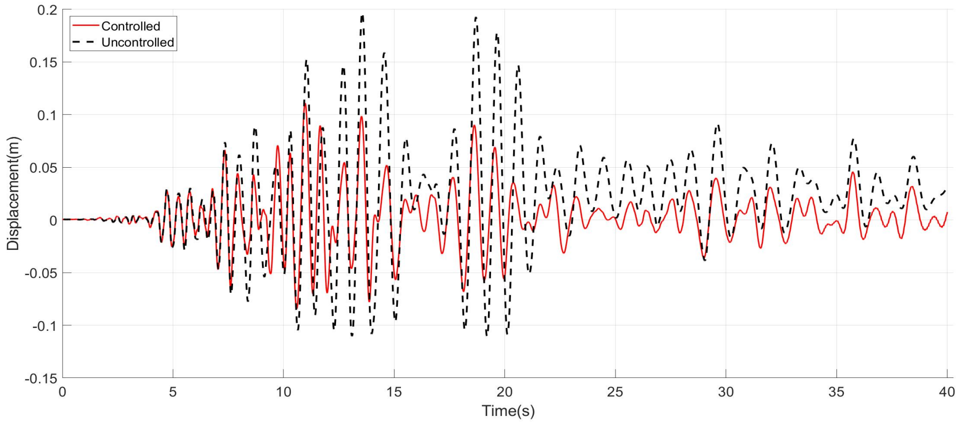

(a) Roof Displacements

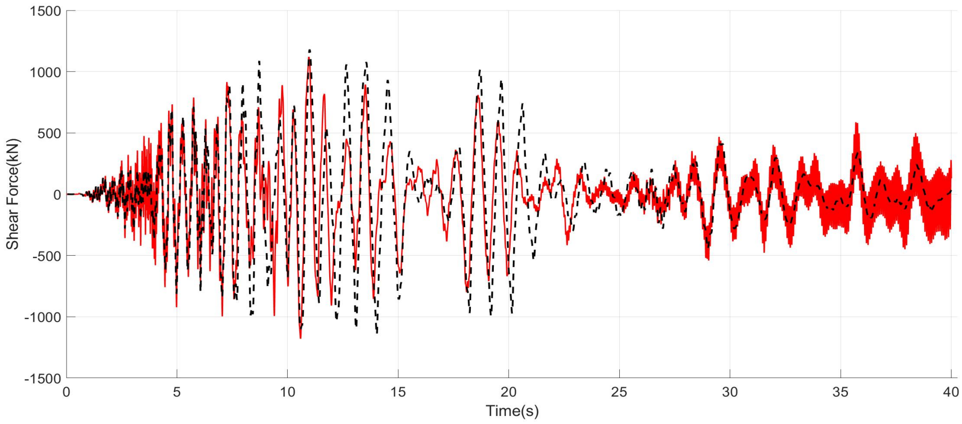

(b) Shear Forces at the base

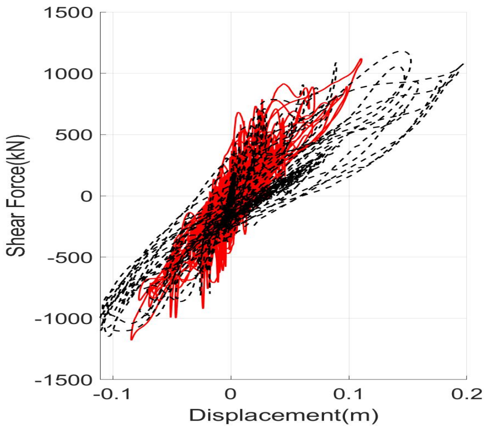

(c) Structural Hysteretic Curve

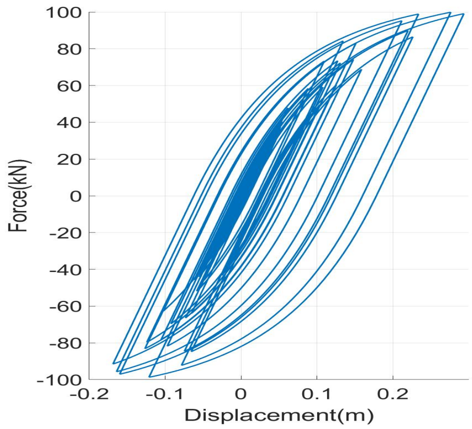

(d) TMD Hysteretic Curve

Figure B.135. Chalfant $f = 0.75$

Chi-Chi

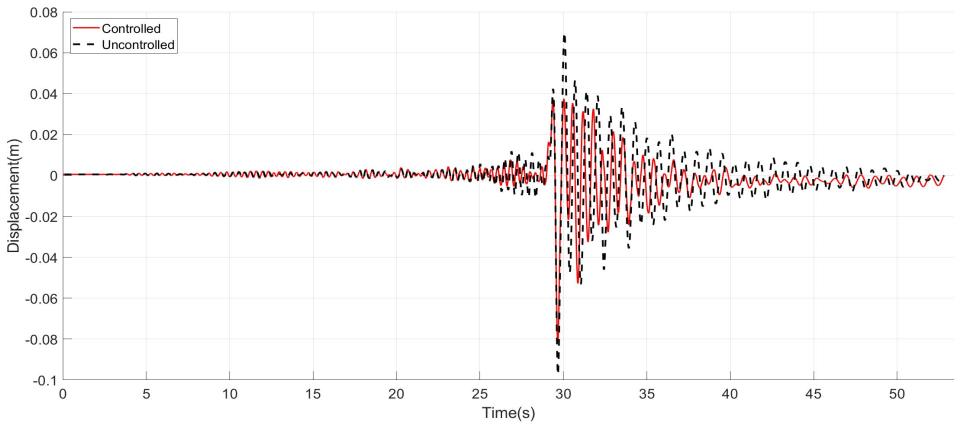

(a) Roof Displacements

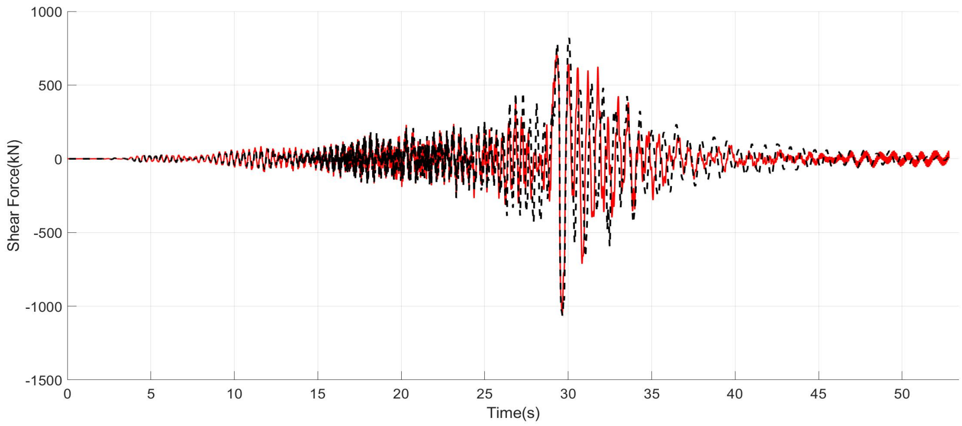

(b) Shear Forces at the base

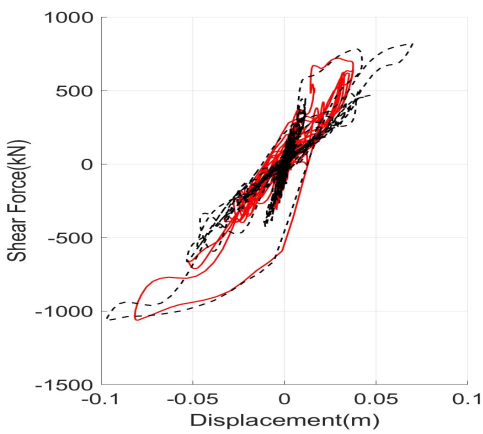

(c) Structural Hysteretic Curve

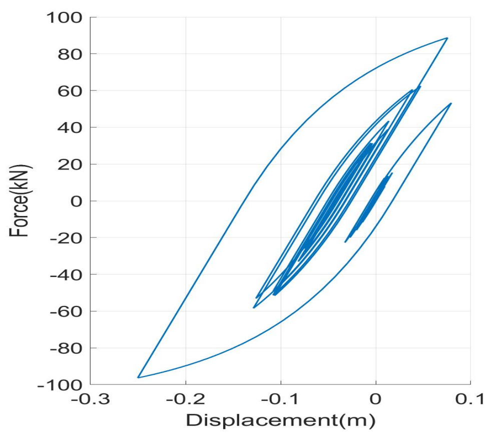

(d) TMD Hysteretic Curve

Figure B.136. Chi Chi $f = 0.75$

Erzincan

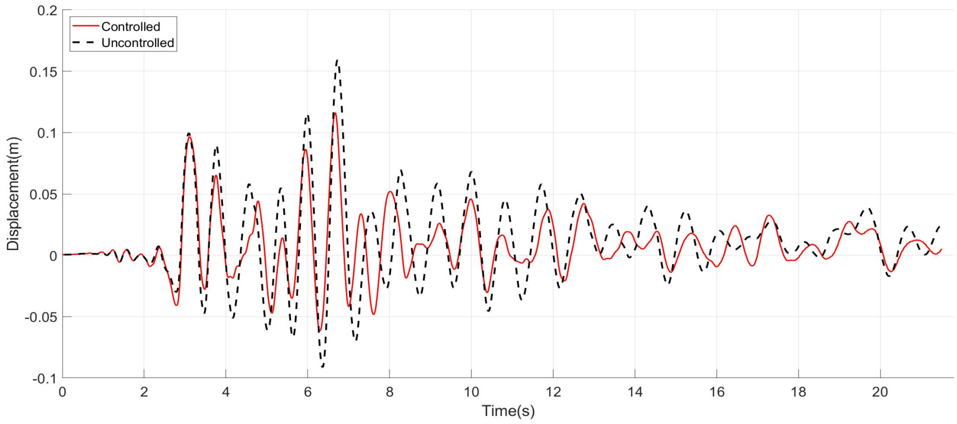

(a) Roof Displacements

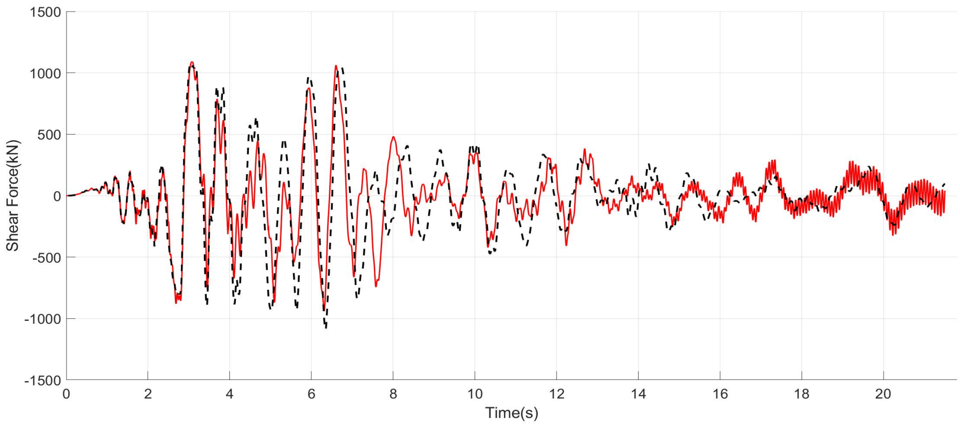

(b) Shear Forces at the base

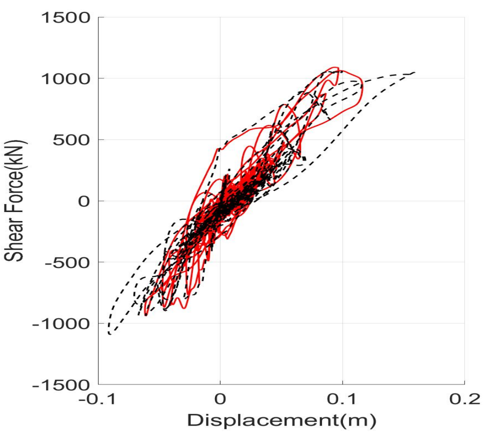

(c) Structural Hysteretic Curve

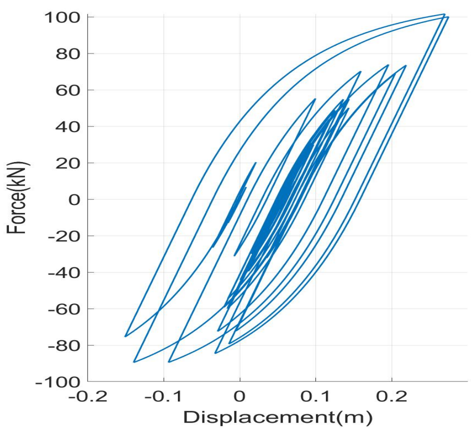

(d) TMD Hysteretic Curve

Figure B.137. Erzincan $f = 0.75$

Friulli

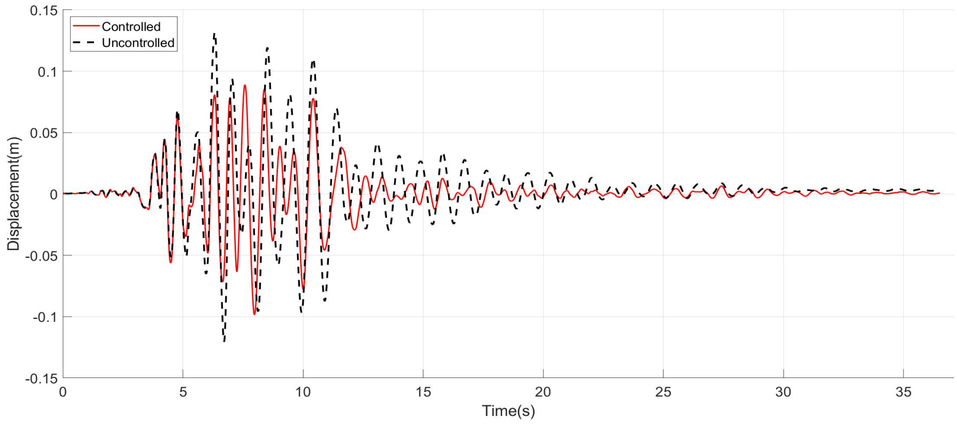

(a) Roof Displacements

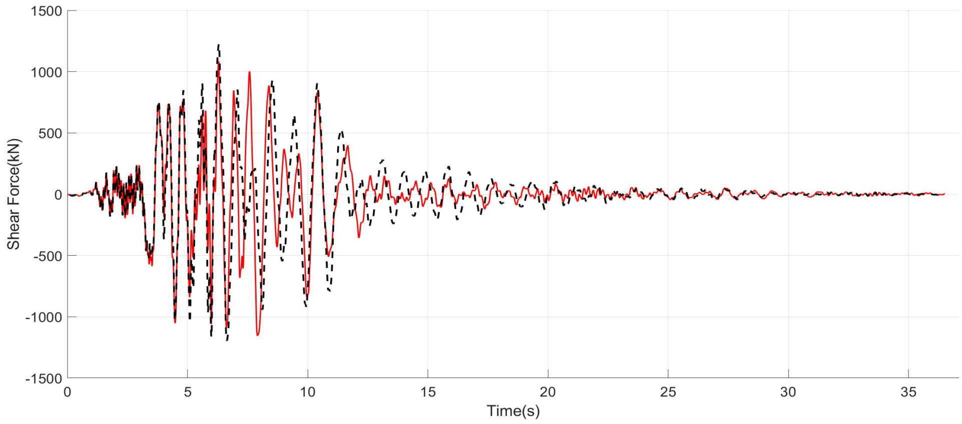

(b) Shear Forces at the base

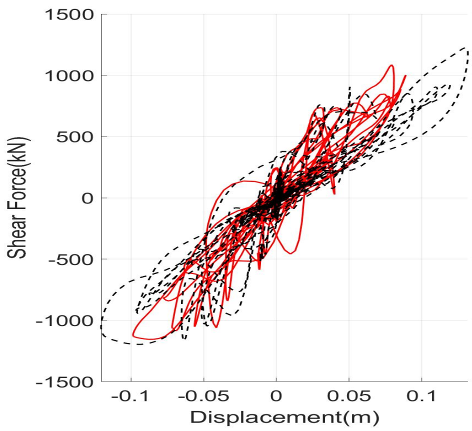

(c) Structural Hysteretic Curve

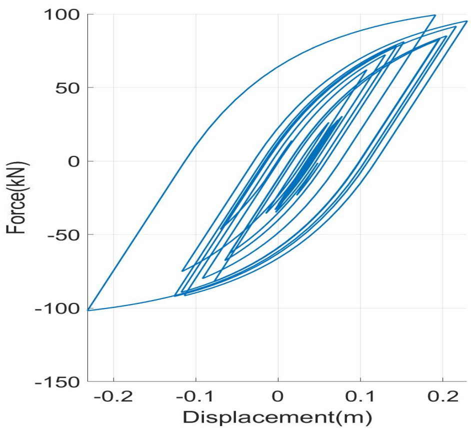

(d) TMD Hysteretic Curve

Figure B.138. Friulli $f = 0.75$

Imperial Valley

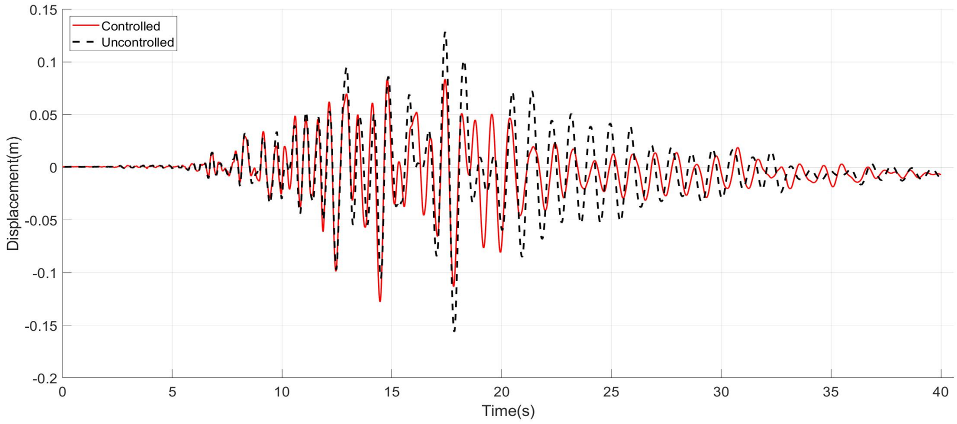

(a) Roof Displacements

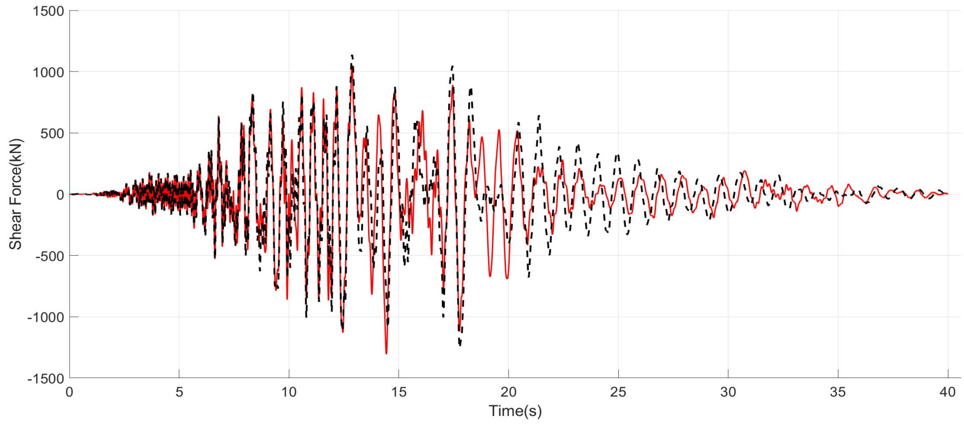

(b) Shear Forces at the base

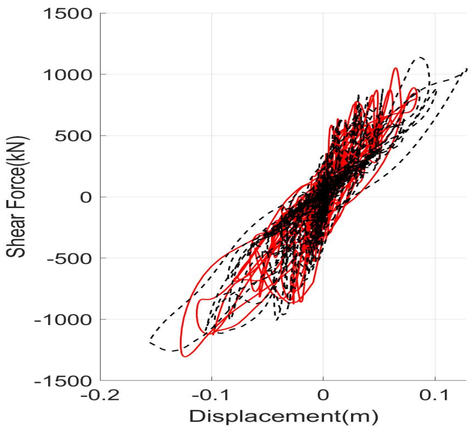

(c) Structural Hysteretic Curve

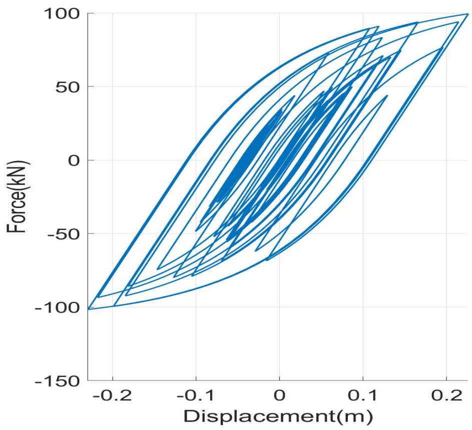

(d) TMD Hysteretic Curve

Figure B.139. Imperial Valley $f = 0.75$

Kobe

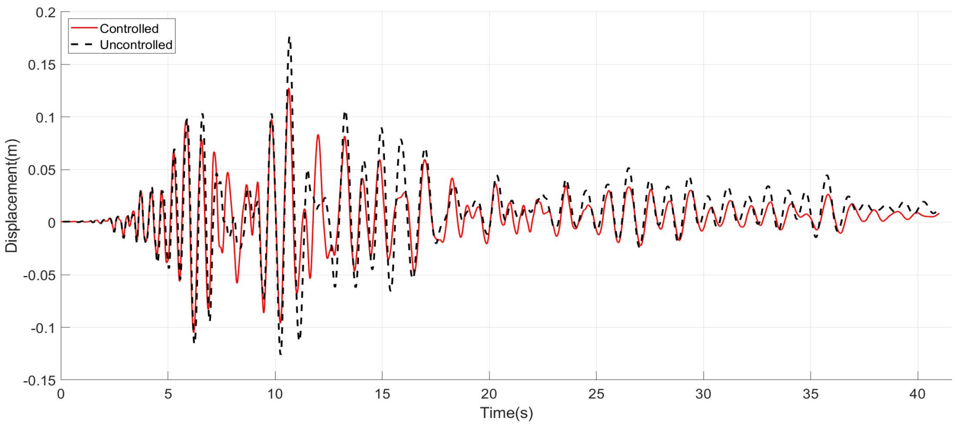

(a) Roof Displacements

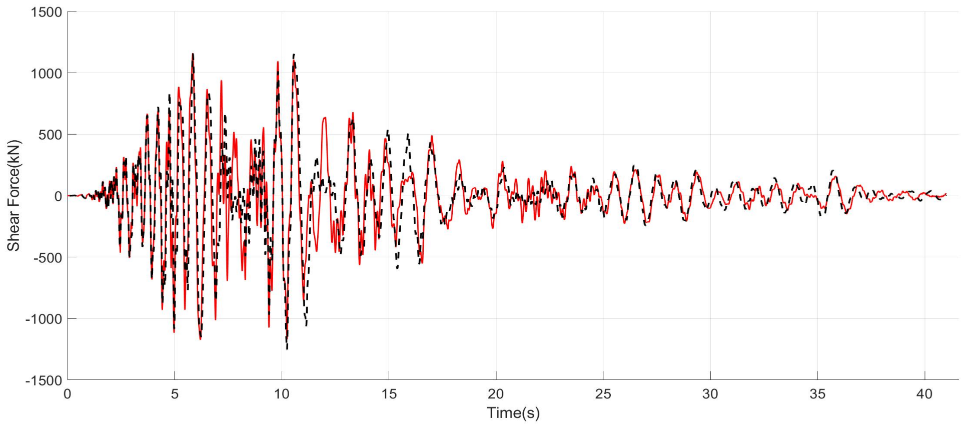

(b) Shear Forces at the base

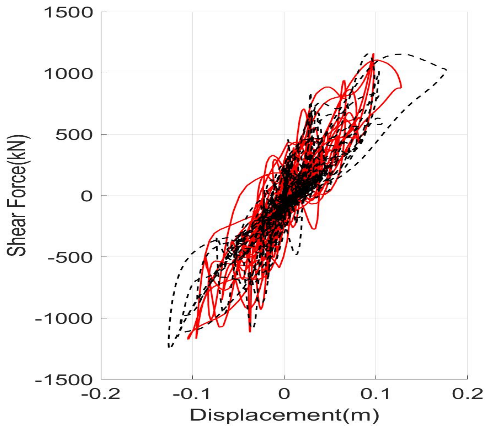

(c) Structural Hysteretic Curve

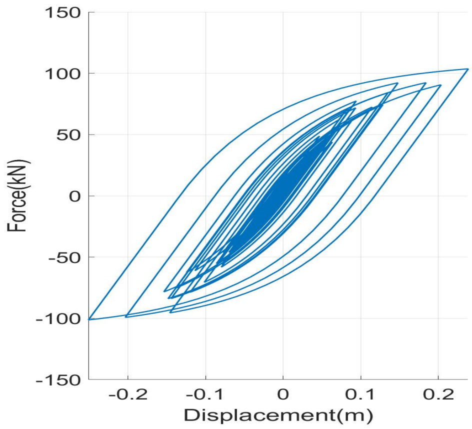

(d) TMD Hysteretic Curve

Figure B.140. Kobe $f = 0.75$

Loma Prieta

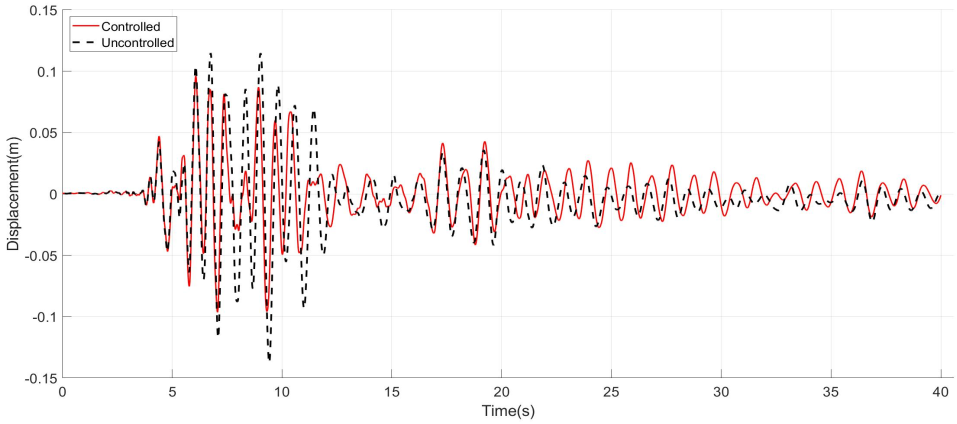

(a) Roof Displacements

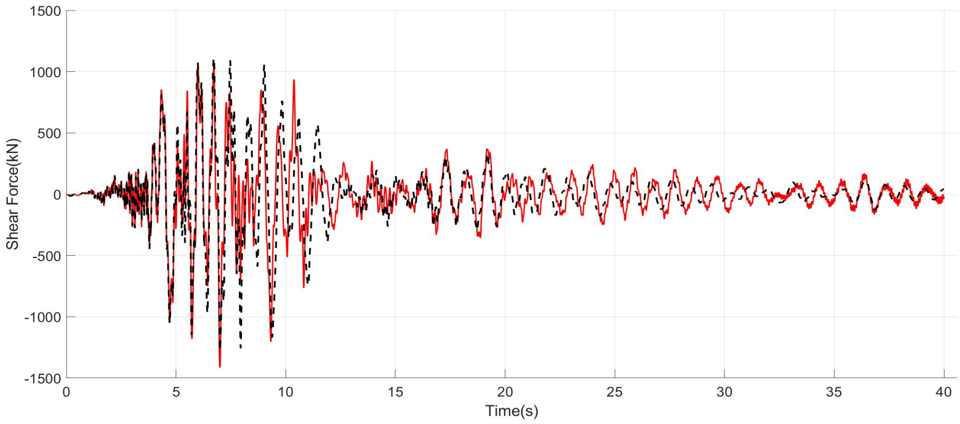

(b) Shear Forces at the base

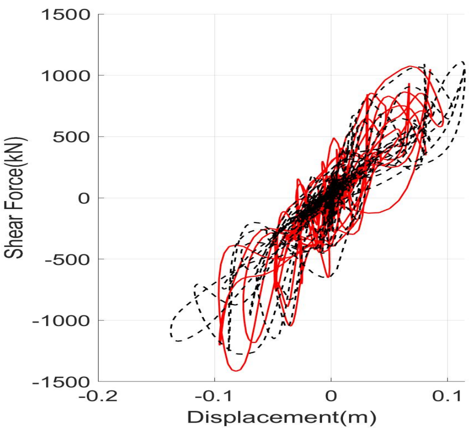

(c) Structural Hysteretic Curve

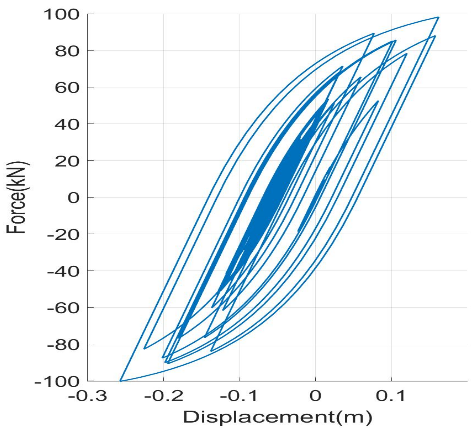

(d) TMD Hysteretic Curve

Figure B.141. Loma Prieta $f = 0.75$

Northridge

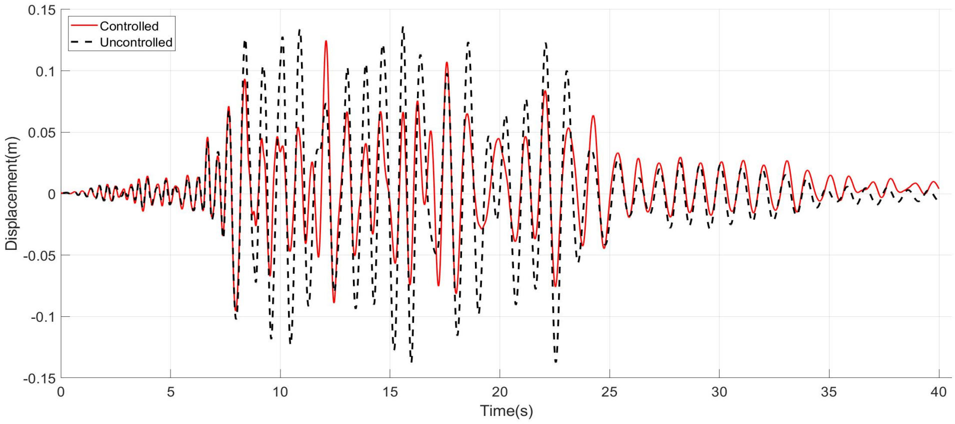

(a) Roof Displacements

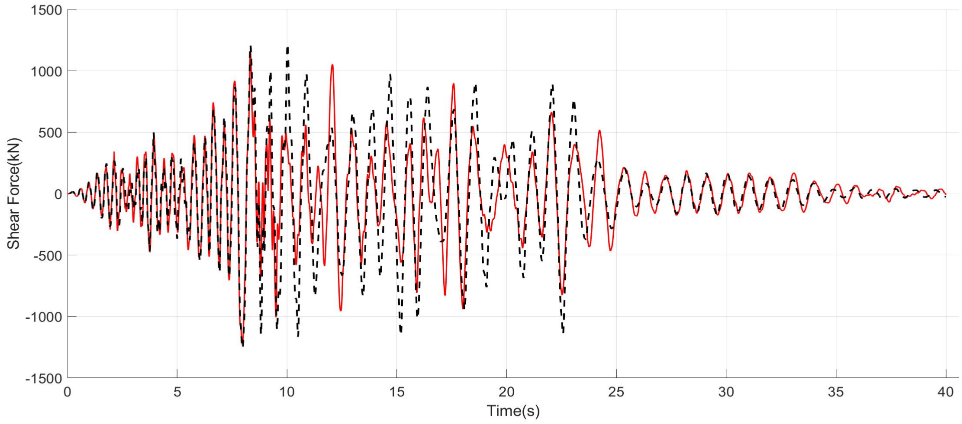

(b) Shear Forces at the base

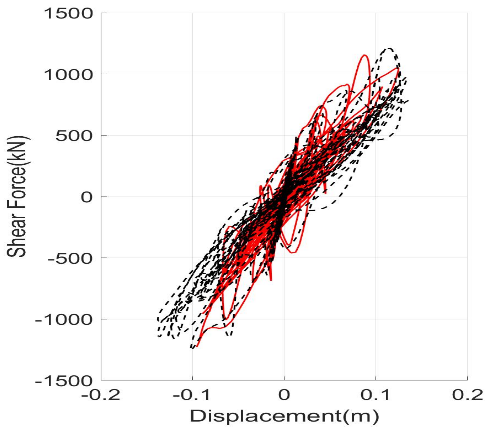

(c) Structural Hysteretic Curve

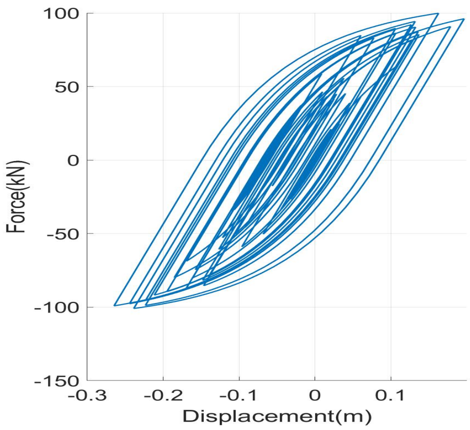

(d) TMD Hysteretic Curve

Figure B.142. Northridge $f = 0.75$

Drifts

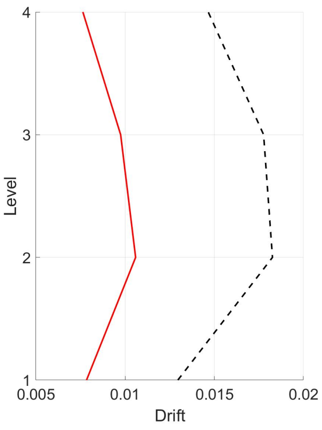

(a) Chalfant

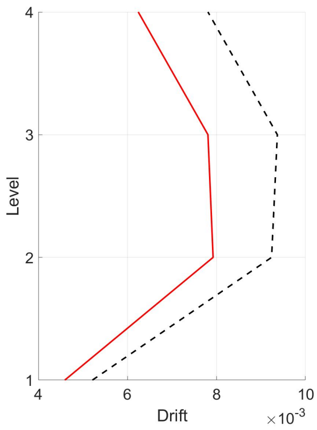

(b) Chi Chi

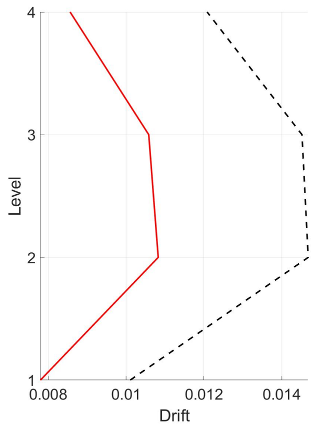

(c) Erzincan

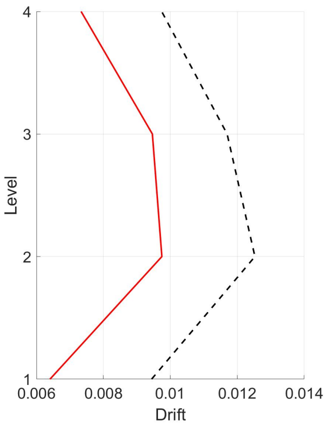

(d) Friulli

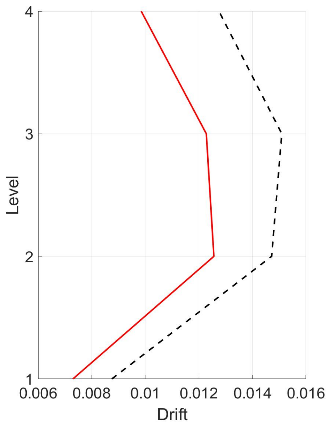

(e) Imperial Valley

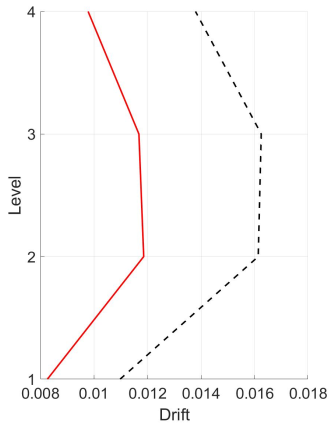

(f) Kobe

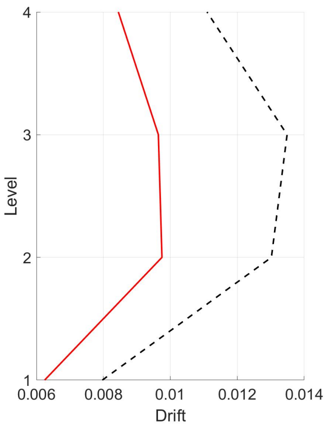

(g) Loma Prieta

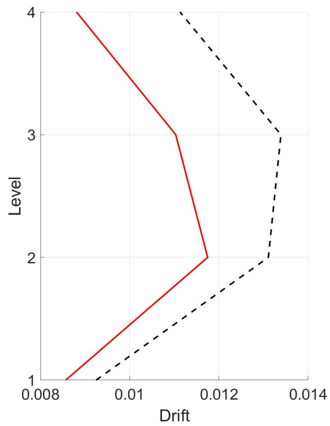

(h) Northridge

Figure B.143. Drifts $f = 0.75$

Drifts

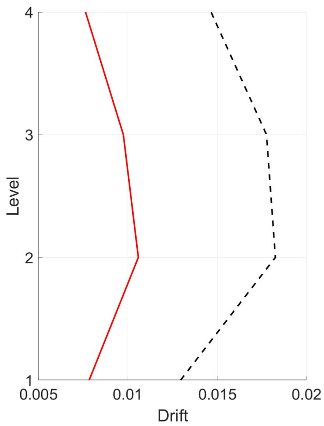

(a) Chalfant

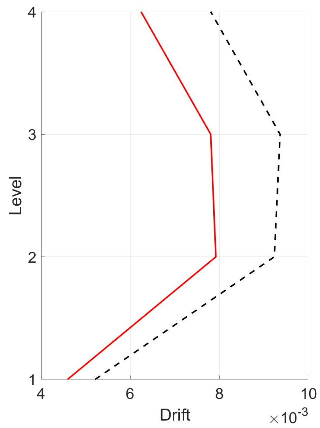

(b) Chi Chi

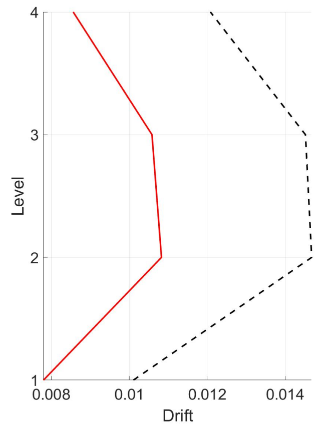

(c) Erzincan

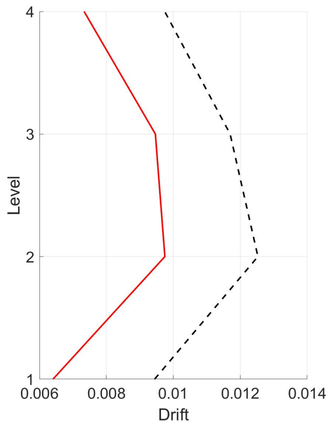

(d) Friulli

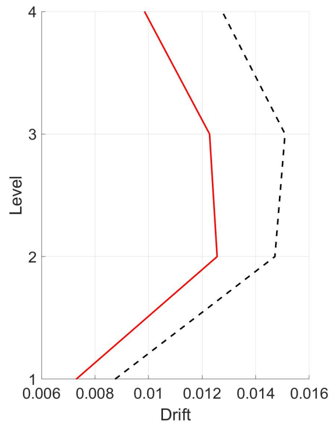

(e) Imperial Valley

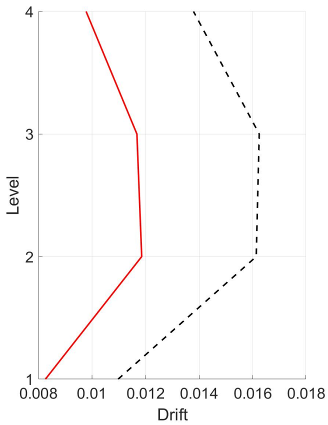

(f) Kobe

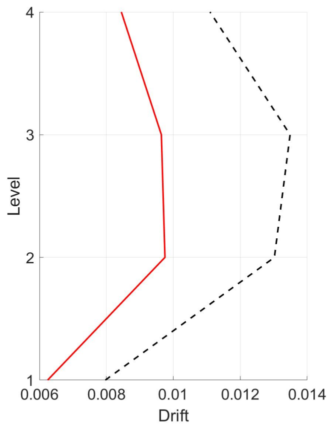

(g) Loma Prieta

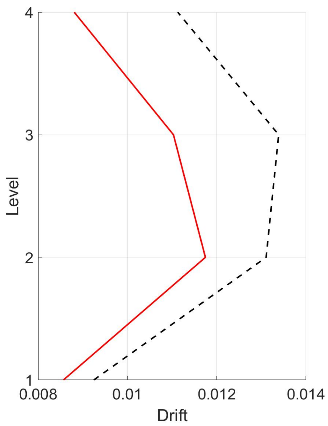

(h) Northridge

Figure B.144. Drifts $f = 0.75$

B.5.4 $f = 0.86$

Using a tuning frequency of 0.86 delivers the following results.

Table B.17. Performance Indices $f = 0.86$

Earthquake	Performance Index						
	J_1	J_2	J_3	J_4	J_5	J_6	J_7(m)
Chalfant	0.535	1.199	1.022	0.546	0.877	0.922	0.244
Chi-Chi	0.824	0.962	0.885	0.593	0.765	0.790	0.216
Erzincan	0.595	1.045	0.939	0.626	0.817	0.868	0.236
Friulli	0.694	0.971	1.054	0.701	0.894	0.911	0.222
Imperial Valley	0.673	0.970	0.999	0.750	0.923	0.948	0.219
Kobe	0.638	0.983	1.174	0.726	0.990	1.033	0.223
Loma Prieta	0.773	1.006	0.966	0.697	0.839	0.876	0.202
Northridge	0.734	0.962	0.903	0.641	0.834	0.804	0.287
Average	0.683	1.012	0.993	0.660	0.867	0.894	0.231

Chalfant

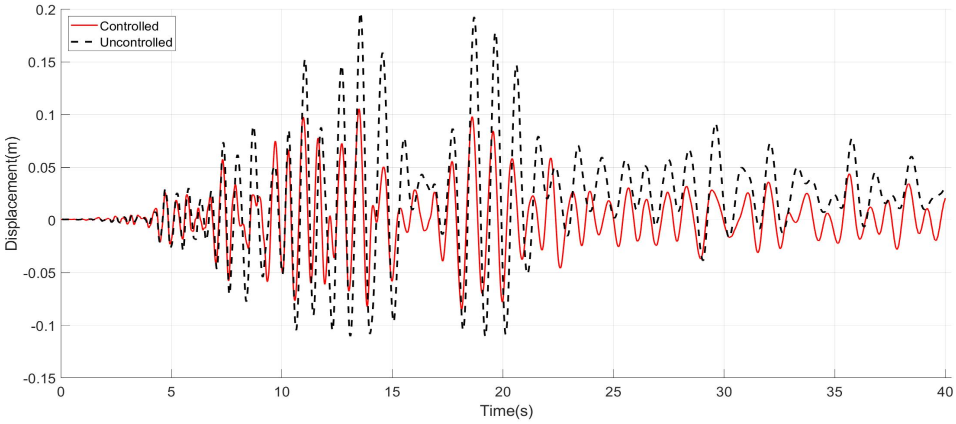

(a) Roof Displacements

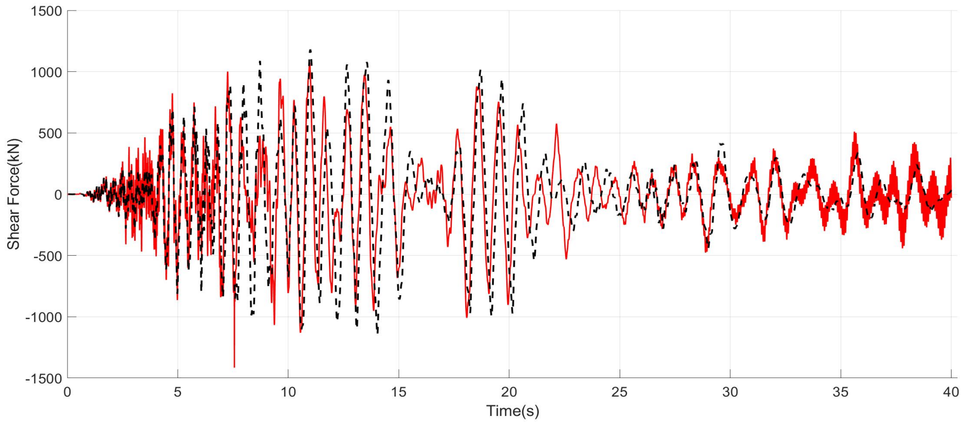

(b) Shear Forces at the base

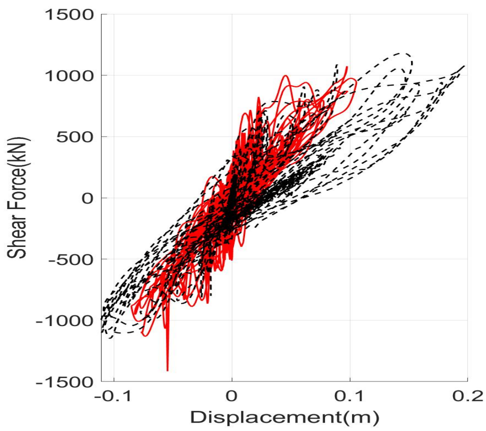

(c) Structural Hysteretic Curve

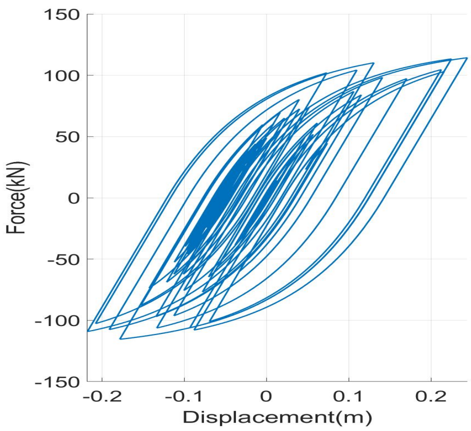

(d) TMD Hysteretic Curve

Figure B.145. Chalfant $f = 0.86$

Chi-Chi

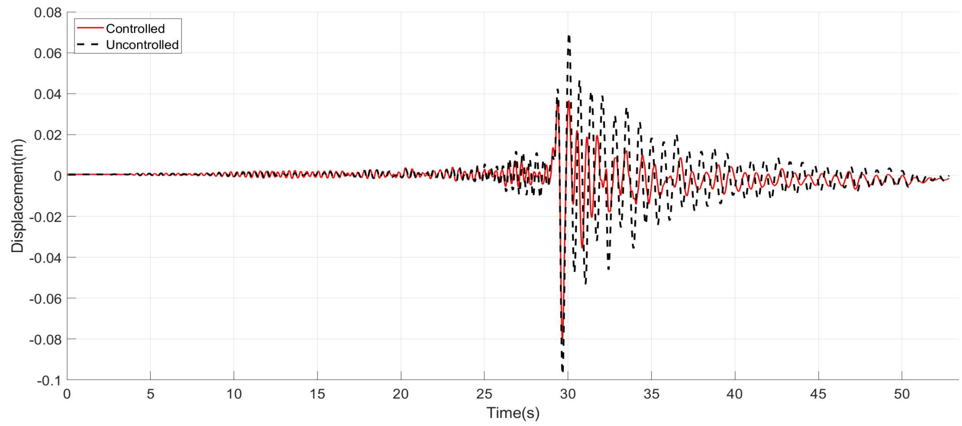

(a) Roof Displacements

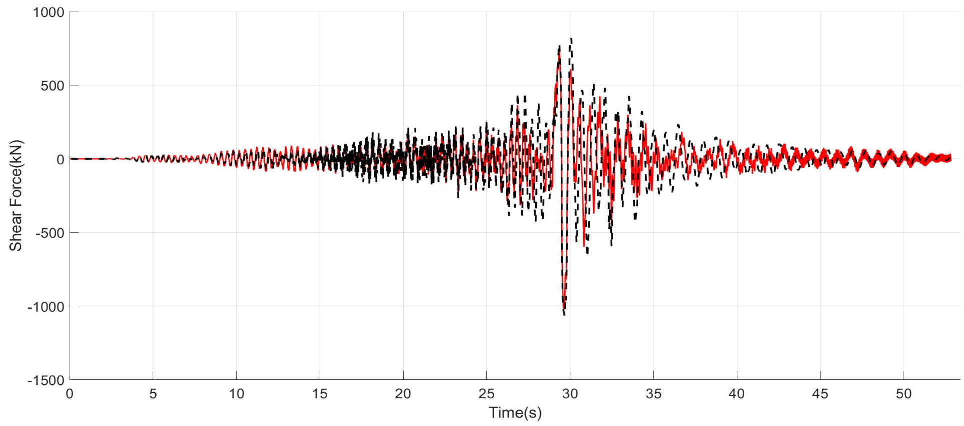

(b) Shear Forces at the base

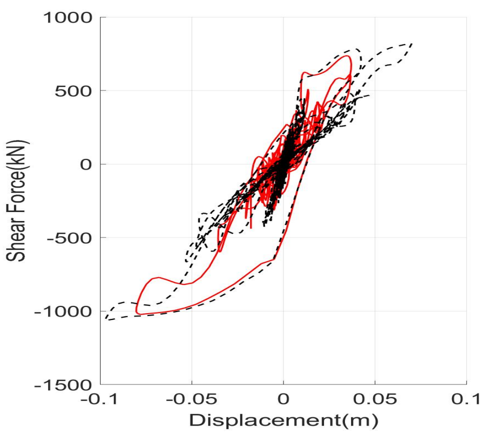

(c) Structural Hysteretic Curve

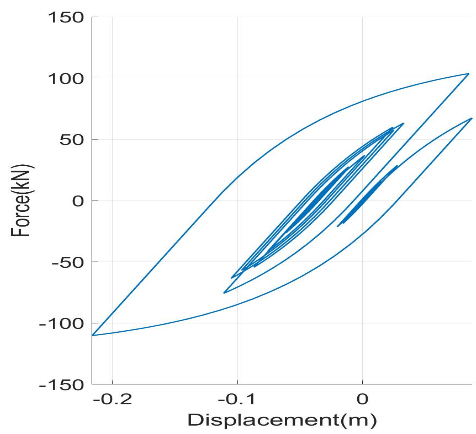

(d) TMD Hysteretic Curve

Figure B.146. Chi Chi $f = 0.86$

Erzincan

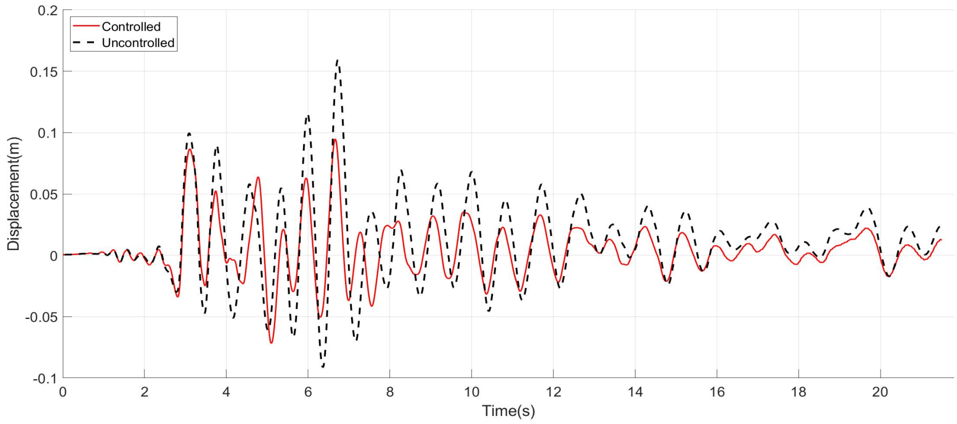

(a) Roof Displacements

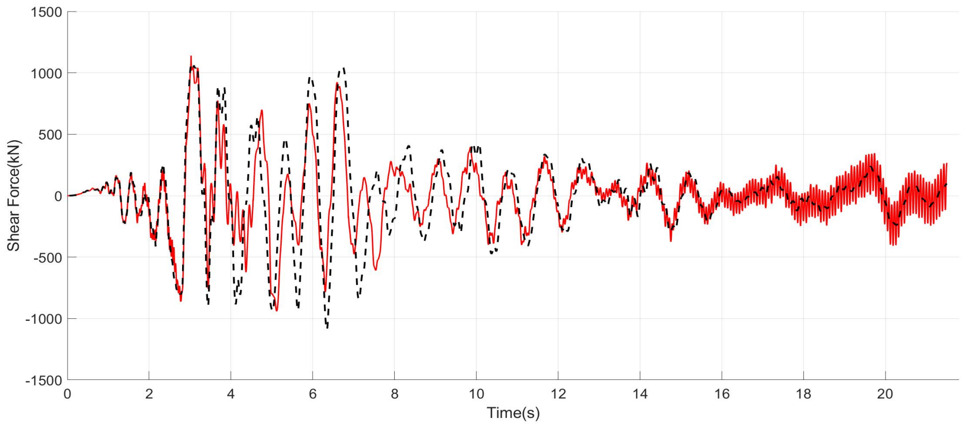

(b) Shear Forces at the base

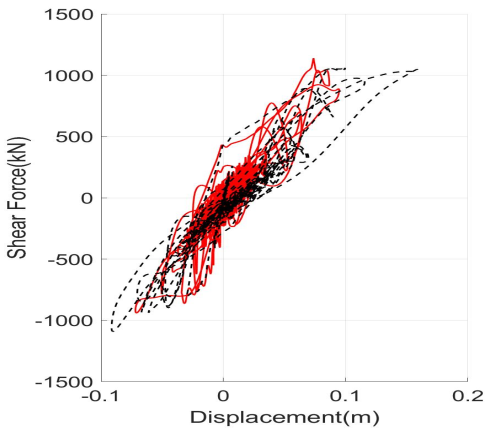

(c) Structural Hysteretic Curve

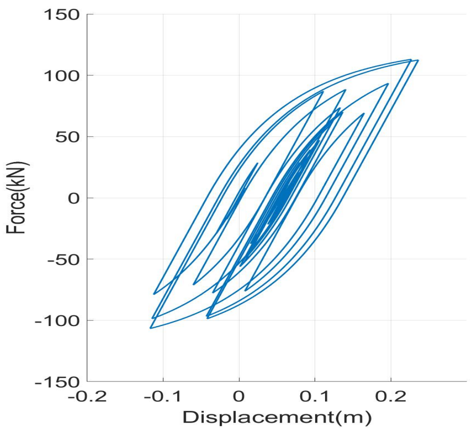

(d) TMD Hysteretic Curve

Figure B.147. Erzincan $f = 0.86$

Friulli

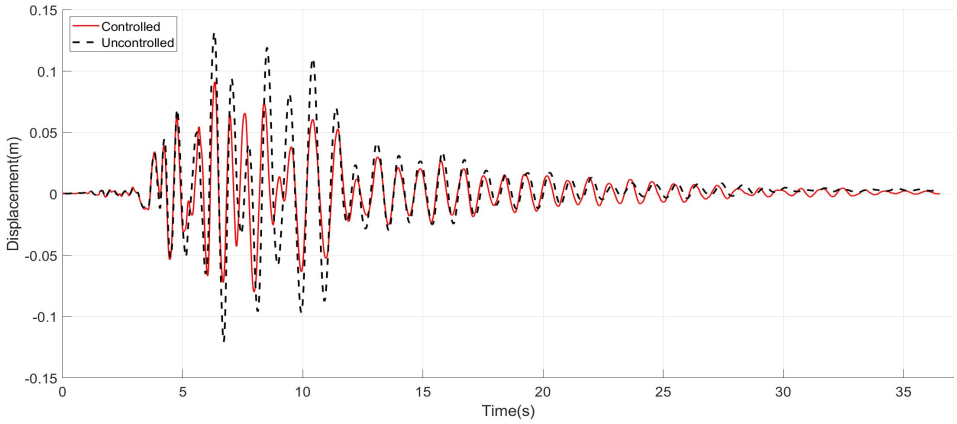

(a) Roof Displacements

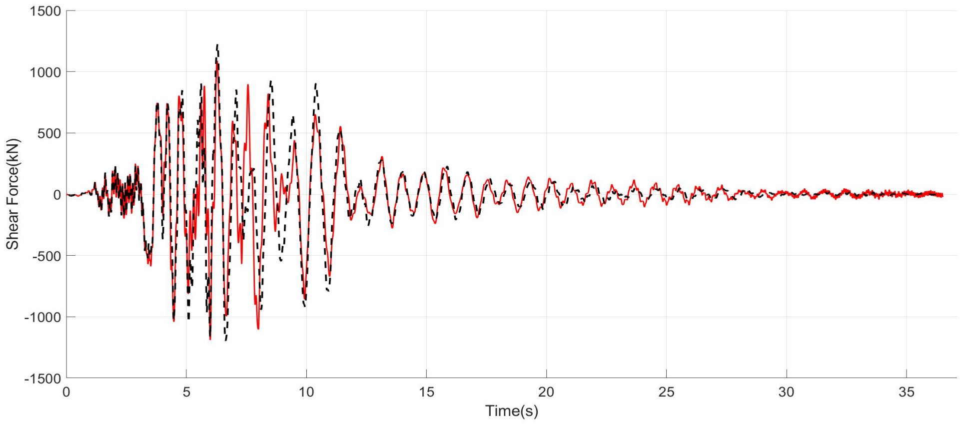

(b) Shear Forces at the base

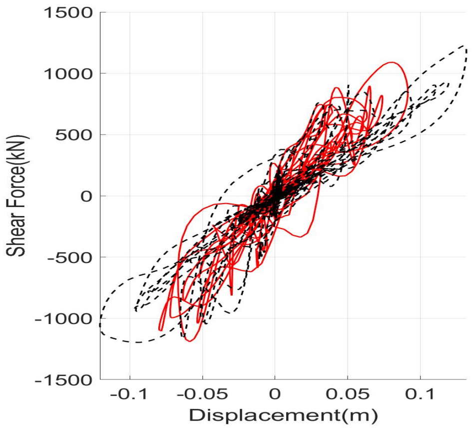

(c) Structural Hysteretic Curve

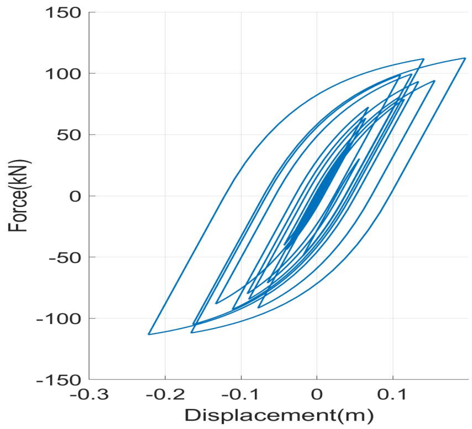

(d) TMD Hysteretic Curve

Figure B.148. Friulli $f = 0.86$

Imperial Valley

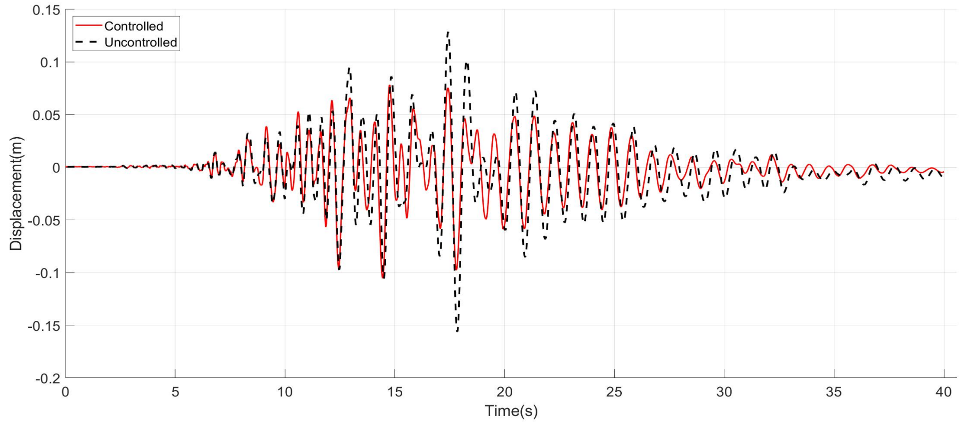

(a) Roof Displacements

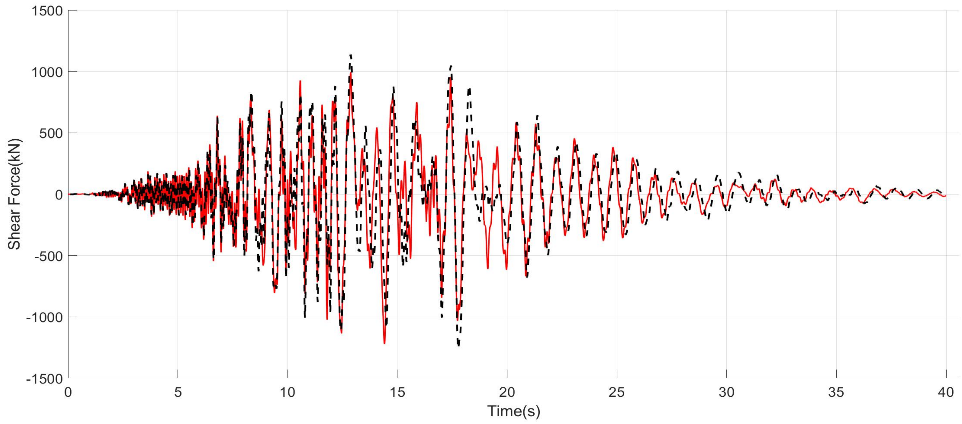

(b) Shear Forces at the base

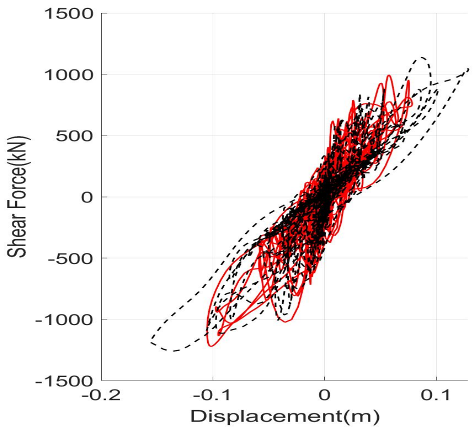

(c) Structural Hysteretic Curve

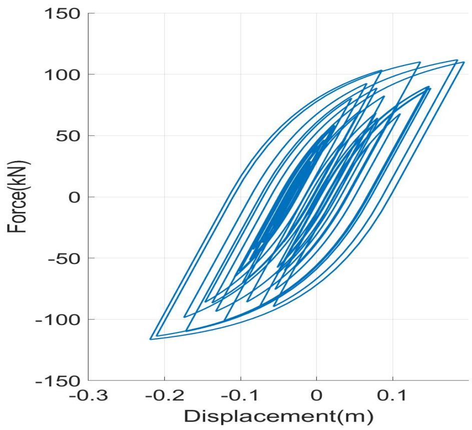

(d) TMD Hysteretic Curve

Figure B.149. Imperial Valley $f = 0.86$

Kobe

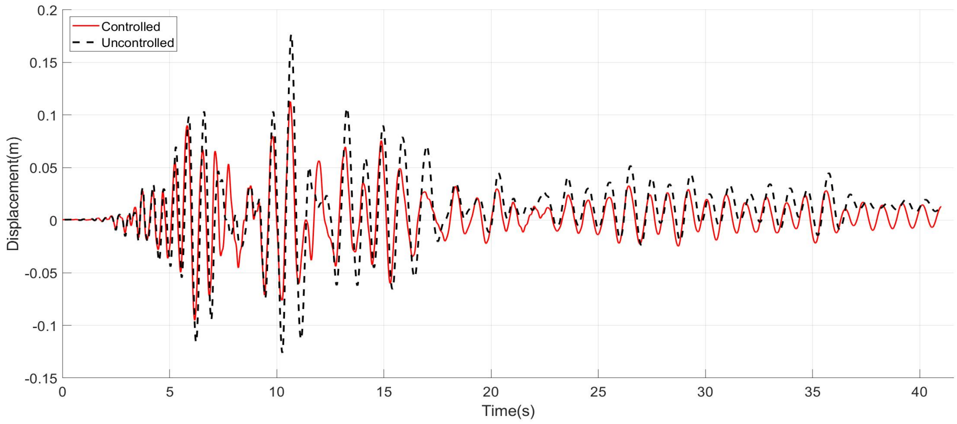

(a) Roof Displacements

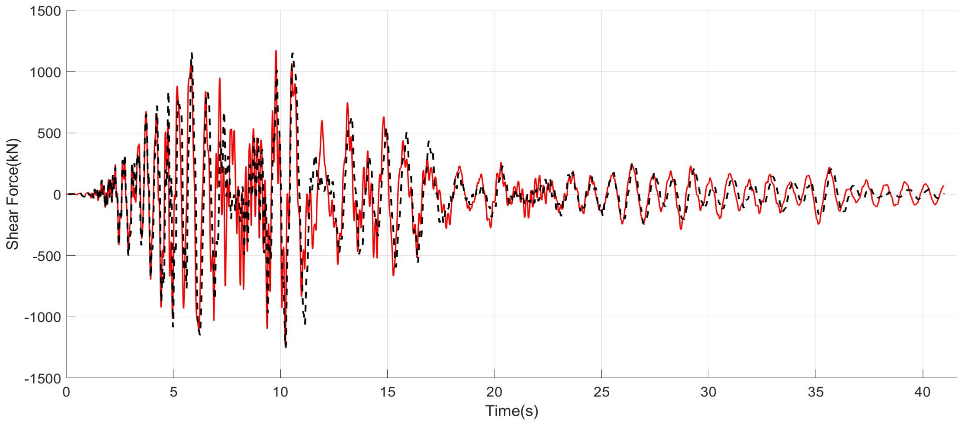

(b) Shear Forces at the base

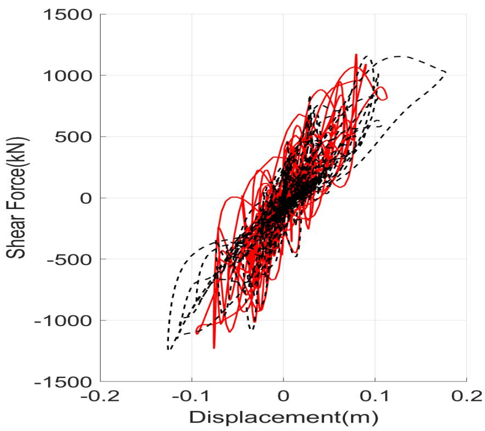

(c) Structural Hysteretic Curve

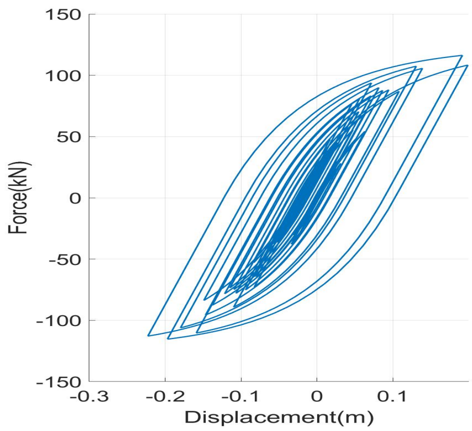

(d) TMD Hysteretic Curve

Figure B.150. Kobe $f = 0.86$

Loma Prieta

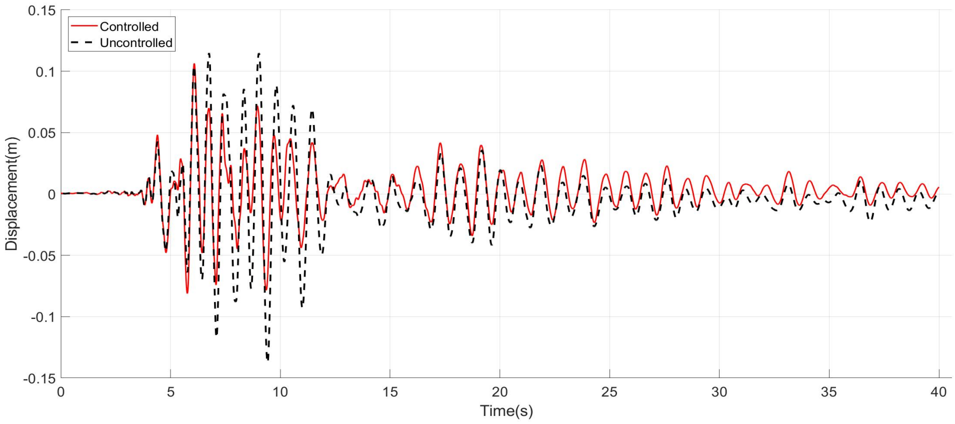

(a) Roof Displacements

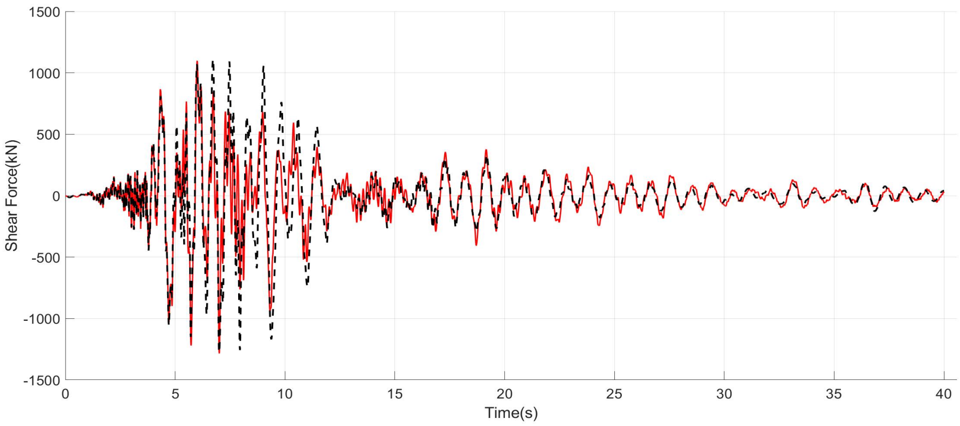

(b) Shear Forces at the base

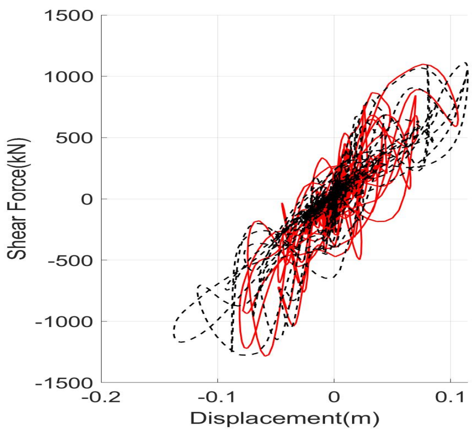

(c) Structural Hysteretic Curve

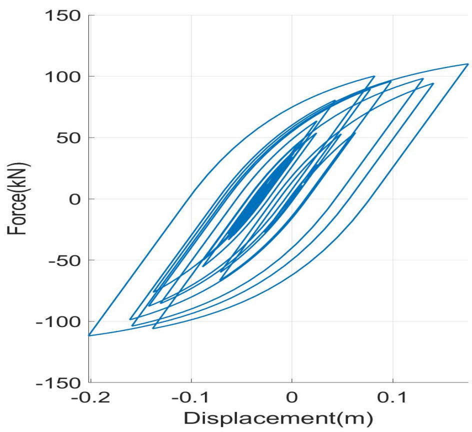

(d) TMD Hysteretic Curve

Figure B.151. Loma Prieta $f = 0.86$

Northridge

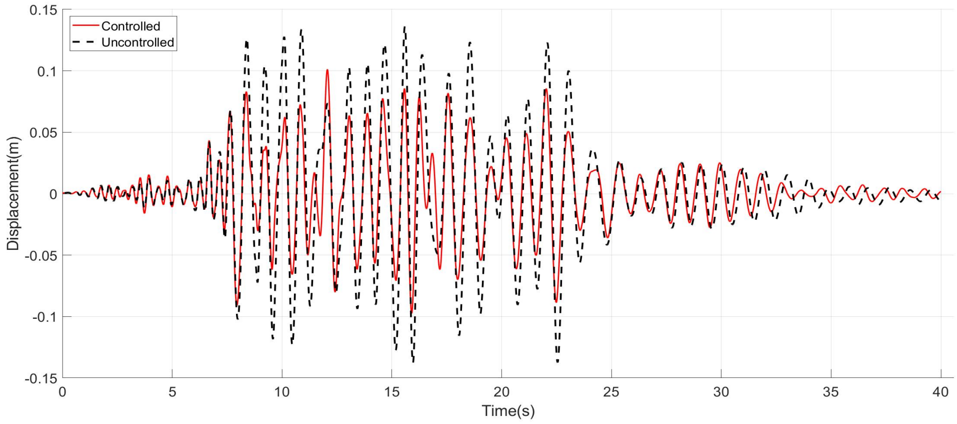

(a) Roof Displacements

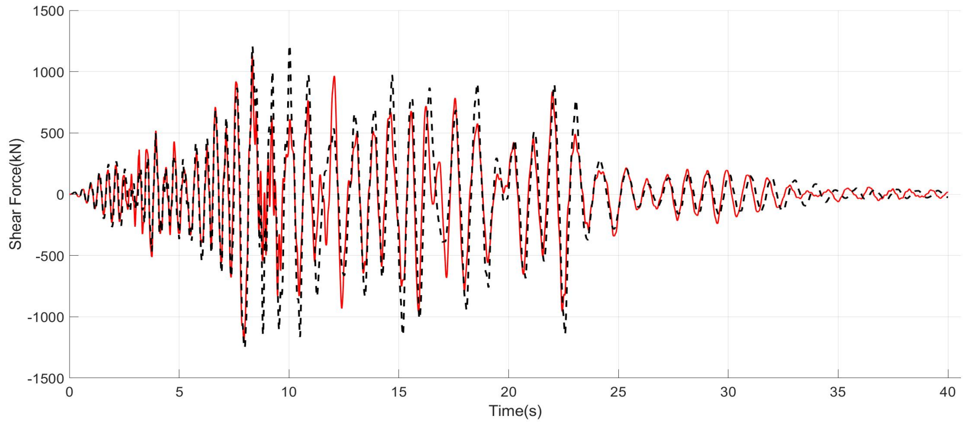

(b) Shear Forces at the base

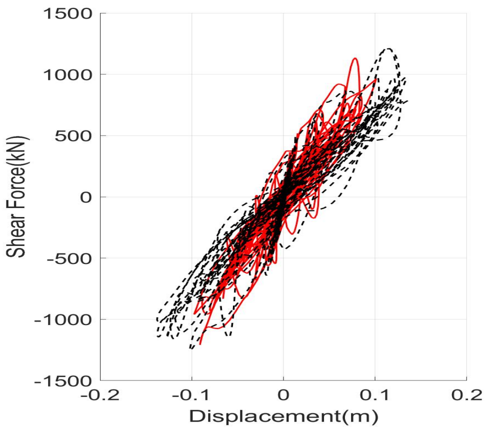

(c) Structural Hysteretic Curve

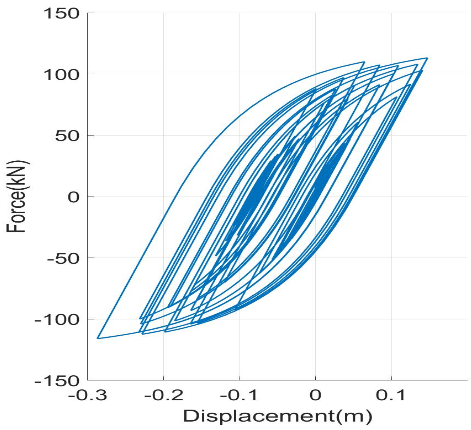

(d) TMD Hysteretic Curve

Figure B.152. Northridge $f = 0.86$

Drifts

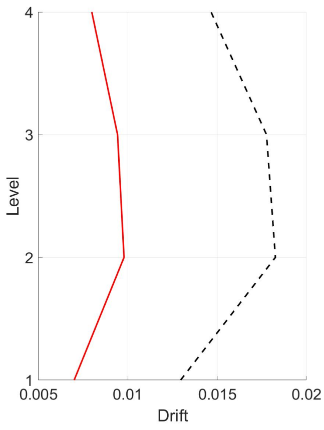

(a) Chalfant

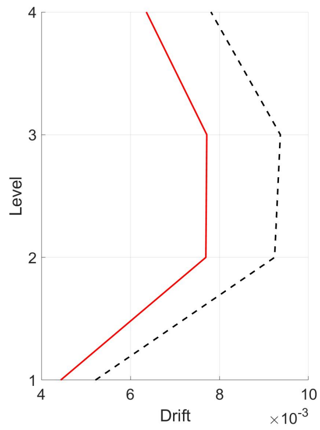

(b) Chi Chi

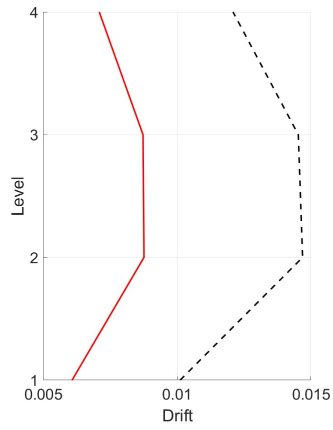

(c) Erzincan

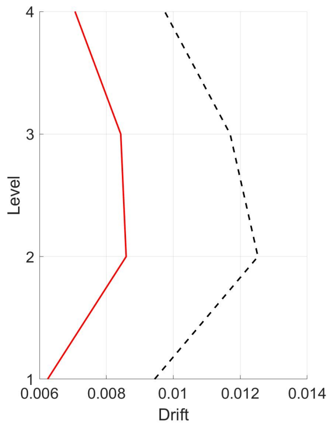

(d) Friulli

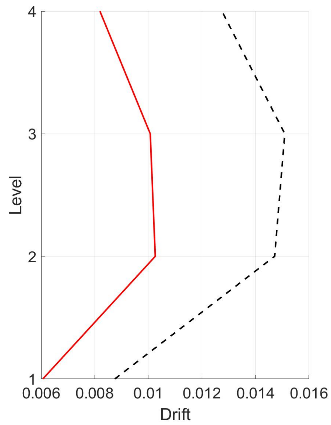

(e) Imperial Valley

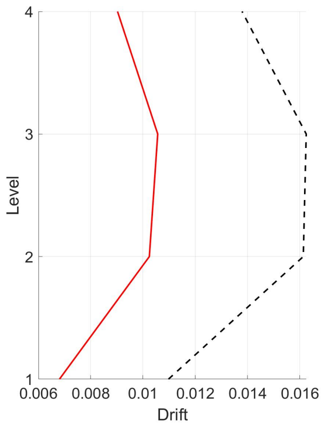

(f) Kobe

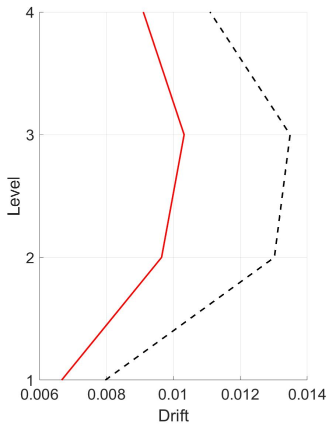

(g) Loma Prieta

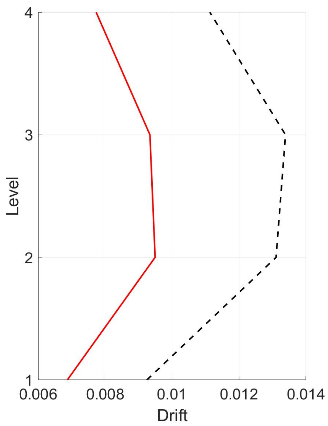

(h) Northridge

Figure B.153. Drifts $f = 0.86$

B.6 Mass ratio

B.6.1 $U_g = 11cm$

Considering a mass ratio of 1% and following the procedure expressed in Chapter 5 the following results are obtained.

Table B.18. Performance Indices $\mu = 0.01$ $U_g = 11cm$

Earthquake	Performance Index						
	J_1	J_2	J_3	J_4	J_5	J_6	J_7(m)
Chalfant	0.814	0.971	1.134	0.809	0.974	1.009	0.254
Chi-Chi	0.999	1.013	0.964	0.822	0.888	0.911	0.220
Erzincan	0.850	0.972	1.013	0.854	0.937	0.937	0.289
Friulli	0.895	0.971	0.977	0.864	0.938	0.943	0.255
Imperial Valley	0.917	0.981	1.089	0.937	0.980	0.984	0.314
Kobe	0.910	1.008	0.959	0.940	0.997	0.992	0.280
Loma Prieta	0.889	1.037	1.013	0.898	0.963	0.969	0.272
Northridge	1.047	0.991	0.940	0.908	0.975	0.963	0.335
Average	0.915	0.993	1.011	0.879	0.956	0.964	0.277

Chalfant

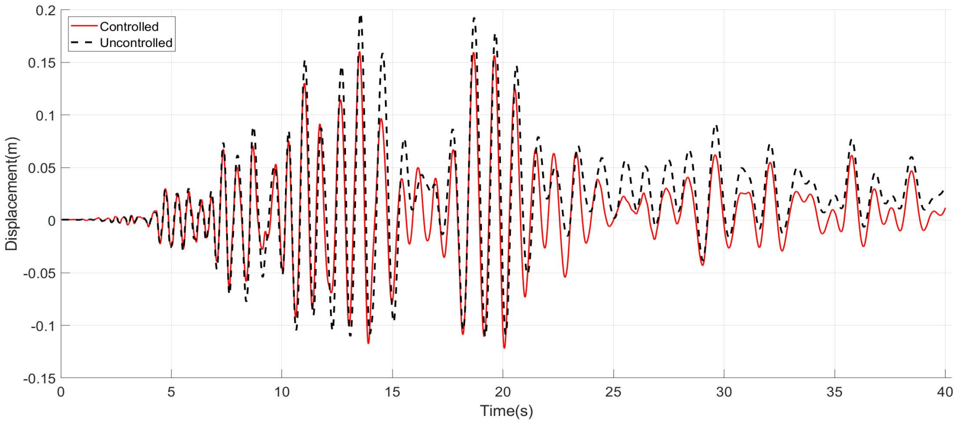

(a) Roof Displacements

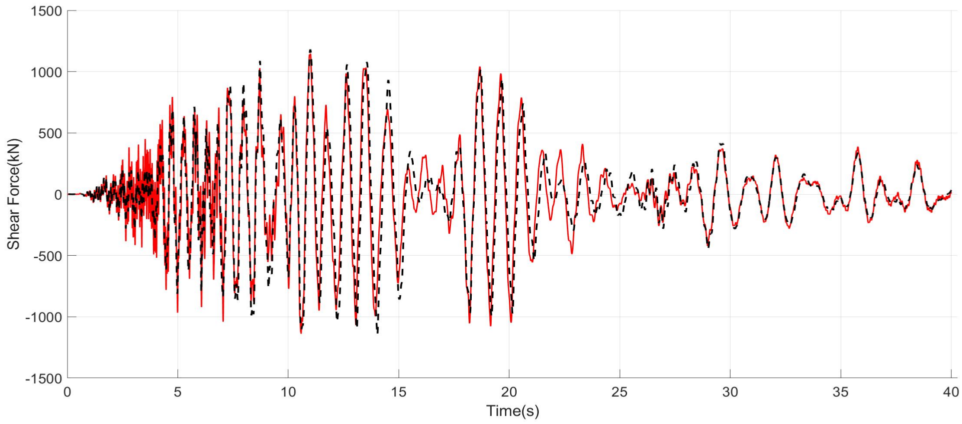

(b) Shear Forces at the base

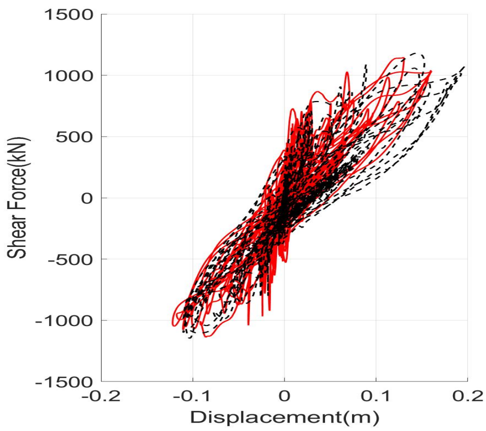

(c) Structural Hysteretic Curve

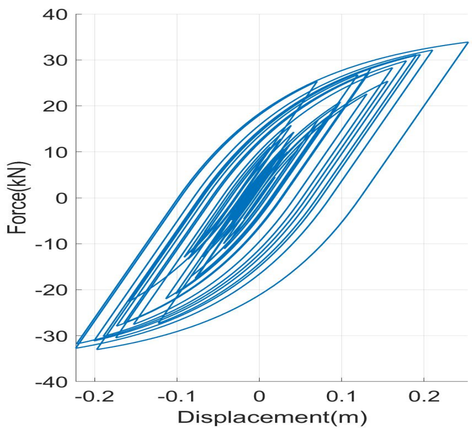

(d) TMD Hysteretic Curve

Figure B.154. Chalfant $\mu = 0.01$ $U_g = 11cm$

Chi-Chi

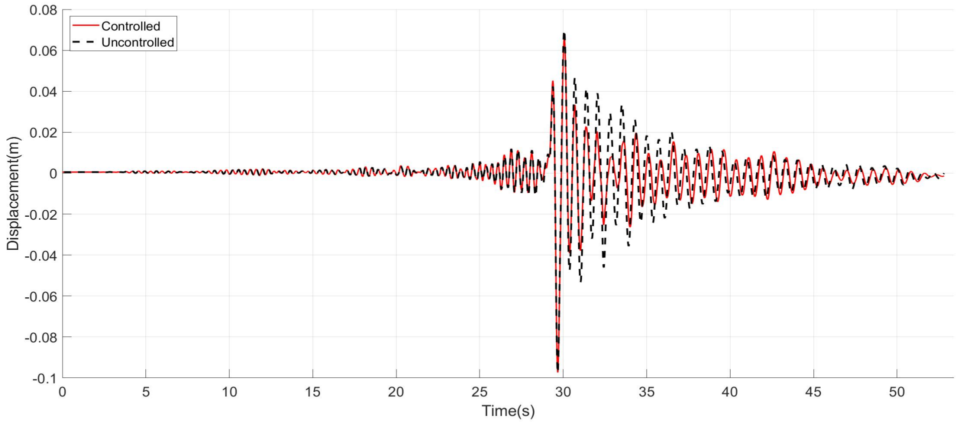

(a) Roof Displacements

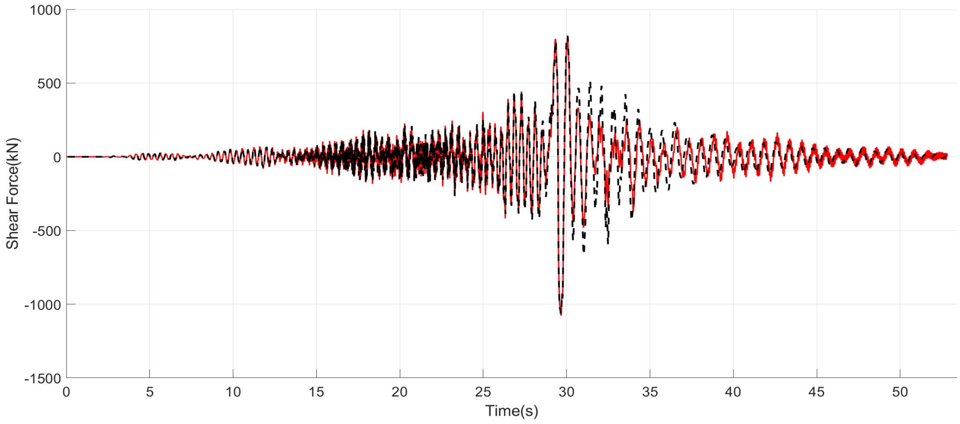

(b) Shear Forces at the base

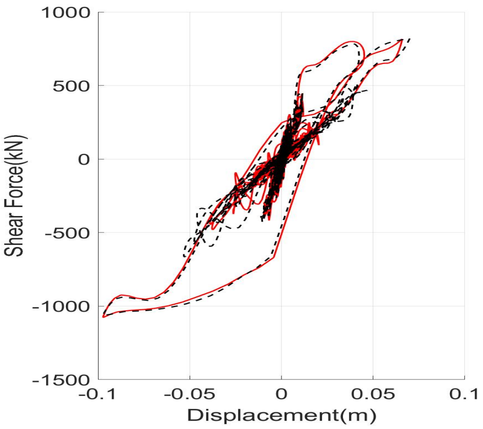

(c) Structural Hysteretic Curve

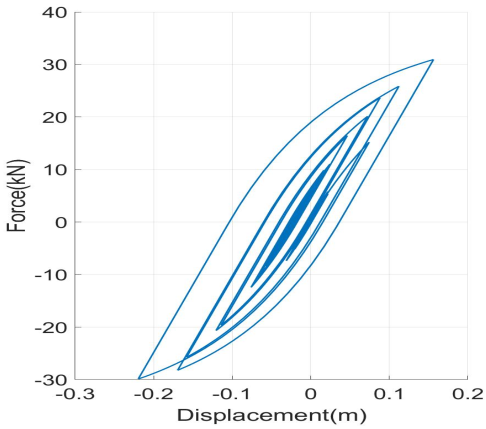

(d) TMD Hysteretic Curve

Figure B.155. Chi Chi $\mu = 0.01$ $U_g = 11cm$

Erzincan

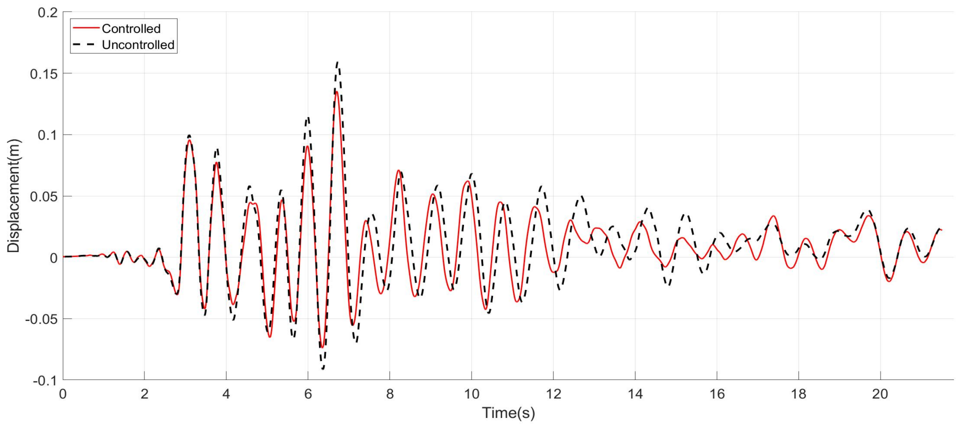

(a) Roof Displacements

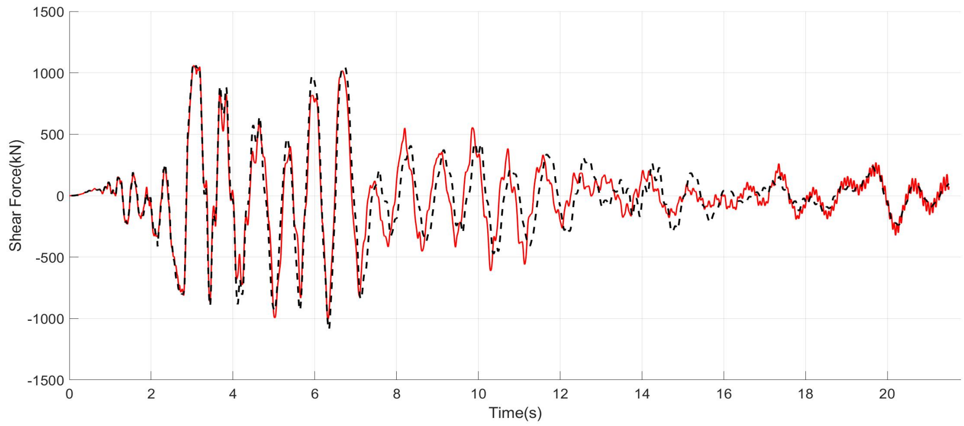

(b) Shear Forces at the base

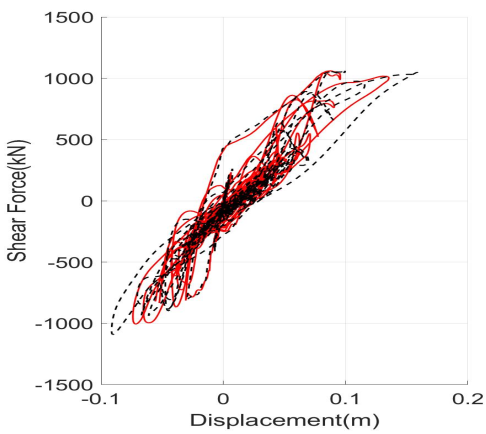

(c) Structural Hysteretic Curve

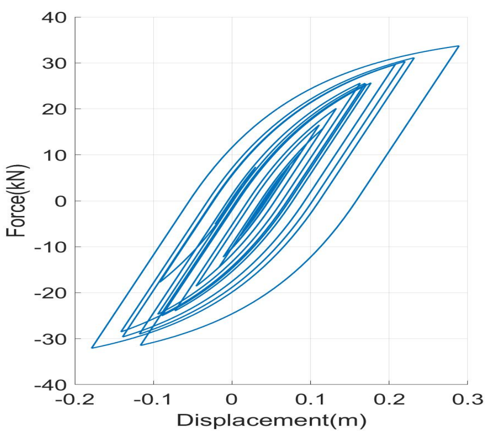

(d) TMD Hysteretic Curve

Figure B.156. Erzincan $\mu = 0.01$ $U_g = 11cm$

Friulli

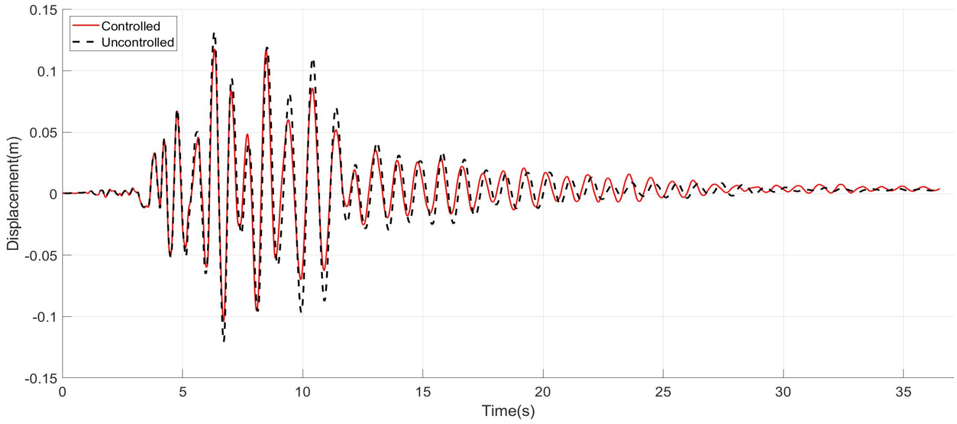

(a) Roof Displacements

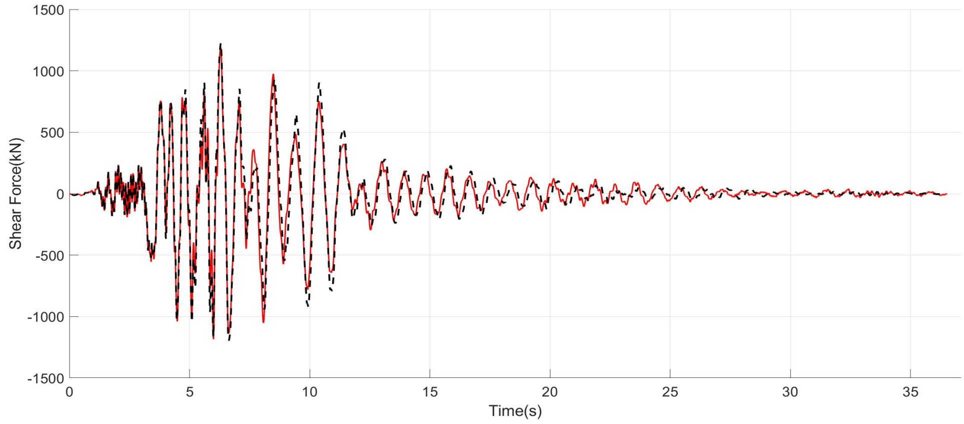

(b) Shear Forces at the base

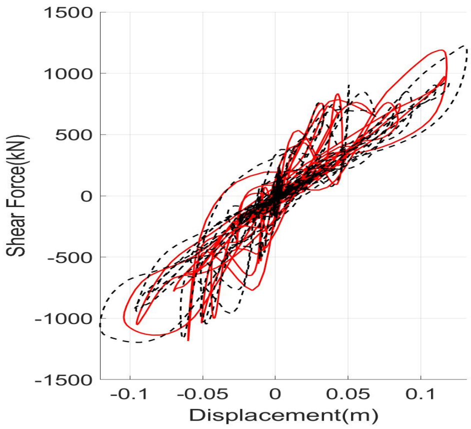

(c) Structural Hysteretic Curve

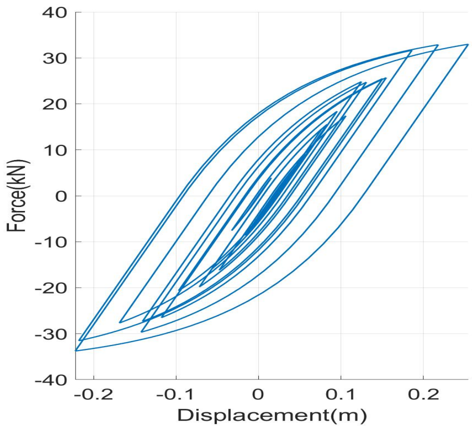

(d) TMD Hysteretic Curve

Figure B.157. Friulli $\mu = 0.01$ $U_g = 11cm$

Imperial Valley

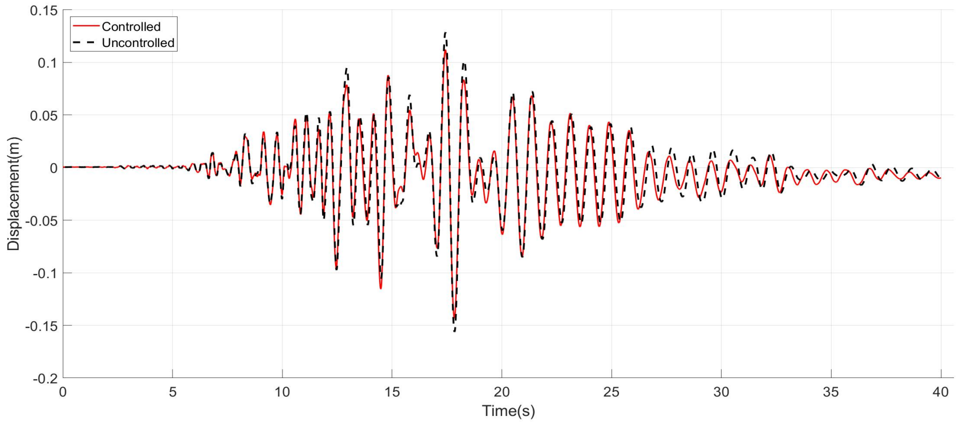

(a) Roof Displacements

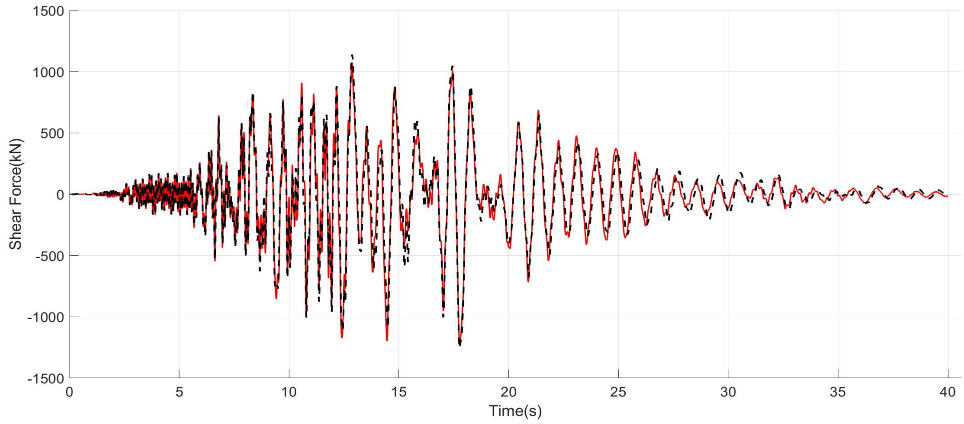

(b) Shear Forces at the base

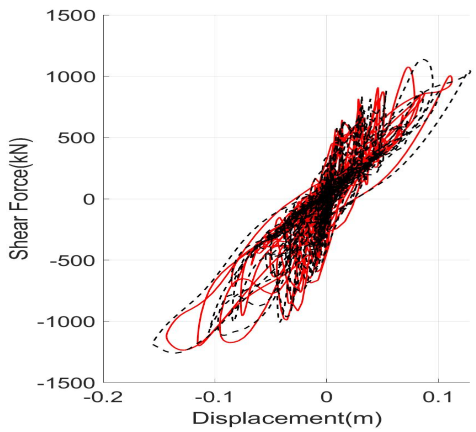

(c) Structural Hysteretic Curve

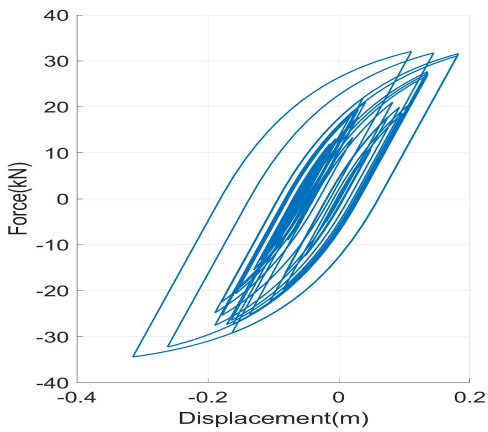

(d) TMD Hysteretic Curve

Figure B.158. Imperial Valley $\mu = 0.01$ $U_g = 11cm$

Kobe

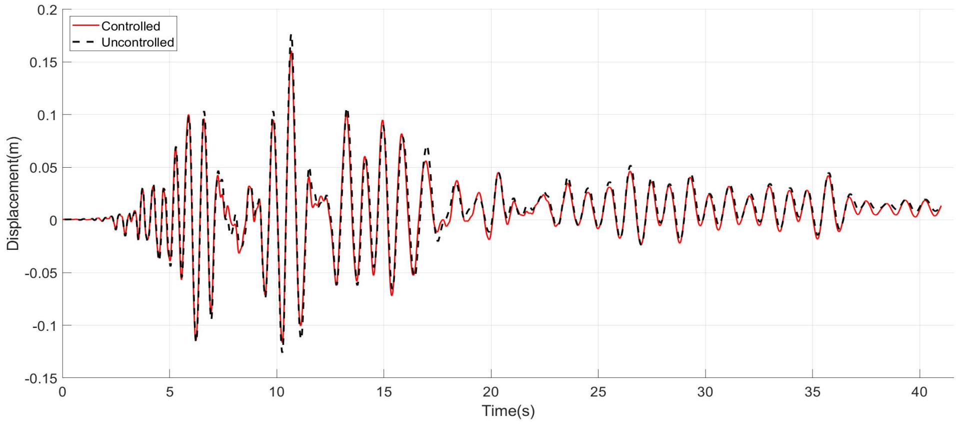

(a) Roof Displacements

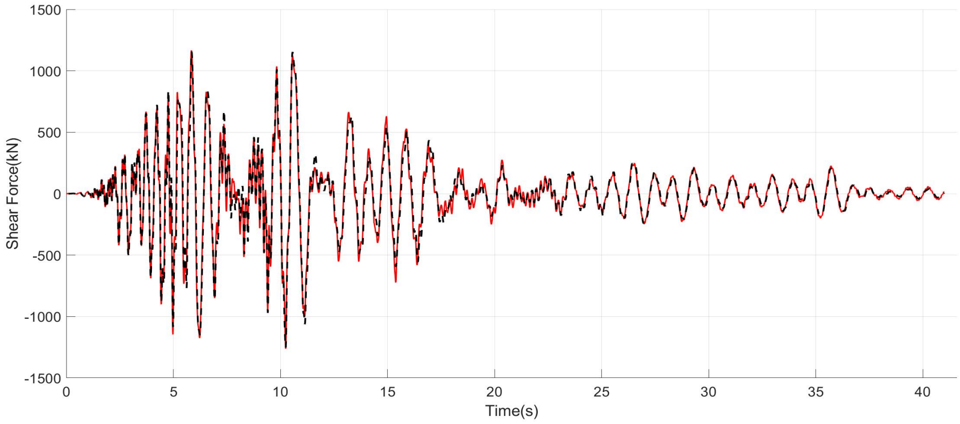

(b) Shear Forces at the base

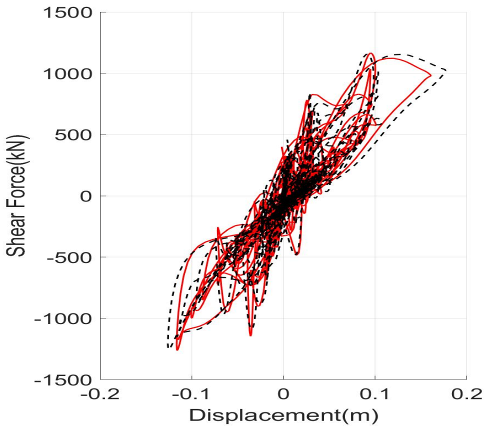

(c) Structural Hysteretic Curve

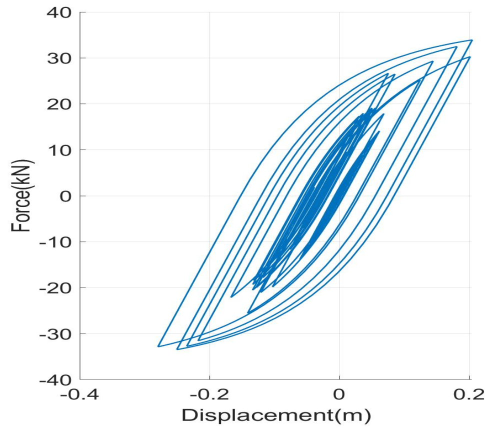

(d) TMD Hysteretic Curve

Figure B.159. Kobe $\mu = 0.01$ $U_g = 11cm$

Loma Prieta

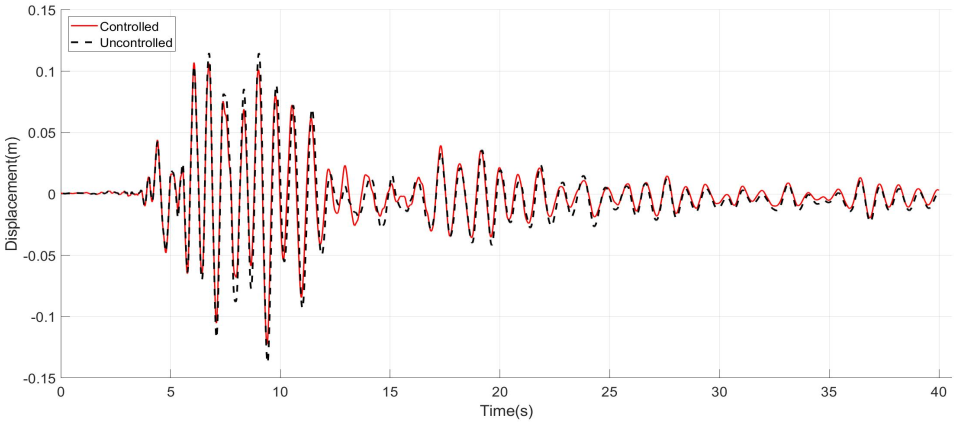

(a) Roof Displacements

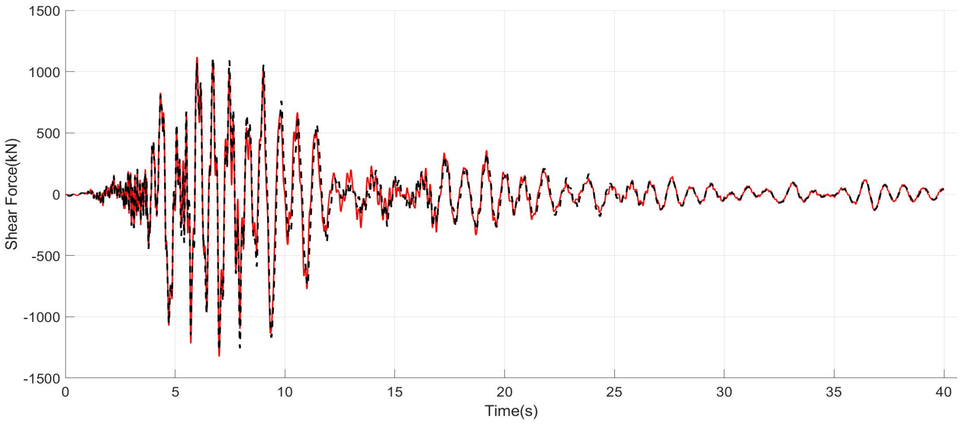

(b) Shear Forces at the base

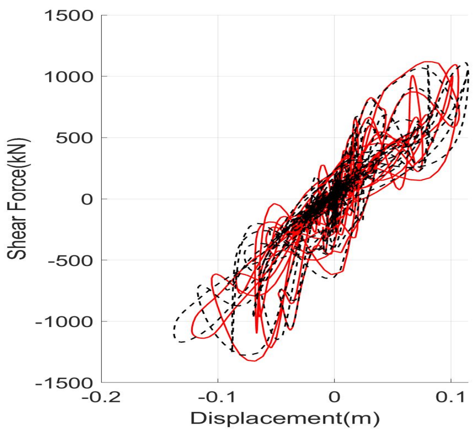

(c) Structural Hysteretic Curve

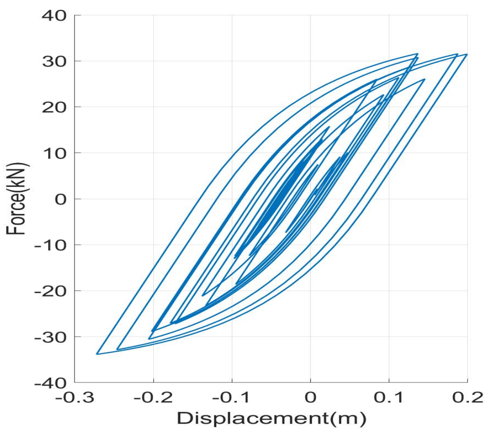

(d) TMD Hysteretic Curve

Figure B.160. Loma Prieta $\mu = 0.01$ $U_g = 11cm$

Northridge

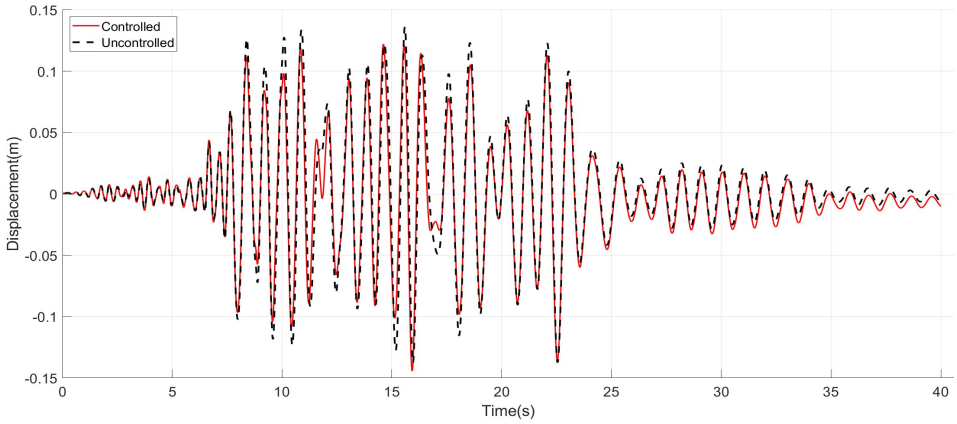

(a) Roof Displacements

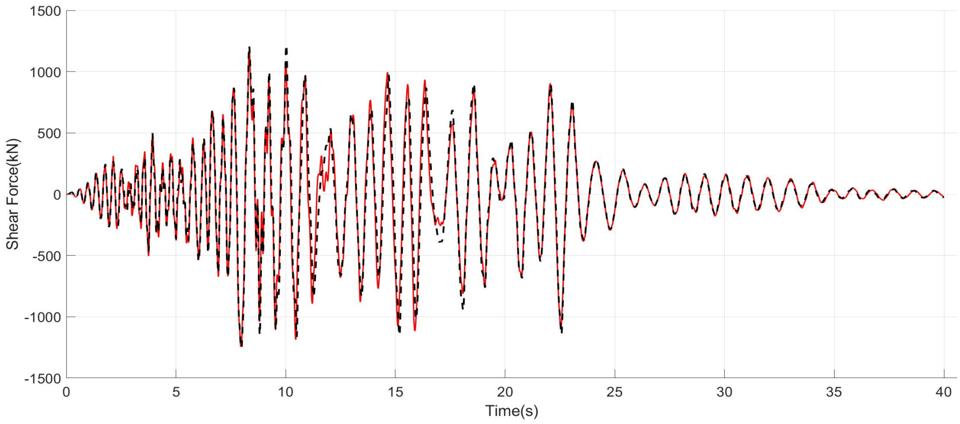

(b) Shear Forces at the base

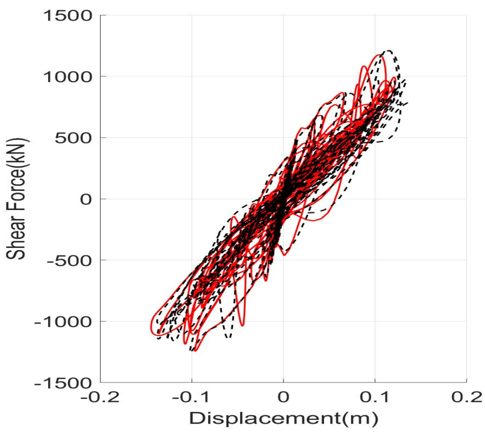

(c) Structural Hysteretic Curve

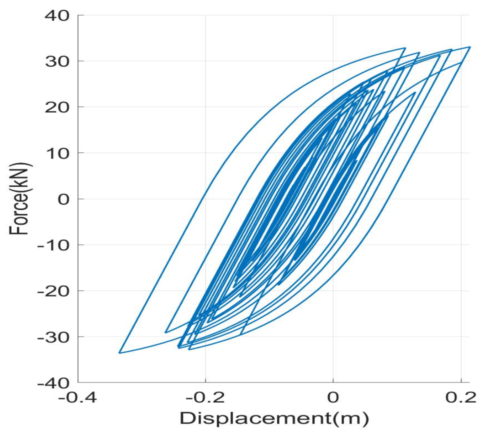

(d) TMD Hysteretic Curve

Figure B.161. Northridge $\mu = 0.01$ $U_g = 11cm$

Drifts

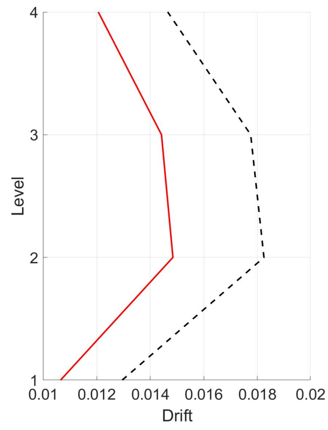

(a) Chalfant

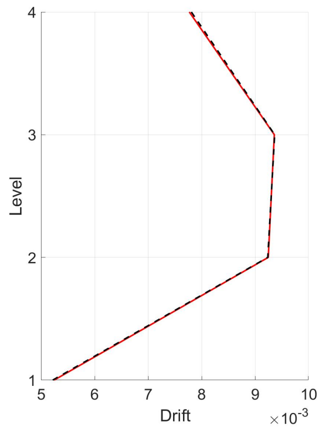

(b) Chi Chi

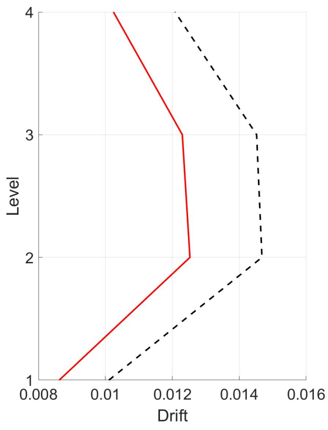

(c) Erzincan

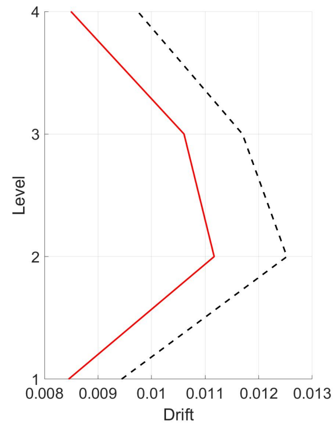

(d) Friulli

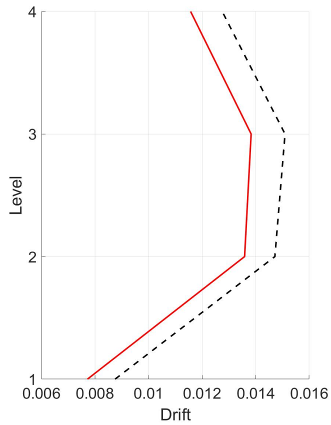

(e) Imperial Valley

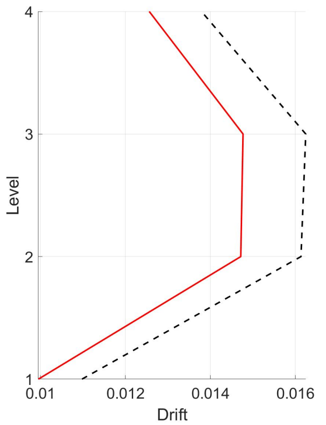

(f) Kobe

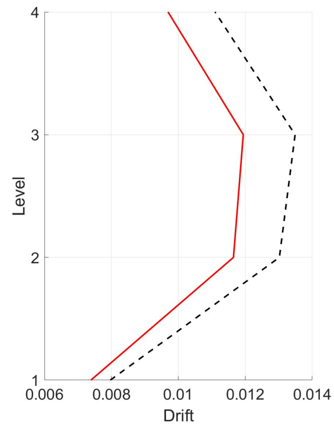

(g) Loma Prieta

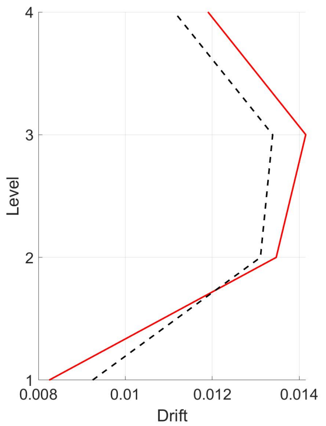

(h) Northridge

Figure B.162. Drifts $\mu = 0.01$ $U_g = 11cm$

B.6.2 $U_g = 13cm$

By updating the expected performance point of the structure to $13cm$ the comparison between the controlled and uncontrolled structure is presented.

Table B.19. Performance Indices $\mu = 0.01$ $U_g = 13cm$

Earthquake	Performance Index						
	J_1	J_2	J_3	J_4	J_5	J_6	J_7(m)
Chalfant	0.814	0.971	1.134	0.809	0.974	1.009	0.244
Chi-Chi	1.006	0.971	0.906	0.833	0.866	0.895	0.225
Erzincan	0.875	0.983	1.006	0.867	0.943	0.945	0.289
Friulli	0.908	0.968	0.978	0.875	0.945	0.953	0.246
Imperial Valley	0.921	0.986	1.118	0.939	0.979	0.985	0.312
Kobe	0.915	1.018	0.980	0.942	0.996	0.992	0.274
Loma Prieta	0.889	1.037	1.013	0.898	0.963	0.969	0.257
Northridge	1.032	0.982	0.957	0.892	0.973	0.963	0.356
Average	0.920	0.990	1.012	0.882	0.955	0.964	0.275

Chalfant

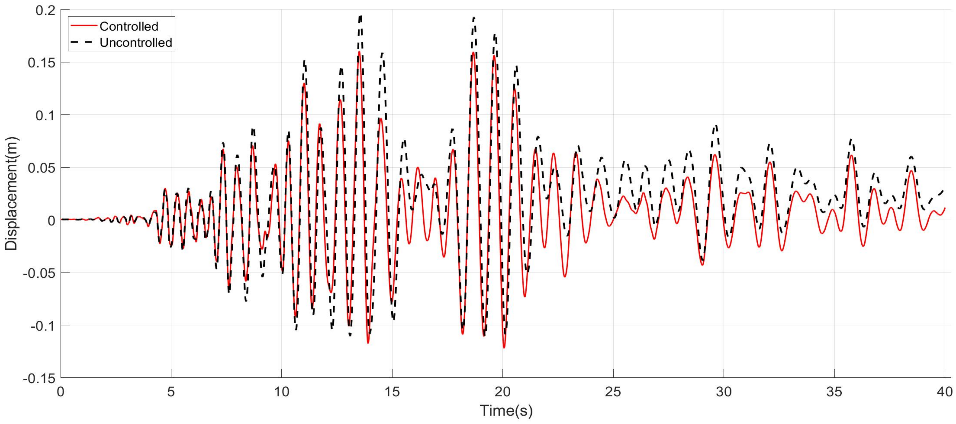

(a) Roof Displacements

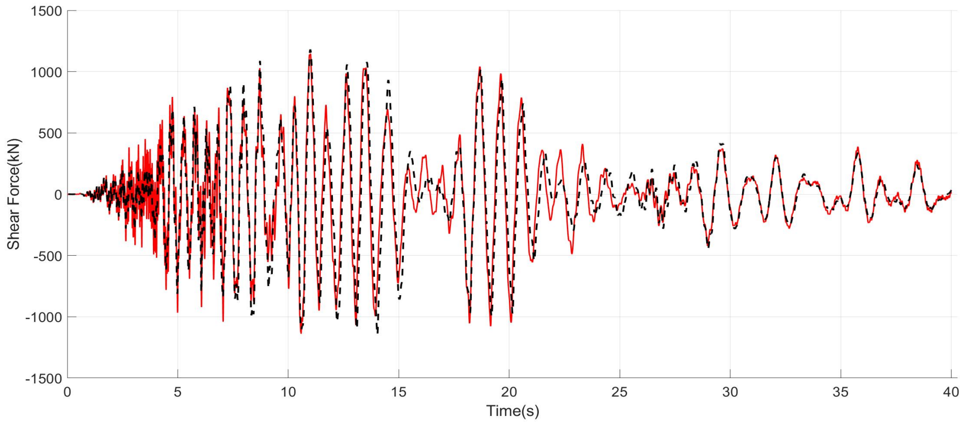

(b) Shear Forces at the base

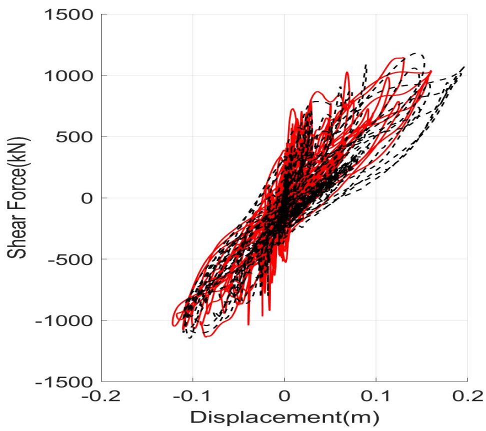

(c) Structural Hysteretic Curve

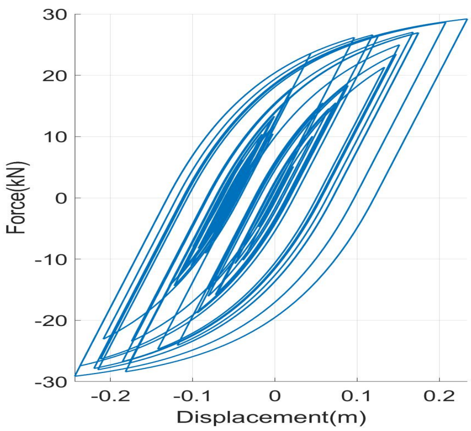

(d) TMD Hysteretic Curve

Figure B.163. Chalfant $\mu = 0.01$ $U_g = 13cm$

Chi-Chi

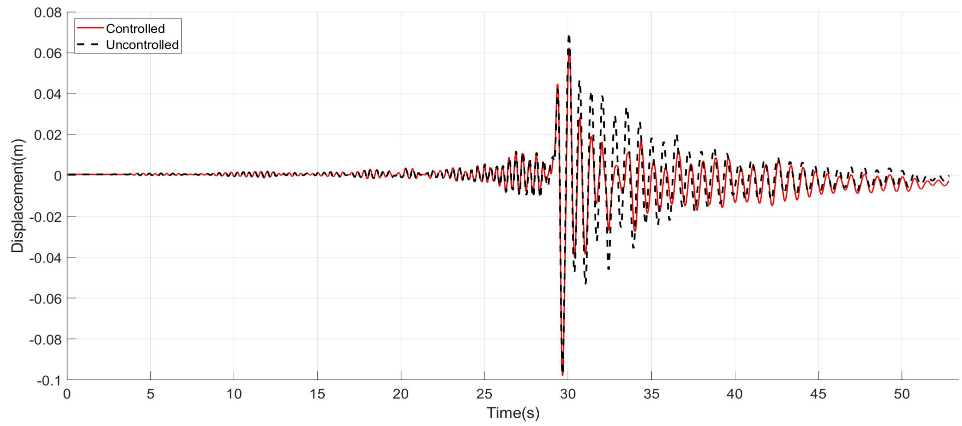

(a) Roof Displacements

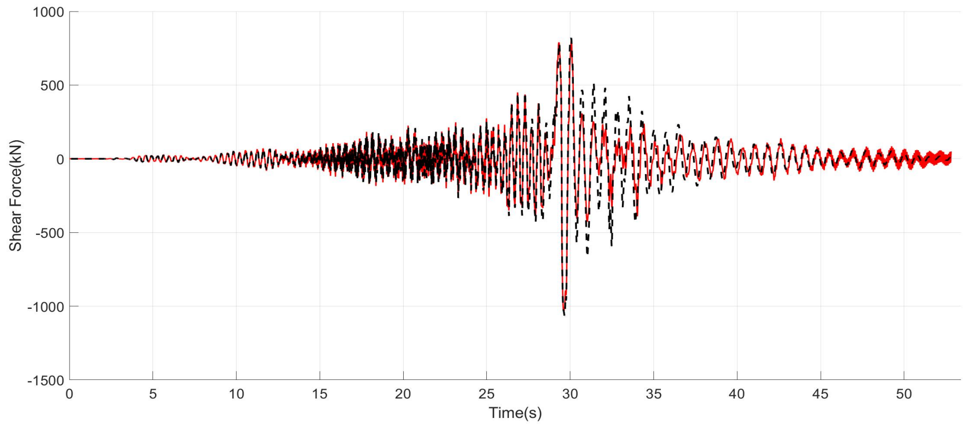

(b) Shear Forces at the base

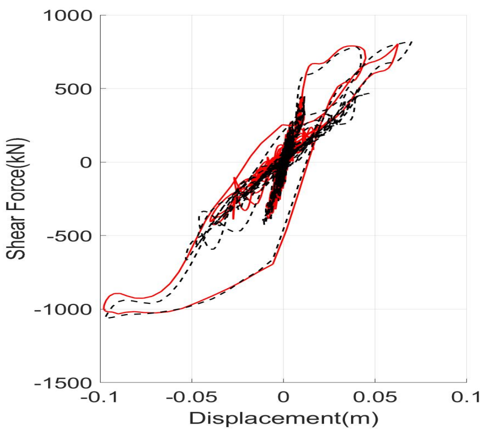

(c) Structural Hysteretic Curve

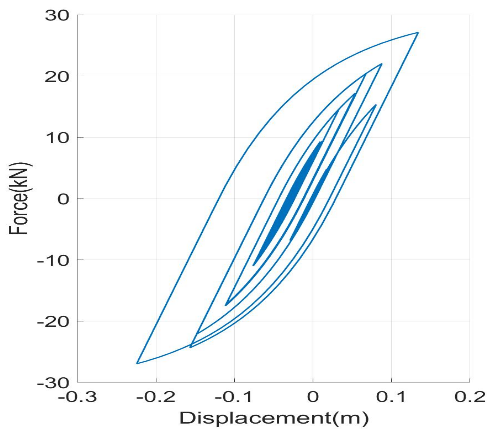

(d) TMD Hysteretic Curve

Figure B.164. Chi Chi $\mu = 0.01$ $U_g = 13cm$

Erzincan

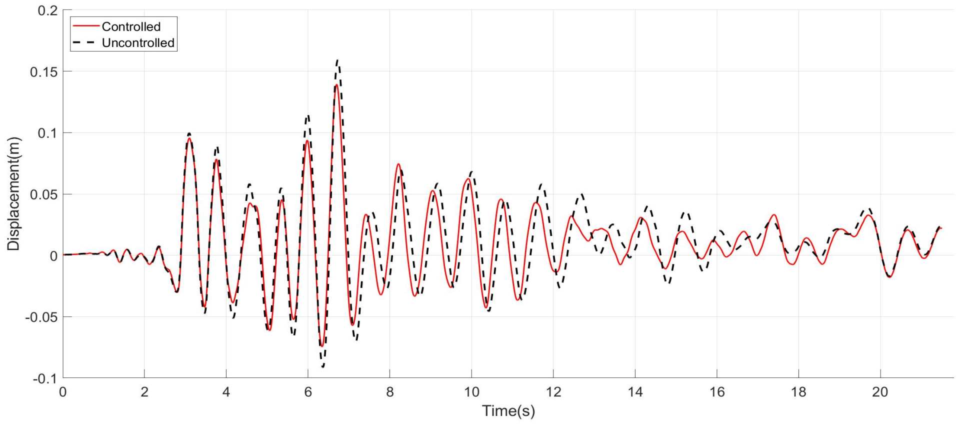

(a) Roof Displacements

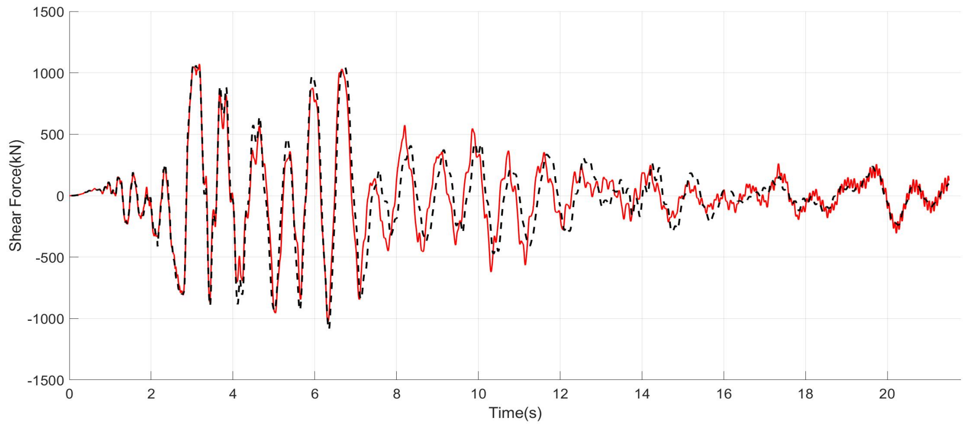

(b) Shear Forces at the base

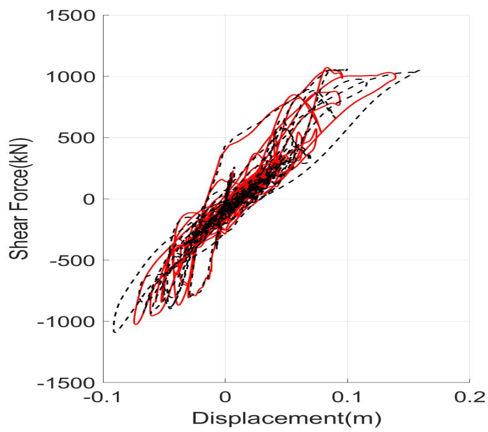

(c) Structural Hysteretic Curve

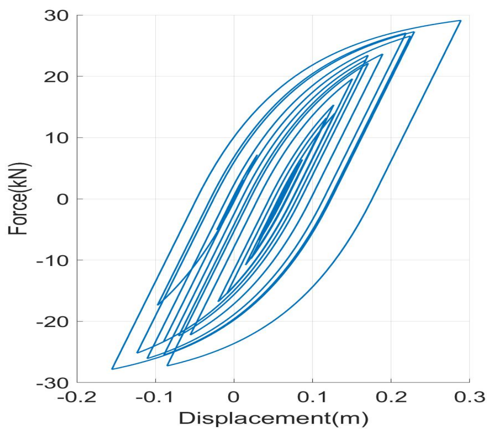

(d) TMD Hysteretic Curve

Figure B.165. Erzincan $\mu = 0.01$ $U_g = 13cm$

Friulli

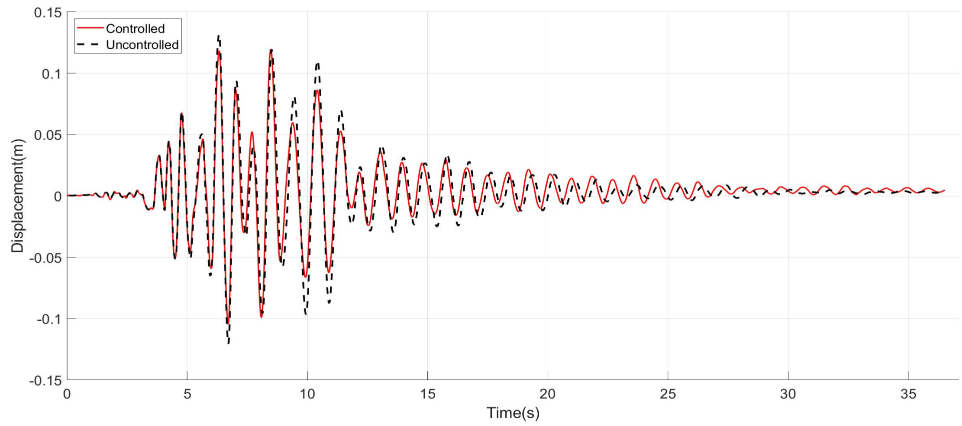

(a) Roof Displacements

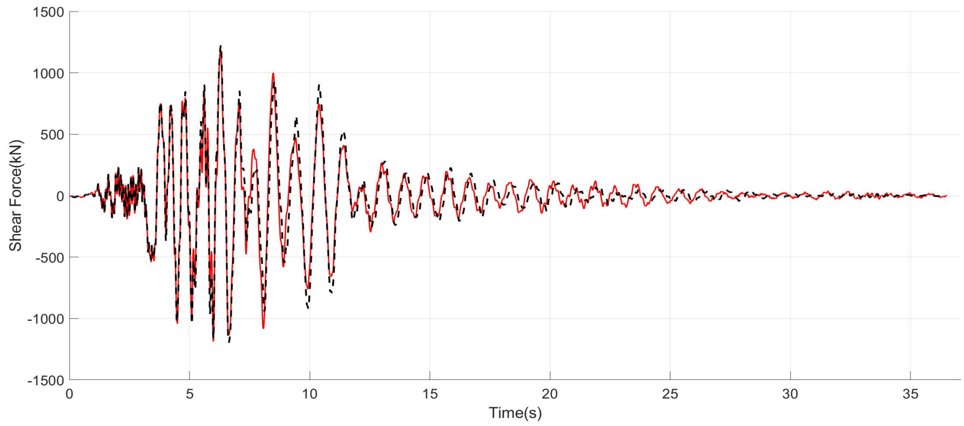

(b) Shear Forces at the base

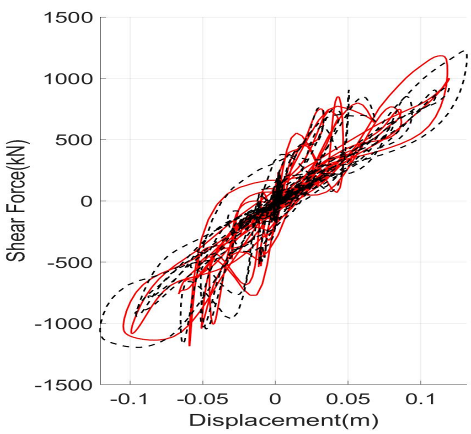

(c) Structural Hysteretic Curve

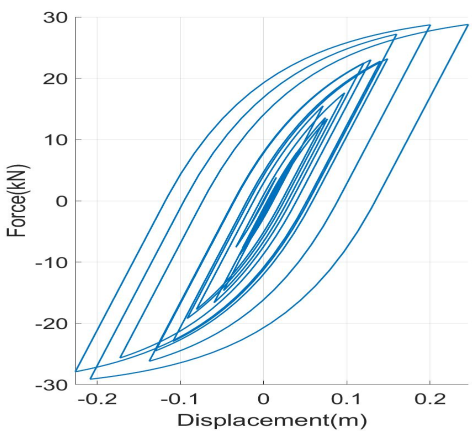

(d) TMD Hysteretic Curve

Figure B.166. Friulli $\mu = 0.01$ $U_g = 13cm$

Imperial Valley

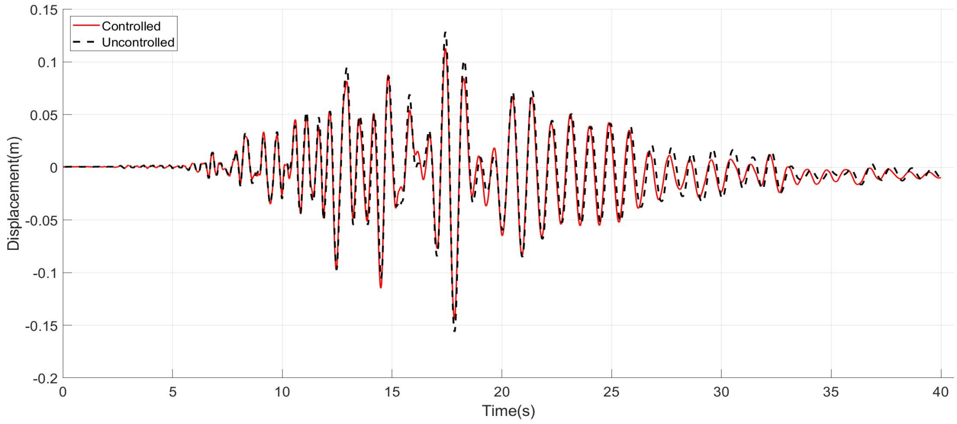

(a) Roof Displacements

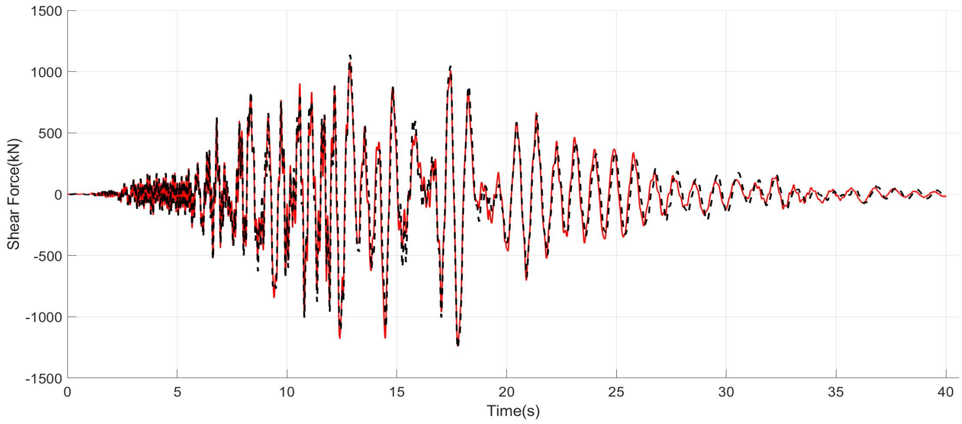

(b) Shear Forces at the base

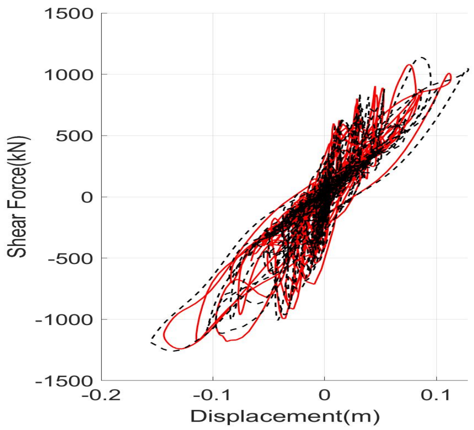

(c) Structural Hysteretic Curve

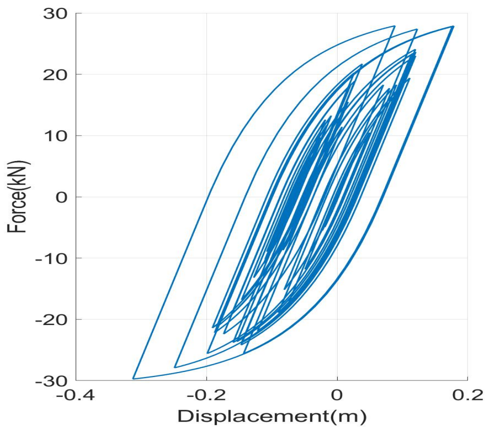

(d) TMD Hysteretic Curve

Figure B.167. Imperial Valley $\mu = 0.01$ $U_g = 13cm$

Kobe

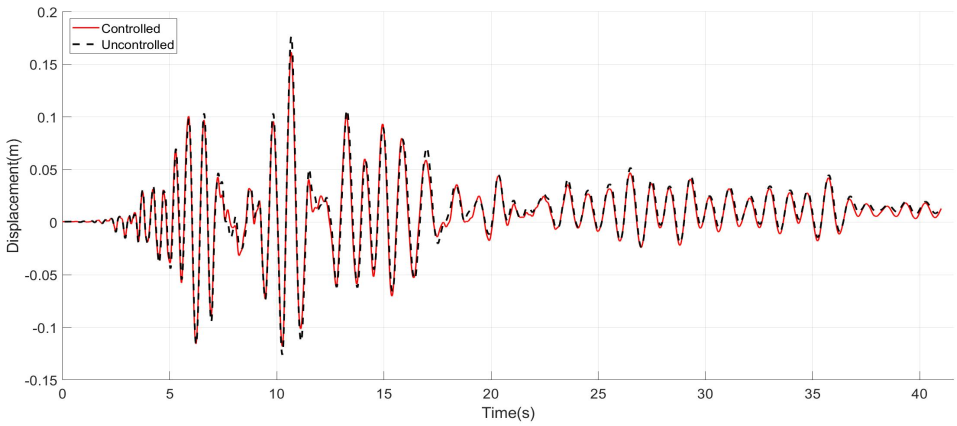

(a) Roof Displacements

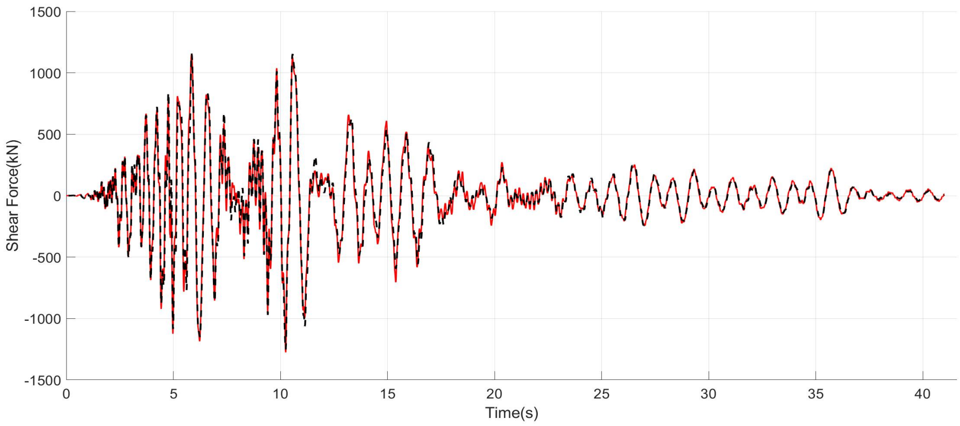

(b) Shear Forces at the base

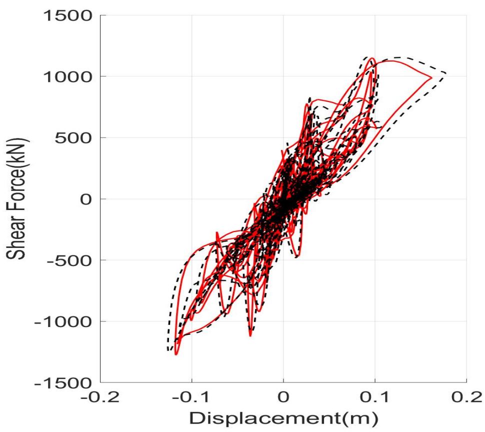

(c) Structural Hysteretic Curve

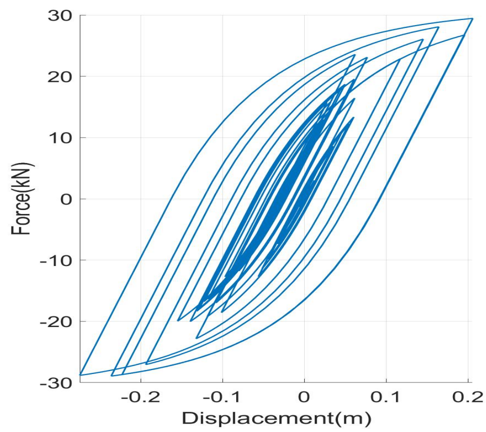

(d) TMD Hysteretic Curve

Figure B.168. Kobe $\mu = 0.01$ $U_g = 13cm$

Loma Prieta

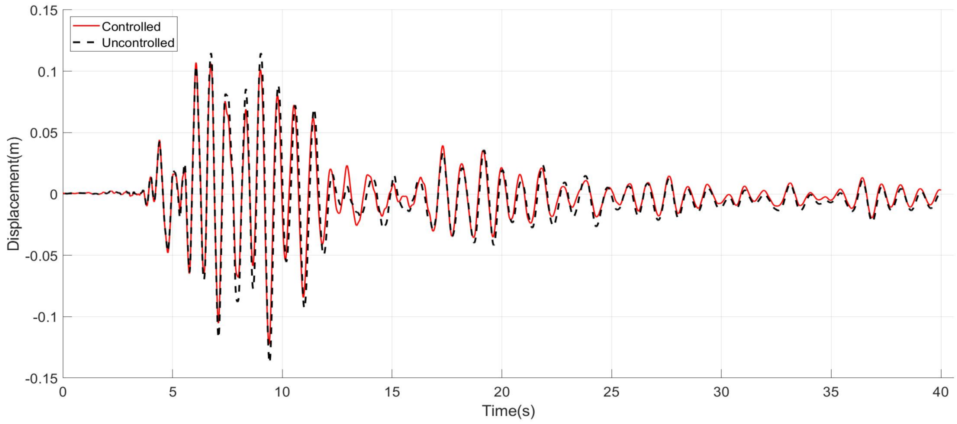

(a) Roof Displacements

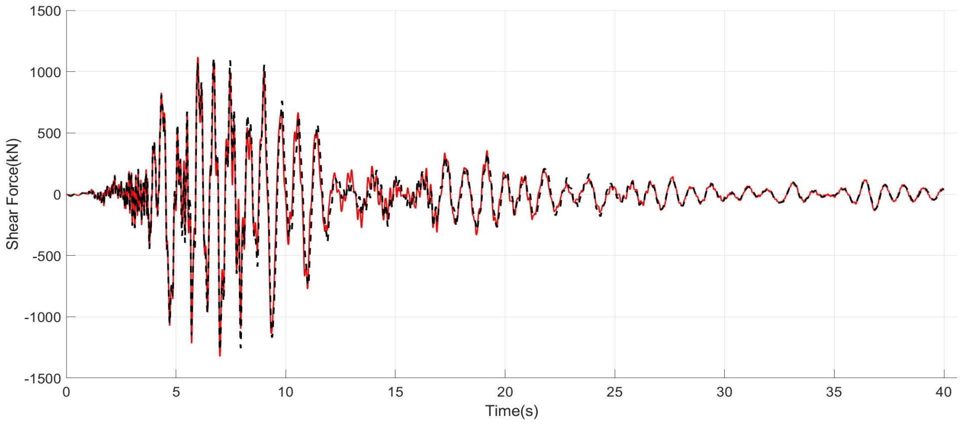

(b) Shear Forces at the base

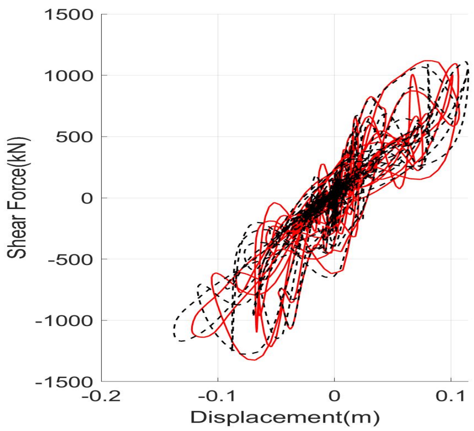

(c) Structural Hysteretic Curve

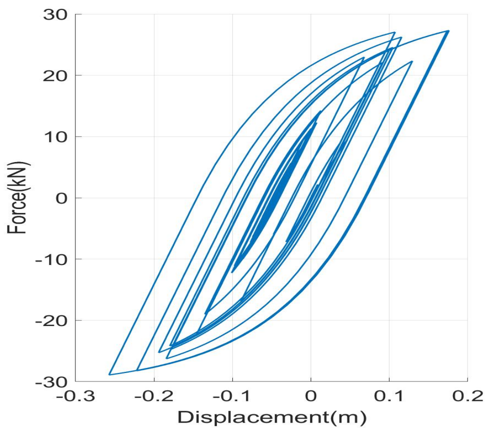

(d) TMD Hysteretic Curve

Figure B.169. Loma Prieta $\mu = 0.01$ $U_g = 13cm$

Northridge

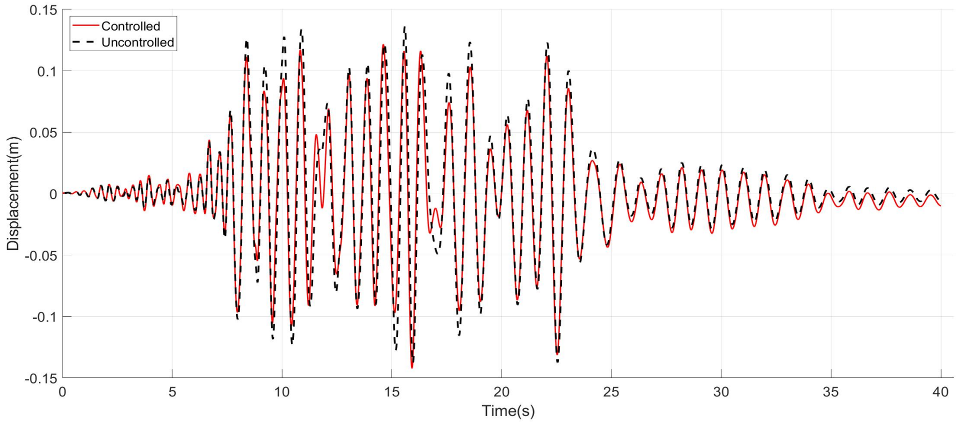

(a) Roof Displacements

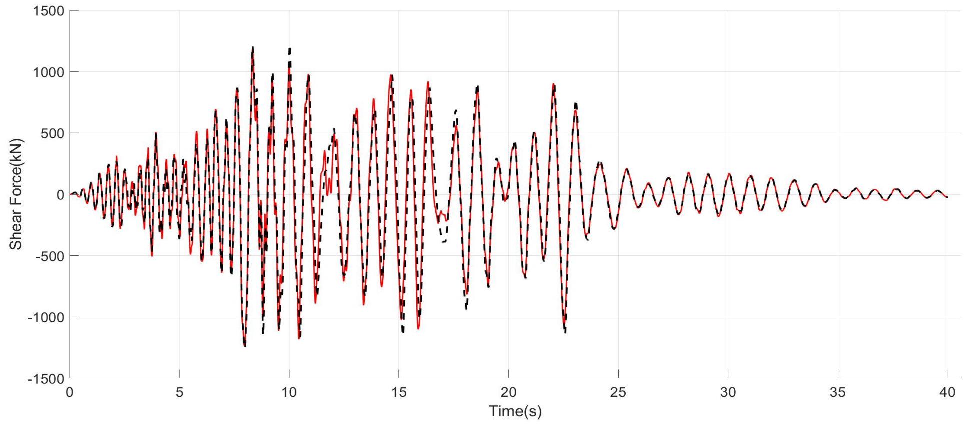

(b) Shear Forces at the base

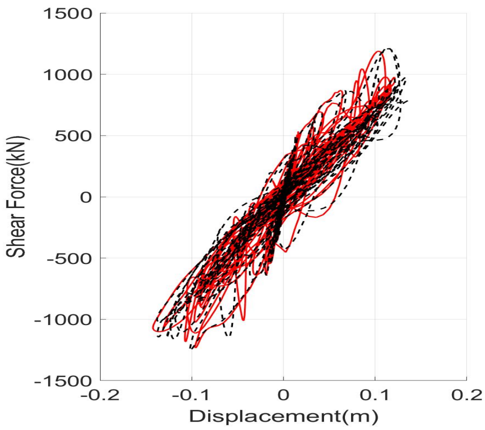

(c) Structural Hysteretic Curve

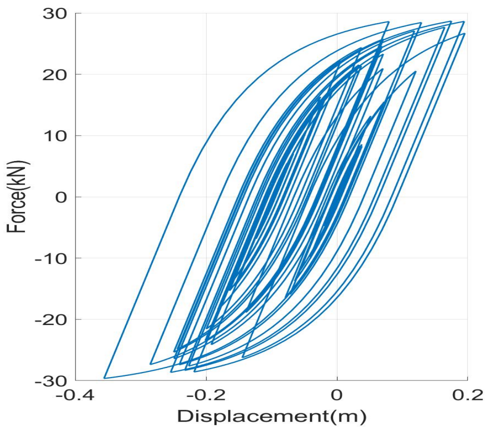

(d) TMD Hysteretic Curve

Figure B.170. Northridge $\mu = 0.01$ $U_g = 13cm$

Drifts

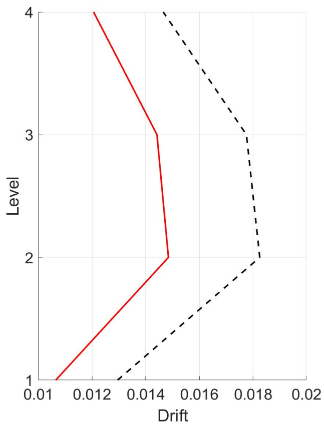

(a) Chalfant

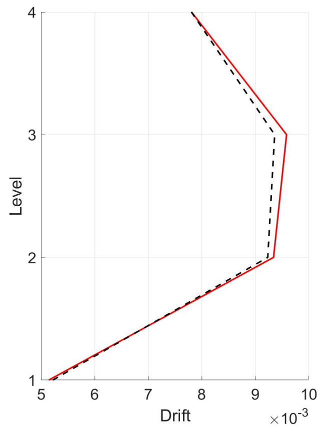

(b) Chi Chi

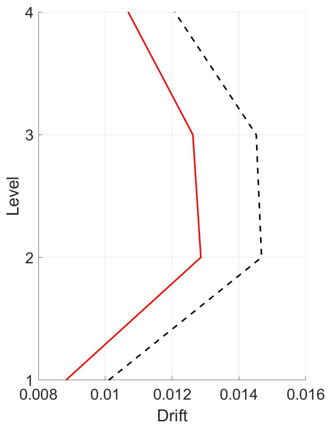

(c) Erzincan

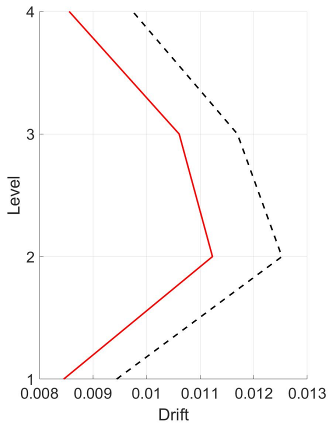

(d) Friulli

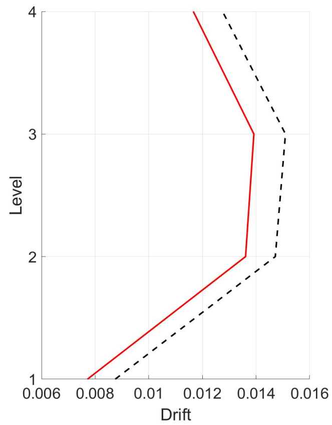

(e) Imperial Valley

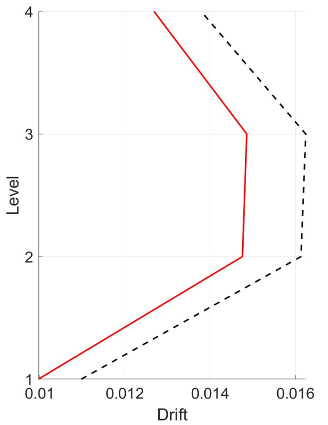

(f) Kobe

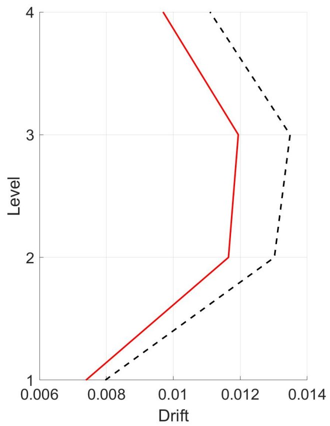

(g) Loma Prieta

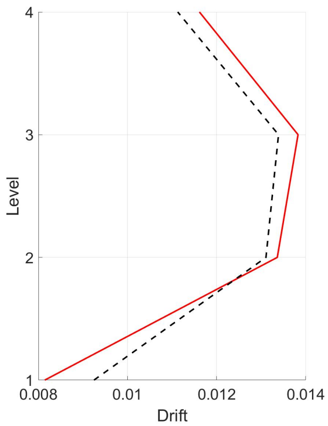

(h) Northridge

Figure B.171. Drifts $\mu = 0.01$ $U_g = 13cm$

B.7 1.5 Design Earthquake

The results of the numerical simulation considering a 1.5 Design Earthquake are here presented. These results may be non representing of the actual behavior of the building under such a severe motion as steel failure, and therefore collapse, are not considered. The green dotted line in B.180 represents the 2% collapse prevention limit for walls stated in [34].

Table B.20. Performance Indices 1.5 Design Earthquake

Earthquake	Performance Index						
	J_1	J_2	J_3	J_4	J_5	J_6	J_7(m)
Chalfant	0.942	0.856	1.069	0.920	1.003	0.954	0.351
Chi-Chi	0.809	0.886	0.905	0.762	0.932	0.952	0.339
Erzincan	0.815	0.930	0.981	0.816	0.970	0.919	0.312
Friulli	0.771	1.103	0.946	0.807	1.001	0.995	0.332
Imperial Valley	0.821	0.957	1.236	0.827	1.010	1.047	0.303
Kobe	0.807	0.944	0.967	0.936	0.836	0.989	0.293
Loma Prieta	0.921	0.989	1.001	1.023	1.005	0.983	0.364
Northridge	0.896	0.993	0.881	0.917	0.985	0.919	0.322
Average	0.848	0.957	0.998	0.876	0.968	0.970	0.327

Chalfant

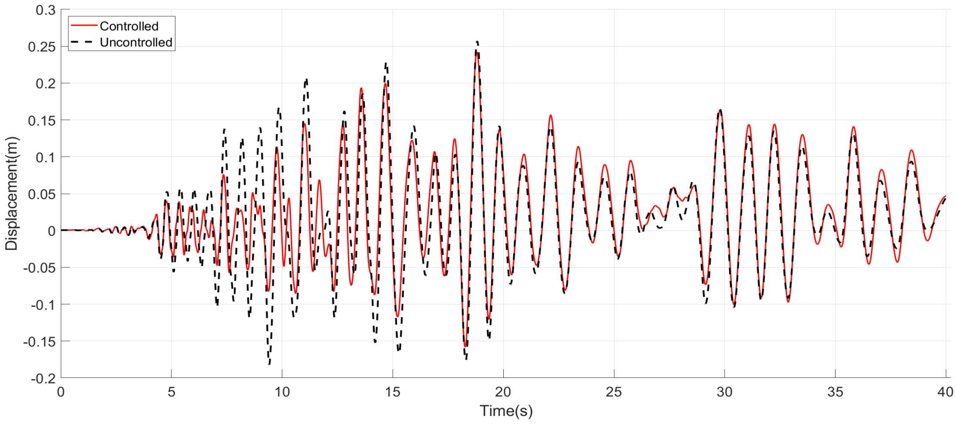

(a) Roof Displacements

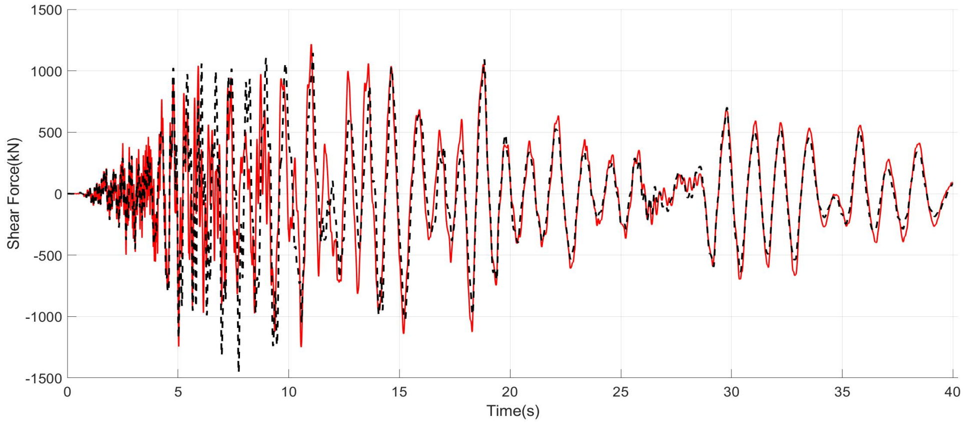

(b) Shear Forces at the base

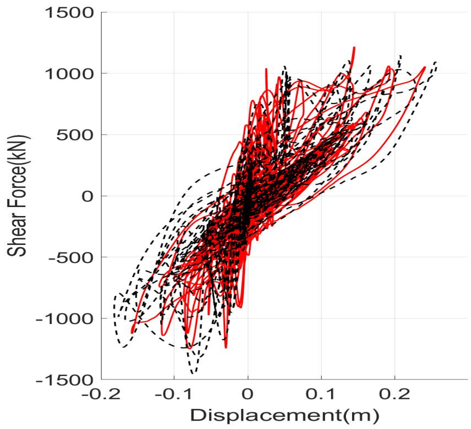

(c) Structural Hysteretic Curve

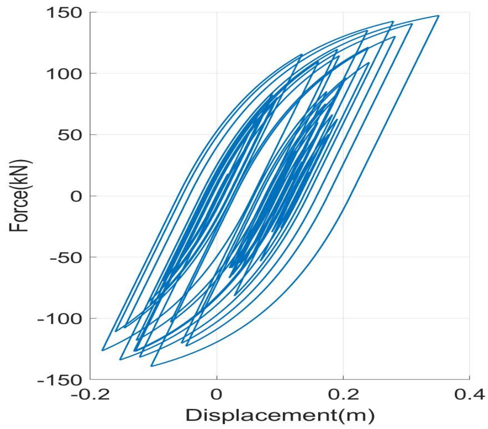

(d) TMD Hysteretic Curve

Figure B.172. Chalfant 1.5 Design Earthquake

Chi-Chi

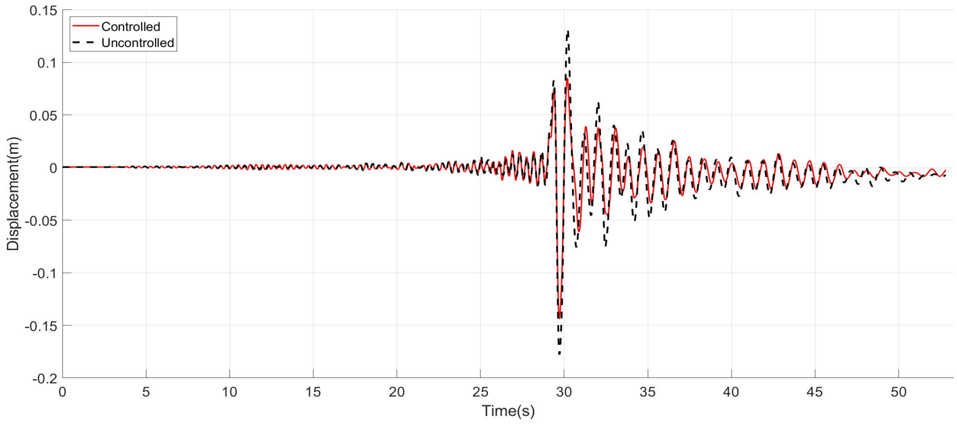

(a) Roof Displacements

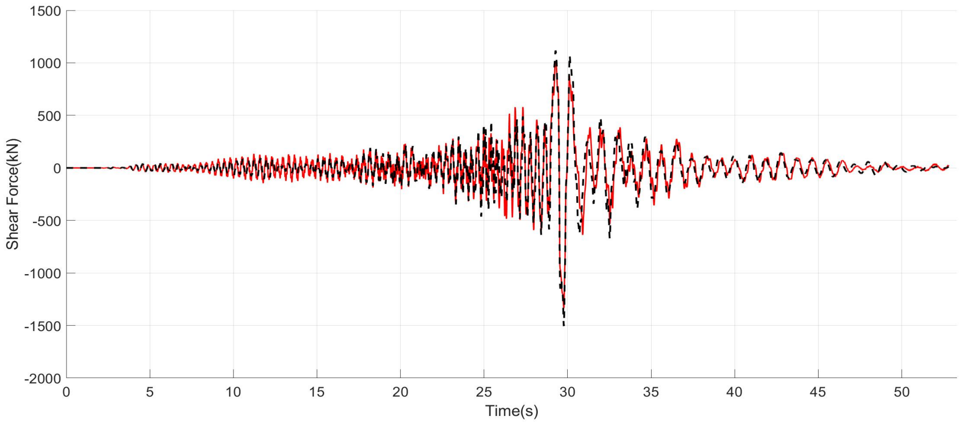

(b) Shear Forces at the base

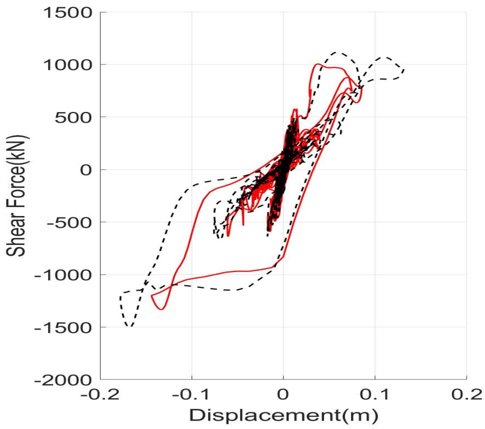

(c) Structural Hysteretic Curve

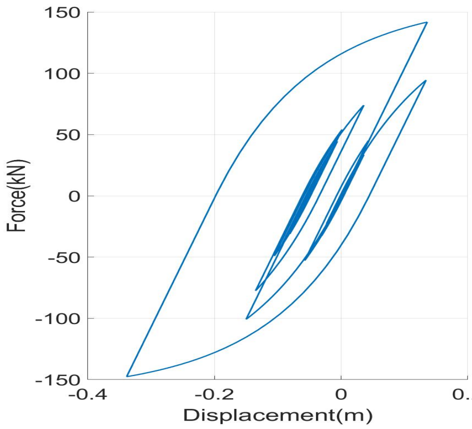

(d) TMD Hysteretic Curve

Figure B.173. Chi Chi 1.5 Design Earthquake

Erzincan

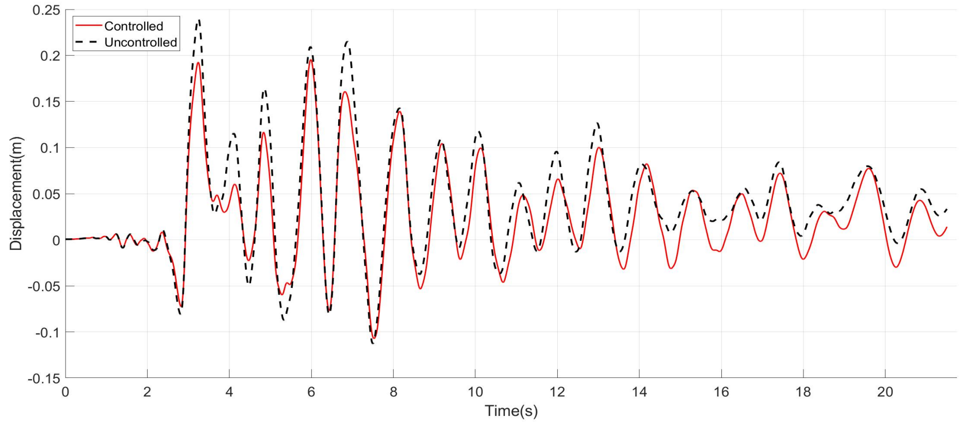

(a) Roof Displacements

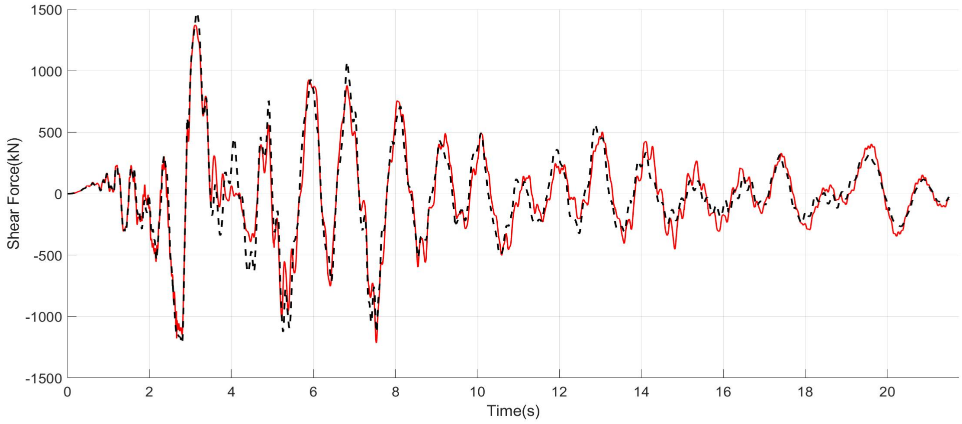

(b) Shear Forces at the base

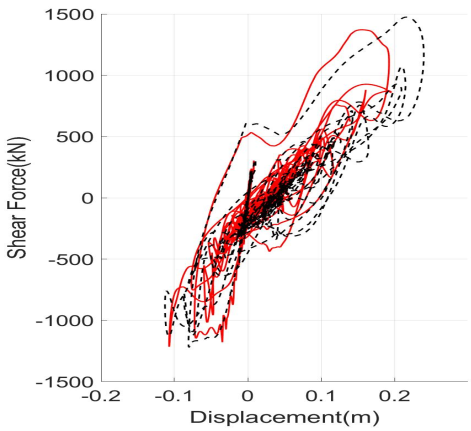

(c) Structural Hysteretic Curve

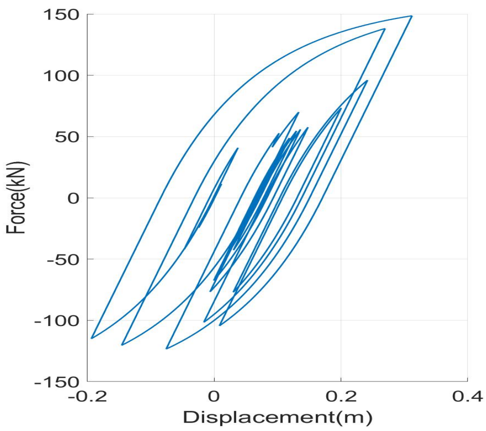

(d) TMD Hysteretic Curve

Figure B.174. Erzincan 1.5 Design Earthquake

Friulli

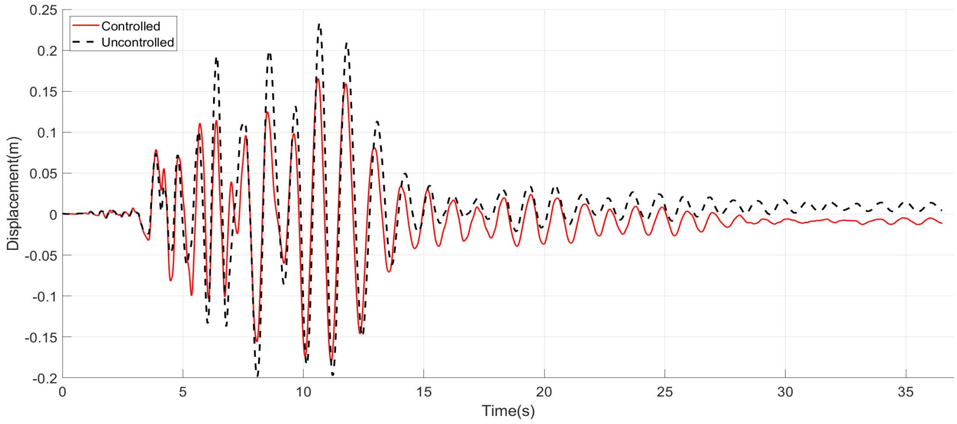

(a) Roof Displacements

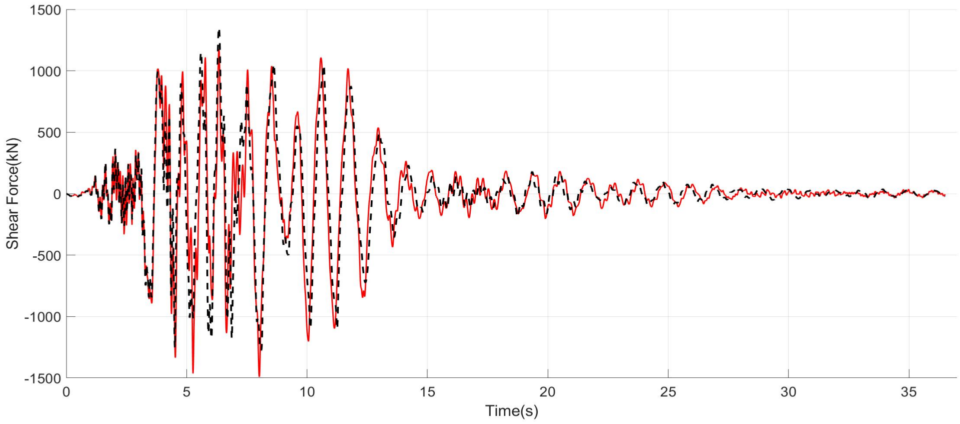

(b) Shear Forces at the base

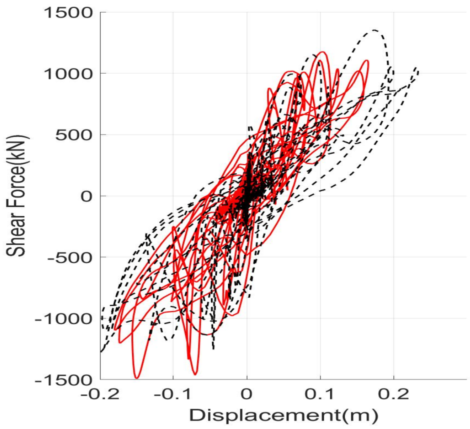

(c) Structural Hysteretic Curve

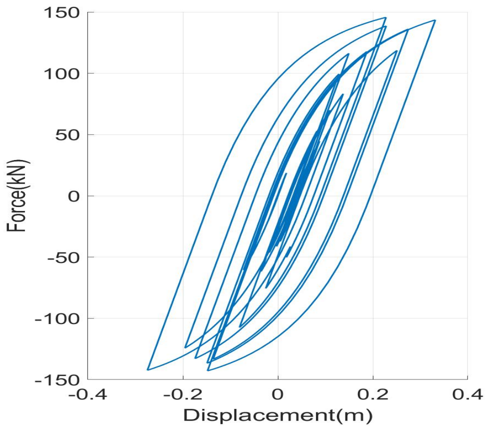

(d) TMD Hysteretic Curve

Figure B.175. Friulli 1.5 Design Earthquake

Imperial Valley

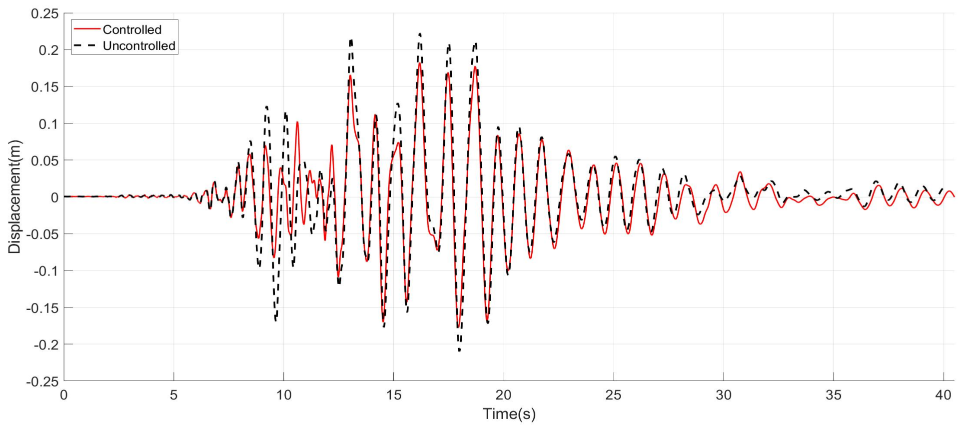

(a) Roof Displacements

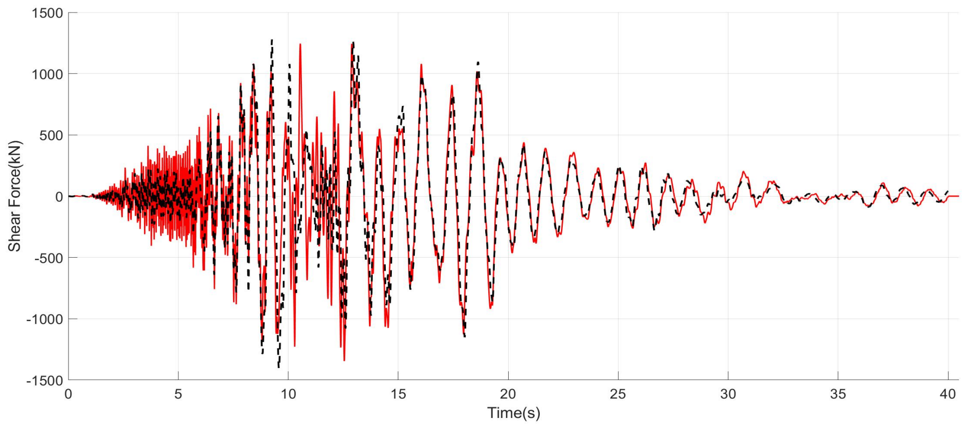

(b) Shear Forces at the base

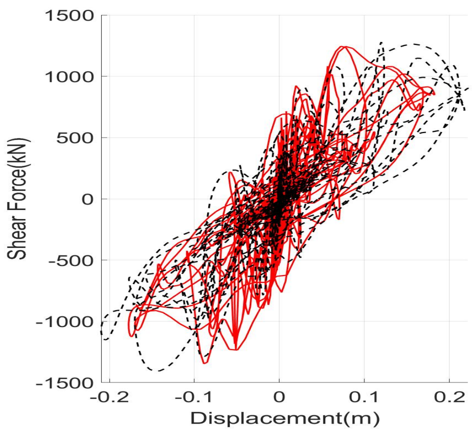

(c) Structural Hysteretic Curve

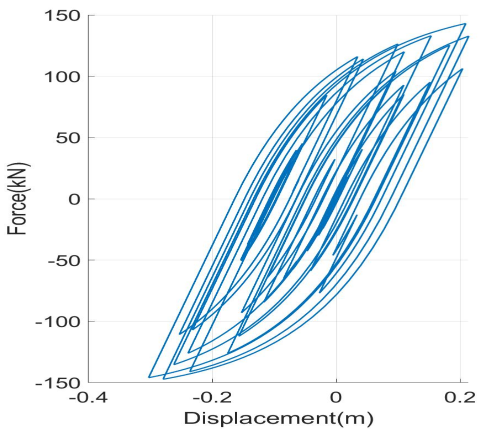

(d) TMD Hysteretic Curve

Figure B.176. Imperial Valley 1.5 Design Earthquake

Kobe

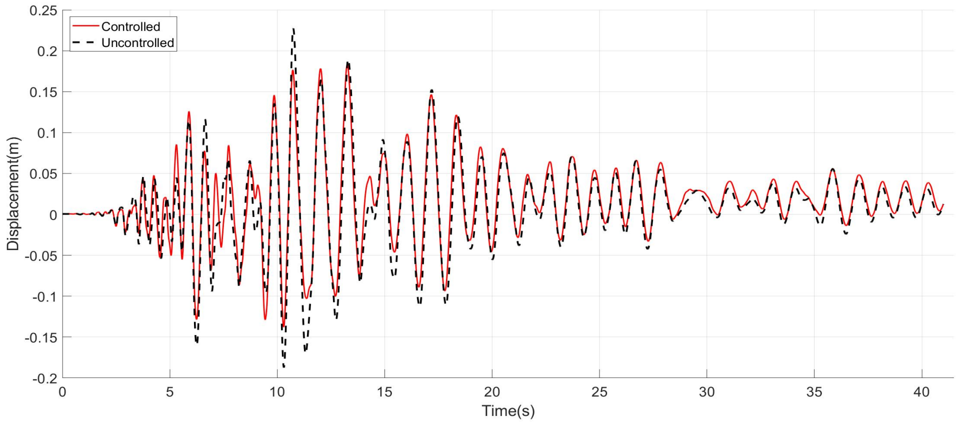

(a) Roof Displacements

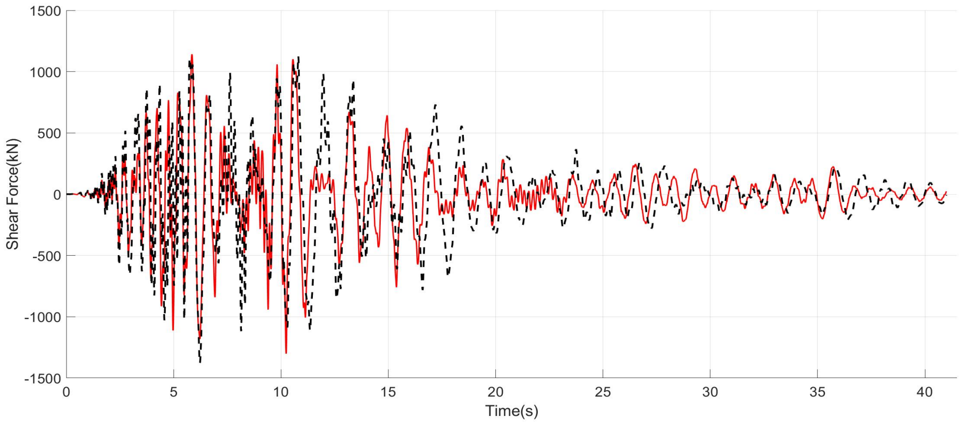

(b) Shear Forces at the base

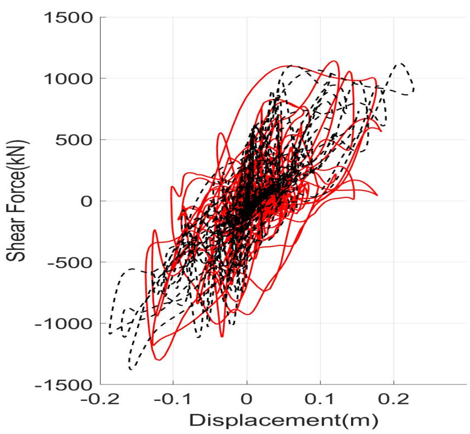

(c) Structural Hysteretic Curve

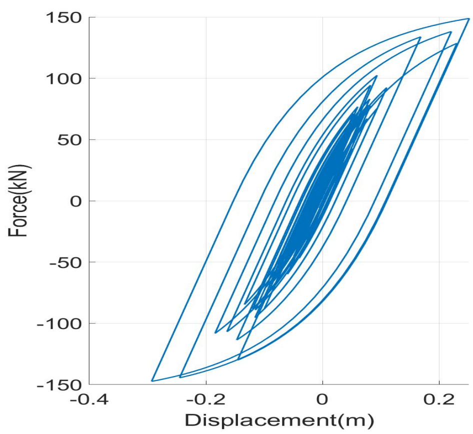

(d) TMD Hysteretic Curve

Figure B.177. Kobe 1.5 Design Earthquake

Loma Prieta

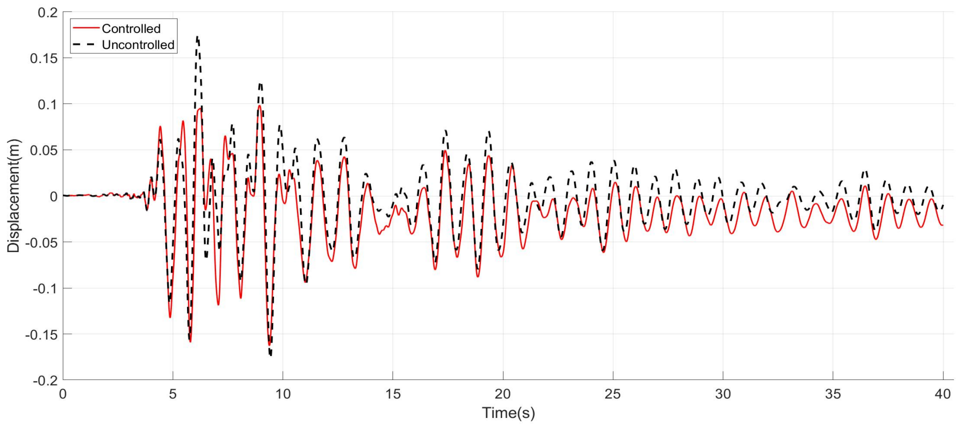

(a) Roof Displacements

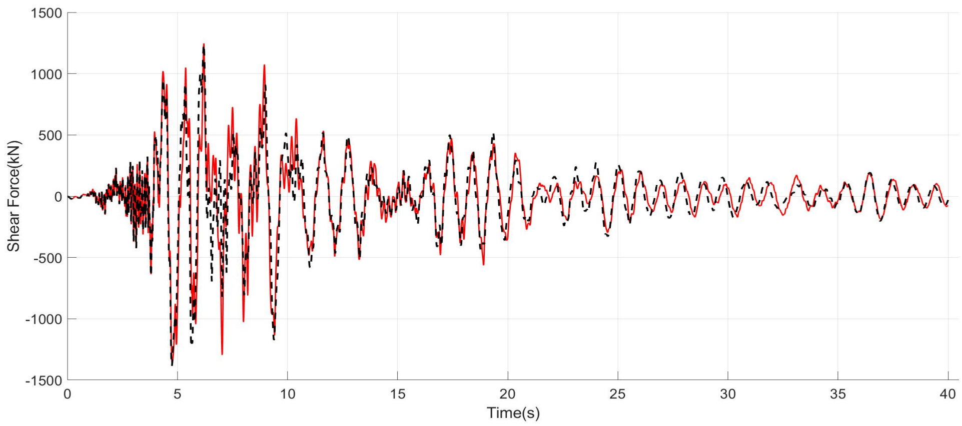

(b) Shear Forces at the base

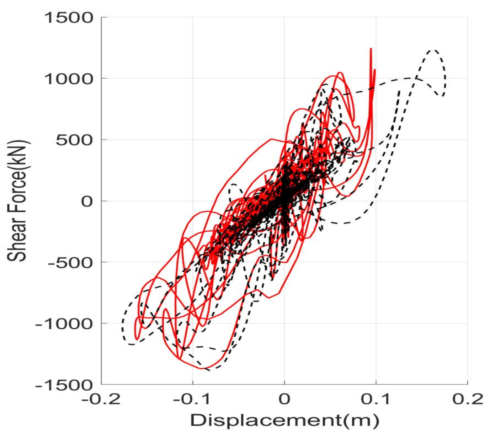

(c) Structural Hysteretic Curve

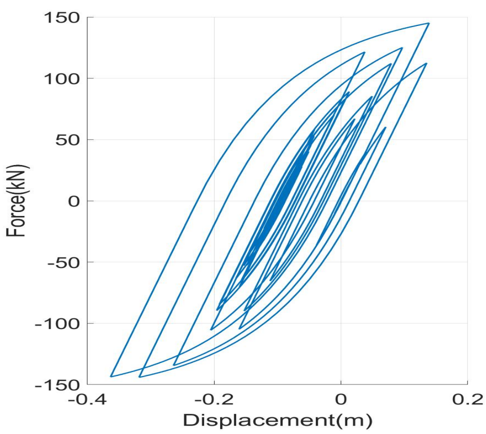

(d) TMD Hysteretic Curve

Figure B.178. Loma Prieta 1.5 Design Earthquake

Northridge

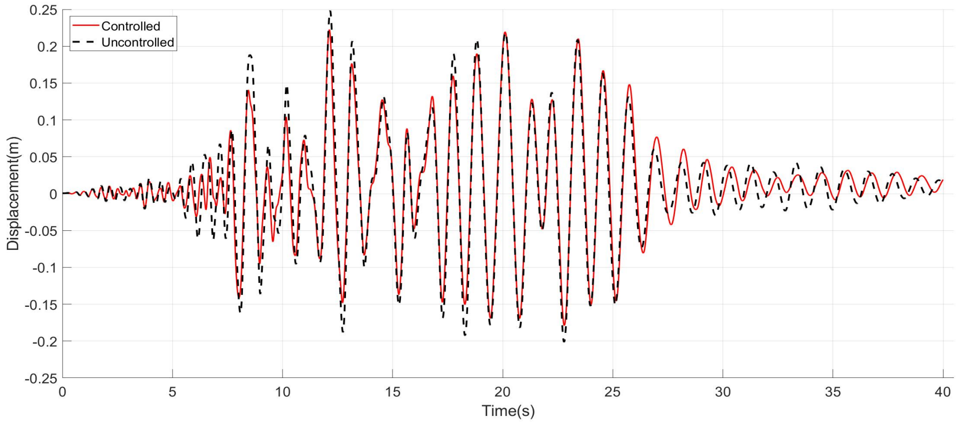

(a) Roof Displacements

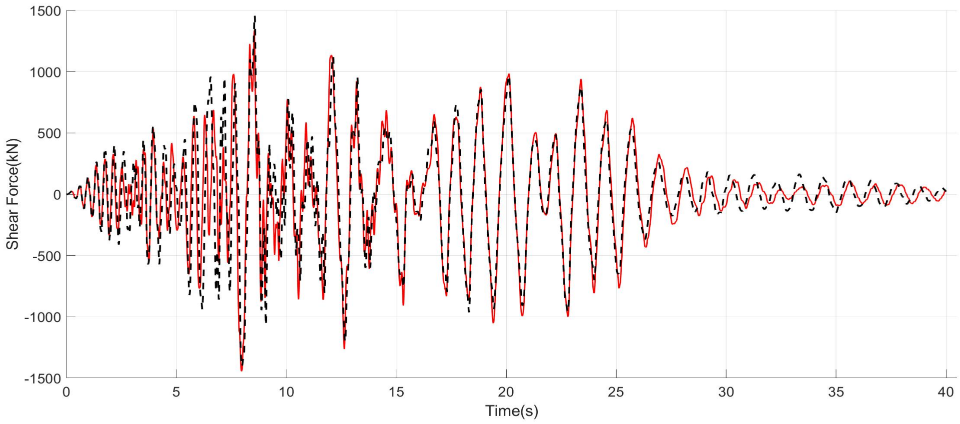

(b) Shear Forces at the base

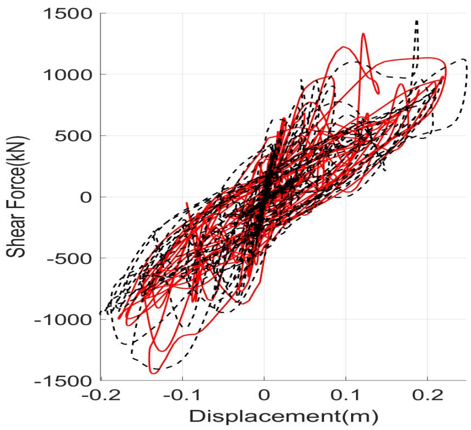

(c) Structural Hysteretic Curve

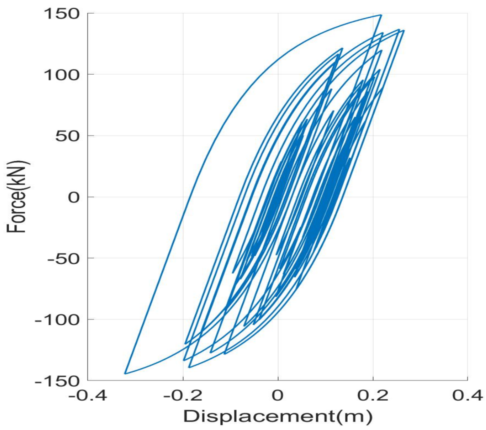

(d) TMD Hysteretic Curve

Figure B.179. Northridge 1.5 Design Earthquake

Drifts

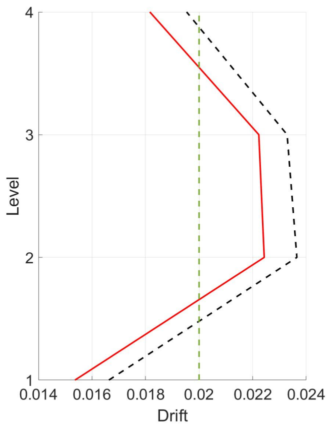

(a) Chalfant

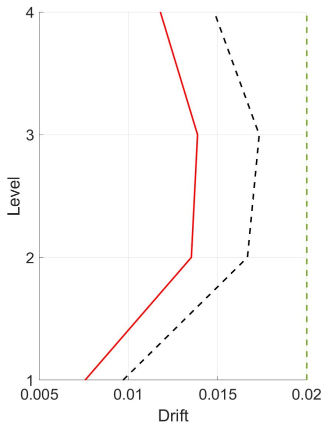

(b) Chi Chi

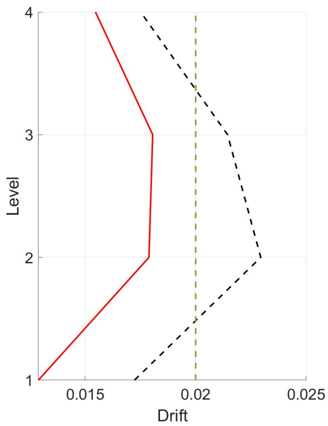

(c) Erzincan

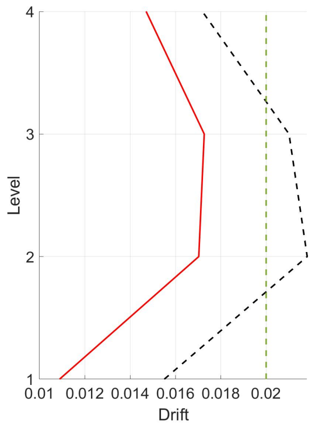

(d) Friulli

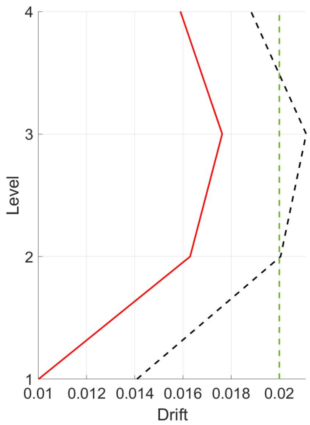

(e) Imperial Valley

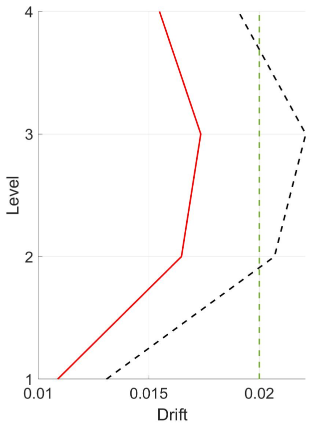

(f) Kobe

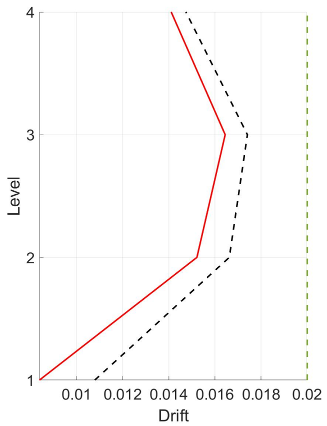

(g) Loma Prieta

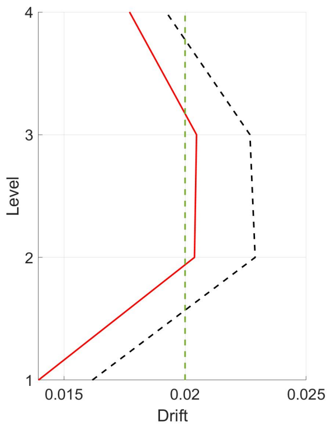

(h) Northridge

Figure B.180. Drifts 1.5 Design Earthquake
The green dotted line represents the [34] collapse prevention limit for walls.

Acronyms

TMD	Tuned Mass Damper
GA	Genetic Algorithms
Ec8	Eurocode 8
NTC2018	Norma Tecniche delle Costruzione 2018
RMS	Root Mean Square
BW	Bouc Wen

Bibliography

[1] B. UCLouvain, Brussels. Em-dat, cred. [Online]. Available: www.emdat.be

[2] R. Bilham, "The seismic future of cities," *Bulletin of earthquake engineering*, vol. 7, no. 4, pp. 839–887, 2009.

[3] S. Elias and V. Matsagar, "Research developments in vibration control of structures using passive tuned mass dampers," *Annual Reviews in Control*, vol. 44, pp. 129–156, 2017.

[4] J. J. Connor, *Structural motion control.* Pearson Education, Inc, 2003.

[5] M. Gaspar. (2017) The mechanism and applications of a tuned mass damper (tmd). [Online]. Available: https://bsbgroup.com/blog/the-mechanism-and-applications-of-tuned-mass-damper-tmd

[6] A. Boccamazzo, B. Carboni, G. Quaranta, and W. Lacarbonara, "Seismic effectiveness of hysteretic tuned mass dampers for inelastic structures," *Engineering Structures*, vol. 216, p. 110591, 2020.

[7] G. P. Hayes, G. M. Smoczyk, A. H. Villaseñor, K. P. Furlong, and H. M. Benz, "Seismicity of the earth 1900–2018," US Geological Survey, Tech. Rep., 2020.

[8] M. Dolce, A. Prota, B. Borzi, F. da Porto, S. Lagomarsino, G. Magenes, C. Moroni, A. Penna, M. Polese, E. Speranza *et al.*, "Seismic risk assessment of residential buildings in italy," *Bulletin of Earthquake Engineering*, vol. 19, no. 8, pp. 2999–3032, 2021.

[9] A. Rosti, M. Rota, and A. Penna, "Empirical fragility curves for italian urm buildings," *Bulletin of Earthquake Engineering*, vol. 19, no. 8, pp. 3057–3076, 2021.

[10] A. Masi, S. Lagomarsino, M. Dolce, V. Manfredi, and D. Ottonelli, "Towards the updated italian seismic risk assessment: exposure and vulnerability modelling," *Bulletin of Earthquake Engineering*, vol. 19, no. 8, pp. 3253–3286, 2021.

[11] L. Facchini and M. Betti, "An efficient bouc & wen approach for seismic analysis of masonry tower," *Frattura ed Integrità Strutturale*, vol. 8, no. 29, pp. 139–149, 2014.

[12] A. E. Charalampakis, "Parameters of bouc-wen hysteretic model revisited," in *9th HSTAM International Congress on Mechanics, Cyprus*, 2010.

[13] P. Sengupta and B. Li, "Modified bouc–wen model for hysteresis behavior of rc beam–column joints with limited transverse reinforcement," *Engineering Structures*, vol. 46, pp. 392–406, 2013.

[14] H. Frahm, "Device for damping vibrations of bodies," *US patent*, vol. 989, 1911.

[15] G. Warburton, "Optimum absorber parameters for minimizing vibration response," *Earthquake engineering & structural dynamics*, vol. 9, no. 3, pp. 251–262, 1981.

[16] S. Randall, D. Halsted III, and D. Taylor, "Optimum vibration absorbers for linear damped systems," 1981.

[17] G. B. Warburton, "Optimum absorber parameters for various combinations of response and excitation parameters," *Earthquake Engineering & Structural Dynamics*, vol. 10, no. 3, pp. 381–401, 1982.

[18] F. Sadek, B. Mohraz, A. W. Taylor, and R. M. Chung, "A method of estimating the parameters of tuned mass dampers for seismic applications," *Earthquake Engineering & Structural Dynamics*, vol. 26, no. 6, pp. 617–635, 1997.

[19] H.-C. Tsai and G.-C. Lin, "Optimum tuned-mass dampers for minimizing steady-state response of support-excited and damped systems," *Earthquake engineering & structural dynamics*, vol. 22, no. 11, pp. 957–973, 1993.

[20] S. Sgobba and G. C. Marano, "Optimum design of linear tuned mass dampers for structures with nonlinear behaviour," *Mechanical Systems and Signal Processing*, vol. 24, no. 6, pp. 1739–1755, 2010.

[21] R. Soto-Brito and S. E. Ruiz, "Influence of ground motion intensity on the effectiveness of tuned mass dampers," *Earthquake engineering & structural dynamics*, vol. 28, no. 11, pp. 1255–1271, 1999.

[22] S. Ruiz and L. Esteva, "About the effectiveness of tuned mass dampers on nonlinear systems subjected to earthquakes," *WIT Transactions on The Built Environment*, vol. 23, 1970.

[23] Y. Arfiadi and M. Hadi, "Optimum placement and properties of tuned mass dampers using hybrid genetic algorithms," *Iran University of Science & Technology*, vol. 1, no. 1, pp. 167–187, 2011.

[24] M. Mohebbi and A. Joghataie, "Designing optimal tuned mass dampers for nonlinear frames by distributed genetic algorithms," *The Structural Design of Tall and Special Buildings*, vol. 21, no. 1, pp. 57–76, 2012.

[25] G. Grillo, "Development and validation of new design strategies for optimal passive non detuning mass dampers," 2021.

[26] W. Lacarbonara and F. Vestroni, "Feasibility of a vibration absorber based on hysteresis," in *Proceedings of the Third World Congress on Structural Control*, 2002, pp. 7–12.

[27] A. Boccamazzo, B. Carboni, G. Quaranta, and W. Lacarbonara, “Hysteretic tuned mass dampers for seismic protection,” 2021.

[28] A. Colombo, M. Fardis, J. Molina, P. Negro, T. Panagiotakos, and G. Tsionis, “Pseudodynamic response of dual rc structure with different designs,” in *Proceedings of the Twelfth European Conference on Earthquake Engineering*, 2002.

[29] T. Panagiotakos and M. Fardis, “A displacement-based seismic design procedure for rc buildings and comparison with ec8,” *Earthquake engineering & structural dynamics*, vol. 30, no. 10, pp. 1439–1462, 2001.

[30] A. Balzarotti, “Modellazione del comportamento sismico di una struttura in c.a. a pareti accoppiate,” 2002.

[31] L. Martinelli, “Numerical modelling of a psd test on a dual rc system,” in *Proceedings of 13th World Conference on Earthquake Engineering (Vancouver, Canada, 2004)*, 2004.

[32] T. Paulay and M. N. Priestley, *Seismic design of reinforced concrete and masonry buildings.* Wiley New York, 1992, vol. 768.

[33] L. Martinelli, “Modeling shear-flexure interaction in reinforced concrete elements subjected to cyclic lateral loading,” *ACI Structural Journal*, vol. 105, no. 6, p. 675, 2008.

[34] ASCE, “Fema356 prestandard and commentary for the seismic rehabilitation of buildings,” 2000.

[35] L. Martinelli, “Modellazione di pile di ponti in ca a travata soggetti ad eccitazione sismica,” *Dottorato di ricerca in ingegneria sismica*, 1998.

[36] L. Martinelli, M. G. Mulas, and F. Perotti, “The seismic response of concentrically braced moment-resisting steel frames,” *Earthquake engineering & structural dynamics*, vol. 25, no. 11, pp. 1275–1299, 1996.

[37] A. Fema, “440, improvement of nonlinear static seismic analysis procedures,” *FEMA-440, Redwood City*, vol. 7, no. 9, p. 11, 2005.

[38] A. Charalampakis and V. Koumousis, “On the response and dissipated energy of bouc–wen hysteretic model,” *Journal of Sound and Vibration*, vol. 309, no. 3-5, pp. 887–895, 2008.

[39] F. Vestroni and P. Casini, “Mitigation of structural vibrations by hysteretic oscillators in internal resonance,” *Nonlinear Dynamics*, vol. 99, no. 1, pp. 505–518, 2020.

[40] M. N. Priestley, F. Seible, and G. M. Calvi, *Seismic design and retrofit of bridges.* John Wiley & Sons, 1996.

[41] A. E. Charalampakis, “The response and dissipated energy of bouc–wen hysteretic model revisited,” *Archive of Applied Mechanics*, vol. 85, no. 9, pp. 1209–1223, 2015.

[42] G. U. della Repubblica Italiana, "Norme tecniche per le costruzioni," *Ministero delle infrastrutture e dei trasporti (in Italian)*, 2018.

[43] S. Pampanin, C. Christopoulos, and T.-H. Chen, "Development and validation of a metallic haunch seismic retrofit solution for existing under-designed rc frame buildings," *Earthquake engineering & structural dynamics*, vol. 35, no. 14, pp. 1739–1766, 2006.

[44] D. De Domenico, G. Quaranta, G. Ricciardi, and W. Lacarbonara, "Optimum design of tuned mass damper with pinched hysteresis under nonstationary stochastic seismic ground motion," *Mechanical Systems and Signal Processing*, vol. 170, p. 108745, 2022.